HANDBOOK ON THE PHYSICS AND CHEMISTRY OF RARE EARTHS

North-Holland is an imprint of Elsevier

Radarweg 29, PO Box 211, 1000 AE Amsterdam, The Netherlands
The Boulevard, Langford Lane, Kidlington, Oxford OX5 1GB, United Kingdom

Notices

Knowledge and best practice in this field are constantly changing. As new research and experience broaden our understanding, changes in research methods, professional practices, or medical treatment may become necessary.

Practitioners and researchers must always rely on their own experience and knowledge in evaluating and using any information, methods, compounds, or experiments described herein. In using such information or methods they should be mindful of their own safety and the safety of others, including parties for whom they have a professional responsibility.

To the fullest extent of the law, neither the Publisher nor the authors, contributors, or editors, assume any liability for any injury and/or damage to persons or property as a matter of products liability, negligence or otherwise, or from any use or operation of any methods, products, instructions, or ideas contained in the material herein.

ISBN: 978-0-444-63851-9
ISSN: 0168-1273

Publisher: Zoe Kruze
Acquisition Editor: Poppy Garraway
Editorial Project Manager: Shellie Bryant
Production Project Manager: Radhakrishnan Lakshmanan
Cover Designer: Mark Rogers

Typeset by SPi Global, India

Contributors

Numbers in Parentheses indicate the pages on which the author's contributions begin.

Eleonora Aneggi (209), Università di Udine, Udine, Italy

Zoila Barandiarán (65), Instituto Universitario de Ciencia de Materiales Nicolás Cabrera, and Condensed Matter Physics Center (IFIMAC), Universidad Autónoma de Madrid, Madrid, Spain

Marta Boaro (209), Università di Udine, Udine, Italy

Jean-Claude G. Bünzli (141), Institute of Chemical Sciences and Engineering, Swiss Federal Institute of Technology Lausanne (EPFL), Lausanne, Switzerland; Haimen Institute of Science and Technology, Hong Kong Baptist University, Haimen, PR China

Banglin Chen (243), State Key Laboratory of Silicon Materials, Cyrus Tang Center for Sensor Materials and Applications, School of Materials Science and Engineering, Zhejiang University, Hangzhou, China; University of Texas at San Antonio, San Antonio, TX, United States

Sara Colussi (209), Università di Udine, Udine, Italy

Yuanjing Cui (243), State Key Laboratory of Silicon Materials, Cyrus Tang Center for Sensor Materials and Applications, School of Materials Science and Engineering, Zhejiang University, Hangzhou, China

Carla de Leitenburg (209), Università di Udine, Udine, Italy

Roderick G. Eggert (19), Critical Materials Institute, Colorado School of Mines, Golden, CO, United States

William J. Evans (337), University of California, Irvine, CA, United States

Dante Gatteschi (91), Dipartimento di Chimica "U. Schiff" and INSTM UdR Firenze, Università degli Studi di Firenze, Sesto Fiorentino, Italy

Karl A. Gschneidner Jr. (1,19), The Ames Laboratory, Iowa State University; Critical Materials Institute, The Ames Laboratory, Ames, IA, United States

Susan M. Kauzlarich (177), University of California, Davis, CA, United States

Nasrin Kazem (177), University of California, Davis, CA, United States

Alexander H. King (19), Critical Materials Institute, The Ames Laboratory, Ames, IA, United States

Lin-Dong Li (301), Beijing National Laboratory for Molecular Sciences, State Key Laboratory of Rare Earth Materials Chemistry and Applications, PKU-HKU Joint Laboratory in Rare Earth Materials and Bioinorganic Chemistry, College of Chemistry and Molecular Engineering, Peking University, Beijing, China

Anja-Verena Mudring (395), Iowa State University and Ames Laboratory, Ames, IA, United States

David Parker (269), Durham University, Durham, United Kingdom

Denis Prodius (395), Iowa State University and Ames Laboratory, Ames, IA, United States

Guodong Qian (243), State Key Laboratory of Silicon Materials, Cyrus Tang Center for Sensor Materials and Applications, School of Materials Science and Engineering, Zhejiang University, Hangzhou, China

Michael F. Reid (47), University of Canterbury, Christchurch; The Dodd-Walls Centre for Quantum and Photonic Technologies, Dunedin; The MacDiarmid Institute for Advanced Materials and Nanotechnology, Wellington, New Zealand

Luis Seijo (65), Instituto Universitario de Ciencia de Materiales Nicolás Cabrera, and Condensed Matter Physics Center (IFIMAC), Universidad Autónoma de Madrid, Madrid, Spain

Roberta Sessoli (91), Dipartimento di Chimica "U. Schiff" and INSTM UdR Firenze, Università degli Studi di Firenze, Sesto Fiorentino, Italy

Lorenzo Sorace (91), Dipartimento di Chimica "U. Schiff" and INSTM UdR Firenze, Università degli Studi di Firenze, Sesto Fiorentino, Italy

Ling-Dong Sun (301), Beijing National Laboratory for Molecular Sciences, State Key Laboratory of Rare Earth Materials Chemistry and Applications, PKU-HKU Joint Laboratory in Rare Earth Materials and Bioinorganic Chemistry, College of Chemistry and Molecular Engineering, Peking University, Beijing, China

Alessandro Trovarelli (209), Università di Udine, Udine, Italy

David H. Woen (337), University of California, Irvine, CA, United States

Chun-Hua Yan (301), Beijing National Laboratory for Molecular Sciences, State Key Laboratory of Rare Earth Materials Chemistry and Applications, PKU-HKU Joint Laboratory in Rare Earth Materials and Bioinorganic Chemistry, College of Chemistry and Molecular Engineering, Peking University, Beijing, China

Jun Zhang (243), State Key Laboratory of Silicon Materials, Cyrus Tang Center for Sensor Materials and Applications, School of Materials Science and Engineering, Zhejiang University, Hangzhou, China

Xiao-Yu Zheng (301), Beijing National Laboratory for Molecular Sciences, State Key Laboratory of Rare Earth Materials Chemistry and Applications, PKU-HKU Joint Laboratory in Rare Earth Materials and Bioinorganic Chemistry, College of Chemistry and Molecular Engineering, Peking University, Beijing, China

Preface

These elements perplex us in our reaches [sic], baffle us in our speculations, and haunt us in our very dreams. They stretch like an unknown sea before us—mocking, mystifying, and murmuring strange revelations and possibilities.

Sir William Crookes (February 16, 1887)

This volume of the *Handbook on the Physics and Chemistry of Rare Earths* has a very special meaning for the series. First and sadly, the initiator of the series, Karl A. Gschneidner Jr., passed away on April 27, 2016 in his 86th year. He had retired three and a half months earlier from his positions of Anson Marston Distinguished Professor at the Department of Materials Science and Engineering at Iowa State University, Senior Scientist at the Department of Energy Ames Laboratory, and Chief Scientific Officer at the Critical Materials Institute, Ames Laboratory, Ames, Iowa, and was working on the first chapter of this volume. Karl started the series with Professor LeRoy Eyring (1919–2005) by soliciting and editing an initial set of four volumes encompassing 40 chapters published in 1978 and 1979. Since then, he has always been an

inspiring editor, finding adequate contributors and convincing them to write authoritative reviews within their respective research fields. Karl served as senior editor for the first 41 volumes of the series. He will be remembered as a dedicated scientist, great communicator, and particularly receptive gentleman. A full-scale tribute to Karl will appear in Volume 51.

In the preface of the first volume of the series Karl and LeRoy wrote: *"[We] have invited experts in various areas write comprehensive, broad, up-to-date, and critical reviews. Some of the subjects were chosen because they are mature and still quite active; others because they are essential as background information and for reference; and some topics because they are relatively new and exciting areas of research."* In a way, jubilee Volume 50 is somehow mimicking this approach. The editors have asked prominent experts in rare-earth physics, chemistry, and materials sciences to come up with short perspective essays not meant to be comprehensive but, rather, showing how a given topic evolved in response to societal and/or scientific challenges and how one can imagine its future development. Given the explosion of rare-earth research during the past two decades, covering all facets of rare-earth science and technology was of course simply impossible, but much in the spirit of the founding fathers of the series, the editors tried to keep a balance between physics, chemistry, basic science, applications, and resources.

Volume 50 features 13 chapters. The first one (Chapter 282) shows how systematic analysis of basic data, e.g., element radii or melting temperatures, may become a powerful tool for predicting properties that can be considered as being unusual, such as contraction of ionic radii or variations in the solubility of alloys. In Chapter 283, the authors define the concept of critical materials, analyze the supplies of rare earths that have become the focus of much attention recently, and describe the research that needs to reduce supply-chain risks. The next two reviews deal with theories developed for understanding spectroscopic properties of the lanthanides. Chapter 284 puts current understanding into historical perspective and presents the impact of theories and models such as crystal field and Judd–Ofelt theories or Newman superposition model. The subject of Chapter 285 is entirely focused on ab initio calculations that are compared to empirical models; in addition, their potential for predicting properties of luminescent materials is assessed. With Chapter 286, the reader is discovering the whereabouts pertaining to the design of new molecular materials, single-ion (or molecule) magnets; the occurrence of magnetic bistability is investigated with respect to anisotropy and exchange interactions. Luminescent materials are one of the key applications of lanthanides; Chapter 287 is unfolding the long path from the first discoveries at the end of the 19th century to present high-technology uses, as well as pointing to cutting-edge developing fields. Transforming heat into electricity is the subject of Chapter 288; contributions of lanthanides to thermoelectric materials are highlighted with reference to newly discovered Zintl phase compounds,

clathrates, and filled skutterudites that yield more efficient thermoelectric materials. One of the oldest industrial applications of rare earths is catalysis, and Chapter 289 takes the reader into the amazing world of cerium dioxide, an oxygen storage compound initially used in automotive three-way catalysts but which enters presently in the composition of numerous catalytic processes, including water splitting and cell fuel technology. The next chapter (Chapter 290) describes the design of porous coordination polymers, also called metal–organic frameworks, which are tailored for luminescence applications in ratiometric sensing, white light-emitting devices, bioanalysis, bioimaging, and thermometry. Coordination chemistry is also in action in Chapter 291 in which a critical assessment of the theoretical background of magnetic anisotropy and relaxation is presented in view of the use of paramagnetic lanthanide complexes in medical imaging; the review is complemented by considerations on luminescent properties. Chapter 292 is also concerned with magnetic resonance imaging but with emphasis on the design of contrast agents based on nanoparticles; the latter can be tailored for fulfilling various functionalities, including multimodal imaging applications. The next review (Chapter 293) describes what appears to be a major and unique discovery in organometallic chemistry of f-elements, namely the isolation of divalent complexes for the entire lanthanide series, yttrium, uranium, and thorium; optical and magnetic data show that some of the divalent lanthanide ions have $4f^{n+1}$ electronic configurations, others $4f^n5d^1$, while a few are crossover ions adopting one or the other configuration depending on the ligand. The final chapter (Chapter 294) explores a still relatively unknown group of compounds: rare-earth ionic liquids in which rare earth ions are part of either the cation or the anion; the structures of these new compounds with large innovation potential are described in detail.

Although quite restrictive in the choice of subjects, this volume shows the ubiquitous contribution of lanthanides to many fields of technology and science. The resulting panorama is diagnostic of a vivid research field in full expansion and not hesitating to deal with entirely new concepts.

CHAPTER 282: SYSTEMATICS

Karl A. Gschneidner Jr.*
The Ames Laboratory, Iowa State University, Ames, IA, United States

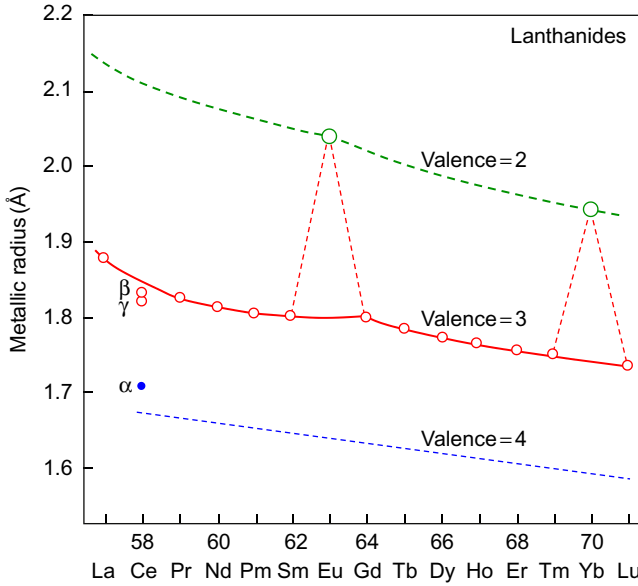

Altogether, the rare earths represent the largest fraction (about 1/6) of naturally occurring elements. Over the last 60 years, many of these elements have become indispensable for modern technology, and the family as a whole has become a poster child for demonstrating the vital role analyses of systematics and anomalies play in science. Indeed, a systematic analysis of trends in structure and properties of materials moving from one member of the rare earth family to another has often resulted in correct predictions that later have been verified either theoretically or experimentally or both. Systematics is a powerful tool in science; in the past, it has for instance predicted yet unknown elements. Applied to rare earths, it has revealed the unusual valence state of Eu and Yb in the metals or the lanthanide contraction. This chapter briefly reviews successful applications of systematics that brought about a great deal of understanding of the fundamentals of chemistry, physics, and materials science of rare earths and their compounds. Among the latter, metals and alloys represent an interesting field of application for systematics that led to understanding anomalous solubility or predicting entropies of fusion. The concept is also extended to some examples in the actinide series.

*Deceased April 27, 2016.

CHAPTER 283: THE RARE EARTHS AS CRITICAL MATERIALS

Alexander H. King*, Roderick G. Eggert†, and Karl A. Gschneidner Jr.*,*

*Critical Materials Institute, The Ames Laboratory, Ames, IA, United States. E-mail: alexking@ameslab.gov

†Critical Materials Institute, Colorado School of Mines, Golden, CO, United States

Recent increase in the demand for rare earth elements (REEs), especially dysprosium and terbium used in the permanent magnet industry, is modifying the industrial approach to REE mineralogy and resources. This is amplified by the REE supply restrictions outside of China and by the fact that rare earths are never mined individually but always as mixtures with various compositions. These compositions, however, do not necessarily correspond to the demand for individual rare earths. Some elements are in surplus (La, Ce), while others are in tight supply (or more utilized) and are classified as "critical." The latter include yttrium, neodymium, europium, terbium, and dysprosium. Exploration has now been extended worldwide to secure the supply of REEs, especially the heavier ones (HREEs, Gd–Lu). In recent years, various attempts have been made to produce HREEs from unconventional sources, such as peralkaline igneous rocks or deep-sea muds (see Vol. 46, Chapter 268, and Vol. 49, Chapter 279).

Potential sources of REEs are reviewed in this chapter with a focus on HREEs, which are the most critical group of elements for future green technologies. The geochemistry and mineralogy of rare earths are first described

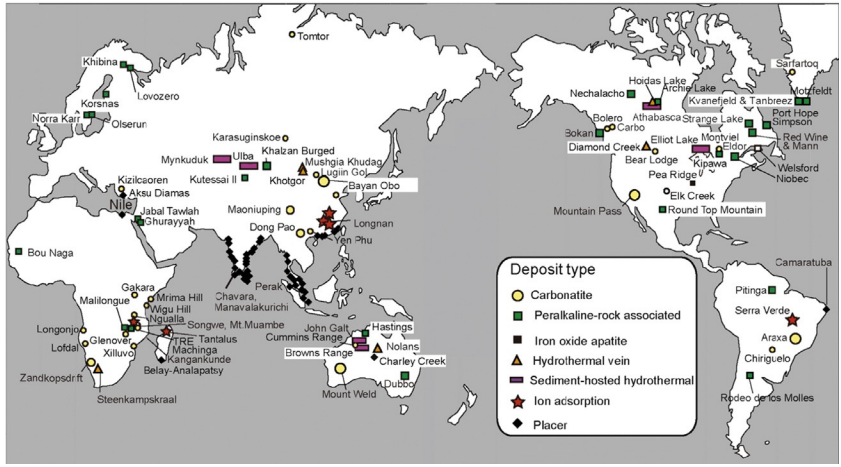

*Deceased April 27, 2016.

before focusing on deposits. Properties of ion-adsorption and apatite deposits are detailed in view of their importance for heavier REEs. The authors conclude that in the future the most promising source of rare earths will be apatite ores.

CHAPTER 284: THEORY OF RARE-EARTH ELECTRONIC STRUCTURE AND SPECTROSCOPY

Michael F. Reid
University of Canterbury, Christchurch, New Zealand.
E-mail: mike.reid@canterbury.ac.nz

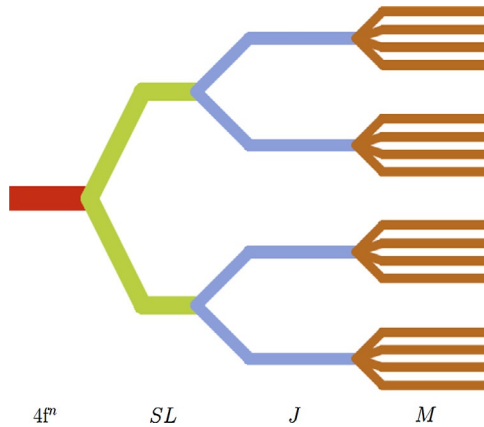

Theoretical analysis and understanding of lanthanide spectra have been important to the development of laser, phosphor, and scintillator materials that are currently ubiquitous in modern life. Analysis techniques developed in the 1960s followed the reporting of high-quality optical spectra in the 1950s by several laboratories and could become effective thanks to developments in computer technology making calculations requiring diagonalization of large matrices tractable. This theoretical work led to two key advances, namely the description of an accurate Hamiltonian operator allowing precise description of energy levels and a model for the intensity of the transitions.

Current theoretical understanding of electronic structure and spectroscopy of rare-earth ions in a condensed-matter environment is reviewed in this chapter. The development of the crystal-field effective Hamiltonian for the $4f^n$ configuration, and its extension to the $4f^{n-1}5d$ configuration, is discussed. The addition of hyperfine and magnetic interactions is reviewed, as well as the use of magnetic-splitting data to improve crystal-field fitting. Judd–Ofelt theory and selection rules for the various transitions encountered in lanthanide optical spectra are also scrutinized before presenting Newman superposition model as an analysis technique for both crystal-field and transition-intensity

parameterization. Finally, the role of ab initio calculations with respect to parameterized models is assessed, as well as their potential impact on the field.

CHAPTER 285: AB INITIO CALCULATIONS ON EXCITED STATES OF LANTHANIDE CONTAINING MATERIALS

Luis Seijo and Zoila Barandiarán

Instituto Universitario de Ciencia de Materiales Nicolás Cabrera, and Condensed Matter Physics Center (IFIMAC), Universidad Autónoma de Madrid, Madrid, Spain. E-mail: luis.seijo@gmail.com, zoila.barandiaran@uam.es

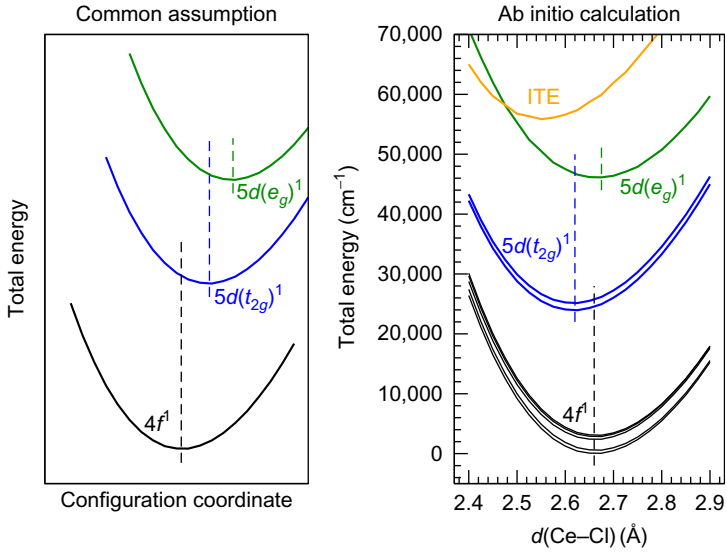

The optical properties derived from the rich manifolds of excited states of lanthanide-containing materials give them a key role in the development of a large variety of luminescent solid-state devices with high societal demand. These include white light-emitting diodes for energy efficient lighting, solid-state lasers for telecommunications, or scintillating detectors; applications range from medical imaging to high-energy physics calorimetry, remote pressure and temperature measurement systems, devices for enhancing the efficiency of solar cells, energy storage phosphors, or persistent luminescence materials for safety signage, among others. Altogether, the rich manifolds of lanthanide $4f^n$ and $4f^{n-1}5d$ electronic configurations feature about 200,000 states and identifying them all requires a good synergy between experimental work and theoretical modeling.

The intense experimental research in this area finds its theoretical grounds mostly in empirical models, but the consideration of ab initio methods as fruitful theoretical tools to handle such a complexity is steadily growing.

These methods do not rely on empirical parameters and are based only on the first principles of quantum mechanics. The chapter is dedicated to give a perspective on their use as basic theoretical tools in the area, which must complement and go together with experiments and empirical models.

CHAPTER 286: MAGNETIC BISTABILITY IN LANTHANIDE-BASED MOLECULAR SYSTEMS: THE ROLE OF ANISOTROPY AND EXCHANGE INTERACTIONS

Dante Gatteschi, Roberta Sessoli, and Lorenzo Sorace

INSTM UdR Firenze, Università degli Studi di Firenze, Sesto Fiorentino, Italy. E-mail: dante.gatteschi@unifi.it

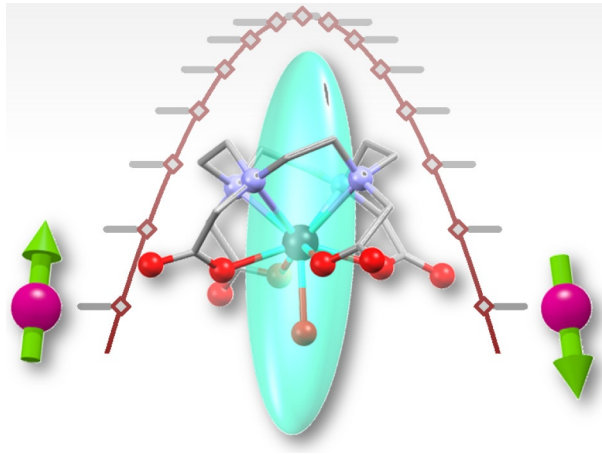

Molecular-based lanthanide magnets started to be systematically investigated in the 2000s, showing new types of magnetic properties and new opportunities. In particular, the discovery that slow relaxation of the magnetization at liquid nitrogen temperature can occur in mononuclear complexes of these ions prompted an intense wave of investigation on these systems. The historical developments in this field are summarized in this chapter along with more recent advances making the point for the need of combined high-level ab initio calculations and single-crystal multitechnique characterization to obtain a reliable picture of the electronic structure of these systems and the way this is reflected in their static and dynamic magnetic properties. Indeed, magnetic bistability in lanthanide-based molecular materials results from a subtle interplay between magnetic anisotropy and magnetic exchange, and the optimization of both is far from trivial. The authors conclude the chapter by raising some prospects into the future development of Ln-based molecular magnets in the emerging fields of quantum information processing and molecular spintronics using molecular-based lanthanide systems.

CHAPTER 287: LANTHANIDE LUMINESCENCE: FROM A MYSTERY TO RATIONALIZATION, UNDERSTANDING, AND APPLICATIONS

Jean-Claude G. Bünzli

Institute of Chemical Sciences and Engineering, Swiss Federal Institute of Technology Lausanne (EPFL), Lausanne, Switzerland. E-mail: jean-claude.bunzli@epfl.ch

Haimen Institute of Science and Technology, Hong Kong Baptist University, Haimen, PR China

Lanthanide luminescence is at the heart of applications as diverse as lighting, telecommunications, lasers, security marking, barcoding, luminescent molecular thermometers, immunoassays, optical medical imaging, or agriculture. The subject is fascinating and has always accompanied the development of lanthanide science and technology, from the early discovery of the 4f elements to present high-technology applications. The large added value of luminescent phosphors, probes, and materials explains the enthusiasm research groups are coming up with in looking for new and better systems, in addition to simple fascination for light emission.

The chapter highlights the various facets of lanthanide luminescence, with special emphasis on historical developments, understanding the underlying mechanisms, and presenting leading applications. The $4f^n$ and $4f^{n-1}5d$ electronic configurations of lanthanide ions generate numerous electronic levels, and most of the transitions are forbidden by Laporte's rule and are very faint. Systematic experimental work had, therefore, to be substantiated by theoretical concepts, leading to the elaboration of energy diagrams and to modeling of the energy migration mechanisms during sensitization of lanthanide luminescence. The major applications mentioned earlier are still vivid today, in parallel to more futuristic ones such as photocatalysis, solar energy conversion, optical cooling, and quantum information processing. All these fields trigger materials developments, particularly at the nanoscale, and elaboration of new theoretical concepts.

CHAPTER 288: THERMOELECTRIC PROPERTIES OF ZINTL ANTIMONIDES

Nasrin Kazem and Susan M. Kauzlarich*

University of California, Davis, CA, United States. E-mail: smkauzlarich@ucdavis.edu

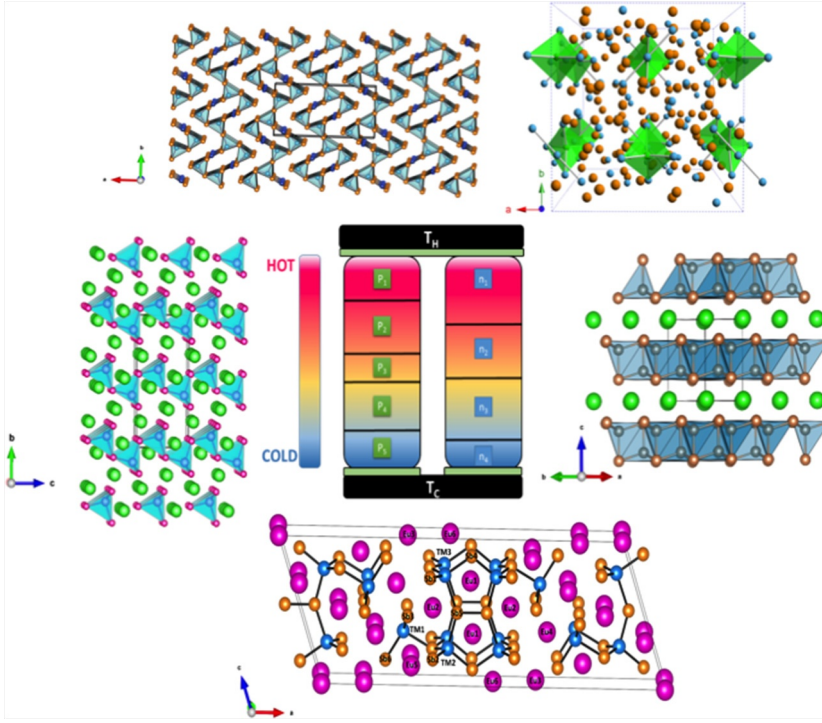

The ever-increasing demand for energy worldwide not only requires more sources but also calls for a much greater versatility in generation of electricity.

In this respect, thermoelectric devices that convert heat into electricity are on an upward trend because of their high reliability, longtime durability, and scalability, along with environmentally friendly operation. In addition to harvesting primary thermal energy sources such as solar energy or geothermal energy, they can also be useful in collecting waste heat produced by nuclear plants or automotive engines. However, enhancing the efficiency of thermoelectric devices is critical for their adoption in commercial large-scale applications. To compete with the present mechanical energy generators, thermoelectric materials need to be at least three times more efficient than today's commercial devices. This high conversion efficiency corresponds to a thermoelectric figure of merit, zT, of $\sim$3, which has remained elusive despite a long history of searching for new thermoelectric materials.

The recent discoveries of high zT among Zintl phase compounds such as $Yb_{14}MnSb_{11}$, $EuZn_2Sb_2$, $Yb_9Mn_{4.2}Sb_9$, clathrates, and filled skutterudites show the potential of this class of compounds for more efficient thermoelectric materials. This perspective summarizes the recent progress on Zintl phases studied for thermoelectric applications with a focus on their chemistry, crystal structure, and transport properties.

CHAPTER 289: CERIA-BASED MATERIALS IN CATALYSIS: HISTORICAL PERSPECTIVE AND FUTURE TRENDS

Eleonora Aneggi, Marta Boaro, Sara Colussi, Carla de Leitenburg, and Alessandro Trovarelli

Università di Udine, Udine, Italy. E-mail: alessandro.trovarelli@uniud.it

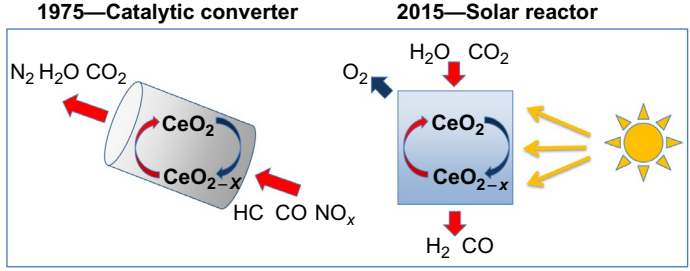

The unique versatile structural arrangement of CeO_2 allows its use in emerging engineering and biological applications like solid oxide fuel cells, materials for protections, antioxidant agent, solar cells, optical films, and gas sensors. However, it is in catalysis that cerium oxide nanoparticles have shown their tremendous potential and impact. The origin of this success dates back to the late 1970s when CeO_2 was first employed as an oxygen storage component of three-way catalysts formulation. The ability of ceria to modify rapidly its average oxidation state in a suitable temperature range while maintaining structural integrity is the key property for this application; after several years, its ability to do so is still unsurpassed. In addition, the pivotal role of ceria in stabilizing metal particles by

binding them to ceria surface defects and the extraordinary role of the ceria–metal interface contributes to its achievements in catalysis.

Other applications for which ceria-based materials are currently being actively investigated include catalysts for soot oxidation, reforming, partial oxidation, water gas shift reaction, water splitting, and fuel cell technology. The fine tuning of these materials is reviewed here, with focus on the understanding of the relationships between activity and morphology and trying to see how the tremendous knowledge gain with ceria-based materials can help in determining future developments.

CHAPTER 290: LANTHANIDE METAL–ORGANIC FRAMEWORKS FOR LUMINESCENT APPLICATIONS

Yuanjing Cui*, Jun Zhang*, Banglin Chen*,†, and Guodong Qian*

*State Key Laboratory of Silicon Materials, Cyrus Tang Center for Sensor Materials and Applications, School of Materials Science and Engineering, Zhejiang University, Hangzhou, China. E-mail: gdqian@zju.edu.cn

†University of Texas at San Antonio, San Antonio, TX, United States

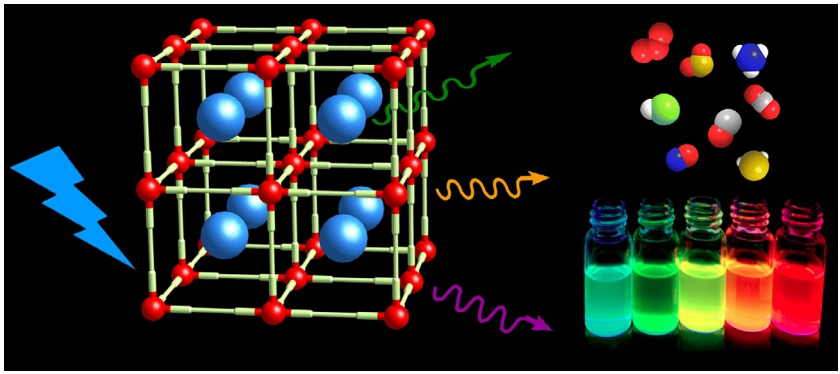

Coordination polymers are built up from metal ions and multidentate bridging inorganic or organic ligands; they are referred to as metal–organic frameworks (MOFs) when they are porous. MOFs have emerged as particularly exciting multifunctional hybrid materials due to combining the properties of organic linkers and inorganic metal ions, as well as tailorability in terms of structure, dimension, size, and shape. As one special type of MOF, the lanthanide MOFs have been successfully developed for several luminescent applications, taking advantage of the unique photophysical properties of lanthanide ions, such as large quantum yield, long-lived excited states, large ligand-induced Stokes shifts, characteristic sharp line emissions, and little propensity to photobleaching.

In this chapter, the latest developments in lanthanide MOFs and their applications in sensing, white light-emitting devices, bioanalysis, and bioimaging, as

well as in ratiometric luminescent thermometry are reviewed. Incorporation of open metal sites, Lewis acidic sites, and Lewis basic pyridyl sites within porous lanthanide MOFs is the key for highly selective luminescence sensing. Mixed lanthanide MOFs can easily be obtained, resulting in simultaneous emission of several lanthanide ions that can be used either to tune the emission color of the framework or as self-reference in ratiometric analysis. Finally, some strategies for effectively improving the luminescence of lanthanide MOFs are described.

CHAPTER 291: RARE EARTH COORDINATION CHEMISTRY IN ACTION: EXPLORING THE OPTICAL AND MAGNETIC PROPERTIES OF THE LANTHANIDES IN BIOSCIENCE WHILE CHALLENGING CURRENT THEORIES

David Parker

Durham University, Durham, United Kingdom. E-mail: david.parker@durham.ac.uk

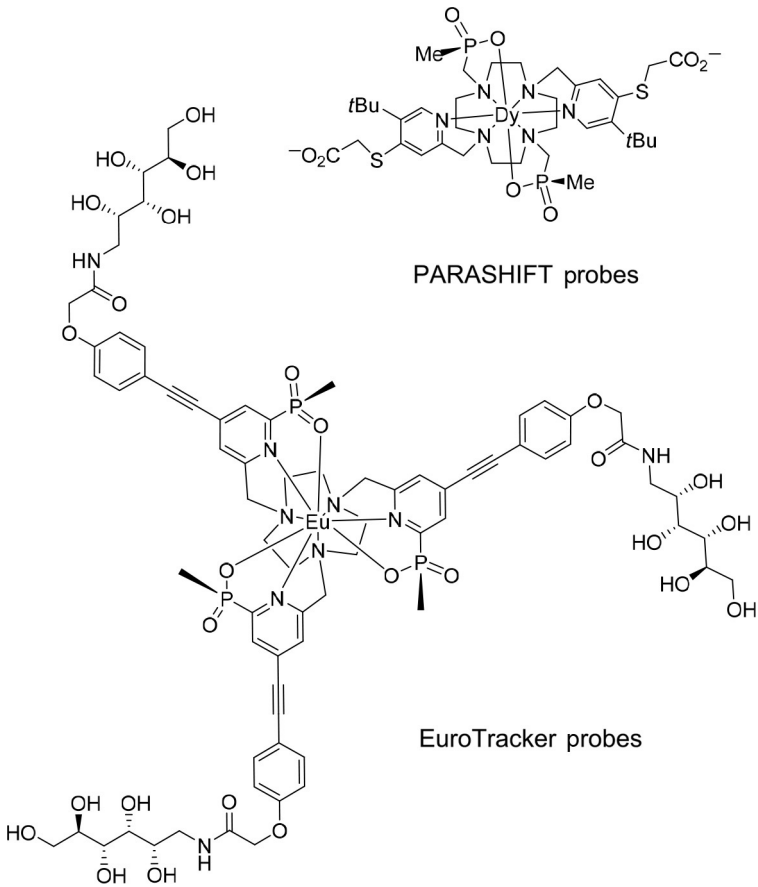

In the 1980s, developments in healthcare led to the introduction of gadolinium complexes as contrast agents for magnetic resonance imaging (MRI) and targeted radiotherapeutic agents, using isotopes such as ^{90}Y. In each case, new rare earth coordination chemistry developed, guided by precise ligand design criteria, to provide kinetically stable systems that resisted premature metal dissociation in vivo. The paramagnetic lanthanide(III) ions have found numerous applications in analysis, imaging science, and the biosciences, notably in magnetic resonance based on fast relaxation processes and large dipolar shifts, and in diverse optical phenomena, associated with the sharp emission spectra and long-lived lifetimes characterizing the parity-forbidden f–f transitions.

The chapter provides a critical assessment of the theoretical background of magnetic anisotropy and relaxation. The theories that were developed to rationalize these experimental phenomena have limitations that preclude their widespread use; a unifying theory of electromagnetic anisotropy is required to aid the future design of functional coordination complexes, enabling realistic structure/property predictions. Paramagnetic complexes of Ln(III) have found use in the development of chemical exchange by saturation (PARACEST) and shift methods (PARASHIFT); these methods are relatively new and the corresponding theoretical background is still insufficient. In addition, luminescent properties are discussed with respect to both in vitro and in vivo analyses.

CHAPTER 292: LANTHANIDE NANOPARTICLES: PROMISING CANDIDATES FOR MAGNETIC RESONANCE IMAGING CONTRAST ENHANCEMENT

Xiao-Yu Zheng, Lin-Dong Li, Ling-Dong Sun, and Chun-Hua Yan

Beijing National Laboratory for Molecular Sciences, State Key Laboratory of Rare Earth Materials Chemistry and Applications, PKU-HKU Joint Laboratory in Rare Earth Materials and Bioinorganic Chemistry, College of Chemistry and Molecular Engineering, Peking University, Beijing, PR China. E-mail: yan@pku.edu.cn

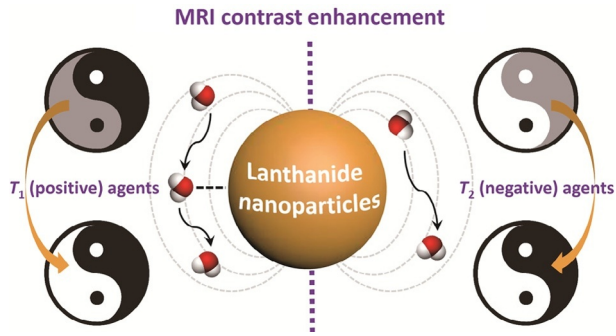

Magnetic resonance imaging (MRI) contrast agents (CAs) are widely used to manipulate the image contrast for enhanced imaging efficiency and accuracy. Novel imaging agents with better performance and desired functions are of great value to meeting diverse practical requirements. Lanthanide nanoparticles (NPs) integrating unique electronic configurations of lanthanide ions and nanometric-size effects have been recognized as promising candidates for MRI contrast enhancement. The chapter focuses on the evolution of lanthanide NPs in the past decade and pays particular attention to the design strategy of novel CAs tailored toward specific purposes. Both T_1-weighted and T_2-weighted MRI contrast enhancements are dealt with. Recent advances in the design and test of various CAs are summarized, and the influence of composition, size, shape, and surface status on the relaxometric properties of lanthanide NPs is discussed based on relaxation mechanism.

In addition, an overview on the multifunctional applications of lanthanide NPs is presented, for instance for simultaneous MRI and optical imaging, or MRI and X-ray computed tomography, or MRI and positron emission tomography, or MRI and single-photon emission computed tomography. The authors also raise some prospects with the hope of providing insights into the future development of lanthanide NPs since many questions remain open, for instance the influence of structure, exposed surface, and impurities on relaxivity.

CHAPTER 293: EXPANDING THE +2 OXIDATION STATE OF THE RARE-EARTH METALS, URANIUM, AND THORIUM IN MOLECULAR COMPLEXES

David H. Woen and William J. Evans
University of California, Irvine, CA, United States. E-mail: wevans@uci.edu

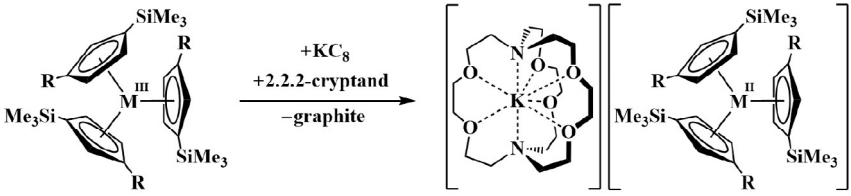

R = H, M = Y, Pr, Gd, Tb, Ho, Er, Lu, U
R = $SiMe_3$, M = Th

This chapter describes recent developments in the low oxidation state chemistry of the rare-earth elements. Since the publication in 2010 of Chapter 246 in Volume 40 of this series on "The Molecular Chemistry of the Rare-Earth Elements in Uncommon Low-Valent States" by Nief, the landscape of low oxidation states in the rare-earth metal series has changed dramatically. The first isolable crystallographically characterizable molecular complexes of the +2 rare-earth metal ions, La^{2+}, Ce^{2+}, Pr^{2+}, Gd^{2+}, Tb^{2+}, Ho^{2+}, Y^{2+}, Er^{2+}, and Lu^{2+} as well as the +2 actinide ions, U^{2+} and Th^{2+}, have

been discovered. Following a background section, these discoveries are presented chronologically to show the evolution of this new chemistry. A section describing previous literature that foreshadowed these discoveries is included to stimulate thinking about how current literature can be used to generate future discoveries. The importance of specific ligand sets which allowed isolation of ions with $4f^n5d^1$, $5f^36d^1$, and $6d^2$ electron configurations is described as well as the special conditions of low temperature and alkali metal chelate choice that provided isolable complexes. The identification of configurational crossover ions, whose electronic ground states can be either $4f^{n+1}$ or $4f^n5d^1$ depending on the ligand set, is also discussed.

CHAPTER 294: COORDINATION CHEMISTRY IN RARE EARTH CONTAINING IONIC LIQUIDS

Denis Prodius and Anja-Verena Mudring

Iowa State University and Ames Laboratory, Ames, IA, United States. E-mail: mudring@ameslab.gov

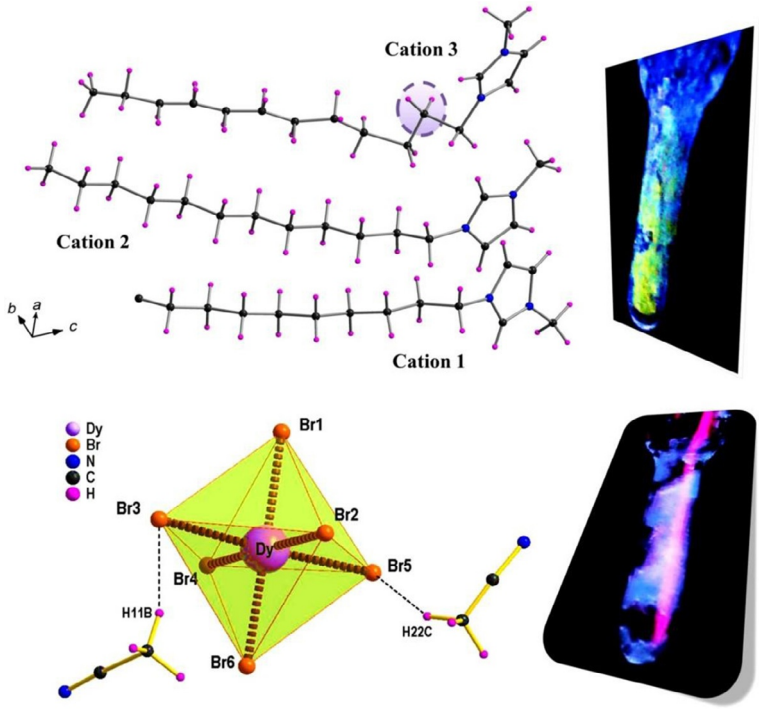

Ionic liquids (ILs) have become an important class of materials in the light of the constantly increasing number of their applications and commercial uses. They are generally defined as salts with a melting point lower than

100°C, but many of them are liquid at room temperature and even below, opening a wide space for applications. Ionic liquids can be true technology enablers because a given liquid can be designed with programmed properties by the simple choice of the constitutive ions.

Combining ILs with rare earths makes potent functional materials with intriguing optical, magnetic, and catalytic properties. This chapter presents a systematic overview of ILs where rare earth ions are integral part of either the cation or the anion and discusses in detail their crystal structure with emphasis on the coordination mode of the ligands used to create rare earth containing ionic liquids. Luminescent and magnetic properties are described as well as thermal behavior and chemical reactivity. It is noteworthy that some of these ILs are being tested in practical applications such as lanthanide extraction and separation or in the design of single ion magnets. Relatively unexplored to date, this new field of research possesses a large innovation potential.

Jean-Claude G. Bünzli
Vitalij K. Pecharsky

Contents of Volumes 1–49

VOLUME 7
1984; ISBN 0-444-86851-8

VOLUME 8
1986; ISBN 0-444-86971-9

VOLUME 9
1987; ISBN 0-444-87045-8

VOLUME 10: High energy spectroscopy
1987; ISBN 0-444-87063-6

VOLUME 11: Two-hundred-year impact of rare earths on science
1988; ISBN 0-444-87080-6

VOLUME 12
1989; ISBN 0-444-87105-5

VOLUME 13
1990; ISBN 0-444-88547-1

VOLUME 18: Lanthanides/Actinides: Chemistry
1994; ISBN 0-444-81724-7

VOLUME 19: Lanthanides/Actinides: Physics – II
1994; ISBN 0-444-82015-9

VOLUME 35

2005; ISBN 0-444-52028-7

VOLUME 36

2006; ISBN 0-444-52142-9

VOLUME 37: Optical Spectroscopy

2007; ISBN 978-0-444-52144-6

VOLUME 38

2008; ISBN 978-0-444-52143-9

VOLUME 44: Including Actinides
2014; ISBN 978-0-444-62711-7

VOLUME 45: Including Actinides
2014; ISBN 978-0-444-63256-2

VOLUME 46
2015; ISBN 978-0-444-63260-9

VOLUME 47
2015; ISBN 978-0-444-63481-8

VOLUME 48: Including Actinides
2015; ISBN 978-0-444-63483-2

VOLUME 49: Including Actinides
2016; ISBN 978-0-444-63699-7

Index of Contents of Volumes 1–50

D

E

F

G

H

I

J

K

L

M

N

O

P

Q

R

S

T

U

V

W

X

Z

Chapter 282

Systematics

Karl A. Gschneidner Jr.[1]
The Ames Laboratory, Iowa State University, Ames, IA, United States
[1]*Corresponding author: e-mail: cagey@ameslab.gov*

Chapter Outline

1 INTRODUCTION

Systematics is a powerful tool in science. It may enable us to understand the basic scientific principle(s) involved in certain studies, eg, in a group of elements or compounds. Or, it may help one to determine if some data are correct or, at least, reasonable, or if they are wrong and, thus, make no sense. Or, it may allow one to decide which of two disagreeing pieces of data is correct, eliminating the erroneously measured datum. Or, it may show an anomaly in a series of data points, or measurements, which is extremely important since anomalies actually bring more knowledge and understanding of the nature of materials, ie, something new, than if everything is in agreement. If there is no anomaly, then all you have done is just verified what we already know, which is also good, but it has not advanced our knowledge much.

Handbook on the Physics and Chemistry of Rare Earths, Vol. 50. http://dx.doi.org/10.1016/bs.hpcre.2016.07.001

Globally, systematics involves most of the periodic table, for example, the prediction of an unknown element scandium, a.k.a. eka-boron or ductile intermetallic compounds. Locally, on the other hand, systematics involves just the rare earth elements, eg, the lanthanide contraction, or the anomalous valence of Eu and Yb, or the standard state (thermodynamics). One may also recognize an intermediate, ie, semi-global case when systematics involves the rare earth series and a portion of the periodic table: an excellent example is the melting point anomaly which led to the notion of 4f bonding—4f-5d hybridization way before this has been verified using rigorous first-principles computations.

2 SYSTEMATICS

The regular and systematic variations of physical and chemical properties of the lanthanides were recognized as soon as scientists had sufficient data about a given property for most of the lanthanide elements. Since then not only systematics but also deviations thereof have been used to understand the lanthanide elements, see, for example, Gschneidner and Daane, including references cited therein [1]. For example, shortly after the lattice parameters of the rare earth sesquioxides—R_2O_3—had been established, Goldschmidt *et al*. [2] noted the gradual, systematic decrease in unit cell dimensions and in the derived ionic radii of lanthanides with increasing atomic number; he also coined the phrase "die Lanthaniden-Kontraktion"—"the lanthanide contraction." Soon after, Klemm and Bommer [3] prepared the pure metals and confirmed the lanthanide contraction. Importantly, they also observed several anomalies, namely, the divalent states for Eu and Yb, and that the valence of Ce was greater than 3+.

Since the middle of the 20th century, various issues related to systematics of the lanthanides including Sc and Y has been the subject of a large number of published papers. By and large, this has led to a deeper understanding and appreciation of the chemical, metallurgical, and physical nature of the rare earths in general and lanthanides in particular. Traditionally, anomalies in the systematic trends have been and are used to date to point out: (1) anomalous valence states of Ce^{4+}, Eu^{2+}, and Yb^{2+} in many compound series; (2) valence fluctuation behaviors of Ce^{3+}/Ce^{4+} and Yb^{2+}/Yb^{3+}; (3) conservation of 4f electrons or 4f valence promotion during vaporization or sublimation; and (4) 4f hybridization with the 5d and 6s valence electrons (4f bonding) [4].

Things are, however, not so simple for compounds. As noted by Gschneidner [4], one of the major problems in working with alloys and compounds is the lack of reliable and sufficient data. Part of this is inherent with the rare earth intermetallic and nonmetallic compounds themselves. Over 50% of binary compounds in the R_xM_y series of phases do not exist for *all* of the rare earth members. Thus, quite often we lack information about La_xM_y and/or, Sc_xM_y and/or Lu_xM_y, which makes it difficult to establish a baseline. The other major problem is that the melting points, phase relationships (eg, solid solubility limits), and thermodynamic properties have been measured by a

number of different investigators and the values reported in the literature many times are so scattered that it is difficult to establish a trend, even for close lanthanide neighbors, let alone for Sc and Lu. Usually the only reliable data that one finds in the literature are those which have been measured by one group of scientists. Fortunately, after an extensive search, several types of information have been found and analyzed [4], and some of them are discussed in this chapter.

As we will see, the use of systematics is a powerful tool for understanding the nature of the lanthanides. Furthermore, it is also important to include yttrium and scandium in such analyses when appropriate. Even today, systematics remains a valuable tool for evaluating the reliability of published data and also for predicting or estimating data which are unknown. But as noted by Gschneidner and Calderwood [5] systematics must be approved cautiously and carefully because incorrect conclusions can be drawn or erroneous values can be estimated.

The use of systematics in other fields of science involving the rare earths/lanthanides can be found in the NATO Conference Proceedings edited by Sinha [6]. Articles on divalent Eu and Yb, the electronic levels in lanthanide gaseous species, the inclined W function of 4f levels, structural chemistry, and future trends are contained in this book.

2.1 The Discovery of New Elements

One of the greatest achievements using systematics was Mendeleev's prediction of three unknown elements (eka-boron, eka-aluminum, and eka-silicon) which included a rare earth element [7]. His predictions were based on the systematic variation of the chemical and physical properties of the known oxides of the elements in the early 1870s and the gaps in the variation of the properties of the compounds. The three elements are scandium (discovered in 1879), gallium (discovered in 1875), and germanium (discovered in 1886). The amazing feature is that this work was done about 50 years ahead of the Bohr model of the electronic structure of the elements. This is indeed an exemplary application of *global systematics* [8].

2.2 Goldschmidt's Lanthanide Contraction and What Do Anomalies Tell Us?

The first application of systematics to the lanthanides was made in the mid-1920s by Goldschmidt. When compiling the ionic radii of the elements he noted that radii of the lanthanide elements decrease in a regular and smooth fashion from lanthanum to lutetium. This is a fantastic example of *localized systematics*. The ionic radii of the lanthanides were calculated from the lattice parameters of the C-form of the sesquioxides [2]. Since both europium and ytterbium are trivalent in the R_2O_3 phase [9], their radii are in line with those of the other trivalent lanthanides; normally this is not the situation for most compounds. Goldschmidt coined the words "lanthanide contraction" to

describe this systematic decrease in ionic radii. He realized that this contraction is due to the fact that the 4f electrons do not effectively screen the outer electrons from the increased nuclear charge as an additional 4f electron is added moving left to right in the periodic table from one element to the next, ie, gradually increasing the atomic number from 57 to 71. The importance of this observation was recognized by the Nobel laureate von Hevesy and given prominence in his classical book on the atomic structure of the rare earths [10].

Klemm and Bommer's pioneering work on preparing the lanthanide metals for the first time [3] (especially the middle and heavy lanthanides) confirmed the lanthanide contraction and also found some departures from Goldschmidt *et al.*'s rule. The authors observed that the densities of Eu and Yb were anomalously low s (ie, their atomic volumes were too large) compared with those of their neighboring lanthanide metals. They proposed that Eu and Yb were divalent metals [3]. These two metals could only be divalent if a valence electron, namely a lone $5d^1$ electron, is "promoted" to the 4f level. The existence and stability of divalent Eu and Yb also confirms Hund's rules that half (ie, $4f^7$) and completely filled (ie, $4f^{14}$) shells are more stable states compared to partially filled states. In this case the use of systematics confirmed an earlier proposed rule.

Today the lanthanide contraction is still one of the most important tools available to us in applying systematics to the behavior of lanthanide materials. Deviations from the lanthanide contraction established for a given compound series give a measure of anomalous valences for cerium, samarium, europium, thulium, and ytterbium, which are important in evaluating the nature of these elements in valence fluctuation, heavy fermion, and spin fluctuation behaviors. Unexpectedly some of the ternary compounds $R_xM_yT_z$ have been found to exhibit a *lanthanide expansion* (also see Section 2.4) which is due to an unusual crystal structure.

In the case of compounds, especially noncubic materials, McMasters *et al.* [11] suggested the use of effective radius, r_{eff}, which they defined as:

$$r_{\text{eff}} = (V/n)^{1/3},$$

where V is the unit cell volume and n is the total number of atoms in the unit cell. This gets around the problem of which lattice constant one should use for a noncubic material to establish the absence or presence of deviations from the lanthanide contraction. There are other advantages of using r_{eff} vs Z (the atomic number) plots for all the compounds formed between R and a given M, and these too were discussed by the authors.

2.3 Melting Behavior

It has long been recognized that the melting behavior of a compound series of the *trivalent* lanthanides does not necessarily follow the approximate linear increase observed in the trivalent metals, which is illustrated in Fig. 1. Indeed four different behaviors have been noted [12] as shown in Fig. 2. But when

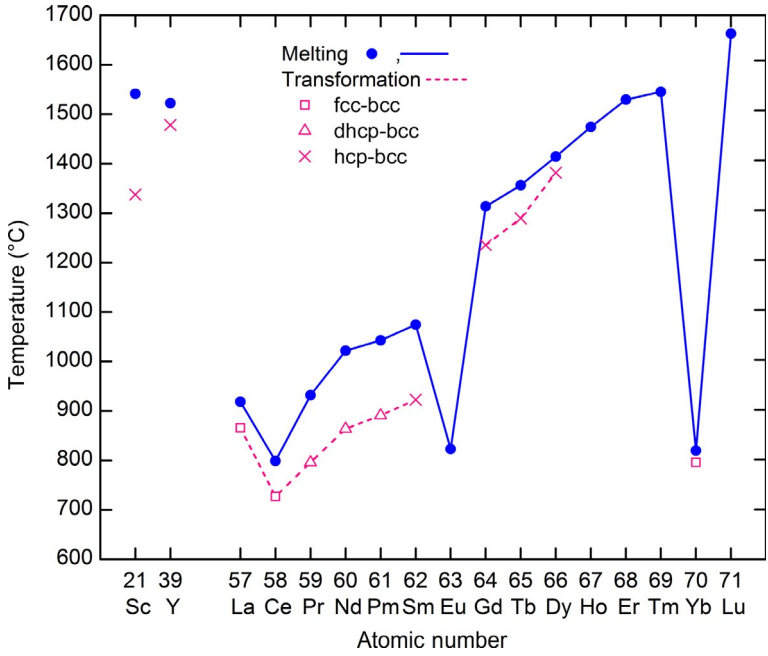

FIG. 1 The high-temperature allotropy, transformation, and melting temperatures of the lanthanides. *Adapted after K.A. Gschneidner Jr., Rare Earth Alloys, D. Van Nostrand Company, Princeton, NJ, 1961, 449 p.*

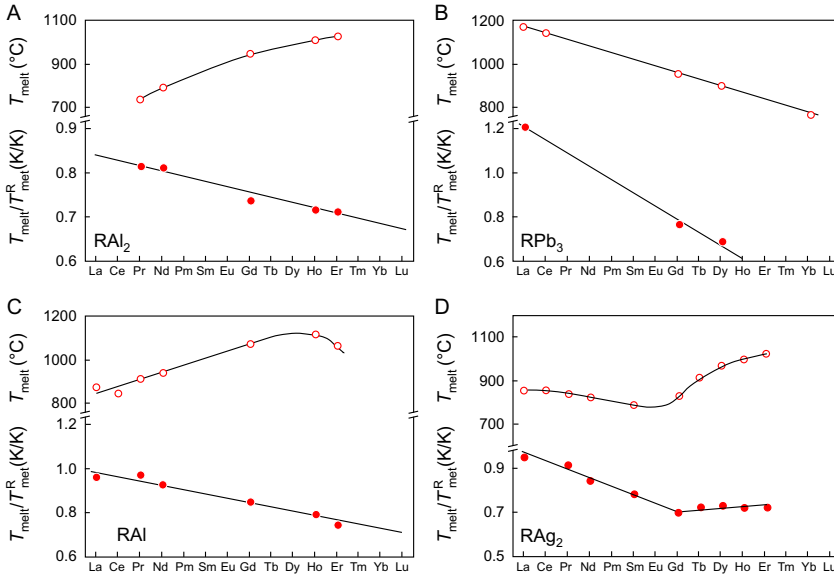

FIG. 2 Melting points and reduced melting points for the four possible melting behaviors: (A) melting point increases, (B) melting point decreases, (C) maximum in melting points, and (D) minimum in melting points [12].

one plots the reduced absolute melting points (the melting point of the compound in K divided by the melting point of the pure rare earth metal in K) many times one obtains a straight line, as is shown in Fig. 2A–C. This can be helpful when estimating melting points for lanthanide compounds by extrapolation, especially if the melting behaviors are not linear functions of the atomic number, see, eg, Fig. 2C. As shown in Fig. 2D, however, the reduced melting temperature vs the atomic number in the case of a melting minimum has two linear segments. This seems to be more prevalent in the case of melting minima; in addition to the RAg_2 series (Fig. 2D) both the RCl_3 and RBr_3 compound series show similar behaviors.

Again we note that one must be careful in using such plots for estimating data. For estimating melting points by interpolation the normal melting point vs atomic number plot serves just as well and saves one the step of calculating the reduced melting temperatures and plotting them.

2.4 Lattice Parameter, Free Energy (Heat) of Formation, and Melting Point Correlation

All lanthanide compound series exhibit the lanthanide contraction when one considers the molar volume of the compounds. But in four of the compound series which have the tetragonal $ThCr_2Si_2$-type structure, the c lattice parameter actually expands, but a decreases sufficiently such that the unit cell volume shows the normal lanthanide contraction [13]. These compound series are: RM_2Si_2, with M = Cu, Ag, and Au, and RCu_2Ge_2. Although this "lanthanide expansion" was originally observed quite some time ago, no one has proposed an explanation.

When one compares the lanthanide contraction in a compound series with that of the metals, three different behaviors are possible; the lanthanide contraction in the compound series relative to that in the metals is: (1) stronger, (2) weaker, and (3) just about the same. Gschneidner [12] argued that since the volume of formation of the compound from the elemental constituents, ΔV_f, is proportional to the free energy (heat) of formation, ΔG_f (ΔH_f), then in the first case ΔG_f should become more negative left to right across the lanthanide series, indicating greater stability in the compound series as the atomic number of the lanthanide increases, and this is what is observed in the R_2O_3 and RH_2 phases [12], and also the R_2C_3 series of compounds. For the second case the converse is expected and this has been verified in the RMg, RCd, and RCl_3 phases [12], and RAl, RAl_2, RAl_3, R_5Bi_3, R_4Bi_3, and RBi compound series. In the last (third) case ΔG_f is expected to remain constant for a compound series and this is the situation for the RAs compounds.

Gschneidner *et al*. [14] used this technique along with some limited available experimental data to predict the free energies of formation at 1100 K, and heats of formation at 298 K of the rare earth oxysulfides. Subsequently, Akila *et al*. [15] measured the free energies of formation of 11 lanthanide

oxysulfides and they noted that there was good to excellent agreement between the experimental and systematics-derived predictions [14].

In the melting process, at least for the normal metallic elements, melting occurs when about 1 bond out of 12 is broken, and if this correlation holds for compounds, then one might expect the melting trends in a compound series to be related to relative lanthanide contraction. This correlation was found to hold for 15 of 17 different compound series [12]. Since then Gschneidner and his coworkers examined 14 additional systems and found that only 8 of these obey the correlation, and that 2 of the original 15 systems found to hold do not. They noted that *about two-thirds of* the 31 compound series obey this correlation, which suggests that the lattice parameter–melting point interrelationship is not as good as originally thought.

2.5 Generalized Phase Diagram

Generalized phase diagrams have been proposed for both intra-lanthanide (Fig. 3A [16]) and intra-actinide (Fig. 3B [17]) alloy systems. These have proven to be quite useful in understanding the phase relationships in the two series of the elements and in predicting the existence of phases when experimental data are lacking, especially in the lanthanide series. The generalized phase diagram for the trivalent lanthanides is shown in Fig. 3A. This single diagram, which is also valid for yttrium–lanthanide binary alloys, represents a total of 91 possible binary phase diagrams. The systematization number shown at the top of the figure is used to calculate the critical points and phase boundaries for any combination of the trivalent lanthanide metals for which no experimental data exist. Indeed, two such calculated diagrams, La-Er and Sm-Ho, have been presented by Gschneidner [16] in his classification of the intra-lanthanide binary systems into the 13 possible types of phase diagram that could form between the trivalent lanthanides. Today, these two systems are listed in the ASM Alloy Phase Diagram Database [18] as "experimental" phase diagrams.

The representation of 91 possible binary alloy phase diagrams in a single diagram is possible because of the regular and systematic variation of the physical properties, such as the metallic radius (Fig. 4) and melting points (Fig. 1) of these elements. One notes significant anomalies in the radii of the lanthanides (which also are evident in other physical properties) for α-Ce, Eu, and Yb. Both Eu and Yb have anomalous radii and physical properties because they are divalent in their room-temperature metallic states. Because of this, the generalized phase diagram shown in Fig. 3A cannot be used to estimate intra binary alloy phase diagrams involving these divalent metals. However, it can be used to estimate the alloying behavior of hypothetical trivalent Eu and Yb. Furthermore, α-Ce is also excluded from the generalized phase diagram, because this phase exists only at high pressure (above 0.7 GPa) at 298 K, or below about 120 K at 1 atm. The other Ce

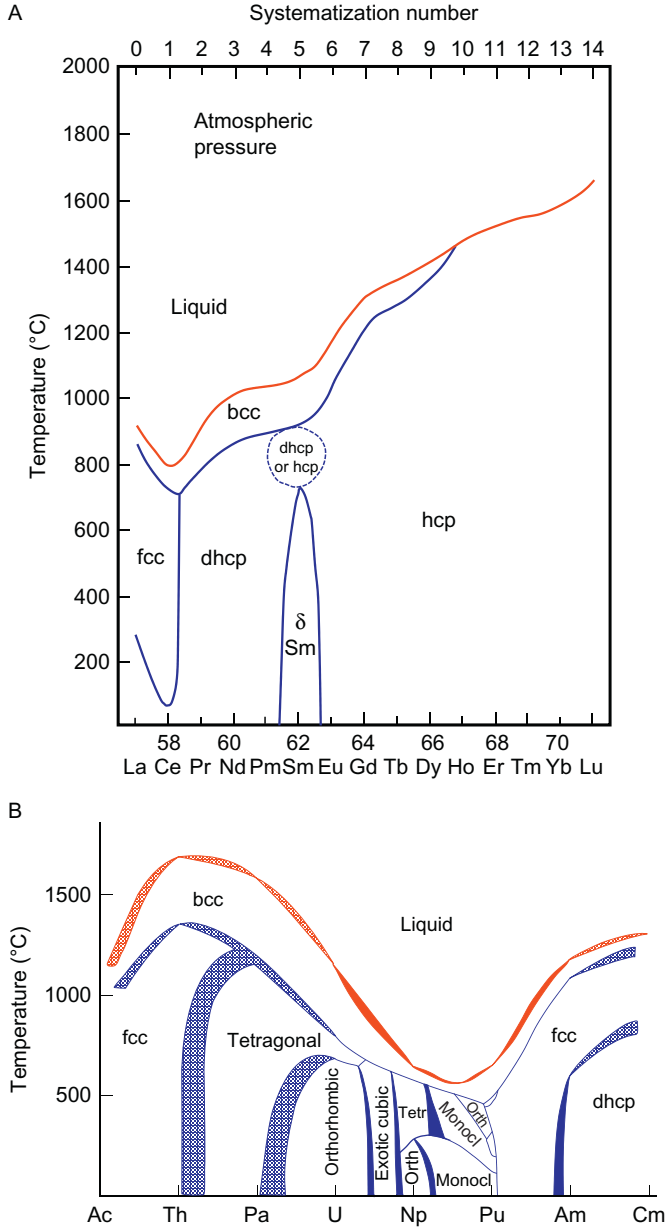

FIG. 3 Generalized phase diagrams for the trivalent intra-lanthanide alloys (A) and for the light actinides (B). In (B), the *hatched areas* are uncertain, and the *solid areas* are two-phase regions. The *blue colors* represent solid–solid, and the *red colors* represent solid–liquid transformations. *Panel (A): After K.A. Gschneidner Jr., Systematics of the intra-rare-earth binary alloy systems, J. Less-Common Met. 114 (1985) 29–42. Panel (B): After J.L. Smith, E.A. Kmetko, Magnetism or bonding: a nearly periodic table of transition elements, J. Less-Common Met. 90 (1983) 83–88.*

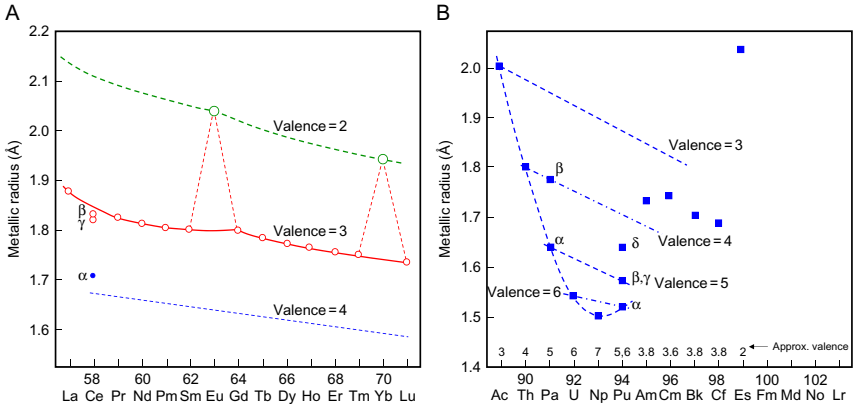

FIG. 4 Metallic radii of the lanthanides (A) and actinides (B) for coordination number of 12 [19].

phases (β and γ) have a valence close enough to three so that Ce can be treated as a normal trivalent lanthanide in the generalized phase diagram.

The generalized phase diagram for the actinide metals is shown in Fig. 3B. This diagram is quite different from that for the lanthanides. Indeed, it was constructed by Smith and Kmetko [17] by connecting the known binary phase diagrams (Np-Pu, Np-U, and Pu-U) and the known elemental phase transformations and melting points to give seven individual, but connected, phase diagrams. Furthermore, from the known Pu-Th and Th-U phase diagrams, it is clear that these seven individual diagrams cannot be compressed into a single generalized phase diagram as was done for the lanthanides [19]. This becomes even more obvious when one examines the metallic radii and the approximate valence states of the actinide elements shown in Fig. 4B.

The occurrence of the various crystal structures in the pure metals across the lanthanide series, in their intra rare earth alloys and at high pressures has generated a great deal of interest in the systematics that are involved (see Ref. [20] for most of the earlier references). Johansson and Rosengren [21] showed that the high-pressure transformations for the various polymorphic forms are systematically related, and they showed this in a three-dimensional projection in which the temperature and pressure axes are shifted for each lanthanide. Later, generalized phase diagrams similar to the one shown in Fig. 3A were also proposed for pressures up to 4 GPa [22] and then extended to 50 GPa [23], further improving the predictive power of systematics.

2.6 Dual Valence of Europium and Ytterbium

One of the best known and understood anomalies in the lanthanide series is the divalent character of europium and ytterbium metals which, as noted earlier, is quite evident in Figs. 1 and 4. In compounds, however, both divalent

and trivalent as well as intermediate valence states are known for these two elements. Since the standard state of these two metals (the pure metallic elements at 298 K and 1 atm pressure) is the divalent state, compounds in which europium and ytterbium are divalent may be easily formed. But in order to form compounds in which these elements are trivalent, one 4f electron must be promoted to the valence level. This promotion energy is 96 and 38 kJ/mol (R) for europium and ytterbium, respectively [24]. Thus the free energy of formation of a compound containing lanthanides in mixed valence states, the promotion energies are proportional to the fractional valence.

It is immediately obvious that ytterbium should form more compounds in which it is trivalent than in the case of europium, and that is what is observed [24]. As one might expect from the electronegativities of the elements in the periodic table and the way the bonding changes with the M element partner in an RM_x compound (Fig. 5), there is a relationship between the M element's position in the periodic table and the valence state of europium and ytterbium in the various compounds. This has been discussed by Gschneidner [24] and Iandelli and Palenzona [25].

In addition to using the lattice parameter(s) of the RM_x compound to estimate the valence state of europium and ytterbium one can use magnetic susceptibility data [24,26] and L_{III} absorption edges, XPS and UPS [26], to distinguish between the $4f^n$ and $4f^{n+1}$ configurations and intermediate valences. For europium one can also use Mössbauer isomer shift data [27–30].

The valence state of europium is important in some technological applications. For example, as a trivalent ion it emits a red light when used as a phosphor and a blue light when it is divalent. Also, the formation of trivalent europium compounds is quite critical for its applications in control rods or

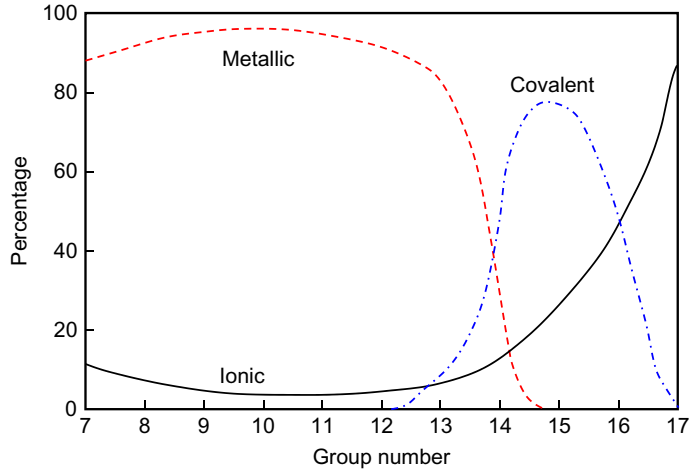

FIG. 5 The bonding character in binary rare earth compounds formed with the elements from Group 7 to Group 17 of the periodic table.

neutron absorbers [31]. Europium has a high neutron cross-section, and as it captures neutrons its eventual decay product is always a gadolinium atom. Thus if europium were divalent in such a material, each atom would undergo ~30% volume contraction when it formed gadolinium, and within a short time the control rod would probably not meet engineering standards and thus be unacceptable for nuclear applications. If europium, however, were trivalent there would be only a 1% volume contraction during the absorption of neutrons and eventual decay, and these materials would be acceptable. Thus there are only a limited number of compounds that could serve as useful europium control rod or neutron absorber materials.

2.7 Contributions to Alloy Theory

The systematic variation of the size and electronegativity and a constant valence of the lanthanide elements and also yttrium make these groups of elements a useful research tool for probing the chemical and alloying nature of materials, and solving some problems, whereby this newly gained knowledge transcends the rare earth group and adds understanding to the entire field.

The anomalous high solid solubility of holmium in gold reported by Wunderlin *et al*. [32] led Gschneidner and coworkers to study the solid solubilities of the rare earths in gold and silver. These studies along with a study of the solid solubility of magnesium in the rare earth metals and of the crystal chemistry of the rare earth-gold and -silver intermetallic compounds revealed that lattice rigidity, compound stoichiometry, and electron transfer are important parameters which govern the formation of solid solutions [33]. In time a new theory evolved for predicting the formation of solid solutions which improved the reliability from ~60% to ~85%.

Another contribution involved the measurement of the high-temperature heat contents of the rare earth metals. An analysis of the data revealed that the entropy of transformation, ΔS_{tr}, for the close packed to bcc transition in the rare earth metals depended upon the number of valence electrons [34], ie, $\Delta S_{tr} \cong 0.2$ entropy units, e.u., per valence electron. Extension of these observations to the remainder of the periodic table indicated that the entropy of transformation of metals which possess two or more of the common metallic structures and the entropy of fusion depend upon both the crystalline structure of the phases involved and the number of valence electrons [35]. These results were then used to predict the entropies of fusion for 16 metals, including 2 lanthanide metals—promethium and lutetium—and the entropies of transformation of 5 metals including promethium, for which no reliable experimental values existed.

Analyses of the systematics involved in various properties, such as the crystal structure sequence and melting points of the metals, have led several authors to conclude that 4f electrons are involved in the bonding of the metals via hybridization with the 5d and 6s valence electrons. This extension of systematics leads naturally into the topic of the next section.

2.8 Correcting Experimental Results

A problem in developing actinide systematics was the radius of actinium: it appeared to be too small relative to that of Th [19]. The change in radius on going from trivalent Ac to tetravalent Th is much too small when one compares the shifts of the radii due to valence changes for the lanthanide series from 2 to 3 and 3 to 4. Zachariasen [36] recognized this problem over 40 years ago, ie, the reported radius of actinium would suggest Ac has a valence greater than 3, which is impossible since it would require removing an electron from the Rn rare gas core level to attain this higher valence. He estimated a hypothetical radius of 1.977 Å for trivalent Ac, and ignored the then known experimental value of 1.877 Å. The Zachariasen radius for Ac is consistent with these valence changes and this implies that the radii for Am, Cm, Bk, and Cf are more appropriate for a valence of about 3.5, instead of 3 as shown in Fig. 4.

Further evidence supporting the larger lattice parameter for Ac metal is that the lattice parameters for all of the known Ac compound are about 3.0% larger than those of the corresponding isostructural La compounds [19]. The lattice parameter of fcc Ac ($a = 5.670$ Å) is 6.9% larger than that of fcc La, which is reasonable since the atomic fraction of Ac (or La) in the various compounds ranges from 0.17 to 0.40, and one would expect smaller increases in the lattice parameters in the compounds owing to this dilution effect.

Finally, the last piece of evidence supporting the larger lattice parameter being the true value for Ac is found in the systematic variation in the metallic radii in the Group 2, 3, and 4 elements, as argued by Gschneidner [19].

3 4F HYBRIDIZATION

For the last item, experimental evidence for 4f bonding in the lanthanide metals was initially presented over 45 years ago and has been subsequently refined since then. However, since 1993 we understand that the 4f hybridization in the lanthanides involves the 4f electrons which lie above the Fermi level and not the localized 4f electrons which give rise to the unique magnetic and optical properties.

About 50 years ago it was rare that any scientist would speak about 4f electrons being involved in bonding, since "everyone" *knew* that the 4f electrons were localized in the ion core and were well shielded by the $5p^6$ and $5s^2$ electrons, especially in the case of the lanthanide metals. However, a few scientists led by Matthias and Gschneidner believed that some of the properties of the lanthanide elements were sufficiently anomalous with respect to the rest of the periodic table that just the ($5d6s^2$) valence electrons could not account for these behaviors. Slowly the evidence built up such that today virtually everyone believes that there is some hybridization of the 4f electrons with the outer 5d and 6s electrons, especially in the light lanthanides (see, eg, Ref. [37]). The work on intermediate valence cerium and more recently the heavy-fermion studies convinced even the most conservative

scientists that 4f electrons must be involved. Reference to the early papers on this subject can be found in the article by Gschneidner [38].

Below we will describe briefly the major early contributions which pointed the way to our present state of knowledge. In addition to these two topics, more recent supporting information is found in the pressure dependence of the superconducting temperatures and the solid solubilities of Sc, Y, and Lu relative to those of lanthanides which have unpaired 4f electrons.

3.1 Crystal Structure Sequence

The existence of a sequence of close-packed structures in which the fcc to hcp stacking percentage changes from 100% fcc to 50% fcc–50% hcp to 33% fcc–67% hcp to 100% hcp as one proceeds along the lanthanide series may not seem so unusual that one needs to invoke 4f hybridization. True enough, but when this information is combined with the facts that (i) intra-lanthanide alloys between a light and a heavy always yield this same sequence of structures (see, eg, Fig. 3A and Ref. [16]) and (ii) application of pressure reverses this sequence [22], most of the explanations proposed for one or two of these facts failed to explain the other two or the third.

In the late 1960s Gschneidner and Valletta [39] and later Langley [20] proposed that 4f hybridization could account for the observed structures both at atmospheric pressure and also under pressure, while Hodges [40] and more recently Skriver [41] suggested that variation in the number of d electrons would account for the observed behaviors. High-pressure studies by Grosshans *et al.* [42], which showed that hcp yttrium transformed successively to the Sm-type to the dhcp and finally the fcc structure, would appear to rule out the need for 4f hybridization to explain the observed crystal structures. But by application of systematics, Gschneidner [22] pointed out that the corresponding phase transformations in the elements which have no unpaired 4f electrons (yttrium and lutetium) transform at pressure $\sim$7 GPa—higher than those elements which have unpaired 4f electrons. He concluded that relative s/d occupancy may play a major role in governing the crystal structure sequence, but 4f hybridization cannot be ignored and also plays a role.

3.2 Melting Points

The melting points for the light lanthanides are much too low relative to the rest of the periodic table, and also the change in the melting temperature from lanthanum to lutetium (Fig. 1) is much too large relative to that observed in a compound series with normal bonding. Matthias *et al.* [43] recognized these anomalies and proposed that the low melting temperature of the lights were due to "some f character in the hybridized wave functions describing the band structure for the valence electrons." This work on the melting points was expanded upon and extended to include the heats of sublimation in the analysis [38]. Gschneidner suggested the low melting points arose because of the low mobility of the 4f electron allowing 1 bond in 12 to break which is

sufficient to permit melting, even though the 4f contribution to the bonding is expected to increase the bond strength.

Kmetko and Hill [44] on the other hand proposed that the angular dependence of the 4f wave functions accounts for the low melting points because they do not have the appropriate directionality to form good bonds in the bcc structure, and that in the liquid state the 4f electrons bond better than in the bcc phase. But in the metallic state the conduction/bonding electrons are mobile and move throughout the "sea" of conduction electrons between the ion cores so that the bonds are continually being broken and reformed between neighboring ions, ie, there are resonating bonds between the atoms. Thus the truth of the matter is that both the mobility and the anisotropy of the 4f electrons contribute and account for the anomalous melting behaviors.

The initial evidence for 4f bonding or hybridization came from an analysis of the melting behavior of the lanthanides (Fig. 1), which at first glance (other than the anomalies at Ce, Eu, and Yb due to nontrivalent valences) seems to increase rapidly and monotonically from La to Lu [4]. However, when these melting points were compared with the systematic trends from the alkali to the alkaline earth to the rare earth to the Ti group metals, it was obvious that the melting point of La was approximately 450°C too low (see Fig. 6).

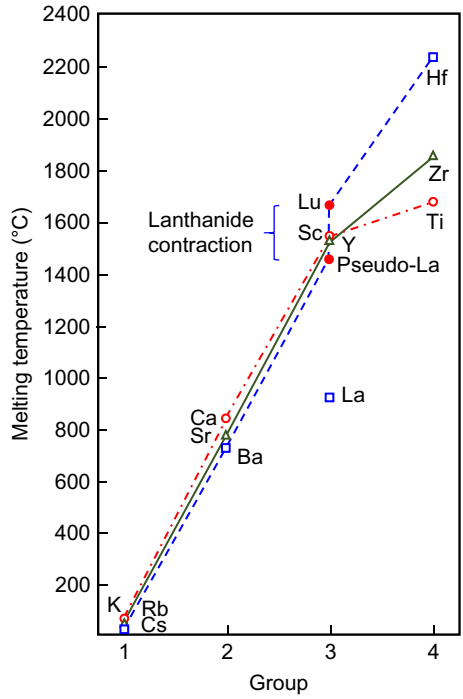

FIG. 6 The melting temperatures of the Group 1 through Group 4 metals. The *dashed line* extending from "pseudo-La" to Lu represents the range expected for the melting points of the lanthanides due to the lanthanide contraction [38].

The expected melting point of La, if no 4f electron hybridization occurred, is indicated by "pseudo-La" in Fig. 6.

3.3 Solid-Solution Behavior

As noted in the previous sections the evidence for 4f hybridization and involvement in the bonding of the lanthanide elements is strong. If this is the case, then surely there should be other evidence for this in alloys and compounds, but it may be difficult to demonstrate clearly that the observed behavior is indeed due to 4f hybridization with the bonding electrons.

One such situation is the room-temperature solid solubility of hydrogen in Sc [45], Y, Gd, Er, Tm, and Lu [46], which is plotted in Fig. 7 as a function of the metallic radius. It is immediately seen that the amount of hydrogen dissolved in the rare earth elements with no unpaired 4f electrons is enormously higher than those in lanthanides with unpaired electrons. If the 4f electrons were *truly localized* and *not involved in the chemical bonding*, one would expect all of the solid solubilities to fall on (or be close to) a smooth curve from scandium to gadolinium, yttrium (which have essentially the same size), but clearly this is not the situation here. Furthermore, any other type of correlation of the hydrogen solubility with a physical property of the rare earth metal (such as the electronegativity, melting point, Debye temperature) will lead to a

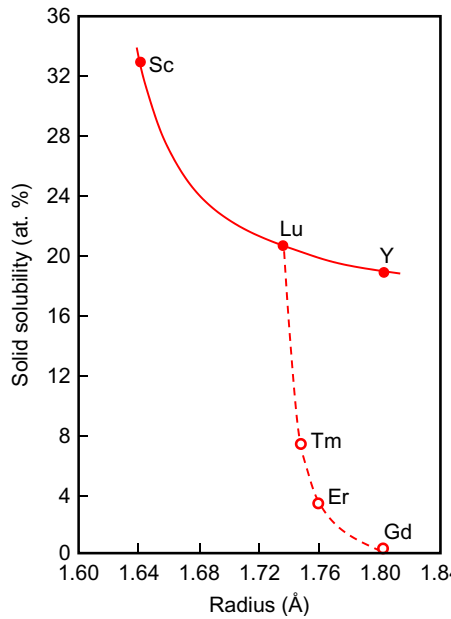

FIG. 7 The room-temperature solid solubility of hydrogen in the rare earth metals as a function of the rare earth radius. The solubility in the light lanthanides (not shown) is less than that in gadolinium.

similar separation of the non-4f rare earths from the 4f-containing ones as shown in Fig. 7. Thus by default we come to the conclusion that 4f hybridization with the valence electrons leads to a much reduced hydrogen solubility, and the larger the amount of hybridization the smaller the solubility.

This application of systematics to the solubility of hydrogen in the rare earth metals actually turns out to be the strongest case that we have to support our claim that 4f electrons are involved in the chemical bonding.

4 EPILOGUE

Karl A. Gschneidner, Jr. has passed away on April 27, 2016 at the age of 85. He was working on this chapter literally to his last day in the office, until the day he was taken to a hospital. The unfinished manuscript was put through our standard editorial process, and both editors unanimously decided that this last work by Karl must be published even if in the unfinished state. Both of us agree that in addition to the content, this chapter illustrates Karl's complete dedication to the rare earth science in general and to the Handbook series that he and LeRoy Eyring started nearly 40 years ago in particular. We hope that the reader will appreciate Karl's passion toward a systematic approach, his willingness to share what he knows, and his unparalleled abilities to deliver the message as both of us do, being privileged to have worked with Karl for many years. We are sad that Karl is no longer with us, but we are glad to see that Karl's work lives on.

REFERENCES

[1] K.A. Gschneidner Jr., A.H. Daane, Physical metallurgy, in: K.A. Gschneidner Jr., L.R. Eyring (Eds.), Handbook on the Physics and Chemistry of Rare Earths, vol. 11, Elsevier Science Publishing, Amsterdam, 1988, p. 409.

[2] V.M. Goldschmidt, T. Barth, G. Lunde, Geochemische Verteilungsgesetze der Elemente, vol. 5, Isomorphie und Polymorphie des Sesquioxyde: die Lanthaniden-Kontraktion und ihre Konsequenzen, Skr. Nor. Vidensk.-Akad. Mat.-Natur. Klasse, Oslo, 1925, 59 p.

[3] W. Klemm, H. Bommer, Zur Kenntnis der Metalle der seltenen Erden, Z. Anorg. Allg. Chem. 231 (1937) 138–171.

[4] K.A. Gschneidner Jr., Systematics and anomalies, J. Alloys Compd. 192 (1993) 1–10.

[5] K.A. Gschneidner Jr., F.W. Calderwood, Use of systematics for the evaluation of rare-earth phase diagrams and crystallographic data, Bull. Alloy Phase Diagr. 4 (1983) 129–131.

[6] S.P. Sinha (Ed.), Systematics and Properties of the Lanthanides, In: NATO ASI Series, Series C, Mathematical and Physical Sciences, vol. 109, D. Reidel Publishing Company, Dordrecht, 1983. 648 p.

[7] M. Kaji, D.I. Mendeleev's concept of the chemical elements and the principles of chemistry, Bull. Hist. Chem. 27 (2002) 4–16.

[8] F. Szabadvary, The history of the discovery and separation of the rare earths, in: K.A. Gschneidner Jr., L.R. Eyring (Eds.), Handbook on the Physics and Chemistry of Rare Earths, vol. 11, Elsevier Science Publishing, Amsterdam, 1988, p. 33.

[9] L.R. Eyring, The binary rare earth oxides, in: K.A. Gschneidner Jr., L.R. Eyring (Eds.), Handbook on the Physics and Chemistry of Rare Earths, vol. 3, North Holland, Amsterdam, 1979, p. 337.
[10] G. von Hevesy, Die Seltenen Erden von Standpunkte des Atombaues, Julius Springer, Berlin, 1927, 138 p.
[11] O.D. McMasters, K.A. Gschneidner Jr., G. Bruzzone, A. Palenzona, Stoichiometry, crystal structures and some melting points of the lanthanide-gold alloys, J. Less-Common Met. 25 (1971) 135–160.
[12] K.A. Gschneidner Jr., On the interrelationships of the physical properties of lanthanide compounds: the melting point, heat of formation and lattice parameter(s), J. Less-Common Met. 17 (1969) 1–12.
[13] K.A. Gschneidner Jr., Systematics of binary rare earth-silver and -gold systems, in: T.B. Massalski, W.B. Pearson, L.H. Bennett, Y.A. Chang (Eds.), Noble Metal Alloys, The Metallurgical Society, Warrendale, PA, 1986, pp. 325–344.
[14] K.A. Gschneidner Jr., N. Kippenhan, O.D. McMasters, Thermochemistry of the Rare Earths, IS-RIC-6, Rare-Earth Information Center, Iowa State University, Ames, IA, 1973.
[15] R. Akila, K.T. Jacob, A.K. Shukla, Gibbs energies of formation of rare earth oxysulfides, Metall. Trans. B 18 (1987) 163–168.
[16] K.A. Gschneidner Jr., Systematics of the intra-rare-earth binary alloy systems, J. Less-Common Met. 114 (1985) 29–42.
[17] J.L. Smith, E.A. Kmetko, Magnetism or bonding: a nearly periodic table of transition elements, J. Less-Common Met. 90 (1983) 83–88.
[18] ASM Alloy Phase Diagram Database. http://mio.asminternational.org/apd/index.aspx.
[19] K.A. Gschneidner Jr., Systematics in lanthanide and actinide solids, J. Alloys Compd. 223 (1995) 165–169.
[20] R.H. Langley, Bond hybrids and the structures of the lanthanide metals, Phys. Status Solidi B 111 (1982) 501–505.
[21] B. Johansson, A. Rosengren, Generalized phase diagram for the rare-earth elements: calculations and correlations of bulk properties, Phys. Rev. B 11 (1975) 2836–2857.
[22] K.A. Gschneidner Jr., Pressure dependence of the intra rare earth generalized binary phase diagram, J. Less-Common Met. 110 (1985) 1–10.
[23] U. Benedict, W.A. Grosshans, W.B. Holzapfel, Systematics of *f* electron delocalization in lanthanide and actinide elements under pressure, Phys. B+C 144 (1986) 14–18.
[24] K.A. Gschneidner Jr., On the valences of europium and ytterbium in compounds, J. Less-Common Met. 17 (1969) 13–24.
[25] A. Iandelli, A. Palenzona, Crystal chemistry of intermetallic compounds, in: K.A. Gschneidner Jr., L.R. Eyring (Eds.), Handbook on the Physics and Chemistry of Rare Earths, vol. 2, North Holland, Amsterdam, 1979, pp. 1–54.
[26] L.M. Falicov, W. Hanke, M.B. Maple (Eds.), Valence Fluctuations in Solids, North Holland, Amsterdam, 1981, p. 1.
[27] P. Brix, S. Hüfner, P. Kienle, D. Quitmann, Isomer shift on Eu^{151}, Phys. Lett. 13 (1964) 140–142.
[28] A.F. Clifford, Mössbauer spectroscopy of the rare earths, Adv. Chem. Ser. 68 (1967) 113–125.
[29] F.J. van Steenwijk, K.H.J. Buschow, Isomer shifts in divalent europium intermetallic compounds, Phys. B+C 85 (1976) 327–330.
[30] J.W.C. de Vries, R.C. Thiel, K.H.J. Buschow, The ^{151}Eu Mössbauer isomer shift in intermetallic compounds containing trivalent europium, Phys. B+C 124 (1984) 291–298.

[31] O.D. McMasters, K.A. Gschneidner Jr., Rare earth intermetallic compounds, Nucl. Metall. 10 (1964) 93–158.
[32] W. Wunderlin, B.J. Beaudry, A.H. Daane, Redetermination of solid solubility of holmium in gold, Trans. Met. Soc. AIME 233 (1965) 436.
[33] K.A. Gschneidner Jr., L. S. (Larry) Darken's contributions to the theory of alloy formation and where we are today, in: L.H. Bennett (Ed.), Theory of Alloys Phase Formation, The Metallurgical Society, Warrendale, PA, 1980, p. 1.
[34] D.H. Dennison, K.A. Gschneidner Jr., A.H. Daane, High-temperature heat contents and related thermodynamic functions of 8 rare earth metals: Sc, Gd, Tb, Dy, Ho, Er, Tm, and Lu, J. Chem. Phys. 44 (1966) 4273–4282.
[35] K.A. Gschneidner Jr., Entropies of transformation and fusion of the metallic elements, J. Less-Common Met. 43 (1975) 179–189.
[36] W.H. Zachariasen, Metallic radii and electron configurations of 5f-6d metals, J. Inorg. Nucl. Chem. 35 (1973) 3487–3497.
[37] A.J. Freeman, B.I. Min, M. Norman, Local density supercell theory of photoemission and inverse photoemission spectra, in: K.A. Gschneidner Jr., L. Eyring (Eds.), Handbook on the Physics and Chemistry of Rare Earths, vol. 10, North Holland, Amsterdam, 1987, pp. 165–229.
[38] K.A. Gschneidner Jr., On the nature of 4f bonding in the lanthanide elements and their compounds, J. Less-Common Met. 25 (1971) 405–422.
[39] K.A. Gschneidner Jr., R.M. Valletta, Concerning the crystal structure sequence in the lanthanide metals and alloys; evidence for 4f contribution to the bonding, Acta Metall. 16 (1968) 477–484.
[40] C.H. Hodges, Stability and axial ratios of various close-packed structures, Acta Metall. 15 (1967) 1787–1794.
[41] H.L. Skriver, Electronic structure and cohesion in rare earth metals, in: S.P. Sinha (Ed.), Systematics and Properties of the Lanthanides, NATO ASI Series, Series C, Mathematical and Physical Sciences, vol. 109, D. Reidel Publishing Company, Dordrecht, 1983, pp. 213–254.
[42] W.A. Grosshans, Y.K. Vohra, W.B. Holzapfel, High pressure phase transformations in yttrium and scandium: relation to rare earths and actinides crystal structures, J. Magn. Magn. Mater. 29 (1982) 282–286.
[43] B.T. Matthias, W.H. Zachariasen, G.W. Webb, J.J. Engelhardt, Melting-point anomalies, Phys. Rev. Lett. 18 (1967) 781–784.
[44] E.A. Kmetko, H.H. Hill, Anomalous melting of f electron metals (with attention to Pu), J. Phys. F Met. Phys. 6 (1976) 1025–1037.
[45] Z.M. Azarkh, V.N. Funin, X-ray structural phase analysis of scandium-hydrogen system, Sov. Phys. Cryst. 10 (1965) 21.
[46] B.J. Beaudry, F.H. Spedding, The solubility of RH_{2-x} in Gd, Er, Tm, Lu and Y from ambient to 850°C, Metall. Trans. B 6 (1975) 419–427.

Chapter 283

The Rare Earths as Critical Materials

Alexander H. King*,[1], Roderick G. Eggert[†] and Karl A. Gschneidner Jr.*
[*]*Critical Materials Institute, The Ames Laboratory, Ames, IA, United States*
[†]*Critical Materials Institute, Colorado School of Mines, Golden, CO, United States*
[1]*Corresponding author: e-mail: alexking@ameslab.gov*

Chapter Outline

1 WHAT IS A CRITICAL MATERIAL?

Substances that are subject to supply risks and for which there are no easy substitutes in their technological applications, may be considered to be *critical materials*.

The level or degree of criticality is usually assessed in some variant of the diagram shown in Fig. 1, where the level of supply risk is depicted on one axis, and the level of essentiality is depicted on the other [1]. A material that is highly essential or very difficult to substitute and also subject to great supply risks is a highly critical material.

The identification of materials as "critical" clearly depends on many things:

- The identification depends on the technological context. What is essential for a manufacturer of lamps may be different from what is essential for a manufacturer of motors.

Handbook on the Physics and Chemistry of Rare Earths, Vol. 50. http://dx.doi.org/10.1016/bs.hpcre.2016.08.001

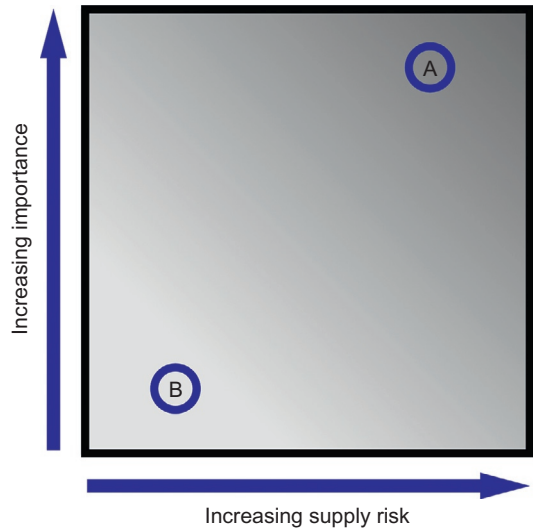

FIG. 1 Classification of materials according to their supply risk and their importance to a particular application. Material A has greater supply risk, and greater consequences ensue from a supply disruption, so it is considered more critical than Material B.

- The identification depends on location. What is unavailable in one country or region may be highly available in other parts of the world.
- The identification depends on time. What is a critical material today may not be critical tomorrow, as technological applications and materials availability evolve.
- The identification depends to some extent on how essentiality and supply risk are quantified, and especially on how different factors are weighted.
- Small differences in the plotted locations of different materials are probably insignificant, but large differences, such as those between materials "A" and "B" in Fig. 1 represent real differences in risk for the users of the materials.

In some cases, additional information is provided in plots of this kind. For example, environmental risks have been added on a third, orthogonal axis in some analyses [2,3]. In some corporate applications of the methodology, other concerns may be applied, for example, the annual cost of the material may be depicted, or the profit generated from products that contain the material.

Notwithstanding the differences in context and methodology, however, many different studies have identified rare earths as critical materials [4–11]. The rare earths are unique in their ubiquity in the critical material category: other elements may or may not be considered critical depending on the parameters of a particular study, but the rare earths are included in nearly every list. The US Department of Energy's Critical Materials Strategy, of

2011, identified yttrium, neodymium, europium, terbium, and dysprosium as critical materials [12].

The fact that a material is classified as critical does not automatically mean that there will be shortfalls of supply: rather, it means that there are significant risks of supply-chain interruptions, coupled with significant consequences if they happen. It is an identification of a need for appropriate concern and planning, not for panic.

Finally, it is important to note that price, per se, is not a good guide to criticality. While a truly critical material may command a high price, price fluctuations occur for many reasons other than the emergence or disappearance of criticality.

1.1 A Brief History of Critical Materials

Although the term "critical material" is relatively new, materials supply-chain shortfalls have impacted technology for many centuries, if not millennia. Historical examples are useful case studies to help us to identify and illustrate the traits of critical materials.

1.1.1 Bronze: 1200 BC

Starting in about 4000 BC, bronze production in the eastern Mediterranean region provided a technological base that underpinned the development of increasingly sophisticated nation-states and civilizations that left extensive records of their wars, treaties, and trading [13]. Bronze production was initially dispersed quite widely, and found wherever sources of copper and tin were found in close proximity. As trade developed, however, production became increasingly concentrated where it was most efficient. Copper production, in particular, eventually came to be dominated by the island of Cyprus, whose name refers directly to copper.

Around 1200 BC there was a general breakdown of civilization that is referred to as the Bronze Age Collapse [14]. Kingdoms that had thrived heretofore, quite suddenly ceased to exist, and others saw great changes in their power and influence. Once-dominant peoples like the Hittites, Trojans, Assyrians, Mycenaeans, and many others are never heard of after this period.

The causes of the Bronze Age Collapse are debated [15] but they probably include natural disasters including volcanic eruptions, earthquakes, and droughts, along with wars and revolts. Events such as these had occurred before, however, and it is not clear why this case was different. One possibility is the fact that Cyprus was invaded by a shadowy group known as the Sea Peoples, possibly making copper unavailable and impacting the availability of bronze for tools of agriculture and weapons of war, alike. When a dominant technology becomes unavailable, civilizations that depend on it may be unable to survive catastrophes that would otherwise not have been fatal.

Following the Bronze Age Collapse, the eastern Mediterranean region entered a Dark Age from which it emerged in around 1000 BC, as the technology of iron-making emerged. This is the period in which ancient Rome emerged as a major power.

1.1.2 Cobalt: 1978

In the 1970s, about 65% of cobalt traded in the world came from the Kolwezi district in the southwest of the African nation of Zaire. It was used primarily in superalloys for jet engines and chemical processing plants. As high-strength samarium–cobalt permanent magnet alloys emerged in the early 1970s, there was initial reluctance to adopt them because of concern about the supply of samarium, but General Motors (GM) eventually opted to use a Sm–Co permanent magnet starter motor in some of its vehicles, taking advantage of the weight and volume advantages of these motors over their traditional counterparts. Unfortunately for GM, the supply of cobalt (rather than samarium) became problematic, with prices rising from about US$5/lb in 1976, to US$25/lb in 1978. The primary reason for this alarming price spike was the threat to the Kolwezi district posed by rebel forces during a period of significant civil unrest. Interestingly, the price spike coincided with significantly increasing global production. Nevertheless, price spikes like this had never been seen before, and GM and other cobalt users tried to find alternatives, one result of which was the development of the neodymium–iron–boron magnet alloy, which first appeared in about 1984 [16].

Since the 1970s, world cobalt production has grown very significantly, going from a peak of 31.5 kt/year at the end of the 1970s to 109 kt/year in 2011. Much of the additional production goes into lithium-ion batteries and is generated through coproduction from primary copper mining.

1.1.3 Molybdenum: 1980 and 2004

In 1979 and 1980, demand for molybdenum significantly outstripped supply, generating a brief price spike. Sources of molybdenum included primary molybdenum mines and coproduction from copper anode sludge, and softness in the copper market suppressed molybdenum production from the latter source as the value of molybdenum was not sufficient to drive production of copper. As the market for copper recovered, supplies of molybdenum also eased [17].

A second molybdenum price spike occurred in 2004. Demand for molybdenum was recovering following an economic recession in 2002, but production was growing, too. In the first quarter of 2004; however, China—then the third largest producer and responsible for about 23% of the world's production [18]—abruptly cut its exports of molybdenum, causing great concern among consumers and driving prices up abruptly. Although Chinese exports returned to their normal levels in the next quarter, the sudden cut left

consumers nervous and drove up prices, which brought more producers into the market, with the result that by the end of 2004, with Chinese exports restored, prices fell [19].

1.1.4 Rhenium: 2006–2008

Among all of the elements, rhenium is one of the rarest, least widely utilized, and least substitutable. It is slightly less abundant in the earth's crust than platinum with only about 45 or 50 t being used, worldwide, each year. More than 80% of this goes into superalloys for jet engines, where it imparts strength at high temperatures, allowing the engines to run hotter, and thus more efficiently. Rhenium is produced as a by-product of copper, specifically when the ore contains molybdenite: effectively, it is a by-product of molybdenum production, in operations where molybdenum is a by-product of copper. The largest single producer is Chile, which commands a little more than half of the world's supply [20,21].

As new generations of passenger aircraft came on line in the mid-2000s, with new and more efficient engines stipulated by the airlines, demand for rhenium grew, threatening to outstrip supply. Although prices rose rapidly starting in 2006, supplies did not respond proportionately because of the negligibly small impact on the revenues of copper producers. Prices continued to rise through 2007 and into 2008, abating only with the onset of the worldwide economic recession, that year.

This is a case in which the economics of coproduction combined with the vulnerability of a small market to demand fluctuations to create a criticality. The aero-engine industry responded with refinements in alloy design to reduce the need for rhenium and changes in the business model to allow for greater recovery and recycling of end-of-life components. With the postrecession recovery in aero-engine production, rhenium prices recovered to some degree, but did not return to the levels of the 2008 peak. Rhenium remains vulnerable to changes in demand as jet engines continue to evolve and supplies are essentially unresponsive to price.

1.1.5 The Lessons from History

We see from these historic examples that lack of substitutability, localization of production and reliance on coproduction are risk factors for criticality, and especially when coupled with small market volumes, they make a material subject to disruptions resulting from changes in the supply chain or the demand for a material. All of these factors impact the rare earths.

1.2 The Emergence of Rare-Earth Criticality

While the focus of this Handbook is on the physics and chemistry of the rare-earth elements and their compounds, their status as critical materials stems from the many technological applications that they enable. Technologies become

effectively essential if society becomes adapted to them and their sudden absence becomes unthinkable. When essential technologies are enabled by specific materials, the supplies of those materials become an issue of great concern.

Uses have been found for rare-earth elements since their first discovery, with some of the earliest of them pioneered by Carl Auer von Welsbach [22]. In many cases, former uses have ended, either because the application became obsolete or more available alternative materials were identified, but Auer's inventions have had a surprising persistence.

Lanthanum, cerium, and yttrium oxides, combined with magnesium oxide, formed the first commercial rare-earth material, and it was used for gas lamp mantles. Auer's 1885 patent on "Actinophor" was the basis of a business that he started in 1887. Although the material had good emissive power, the color spectrum was not attractive, and in 1890 Auer and Haittinger patented a gas mantle comprised of 99% thoria and 1% ceria [22]. This became the dominant gas mantle material, worldwide, lasting until electric lighting eventually replaced gas: it remains in use today for gas lanterns such as those used by recreational campers.

Carbon arc lamps, especially those used in large film projectors, were significantly enhanced by additions of lanthanum and other rare-earth elements to the carbon electrodes but, like gas lamps, this technology is largely a thing of the past.

Mischmetal was originally developed by Auer as a mixture of 30% iron and 70% rare earths, and today typically contains roughly 50% cerium, 25% lanthanum, and small amounts of neodymium and praseodymium. It is used as a spark generator for cigarette lighters and welding torch igniters—an enduring use over many decades [22].

In the 1920s, praseodymium began to be used as a yellow–orange stain for ceramics and remains in use for this application today. Around the same time, neodymium began to be used to tint glass for both decorative use, and for industrial goggles for glassworkers and welders. It also remains in use for this purpose. General Electric's (GE) premium Reveal® light bulb line uses neodymium-tinted glass envelope to provide an improved color balance relative to other incandescent lamps. This use is rapidly being replaced by a new light-emitting diode (LED) version of the reveal product line.

All of these uses of rare earths (with the possible exception of welding goggles) may now be considered to be somewhat inessential, optional, or "boutique" applications that are either small in volume, easily replaced or have otherwise been made obsolete.

The 1960s, however, saw two new applications for rare-earth elements, in which unique benefits emerged from the electronic structure of the lanthanides. These are the first large-scale, initially nonsubstitutable uses for rare-earth materials. Zeolite catalysts for crude oil cracking, known as fluid cracking catalysts, or fluid cracking catalyst (FCCs), are stabilized by the addition of rare earths, and achieve significantly longer life as a result of the addition of yttrium and other rare earth elements. First-generation color televisions suffered from

poor color saturation because of the low output of the available red phosphors and the need to "mute" the green and blue phosphors to maintain a reasonable color balance. This changed with the discovery of a bright red phosphor, europium-doped yttrium orthovanadate, which was first adopted by Zenith Electronics, and then industry wide. The rare-earth mine at Mountain Pass, California, proved to be a good source for the elements in question, and critical uses for the rare earths were in place for the first time, although flat panel televisions and screens of various kinds make europium much less essential, today, and rare-earth-free FCCs are also now available.

Other uses of rare earths have come and gone, over time. Gadolinium gallium garnet single crystals, for example, were used as substrates for permanent computer memory chips based on the technology of magnetic bubbles in the 1970s and 1980s.

Current uses of the rare earths tend to focus particularly on the properties imparted by 4f electrons, which are traits unique to the lanthanides, and result in applications related to optical properties, magnetic properties, catalysis, and to some extent mechanical properties. Yttrium has a wide range of uses related to oxidation resistance, and rare earths are sometimes used to modify microstructures of major metal products, appearing as grain refiners for aluminum, for example. A partial list of current applications is provided in Table 1. In each of these applications, rare-earth elements are considered to be difficult or impossible to substitute. Particularly important and persistently unsubstitutable uses for the rare earths include europium, for red-emitting phosphors, terbium for green-emitting phosphors, and samarium and neodymium for high-strength permanent magnets.

Growth in the demand for rare earths is expected for coming years as a result of increasing dependence on advanced technologies, calling for increased production of display technologies; increasing electrification of mechanical devices, calling for more magnets to convert between electrical and mechanical work; increased use of solid-state lighting; and rapidly increasing numbers of consumers for these devices, worldwide [23].

Despite the challenges of maintaining a supply chain for rare-earth materials, new potential uses continue to emerge, and a partial list of these is provided in Table 2. It is likely, of course, that many of these technologies will fail to penetrate the market as a result of the usual barriers to commercialization (often characterized as the "valley of death"), but the challenges are increased in the case where an essential material is known to be critical in the sense described in this chapter, as this tends to deter interest from investors.

Even while the uses of rare-earth elements have grown in variety and volume, production has become localized. By the late 2000s, the world's production was around 140,000 t of contained rare-earth oxide, 97% of which were produced by China, after the closure of the Mountain Pass mine in 2002, with only very small quantities being sourced from the rest of the world (or ROW).

TABLE 1 Principal Current Uses of the Rare Earths

Element	Current Uses
Scandium	Structural alloys, medical lasers, metal-halide lamps
Yttrium	Phosphors, catalysts, propane gas mantles, oxygen sensors, structural metal alloys, structural ceramics, thermal barrier coatings, microwave filters, transducers, gemstones, pharmaceuticals, high-temperature superconductors
Lanthanum	Ni-M-H rechargeable batteries, lighter flints, electron emitters, fiber-optic glasses, scintillators for radiation detection, high-refractive index optics, abrasives, steels, welding, phosphors, phosphate control
Cerium	Structural metal alloys, polishing, fuel cracking catalysts, self-cleaning ovens, automotive catalytic converters, phosphors, pigment stabilization
Praseodymium	Pigments, magnets, structural metal alloys, lighting, welders' goggles, fiber-optic amplifiers, catalysts, lighter flints
Neodymium	Pigments, magnets, lasers, cryocoolers, fertilizers, automobile rear-view mirrors
Promethium	
Samarium	Magnets, cancer treatment, nuclear reactor control rods, IR absorbers
Europium	Phosphors
Gadolinium	Cancer treatment, neutron radiography, MRI contrast agents, neutron shielding, structural metal alloys
Terbium	Phosphors, magnets (vs. Dy), magnetostrictive actuators, SOFCs (vs. Y)
Dysprosium	Magnetostrictive actuators, thermal neutron absorbers, lasers, IR sources, metal-halide lamps, radiation dosimeters, catalysts, adiabatic refrigeration, additive in magnets
Holmium	Magnetic flux concentrators, neutron absorbers, lasers, fiber-optics, pigments, magnets (vs. Dy)
Erbium	Lasers, optical amplifiers, medical lasers, neutron absorbers, vanadium alloys, pigments for artificial gemstones, cryocoolers
Thulium	Portable X-ray sources, lasers (especially in surgery), radiation dosimeters, fluorescent anticounterfeiting banknote dyes
Ytterbium	Gamma-ray sources, stainless steels, lasers, fiber-optics
Lutetium	Metal alloys, catalysts, cancer treatment

TABLE 2 Potential and Emerging Uses of the Rare Earths

Element	Potential and Emerging Uses
Scandium	Lightweight high-strength structural materials
Yttrium	Increasing concentrations in next-generation YSZ
Lanthanum	Hydrogen storage
Cerium	Solid-oxide fuel cells, electronic applications (in fullerenes), magnets, structural metal alloys, catalysts
Praseodymium	Magnetic refrigeration
Neodymium	Downconversion of UV light to improve the efficiency of silicon solar cells
Promethium	
Samarium	Quantum computing, X-ray lasers, thermoelectrics
Europium	Quantum computing
Gadolinium	Magnetic refrigeration solid-oxide fuel cells
Terbium	SOFCs
Dysprosium	
Holmium	
Erbium	
Thulium	Pigments
Ytterbium	Ultra-high-precision clocks military pyrotechnics
Lutetium	Pigments, lithographic lenses, X-ray phosphors

While China often appears to be a single source from viewpoints in the ROW, it actually has a diverse group of suppliers that can be categorized in a number of different ways. The Association of Chinese Rare-Earth Industries counts about 350 corporations among its membership, across a spectrum of rare-earth producers and users. Production of rare earths in China comes from bastnaesite mining in Baotou, in Inner Mongolia, and from lateritic ion-adsorption clays located broadly in southern China. The bastnaesite ores are relatively richer in light rare earths, while the lateritic clay deposits are richer in the heavier ones. In either case, the ores always contain multiple rare-earth elements, which can be separated from each other or sold as mixed products such as mischmetal or didymium (a mixture of praseodymium and neodymium). The amounts of each element that are produced depend upon the geology of the mine, and typically do not match the market demand for the individual

elements. The mismatch between production and demand leads to a variety of challenges for the miners, and is a classic case of the difficulties presented by coproduction. Many of the mines in China are unlicensed operations, falling outside the control of the government, and are referred to as "illegal." By some estimates, up to 40% of China's production is illegal, although the Beijing government is making some efforts to establish greater control.

As illustrated in the case of the 2004 molybdenum price spike, without a clear view of the operation of Chinese commodity markets, actions taken by China are often hard to interpret and agendas or goals are ascribed to China by ROW pundits, based on reported actions. This leads to concerns about security of supply, and a degree of market nervousness. Starting in 2006, the Chinese government imposed export quotas on rare earths, and notably reduced the quotas by 40% in 2010, as Chinese domestic industries increased their utilization of these materials. One impact of the quotas was a marked differential between the prices of rare earths in China and the ROW, and the attention of various ROW governments was drawn to the issue as the prices of imported rare earths began to grow. The price history of the rare earths from the mid-2000s to the mid-2010s is illustrated in Fig. 2.

In September 2010, a Chinese fishing vessel collided with a Japanese Coast Guard patrol boat near the disputed islands in the East China Sea, known as Senkaku in Japan, and Diaoyu in China. The Chinese vessel, its captain and crew were arrested by the Japanese Coast Guard resulting in a diplomatic incident between the two nations. While it was widely reported that China cut off rare-earth exports to Japan in an effort to win the release

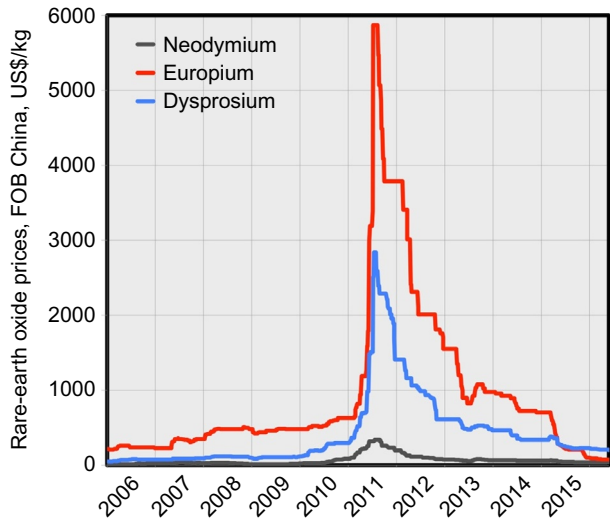

FIG. 2 The prices of three representative rare earths from 2006 to 2016. *Source of raw price data: Argus Media Inc. (direct.argusmedia.com).*

of its citizens, the full truth may be more complicated. Some diplomatic meetings were cancelled at this time, as often occurs in the wake of such incidents between nations, but China officially denies that any embargo was imposed. The reports of an embargo against Japan may have stemmed from the actions of an individual harbormaster in refusing to allow certain ships to sail, without any approval from the central government in Beijing. In any case, the perception in the ROW was that the Chinese had, indeed, imposed an embargo and buyers of rare earths, already nervous about the increasingly stringent export quotas, drove the prices to new highs. Neodymium prices eventually peaked in 2011, at around 10 times their precrisis prices and dysprosium prices at around 25 times.

The Chinese rare-earth export quotas and tariffs were eventually dropped in 2015, after the World Trade Organization ruled them illegal in response to a complaint filed jointly by the United States, the European Union, and Japan. The removal of the quotas and tariffs, however, had little observable impact on rare-earth prices, which by then had returned to within two or four times their precrisis lows.

The events of 2010 and 2011 notwithstanding, the world's immediate production capacity for rare-earth elements has grown very little, with the sole surviving addition of the Lynas Corporation's mine at Mount Weld, Australia, producing around 8000 t of rare-earth oxide per year. Heavy rare-earth production is arguably threatened as leaching operations some of the ionic clay deposits in China become less productive, and the Chinese government attempts to regain control of some of the unlicensed operations. In comparison with static or slowly growing supply, many projections suggest that demand for rare earths will continue to rise. The currently low prices, concerns about the accuracy of growth predictions, and the potential for price instability (in both directions) limit investment in new mining operations. Investors in mining projects face long payback times under good circumstances, with mine development and commissioning often taking as long as 15 years: uncertainty about the markets makes the time to achieve a return on investment seems potentially even longer.

2 RESOURCES, SUPPLY CHAINS, AND LIFE CYCLES

Rare earths are transformed from resources in the ground to components in final products in a series of steps that make up the rare-earth supply chain. The supply chain becomes a life cycle with consideration of what happens to rare earths after rare-earth-containing products reach the ends of their lives—that is, are the products, components or rare-earth raw materials reused, recycled, or disposed of as wastes.

The first step in the supply chain occurs prior to mining—basic geoscientific research, mineral exploration, and mine development. Research and exploration lead to the identification of rare-earth resources—using the word

resource in a narrower and more specialized sense than it commonly is used. A rare-earth resource here is the subset of all rare earths in the earth's crust that are known to exist with a high degree of certainty and might conceivably be developed into a mine at some point in the future. Resources are the result of mineral exploration, including sampling, drilling, and other activities that locate a mineral deposit and define its basic characteristics.

In advanced mineral exploration and then mine development, the best mineral resources become reserves—that is, mineralization that is known to exist in a geologic sense with an even higher degree of certainty than are resources and, moreover, that is capable of being mined for a profit with known technologies for extraction and recovery and current market conditions. Just as rare-earth resources are a subset of all the rare earths in the earth's crust, mineral reserves are a subset of resources. For any element, both resources and reserves change over time—declining as the result of mining, increasing as the result of mineral exploration and mine development. During mine development, a mineral deposit is prepared for mining through investment in infrastructure, extraction and recovery equipment, and other facilities necessary for mining. Think of reserves as the working inventory of rare earths that form the basis for mining.

Although rare earths appear in a large number of minerals, almost all production comes today from three of these minerals: bastnaesite, a carbonate mineral; monazite, a phosphate mineral; and lateritic, ion-adsorption clays, which are aluminosilicate minerals.

Different rare-earth deposits have widely differing rare-earth contents. Most bastnaesite and monazite deposits have relatively high concentrations of the lighter rare earths lanthanum and cerium. Most ion-adsorption clays are cerium-poor and relatively more enriched in the heavier rare earths, including yttrium.

The second step in the supply chain is mining and concentration. Mining, either underground or open pit, involves extracting ore containing from <1 to approximately 10% by weight rare-earth oxide or equivalent. This wide range in ore grades reflects the diverse nature of minerals that contain rare-earth elements. In concentration, ore is upgraded to concentrate, which contains 50–70% rare-earth oxide or equivalent for bastnaesite and monazite ores and greater than 90% for ion-adsorbed clay ores. The output of mining and concentration is a mixed rare-earth oxide, which is considered "mixed" because the concentrate contains a mixture of all the rare earths.

The third step in the supply chain is separation, necessary because almost all rare-earth uses require separated rare earths, either individual rare earths or sometimes mixtures of only two or three of the rare-earth elements. The output of this step in the supply chain is compounds of separated rare earths such as oxides, fluorides, nitrates, and carbonates. By industry convention, production usually is reported in terms of rare-earth oxide or equivalent, regardless of the exact chemical form of the output.

The fourth step is conversion to metals, alloys, and other intermediate products that are inputs to the manufacture of products and assemblies containing rare earths. The elements iron, nickel, magnesium, and copper, for example, are alloyed with rare earths.

The fifth step is manufacturing of products and use of these products by consumers.

The sixth step, disposition of material after a product reaches the end of its useful life, completes the rare-earth life cycle and includes reuse, recycling, and disposal.

2.1 Geography and Future Production

Data help illustrate the geography of rare-earth supply chains. Rare-earth resources, reserves, and mine production are concentrated in China. Documented, legal mine production in China accounted for some 85% of world production in 2015 (Table 3); the percentage would be larger if the several tens of thousands of tonnes of undocumented Chinese production were included. One Chinese iron-ore mine, Bayan Obo, produces rare earths as by-products, accounting for more than half of Chinese production capacity for rare earths [24]. One mine in Australia, Mount Weld, with about

TABLE 3 Mine Production and Reserves, 2015 (Metric Tons of Rare-Earth Oxide Equivalent)

	Mine Production	Reserves
Australia	10,000	3,200,000
Brazil	—	22,000,000
China	105,000[a]	55,000,000
India	NA	3,100,000
Malaysia	200	30,000
Russia	2500	Included in "other"
Thailand	2000	NA
United States	4100	1,800,000
Other	NA	41,000,000
Total	124,000	130,000,000

Notes: —, negligible or zero; NA, not available.
[a]*Excludes undocumented, illegal production.*
Source: U.S. Geological Survey, Mineral Commodity Summaries 2016, accessed May 11, 2016, minerals.usgs.gov.

10–15% of world production capacity, is the only significant non-Chinese producer of rare-earth ore and concentrate. Smaller amounts of production occur in India, Malaysia, Russia, and Thailand.

Chinese reserves account for 40–45% of estimated world reserves (Table 3), although many of the non-Chinese reserves likely are not commercially viable in 2016 but rather reflect reserve calculations made in 2012 and 2013 when rare-earth prices were substantially higher than in 2016. Compared to reserves, rare-earth resources are distributed more broadly worldwide (Figs. 3 and 4).

Looking to the future, data on reserves and resources provide clues about what new mines might come into production. Data for China are sufficiently limited that this chapter focuses only on possible new non-Chinese mines.

The Mountain Pass mine in the United States is a likely source of additional rare-earth production in the future. From the 1960s to the 1980s, it was the largest rare-earth mine in the world. It shut down in the early 2000s and reopened in 2012 following major investments in new processing and separations facilities. It closed in 2015, and the North American operations of the mine's owner, Molycorp, entered bankruptcy. In 2016, Molycorp's

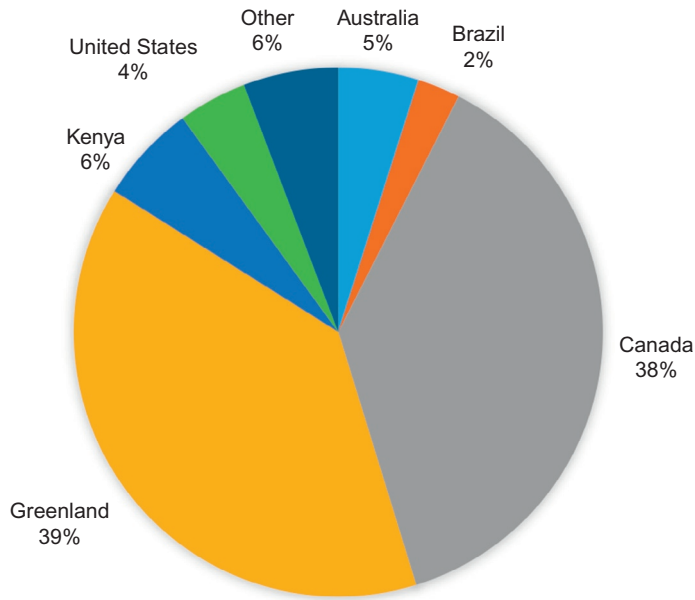

FIG. 3 Distribution of non-Chinese resources prepared according to recognized reporting guidelines (% of total). Notes: Recognized reporting guidelines include the Canadian 43-101, Australian JORC and South African SAMREC sets of guidelines. *Source: Prepared with data from Technology Metals Research, accessed May 11, 2016, techmetalsresearch.com. The data represent estimates collected in November 2015.*

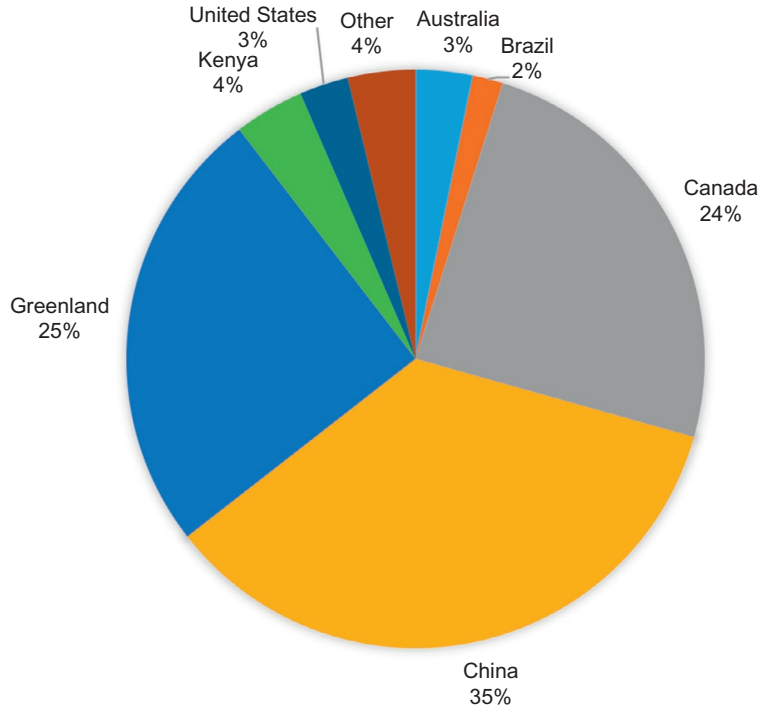

FIG. 4 Comparing Chinese reserves with non-Chinese resources (% of total). *Source: Chinese reserve data from U.S. Geological Survey as reported in Table 3. Non-Chinese resource data from Technology Metals Research as reported in Fig. 3.*

assets are being restructured, and ownership is changing. It is unclear whether the mine will be reopened or, alternatively, the new mine owners will liquidate the mine's assets. What is clear is that the mineral deposit and tailings (wastes) from previous mining contain significant quantities of bastnaesite and other rare-earth mineralization, which remain a likely source of production at some point in the future.

Additional new mining outside of China will require mine development of deposits for which some degree of mineral exploration already has occurred. More than 50 rare-earth deposits were explored sufficiently during and following the spike in rare-earth prices in 2010–2011 to allow for estimates of resources and in some cases reserves to be developed according to recognized guidelines such as the Canadian NI-43101 [25], Australian JORC [26], and South African SAMREC [27]; these resource and reserve estimates sum to more than 100 million metric tons of contained rare-earth oxide or equivalent [28]. Eight deposits in five countries have reserve estimates expressed in million tonnes (Mt) [24]:

1. Tanzania (Ngualla deposit), 0.94 in situ total rare-earth oxides (TREO) (Mt)
2. Australia (Browns Range, Nolans Bore, Dubbo Zirconia deposits), 0.87 in situ TREO (Mt)
3. Canada (Nechalacho Basal Zone and Kipawa deposits), 0.33 in situ TREO (Mt)
4. USA (Bear Lodge deposit), 0.18 TREO (Mt)
5. South Africa (Steenkampskraal deposit), 0.07 TREO (Mt)

These reserve estimates were developed when rare-earth prices were significantly higher than in early 2016. For these or other deposits to proceed to mine development and full-scale operation, developers need to, among other things:

- Demonstrate that the ore is capable of being converted into saleable products though pilot-plant testing and interactions with potential customers;
- Obtain the necessary preproduction permits and approvals from governments and local communities;
- Raise the necessary financial capital;
- Construct the mine and associated processing facilities;
- Start up the mine and processing facilities at a small scale, overcome the inevitable start-up challenges, and gradually increase the scale of operations.

Successfully achieving these preproduction requirements takes 2 or 3 years at a minimum. The Dubbo Zirconia deposit is the furthest along in these preproduction steps, having run a pilot plant for several years. Russian operations, primarily in the Kola peninsula, have produced about 2500 t of rare-earth oxide per year in recent years and have plans to renovate and develop their operations [29]. Most of the other non-Chinese projects with reserve or resource estimates are idled in early 2016 due to lack of funds or other problems. For example, the heavy rare-earth deposit of Nora Kärr, Sweden, was due to start operations in 2016–2017 but development of the project has been stalled due to environmental problems [30].

In addition to these mineral exploration and development projects, several nonconventional sources of rare earths are possible sources of rare earths as by-products over the longer term: deposits of heavy mineral sands, especially in Brazil, India, and the United States, which are mined today for titanium and zirconium; coal ash, a waste product from coal combustion; phosphate rock, the principal raw material for phosphorus used in fertilizers; and polymetallic base metal mines such as the Olympic Dam mine, Australia. All of these potential rare-earth sources produce something else as a principal product but contain large quantities of rare earths at very low concentrations.

At the height of the rare-earth crisis of 2010–2011, a great deal of interest emerged in recycling as a means of overcoming shortages. The Japanese government announced that it would develop “urban mining” of postconsumer

scrap to meet some of its needs, and many research efforts were also funded in Europe, to meet the same goals, effectively treating scrap as a new resource [31]. In practice, however, recycling faces severe economic challenges. Dahmus and Gutowski [32] have considered the question of "what gets recycled" and they conclude that simple objects (such as beverage cans) are economically recyclable, even if they have low value, but as the complexity of an object and its "material mixity" increases, recycling only occurs when the materials have proportionately higher value. Rare earths tend to be used in small quantities, in complex devices. The cost of collecting scrapped objects that contain rare earths, and separating the rare earths from the other materials, is often larger than the value of the materials that they contain. For more on recycling of rare earths, see Tanaka *et al*. [31].

Despite the evident challenges of recycling rare earths from scrapped devices like motors embedded in products like vehicles and appliances, there have been a few successes, largely in line with the findings of Dahmus and Gutowski.

Cerium oxide is widely used as an abrasive for polishing glass and silicon wafers, because it combines a mild chemical attack of the silicon with mechanical abrasion, resulting in excellent surface finish provided by "chemical mechanical polishing." Although technologies had been developed for recycling ceria polishing powders through the early 2000s, and polishing slurries are effectively very low-mixity materials, these methods were not widely applied before the rare-earth crisis at the end of the decade, as ceria was a very low-cost material and the capital expenditures (CAPEX) of recycling systems could not be justified. With the emerging concerns about the supply chain, and the fact that Chinese export quotas were initially applied to rare earths across the board; however, the recycling of ceria polishing powder became very widespread, and up to 80% reductions of demand were achieved in short order. This represents a destruction of demand that is arguably a negative result for the rare-earth mining industry, since cerium production exceeded demand, anyway.

A moderately low-mixity use of rare earths is in fluorescent lamp phosphors. These contain yttrium oxide (as a host material) doped with various compounds of europium (producing red light) and terbium (producing green). Europium and terbium are present at fairly low concentrations, but higher than in many ore bodies, and the separations challenge is much lower than it is for separating these from a typical ore body because of the absence of other rare-earth elements. Furthermore, fluorescent lamps are already recycled as a means of keeping mercury out of landfills, so a collection system was already in place. Lamp recyclers were excited about the prospect of a new revenue stream, and systems for extracting and separating the rare earths were developed by Global Tungsten & Powders (GTP) in the United States and Solvay in France. After a large effort to build a plant, GTP abandoned its project before commissioning, and although the Solvay process has been in operation

for some time, the operation is likely to be suspended by the end of 2016. The reasons for the failure of this effort are complex, and they include factors such as (1) the cost of disposal of the glass envelopes of the lamps; (2) the reluctance of lamp manufacturers to qualify the recycled materials for use in production, possibly because of the low volumes involved; and (3) the rapid decline in fluorescent lamp sales, resulting from the availability of lower-cost LED lamps, starting in 2013.

Yttria-stabilized zirconia (YSZ) is a tough ceramic material that is used as a thermal barrier coating for gas turbine blades, allowing them to operate in environments above the nominal melting temperatures of the base alloys. At a concentration of around 7 or 8 mol%, yttria use in this application is a small fraction of the world market, but technology advancements threaten to increase the yttria concentration up to as much as 50%. YSZ coatings are applied to turbine blades by plasma spraying, a process in which as much as 80% of the feedstock powder either bounces off or misses the target completely. This "overspray" material has traditionally been discarded as waste but, again, it is a low-mixity resource and according to the analysis of Dahmus and Gutowski, should be readily recyclable. Following a joint research effort between the Critical Materials Institute and the GE corporation, a process for reverting the overspray material for use as feedstock is now being adopted by GE.

It is unlikely that recycling of rare-earth elements from postconsumer scrapped devices like electric motors, hard disk drives, and LEDs will become economical at current price levels, or even at significantly higher prices unless the costs of collection and separation can be very significantly reduced. Umicore (Hoboken, Belgium) has developed a process to recycle rechargeable batteries, including Li-ion and NiLnH batteries: the process slag is sent to Solvay for rare-earth recovery and separation.

3 BARRIERS TO RARE-EARTH PRODUCTION

Estimated rare-earth reserves and resources, presented in the previous section, would last for more than 1000 years at current rates of production and use. Rare-earth resources outside of China, by themselves, would last for more than 800 years. Even allowing for demand growth, these are large numbers.

But they are misleading. Rare earths are not rare in a geologic sense. What is rare, and what creates barriers to greater production and use of rare earths, is technology for efficiently extracting, recovering, and converting rare earths in the ground into saleable products.

For all actual and potential producers of rare earths, in China and elsewhere, current methods of concentrating, separating, and converting rare earths to saleable products involve many steps, make substantial use of chemicals, are energy intensive, and can be highly polluting. Thus most of the rare earths contained in the resource estimates above are unlikely to be produced

without technological innovation that improves the technical efficiency of production, at lower costs with less environmental damage than at present.

From the narrower perspective of non-Chinese producers and users of rare earths, the barriers to rare-earth production are not just technical but also, more prosaically, economic and commercial in nature. Consider the rare-earth supply chain for NdFeB magnets (Table 4). For the first three steps in the supply chain—mining and concentration, separations, conversion to metals and alloys—the vast majority of existing production capacity is in China. Moreover, there is more production capacity in China than necessary to meet current rare-earth demands [33]. Although some of this excess capacity is slated to be closed, the lack of clarity about Chinese production capacity discourages potential non-Chinese producers from investing in new capacity because of the implied threat to use idled capacity should non-Chinese producers enter the market. Much Chinese rare-earth production comes as a by-product of iron-ore mining, which has inherently lower costs of rare-earth production than mines producing rare earths as principal products because of the sharing of costs among multiple products. Another barrier to entry for non-Chinese mines is the lack of downstream customers outside of China. Still another entry barrier outside of China is lack of intellectual capital outside of China;

TABLE 4 China's Role in the NdFeB Magnet Supply Chain and Barriers to a More-Diverse (non-Chinese) Supply Chain

Step in Supply Chain	% in China, 2015	Significant Barriers to Production Outside of China
Mining and concentration	80–85	– Market uncertainties and potential lack of downstream customers – Low-cost by-product mine production in China – Lack of intellectual capital – Apparent excess capacity in China
Separations	80–85	
Conversion of metals and alloys	>95	
Magnet manufacturing	>80	– Intellectual property for sintered NdFeB magnets held by Hitachi in Japan
Manufacturing of components	Not available	– Lack of secure upstream supply chain
Recycling	Not available	– Market uncertainties, including reluctance of manufacturers to use recycled material – Collection logistics and costs – Coproduction economics

Source: Adapted from U.S. Department of Energy, Quadrennial Technology Review 2015, http://energy.gov/qtr, accessed May 11, 2016.

most of the metallurgists with expertize and experience with rare earths are now in China.

Over time, these economic and commercial entry barriers for non-Chinese producers—excess capacity and inherently low-cost production in China, lack of intellectual capital outside of China—can be overcome, but the technical barriers to more efficient and more diversified production of rare earths remain.

4 RESEARCH EFFORTS AND NEEDS

The Critical Materials Strategy presented by the US Department of Energy [12] identifies three approaches that can be applied to reduce the criticality of any material. These are:

i. Source diversification
ii. Materials substitution
iii. Improved utilization of existing resources through improvements in manufacturing efficiency and end-of-use recycling.

Interestingly, it appears that exactly the same strategies were applied to the crisis in copper supply that accompanied the end of the Eastern Mediterranean Bronze Age. In the context of the rare earths, the three strategies have been applied with varying success to different sources and uses of the materials. There are also striking differences of research agenda emphasis depending on the location of the effort. Countries with rare-earth resources, such as Canada, Australia, and others, have a tendency to focus their research efforts on issues related to source diversification. Regions that are primarily users rather than producers (including the European Union and Japan) tend to focus more on substitution and recycling. In the United States, which has potential as a producer and a user of rare earths, the research strategy is more broadly based.

4.1 Source Diversification

Research and development efforts intended to promote source diversification generally fall into two categories: the identification and evaluation of new resources (typically through exploratory geology), and the development of new or improved technologies for extraction. As noted earlier, the number of rare-earth resources is not a limiting factor. Since the postcrisis collapse in rare-earth prices, however, investment funds for new mines have become increasingly difficult to find. New mines will eventually be established when the cost of producing rare earths is lower than the price that they command in the market place: if prices rise, then, source diversification can be expected to occur. If the cost of production can be reduced, then the establishment of new sources will occur at a lower price point, so much of the effort toward source diversification is actually addressed toward reducing mining costs.

As with any major production facility, the cost of operating a rare-earth mine has two primary components: CAPEX which are the costs of acquiring the land and building the mine's facilities. These costs are one-time expenditures that are amortized over the life of the mine. Operating expenditures (OPEX) are recurring costs for labor, energy, and consumables, which are broadly proportional to the amount of material produced. In the case of the rare-earth elements, consideration also needs to be given to the generation of revenue: rare-earth mines produce a range of different elements, and in most cases production levels are skewed very significantly to the lighter rare earths. While a mine may produce large amounts of cerium and lanthanum, however, there is not such a strong market for these elements, and the majority of the revenue typically comes from neodymium. If more uses can be found for the under-utilized elements, then more revenue can be generated, allowing the production of the critical rare earths. If cerium and lanthanum are not utilized, they are considered "by-products" that do not contribute to a mine's profits. If they are utilized, they become "coproducts" that have value. In some cases rare-earth mines have by-products that go beyond having no value, and generate actual costs. Typical rare-earth deposits have some concentration of thorium or uranium, and there can be considerable regulatory issues with handling these radioactive materials, and costs for disposing of them if they cannot be sold.

R&D opportunities that can assist in source diversification include efforts to reduce CAPEX, including work to reduce the amount of infrastructure needed to produce saleable goods. For rare-earth mines, a very large part of the CAPEX relates to the separation facilities, which have typically been based on solvent extraction technologies. In some cases, a solvent extraction system can have as many as 400 mixer-settler stages, and reductions in this footprint are an attractive research target—especially if the reduction can be achieved with a reduction in OPEX.

Even greater reductions in CAPEX can be achieved by avoiding the development of a new mine. Rare earths are found in many resources that would not typically be classified as rare-earth ores, albeit at much lower concentration than would be associated with a classical ore. Phosphate fertilizer production streams contain total concentrations of rare earths in the range of 500 ppm, but phosphate is produced in very large quantities. If existing phosphate mines can be accessed to produce rare earths, then the CAPEX for developing a mine is avoided, although the OPEX for extraction from a low concentration source may be higher than for a traditional rare-earth mine. Research on efficient methods to extract rare earths from phosphate production streams therefore has potential value. Similar considerations apply to the extraction of rare earths from sources such as geothermal brines, fly-ash from coal-fired power plants, "red mud" waste from the conversion of bauxite to alumina, and even to tailings heaps at rare-earth mines.

OPEX considerations for rare-earth extraction include efforts to improve the efficiency of beneficiation processes such as ore sorting and froth flotation, where relatively large impacts may be achieved at moderate cost. Improvements in separations technologies include enhancing the efficiency of solvent extraction, in addition to a number of completely new technologies from membrane solvent extraction, to electrolytic methods and others. While it has been the traditional practice to have a separation facility associated with a mine, there is current discussion about the possibility of building "toll" facilities that serve several mines. Such facilities must either operate a single flow sheet which will typically be under-optimized for any single ore body, or be easily reconfigurable to optimize themselves for the feed received for a given run, and significant research and development is needed to identify the best path forward.

Growing efforts are being applied to developing new uses for rare earths in oversupply situations, including the search for novel thermoelectric, magnetic, catalytic, and fluorescent applications for light rare-earth elements. A particularly encouraging development has been the emergence of a new class of Al–Ce–X alloys that is highly castable, strong, and heat resistant [34].

4.2 Materials Substitution

Just a few years after the cobalt crisis of 1978 deterred the use of Sm–Co permanent magnets, Nd–Fe–B magnets emerged not only as a replacement, but a significant improvement in many ways. This rather surprising outcome gives some hope that a new magnet material is out there, waiting to be discovered, and that, by extension, other uses of rare earths can be enabled by new, more easily obtained materials. The search for such materials is challenging, but is yielding some encouraging results.

While it is commonly accepted that it takes about 20 years to develop and commercialize a new material, there have been several initiatives to accelerate the process. These include the Materials Genome Initiative, which is effectively an effort to harness data-mining and advanced computational tools to identify candidate materials as rapidly as possible. The process of identifying candidate materials, however, is just the start of a process through which candidates are successively eliminated as they fail a series of tests including

- Thermodynamic stability
- Manufacturability
- Performance
- Durability
- System compatibility—does it interact with other components in the device?
- Safety and toxicity
- Supply-chain security
- Price

In addition to these, an additional, but arguably optional consideration is compatibility with existing processes. A new material that can be introduced into the manufacture of a device without changing the design of the device or the process used to make it—a "plug-in" replacement—is always more readily accepted than a new material that requires such changes. It is frequently possible to coarse-filter a list of candidate materials for the latter four items in the test list, simply by asking the end users of the material. Making this check early in the process can help the researcher to avoid much work on materials that would never be adopted by manufacturers, thus accelerating development. A simple depiction of the process of downselecting materials is provided in Fig. 5.

Following the rare-earth price spike of 2010–2011, there has been renewed interest in the discovery of new magnetic materials, and there has been renewed interest in producing magnetic materials that have been known in theory or practice, but for which no manufacturing method has been developed. Among the promising materials are the ordered phase of stoichiometric FeNi. While this is an excellent permanent magnet, it only forms below 347°C, and is therefore burdened by extremely slow kinetics. A challenge of a different kind is provided by iron nitride, which theoretically forms an excellent magnet, but decomposes rapidly during most processing schemes.

While these opportunities offer magnetic properties that may exceed those of $Nd_2Fe_{14}B$ and therefore represent "grand slam" substitutes, there are other opportunities. Fig. 6 shows the ranges of energy products provided by different classes of permanent magnet materials. There is a notable gap, from about 11 to 15 mega-gauss-oersteds and for applications that need strengths

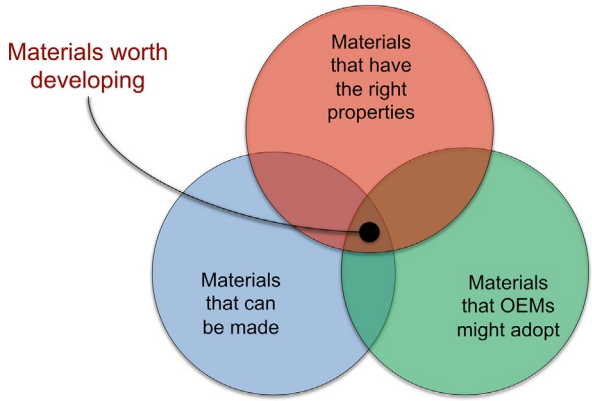

FIG. 5 The development of a new material is a process of eliminating all candidates, on the basis of three criteria: first, we find all materials that should *theoretically* embody the desired properties; second, we determine which of these materials can actually be made; and third, we consider which materials might actually be used after taking account of considerations of compatibility, reliability, toxicity, cost, etc. The key to rapid development is the earliest possible elimination of nonviable candidates.

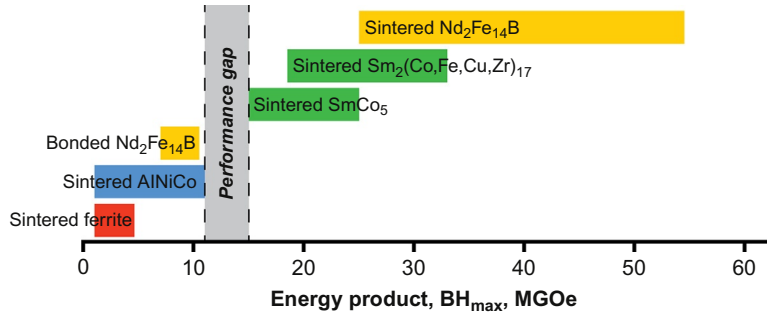

FIG. 6 Energy product ranges, BH_{max}, in units of mega-gauss-oersted, provided by different materials currently available for permanent magnets. Although the energy product is an important figure of merit for a magnet material, other measures of performance may be more important than the energy product, depending on the specific application.

in this range, rare-earth magnets have to be used, even though they are over-specified. The development of a material in the "gap" range would displace the rare-earth magnets from these applications, and make more available for the uses in which the properties of these magnets are truly necessary.

Compounding the need for new magnet materials, there are several trends in the use of magnets, which generate new requirements. Among these are the shrinking sizes of some devices such as microphones and loudspeakers used for personal electronics. The magnets in these are typically cut from larger blocks of material, and the fraction of the material that ends up as swarf grows larger as the magnets shrink. Alternative forms of magnet manufacturing, such as thin film formation and lithography start to become desirable, especially if very strong magnetic materials can be produced. Even at larger sizes, many devices such as motors, actuators, and generators can be made more efficient if more intricate magnet shapes can be produced, and there is therefore some interest in additive manufacturing of magnets, for which new processes and new materials will be required.

The search for new phosphors to replace terbium-based green light emitters and europium-based red light emitters is also challenged by ongoing technological change. New materials that are suitable replacements for fluorescent lamps are not necessarily (or perhaps not even likely to be) good phosphors for LEDs, which are rapidly taking over the lighting market. In its infancy, LED technology is also advancing at a noticeable pace and there is some likelihood that current broad-spectrum white light phosphors will be replaced with more efficient and tunable tri-band phosphors within a few years, and a number of other technologies such as organic LEDs (OLEDs) and light-emitting electrochemical cells are also on the horizon. With each new technology, there are new challenges for the materials, and fresh opportunities to commercialize new phosphors.

4.3 Improved Utilization of Existing Resources

As noted in Section 2, recycling has had limited impact on rare-earth supplies, largely as a result of the cost of extracting the materials from complex devices, such as a smart-phone, in which there are small quantities of the target materials, combined with large numbers of additional elements. In most cases, the cost of extracting rare earths from postconsumer waste is greater than the cost of extracting it from ore. Commercial success in recycling, therefore, depends largely on eliminating the costs that are specific to recycled materials: many of the processes used to recover materials from postconsumer waste are identical to those used in extraction from ores, and although reduction of these costs is helpful, in general, it does not advance recycling, per se.

The processes that distinguish recycling from mining are associated with collection and separation. Collection of sufficient quantities of recyclable material is a significant challenge that raises the cost, the energy budget, and the carbon footprint for recycling. Postconsumer scrap is particularly challenging in this regard. Large-scale use facilities represent a significant advantage over dispersed single users of a device, so as data servers that colocate hundreds of thousands of hard disk drives represent a better target than home or office computers. The separation of rare earths or other target metals from devices is also a major challenge, and there are two schools of thought on how to achieve this: in the first case, a device is shredded and the component materials are separated by physical and chemical processes; in the second case, the device is disassembled to some degree, allowing greater isolation of target-rich metals, such as the voice-coil magnets in hard disk drives, that can possibly even be reused rather than being recycled. Disassembly, however, comes at a cost and is most easily implemented when all of the devices are identical. For a mixed stream of scrap devices, shredding is usually the most economical approach, and although shredding devices that contain rare-earth magnets provides for relatively simple separation, it is not typically easy to extract the magnetized shards from a machine constructed of steel.

There are considerable opportunities to reduce the costs of collection and separation of postconsumer devices, across a range of social, regulatory, and engineering disciplines.

Compared to postconsumer recycling, in-process reuse of waste material is relatively simple and has lower costs, although the processes are not necessarily trivial. Examples include the reuse of ceria polishing powder and the reversion of YSZ plasma spray powder, described in Section 2, and also the remelting of swarf from magnet cutting and slicing. Other opportunities may exist, as do opportunities for reducing the amounts of such waste through the application of more material-efficient manufacturing processes, such as additive manufacturing.

4.4 Crosscutting Research

In many cases, research directed toward the economic opportunities outlined earlier requires underlying information in areas of basic physical science,

for the development of datasets and research tools. Work on environmental impacts also provides essential information regarding the ability to deploy particular technologies, and economic analysis underlies almost all decisions on which research to pursue.

5 SUMMARY AND CONCLUSIONS

Rare earths are the most recent group of elements to emerge in the category of critical materials. Because of their importance across a wide range of technological uses, the security of the supply chains for rare earths has raised great concerns, worldwide. Focused research and development efforts can reduce the level of criticality, but we are often faced with a set of shifting targets as new uses emerge and existing ones decline. In this environment, there is a great need to enhance the speed at which R&D can be transformed into commercialized materials or processes. Detailed understanding of the economics of rare-earth production and use are essential to identifying the most appropriate research opportunities.

ACKNOWLEDGMENTS

This work was supported by the Critical Materials Institute, an Energy Innovation Hub funded by the US Department of Energy, Office of Energy Efficiency and Renewable Energy, and Advanced Manufacturing Office.

ABBREVIATIONS

CAPEX	capital expenditures
FCC	fluid cracking catalyst
GE	General Electric
GM	General Motors
LED	light-emitting diode
OLED	organic light-emitting diode
OPEX	operating expenditures
ROW	rest of the world
TREO	total rare-earth oxide
YSZ	yttria-stabilized zirconia

REFERENCES

[1] National Research Council (U.S.), Committee on Critical Mineral Impacts on the U.S. Economy, National Research Council (U.S.), Committee on Earth Resources, National Research Council (U.S.), Board on Earth Sciences and Resources, National Research Council (U.S.), Division on Earth and Life Studies, Minerals, Critical Minerals, and the U.S. Economy, National Academies Press, Washington, DC, 2008.

[2] T.E. Graedel, R. Barr, C. Chandler, T. Chase, J. Choi, L. Christoffersen, E. Friedlander, C. Henly, C. Jun, N.T. Nassar, D. Schechner, S. Warren, M.Y. Yang, C. Zhu, Methodology of metal criticality determination, Environ. Sci. Technol. 46 (2012) 1063–1070.
[3] N.T. Nassar, X.Y. Du, T.E. Graedel, Criticality of the rare earth elements, J. Ind. Ecol. 19 (2015) 1044–1054.
[4] APS Panel on Public Affairs and the Materials Research Society, Report: "Energy Critical Elements: Securing Materials for Emerging Technologies", APS, Washington, DC, 2011.
[5] R. Moss, E. Tzimas, P. Willis, J. Arendorf, P. Thompson, A. Chapman, N. Morley, E. Sims, R. Bryson, J. Pearson, E.L. Tercero, F. Marscheider-Weidemann, M. Soulier, A. Lüllmann, C. Sartorius, K. Ostertag, Critical Metals in the Path Towards the Decarbonisation of the EU Energy Sector, European Union, Luxembourg, 2013.
[6] R. Silberglitt, J.T. Bartis, B.G. Chow, D.L. An, K. Brady, Report: "Critical Materials: Present Danger to U.S. Manufacturing", Rand Corporation, Santa Monica, California, 2013.
[7] J. Adams, Remaking American Security: Supply Chain Vulnerabilities and National Security Risks Across the U.S. Defense Industrial Base, Alliance for American Manufacturing, Washington, DC, 2013.
[8] D.R. Wilburn, Report: "Byproduct Metals and Rare-Earth Elements Used in the Production of Light-Emitting Diodes—Overview of Principal Sources of Supply and Material Requirements for Selected Markets", U.S. Department of the Interior, Reston, Virginia, 2012.
[9] Ad Hoc Working Group on Defining Critical Raw Materials, Report: "Report on Critical Raw Materials for the EU", European Commission, Brussels, 2014.
[10] Federal Ministry of Economics and Technology, Report: "The German Government's Raw Materials Strategy: Safeguarding a Sustainable Supply of Non-Energy Mineral Resources for Germany", German Federal Government, Berlin, 2010.
[11] Minerals UK Center for Sustainable Mineral Development. Risk List 2015. http://www.bgs.ac.uk/mineralsuk/statistics/risklist.html, British Geological Survey, Accessed June 23, 2016.
[12] U.S. Department of Energy, Report: "Critical Materials Strategy", U.S. Department of Energy, Washington, DC, 2011.
[13] M. Otte, Vers la Préhistoire: Une Initiation, De Boeck, Brussels, 2007.
[14] O.T.P.K. Dickinson, The Aegean Bronze Age, Cambridge University Press, Cambridge, 1994.
[15] E.H. Cline, 1177 B.C. The Year Civilization Collapsed. Turning Points in Ancient History, Princeton University Press, Princeton, 2014. p. 1 online resource (260 p.).
[16] H. Onodera, Y. Yamaguchi, H. Yamamoto, M. Sagawa, Y. Matsuura, H. Yamamoto, Magnetic-properties of a new permanent-magnet based on a Nd-Fe-B compound (Neomax). 1. Mössbauer study, J. Magn. Magn. Mater. 46 (1984) 151–156.
[17] R.Q. Barr, Molybdenum statistics and technology 1979, J. Met. 32 (1980) 60–63.
[18] U.S. Geological Survey, Report: "Mineral Commodity Summaries", U.S. Department of the Interior, Washington, DC, 2016. accessed June 23 http://minerals.usgs.gov/minerals/pubs/mcs/2004/mcs2004.pdf.
[19] Casey Research, Report: "Molybdenum's Perfect Storm", Casey Research, Delray Beach, FL, 2005.
[20] G. Gunn, Critical Metals Handbook, Wiley, Chichester, England, 2014.
[21] U.S. Geological Survey, Report: "Mineral Commodity Summaries", U.S. Department of the Interior, Washington, DC, 2016. accessed June 23, 2016. http://minerals.usgs.gov/minerals/pubs/mcs/2016/mcs2016.pdf.
[22] E. Greinacher, History of rare earth applications, rare earth market today, in: K.A. Gschneidner Jr. (Ed.), ACS Symposium Series, vol. 164, American Chemical Society, Washington, DC, 1981, pp. 3–17.

[23] H. Kharas, Report: "The Emerging Middle Class in Developing Countries", OECD Development Center, Paris, 2010.
[24] Adamas Intelligence. Rare Earth Market Outlook: Supply, Demand and Pricing from 2014–2020, Adamas Intelligence, Sudbury, Ontario, Canada, 2014 and 2015 update.
[25] Canadian Institute of Mining Metallurgy and Petroleum. National Instrument 43-101: Standards of Disclosure for Mineral Projects. http://web.cim.org/standards/MenuPage.cfm?sections=177,181&menu=229, Canadian Institute of Mining, Metallurgy and Petroleum. Accessed June 16, 2016.
[26] Joint Ore Reserves Committee. The Australasian Code for Reporting of Exploration Results, Mineral Resources and Ore Reserves. http://www.jorc.org/index.asp, accessed June 16, 2016.
[27] Samcodes Standards Committee. The South African Code for the Reporting of Exploration Results, Mineral Resources and Mineral Reserves. http://www.samcode.co.za, accessed June 16, 2016.
[28] Technology Metals Research. TMR Advanced Rare-Earth Projects Index. http://www.techmetalsresearch.com/2015/11/october-2015-updates-to-the-tmr-advanced-rare-earth-projects-index/, accessed June 16, 2016.
[29] Roskill Information Services, Report: "Rare Earths: Market Outlook to 2020", Services RI, London, 2015.
[30] Tasman Metals Ltd. Tasman Announces Date of Annual and Special Meeting of Shareholders and Provides Additional Update on Norra Karr Mining Lease (Press release). http://www.tasmanmetals.com/s/NewsReleases.asp?ReportID=754553&_Type=News-Releases&_Title=Tasman-Announces-Date-of-Annual-and-Special-Meeting-of-Shareholders-and-Pro, Tasman Metals Ltd. Accessed July 7, 2016.
[31] N. Tanaka, T. Oki, K. Koyama, H. Narita, T. Oishi, Recycling of rare earths from scrap, in: J.C.G. Bünzli, V.K. Pecharsky (Eds.), Handbook on the Physics and Chemistry of Rare Earths, vol. 43, Elsevier, Oxford, 2013, pp. 159–211.
[32] J.B. Dahmus, T.G. Gutowski, What gets recycled: an information theory based model for product recycling, Environ. Sci. Technol. 41 (2007) 7543–7550.
[33] Roskill Information Services, Rare Earths: Market Outlook to 2020, 15th ed., Roskill Information Services, London, 2015.
[34] Z.C. Sims, D. Weiss, S.K. McCall, M.A. McGuire, R.T. Ott, T. Geer, O. Rios, Cerium based intermetallic strengthened aluminum casting alloy: high volume co-product development, JOM 68 (2016) 1940–1947.

Chapter 284

Theory of Rare-Earth Electronic Structure and Spectroscopy

Michael F. Reid[1]

University of Canterbury, Christchurch, New Zealand
The Dodd-Walls Centre for Quantum and Photonic Technologies, Dunedin, New Zealand
The MacDiarmid Institute for Advanced Materials and Nanotechnology, Wellington, New Zealand
[1]*Corresponding author: e-mail: mike.reid@canterbury.ac.nz*

Chapter Outline

1 INTRODUCTION

This chapter gives a perspective on current understanding of electronic energy levels and transition intensities of rare-earth ions, in a condensed matter environment, either solid state or solution. The intention is not to give a detailed history, but to put current understanding into a somewhat historical perspective. This perspective is shaped by my participation in the field from the late 1970s. My description of earlier times is based on what I found important to my understanding and on personal interactions with many of the key people mentioned in this chapter.

Handbook on the Physics and Chemistry of Rare Earths, Vol. 50. http://dx.doi.org/10.1016/bs.hpcre.2016.09.001

The theoretical techniques that matured during the 1960s, and were refined in subsequent decades, were important in the development of laser, phosphor, and scintillator materials that are currently ubiquitous, and one might speculate that modern developments will be important for new applications such as quantum information and bioimaging.

There are many reviews of different aspects of the theory of rare-earth spectroscopy, including a number of articles in this handbook [1–3], and it is not the intention of this article to cover all of the details.

Early work on crystal-field theory, beginning with Bethe's 1929 article [4], assumed that the effect of the crystal was due to electrostatic interactions. Though this assumption was later shown to be highly inaccurate, this work was notable in establishing the importance of the application of point group theory in spectroscopy, allowing the analysis of complex spectra. The 1940s and 1950s saw steady development of theory, with applications not only to optical and magnetic susceptibility data, but also to magnetic resonance [5].

A key factor that drove the development of the "standard model" of crystal-field theory for the $4f^n$ configuration was high-quality optical spectral data, from laboratories such as Dieke's [6]. These data provided enough spectroscopic information to make accurate calculations both possible and worthwhile. At the same time, developments in computer technology made calculations requiring the diagonalization of large matrices tractable.

The theoretical developments led to two key advances:

1. A Hamiltonian that allowed accurate explanations of energy levels.
2. A transition-intensity model that was also crucial to optical applications development.

This chapter will review those models and discuss some recent advances in parametrization techniques and ab initio calculations.

2 ENERGY LEVELS

The "crystal-field" model is often misunderstood. It is early origins in calculations that treated crystals as an array of point charges has obscured the generality of the method. We have come to understand the crystal-field model as a particular case of an "effective Hamiltonian." Effective Hamiltonians and effective operators are defined within a *model space* M. For our purposes the model space will often be the $4f^n$ configuration, sometimes supplemented by the $4f^{n-1}5d$ configuration.

Suppose that the eigenvalue equation for the full Hamiltonian H is given by:

$$H|a\rangle = E_a|a\rangle. \tag{1}$$

The aim is to define an *effective Hamiltonian* H_{eff} that gives identical *eigenvalues* E_a for model-space eigenstates $|a_0\rangle$, i.e.

$$H_{\text{eff}}|a_0\rangle = E_a|a_0\rangle. \tag{2}$$

The spin Hamiltonians used in EPR analyses [5] are examples of effective Hamiltonians. In the simplest spin-Hamiltonian case, any doublet can be treated as if it has a spin of 1/2. Clearly, in that case the "effective spin" quantum numbers are not the physical quantum numbers of the electrons, though they can be related (see Sections 2.3 and 2.4).

An effective Hamiltonian may be related to the full Hamiltonian by a linear-algebra transformation between the full space and model space. Effective operators (such as an effective dipole moment operator—see Section 3.2) may also be defined. For further details see appendix A of [7].

2.1 Free-Ion and "Crystal-Field" Interactions

The effective Hamiltonian acting within the $4f^n$ configuration is commonly written [8]:

$$H_{\text{eff}} = E_{\text{avg}} + \sum_{k=2,4,6} F^k f_k + \zeta_f A_{\text{so}} + \alpha L(L+1) + \beta G(G_2) + \gamma G(R_7) + \sum_{i=2,3,4,6,7,8} T^i t_i + \sum_{h=0,2,4} M^h m_h + \sum_{k=2,4,6} P^k p_k + \sum_{k=2,4,6} B_q^k C_q^{(k)}. \quad (3)$$

E_{avg} is the energy difference between the ground-state energy and the configuration center of gravity (barycenter) and is included to allow the ground-state energy to be set to zero. The Coulomb interaction between the 4f electrons is parametrized by the radial electrostatic integrals, F^k, which multiply the angular part of the electrostatic interaction, f_k. The coupling of the electron spin magnetic moment and the magnetic field originating in the orbital motion of the electron is represented by the spin–orbit coupling constant, ζ_f, which multiplies the angular part of the spin–orbit interaction, A_{so}.

Higher-order terms in the Hamiltonian include two-electron Coulomb correlation contributions represented by parameters α, β, and γ, and three-electron Coulomb correlation contributions are parametrized by the T_i. The M^h and P^k parametrize higher-order spin-dependent effects. Though their effects are subtle, the introduction of these parameters was essential. Without the two- and three-body correlation effects and higher-order magnetic effects, errors in the treatment of the free-ion part of the Hamiltonian make it impossible to fit the crystal field accurately. In complex systems the J multiplets can even be in the wrong order [9]. Judd's analysis of the three-body operators [10] showed that some of the parameters could be eliminated, since they would only have contributions at third order in perturbation theory. This reduction in the number of parameters was crucial in making parameter fits tractable.

The terms in the Hamiltonian that represent the nonspherical part of the interaction with the crystal are modeled using the so-called crystal-field Hamiltonian. It is important to recognize that this Hamiltonian is not restricted to electrostatic effects, which are only a fraction of the total

crystal-field effect [11]. When the parameters are fitted to experimental energies, their values reflect all one-electron nonspherical interactions. The crystal-field Hamiltonian is expressed in Wybourne [12] notation as

$$H_{\mathrm{cf}} = \sum_{k,q} B_q^k C_q^{(k)}, \tag{4}$$

where the B_q^k parameters define the one-electron crystal-field interaction and the $C_q^{(k)}$ are spherical tensor operators for the $4f^n$ configuration. For f^n configurations, $k = 2$, 4, 6, and q values for which the parameters are nonzero depend upon the site symmetry of the rare-earth ion in the host lattice. The total number of crystal-field parameters ranges from 27 parameters for C_1 or C_i symmetry, down to only two parameters for octahedral or cubic symmetry.

Most calculations use basis vectors of the form $|\alpha SLJM\rangle$, where the last four labels are the total spin angular momentum, total orbital angular momentum, total angular momentum, and the projection of the total angular momentum along the quantization axis. The label α distinguishes basis states with the same SL quantum numbers. These extra labels are defined by the group theory developed by Racah, and the calculation of matrix elements make use of these powerful techniques (see, for example, [12, 13]).

The Hamiltonian parameters may be fitted to the energies of the sharp transitions within the $4f^n$ configuration, e.g., see [1, 7, 8]. The largest splittings are caused by the Coulomb interaction, which splits the configuration into SL terms separated by the order of 10^4 cm^{-1}. The spin–orbit interaction splits these terms into SLJ multiplets separated by the order of 10^3 cm^{-1} and mixes states with different S and L quantum numbers. Finally, the crystal-field interaction splits the multiplets in to mixtures of the $|\alpha SLJM\rangle$ basis states, split by order of 10^2 cm^{-1}.

The crystal-field parameters vary between crystals, since they depend on the site symmetry and the nature of other ions in the crystal. However, the free-ion interactions, and therefore the positions of the multiplets, are almost independent of the crystal. Since the crystal field generally splits the J multiplets by less than their separation, it is useful to construct, a "Dieke" or "Dieke-Carnall" diagram for the entire series of trivalent ions to give an overview of the energy levels of the $4f^n$ configuration (Fig. 1). Studies such the exhaustive analysis of rare-earth ions in LaF_3 by Carnall and coworkers [8] show that both free-ion and crystal-field parameters have systematic trends across the series.

2.2 The $4f^{n-1}5d$ Configuration

The crystal-field model for the $4f^{n-1}$ configuration may be extended in a straightforward way to the higher-energy $4f^{n-1}5d$ configuration. Early calculations [14] for this configuration date back to the 1960s, on divalent ions, where the $4f^{n-1}5d$ configuration has lower energy than in trivalent ions.

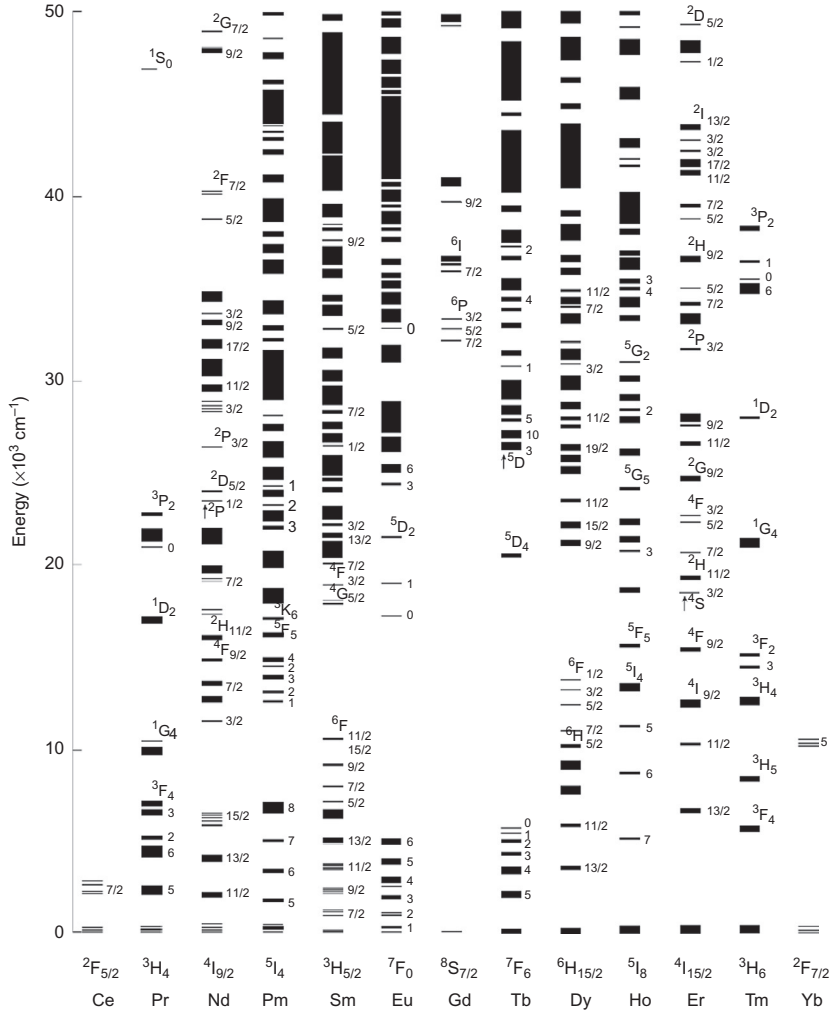

FIG. 1 Dieke diagram for trivalent rare-earth ions in LaF_3, after [7, 8]. The configurations range from $4f^1$ (Ce^{3+}) to $4f^{13}$ (Yb^{3+}). The *lines* indicate the energies of the multiplets, with the widths of the *lines* representing the crystal-field splittings of the multiplets.

However, it was the availability of vacuum ultraviolet synchrotron sources, and the investigation of wide band-gap materials such as fluorides, that generated enough data to make detailed analysis across the series possible [15, 16].

For the $4f^{n-1}5d$ configuration we must add 5d spin–orbit and crystal-field parameters, the direct (F) and exchange (G) Coulomb interaction between the f and d electrons, and a parameter Δ_E(fd) representing the average energy difference between the configurations. The additional terms are [3]:

$$H_{\mathrm{d}} = \Delta_E(\mathrm{fd}) + \sum_{k=2,4} F^k(\mathrm{fd}) f_k(\mathrm{fd}) + \sum_{k=1,3,5} G^k(\mathrm{fd}) g_k(\mathrm{fd}) + \zeta_d A_{\mathrm{so}}(\mathrm{d}) + \sum_{k=2,4,} B_q^k(\mathrm{d}) C_q^{(k)}(\mathrm{d}). \tag{5}$$

Transitions between the $4f^n$ and $4f^{n-1}5\mathrm{d}$ configurations are vibronically broadened, so detailed fitting is not possible, and a mixture of atomic calculations and fitting "by eye" has been used in most cases [3].

Since the $5d$ orbitals are much more extensive radially than the $4f$ they interact more strongly with the ligands, and the crystal-field parameters are generally about 40 times larger. Whereas for $4f^n$ the crystal-field is a small perturbation, for $4f^{n-1}5\mathrm{d}$ it is comparable with the Coulomb interaction, and dominates the spectra.

2.3 Hyperfine Calculations

Hyperfine interactions between the electronic and nuclear states give small splittings which generally require high-resolution techniques to measure. Analysis is typically done with spin Hamiltonians, as in EPR analyses [5, 17]. However, tensor-operator techniques may be used to derive additions to the Hamiltonian that may be simply applied to all transitions (see, for example, [18–21]). This approach has the advantage that it is not necessary to fit spin-Hamiltonian parameters for each electronic level separately. If spin-Hamiltonian parameters are required, they may be derived from the crystal-field calculation.

2.4 Magnetic Fields and a Solution to the Low-Symmetry Problem

The effects of magnetic fields are an important diagnostic tool, and, along with hyperfine interactions, crucial to applications such as quantum information [22, 23].

Early optical work concentrated on the magnetic-splitting g values along particular directions. In high-symmetry crystals measurements along one or two directions, typically parallel and perpendicular to the symmetry axis, are enough to completely determine the magnetic response. However, in low symmetries this is not the case. High-resolution laser experiments may be used to generate rotation curves for the magnetic splittings, and hence determine the g tensors describing the magnetic properties of the ground and excited states [17], analogous to EPR analyses [5].

The fitting of crystal-field parameters to systems with low site symmetries is a difficult problem. In the complete absence of symmetry there are 27 crystal-field parameters (including real and imaginary parts), and it is not possible to determine them from energy-level data alone. Not only do rotations of the axes lead to the same energy levels [24], but the energy levels

are often not sensitive to the phases of off-diagonal matrix elements. For this reason, many crystal-field analyses use a higher symmetry than the actual site symmetry. For example, for LaF_3 it is usual to restrict the parameters to be real [8], equivalent to using C_{2v}, rather than the actual C_2, symmetry.

Recent work by Horvath and coworkers [25, 26] has demonstrated a way forward. By adding magnetic splitting data to the fitting process, it is possible to determine parameters even in such low-symmetry crystals such as yttrium orthosilicate (YSO), which is an important material for quantum-information applications [22, 23]. What makes this approach tractable is that the magnetic splitting data for each electronic level contains significant geometric data. In low symmetries each g tensor has six independent components [5]. Adding this magnetic splitting data for several electronic states can give enough information to uniquely determine the crystal-field parameters.

2.5 Extending and Simplifying the Analysis

There are many interesting effects and analyses that we do not have space to cover here. For example, in the late 1960s it became clear that correlation effects could give rise to two-body crystal-field interactions, which give additional parameters [27–29], and additional insight into electronic structure.

In some cases simple models can be extremely powerful. In the early 2000s Dorenbos realized that it was possible to develop parametrizations for key energies, such as the lowest energy of the $4f^{n-1}5d$ configuration [30, 31]. These analyses are possible because the free-ion parameters are almost independent of the host, and the crystal-field and free-ion parameters have predictable trends across the series (with the 5d parameters varying much less than 4f). Consequently, from measurements for one ion, it is possible to predict the values for other ions.

3 TRANSITION INTENSITIES

In 1962 Judd [13] and Ofelt [32] published detailed analyses of transition probabilities within the $4f^n$ configuration. The first applications were to total intensities of transitions between J multiplets. However, Axe [33] examined transitions between crystal-field levels soon after, and also did the first calculations for two-photon processes [34]. In the absence of an odd-parity interaction with the crystal, electric dipole transitions within the $4f^n$ configuration are forbidden. Early work considered only the mixing of atomic configurations by the crystal field but subsequent work, summarized in [35], indicated that excitations involving ligand states (dynamic polarization and charge transfer) were also important. Over the following decades, significant progress was made in both phenomenological modeling, and the understanding the underlying mechanisms, for both one-photon [2, 36–38] and two-photon transitions [39, 40]. Here we provide a brief overview. Further details may be found in [37, 38].

Spectroscopic experiments measure observables such as oscillator strengths, absorption cross-sections, branching ratios, and radiative lifetimes. These observables may, in principle, be calculated from squares of matrix elements of electric dipole, magnetic dipole, and higher-order operators. A comprehensive discussion of these basic principles may be found in [38, 41–43].

The electric dipole operator is

$$-eD_q^{(1)} = -erC_q^{(1)}, \tag{6}$$

and the magnetic dipole operator

$$M_q^{(1)} = \frac{-e\hbar}{2mc}\left(L_q^{(1)} + 2S_q^{(1)}\right). \tag{7}$$

In these equations $C_q^{(1)}$ is a spherical tensor operator and r is the distance from the origin. The other operators and physical constants have their usual meanings. We consider only electric dipole and magnetic dipole transitions in what follows. Electric quadrupole contributions to the transition intensities are also possible [44] but are usually too small to be significant.

For linearly polarized light there is no interference between electric dipole and magnetic dipole moments, so the observables may be evaluated by adding the contributions fro m electric and magnetic dipole strengths. However, for circularly polarized light interference is possible, leading to circular dichroism and circularly polarized luminescence [38, 45, 46].

Derivations of the selection rules for optical transitions may be found in many references [2, 12, 42, 43, 47, 48]. For a recent discussion see [38].

The initial and final states need not be pure electronic states, but may be combinations of electronic and vibrational (vibronic) states. If the vibrational part of the wavefunction does not change during the transition then it may be ignored. However, if it does change then it is necessary to use wavefunctions that include both electronic and vibrational parts.

There are two particular cases of interest. The first case applies to transitions within the $4f^n$ configuration. In this case the coupling to the lattice is almost identical for the initial and final states. As a result, vibronic transitions are weak, and generally only become important for centrosymmetric systems, where purely electronic electric dipole transitions are forbidden. The other case applies to transitions between the $4f^n$ configuration and the $4f^{n-1}5d$ configuration or charge-transfer states. In this case the coupling to the lattice is very different for the initial and final states and transitions may involve a change of several quanta of vibration. For details the reader is referred to section 2.2.3 of [38] and other references, such as [49, 50].

3.1 Allowed Electric and Magnetic Dipole Transitions

Magnetic dipole (MD) transitions within the $4f^n$ configuration and electric dipole (ED) transitions between the $4f^n$ and $4f^{n-1}5d$ configurations are

allowed by parity selection rules [38], so it is relatively straightforward to calculate the intensities. As discussed earlier, for transitions between the $4f^n$ and $4f^{n-1}5d$ configurations there is considerable vibronic broadening. In many cases it is adequate to represent this by a Gaussian function, though more sophisticated approaches are also possible [49, 50].

3.2 One-Photon Transitions Within the $4f^n$ Configuration

As in the case of energy-level calculations, most analyses of ED transitions within the $4f^n$ configuration rely on parametrization schemes, making use of effective operators and perturbation theory. Here we will concentrate on some key issues. The reader is referred to [37, 38], and references therein, for further details.

The electric dipole moment vanishes between pure $4f^n$ states, so instead of the dipole moment operator $D_q^{(1)}$ an *effective* dipole moment operator is required. This may be derived from a perturbation expansion for a general effective operator:

$$D_{\mathrm{eff},q} = D_q^{(1)} + D_q^{(1)} \sum_{\beta \notin \mathrm{M}} \frac{|\beta\rangle\langle\beta|V}{E_0 - E_\beta^{(0)}} + \sum_{\beta \notin \mathrm{M}} \frac{V|\beta\rangle\langle\beta|}{E_0 - E_\beta^{(0)}} D_q^{(1)} + \cdots \tag{8}$$

In this equation the $|\beta\rangle$ are excited states on the rare-earth *or* ligand. This operator is evaluated within the $4f^n$ model space (M). In this case, the first-order term, $D_q^{(1)}$, vanishes because this odd-parity operator cannot connect states of the same parity.

As discussed in appendix A of [7], and [51], the denominators in the two summations in Eq. (8) are equal term by term and the effective operator is Hermitian. Time-reversal and Hermiticity symmetry restricts the one-electron phenomenological crystal field to even-rank operators (see, for example, chapter 1 of [7] and [52]). The same argument may be applied to the effective dipole moment operator, so only even-rank operators are required to parametrize the one-electron, spin-independent, part of the effective dipole moment operator. Since they are one-electron operators for the $4f^n$ configuration, with $l = 3$ the rank of the effective operators is restricted to be less than or equal to 6.

3.3 Transitions Between Crystal-Field Levels

Judd [13] and Ofelt [32] derived parametrizations based on the perturbation-theory expansion (Eq. (8)). An adaption of their parametrization by Reid and Richardson [53, 54] is now in common use. The effective electric dipole moment operator is written as

$$D_{\mathrm{eff},q} = \sum_{\lambda,t,p} A_{tp}^{\lambda} U_{p+q}^{(\lambda)} (-1)^q \langle \lambda(p+q), 1-q | tp \rangle, \tag{9}$$

with $\lambda = 2, 4, 6$, $t = \lambda - 1, \lambda, \lambda + 1$ and p restricted by the site symmetry. In this expression, t and p are the angular momentum labels for the odd-parity potential felt by the rare-earth ion, q is the polarization of the light, and λ and $p + q$ are the angular momentum labels for the operator that acts on the 4f electrons. Under the superposition approximation (Section 4), which is implicit in the point-charge potentials considered by Judd and Ofelt, parameters with $t = \lambda$ are zero.

Eq. (8) indicates that the effective dipole moment arises from coupling the dipole moment operator $D_q^{(1)}$ with the perturbation operator V. Since the perturbation is a scalar of the site symmetry, the A_{tp}^{λ} are nonzero only if $|tp\rangle$ (or linear combinations of $|tp\rangle$) transforms as the identity irreducible representation of the site symmetry group. Eq. (9) emphasizes the coupling between the perturbation (transforming as $|tp\rangle$), and the dipole moment operator (transforming as $1q$) to give an effective operator (transforming as $|\lambda(p + q)\rangle$).

3.4 Transitions Between *J* Multiplets

The vast majority of transition-intensity analyses are for measurements of total J-multiplet to J-multiplet transitions, at room temperature, and often in solutions. Judd [13] showed that in these cases the intensities may be fitted to a three-parameter linear model, which is straightforward to apply. The standard parameters are now labeled Ω_λ, with $\lambda = 2, 4, 6$ [2, 35]. Consider transitions from an initial multiplet $|\alpha_I J_I\rangle$ to a final multiplet $|\alpha_F J_F\rangle$. If all components of the initial multiplet are assumed to be equally populated (a good approximation at room temperature) then it is possible to average over all polarizations, sum the dipole strength over the M components of the multiplets, and use the orthogonality of $3j$ symbols to derive an expression for the dipole strength proportional to

$$\sum_{\lambda} \Omega_\lambda \langle \alpha_F J_F \| U^{(\lambda)} \| \alpha_I J_I \rangle^2, \tag{10}$$

with

$$\Omega_\lambda = \sum_{t,p} \frac{1}{2\lambda + 1} \left| A_{tp}^{\lambda} \right|^2. \tag{11}$$

Note that the reduced matrix elements in Eq. (10) are “intermediate-coupled”, i.e. the eigenvectors of the free-ion Hamiltonian have been calculated and the matrix elements are taken between these eigenvectors.

The parametrization (Eq. (10)) has the virtue of being linear in the Ω_λ parameters which makes fitting to experimental data straightforward, and thousands of papers have used this parametrization. In forming the sum and reducing the parametrization to just three parameters a considerable amount of information is lost, since each Ω_λ parameter is a combination of A_{tp}^{λ} parameters with $t = \lambda - 1, \lambda, \lambda + 1$ and vibronic intensity is absorbed into the

Ω_λ parametrization. Thus these parameters are not ideal for tests of models, or ab initio calculations. Also, the assumption that the states of the initial multiplet are evenly populated may not be accurate in some cases. Nevertheless, the relative simplicity of the measurements and calculations have permitted extremely useful analyses of huge amounts of experimental data.

The multiplet–multiplet parametrization can give important input to materials engineering. Many applications require particular transitions to be strong or weak, and Judd's parametrization can often be used to evaluate the feasibility of such manipulations. For example, from table 1 of [55] we can conclude that in Pr^{3+} transitions from the $^1G_4$ multiplet to the $^3H_4$ multiplet will always be weaker than transitions to $^3H_5$ and $^3H_6$ in *any* material.

3.5 Other Processes

The theory discussed earlier may be extended to other processes, such as two-photon absorption and Raman scattering [39, 56, 57]. Nonradiative excitation and energy transfer processes may also be modeled [7].

4 THE SUPERPOSITION MODEL

The superposition model, developed by Newman and coworkers in the late 60s [52, 58, 59], is an important framework for understanding both crystal-field and intensity parameters. The idea is to use the approximation that the contributions to the effective potential from different ligands is superposable (obviously for an electrostatic potential this is exact). If we had only one ligand on the Z-axis at distance R_0 only crystal-field parameters with $q = 0$ would be nonzero, due to the cylindrical symmetry. We define the *intrinsic* parameters, $-B_k(R_0)$ as those $B_0^{(k)}$ parameters for this single ligand. Adding together the effects of all the ligands yields

$$B_q^k = \sum_L \bar{B}_k(R_0)(-1)^q C_{-q}^{(k)}(\theta_L, \phi_L)\left(\frac{R_0}{R_L}\right)^{t_k}. \tag{12}$$

Here $(-1)^q C_{-q}^{(k)}(\theta_L, \phi_L)$ is required to take into account the effect of rotating a ligand from the Z-axis to orientation (θ_L, ϕ_L). This angular term has the same form as in a point-charge model. The term $(R_0/R_L)^{t_k}$, which takes into account the variation of the interactions with distance, would be the same as for a point-charge potential if we chose $t_k = k + 1$. However, analyses of experimental crystal-field parameters suggest that the power law is generally higher than electrostatic power laws. This is because the quantum-mechanical effects that give rise to the majority of the "crystal field" involves overlap of ligand orbitals, which fall off faster than electrostatic potentials. An important feature of the superposition model is that by reducing the parametrization to single ligands it is possible to compare crystal-field interactions between sites

of different symmetry. For detailed discussion of such applications see the papers and book by Newman and coworkers [52, 58, 59].

The superposition model may also be applied to intensity parameters [60, 61]. Under the superposition approximation the A_{tp}^{λ} intensity parameters with $t = \lambda$ are zero. In crystals with simple ionic ligands these parameters appear to be small but in some systems, particularly those with polarizable bonds close to the rare-earth ion, the superposition model breaks down [62], and parameters with $t = \lambda$ are required to fit the data. The relative signs of fitted intensity parameters give important information. We have suggested that these signs give restrictions on the possible mechanisms contributing to the transition intensities [63]. For further details the reader is referred to [37, 38].

5 AB INITIO CALCULATIONS

Atomic ab initio calculations can now give a very accurate description of the free-ion energy levels and parameters [64, 65]. However, the vast majority of energy-level and transition-intensity calculations for $4f^n$ configurations of rare-earth ions in solids or solutions make use of the parametrized "crystal-field" Hamiltonian, and it is common to invoke a point-charge model when attempting to rationalize the crystal-field parameters. However, even in the early 1960s [66] it was clear that quantum-mechanical effects were important.

Newman and coworkers performed a number of calculations of increasing sophistication in the 1960s, 1970s, and 1980s [67–69]. Those calculations used specialized computer code. However, advances in quantum-chemistry packages have made good-quality calculations practical with standard codes. An extensive set of calculations by Ogasawara and coworkers is described in [70]. Recent calculations by Seijo, Barandiarán and coworkers (see Chapter "Ab Initio Calculations on Excited States of Lanthanide Containing Materials" by Seijo and Barandiarán of this volume) give excellent agreement with experiment, see, for example, their calculations for $SrCl_2$:Yb^{2+} in [71, 72].

These ab initio calculations give energy levels, not parameters. This limits their usefulness. Energy levels are restricted to a single ion, whereas parameters can be interpolated and extrapolated to other ions, and used for further calculations or analysis. Though it is possible to fit the effective Hamiltonian parameters to calculated energy levels, as in [65, 73], it is desirable to have a more robust method.

We have shown that that it is possible to construct an effective Hamiltonian matrix from ab initio calculations [74–76], and hence determine crystal-field and other parameters by a straightforward projection technique. The crystal-field parameters obtained by this method with modern quantum-chemical codes are quite accurate. We give an example of a calculation for Ce^{3+} in $LiYF_4$ in Table 1. Recently this method has been used to calculate parameters for a variety of Ce^{3+} systems [77], notably YSO [78], where excellent agreement with EPR data is obtained despite the complete lack of site symmetry.

TABLE 1 Crystal-Field Parameters for the $5d^1$ Configuration of Ce^{3+} in $LiYF_4$

Parameter	Experiment	Theory
$B_0^2(4f)$	481	310
$B_0^4(4f)$	−1150	−1104
$B_4^4(4f)$	−1228	−1418
$B_0^6(4f)$	−89	−70
$B_4^6(4f)$	−1213	$-1140+237i$
$B_0^2(5d)$	4673	4312
$B_0^4(5d)$	−18649	−18862
$B_4^4(5d)$	−23871	−23871

Units are cm^{-1}. Note that the experimental fit approximated the actual symmetry by choosing all parameters to be real.
Source: From J. Wen, L. Ning, C.-K. Duan, Y. Chen, Y. Zhang, M. Yin, A theoretical study on the structural and energy spectral properties of Ce^{3}+ ions doped in various fluoride compounds, J. Phys. Chem. C 116 (2012) 20513–20521.

Ce^{3+} systems have only one valence electron. It is possible to use known trends across the rare-earth series to estimate parameters for other ions, but detailed comparisons for complex systems may give important insights. For systems with more than one valence electron it is not straightforward to apply the projection method to transform from the eigenstates of the ab initio calculations to a crystal-field basis. We anticipate that these technical problems will be solved in the near future. In the meantime, parameters may be obtained by fitting the ab initio energies to a crystal-field model [73].

6 CONCLUSIONS

The crystal-field and transition-intensity models described in this chapter were the result of decades of development, drawing on a variety of theoretical techniques, including group theory, atomic structure theory, and quantum chemistry. Extensive experimental data were required to determine the parameters in the models. Advances in technology have been important to this effort, with conventional spectroscopy and EPR spectroscopy supplemented by laser and synchrotron spectroscopy.

Crystal-field and transition-intensity models have been crucial to the understanding and application of optical properties of rare-earth ions. The applications are numerous and we have only been able to hint at the usefulness of the models in optical engineering.

There are two recent developments that we would like to emphasize. One is the use of magnetic-splitting data to supplement optical data as input to crystal-field fits. Low-symmetry systems such as YSO, doped with rare-earths, have potential as components of quantum-information devices, and good crystal-field modeling will aid the analysis required for optimization. The other development is the advances in ab initio techniques. Accurate ab initio calculations are now possible, though far from routine, and it is possible to use these calculations to predict positions and intensities of transitions. This has obvious potential for design of materials for phosphor and other applications.

For many decades, the richness of rare-earth spectra have offered the tantalizing possibility of deriving local structure from spectra. Current developments in modeling and ab initio calculations are close making this dream a reality.

ACKNOWLEDGMENTS

It has been a pleasure to have known some of the people who made crucial contributions to this field in the 1950s and 1960s, several of whom are no longer with us. I would like to particularly acknowledge the generous help and encouragement that that I received early in my career from Brian Wybourne, Brian Judd, Bill Carnall, Hannah Crosswhite, and Doug Newman. I would also like to thank my numerous coworkers who have made working in this area so enjoyable.

LIST OF SYMBOLS

A_{tp}^{λ}	crystal-field level intensity parameter
α, β, γ	parameter for two-body Coulomb interactions
B_q^k	crystal-field parameter
$\bar{B}_k(R_0)$	intrinsic crystal-field parameter for a ligand at R_0
$C_q^{(k)}$	many-electron spherical tensor operator
$D_q^{(k)}$	dipole operator
$D_{\mathrm{eff},q}$	effective dipole operator
$\Delta_E(\mathrm{fd})$	energy difference between configurations
E_{avg}	average energy of configuration barycenter above the ground state.
F^k	Slater parameter for direct Coulomb interaction
G^k	Slater parameter for exchange Coulomb interaction
g	magnetic splitting parameter or tensor
H	full Hamiltonian
H_{cf}	crystal-field Hamiltonian
H_{d}	d-electron portion of the Hamiltonian
H_{eff}	effective Hamiltonian
$L_q^{(1)}$	orbital angular momentum operator
M	model space for effective Hamiltonian

$M_q^{(1)}$	magnetic dipole operator
M^h	spin–spin and spin-other-orbit parameter
Ω_λ	J-multiplet intensity parameter
P^k	electrostatically correlated spin–orbit interaction
$S_q^{(1)}$	spin angular momentum operator
T^i	parameter for three-body Coulomb interaction
U_{p+q}^λ	unit tensor operator
ζ	spin–orbit interaction parameter

REFERENCES

[1] C. Görller-Walrand, K. Binnemans, Rationalization of crystal-field parameterization, in: J.K. A. Gschneidner, L. Eyring (Eds.), Handbook on the Physics and Chemistry of Rare Earths, vol. 23, North-Holland, Amsterdam, 1996, pp. 121–283.

[2] C. Görller-Walrand, K. Binnemans, Spectral intensities of f–f transitions, in: K.A. Gschneidner Jr., L. Eyring (Eds.), Handbook on the Physics and Chemistry of the Rare Earths, vol. 25, North Holland, Amsterdam, 1998, pp. 101–264.

[3] G.W. Burdick, M.F. Reid, $4f^N \rightarrow 4f^{N-1}5d$ transitions, in: K.A. Gschneidner Jr., J.C. Bünzli, V.K. Percharsky (Eds.), Handbook on the Physics and Chemistry of the Rare Earths, vol. 37, North Holland, Amsterdam, 2007, pp. 61–91.

[4] H. Bethe, Termaufspaltung in Kristallen, Ann. Phys. 395 (1929) 133–208.

[5] A. Abragam, B. Bleaney, Electron Paramagnetic Resonance of Transition Ions, Clarendon Press, Oxford, 1970.

[6] G.H. Dieke, Spectra and Energy Levels of Rare Earth Ions in Crystals, Interscience, New York, 1968.

[7] G. Liu, B. Jacquier (Eds.), Spectroscopic Properties of Rare Earths in Optical Materials, Springer, New York City, 2005.

[8] W. Carnall, G.L. Goodman, K. Rajnak, R.S. Rana, A systematic analysis of the spectra of the lanthanides doped into single crystal LaF_3, J. Chem. Phys. 90 (1989) 3443–3457.

[9] K. Rajnak, Configuration-interaction effects on the "free-ion" energy levels of Nd^{3+} and Er^{3+}, J. Chem. Phys. 43 (1965) 847–855.

[10] B.R. Judd, Three-particle operators for equivalent electrons, Phys. Rev. 141 (1966) 4–14.

[11] B. Ng, D.J. Newman, Many-body crystal field calculations I: methods of computation and perturbation expansion, J. Chem. Phys. 87 (1987) 7110–7117.

[12] B.G. Wybourne, Spectroscopic Properties of Rare Earths, Wiley-Interscience, New York, 1965.

[13] B.R. Judd, Optical absorption intensities of rare-earth ions, Phys. Rev. 127 (1962) 750–761.

[14] T.S. Piper, J.P. Brown, D.S. McClure, fd and $f^{13}d$ configurations in a crystal field and the spectrum of Yb^{++} in cubic crystals, J. Chem. Phys. 46 (1967) 1353–1358.

[15] L. van Pieterson, M.F. Reid, R.T. Wegh, S. Soverna, A. Meijerink, $4f^n \rightarrow 4f^{n-1}5d$ transitions of the light lanthanides: experiment and theory, Phys. Rev. B 65 (2002) 045113.

[16] L. van Pieterson, M.F. Reid, G.W. Burdick, A. Meijerink, $4f^n \rightarrow 4f^{n-1}5d$ transitions of the heavy lanthanides: experiment and theory, Phys. Rev. B 65 (2002) 045114.

[17] Y. Sun, T. Böttger, C.W. Thiel, R.L. Cone, Magnetic g tensors for the $^4I_{15/2}$ and $^4I_{13/2}$ states of Er^{3+}:Y_2SiO_5, Phys. Rev. B 77 (2008) 085124.

[18] D.P. McLeod, M.F. Reid, Intensities of hyperfine transitions of Pr^{3+} and Ho^{3+} in CaF_2, J. Alloys Comp. 250 (1997) 302–305.
[19] J.P.R. Wells, G.D. Jones, M.F. Reid, M.N. Popova, E.P. Chukalina, Hyperfine patterns of infrared absorption lines of Ho^{3+} C_{4v} centres in CaF_2, Mol. Phys. 102 (2004) 1367–1376.
[20] O. Guillot-Noel, Y. Le Du, F. Beaudoux, E. Antic-Fidancev, M.F. Reid, R. Marino, J. Lejay, A. Ferrier, P. Goldner, Calculation and analysis of hyperfine and quadrupole interactions in praseodymium-doped $La_2(WO_4)_3$, J. Lumin. 130 (2010) 1557–1565.
[21] D.S. Pytalev, E.P. Chukalina, M.N. Popova, G.S. Shakurov, B.Z. Malkin, S.L. Korableva, Hyperfine interactions of Ho^{3+}:KY_3F_{10}: electron paramagnetic resonance and optical spectroscopy studies, Phys. Rev. B 86 (2012) 115–124.
[22] P. Goldner, A. Ferrier, O. Guillot-Nöel, Rare earth-doped crystals for quantum information processing, in: J.C. Bunzli, V.K. Percharsky (Eds.), Handbook on the Physics and Chemistry of the Rare Earths, vol. 46, North Holland, Amsterdam, 2015, pp. 1–78.
[23] M. Zhong, M.P. Hedges, R.L. Ahlefeldt, J.G. Bartholomew, S.E. Bevan, S.M. Wittig, J.J. Longdell, M.J. Sellars, Optically addressable nuclear spins in a solid with a six-hour coherence time, Nature 517 (2015) 177–181.
[24] G.W. Burdick, M.F. Reid, Crystal field parametrizations for low symmetry systems, Mol. Phys. 102 (2004) 1141–1147.
[25] S.P. Horvath, M.F. Reid, J.P.R. Wells, M. Yamaga, High precision wavefunctions for hyperfine states of low symmetry materials suitable for quantum information processing, J. Lumin. 169 (2016) 773–776.
[26] S.P. Horvath, High-resolution spectroscopy and novel crystal-field methods for rare-earth based quantum information processing (Ph.D. thesis), University of Canterbury, Christchurch, New Zealand, 2016.
[27] D.J. Newman, S.S. Bishton, Theory of the correlation crystal field, Chem. Phys. Lett. 1 (1968) 616–618.
[28] B.R. Judd, Correlation crystal fields for lanthanide ions, Phys. Rev. Lett. 39 (1977) 242–244.
[29] M.F. Reid, D.J. Newman, Correlation crystal fields, in: D.J. Newman, B. Ng (Eds.), Crystal Field Handbook, Cambridge University Press, Cambridge, 2000, pp. 122–141.
[30] P. Dorenbos, The 5d level positions of the trivalent lanthanides in inorganic compounds, J. Lumin. 91 (2000) 155–176.
[31] P. Dorenbos, Relation between Eu^{2+} and Ce^{3+} f $\Leftrightarrow$ d-transition energies in inorganic compounds, J. Phys. Condens. Matter 15 (2003) 4797–4807.
[32] G.S. Ofelt, Intensities of crystal spectra of rare-earth ions, J. Chem. Phys. 37 (1962) 511–520.
[33] J.D. Axe, Radiative transition probabilities within $4f^n$ configurations: the fluorescence spectrum of europium ethylsulphate, J. Chem. Phys. 39 (1963) 1154–1160.
[34] J.D. Axe, Two-photon processes in complex atoms, Phys. Rev. 136A (1964) 42–45.
[35] R.D. Peacock, The intensities of lanthanide *f–f* transitions, Struct. Bond. 22 (1975) 83–122.
[36] L. Smentek, Theoretical description of the spectroscopic properties of rare earth ions in crystals, Phys. Rep. 297 (1998) 155–237.
[37] M.F. Reid, Transition intensities, in: D.J. Newman, B. Ng (Eds.), Crystal Field Handbook, Cambridge University Press, Cambridge, 2000, pp. 193–230.
[38] M.F. Reid, Transition intensities, in: G. Liu, B. Jacquier (Eds.), Spectroscopic Properties of Rare Earths in Optical Materials, Springer, New York City, 2005, pp. 95–127.
[39] M.C. Downer, The puzzle of two-photon rare earth spectra in solids, in: W.M. Yen (Ed.), Laser Spectroscopy of Solids II, Springer-Verlag, Berlin, 1989, pp. 29–75.

[40] A.D. Nguyen, Polarization dependence of two-photon absorption and electronic Raman scattering intensities in crystals, Phys. Rev. B 55 (1997) 5786–5798.
[41] M. Weissbluth, Atoms and Molecules, Academic Press, New York, 1978.
[42] S.B. Piepho, P.N. Schatz, Group Theory in Spectroscopy, with Applications to Magnetic Circular Dichroism, Wiley, New York, 1983.
[43] B. Henderson, G.F. Imbusch, Optical Spectroscopy of Inorganic Solids, Clarendon Press, Oxford, 1989.
[44] P.A. Tanner, G.G. Siu, Electric quadrupole allowed transitions of lanthanide ions in octahedral symmetry, Mol. Phys. 75 (1992) 233–242.
[45] P.S. May, M.F. Reid, F.S. Richardson, Circular dichroism and electronic rotatory strengths of the samarium 4*f*–4*f* transitions in $Na_3[Sm(oxydiacetate)_3]\cdot 2NaClO_4\cdot 6H_2O$, Mol. Phys. 62 (1987) 341–364.
[46] J.P. Riehl, G. Muller, Circularly polarized luminescence spectroscopy for lanthanide systems, in: K.A. Gschneidner Jr., J.C. Bunzli, V.K. Percharsky (Eds.), Handbook on the Physics and Chemistry of the Rare Earths, vol. 34, North Holland, Amsterdam, 2004, pp. 289–357.
[47] S. Hüfner, Optical Spectra of Transparent Rare Earth Compounds, Academic Press, New York, 1978.
[48] G.E. Stedman, Diagram Techniques in Group Theory, Cambridge University Press, Cambridge, 1990.
[49] G.K. Liu, X.Y. Chen, N.M. Edelstein, M.F. Reid, J. Huang, Analysis of f-element multiphonon vibronic spectra, J. Alloys Comp. 366 (2004) 240–244.
[50] M. Karbowiak, A. Urbanowicz, M.F. Reid, $4f^6 \rightarrow 4f^5 5d^1$ absorption spectrum analysis of Sm^{2+}: $SrCl_2$, Phys. Rev. B 76 (2007) 115125.
[51] A.R. Bryson, M.F. Reid, Transition amplitude calculations for one- and two-photon absorption, J. Alloys Comp. 275–277 (1998) 284–287.
[52] D.J. Newman, Theory of lanthanide crystal fields, Adv. Phys. 20 (1971) 197–256.
[53] M.F. Reid, F.S. Richardson, Anisotropic ligand polarizability contributions to lanthanide 4*f*–4*f* intensity parameters, Chem. Phys. Lett. 95 (1983) 501–507.
[54] M.F. Reid, F.S. Richardson, Lanthanide 4*f*–4*f* electric dipole intensity theory, J. Phys. Chem. 88 (1984) 3579–3586.
[55] L. Aarts, B. van der Ende, M.F. Reid, A. Meijerink, Downconversion for solar cells in YF_3: Pr^{3+}, Yb^{3+}, Spectrosc. Lett. 43 (2010) 373–381.
[56] B.R. Judd, D.R. Pooler, Two-photon transitions in gadolinium ions, J. Phys. C 15 (1982) 591–598.
[57] P.C. Becker, N. Edelstein, G.M. Williams, J.J. Bucher, R.E. Russo, J.A. Koningstein, L.A. Boatner, M.M. Abraham, Intensities and asymmetries of electronic Raman scattering in $ErPO_4$ and $TmPO_4$, Phys. Rev. B 31 (1985) 8102–8110.
[58] D.J. Newman, B. Ng, The superposition model of crystal fields, Rep. Prog. Phys. 52 (1989) 699–763.
[59] D.J. Newman, B.K.C. Ng (Eds.), Crystal Field Handbook, Cambridge University Press, Cambridge, 2000.
[60] D.J. Newman, G. Balasubramanian, Parametrization of rare-earth ion transition intensities, J. Phys. C: Solid State Phys. 8 (1975) 37–44.
[61] M.F. Reid, F.S. Richardson, Electric dipole intensity parameters for lanthanide 4*f*–4*f* transitions, J. Chem. Phys. 79 (1983) 5735–5742.
[62] M.F. Reid, F.S. Richardson, Anisotropic ligand polarizability contributions to lanthanide 4*f*–4*f* intensity parameters, Chem. Phys. Lett. 95 (1983) 501–507.

[63] M.F. Reid, J.J. Dallara, F.S. Richardson, Comparison of calculated and experimental 4*f*–4*f* intensity parameters for lanthanide complexes with isotropic ligands, J. Chem. Phys. 79 (1983) 5743–5751.

[64] J.C. Morrison, K. Rajnak, Many-body calculations for heavy atoms, Phys. Rev. A 4 (1971) 536–542.

[65] C.K. Duan, M.F. Reid, S. Xia, Parameterized analysis of the ab initio calculation of Pr^{3+} energy levels, J. Lumin. 122 (2007) 939–941.

[66] C.K. Jørgensen, R. Pappalardo, H.H. Schmidtke, Do the "Ligand Field" parameters in lanthanides represent weak covalent bonding? J. Chem. Phys. 39 (1963) 1422–1430.

[67] M.M. Ellis, D.J. Newman, Crystal field in rare-earth trichlorides I. Overlap and exchange effects in $PrCl_3$, J. Chem. Phys. 47 (6) (1967) 1986–1993.

[68] B. Ng, D.J. Newman, Ab initio calculation of crystal field correlation effects in Pr^{3+}-Cl^-, J. Phys. C: Solid State Phys. 19 (1986) L585–588.

[69] M.F. Reid, B. Ng, Complete second-order calculations of intensity parameters for one-photon and two-photon transitions of rare-earth ions in solids, Mol. Phys. 67 (1989) 407–415.

[70] K. Ogasawara, S. Watanabe, H. Toyoshima, M.G. Brik, First-principles calculations of $4f^n \rightarrow 4fn15d$ transition spectra, in: K.A. Gschneidner Jr., J.C. Bunzli, V.K. Percharsky (Eds.), Handbook on the Physics and Chemistry of the Rare Earths, vol. 37, North Holland, Amsterdam, 2007, pp. 1–59.

[71] G. Sánchez-Sanz, L. Seijo, Z. Barandiarán, Yb^{2+}-doped $SrCl_2$: electronic structure of impurity states and impurity-trapped excitons, J. Chem. Phys. 133 (2010) 114509.

[72] G. Sánchez-Sanz, L. Seijo, Z. Barandiarán, Electronic spectra of Yb^{2+}-doped $SrCl_2$, J. Chem. Phys. 133 (2010) 114506.

[73] A.J. Salkeld, M.F. Reid, J.P.R. Wells, G. Sanchez-Sanz, L. Seijo, Z. Barandiaran, Effective Hamiltonian parameters for ab initio energy-level calculations of $SrCl_2$:Yb^{2+} and $CsCaBr_3$:Yb^{2+}, J. Phys. Condens. Matter 25 (2013) 415504.

[74] M.F. Reid, C.K. Duan, H. Zhou, Crystal-field parameters from ab initio calculations, J. Alloys Comp. 488 (2009) 591–594.

[75] M.F. Reid, L. Hu, S. Frank, C.K. Duan, S. Xia, M. Yin, Spectroscopy of high-energy states of lanthanide ions, Eur. J. Inorg. Chem. 2010 (2010) 2649–2654.

[76] L. Hu, M.F. Reid, C.K. Duan, S. Xia, M. Yin, Extraction of crystal-field parameters for lanthanide ions from quantum-chemical calculations, J. Phys. Condes. Matter 23 (2011) 045501.

[77] J. Wen, L. Ning, C.-K. Duan, Y. Chen, Y. Zhang, M. Yin, A theoretical study on the structural and energy spectral properties of Ce^{3+} ions doped in various fluoride compounds, J. Phys. Chem. C 116 (2012) 20513–20521.

[78] J. Wen, C.-K. Duan, L. Ning, Y. Huang, S. Zhan, J. Zhang, M. Yin, Spectroscopic distinctions between two types of Ce^{3+} ions in X2-Y_2SiO_5: a theoretical investigation, J. Phys. Chem. A 118 (2014) 4988–4994.

Chapter 285

Ab Initio Calculations on Excited States of Lanthanide Containing Materials

Luis Seijo[1] **and Zoila Barandiarán**[1]

Instituto Universitario de Ciencia de Materiales Nicolás Cabrera, and Condensed Matter Physics Center (IFIMAC), Universidad Autónoma de Madrid, Madrid, Spain

[1]*Corresponding authors: e-mail: luis.seijo@uam.es, zoila.barandiaran@uam.es*

Chapter Outline

1 INTRODUCTION

1.1 Applications of the Materials

Luminescent materials made of imperfect crystals that incorporate lanthanide ions as substitutional impurities are the subject of intense scientific and technological research as a consequence of their utility in a wide variety of solid-state devices with high societal demand. These include white light emitting diodes or solid-state lighting devices for energy efficient general illumination,

Handbook on the Physics and Chemistry of Rare Earths, Vol. 50. http://dx.doi.org/10.1016/bs.hpcre.2016.03.003

liquid crystal displays, solid-state lasers of wavelengths spanning from ultraviolet to infrared, scintillating detectors with applications ranging from medical imaging to high-energy physics calorimetry, remote pressure and temperature measurement systems, systems for enhancing the efficiency of solar cells, energy storage phosphors, persistent luminescence materials, quantum information processing materials, and more.

1.2 Rich Manifolds of Excited States

All these applications ultimately rest on the rich manifolds of excited states of the lanthanide ions in the hosts, which makes these materials exceptional for photon engineering. Such excited states are not only abundant, their number ranging from tens to tens of thousands, but also show a variety of natures depending on their electronic configuration and degree of localization/delocalization. Besides the most common $4f^n$ and $4f^{n-1}5d$ configurations, $4f^{n-1}6s$ configurations are also found, as well as impurity-trapped exciton (ITE) configurations $4f^{n-1}\phi_{ITE}$, where a hole is localized in the $4f$ shell and an electron is in molecular orbitals ϕ_{ITE} partly delocalized outside the first coordination shell of the lanthanide ion. But also ligand-to-metal charge transfer (LMCT) states, intervalence charge transfer (IVCT) states where electrons are transferred between different oxidation states of a given element, or metal-to-metal charge transfer (MMCT) states where electrons are transferred between different lanthanide elements, between the lanthanide ions and other dopants, or between the lanthanide ions and the host cations and viceversa.

1.3 Many Possible Processes

The large number of excited states makes feasible many possible processes: absorbing and emitting light from and to several states, of either one photon in regular absorptions and emissions, or several photons in upconversion and downconversion processes; nonradioactively decaying to the ground state or to several stable excited states with a wide range of radiative lifetimes; or transferring energy and electrons between different active centers.

1.4 Empirical Models and Ab Initio Calculations

The advances in understanding the interplays between all these processes, in new materials and mastering their absorptions and emissions of light, have been driven mainly by intense experimental work relying on empirical theoretical models, like Crystal or Ligand Field Theory [1–3] or Judd–Ofelt theory of the intensities of *f–f* transitions [4, 5]. The role of ab initio calculations has been rather modest in this respect up to now, as a consequence of the methodological difficulties inherent to these systems. Though, they have been recognized as a desirable source of reliable information complementary to

experiments and to empirical models, with the potential to predict and shed light into issues where the complicated nature of the ground and excited states prevented the empirical models from giving clear-cut answers [6]. The continuous methodological advances in ab initio quantum chemical methods for lanthanide atoms and molecules containing them [7] and for their local excited states in solids [8] led to a present state of the art in which the contribution of ab initio methods to the chemistry and physics of lanthanide-containing molecules and solids is significant and grows steadily [9], this including the luminescence of lanthanide-containing materials [10]. We discuss this issue in Section 2.

1.5 Wave Function Theory Methods

The excited states of lanthanide-containing materials result, basically, from the partial filling of shells of molecular orbitals. The molecular orbitals retain a strong parentage with the lanthanides' atomic orbitals 4*f*, 5*d*, and 6*s*, as a consequence of the considerable ionic character of the bonds between the lanthanides and their coordinating ligands, up to the point that it is normal to label these molecular orbitals with the atomic notation. Then, the unfilled or open shells produce manifolds of excited states that can be linked with their atomic counterparts. In effect, the 4*f* shells are inner unfilled shells that are protected from the environment by the outer 5*s* and 5*p* filled shells, so that the states of the $4f^n$ configuration retain the multiplet structure of the free ions, where spin–orbit coupling is an important factor, split by the action of a weak external ligand field. The 5*d* shells are far more exposed to the environment and suffer large ligand field splittings into subshells, so that $5d(t_{2g})$, $5d(e_g)$, and, in general, analogous labels referring to the 5*d* subshells' symmetries are compulsory. Then, for example, $4f^{n-1}5d(t_{2g})$ excited states reproduce the $4f^{n-1}$ multiplet structure coupled with the $5d(t_{2g})$ subshell, and the same multiplet structure is reproduced again, this time coupled with $5d(e_g)$, for the states of the $4f^{n-1}5d(e_g)$ configuration. For n close to 7, these manifolds can be extremely crowded.

The excited states that form such crowded manifolds are multiconfigurational in nature, because they result from the coexistence of several unfilled shells and their mutual interactions, and, in consequence, the ab initio multiconfigurational methods of quantum chemistry emerge as convenient tools for their theoretical study. These methods were developed within the wave function theory of atoms and molecules and specially designed to handle the complex multiplet structure of atoms and the rich variety of excites states of all kinds of molecules. Their applicability to local excited states of solids associated with the presence of lanthanide ions is made possible, thanks to embedded cluster methods. In these, the bonding interactions between the lanthanide ions and their close neighbors in the solid are calculated with the full accuracy of the adopted molecular quantum chemical method, and the embedding

effects brought about by the solid environment onto those atoms are calculated at a lower level of accuracy. Besides being multiconfigurational, the methods should be able to consider dynamic correlation at a high level of accuracy, because many tight 4*f*–4*f* electron pairs and their breakings are commonly involved in the processes of interest. They should also make use of relativistic Hamiltonians and wave functions because, the lanthanides being heavy elements: (1) the scalar (spin independent) relativistic effects are large enough so as to affect the radial extent and relative orders of *s*, *p*, and *d* shells of similar energy and they can have a strong impact on the electronic structure, bond lengths, and structural properties in general, and (2) the spin–orbit coupling relativistic effects are very important and basic for the understanding of their multiplet structure and spectroscopic properties. We dedicate Section 3 to the discussion of the use of multiconfigurational wave function theory methods for the ab initio calculation of the complex manifolds of excited states of lanthanide-containing materials.

1.6 Density Functional Theory Methods

Contrary to wave function theory multiconfigurational methods, density functional theory (DFT) related methods [11–13] find difficulties to properly calculate the complex manifolds of local excited states of lanthanide-containing materials, mostly as a consequence of its monoconfigurational grounds. Nevertheless, periodic-boundary conditions (PBC) DFT has been proven to be able to calculate atomistic structures of pure and defective materials in their ground states with high accuracy, at a much lower cost than wave function theory multiconfigurational methods. In these circumstances, it seems natural to exploit the strengths of both families of methods and combine them in a mixed procedure in which the ground state structures of complex defects involving large numbers of atoms are calculated at a DFT level, and the energies of the excited states are calculated with wave function theory. This mixed approach finds limitations when the atomistic structures in the excited states are important, eg, for emissions and Stokes shift calculations, nonradiative decays, or energy transfer mechanisms between excited states. Nevertheless, in many of these problematic cases only some limited structural changes are expected to play important roles, so that the ground state DFT structures can be taken as a starting point for the excited state structural studies with wave function theory methods. We discuss further on this issue in Section 4.

1.7 Reducing the Gap with Experiments

In spite of the theoretical and methodological advances, the contributions from ab initio calculations to a better understanding of the excited states of lanthanide-containing materials are still limited and there is still a considerable

gap between calculations and experiments. In Section 5, we discuss the challenges met by ab initio methods in order to reduce this gap, related with improving their accuracy, becoming applicable to more complex problems, and extending their list of calculated properties.

2 AB INITIO METHODS VS EMPIRICAL MODELS

2.1 Empirical Models

Crystal or ligand field theory was proposed long ago as an empirical approach to understand and predict the complicated structure of multiplets of transition metal ions and lanthanide and actinide ions in complexes and solids [1, 2]. It was and it still is very successful and fruitful at analyzing and systematizing the $4f^n$ energy levels of all lanthanide ions in solid hosts [3, 14], and it was extended to the even more complicated case of $4f^{n-1}5d$ energy levels [15, 16]. Complementing ligand field theory, the empirical theory of Judd and Ofelt [4, 5] allowed for a systematic understanding of the intensities of the transitions between $4f^n$ levels [17]. A revision on this issue is presented elsewhere in this volume [18].

Also, empirical relationships have been found between the lowest $4f \rightarrow 5d$ transitions of all lanthanide ions of equal charge in the same solid host [19], as well as between the lowest energies of their $4f$ shells relative to the top of the valence band of a given host, or LMCT transitions [20, 21], and empirical models have been developed to explain the regularities and allow for predictions. These have recently been reviewed [22] and their uncertainties have been critically assessed [23]. The model for the lowest $4f \rightarrow 5d$ transitions was initially proposed by Morrison [24] after considering the change in ligand polarization interactions caused by the $4f \rightarrow 5d$ transition according to Judd [25], as pointed out by Bettinelli and Moncorgé [26]. The trends of these transitions and of the $4f$ energies across the lanthanide series follow the trend of the $4f$ ionization potentials very closely. This is what has to be expected for the energies of the $4f$ shells relative to the top of the valence band of a given host. For the $4f \rightarrow 5d$ transitions , the trend is a consequence of the lanthanides' $5d$ ionization potentials rising very smoothly across the series (the energy of the lowest $4f \rightarrow 5d$ transition equals the difference between $4f$ and $5d$ ionization potentials), both as free ions and as dopants in a solid host [27], which, in turn, is due to the fact that the increase in the effective nuclear charge acting on the $5d$ shell across the series is very small (as a result of the high screening efficiency of $4f$ electrons).

Empirical models have also been proposed for other types of excited states of lanthanide-containing materials, eg, ITEs [28] or IVCT and MMCT states [29].

The strength of empirical models lies on the simplicity of their description of complex physical phenomena, and on their ability to make fast predictions of sufficient quality so as to help the design of new enlightening experiments.

The empirical models have limitations, though. A fundamental one is their reliability, because the fact that some experimental data are well reproduced with a model when some specific values of its parameters are used, does not guarantee that the real physics is the one behind the model. A practical limitation lies on their application boundaries, because these models are focused on rationalizing and predicting certain properties only, rather than all or at least many different properties of the materials. So, whereas empirical models can often make good predictions when they are used as interpolation tools, they are usually not expected to be used as extrapolation tools. For instance, ligand field theory parameters obtained from a set of states of a lanthanide ion in a given host can be safely used to predict energies of its other states, but less safely to predict energies of the same lanthanide ion in a related host, and extrapolations become more unreliable for more different hosts. Also, ligand field theory calculations are not meant to inform on other, though related issues, like, eg, equilibrium structures and vibrational frequencies in the ground and excited states, bond length changes associated with spectroscopic transitions, Stokes shifts, etc. Similarly, the estimated trends of $4f \rightarrow 5d$ transitions have to be used in a given host and apply only to the band maxima of the lowest transitions, but they can neither be used for zero-phonon lines, $5d \rightarrow 4f$ emissions, or their corresponding Stokes shifts [22], nor they are meant to give details of nonradiative processes after $4f \rightarrow 5d$ or other types of absorptions.

2.2 Ab Initio Methods

In general, ab initio methods cannot provide as fast answers and as simple descriptions as empirical models do, and they are not expected to do so. On the other hand, they evolve and the pace at which they deliver practical answers, the simplicity of their descriptions, and the accuracy of their results can improve with time. They can do it based on their systematicity.

In effect, the fact that ab initio methods rely only on the first principles and well-defined approximations, means that substitutions of some approximations by others more sound from the point of view of efficiency (balance between accuracy and computational demand) can speed up the production of results without damaging their accuracy. This, together with the development of new computational algorithms that implement the approximations, creates a state of continuous methodological improvement which adapts to and adds up to the technological developments in computers and makes a given ab initio calculation much faster every time. And, perhaps even more importantly, it makes affordable, at a point in time, ab initio calculations that were previously unfeasible.

At the same time, the raw numerical results of ab initio calculations can be systematically analyzed. This can be done with the help of concepts and

analysis procedures which are constantly developed, but also with as simple procedures as switching on and off interactions represented by Hamiltonian terms. Examples of the former are: the simple and famous Mulliken population analysis [30] and the analysis of dominant electronic configurations in a very complex wave function, etc., or the more elaborate natural orbital analysis NO [31], constraint-space orbital variation method CSOV [32], etc. Examples of the latter are: the analysis of the effects of dynamic correlation, spin–orbit coupling, embedding electrostatic interactions, embedding Pauli repulsion [10], etc. Carrying on many of these analyses involves additional costs in computing and human time and effort with respect to the costs of the calculations themselves, but they are almost always compensated by the benefits of the light shed on the issues under study.

A final, key consequence of the systematicity of ab initio methods is that removing approximations leads, in principle, to more accurate methods. This constitutes the basic support for the reliability of the description of a physical phenomenon obtained from ab initio calculations that agree with the experiments. It also gives the basic motivation for methodological improvement of state-of-the-art ab initio methods when they fail at reproducing experimental data with sufficient accuracy. We must be aware, nevertheless, that a particular agreement with experiment is not a guarantee of reliability for an ab initio method, because it can eventually be due to a compensation of errors associated with several approximations [33]. The reliability of a given ab initio method requires systematic agreements between its results and the experiments. It also requires successful performances in quality and stability analyses: eg, an improvement in the basis set or other methodological ingredients cannot worsen the results.

Besides being systematic, ab initio methods are general and rely on a minimum number of assumptions. They are general because the same method estimates several properties of a luminescent material, no matter how related they are; and the properties of many materials, no matter how similar or different from each other they are. So, an ab initio method used to calculate the relative energies of the $4f^n$ states of a lanthanide-containing material also gives the energies of its $4f^{n-1}5d$ states, ITEs , or IVCT and MMCT states; it also calculates the oscillator strengths of the transitions between them and their radiative lifetimes; furthermore, the equilibrium structures and vibrational frequencies of all these states, as well as structures at which the potential energy surfaces of different states cross and activation energy barriers of nonradiative processes can be calculated; in addition, ab initio methods provide the analysis of the bonding that explains why the structures are as different as they are in the different excited states. Also, the results of an ab initio calculation can be used for subsequent theoretical studies; eg, the complete potential energy surfaces of all states resulting from an ab initio calculation are useful for kinetics studies and dynamic analyses in general. Even more,

the generality of ab initio methods extends beyond the field of a given family of materials and states, so that the same ab initio methods that are able to calculate all of the above properties in a lanthanide-containing material, are also used to calculate, for instance, the photochemistry of an organic compound of biological interest in gas phase or in aqueous solution.

The generality of ab initio methods rests upon the minimum number of assumptions that have to be made prior to an ab initio calculation, which are limited in principle to the chemical composition and in practice to specific atomistic configurations of the material or compound under investigation.

2.3 Ab Initio Methods vs Empirical Models

As a consequence of the above it can be said that, in the field of lanthanide-containing luminescent materials, when a purely empirical approach is unable to give answers to a given problem because of its complexity, ab initio methods still have the potential to shed light into the issue. This observation was made long before ab initio calculations were systematically performed in these materials by Blasse in a delightful paper [6] in which he briefly reviewed the state of the art of the fundamental understanding of a large number of well-known luminescent ions and concluded that, in many luminescent studies, especially of broad-band luminescence in inorganic materials, there was a lack of quantitative and even qualitative understanding. He metaphorically described those problems as the evils that escaped from *Pandora's box of classical phosphors* when she opened it. Bravely enough, he continued the metaphor and saw ab initio calculations of the ground and excited states of luminescent materials as the hope that remained in Pandora's box after she immediately closed it. Cautiously, he called attention to the fact that "such type of calculations are by no means easy and will require a years-taking effort." His work was recently revisited and reminded to the community by [34].

Fortunately, as a result of continuous methodological improvements in ab initio quantum chemical methods for lanthanides and actinides [7] and for their local excited states in solids [8], the performance of state-of-the-art ab initio calculations in luminescent lanthanide-containing materials is today significant [10] and grows steadily [9]. Yet, the throughput is lower than desired and strong limitations and interesting challenges still exist.

Ab initio methods have a great potential, but they are never meant to substitute empirical models. Rather, both approaches can support and enhance each other [35] and both of them need to go together with and complement experiments. In such a collaboration, each of the approaches can provide its strengths. In this sense, we may move from a competition between opposites, which is often expected and provocatively stated in the title of this section "ab initio methods vs empirical models," towards the more realistic and practical paradigm "ab initio methods and empirical models."

3 WAVE FUNCTION THEORY METHODS

3.1 Periodic vs Molecular Boundary Conditions Methods

The electronic structure ab initio methods are grouped in two families according to the boundary conditions they adopt: PBC methods and molecular boundary conditions methods. The former methods take advantage of translational symmetry of crystalline solids and obtain properties of an infinite crystal by means of calculations on the atoms that constitute the unit-cell only. They are specially indicated for solving one-electron effective Schrödinger or Dirac equations, like the one-component and four-component Kohn–Sham DFT equations [12], in which one-electron wave functions are obtained in order to compute the electronic density of the system. However, PBC have difficulties in solving many-electron Schrödinger or Dirac equations, where many-electron wave functions are central. As a consequence, except for anecdotic cases, the methods that make use and take full advantage of many-electron wave functions (let us call them wave function theory methods) use molecular boundary conditions. These methods have been developed within the framework of quantum chemistry and they are very successful in the description and understanding of the electronic structure of the ground and excited states of atoms (multiplet structure) and molecules of all kinds, ranging from small diatomics to organic molecules of biological interest to molecules containing lanthanides, actinides, or other heavy elements. Obviously, molecular boundary conditions wave function theory methods are not appropriate for the description of infinite solids, in general. However, they are adequate for calculating and giving insight into the properties of an infinite periodic solid that are local in nature. Furthermore, many solids are in fact solid solutions and defective materials whose impurities and local defects of all kinds give them their interesting properties, which are local properties. This is the case of most of the excited states involved in the optical activity of lanthanide-containing materials. Regarding local properties of solids, it has long ago been recognized that they depend to first order on a reduced number of atoms, which can be called *the cluster*, and to second order on the embedding effects brought about by the remaining atoms of the solid [36]. This idea led to the concept of *embedded cluster*, which is a pseudomolecule made of the atoms of the cluster under the effects of an embedding potential created by the solid [37]. Once the cluster is chosen and the embedding potential is obtained, any wave function theory method developed for molecules can be applied to it. This is the power of embedded cluster methods: all the molecular artillery that resulted from decades of development in quantum chemistry can be applied to the local properties of solids, provided an embedding potential of sufficient quality is available. Although a general, practical theory of embedding does not exist, efficient embedding methods have been developed to be used in particular contexts, like the ab initio model potential (AIMP) embedding method for ionic materials

[37] based on the group wave function theory of [38], or the frozen density functional approach in DFT calculations [39].

3.2 Multiconfigurational Methods

The crowded manifolds of excited states of lanthanide-containing materials result from the coexistence of several unfilled shells (open shells) and their mutual interactions. Thus, any detailed ab initio description of all these excited states must necessarily be multiconfigurational. Besides, these open shells are linked to orbitals more or less localized on a limited number of atoms in the solid; such is the case of the states of $4f^n$, $4f^{n-1}5d$, and $4f^{n-1}6s$ configurations, but also of ITE $4f^{n-1}\phi_{ITE}$, LMCT states, IVCT states, and MMCT states. Then, they are susceptible of being studied with embedded cluster methods that adopt molecular boundary conditions. This allows one to apply to these materials all the ab initio methods that were specially designed to handle complex manifolds of states of multiconfigurational nature within the framework of wave function theory of atoms and molecules. The most successful of them are, perhaps, those derived from the complete active-space self-consistent-field method, CASSCF [40–42]. This is a variational method in which the wave functions of the states are ultimately written as full configuration interaction functions (full CI, "full" meaning that the electrons are distributed among the available orbitals in all possible ways) in a limited set of molecular orbitals (the "active" orbitals, which are those of the relevant open shells), and both the molecular orbitals and the full CI coefficients are variationally optimized. For instance, a CASSCF wave function of one of the states of the $4f^{n-1}5d$ configuration can be a linear combination of all Slater determinants resulting from distributing n electrons among the seven molecular orbitals of main $4f$ character and the five molecular orbitals of main $5d$ character in all possible ways, spin and spatial symmetry restrictions applying. In this combination, all the molecular orbitals of the embedded cluster (the open shells of main $4f$ and $5d$ characters, but also all the doubly occupied molecular orbitals or closed shells) and all the CI linear coefficients are obtained by variation methods.

Being multiconfigurational, CASSCF wave functions represent some degree of electron correlation, because the probability density of finding one electron at one site and another at a second site is not equal to the product of the probability densities of finding the respective electrons at the given sites (the two-electron density function cannot be written as the product of the two one-electron density functions). However, the CASSCF multiconfigurational expansions are limited to those Slater determinants (N-electron wave functions built as an antisymetric product of N orthonormal spin orbitals) that are required for proper bond breakings and multiplet structures, but they do not contain all those required for a correct representation of the Coulomb hole. Hence, CASSCF wave functions are successful at describing

the complex structure of the manifolds of excited states of lanthanides in solids in a qualitative manner, but they fail at representing most of the dynamic correlation and, consequently, at providing quantitatively correct descriptions of the relative energies of such states.

Quantitative results demand a correct treatment of dynamic correlation effects. And, although doing it from a CI perspective is an extremely demanding route, if not prohibitive, obtaining them as additional second-order perturbation theory corrections is a reasonable alternative to achieve a good balance between accuracy and feasibility; this is what is done in the so-called CASSCF/CASPT2 method [43–46].

3.3 Spin–Orbit Coupling: One-Step vs Two-Step Methods

Ab initio studies of lanthanide atoms and of molecular and solid systems containing them must use relativistic Hamiltonians [7]. This is so because lanthanides are heavy elements and the large values of their nuclear charges make the innermost electrons to move extremely fast and to need a relativistic treatment. These relativistic effects ultimately propagate to all of their electrons. They can be divided into scalar or spin-independent effects and spin-dependent effects. The former have a large impact on the radial extent and relative ordering of the electronic shells and, as a consequence, on the electronic structure and the bonding; so, they largely affect bond lengths and angles, vibrational frequencies, and bond properties in general. Among the spin-dependent effects, spin–orbit coupling effects are the most important. They make the quantum numbers of angular momentum ℓ and internal momentum or spin s to fail as good quantum numbers and be substituted by the total angular momentum quantum number j, and create important energy splittings of the $n\ell$ shells into $n\ell_j$. While these spin–orbit coupling splittings cancel out in filled shells, they do not in unfilled shells and they become central for the understanding of the multiplet structure resulting from them, ie, the number, symmetry, and relative energy of all the energy levels and states of a given electronic configuration. The magnitude of the spin–orbit coupling splittings of lanthanides is relevant for all of them, and it can take really large values: The ^2F Russell–Saunders terms of Ce^{3+} and Yb^{3+} as free-ions split with spin–orbit coupling into the $^2F_{7/2}$ and $^2F_{5/2}$ levels, whose energy difference is 2253 cm^{-1} in Ce^{3+} and $-$ 10214 cm^{-1} in Yb^{3+} [47].

Studying scalar and spin-dependent effects on the electronic structure of atoms, molecules, and solids, can be done with four-component Hamiltonians, directly related with the four-component kinetic energy operator of Dirac, and with two-component Hamiltonians, resulting from 4×4 matrix transformations of the former [48]. Different choices of transformations led to different two-component Hamiltonians; among all of them, the Douglass–Kroll–Hess Hamiltonian [49, 50] reached the maximum popularity. In some four-component methods and in most of two-component methods it is possible to

split the Hamiltonians into a scalar or spin-independent part and a spin-dependent part, and to identify a spin–orbit coupling operator. Then, it is possible to handle the full relativistic Hamiltonian as a whole and apply the available electronic structure methods developed for nonrelativistic Hamiltonians after the adequate methodological adaptations. These, however, are not obvious nor simple, and limit in practice the amounts of correlation that can be included in a given calculation. This procedure leads to the so-called one-step methods. The name indicates that all scalar effects (mean field including bonding, dynamic correlation, scalar relativistic effects) and spin–orbit coupling effects are treated in one single step in an equal footing. An example of this is the spin–orbit coupling singles and doubles CI method of [51]. Alternatively, it is also possible to take only the scalar components of the relativistic Hamiltonians (which have nonrelativistic and relativistic contributions and the structure and symmetry of the nonrelativistic Hamiltonian) in a first step, and apply the available electronic structure methods developed for nonrelativistic Hamiltonians as they are, without adaptations of any kind. This means that electron correlation can be considered at the highest possible level, exactly as in the nonrelativistic case. Then, the spin–orbit coupling terms can be switched on in a second step that uses the full relativistic Hamiltonian in a CI calculation on the basis of the many-electron wave functions of step one. In this way, all the spin–orbit couplings between the states of the spin–orbit coupling free Hamiltonian are taken into account. This procedure leads to the so-called two-step methods. Having a relatively simple second step to include spin–orbit coupling and, at the same time, incorporating in it all the correlation effects calculated in a cumbersome first step, is achieved by a spin-free state shifting technique [52]. An example of a very practical and convenient two-step method is the restricted active-space state-interaction with spin–orbit method (RASSI-SO) of [53].

One-step methods are in a better position to represent effects of spin–orbit coupling on orbital polarizations, but two-step methods have advantages in the calculation of electron correlations. This is, in fact, the feature that made two-step methods very popular and especially attractive, because correlation has in general been found as being the limiting factor or bottleneck governing the quality of ab initio results on molecules in which scalar and spin–orbit coupling relativistic effects are important.

3.4 Results

The results of ab initio wave function theory studies on the ground and excited states of lanthanide-containing materials can be divided into: those properties and data that have been or can be obtained experimentally, and those that are very hard or even impossible to get from experiments. The former are useful to validate the ab initio methods and establish their degrees of accuracy by direct comparison with measurements. Also, when the experimental data are

not primary information, but deduced from experiments after elaborations based on the acceptance of models and assumptions, the ab initio results play the role of independent tools for the confirmation, support, or rejection of hypotheses, and for the suggestion of new ones. And, when the properties have not yet been measured, or the materials not even been synthesized, the results predicted from ab initio calculations can help and orient the decision making process in experimental research, so saving time and money. On the other hand, the calculated properties that are hard or impossible to get from experiments are very useful for the purposes of interpreting the physics behind experimental observations, giving insight, and building coherent, complete, and detailed pictures of the atomistic and electronic structures of the materials.

Let us summarize some of the available results of ab initio wave function theory studies on the excited states of lanthanide-containing materials that illustrate the above comments.

As a rule, the expected accuracies are the same as those already established in molecular quantum chemistry, after consideration of the inaccuracies associated with the embedding approximations. As in isolated molecules, the accuracies of embedded cluster calculations are almost always controlled by the quality of the dynamic electron correlation effects included, whose treatment is the most computationally demanding issue. In correct CASSCF/CASPT2/RASSI-SO embedded cluster calculations, as in others of a similar level of theory, ground and excited state bond length accuracies are estimated to be around 0.01 Å, bond length changes to be qualitatively correct and of the order of 0.002 Å, vibrational frequencies around 5%, and the energies of electronic transitions of the order of 10%; small transition energy shifts of physical or chemical origin are expected to be qualitatively and even semiquantitatively correct, and the same can be said about the oscillator strengths and the relative intensities of electronic transitions.

3.4.1 Calculating Data: Ground and Excited State Structures

The relative energies of the absorbing and emitting states are accurately obtained from experiments, in general, but structural data of optically active defects in their ground and excited states are much harder to extract. This structural information is very often missing. Sometimes, it is obtained by means of extended X-ray absorption fine structure(EXAFS) spectroscopy experiments ; in these cases, the information is usually limited to the coordination number of the lanthanide impurity and its distances with the first and second neighbors in the ground state, which are probably the most important structural parameters, without further details on bond angles and bond torsion angles: eg, the first coordination shell of trivalent Ce in the doped garnet $Y_3Al_5O_{12}$:Ce is made of four oxygen atoms at a Ce–O distance of 2.38(1) Åand four oxygen atoms at a Ce–O distance of 2.52(2) Å[54]. Direct structural experimental information on excited states is usually missing. On the

other hand, DFT and wave function based ab initio calculations regularly report reliable atomistic structures for the ground state, and the latter methods also for excited states. For example, in the ground state structure of the Ce_Y substitutional defect of $Y_3Al_5O_{12}$:Ce the Ce–O distances have been found to be 4 × 2.37 Åand 4 × 2.47 Åby DFT calculations [55] and 4 × 2.37 Åand 4 × 2.44 Åby wave function theory calculations [56]. In both cases the complete structure of the first coordination shell is given; in the DFT calculations, also the one of the second shell. Wave function theory calculations also provided the structure of the first shell in the six excited states of the $4f^1$ configuration, which were basically identical to that in the ground state, and of the five excited states of main $5d^1$ configurational character; in the lowest of these states the Ce–O distances become shorter than in the ground state: 4 × 2.36 Åand 4 × 2.43 Å[56]. Similar results have been obtained for Ce^{3+} as a dopant in other garnets like $Lu_3Al_5O_{12}$, $Y_3Ga_5O_{12}$, $Lu_3Ga_5O_{12}$, and $Ca_3Sc_2Si_3O_{12}$ [57].

3.4.2 Giving Insight: Some Extended Assumptions Under Question

Giving insight into complex or puzzling issues is another way of complementing experiments, besides providing data hard to obtain from experiments alone. One of its forms is by checking assumptions that became extended and more or less general at some point. Let us comment here some of them that have been put under question by ab initio calculations.

It was very common, and it still is, to find configuration coordinate diagrams in articles and books in which the lowest states of the $4f^{n-1}5d$ configuration are represented with parabolas shifted to higher energies and to longer lanthanide-ligand distances with respect to that of the ground state of $4f^n$ configuration. The shift to higher energy is obvious if the $4f \rightarrow 5d$ transition is an absorption, but the shift to longer distances seems to be based only on an unchecked assumption, perhaps induced by the fact that the $4f$ orbitals are tight, inner orbitals, whereas the $5d$ orbitals are much more extended in space. However, wave function theory calculations on lanthanide (and actinide) ions in solids and in liquid solution found a bond length shortening between the lanthanide and the ligands associated with the lowest $4f \rightarrow 5d$ absorptions and explained the reasons for it [58, 59]. They also found a corresponding elongation associated with the highest $4f \rightarrow 5d$ transitions. These findings seem to be general for all kind of solid hosts [10]. Bond length shrinkages and elongations with respect to the $4f^n$ configuration in, respectively, the lowest and highest $4f^{n-1}5d$ configurations, are often of around 0.02 Å. A few examples are: shortenings of − 0.04 Åand − 0.03 Åfor the $5d(t_{2g})^1$ configuration of Ce^{3+} in the octahedral sites of $Cs_2LiLuCl_6$ and Cs_2NaYCl_6, and respective +0.01 Åand +0.03 Åelongations for the $5d(e_g)^1$ configuration; − 0.02 Å/+0.03 Åfor the $5d(e_g)^1/5d(t_{2g})^1$ configurations of Ce^{3+} in the cubic

site of CaF_2; and − 0.02 Å/+0.02 Åin average for the lowest/highest $5d^1$ state in the D_2 site of $Y_3Al_5O_{12}$; − 0.02 Å/+0.03 Åfor the $4f^1 5d(e_g)^1/4f^1 5d(t_{2g})^1$ configurations of Pr^{3+} in CaF_2; or − 0.02 Å/+0.02 Åfor the $4f^{13}5d(t_{2g})^1/4f^{13}5d(e_g)^1$ configurations of Yb^{2+} in the O_h site of $CsCaBr_3$. The bond length shrinkage is related to the $4f \rightarrow 5d$ excitation making one electron to cross the $5s^2 5p^6$ barrier from the inside ($4f$) to the outside ($5d$); in particular it was found to be due to the following combination of facts: First, the purely ionic contribution to the bond length change in a $4f \rightarrow 5d$ excitation is not the difference between the $5d$ and $4f$ orbital radii, but a much smaller positive number: 1/7 of the difference between the $5d$ and $5p$ orbital radii (the difference between the sizes of the $5p^6 5d^1$ and $5p^6$ shells, which are the ones determining the bond lengths in the $4f^{n-1}5d$ and $4f^n$ configurations, respectively). Second, this small bond length increase has to be corrected with two negative contributions: one due to the more intense covalent interactions of the $5d$ electron with the ligands, and another due to the hole left in the $4f$ shell promoting charge transfer from the ligands. Finally, the large ligand field splitting of the $5d$ shell (enhanced by covalency) means a third negative contribution to the bond length change in the lower states of the $4f^{n-1}5d$ configuration and a positive contribution in the upper states. The magnitudes of the covalent, charge transfer, and ligand field splitting contributions are similar. Altogether, they dominate over the ionic expansion in the lowest $4f^{n-1}5d$ state, all of it leading to a bond length shrinkage. In the upper $4f^{n-1}5d$ states, the positive ionic and ligand field splitting contributions are larger in general than the negative covalent and charge transfer contributions, so leading to a bond length elongation . This, however, can be of a very small size, so leading to upper $4f \rightarrow 5d$ excitation bands narrower than the lowest ones (Fig. 1).

The bond length shortening in the lowest $4f \rightarrow 5d$ absorptions has been shown to produce red shifts of the $5d \rightarrow 4f$ emission and the lowest $4f \rightarrow 5d$ absorptions under high pressure in $Cs_2NaYCl_6:Ce^{3+}$ [61] and $SrF_2:Sm^{2+}$ [62]. In absence of direct measurements of lanthanide-ligand distances in the ground and excited states, the previous observation of pressure induced red shifts in the latter material [63] and the subsequent measurements in the former material [64] give a strong support to the insight provided by ab initio calculations.

Another assumption is commonly accepted on the spin character of the low-lying states of the $4f^{n-1}5d$ configuration of heavy lanthanide ions ($n > 7$): The lowest part of their $4f \rightarrow 5d$ absorption spectra is normally made of a first low-intensity band followed by one or several high-intensity bands. They are usually interpreted as spin-forbidden and spin-allowed transitions, respectively, taking place from a ground state of the $4f^n$ configuration, which has a lower spin than the first $4f^{n-1}5d$ state due to $n > 7$. Ab initio calculations on $CsCaBr_3:Yb^{2+}$ [65] have shown that the lower states of the $4f^{n-1}5d$ configuration, which are associated with the low-intensity band, have indeed a clear high-spin character, higher than 90%. However, they have also shown

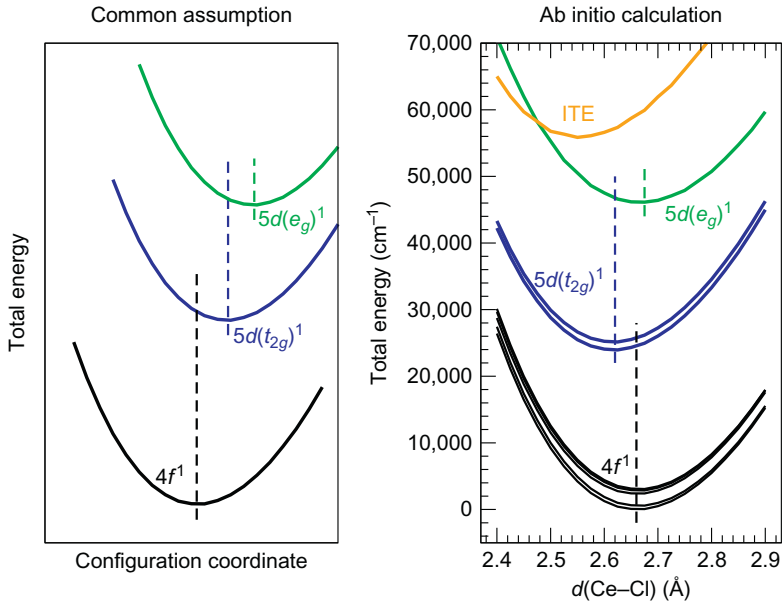

FIG. 1 *Left*: Qualitative configuration coordinate diagram of the $4f$ and $5d$ states of Ce^{3+} in an octahedral site of a host as it is commonly found in the literature. *Right*: Ab initio potential energy curves of Ce^{3+} along the totally symmetric breathing vibrational mode in the cubic elpasolite $Cs_2LiLuCl_6$ [60].

that the states immediately above them, which are responsible for the strong absorption bands, also have a dominant high-spin character, are higher than 55%. Their low-spin contributions (of a spin identical to that of the ground state) are not dominant, which makes it misleading to name these states low-spin states; as it is misleading to call the strong absorption bands spin-allowed transitions. However, their low-spin character, not being dominant, is sufficient to give them the observed high intensity. This converts the transitions into spin-enabled transitions.

A few other common assumptions have been corrected by ab initio calculations. First, the lowest state of the $4f^15d^1$ configuration of Pr^{3+} in solid hosts is a spin triplet; however it is 80% spin singlet, as it has been shown by [66]. An incorrect extension of Hund's rule to the case of electrons not sharing the same orbital shell might be behind this misconception. Second, the $4f^1$ levels of Ce^{3+} in garnets and other hosts split into two sets, basically associated with the free-ion levels $^2F_{5/2}$ and $^2F_{7/2}$; however they have been shown to split into three sets well separated in energy in $Y_3Al_5O_{12}$:Ce^{3+} and other Ce-doped garnets [67]: a first set of three levels results from the splitting of $^2F_{5/2}$, a second set of three levels from the splitting of $^2F_{7/2}$, and the seventh level from a strong interaction between $^2F_{5/2}$ and $^2F_{7/2}$ components; $5d \rightarrow 4f$ emission to

the upper level has a very low intensity, hence the $5d \rightarrow 4f$ emission band shows two clear main components only. Third, the energies of the states of $4f^{n-1}6s$ configuration of lanthanides above the ground state are similar in solids and in the gas phase, but ab initio calculations have shown that they undergo a large blue shift in the solid host as a consequence of the confinement of the 6*s* electron [68]. Since the above assumptions are not special and they do not have an issue common to all of them, we may expect more assumptions needing reconsideration when they are confronted with ab initio results in future calculations.

3.4.3 Giving Insight: Helping Understanding Spectroscopy and Excited States

Another form of giving insight is providing information that complements spectroscopic experiments, evaluates contradictory interpretations, and extends the understanding of the complex manifolds of excited states. We summarize here some examples that illustrate how wave function theory ab initio calculations work together with experiments for drawing a complete picture of the excited states of lanthanide-containing materials.

A long standing puzzle in the attempts to control the color of the $5d \rightarrow 4f$ emission of YAG:Ce^{3+}, which is one of the most heavily studied lanthanide-activated phosphor material since the pioneering work of [69], was that it showed an opposite shift (blue and red) when it was co-doped with Ga^{3+} and La^{3+} respectively, in spite of the fact that both co-dopings produced a lattice expansion. The reduction of the $Ce^{3+}5d$ ligand field splitting by the lattice expansion could only account for the blue shift. The red shift was explained by ab initio calculations [70, 71] as due to the fact that the preferred site for La^{3+} as a co-dopant is at the Y^{3+} site closest to Ce^{3+}. This enhances the splitting of the $Ce^{3+}5d$ orbitals because the Pauli repulsion exerted on them by the $La^{3+}5p$ orbitals is larger than by the original, smaller $Y^{3+}4p$ orbitals (the Pauli repulsion is a short-range interaction created by the need of the $Ce^{3+}5d$ orbitals of being orthogonal to environmental orbitals and it ultimately acts in a way equivalent to an external negative charge).

Other examples that involve an ab initio analysis of either a relatively simple excited manifold like that of Ce^{3+}, or selected transitions of more complex manifolds, are: The effects of local charge compensations on $4f \rightarrow 5d$ transitions in CaF_2:Ce^{3+} [72]; the comparison of the lowest $4f \rightarrow 5d$ absorptions and their corresponding $5d \rightarrow 4f$ emissions of Ce^{3+}, Pr^{3+}, Nd^{3+}, Pm^{3+}, Sm^{3+}, Eu^{3+}, Gd^{3+}, and Tb^{3+} active ions in the elpasolite Cs_2NaYCl_6 [27], with $4f^{1-8}$ and $4f^{0-7}5d^1$ manifolds involved; the effects of high hydrostatic pressures on selected $4f \rightarrow 5d$ transitions in SrF_2:Sm^{2+} [62], which involves $4f^6$ and $4f^5 5d^1$ configurations.

Detailed analyses of excited manifolds with tens or hundreds of states have also been performed, for instance, for the $4f^7$ and $4f^6 5d^1$ manifolds of Eu^{2+} as a dopant in CaF_2 [73], the $4f^8$ and $4f^7 5d^1$ manifolds of Tb^{3+} as a

dopant in BaF_2 [74], or the $4f^{13}5d^1$, $4f^{13}6s^1$, and $4f^{13}\phi^1_{ITE}$ ITE manifolds of Yb^{2+} as a dopant in $SrCl_2$ [75].

Also, ab initio studies involving two cations led to new interpretations of the so-called anomalous emissions of some materials: The very broad, anomalous emission of Ce^{3+} in elpasolites, which shows a very large red-shift with respect to the expected, regular $Ce^{3+}5d(e_g) \rightarrow 4f$ emission, has been shown not to be due to any ITE emitter of unknown nature, as previously assumed, but to an IVCT emission in which an electron is transferred from $5d(e_g)$ orbitals of Ce^{3+} to $4f$ orbitals of a Ce^{4+} ion lying in its neighborhoods [60]. The broadness and the very large red shift of the emission are a consequence of the very large atomistic reorganizations that take place around the two Ce centers after the electron transfer. Equivalently, the very broad and very much red-shifted anomalous luminescence of Yb^{2+} in fluorite-like crystals is interpreted as an IVCT emission made of a two electron deexcitation: $Yb^{2+}5(de_g) \rightarrow Yb^{3+}4f_{7/2}$ accompanied by a $4f_{7/2} \rightarrow 4f_{5/2}$ deexcitation within the $Yb^{2+}4f^{13}$ subshell [76]. This emission is excited by a $Yb^{2+}4f \rightarrow 5d(e_g)$ absorption, followed by a $Yb^{2+}5d(e_g) \rightarrow Yb^{3+}4f_{7/2}$ IVCT nonradiative decay, and a second $Yb^{2+}4f \rightarrow 5d(e_g)$ absorption. Besides an interpretation of the anomalous emission, these ab initio studies explain why there is such a complex interplay between the anomalous and regular $5d \rightarrow 4f$ emissions of Yb^{2+} in fluorite crystals: only anomalous emission, only $5d \rightarrow 4f$ emission, both of them, and none of them, respectively, are observed in CaF_2:Yb^{2+}, $SrCl_2$:Yb^{2+}, SrF_2:Yb^{2+}, and BaF_2:Yb^{2+}. The IVCT also explains that in partly reduced CaF_2:Yb^{3+} the excitation spectrum of the $Yb^{3+}4f_{7/2} \rightarrow 4f_{5/2}$ NIR emission shows the $Yb^{2+}4f \rightarrow 5d$ absorptions . And it can reproduce in detail the results of fine transient photoluminescence enhancement experiments in CaF_2:Yb^{2+} and SrF_2:Yb^{2+} [77]. Along the same line, ab initio calculations have also been able to explain the details of photoconductivity experiments on CaF_2:Yb^{2+} and SrF_2:Yb^{2+} as due to two-photon Yb^{2+}-to-Ca^{2+} and Yb^{2+}-to-Sr^{2+} MMCT absorptions [78].

4 DFT METHODS

Although standard DFT methods use correlation functionals that allow them to calculate dynamic correlation with sufficient accuracy in many cases, they are based on the use of a single determinant reference and have difficulties representing the nondynamic correlations accompanying relatively short multiconfigurational expansions like those in the CASSCF wave function method. As a consequence of this, they cannot reproduce the multiplet structure of unfilled shells.

In an attempt to overcome this difficulty and make the DFT methods useful in the context of excited states of lanthanide-containing materials with optical activity, a mixed procedure has been used in which a DFT calculation is done firstly on an embedded cluster and, later, the DFT molecular orbitals are used to calculate (wave function theory) ligand field matrices of

$4f^n$ and $4f^{n-1}5d$ configurations, which are finally diagonalized to give the target states of these configurations. The ligand field matrices are CI matrices of a relatively small size and are not to be confused with CASSCF matrices, which are in general much larger, nor with the matrices of standard CI quantum chemical calculations that are several orders of magnitude larger; CASSCF matrices include all kinds of excitations within the active orbitals and CI matrices like SDCI include single and double excitations to many empty or virtual orbitals. Such mixed procedure has been applied with the choice of a Four-component Discrete Variational Xα (DV-Xα) calculation (which can be understood as a Four-component DFT calculation with an exchange-correlation functional that uses Slater's Xα exchange functional and lacks dynamic correlation), eg, on $4f \rightarrow 5d$ transitions of Pr^{3+}-doped LaF_3, $LiYF_4$, and CaF_2 [79]. With a choice of one-component DFT calculations using standard local density approximation (LDA) and generalized gradient approximation (GGA) functionals, it has been applied, eg, to Pr^{3+}-doped Cs_2KYF_6 under the name ligand field DFT (LFDFT) [80].

Other approaches have also been followed in order to obtain information on the excited states of lanthanides in solids by means of PBC DFT. For instance, PBC DFT+U calculations in which the energy difference between the valence-band maximum (VBM) of the host and the 4*f* levels are empirically tunned by means of the U parameter, and the energies of the 5*d* levels with respect to the conduction band minimum (CBM) are obtained by substracting experimental $4f \rightarrow 5d$ absorption energies and calculated 4*f* VBM differences from the calculated band gap of the material have been used to predict the scintillation or nonscintillation of Ce^{3+}-doped and Eu^{2+}-doped inorganic solids [81, 82]. Also, the one-electron transitions between occupied and unoccupied Bloch orbitals obtained as the imaginary part of the dielectric function in PBC DFT calculations have been compared with experimental $4f \rightarrow 4f$ and $4f \rightarrow 5d$ absorption spectra of Ce-doped and co-doped $Y_3Al_5O_{12}$ [83].

PBC DFT ground state structural calculations have also been combined with embedded cluster wave function theory calculations of excited states. For instance, in $Y_3Al_5O_{12}$ doped with Ce and co-doped with La and Ga [70, 71], the blue shift of the Ce^{3+} lowest $4f - 5d$ transition upon Ga co-doping, which becomes a red shift upon La co-doping in spite of the fact that both co-dopings produce lattice expansions, has been explained using atomistic structures of $Ce,Ga:Y_3Al_5O_{12}$ and $Ce,La:Y_3Al_5O_{12}$ calculated at the PBC DFT level and energies of the $4f^1$ and $5d^1$ manifolds calculated with the CASSCF-/CASPT2/RASSI-SO wave function methods. The same procedure was followed in a number of works; see, for instance [84, 85].

One of the limitations of DFT calculations lies in the difficulties for structural optimization of excited states, which causes problems to calculate emission energies and Stokes shifts. This limitation is partially overcome by forcing the occupation of the one electron levels, which facilitates structural optimizations in excited configurations (not excited many-electron states)

[81, 82]. Another way is to use atomistic structures within the unit cell as obtained in ground state DFT calculations with PBC, and reoptimize the position of a number of atoms in every excited state in embedded cluster wave function theory calculations. Such kind of excited state partial structural reoptimization has been done at the CASSCF/CASPT2/RASSI-SO level of calculation in a number of Ce^{3+}-doped garnets in order to study the effect of local relaxations on the $5d \rightarrow 4f$ emissions [57], which have been found responsible, eg, for the differences between Ce^{3+}:$Y_3Al_5O_{12}$ and Ce^{3+}:$Lu_3Al_5O_{12}$.

5 REDUCING THE GAP WITH EXPERIMENTS

Although ab initio calculations are already contributing to a better understanding of the excited states of lanthanide-containing materials as a consequence of the developments in the last decades, their potential is far from being fully exploited and the gap between calculations and experiments can be largely reduced. For this to happen, ab initio methods should face the following challenges: Improving their accuracy; becoming applicable to more complex problems, both in atomistic terms (number of atoms in the active defects) and in numbers and types of excited states; and extending the list of properties delivered.

The accuracy of the calculations seems to be limited by the treatments of electron correlation and embedding effects. In wave function theory methods, new developments in the calculation of dynamic correlation might give an important impulse, together with the developments of improved embedding techniques. In PBC DFT methods, the developments in the consideration of nondynamic correlation and the access to excited states might have the strongest impact. Fortunately, the accuracies already achieved for the relativistic effects up to spin–orbit coupling are very high.

Nowadays, ab initio calculations can be systematically applied to excited manifolds of active centers containing one active lanthanide with unfilled orbital shells and tens of other atoms, and tens or hundreds of local excited states. The development of efficient low scaling and parallel algorithms, together with more powerful computers, might perhaps increase the above numbers by one order of magnitude in the coming years. Being able to handle active centers involving several lanthanide ions with unfilled shells (which implies being able to calculate electronic couplings, intensities, etc. of IVCT and MMCT excited states) poses a major challenge. It can perhaps be met with new developments on perturbation theory methods based on general active-space self-consistent field wave functions.

Some of the spectroscopically interesting properties regularly calculated in ab initio calculations of lanthanide-containing luminescent materials include: (i) potential energy surfaces of the ground and excited states and, from them, properties such as equilibrium structures, vibrational frequencies, absorption and emission band maxima, zero-phonon lines, and some nonradiative decay

mechanisms; (ii) electric (and magnetic) dipole oscillator strengths and radiative rates of purely electronic transitions. A few other interesting properties harder to calculate, that would help drawing much more complete pictures are: vibronic couplings and their induced intensities; nonradiative decay rates deduced from multistate molecular dynamics; intensities of IVCT and MMCT transitions; and energy transfer rates in general. The two latter types of properties would be directly attainable from the more complex calculations mentioned in the last paragraph; the others imply handling nuclear dynamics and involve complexities specific to this field and external to the pure electronic structure issues.

ACKNOWLEDGMENTS

This work was partly supported by a grant from Ministerio de Economía y Competitivad, Spain (Dirección General de Investigación y Gestión del Plan Nacional de I+D+I, MAT2014-54395-P).

ABBREVIATIONS AND ACRONYMS

CASPT2	complete active-space second-order perturbation theory
CASSCF	complete active-space self-consistent field
CI	configuration interaction
DFT	density functional theory
EXAFS	extended X-ray absorption fine structure
ITE	impurity-trapped exciton
IVCT	intervalence charge transfer
LMCT	ligand-to-metal charge transfer
MMCT	metal-to-metal charge transfer
PBC	periodic-boundary conditions
RASSI-SO	restricted active-space state-interaction with spin–orbit coupling
VBM	valence-band maximum

REFERENCES

[1] H. Bethe, Termaufspaltung in kristallen, Ann. Phys. 395 (1929) 133–208.
[2] R. Finkelstein, J.H. Van Vleck, On the energy levels of chrome alum, J. Chem. Phys. 8 (1940) 790–797.
[3] M.F. Reid, F.S. Richardson, Free-ion, crystal-field, and spin-correlated crystal-field parameters for lanthanide ions in $Cs_2NaLnCl_6$ and Cs_2NaYCl_6:Ln^{3+} systems, J. Chem. Phys. 83 (1985) 3831.
[4] B.R. Judd, Optical absorption intensities of rare-earth ions, Phys. Rev. 127 (1962) 750–761.
[5] G.S. Ofelt, Intensities of crystal spectra of rare-earth ions, J. Chem. Phys. 37 (1962) 511–520.
[6] G. Blasse, Classical phosphors: a Pandora's box, J. Lumin. 72-74 (1997) 129–134.

[7] M. Dolg, H. Stoll, Electronic structure calculations for molecules containing lanthanide atoms, in: Handbook on the Physics and Chemistry of Rare Earths, 22, Elsevier, 1996, pp. 607–729. chap. 152.
[8] L. Seijo, Z. Barandiarán, Relativistic ab-initio model potential calculations for molecules and embedded clusters, in: P. Schwerdtfeger (Ed.), Relativistic Electronic Structure Theory: Part 2. Applications, Elsevier, Amsterdam, 2004, pp. 417–475.
[9] D. Michael (Ed.), Computational Methods in Lanthanide and Actinide Chemistry, Wiley Online Library, 2015.
[10] Z. Barandiarán, L. Seijo, 4*f*, 5*d*, 6*s*, and impurity-trapped exciton states of lanthanides in solids, in: M. Dolg (Ed.), Computational Methods in Lanthanide and Actinide Chemistry, John Wiley & Sons, New York, 2015, pp. 217–240.
[11] P. Hohenberg, W. Kohn, Inhomogeneus electron gas, Phys. Rev. B 136 (1964) B864.
[12] W. Kohn, L.J. Sham, Self-consistent equations including exchange and correlation effects, Phys. Rev. 140 (1965) A1133.
[13] Erich Runge, E.K.U. Gross, Density-functional theory for time-dependent systems, Phys. Rev. Lett. 52 (1984) 997–1000.
[14] G.H. Dieke, Spectra and Energy Levels of Rare Earth Ions in Crystals, Interscience Publishers, New York, 1968.
[15] L. van Pieterson, M.F. Reid, G.W. Burdick, A. Meijerink, $4f^n \rightarrow 4f^{n-1}5d$ transitions of the heavy lanthanides: experiment and theory, Phys. Rev. B 65 (2002) 045114.
[16] L. van Pieterson, M.F. Reid, R.T. Wegh, S. Soverna, A. Meijerink, $4f^n \rightarrow 4f^{n-1}5d$ transitions of the light lanthanides: experiment and theory, Phys. Rev. B 65 (2002) 045113.
[17] Lidia Smentek, Judd-Ofelt theory–the golden (and the only one) theoretical tool of f-electron spectroscopy, in: M. Dolg (Ed.), Computational Methods in Lanthanide and Actinide Chemistry, John Wiley & Sons, New York, 2015, pp. 241–268.
[18] M.F. Reid, Theoretical accounts of rare-earth spectroscopy, in: Handbook on the Physics and Chemistry of Rare Earths, 50 Elsevier, 2016. chap. 50-4.
[19] P. Dorenbos, The 5d level positions of the trivalent lanthanides in inorganic compounds, J. Lumin. 91 (2000) 155.
[20] C.W. Thiel, H. Cruguel, H. Wu, Y. Sun, G. Lapeyre, R.L. Cone, R. Equall, R. Macfarlane, Systematics of 4*f* electron energies relative to host bands by resonant photoemission of rare-earth ions in aluminum garnets, Phys. Rev. B 64 (2001) 085107.
[21] P. Dorenbos, Systematic behaviour in trivalent lanthanide charge transfer energies, J. Phys. Cond. Matter 15 (49) (2003) 8417–8434.
[22] P. Dorenbos, A Review on how lanthanide impurity levels change with chemistry and structure of inorganic compounds, ECS J. Solid State Sci. Technol. 2 (2) (2013) R3001–R3011.
[23] JonasJ. Joos, Dirk Poelman, PhilippeF. Smet, Energy level modeling of lanthanide materials: review and uncertainty analysis, Phys. Chem. Chem. Phys. 17 (2015) 19058–19078.
[24] C.A. Morrison, Host dependence of the rare-earth ion energy separation $4f^N - 4f^{N-1}nl$, J. Chem. Phys. 72 (1980) 1001.
[25] B.R. Judd, Correlation crystal fields for lanthanide ions, Phys. Rev. Lett. 39 (1977) 242.
[26] M. Bettinelli, R. Moncorgé, Correlation between the 5*d*-level position of Ce^{3+} and of the other Ln^{3+} ions in solids, J. Lumin. 92 (2001) 287–289.
[27] F. Ruipérez, Z. Barandiarán, L. Seijo, Quantum chemical study of $4f - 5d$ transitions of trivalent lanthanide ions doped in the cubic elpasolite Cs_2NaYCl_6 Ce^{3+} to Tb^{3+}, J. Chem. Phys. 123 (2005) 244703.
[28] D.S. McClure, C. Pédrini, Excitons trapped at impurity centers in highly ionic crystals, Phys. Rev. B 32 (1985) 8465.

[29] Z. Barandiarán, A. Meijerink, L. Seijo, Configuration coordinate energy level diagrams of intervalence and metal-to-metal charge transfer states of dopant pairs in solids, Phys. Chem. Chem. Phys. 17 (2015) 19874.
[30] R.S. Mulliken, Electronic population analysis on LCAO-MO molecular wave functions. I, J. Chem. Phys. 23 (1955) 1833–1840.
[31] Per-Olov Löwdin, Harrison Shull, Natural orbitals in the quantum theory of two-electron systems, Phy. Rev. 101 (1956) 1730–1739.
[32] P.S. Bagus, K. Hermann, C.W. Bauschlicher, A new analysis of charge transfer and polarization for ligand-metal bonding: model Studies of Al_4CO and Al_4NH_3, J. Chem. Phys. 80 (1984) 4378–4386.
[33] M.A. Nygren, L.G.M. Pettersson, Z. Barandiarán, L. Seijo, Bonding between CO and the MgO(001) surface: a modified picture, J. Chem. Phys. 100 (1994) 2010.
[34] A. Meijerink, Revisiting Pandora's box of luminescence, in: 9th Annual Phosphor Global Summit, San Antonio, TX, 2011.
[35] A.J. Salkeld, M.F. Reid, J.-P.R. Wells, G. Sánchez-Sanz, L. Seijo, Z. Barandiarán, Effective Hamiltonian parameters for abinitio energy-level calculations of $SrCl_2$:Yb^{2+} and $CsCaBr_3$:Yb^{2+}, J. Phys. Cond. Matter 25 (2013) 415504.
[36] R.G. Shulman, S. Sugano, Covalency effects in KNiF3. I. Nuclear magnetic resonance studies, Phys. Rev. 130 (1963) 506.
[37] L. Seijo, Z. Barandiarán, The ab initio model potential method: a common strategy for effective core potential and embedded cluster calculations, in: J. Leszczyński (Ed.), Computational Chemistry: Reviews of Current Trends, 4, World Scientific, Singapore, 1999, pp. 55–152.
[38] R. McWeeny, Methods of Molecular Quantum Mechanics, second, Academic Press, London, 1989. chap. 14.
[39] T. Wesolowski, A. Warshel, Frozen density functional approach for ab initio calculations of solvated molecules, J. Phys. Chem. 97 (1993) 8050–8053.
[40] B.O. Roos, P.R. Taylor, P.E.M. Siegbahn, A Complete active space SCF method (CASSCF) using a density-matrix formulated super-CI approach, Chem. Phys. 48 (1980) 157–173.
[41] P.E.M. Siegbahn, A. Heiberg, B.O. Roos, B. Levy, Comparison of the super-CI and the Newton-Raphson scheme in the complete active space SCF method, Phys. Scr. 21 (1980) 323–327.
[42] P.E.M. Siegbahn, A. Heiberg, J. Almlöf, B.O. Roos, The complete active space SCF (CASSCF) method in a Newton-Raphson formulation with application to the HNO molecule, J. Chem. Phys. 74 (1981) 2384–2396.
[43] K. Andersson, P.-Å. Malmqvist, B.O. Roos, A.J. Sadlej, K. Wolinski, Second-order perturbation theory with a casscf reference function, J. Phys. Chem. 94 (1990) 5483–5488.
[44] K. Andersson, P.-Å. Malmqvist, B.O. Roos, Second-order perturbation theory with a complete active space self-consistent field reference function, J. Chem. Phys. 96 (1992) 1218–1226.
[45] A. Zaitsevskii, J.-P. Malrieu, Multi-partitioning quasidegenerate perturbation theory. A new approach to multireference Møller-Plesset perturbation theory, Chem. Phys. Lett. 233 (1995) 597–604.
[46] J. Finley, P.-Å. Malmqvist, B.O. Roos, L. Serrano-Andrés, The multi-state CASPT2 method, Chem. Phys. Lett. 288 (1998) 299–306.
[47] A. Kramida, Yu. Ralchenko, J. Reader, NIST ASD Team, NIST atomic spectra database (ver. 5.3), 2015). http://physics.nist.gov/asd. [2015, November 26]. National Institute of Standards and Technology, Gaithersburg, MD.

[48] Trond Saue, Lucas Visscher, Relativistic all-electron approaches to the study of *f* element chemistry, in: M. Dolg (Ed.), Computational Methods in Lanthanide and Actinide Chemistry, John Wiley & Sons, New York, 2015, pp. 55–87.
[49] M. Douglas, N.M. Kroll, Quantum electrodynamical corrections to the fine structure of helium, Ann. Phys. (N.Y.) 82 (1974) 89–155.
[50] B.A. Hess, Relativistic electronic-structure calculations employing a two-component no-pair formalism with external-field projection operators, Phys. Rev. A 33 (1986) 3742–3748.
[51] S. Yabushita, Z. Zhang, R.M. Pitzer, Spin-orbit configuration interaction using graphical unitary group approach and relativistic core potential and spin-orbit operators, J. Phys. Chem. A 103 (1999) 5791.
[52] R. Llusar, M. Casarrubios, Z. Barandiarán, L. Seijo, Ab initio model potential calculations on the electronic spectrum of Ni^{2+}-doped MgO including correlation, spin-orbit and embedding effects, J. Chem. Phys. 105 (1996) 5321–5330.
[53] P.A. Malmqvist, B.O. Roos, B. Schimmelpfennig, The RASSI approach with spin-orbit coupling, Chem. Phys. Lett. 357 (2002) 230–240.
[54] P. Ghigna, S. Pin, C. Ronda, A. Speghini, F. Piccinelli, M. Bettinelli, Local structure of the Ce^{3+} ion in the yellow emitting phosphor YAG:Ce, Opt. Mater. 34 (2011) 19–22.
[55] A.B. Muñoz-García, L. Seijo, Ce and La single- and double-substitutional defects in yttrium aluminum garnet: first-principles study, J. Phys. Chem. A 115 (2011) 815.
[56] J. Gracia, L. Seijo, Z. Barandiarán, D. Curulla, H. Niemansverdriet, W. van Gennip, Ab initio calculations on the structure and the $4f - 5d$ absorption and emission spectra of Ce^{3+}-doped YAG, J. Lumin. 128 (2008) 1248.
[57] QuanManh Phung, Zoila Barandiarán, Luis Seijo, Structural relaxation effects on the lowest $4f - 5d$ transition of Ce^{3+} in garnets, Theor. Chim. Acc. 134 (2015) 37.
[58] Z. Barandiarán, L. Seijo, Quantum chemical analysis of the bond lengths in f^n and $f^{n-1}d^1$ states of Ce^{3+}, Pr^{3+}, Pa^{4+}, and U^{4+} defects in chloride hosts, J. Chem. Phys. 119 (2003) 3785.
[59] Z. Barandiarán, N.M. Edelstein, Belén Ordejón, F. Ruipérez, L. Seijo, Bond lengths of 4f(1) and 5d(1) states of Ce^{3+} hexahalides, J. Solid State Chem. 178 (2005) 464.
[60] L. Seijo, Z. Barandiarán, Intervalence charge transfer luminescence: the anomalous luminescence of Ce-doped $Cs_2LiLuCl_6$ elpasolite, J. Chem. Phys. 141 (2014) 214706.
[61] F. Ruipérez, L. Seijo, Z. Barandiarán, Prediction of pressure-induced redshift of $f^1 \rightarrow d(t_{2g})^1$ excitations in $Cs_2NaYCl_6:Ce^{3+}$ and its connection with bond-length shortening, J. Chem. Phys. 122 (2005) 234507.
[62] J.L. Pascual, Z. Barandiarán, L. Seijo, Relation between high-pressure spectroscopy and $f^{N-1}d^1$ excited-state geometry: a comparison between theoretical and experimental results in $SrF_2:Sm^{2+}$, Phys. Rev. B 76 (2007) 104109.
[63] C.S. Yoo, H.B. Radousky, N.C. Holmes, N.M. Edelstein, Luminescence of Sm^{2+} ions as a probe of pressure-induced phase transitions in SrF_2, Phys. Rev. B 44 (1991) 830.
[64] R. Valiente, F. Rodríguez, J. González, H.U. Güdel, R. Martín-Rodríguez, L. Nataf, M. N. Sanz-Ortiz, K. Krämer, High pressure optical spectroscopy of Ce^{3+}-doped $Cs_2NaLuCl_6$, Chem. Phys. Lett. 481 (2009) 149.
[65] G. Sánchez-Sanz, L. Seijo, Z. Barandiarán, Spin-forbidden and spin-enabled $4f^{14} - 4f^{13}5d$ transitions of Yb^{2+}-doped $CsCaBr_3$, J. Chem. Phys. 131 (2009) 024505.
[66] Marek Krośnicki, Andrzej Kdziorski, Luis Seijo, Zoila Barandiarán, Ab initio theoretical study on the $4f^2$ and $4f5d$ electronic manifolds of cubic defects in $CaF_2:Pr^{3+}$, J. Phys. Chem. A 118 (2014) 358–368.
[67] L. Seijo, Z. Barandiarán, Large splittings of the 4f shell of Ce^{3+} in garnets, Phys. Chem. Chem. Phys. 16 (2014) 3830–3834.

[68] G. Sánchez-Sanz, L. Seijo, Z. Barandiarán, Energy shift of the $4f^{13}6s$ excited states of Yb^{2+} from gas phase to the $CsCaBr_3$ solid, Spec. Lett. 43 (2010) 393.
[69] G. Blasse, A. Bril, Investigation of some Ce^{3+}-activated phosphors, J. Chem. Phys. 47 (1967) 5139.
[70] A.B. Muñoz-García, J.L. Pascual, Z. Barandiarán, L. Seijo, Structural effects and $4f - 5d$ transition shifts induced by La codoping in Ce-doped yttrium aluminum garnet: first-principles study, Phys. Rev. B 82 (2010) 064114.
[71] A.B. Muñoz-García, L. Seijo, Structural, electronic, and spectroscopic effects of Ga codoping on Ce-doped yttrium aluminum garnet: first-principles study, Phys. Rev. B 82 (2010) 184118.
[72] L. Ning, C. Wu, L. Li, L. Lin, C. Duan, Y. Zhang, L. Seijo, First-principles study on structural properties and $4f - 5d$ transitions of locally charge-compensated Ce^{3+} in CaF_2, J. Phys. Chem. C 116 (2012) 18419–18426.
[73] F. Aiga, R. Hiramatsu, K. Ishida, Ab initio theoretical study of $4f - 5d$ transitions in Eu^{2+}-doped CaF_2, J. Lumin. 145 (2014) 951–955.
[74] J.L. Pascual, Z. Barandiarán, L. Seijo, Ab initio theoretical study of the $4f^8$ and $4f^7 5d$ manifolds of Tb^{3+}-doped BaF_2 cubic sites, J. Lumin. 145 (2014) 808.
[75] G. Sánchez-Sanz, L. Seijo, Z. Barandiarán, Yb^{2+}-doped $SrCl_2$: electronic structure of impurity states and impurity-trapped excitons, J. Chem. Phys. 133 (2010) 114509.
[76] Z. Barandiarán, L. Seijo, Intervalence charge transfer luminescence: interpaly between anomalous and $5d - 4f$ emissions in Yb-doped florite-type crystals, J. Chem. Phys. 141 (2014) 234704.
[77] M.F. Reid, P.S. Senanayake, J.-P.R. Wells, G. Berden, A. Meijerink, A.J. Salkeld, C.-K. Duan, R.J. Reeves, Transient photoluminescence enhancement as probe of the structure of impurity-trapped excitons in CaF_2:Yb^{2+}, Phys. Rev. B 84 (2011) 113110.
[78] Z. Barandiarán, L. Seijo, Metal-to-metal charge transfer between dopant and host ions: photoconductivity of Yb-doped CaF_2 and SrF_2 crystals, J. Chem. Phys. 143 (2015) 144702.
[79] T. Ishii, M.G. Brik, K. Ogasawara, First-principles analysis method for the multiplet structures of rare-earth ions in solids, J. Alloys Compd. 380 (2004) 136.
[80] H. Ramanantoanina, W. Urland, F. Cimpoesu, C. Daul, Ligand field density functional theory calculation of the $4f^2 - 4f^1 5d^1$ transitions in the quantum cutter Cs_2KYF_6:Pr^{3+}, Phys. Chem. Chem. Phys. 15 (2013) 13902–13910.
[81] A. Canning, A. Chaudhry, R. Boutchko, N. Grønbech-Jensen, First-principles study of luminescence in Ce-doped inorganic scintillators, Phys. Rev. B 83 (2011) 125115.
[82] A. Chaudhry, R. Boutchko, S. Chourou, G. Zhang, N. Grønbech-Jensen, A. Canning, First-principles study of luminescence in Eu^{2+}-doped inorganic scintillators, Phys. Rev. B 89 (2014) 155105.
[83] K. Choudhary, A. Chernatynskiy, K. Mathew, E.W. Bucholz, S.R. Phillpot, S.B. Sinnott, R. G. Hennig, Computational discovery of lanthanide doped and Co-doped $Y_3Al_5O_{12}$ for optoelectronic applications, Appl. Phys. Lett. 107 (2015) 112109.
[84] J. Wen, L. Ning, C.-K. Duan, Y. Chen, Y. Zhang, M. Yin, A theoretical study on the structural and energy spectral properties of Ce^{3+} ions doped in various fluoride compounds, J. Phys. Chem. C 116 (2012) 20513.
[85] L. Ning, F. Yang, C. Duan, Y. Zhang, J. Liang, Z. Cui, Structural properties and $4f - 5d$ absorptions in Ce-doped $LuAlO_3$: a first-principles study, J. Phys. Condens. Matter 24 (2012) 05502.

Chapter 286

Magnetic Bistability in Lanthanide-Based Molecular Systems: The Role of Anisotropy and Exchange Interactions

Dante Gatteschi[1], **Roberta Sessoli and Lorenzo Sorace**
Dipartimento di Chimica "U. Schiff" and INSTM UdR Firenze, Università degli Studi di Firenze, Sesto Fiorentino, Italy
[1]*Corresponding author: e-mail: dante.gatteschi@unifi.it*

Chapter Outline

1 INTRODUCTION

The magnetic properties of lanthanides have long been investigated for applications. Even if all the technologically relevant permanent magnets are inorganic in nature, in the last years there has been an increasing interest in molecular magnets, i.e., systems having molecular structures that transfer unique properties to the materials. The investigation of molecular magnets

Handbook on the Physics and Chemistry of Rare Earths, Vol. 50. http://dx.doi.org/10.1016/bs.hpcre.2016.09.003

started with simple paramagnets, then moved to oligonuclear material, to low dimensional (one dimensional and two dimensional) and finally three-dimensional bulk magnets, which proved to be a fashionable research field. We just remind here the quest for "molecular ferromagnets," i.e., of molecular systems which could provide the same performance of permanent inorganic magnets [1]. The first evidence of magnetic order in a pure organic material dates back to 1973 [2], while ferromagnetism was observed for the first time in a nitronyl nitroxide radical in 1991 [3]. Most investigations focused however on transition metal ions [4,5].

More recent is the interest for molecular-based lanthanide magnets, which started to be systematically investigated in the 2000s. There are several good reasons for justifying the late arrival of lanthanide molecular magnets. The characterization of the magnetic properties of lanthanide-based molecular magnets requires the use of lower temperature compared to transition metal ions because the deviations from Curie law are small and therefore can only be measured in the liquid Helium range and below [6]. The unique properties of these complexes are associated with unquenched orbital momentum, which gives rise to strong anisotropy effects. This is an appealing feature, but there is a heavy toll to pay because the unquenched orbital momentum makes the interpretation of the magnetic properties much more complex, requiring a deep understanding of the electronic structure of the paramagnetic centers.

The efforts, both experimental and theoretical, for characterizing molecular Ln-based magnets, requested the use of several different techniques and sophisticated instrumentation, often difficult to financially justify. Matters started to change when the development of the so-called single-molecule magnets (SMMs) [7], became a hot topic for molecular magnetism. These polynuclear complexes show magnetic hysteresis like bulk magnets, but this is a molecular property, suggesting that they could be a good system for storing information. The characterization of these systems suggested that large easy axis type magnetic anisotropy, i.e., one favorite direction for the magnetization, is needed for achieving SMM behavior. Since the lanthanides are characterized by large anisotropy they represented an appealing set of materials to be investigated in this direction.

The development of molecular magnetism based on lanthanides has discovered new types of magnetic properties and new opportunities. There is an excitement for the development of materials which display the coexistence of quantum and classical effects and may contribute to the emerging field of quantum computing. These points will be worked out in the following in some detail and the opportunities for obtaining new magnetic properties will be described.

1.1 Magnetism of Isolated Ln Ions

The magnetic properties of single lanthanide ions can be described using a simple Hamiltonian which, in addition to hydrogen-like terms, encloses the

electron–electron, the spin–orbit interaction, and the ligand field in decreasing order of magnitude. One starts from the electron configuration $4f^n$ where n ranges from 1 to 14. The low-lying electron states are described by the L, S, and J quantum numbers, where S is the total electron spin, L is the orbital quantum number, and J is the total angular momentum arising from spin–orbit coupling. For the ground state $S=n/2$ and $J=L-S$ for $n\leq 7$, while $S=(14-n/2)$ and $J=L+S$ for $n\geq 7$. The corresponding L values are shown in Table 1, where we also indicate the spectroscopic term (F, H, …) of the ground state.

As long as we are interested in magnetic data, the consideration of only the ground J state is enough, with the exception of Sm(III) ($n=5$) and Eu(III) ($n=6$), for which low-lying excited states provide a remarkable second-order contribution to the susceptibility [8]. In a magnetic field, the use of standard theory provides the paramagnetic behavior of the various $4f^n$ ground states which, on the assumption of noninteracting ions, with no ligands yields:

$$\chi T=\frac{Ng_J^2\mu_B^2J(J+1)}{3k_B} \tag{1}$$

The coupling to the magnetic field is described by the g_J values

$$g_J=1+\frac{J(J+1)+S(S+1)-L(L+1)}{2J(J+1)} \tag{2}$$

For Eu(III), the ground state has $J=0$ and there is no first-order Zeeman splitting: however, application of a magnetic field provides second-order splitting for which the corresponding g_J factor can be calculated as $g_0=2+S=2+L=5$ [1]. The so-called free-ion limit for χT (reported in Table 1 for all the tripositive lanthanide ions) is a useful parameter to compare with room temperature χT value, to obtain an indication of deviations from single-ion spherical behavior. These deviations depend on the influence of the ligands on the energies of the single-ion states. Eventually, also spin–spin interactions, i.e., interactions between the ions, affect the magnetic properties.

1.2 Magnetic Bistability in Molecular Systems

The most relevant magnetic bistability in molecular material is the SMM behavior previously mentioned. Literature on the topic is very rich [7] and here only some very basic concepts will be introduced. The archetypal example of SMM is a molecular cluster comprising 12 manganese ions connected by oxide and carboxylate ions of formula $[Mn_{12}O_{12}(CH_3COO)_{16}(H_2O)_4]$, known as Mn_{12}acetate [9]. The temperature dependence of the magnetic moment of a single crystal of this cluster shows that, due to uncompensated intramolecular antiferromagnetic (AF) interactions, the ground state has a total spin $S=10$ and the component of the magnetization along the tetragonal axis of the molecule is much higher than the perpendicular one. This is the

TABLE 1 *S*, *L*, and *J* values and resulting Free–Ion χT product (in $cm^3\ K\ mol^{-1}$) for the Ground States of Ln(III) Ions

n	**1**	**2**	**3**	**4**	**5**	**6**	**7**	**8**	**9**	**10**	**11**	**12**	**13**
S	½	1	3/2	2	5/2	3	7/2	3	5/2	2	3/2	1	½
L	3(F)	5(H)	6(I)	6(I)	5(H)	3(F)	0(S)	3(F)	5(H)	6(I)	6(I)	5(H)	3(F)
J	5/2	4	9/2	4	5/2	0	7/2	6	15/2	8	15/2	6	7/2
g_J	6/7	4/5	8/11	3/5	2/7	5	2	3/2	4/3	5/4	6/5	7/6	8/7
χT	0.80	1.60	1.64	0.90	0.09	0.00	7.88	11.82	14.17	14.07	11.48	7.15	2.57

so-called Ising type magnetic anisotropy. This behavior can be modeled in first approximation with the spin Hamiltonian $H = DS_z^2$, where $D < 0$, which gives rise to the double-well potential schematized in Fig. 1. If the sample is magnetized at low temperature, i.e., only one of the two wells is populated, the return to equilibrium, corresponding to the demagnetization process, occurs through climbing the stair of levels inside the well. This gives rise to a relaxation time that increases exponentially at low temperature according to the Arrhenius law:

$$\tau = \tau_0 \exp\left(\frac{\triangle E}{k_B T}\right) \tag{3}$$

where $\triangle E \approx DS^2$ is the height of the barrier and τ_0 is a preexponential factor mainly reflecting the efficiency of spin–phonon coupling. As a result of Eq. (3) the relaxation time of Mn_{12}acetate is of the order of months below 2 K. In contrast to magnetic nanoparticles, the return to equilibrium can occur also via tunneling as expected for a quantum object. The efficiency of the tunneling is related to the possibility to delocalize the wavefunction on the two wells, which, in turn, depends on the presence of transverse terms in the spin Hamiltonian that admix states with different projection of the spin along the anisotropy axis, i.e., different $|m_S>$ states. While these transverse terms can have different origin, those arising from magnetocrystalline anisotropy are particularly relevant, especially when the spin of the system is large.

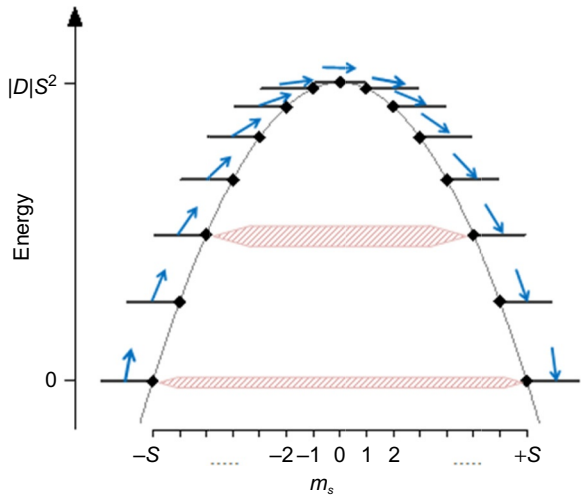

FIG. 1 Scheme of the double-well potential generated by uniaxial magnetic anisotropy on a system characterized by an integer spin state *S*. In the presence of transverse terms in the spin Hamiltonian admixing of states on opposite sides of the barrier is possible but strongly reduced for the ground doublet if *S* is large, as evidenced by the *pale shaded area* (the splitting of the levels is enhanced for clarity).

A gold rush started to design magnetic molecules showing magnetic bistability at higher temperatures than that exhibited by Mn_{12}acetate (ca. 4 K to observe an opening in the hysteresis cycle). Large spin, highly axial magnetic anisotropy with large and negative D values, are the key ingredients. Notwithstanding efforts and the many new SMMs based on d-block metal ions only marginal increase in ΔE and in the critical temperature for blocking the magnetization have been achieved [10].

In this scenario, where magnetic anisotropy is the key of magnetic bistability, it was immediately evident that lanthanide ions could contribute significantly. The anticipated improvements have been actually achieved and systems with barriers for the reversal of the magnetization estimated as high as 1000 K is now available [11], though hysteresis is only observable up to 15 K due to the efficiency of underbarrier mechanisms of relaxation.

In addition to these significant achievements, the use of lanthanide ions has also provided a qualitative breakthrough. In 2003, Ishikawa and coworkers [12] reported for the *bis*-phthalocyaninate complex $[TbPc_2]^-$ with the tetrabutyl ammonium cation slow relaxation of the magnetization detected by ac susceptibility at temperatures as high as 40 K. The peculiarity was that the molecule comprised just one lanthanide ion, indicating that intramolecular exchange interactions to build up a collective spin were not necessary to observe SMM behavior. This allowed focusing more on the magnetic anisotropy as the unique parameter to control at the synthetic level. The new term single-ion magnet (SIM) was employed, though the magnetic properties, including the bistability, were correlated to the molecular structure, in particular the highly uniaxial coordination environment dictated by the staggered configuration of the phthalocyaninate rings in the double-decker structure (see Fig. 2) [13].

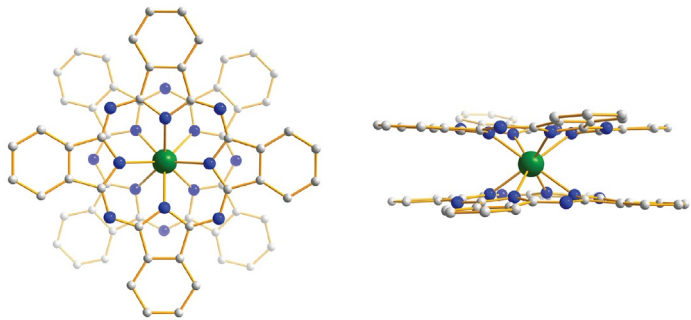

FIG. 2 Schematic top and side views of the double-decker structure that characterizes the series of *bis*-phthalocyaninate complexes $[LnPc_2]^{-,0,+}$. Lanthanide ion: *large green balls*; nitrogen atoms: *small blue balls*; carbon atoms: *small light gray balls*. Hydrogen atoms are omitted for clarity.

The family of double-decker lanthanide complexes has grown significantly in the last 10 years. The possibility to modify the redox state of the ligands [14,15], to functionalize the ring to achieve new functionalities or phases, such a liquid crystals [16] or self-assembled monolayers [17], as well as the possibility to evaporate the neutral species in vacuum [18], have further increased interest in these materials.

To conclude this short historical introduction, it is interesting to recall that SMM behavior is not the only type of magnetic bistability observable for molecular materials in the absence of long-range magnetic order. Paramagnetic metal ions arranged in one-dimensional structure with a magnetic interaction mediated by bridging ligands were used in the '80s as building blocks to obtain bulk magnets. Among the different bridges employed, nitronyl nitroxide radicals as the one schematized in Fig. 3 revealed to be particularly efficient in transmitting the magnetic interaction, thanks to the unpaired electron delocalized on the two N–O groups [19]. Exchange interactions of hundreds of cm^{-1} were found for dipositive 3d metal ions, e.g., Mn(II). The use of an anisotropic spin, such as Co(II), induced a slowing down of the magnetization that was then observed in other one-dimensional systems comprising metal ions with Ising type anisotropy [20]. The term single-chain magnet (SCM) was introduced for this novel behavior [21], indeed predicted in 1963 by Glauber for an Ising chain [22]. As the barrier for the reversal of the magnetization in SCM contains a term due to the exchange interactions, this suggested the possibility to act at the synthetic level on the magnetic exchange to achieve higher blocking temperatures. This has however occurred at the expenses of the richness in quantum effects that characterize SMM. Moreover, addressing single chains appear much more demanding than probing single molecules, which can be deposited on solid surfaces and investigated for instance with a scanning probe microscope.

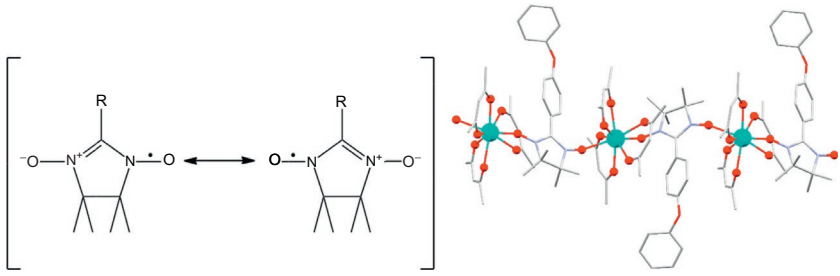

FIG. 3 (*Left*) Resonating structure of nitronyl nitroxide radicals used as bridging paramagnetic ligands thanks to the delocalization of the unpaired electron on the two equivalent N–O groups. (*Right*) Structure of the Dy(III) SCM obtained by using the radical with $R = C_6H_4–O–C_6H_5$. *Crystallographic data available in L. Bogani, C. Sangregorio, R. Sessoli, D. Gatteschi, Molecular engineering for single-chain-magnet behavior in a one-dimensional dysprosium-nitronyl nitroxide compound, Angew. Chem. Int. Ed. 44 (2005) 5817–5821.*

Given the key role played by anisotropy in the phenomenon, lanthanide ions were also employed to build SCMs but the inner nature of 4*f* orbitals hampered to achieve significantly improved performances. Despite the many reports of one-dimensional structures based on lanthanide ions it is often difficult to discern if the observed bistability comes from the anisotropy of the single ion, or is indeed associated to the magnetic correlation along the chain. A noticeable exception is the Dy(III) coordination polymer reported in Fig. 3, *right*, which actually shows genuine SCM behavior [23].

Depending on the nature of the radical it is possible to switch on the three-dimensional ordering to a ferrimagnetic phase [24]; this is hampered by bulky organic substituents like the one reported in Fig. 3, which reduce the interaction between chains.

It should be evident from the described examples that magnetic bistability in lanthanide-based molecular materials results from a subtle interplay between magnetic anisotropy and magnetic exchange. The optimization of both is far from trivial and requires sophisticated tools, at the experimental level and for the modeling. A brief survey of the state of the art in the field is the goal of the remaining of the chapter.

2 MAGNETIC ANISOTROPY IN LOW SYMMETRY COORDINATION ENVIRONMENTS

2.1 Most Employed Formalisms

Most of the relevant magnetic properties of lanthanide-based compounds stem from their large magnetic anisotropy. This occurs even in systems like molecular ones where low symmetry is rather the rule than the exception. The magnetic anisotropy is brought in by the effect of the ligand surrounding the Ln(III) ion on the ground multiplet characterized by a global J value arising from the spin–orbit coupling of L and S. The resulting levels cover an energy range which can easily be hundreds of cm^{-1}, and they will not be, in general, pure m_J states, but rather a combination of them. In this view, which considers the effect of the ligands as a perturbation on the prevailing electron–electron and spin–orbit interactions, the energy levels and their corresponding wavefunctions are obtained by applying a "crystal-field" Hamiltonian acting on the basis of the $2J+1$ functions of the $^{2S+1}L_J$ ground multiplet. In Stevens' notation, this electrostatic potential is expanded using a sum of equivalent angular momentum operators, and the corresponding matrix elements can be easily computed if mixing between different J multiplets is neglected [25–27]:

$$\mathcal{H}_{CF} = \sum_{k=2,4,6} \beta^k \sum_{q=0}^{k} A_k^q \langle r^k \rangle \hat{O}_k^q \tag{4}$$

where $\hat{O}_k^q$ are Stevens' operators, $A_k^q \langle r^k \rangle$ crystal field (CF) parameters, and β^k is a number which depends on the $4f^n$ configuration and on the k values

($k=2, 4, 6$) [25], accounting for the proportionality between angular momentum operators and CF potential. $\beta^2 < 0$ identifies so-called prolate ions, i.e., those for which the quadrupolar charge distribution of the highest m_J state has a prolate shape, whereas $\beta^2 > 0$ identifies oblate ions [28]. The number of terms with $q \neq 0$ to be included in (4) is limited by the point group of the rare-earth site, since the Hamiltonian has to be invariant under all symmetry operations of the point group. Alternatively, the effect of the ligands can be described using the Wybourne formalism [29], more suited when excited energy levels have to be explicitly taken into account, such as in optical spectroscopy. In this approach, the ligand field potential is expressed as:

$$\mathcal{H} = \sum_{k=0}^{\infty} \left[B_0^0 C_0(i) + \sum_{q=1}^{k} \left(B_q^k \left(C_{-q}^k(i) + (-1)^q C_q^k(i) \right) + iB'^k_q \left(C_{-q}^k(i) + (-1)^q C_q^k(i) \right) \right) \right] \tag{5}$$

where B_q^k and B'^k_q are the CF parameters, which are all real, and $C_q^k(i)$ are tensor operators, related to the spherical harmonics $Y_q^k(i)$ by:

$$C_q^k(i) = \sqrt{\frac{4\pi}{2k+1}} Y_q^k(i) \tag{6}$$

In much the same way as for Stevens' operators, the summation in Eq. (5) is limited to well-defined values: for *f*-electrons, the restriction $k \leq 7$ holds, while q is limited to those values consistent with the point symmetry of the site.

Whatever the formalism used, then, the number of independent CF parameters is small for highly symmetric coordination environments, while in the low symmetry environment that often characterizes molecular complexes it is too large to be extracted from simple magnetic data on powder samples. In this sense, additional experimental knowledge on the energy level structure of the Ln(III) molecular complexes can be gained by luminescence and far infrared (FIR) spectroscopy, inelastic neutron scattering, magnetic circular dichroism, electron and nuclear paramagnetic resonances and, as detailed in Section 2.3, by single-crystal angular-dependent magnetic characterization. However, even with the aid of these techniques, interpretation of data based on ligand field approach requires an intractable high number of parameters (27 for C_i symmetry), clearly too large to provide meaningful information.

A way to partially circumvent this problem is to describe the low temperature magnetic properties of lanthanide-based complexes by considering a pseudospin Hamiltonian, where the pseudospin is either a doublet (for Kramers ions) or a triplet (for non-Kramers ones) [30]. The parameters of these pseudospin Hamiltonians are effective, highly anisotropic **g** and, for pseudotriplet, zero-field splitting tensors: their values depend on the composition of the wavefunction and can thus provide some relevant information

about the effect of the ligand field on the electronic structure of the complexes. Nonetheless, to obtain a more precise interpretation of spectroscopic and magnetic data of molecular-based Ln complexes, one should rely on some kind of *theoretical* calculation of the CF parameters. In the following, we will briefly outline the main principles underlying these methods and provide a short survey of the pros and cons for each of them.

2.2 Modeling and Calculation of CF Parameters

The number of theoretical approaches for the calculation of the electronic structure of Ln(III) complexes is extremely vast, ranging from empirical, electrostatic-based models to extremely sophisticated ab initio ones. A detailed discussion on these methods is beyond the scope of this chapter, so that we will focus here on the two general approaches which are most used in molecular magnetism studies. The first and simpler approach is based on point-charge electrostatic model (PCEM), for which the CF effect on the Ln(III) is obtained as the sum of n point charges placed at the atomic positions corresponding to the ligating atoms. The second one, much more expensive in term of computational resources, is the complete active space self-consistent field (CASSCF) calculations, which is currently the most common ab initio method for Ln-based molecular magnets.

It is evident that the first approach neglects, in principle, any covalency and thus is suited for ionic compounds but is not working properly for molecular systems. For these complexes, covalency is then introduced semiempirically in the PCEM model [31–33] by considering effective charges located at some points along the Ln-ligand bond. Application of such methods is quite common in the interpretation of spectroscopic data, but specific adaptation to molecular magnetism problems were developed only recently. Some of these methods found specific applications for rationalizing the magnetic anisotropy in easy axis type Dy(III) molecular complexes [34]. More general, and as such more complex, methods have been developed in recent years by Coronado's group, and we will discuss them here briefly [33,35,36]. In the simplest approximation (termed REC, radial effective charge), which works properly for derivatives of spherical ligands, the effect of the ligating atom is modeled through an effective point charge, situated along the lanthanide–ligand axis at a distance D_r, as schematized in Fig. 4. Both the charge value and its distance to the lanthanide are considered as free parameters and varied to achieve the best fit of the magnetic observables.

It is interesting that in this approach a collective fit, assuming the same value of D_r and effective charge for different Ln derivatives, can be attempted, thus reducing the number of parameters compared to the observables. Furthermore, some specific chemical meaning can be attributed to the parameters and, indeed, their behavior in different series of complexes was found to follow chemical-based expectations [37]. When ligands coordinate

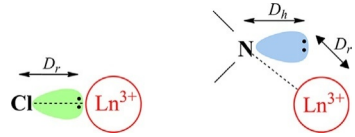

FIG. 4 Different orientations of the electronic pair of a ligand and a lanthanide cation. (*Left*) The lone pair is directly oriented toward the lanthanide cation; in the REC approach, the effect of covalent electron sharing is taken into account by defining a radial displacement vector (D_r) for an effective charge q. (*Right*) The lone pair is not directly oriented toward the lanthanide cation. To define the position of the effective charge q a further vector, D_h, is necessary.

through a nonradial lone pair this model fails, and a further parameter has to be added to identify the position of the effective charge, namely the horizontal displacement vector D_h (Fig. 4). This approach (termed LPEC, lone pair effective charge) has been shown to work properly, once considered its relative simplicity, to describe the magnetic susceptibility and the energy splitting for the $LnPc_2$ series of complexes [33], first reported by Ishikawa [38].

Despite these successes, and its relative simplicity, limitations of this approach are also evident: indeed, as acknowledged by the same authors, it neglects effects arising beyond the first coordination sphere, making the prediction of the magnetic anisotropy direction more sensitive to small perturbations in the coordination sphere [39]. Furthermore, its simplicity is rapidly lost when complexes of heteroleptic ligands are involved, since each different set of ligating atoms requires a set of semiempirical parameters to be determined.

In this respect, this approach shares some of the problems encountered by applying the angular overlap model (AOM) [40,41] to Ln-based molecular complexes, i.e., the rapid growth of the number of parameters on increasing the complexity of the ligand. We remind here that within the AOM, the interaction between the ligand and the lanthanide is described by parameters which are directly related to the σ-, π-, δ-, and φ-bonding ability of the ligands, which may be in principle influenced by the synthetic chemist and for a specific ligand should be transferable from a complex to another [40]. Given the large number of parameters, the δ- and φ-bonding are usually not considered in the approach and in first approximation only isotropic π-interaction have been included [42]. A successful application of this approach to a relevant magnetic molecular system has been reported 15 years ago by Flanagan et al. [41] who applied it to a global fit of CF parameters derived by polarized luminescence spectroscopy for the series of homologous compounds [Ln(trensal)] (where H_3trensal = 2,2′,2″-tris(salicylideneimino)triethylamine), whose structure, with crystal imposed threefold symmetry, is reported in Fig. 5 [43].

In the last part of this section, we will briefly present CASSCF methods, introduced earlier, which are now almost routinely applied to rationalize and predict the peculiar properties of magnetic molecular materials based on lanthanides. While covering all the molecular magnetism literature where

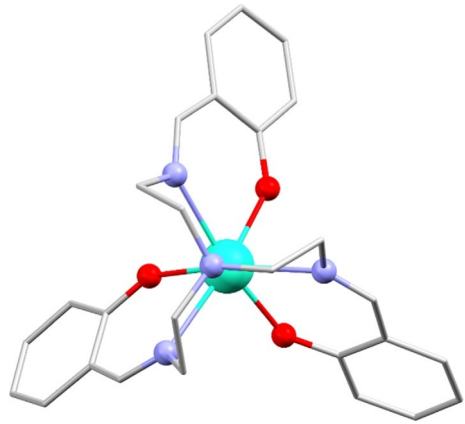

FIG. 5 View of the molecular structure of [Ln(trensal)] slightly off C_3 crystallographic axis. *Stick*: carbon atoms; *large cyan ball*: Lanthanide ion; *small red balls*: oxygen atoms; *small pale blue balls*: nitrogen atoms. Hydrogen atoms are omitted for clarity. *Crystallographic data available in M. Kanesato, T. Yokoyama, Synthesis and structural characterization of Ln(III) complexes (Ln = Eu, Gd, Tb, Er, Tm, Lu) of tripodal tris[2-(salicylideneamino)ethyl]amine, Chem. Lett. 28 (1999) 137–138.*

use is made of this theoretical technique is far beyond the scope of this chapter, we will rather point out the essential features of this method and highlight its potentialities and limitations. This ab initio method consists in two steps: one considers first electron correlation, via CASSCF calculation [44] and relativistic scalar effects by evaluating the single- and double-excitation contributions by second-order perturbation (CASPT2) [45]. Since spin–orbit coupling is not considered in this step, it provides a "spin-free picture" of the electronic structure of the Ln ion. In the following step, spin–orbit coupling is introduced by treating it via a restricted active space state interaction computation (RASSI-SO), which uses the CASSCF wave functions as the basis states. This procedure is necessary due to the complexity of the electronic structure of Ln(III) ions, for which the high degeneracy and the localized nature of the *4f* orbitals result in strong static and dynamic electron correlations, while their large nuclear masses result in large relativistic effects.

This methodology finally leads to obtain the composition of the eigenstates in term of m_J's and their energies, as well as the orientation of the anisotropy axis for each of them. Parameters of the pseudospin Hamiltonian discussed earlier can also be derived [30]. These represent valuable information for the rationalization of the behavior of Ln-based molecular magnets, and indeed, large use has been made of ab initio methods in molecular magnetism studies. We stress here that it would be however advisable to validate the results of calculations with detailed single-crystal studies [46] or spectroscopic characterization. In this sense, it is to be noted that in some cases

where comparison between the energy structure obtained by ab initio calculations and that directly probed by spectroscopic means, such as in the case of $(NBu_4)^+[LnPc_2]^-$ family [13] or [Er(trensal)] derivative [47], nonnegligible systematic deviations have been reported. These have been accounted for by applying an arbitrary scaling factor to the calculated energies, which was attributed to the limited size of the basis set used and unaccounted dynamical correlations [39]. It is clear that this point brings us directly to the major issue related to this theoretical approach, i.e., the size limitations of the problem due to its complexity. This requires extracting a quantum cluster of dimensions reasonable to be handled, but without compromising the accuracy of the computation. To validate these unavoidable approximations, an accurate experimental characterization of the magnetic properties is necessary and the principal magnetometric techniques that can be employed will be the focus of the next section.

2.3 Experimental Methods for the Characterization of Magnetic Anisotropy

First investigations on the CF effects on the magnetic anisotropy of lanthanide ions were based on the use of electron paramagnetic resonance (EPR) spectroscopy. This technique presents several advantages such as the high sensitivity and the possibility to extract information on magnetic anisotropy from randomly oriented powder experiments, though single-crystal experiments on ions in highly symmetric environments formed the precious database collected by Abragam and Bleaney in their seminal book [26]. EPR is continuously providing important information on lanthanide-based molecular materials, in particular if multifrequency experiments are performed. When flanked by an accurate modeling, the technique provides also information on the weak exchange interactions that characterize these ions [48,49]. A drawback, however, is that not all systems are suitable for this technique as many compounds do not provide a significant EPR signal. This may occur because either the lines are broadened by fast relaxation or EPR-allowed transitions are too high in frequency/field to be detected with standard instruments or the transition probability is too weak. As a result, investigations on molecular complexes of lanthanide ions other than Gd(III), which has no orbital angular momentum, are limited to low temperatures and few data are available on ions with even numbers of *4f* electrons, i.e., non-Kramers ion [50,51], which are often EPR silent. In the following, we will therefore focus on single-crystal magnetometric techniques that are always applicable and do not require elaborate modeling of the data.

The ample diffusion of very sensitive magnetometers based on superconducting quantum interference devices (SQUIDs) and the commercialization of automated rotators allow the investigation of single crystals of reduced dimensions, with masses smaller than 1 mg. In the absence of any symmetry

or a priori information on the magnetic anisotropy, three independent rotations are necessary to fully determine the susceptibility tensor through the relation:

$$\vec{M} = \underline{\chi}\,\vec{H} \tag{7}$$

It should be reminded that conventional inductive magnetometers are only sensitive to the component of the magnetization parallel to the applied magnetic field. Thus the detected angular dependence of the magnetization is given by:

$$M(\theta) = \chi_{\alpha\alpha} H (\cos\theta)^2 + \chi_{\beta\beta} H (\sin\theta)^2 + 2\chi_{a\beta} H \sin\theta\cos\theta \tag{8}$$

where α and β correspond to the versors (unit vectors) of the laboratory reference frame X, Y, and Z in a cyclic permutation and θ is the angle between H and the α vector. The susceptibility is here assumed to be independent of the magnetic field, thus weak to moderate fields must be employed to avoid saturation effects.

A very efficient way to correlate the laboratory reference frame to the molecular one is to attach a crystal on a millimetric cube of Teflon or other non-magnetic materials and to index the faces of the cube (X, Y, Z) with an X-ray diffractometer using the diffraction peaks of the crystals. Thus, the laboratory reference frame is directly expressed in term of the orthogonalized crystal reference frame, e.g., $ab'c^*$ for the triclinic system. Crystals with poorly defined faces can thus be employed and problems due to air sensitivity or loss of solvent of crystallization can be avoided by embedding the crystal in grease or glue.

A simple least squares procedure to reproduce $M(\theta)$ in the three rotations along X-, Y-, and Z-axes provides the six independent terms of the susceptibility tensor. Diagonalization of the tensor gives access to the principal values and the principal directions of the susceptibility in the laboratory reference frame that can be easily transformed in the crystal one. An example of the procedure is schematized in Fig. 6.

A textbook example of the power of the technique is represented by the investigation of the magnetic anisotropy of isostructural crystals of formula $Na[Ln(DOTA)(H_2O)]\cdot 4H_2O$, with Ln = Tb, Dy, Er, and Yb, and H_4DOTA = tetraaza-cyclododecane-tetraacetic acid [52,53]. Thanks to the stability of the complex induced by this octadentate macrocyclic ligand [54,55], and the accessibility of the axial coordination site occupied by a water molecule, the gadolinium derivative is one of the most common contrast agent in magnetic resonance imaging [56]. Despite the interest for anisotropic lanthanides [57] to be employed as more efficient T_2 contrast agents in high-field applications [58], few studies have been devoted to characterize the magnetic anisotropy axis of these complexes in solid state. Since the complexes crystallize in the triclinic crystal system with one metal ion in the asymmetric unit, all metal centers in the crystal have collinear magnetic anisotropy, providing a fortunate situation for application of angle-resolved magnetometry [52,53]. This is often not the case for molecular complexes, as discussed later.

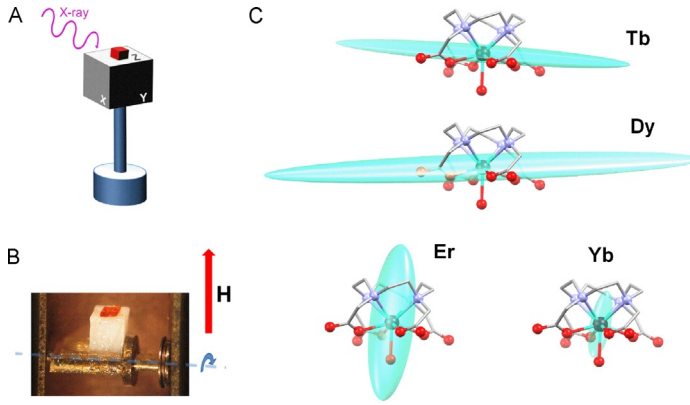

FIG. 6 Single-crystal magnetometry for investigating the magnetic anisotropy: (A) indexing of the laboratory reference frame in the molecular one by X-ray diffraction; (B) view of a sample rotator for angle-resolved magnetometry analysis; and (C) extracted magnetic susceptibility tensors at $T = 5$ K for the Na[Ln(DOTA)(H_2O)]·$4H_2O$ series: the one of Yb has been multiplied by two to allow a better comparison.

The DOTA ligand imposes an almost tetragonal coordination polyhedron but the symmetry is broken by the presence of the Na^+ counterion and by the hydrogen atoms of the apical water ligand. In Fig. 6C, the low temperature susceptibility tensor of the Dy(III) ion is reported superimposed to the molecular structure. It is well evident that the system exhibits strong easy axis anisotropy, i.e., one direction possesses a much larger susceptibility than the other two. This is rather common for Dy(III). What is more surprising is that the easy direction does not coincide with the idealized tetragonal symmetry axis of the coordination polyhedron.

The results of a similar investigation extended to Tb, Er, and Yb analogs are collected in Fig. 6C. It is interesting to notice that Tb behaves similarly to Dy, while in Er and Yb the easy axis is oriented along the M–O_{water} bond, i.e., the pseudotetragonal axis. This behavior can be rationalized taking into account that in the DOTA complexes the negative charges of the carboxylates moieties are localized in the equatorial plane. This stabilizes the largest $|m_J|$ states of the ground J manifold, where the projection is referred to the pseudotetragonal axis, for the prolate ions, like Er and Yb. An easy plane magnetic anisotropy, i.e., stabilization of states with the lowest $|m_J|$ projection, would be expected for oblate ions, like Tb and Dy. However, low symmetry components of the CF are sufficient to pin one direction in the easy plane. A detailed analysis, based on post-Hartree–Fock ab initio calculations, has demonstrated that the positions of hydrogen atoms of the apical water molecules play a key role in pinning the easy axis of magnetization [52]. Even if different results can be obtained depending on the degree of simplification of the molecular structure [34], it is evident that a simple electrostatic description of the CF is inadequate to understand the magnetic anisotropy of lanthanide-based

molecular systems. These results underline the need for accurate experimental and theoretical investigations to extract sound magnetostructural correlations.

Angle-resolved magnetometry has intrinsic limitations. Measuring the crystal magnetization does not provide information on individual magnetic centers if these do not present collinear anisotropy tensors. In fact, when the symmetry of the metal site, often reduced in molecular systems by the use of different ligands, is lower than the symmetry of the crystal, more than one symmetry-related orientations of the anisotropy tensor are present. The different contributions can only be disentangled in very special cases, like in presence of magnetic hysteresis or when additional information are available [59]. This difficulty can be however circumvented by using torque magnetometry. This a simple characterization technique widely employed in the past to characterize the magnetic anisotropy of inorganic compounds. Despite its simplicity the technique has been scarcely used in molecular magnetism [60]. Modern torquemeters are based on millimeter-sized cantilevers of conductive hard materials like silicon or Cu–Be that act as the upper plate of a capacitor, as schematized in Fig. 7.

The magnetic torque exerted by the applied field on the anisotropic crystal attached on the cantilever induces a deflection of the latter and a change in the capacitance. If deformations are small enough that a linear response of the cantilever can be assumed, the change in capacitance is directly proportional to the magnetic torque, which is defined as:

$$\vec{\tau} = \vec{M} \times \vec{B} \tag{9}$$

For a permanent magnet, Eq. (9) gives a sinusoidal dependence with 2π periodicity. In the case of a paramagnet only a field-induced magnetic polarization is present. Taking also into account that only one component of the torque, the Y one in the chosen reference frame, is measured, Eq. (9) becomes

$$\tau_Y = M_\gamma B_\alpha - M_\alpha B_\gamma = B^2 \sin\theta\cos\theta\left(\chi_{\gamma\gamma} - \chi_{\alpha\alpha}\right) + B^2 \chi_{\alpha\gamma}\left(2\sin^2\theta - 1\right) \tag{10}$$

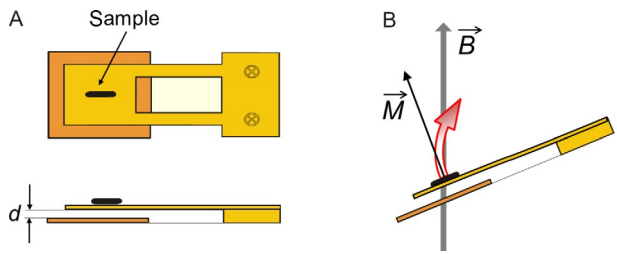

FIG. 7 (A) Top and side schematic views of a capacitive cantilever and (B) the rest distance, d, between the two plates is modified if an anisotropic sample has its magnetization noncollinear with the external magnetic field and a torque is exerted (*curved arrow*).

where θ is the angle formed by the field, applied along the Z laboratory axis, with the γ molecular axis, and $Y = \beta$. By changing θ, three components of the susceptibility tensor can be estimated. In absence of any symmetry three orthogonal rotations, corresponding to a cyclic permutation of α, β, γ, provide access to the full tensor whose diagonalization, as in the previous case, gives the principal values and direction in the molecular reference frame.

The first advantage of cantilever torque magnetometry (CTM) technique relies in its exceptional sensitivity, given not only by the detection mode, but also by the fact that the isotropic susceptibility does not contribute to the signal. The quadratic field dependence allows enhancing significantly the signal-to-noise ratio by using strong magnetic fields, though comparatively strong anisotropies are necessary. This is the case of lanthanide ions for which the anisotropy field is often higher than any field that can be reached in a standard laboratory.

A nice demonstration of the potentialities of the technique is the determination of the CF Hamiltonian parameters for the trigonal complexes [Ln(trensal)], where Ln = Tb, Dy, Er, already introduced in Section 2.2 (see Fig. 5). CF parameters extracted from the simulation of the luminescence spectra are available for these complexes [41,61].

The CTM investigation has evidenced easy plane magnetic anisotropy for Tb and Dy, while Er possesses easy axis anisotropy, with the axis obviously coincident with the C_3 axis of the molecule [62]. This is immediately seen in Fig. 8A where the torque signal is investigated rotating the crystal along a direction in the *ab* plane of the trigonal crystal. The detected torque is in this case given by:

$$\tau_Y = B^2 \sin\theta \cos\theta (\chi_c - \chi_{ab}) \tag{11}$$

where θ is the angle between the magnetic field and c is the crystal axis.

The torque is zero along the principal axes, i.e., $\theta = 0$ and 90 degrees, and is negative in the first quadrant for Tb and Dy, indicating that $\chi_{ab} > \chi_c$, i.e., these ions possess easy plane anisotropy. This is a very rare case for Dy(III) ions. It must be said that EPR spectra of powder samples have also been able to elucidate the nature of the magnetic anisotropy of Dy and Er, but not of Tb [63]. Moreover, thanks to the high sensitivity of CTM, data have been collected for temperatures as high as 100 K, thus populating also other states of the ground J manifold. This has allowed to simulate a rich set of data providing information on the eight nonzero elements of the CF potential. In Fig. 8B, the extracted energy levels of the ground J multiplet for the three complexes are reported and compared with those estimated from luminescence spectra [41,61].

It is interesting to notice that the two techniques provide comparable results only for [Er(trensal)], for which luminescence data are available also for the ground $J = 15/2$ multiplet, which is not the case for Tb and Dy

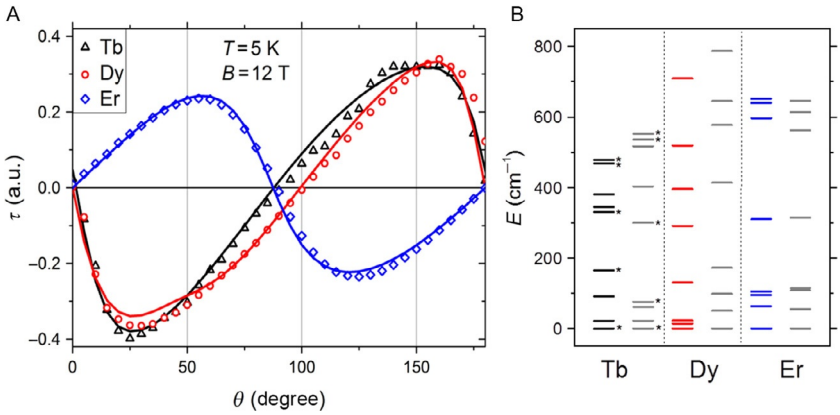

FIG. 8 (A) Experimental (*symbol*) and calculated (*solid lines*) angular dependence of the magnetic torque measured on single crystals of [Ln(trensal)] for Ln = Tb, Dy, and Er, when rotating the field in the *ac* crystallographic plane ($\theta = 0$ degree corresponds to $B//c$) and (B) calculated energy levels of the ground J multiplet for the three lanthanides from the best fit of the torque data (color code is the same as in (A)), and from luminescence data (*pale gray*). The *star* indicates singlet states for the Tb ion. *Adapted with permission from M. Perfetti, E. Lucaccini, L. Sorace, J.P. Costes, R. Sessoli, Determination of magnetic anisotropy in the LnTRENSAL complexes (Ln = Tb, Dy, Er) by torque magnetometry, Inorg. Chem., 54 (2015) 3090–3092, © 2015 The American Chemical Society.*

derivatives. CTM seems therefore a precious tool to estimate energy splitting of the ground multiplet when optical data of good quality are not available.

Torque magnetometry presents also another advantage on standard magnetometry: the possibility to extract information on the single-ion anisotropy from data on single crystals that comprise more than one orientation of the anisotropy tensor. The latter case is often encountered in molecular magnetism. Let suppose we have two centers with their easy axis pointing at 90 degree one from each other. When scanning the plane that contains the two directions Eqs. (10) and (11) provide a zero-resulting signal, due to cancelation of the two contribution. This, however, only occurs when the magnetization is linear with the field, i.e. in the weak field limit. On the contrary, using a strong magnetic field at low temperature, the curves of the individual centers are strongly distorted, with a strong increase in the slope around the position of zero signal corresponding to the hard direction, as shown in Fig. 9. This can be intuitively understood recalling the first part of Eq. (10). When the field is close to the hard direction any minimal deviation induces a nonzero component of the field along the easy axis that at low temperature quickly saturates the magnetization. This maximizes the cross product between the magnetization along its easy axis and the component of the magnetic field along the hard axis. As a result of the asymmetry, the components arising from different sites do not cancel anymore as can be seen in Fig. 9.

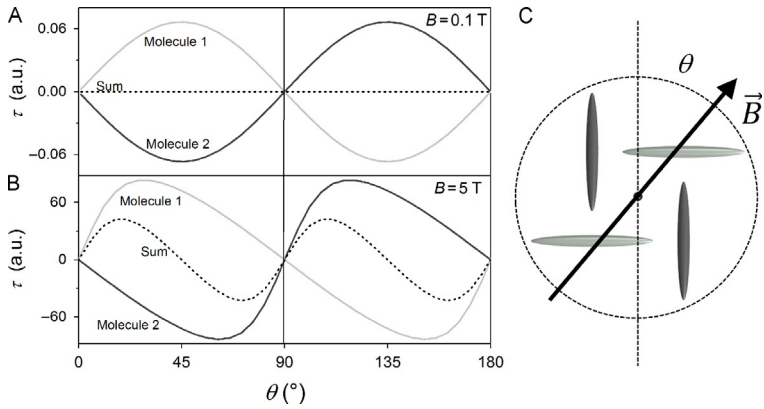

FIG. 9 (A) Calculated angular dependence of two Ising centers (*pale and middle gray*) oriented at 90° one from each other and the resulting total torque (*black dashed line*) when the magnetization is linear with the magnetic field (weak field limit), (B) same graph in strong magnetic field when saturation along the easy axis is achieved, and (C) schematic view of the orientation of the easy axis for the two families of molecules (same *gray code* as in A and B). The torque is measured along the axis that exits from the page.

Even if the two contributions can be disentangled with this procedure, when associating a certain signal to a specific site in the crystallographic unit cell an ambiguity remains that can be only resolved through a qualitative analysis of the chemical structure and the associated CF potential.

This feature of torque magnetometry has been exploited to investigate the magnetic anisotropy of the organometallic sandwich complex [Cp*Er-COT] [64], where COT is the cyclooctatetraene dianion, crystallizing in a orthorhombic space group [65,66]. The more spectacular application at the moment is the investigation of spin helicity in the chiral one-dimensional structures of formula $[Ln(Hnic)(nic)_2(NO_3)]_n$ (Hnic = nicotinic acid, Ln = Gd, Tb, Dy, and Er) whose structure is reported in Fig. 10 [67]. Even if no chiral ligand is present and the lanthanide coordination polyhedron has approximate C_{2v} symmetry, which would not allow chirality, the compounds spontaneously forms enantiomeric pure crystals in the hexagonal space groups $P6_1/P6_5$. The sixfold symmetry axis generates six magnetic nonequivalent metal sites, whose anisotropy tensors have no particular relationship to the crystallographic axes, except being related among themselves by a rotation along the c axis of an angle $i \cdot 60$ degree, where $i = 0–5$.

By performing torque experiments rotating the crystals along the c axis and an axis in the ab plane, it has been possible to extract the susceptibility tensor of the lanthanide single ion [68]. The results are shown in Fig. 10, where the orientation of the tensors are superimposed to a schematized helical structure, as the ambiguity previously mentioned cannot be resolved and a particular orientation cannot be associated to a particular site of the unit cell. However, very important information is provided by this analysis. First of all,

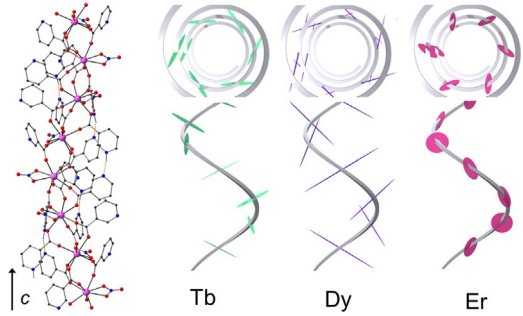

FIG. 10 On the *left*, view of the structure of the molecular helices $[Ln(Hnic)(nic)_2(NO_3)]_n$. (Online color scheme: Ln in *pink*, oxygen in *red*, nitrogen in *blue*, carbon in *gray*.) On the *right*, the susceptibility tensors extracted from the simulation of the torque data highlighting the easy axis character of Tb and Dy and easy plane character of Er as well as the pronounced non-collinearity resulting from the sixfold screw axis. *Adapted with permission from I. Mihalcea, M. Perfetti, F. Pineider, L. Tesi, V. Mereacre, F. Wilhelm, A. Rogalev, C.E. Anson, A.K. Powell, R. Sessoli, Spin helicity in chiral lanthanide chains, Inorg. Chem., (2016), © 2016 the American Chemical Society.*

the nature of the single-ion anisotropy, which is practically of the Ising type for the Dy derivative, i.e., transverse susceptibility is practically zero. The Tb derivative shows also a pronounced easy axis anisotropy but with a sizeable rhombicity, i.e., one transverse component of the susceptibility is not negligible. Completely different is the situation for Er that has easy plane magnetic anisotropy, i.e., two large components of the magnetic susceptibility. Interestingly, tensors are significantly tilted from the *c* axis with the results that the crystal anisotropy is small and with a nature that is opposite to that of the single-ion contributions: easy plane for Tb and Dy, easy axis for Er. The extracted single-ion magnetic anisotropy correlates well with the dynamic behavior of these materials, where only the Dy derivative shows slow dynamics of the magnetization. As already anticipated, the easy axis anisotropy is at the origin of a barrier hampering the reversal of the magnetization.

These chiral crystals showing helicity in the arrangement of magnetic moments are particularly interesting to investigate the interplay between structural chirality and magnetism that can result in interesting optical effects such as magnetochiral dichroism [69,70], i.e., the different absorption of unpolarized light depending on the orientation of light propagation, structural chirality, and magnetic polarization. This effect, first observed in the luminescence of an Eu(III) chiral complex [71], has been found to be particularly intense in a Co(II) molecular helix by employing X-ray at the Co K edge [72]. Unfortunately, the small mixing of *4f* orbitals with other ones makes the use of hard X-ray not well suited to investigate magnetochiral effects in lanthanide-based compounds.

2.4 Magnetic Anisotropy and Magnetization Dynamics

We have seen in Section 1 that the magnetic anisotropy can be at the origin of a potential barrier separating states with opposite magnetic polarization, thus originating magnetic bistability that is known as SMM behavior [7,73], or in the case of mononuclear complex also as SIM. SMMs and SIMs present bistability only at cryogenic temperatures and are often investigated by employing a weak alternating field of variable frequency, usually in the range 1–10,000 Hz. *Ac* susceptometry, a relatively common technique available in most commercial magnetometers, provides information on the magnetization dynamics by monitoring the dephasing of the signal induced by the sample, whose magnetization is no more able to follow the oscillating field. When the relaxation time is of the order of hundreds of second a hysteresis appears in the magnetization cycle.

The number of reports on slow dynamics of the magnetization of lanthanide-based molecules is increasing continuously and an exhaustive survey is not the scope of this chapter, addressing the reader to dedicated reviews [74–78] and books [79,80]. It is more relevant here to make a clear distinction between the two most commonly observed behaviors. In fact, in many cases no dephasing of the signal in *ac* susceptibility is observed in zero static field, but can be observed if a static field is applied. This behavior is relatively common in paramagnetic materials. Let us start from the simplest case: a doublet state. In zero static field, the spin–spin interactions have magnitude comparable to the oscillating Zeeman splitting induced by the *ac* field. As a result, there is no need of energy exchange with lattice and spin–spin relaxation, usually rather fast and weakly dependent on temperature, allows reaching equilibrium. On the contrary, when a moderate static field is applied, transitions between states well separated in energy are observed. These states are in equilibrium when the oscillating field is superimposed to the static one and require an exchange of relatively large quanta of energy with the lattice by coupling to lattice vibrational modes, i.e., phonons. As the population of phonon modes depends on temperature, a temperature-dependent dynamics is observed. In this case what is usually observed is that the most isotropic ion, Gd(III), exhibits the slower dynamics [81]. However, such a system cannot exhibit any remnant magnetization due to the intrinsic fast relaxation in zero field, and it is not correct to associate this dynamics to SMM behavior and to the presence of a potential barrier originated by magnetic anisotropy.

An example of this behavior is encountered again in the [Ln(trensal)] series. Both Dy and Er derivatives exhibit a similar field-induced slow relaxation, despite the different magnetic anisotropy of the two complexes discussed in the previous section. Interestingly no slow dynamics is observed for the Tb derivative, which in this coordination is characterized by a singlet state, though with a small separation from the first excited state. Lanthanide ions with even number of *4f* electrons, are less prone to show slow dynamics

of the magnetization and a "spin parity" effect is often encountered, when series are investigated [53].

The situation is conceptually different when slow relaxation is observed in zero static field. In this case, the easy axis anisotropy of the molecule is important as it hampers the admixing of states on opposite sides of the barrier, thus requiring that excited states are involved in the reversal of the magnetization. Exchange of energy with the lattice is then required even if the initial and final states are practically degenerate in zero field. Also in this case the external field can play an important role. In fact, in a real system there are many sources of interactions with transverse components of the angular momentum of the molecule, either J or S. These can be transverse anisotropy terms of the CF, as in Eq. (4), dipolar interactions between molecules, or hyperfine interactions with magnetic nuclei, that of the metal itself of those of the ligands. These transverse terms, not commuting with the leading axial magnetic anisotropy terms, induce admixing of the states on opposite sides of the barrier, making the barrier more "transparent" to quantum effects. This is the quantum tunneling of the magnetization, a phenomenon that affects matter at the nanoscale and that has been investigated in detail in molecules [7,73].

The admixing is maximum when the states on opposite sides of the barrier are closest in energy, as described by perturbation theory. The application of a magnetic field removes the quasi-degeneracy in zero field and slows down the magnetization. A more efficient underbarrier or tunneling mechanism is reestablished for certain values of the magnetic field when two levels are brought closer in energy. For lanthanide ions, the CF splitting of the ground J multiplet is in general large, so that this type of field-induced level crossing is not observed. It can be however observed among hyperfine levels. This is the case of the archetypal SIM, the $[TbPc_2]^-$ molecules, whose low temperature magnetization hysteresis reveals acceleration at regular spacing corresponding to $m_J = \pm 6$ and different m_I values, as schematized in Fig. 11 [82]. Very low temperatures are however necessary to evidence these tunneling resonances due to the energy separation between hyperfine levels not exceeding 1 K.

The hyperfine level crossings have been exploited by Wernsdorfer and colleagues [83,84] as a fingerprint of the quantum tunneling of the magnetization of this class of molecules in experiments where isolated molecules are electrically addressed, as briefly discussed in Section 4.

It is interesting to underline that the nuclear magnetic moments can significantly affect the magnetization dynamics of SMMs. Isotopic enrichment to accelerate or decelerate the magnetic relaxation was first used in polynuclear 3d SMMs [85] but a recent report on a Dy(III) complex has revealed a dramatic increase of four order of magnitudes for the relaxation time in zero static field when the system is diluted in a diamagnetic matrix and ^{164}Dy, characterized by $I = 0$, is employed [86].

This short overview should have highlighted which are the main ingredients to obtain lanthanide-based SMMs with improved magnetic bistability [87].

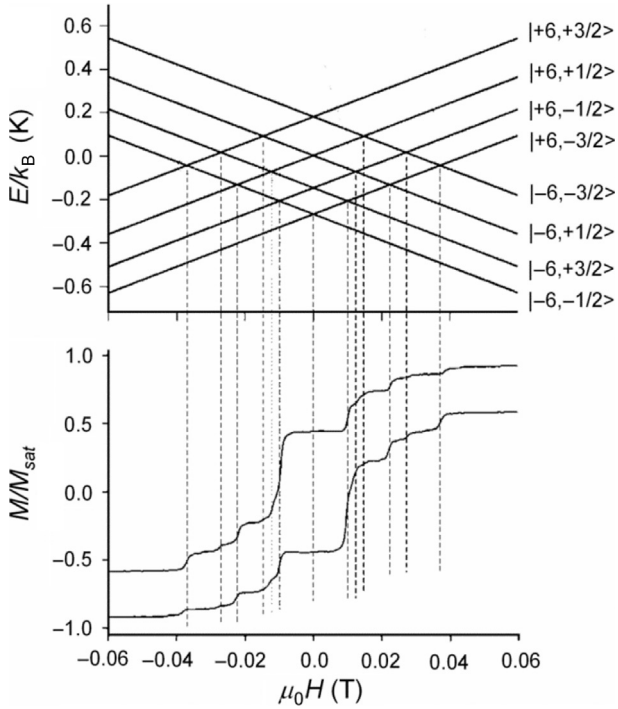

FIG. 11 (A) The $J = 6$, $m_J = \pm 6$ pseudodoublet of $[TbPc_2]^-$ is split by hyperfine interaction with the $I = 3/2$ of ^{159}Tb nuclei. At the hyperfine levels crossings acceleration of the relaxation is observed as highlighted in the hysteresis loop recorded at $T = 0.04$ K diluting the Tb complexes in the diamagnetic Y analogs (B). *Adapted with permission from N. Ishikawa, M. Sugita, W. Wernsdorfer, Quantum tunneling of magnetization in lanthanide single-molecule magnets: bis(phthalocyaninato)terbium and bis(phthalocyaninato)dysprosium anions, Angew. Chem. Int. Ed., 44 (2005) 2931–2935, © 2005 Wiley-VCH.*

First of all comes the tuning of the CF that, in order to generate an anisotropy barrier, should stabilize the largest J projections along one direction. Simple rules based on the distribution of the negative charges of the ligands in axial position for prolate ions like Dy(III) and Tb(III) or in the equatorial plane for the oblate ones, e.g., Er(III) and Yb(III) are the first tool for the synthetic chemists [28], though we have previously shown that covalency is not always negligible. Following this strategy, large barriers for the reversal of the magnetization have been obtained by linear arrangement of negatively charged donor atoms in a Dy(III) bis(methanediide) complex [88]. The C=Dy=C bond angle deviates significantly from 180 degree and the energy barrier, ca. 800 K, though remarkable does not reach the limit estimated for a linear coordination mode [89]. A strong axial CF characterizes also prolate Ln(III) ions coordinated to a single nitride ion encapsulated in a fullerene as observed for $DySc_2N@C_{80}$ [90].

The opposite chemical design is followed with oblate ions. Indeed, the highest blocking temperatures for these ions have been achieved in organometallic sandwich compounds, such as $[Er(COT)_2]^-$ [91] and [Cp*ErCOT] [66], because of the lack of ligand charge density in axial positions.

The continuous improvement of our understanding of the factors determining the magnetic bistability in lanthanide-based molecules is leading to a steady increase in the performances of these SMMs [74]. It should be stressed, however, that the magnetic remanence is generally rather low due to efficient tunneling in zero field. Coupling more lanthanide ions between themselves or with other paramagnetic centers can partially solve this issue, as explained in the next section.

3 EXCHANGE INTERACTIONS IN LANTHANIDE-BASED MOLECULAR MATERIALS

In addition to the analysis of the interesting dynamic magnetic properties of mononuclear lanthanide complexes, studies in molecular magnetism have, since the beginning, addressed the investigation of di- and polynuclear complexes with particular focus on their exchange interaction. This, however, results in some difficulties because the unquenched orbital momentum of all the tripositive lanthanides except Gd(III), prevents the possibility of using the isotropic exchange Hamiltonian for the analysis. As such, much of the initial studies were restricted to Gd(III)-containing complexes, coupled to either transition metal ions or organic radicals. The rationale for this choice reside in the weak exchange interaction involving *f* orbitals, due to their inner nature compared to *d* or *p* ones. The use of a second paramagnetic center capable of promoting stronger interaction was then a necessity to obtain exchange interactions of reasonable magnitude. The initial idea was that the use of model dinuclear systems could yield useful indications about the factors governing the magnitude and sign of the exchange coupling in higher dimensional systems, such as one- or three-dimensional structures. Furthermore, this type of studies was aimed at obtaining magnetostructural correlations for systems containing exchange-coupled lanthanide ions, in view of developing suitable synthetic strategies for obtaining complexes characterized by a large ground spin state.

The first relevant contribution came from one of us who, in collaboration with Carlin's group, showed that for Cu(II)–Gd(III) the observed exchange interaction is usually ferromagnetic [92]. This result, unexpected at first sight, was rationalized by considering that the overlap of the magnetic orbital of Cu(II) is relatively larger with the empty *d* or *s* orbitals of Gd(III) than with the *4f* orbitals. It was then suggested that a fraction of unpaired electron of the Gd(III) is transferred, with the same spin it had in the original magnetic orbital, into the empty *6s* [93] or *5d* [94] orbitals, keeping the spins of the electrons in the *f* orbitals parallel according to the Hund's rule (see Fig. 12).

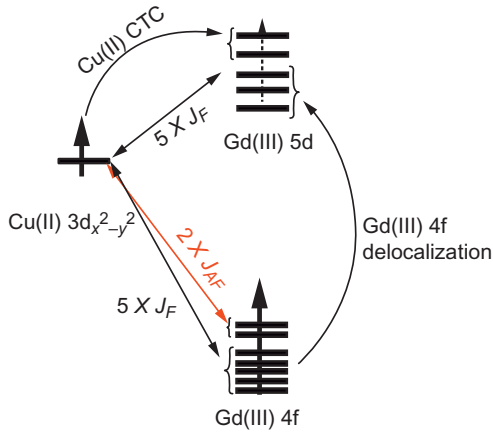

FIG. 12 A schematic mechanism for the magnetic coupling in Gd(III)–Cu(II) pairs obtained from the DFT calculations. The nature and the number of interactions between the Cu(II) and the Gd(III) are shown by *double headed arrows*. The Gd(III) *5d* orbitals gain density via the Cu(II) charge transfer and also via the *4f* delocalization. *Reprinted with permission from G. Rajaraman, F. Totti, A. Bencini, A. Caneschi, R. Sessoli, D. Gatteschi, Density functional studies on the exchange interaction of a dinuclear Gd(III)–Cu(II) complex: method assessment, magnetic coupling mechanism and magneto-structural correlations, Dalton Trans. (2009) 3153–3161, © 2009 The Royal Society of Chemistry.*

This may be seen as a generalization of the Goodenough–Kanamori rules [95,96] suggesting a ferromagnetic pathway when a magnetic orbital of one site has nonzero overlap with an empty orbital of the other site. An elementary semiquantitative treatment of this mechanism was first proposed by the group of Kahn [94] for the copper case and yielded a value of ferromagnetic coupling in fair agreement with the experimental data, confirming at least the feasibility of the suggested ferromagnetic exchange pathway. More recently, detailed theoretical investigations based on both CASSCF and DFT calculations confirmed the prominent role of *5d* orbitals in determining the exchange coupling in Gd(III)-based systems [97,98]. In particular, it has been shown that the *5d* orbitals of Gd(III) gain partial occupancy both via Cu(II) charge transfer as well as from the Gd(III) *4f* orbitals. The interaction between the Cu(II) *3d* and the Gd(III) *5d* orbitals contribute to the ferromagnetic part of the total exchange while the interaction with the *4f* orbitals of Gd(III) has two contributions: two orbitals that overlap with the Cu(II) $d_{x^2-y^2}$ orbital, which in most cases contains the unpaired electron, contribute to the AF term while the remaining five orbitals, being orthogonal to the Cu(II) magnetic orbital, give rise to the ferromagnetic contribution to the total exchange coupling. The net interaction is therefore ferromagnetic and, since none of the interaction terms derived are first-order effect, the overall magnitude of the exchange is very small.

In the past 15 years, some exceptions to the ferromagnetic coupling involving Gd(III) have been reported both for Cu(II) complexes and organic radicals [99–102], with quite relevant magnitude for the latter case [103,104]. For Cu(II)–Gd(III) systems, the observation of AF coupling has been attributed to large O–Cu–O–Gd dihedral angle, which affects the spin density distribution on the Cu(II) and Gd(III) atoms [98,105–107]. Interestingly, the variation of the sign of the exchange coupling from ferro- to AF has been recently reported by Costes and coworkers and attributed to active spin polarization effects [108]: an odd number of bridging atoms in between the ions bearing the spins favors a parallel alignment of the spins, whereas an even number of bridging atoms favors an antiparallel alignment. As for the AF exchange observed in Gd-organic radical systems, this clearly indicates that the resulting coupling is actually the sum of two contributions. One arises from the direct overlap of the magnetic orbitals of the ligands with the *f* orbitals, which presumably yields an AF pathway. The other comes from the overlap between the *5d* (and even *6s*/*6p*) orbitals of Gd(III), partially occupied due to charge transfer, and the π^* magnetic orbital of the radical ligands. The AF contribution may become dominant when the radical ligands become stronger donors [76]. Also in this case DFT results, providing access to molecular orbital (MO) and natural bond orbital (NBO) analysis, confirmed this interpretation, highlighting the active role of the formally empty orbitals of Gd(III) in the exchange mechanism. However, at variance with Cu(II)–Gd(III) complexes discussed earlier, in this case all *5d*/*6s*/*6p* orbitals were found to play a role in mediating the exchange coupling [109]. Recently, a different explanation has been provided to rationalize the strong AF exchange reported by Long's group in the radical-bridged complex Gd–N_2^{3-}Gd, belonging to an isostructural family described in more detail in the following section [76]. For this system, Chibotaru and coworkers demonstrated by DFT calculations that the extremely large AF exchange coupling is essentially due to a large energy gap between the $4f_{xyz}$ orbital and the π^* radical one. This makes the average promotion energy U for $4f^7\,\pi^{*1} \rightarrow 4f^8$ smaller than usual and the corresponding contribution to AF exchange, which is inversely proportional on U, very large [110].

3.1 Exchange Interactions for Orbitally Nondegenerate Lanthanide Ions

As interesting as it can be, the use of Gd(III) ions as the only lanthanide in exchange-coupled molecular systems was not to last: the remaining Ln(III) ions, and especially those of the second half of the series have indeed, from the point of view of potential applications, more interesting properties, such as ground states with large J values and large anisotropy. These two advantages come unfortunately at a prize when exchange interactions have to be evaluated and rationalized. Indeed, the combined effect of unquenched orbital angular momentum and ligand field results in neither S nor J being good quantum numbers anymore. As such, Ln(III) complexes will show large

deviation from Curie type behavior even in the absence of exchange interactions, and the isotropic exchange Hamiltonian which provides a simple conceptual framework to analyze the data in case of orbitally nondegenerate systems, cannot be applied to these systems.

A quantitative interpretation of the magnetic data in term of exchange interactions for Ln(III)-based complexes is then not straightforward and most often only a qualitative explanation is provided. In particular, the disentanglement of ligand field and exchange effects in either heterometallic or lanthanide-radical complexes is usually carried out by the so-called diamagnetic substitution method [111–116]. This involves the determination of magnetic properties of a complex in which the paramagnetic species coupled to the Ln(III) ion is substituted by a diamagnetic one, while preserving the molecular structure, so that ligand field effects on the Ln(III) can be considered equal in the two complexes. The exchange interaction is then made apparent by subtracting the temperature-dependent contribution arising from the thermal depopulation of the excited levels of the ground J multiplet of Ln(III), χT_{Ln}, measured on the reference complex, from χT of the exchange-coupled complex. As an example, in the investigation of Ln(III)–Cu(II) couples paramagnetic Cu(II) can be replaced by either square-planar Ni(II) or Zn(II), whereas in *4f–2p* complexes, organic radicals can be substituted by diamagnetic analogs carrying the same charge on the binding atoms [111,113,116,117].

Two of us extended this approach to a more quantitative analysis of the exchange coupling in pairs containing an orbitally degenerate ion coupled to the Ln(III) [118]. We focused our attention on $[Ce(dmf)_4(H_2O)_3(\mu\text{-}CN)Fe(CN)_5]$ (Fig. 13A), characterized by a weak exchange interaction between Ce(III) and low spin Fe(III) ($^2T_{2g}$ in octahedral strong field) [117]. A first

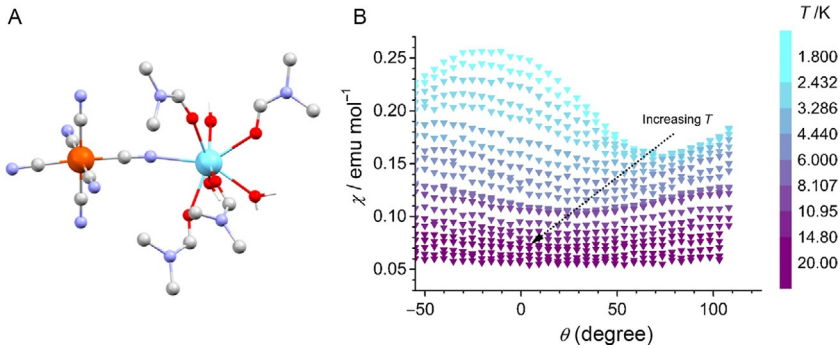

FIG. 13 (A) View of the structure of $[Ln(dmf)_4(H_2O)_3(\mu\text{-}CN)M(CN)_5]$ complexes (M = Fe, Co, Ln = La, Ce). Hydrogen atoms, except for coordinated water molecules, are omitted for clarity. (B) Single-crystal magnetic data of the same complex evidencing the rapid rotation of the magnetic anisotropy axis on increasing temperature. *Adapted with permission from L. Sorace, C. Sangregorio, A. Figuerola, C. Benelli, D. Gatteschi, Magnetic interactions and magnetic anisotropy in exchange coupled 4f–3d systems: a case study of a heterodinuclear Ce^{3+}–Fe^{3+} cyanide-bridged complex, Chem. Eur. J., 15 (2009) 1377–1388, © 2009 Wiley-VCH.*

rationalization of its low temperature properties was attempted by considering the exchange-coupled species to behave at low temperature as a pseudo-triplet with noncollinear **g** and **D** tensors. This approach was however unable to explain the rapid rotation of the magnetic axes evidenced by single-crystal magnetometry (Fig. 13B); it is clear that a more detailed picture of the magnetic properties of the system requires the evaluation of the exchange interactions between the two paramagnetic centers.

Levy first pointed out that the exchange interaction among orbitally degenerate paramagnetic centers should be expressed as a combination of irreducible tensor operators up to the sixth order [119,120]; even if only first-order term of the expansion is retained, the exchange interaction is required to be completely anisotropic and to occur between two anisotropic effective doublet, which are well separated in energy from the excited ones [110,121]:

$$\mathcal{H} = \hat{\mathbf{S}}_1 \cdot \mathbf{D}_{12} \cdot \hat{\mathbf{S}}_2 - \mu_B \vec{B} \cdot \left(\mathbf{g}_1 \cdot \hat{\mathbf{S}}_1 + \mathbf{g}_2 \cdot \hat{\mathbf{S}}_2 \right) \tag{12}$$

where $\mathbf{D_{12}}$ is the 3×3 exchange matrix, containing one isotropic, five symmetric anisotropic, and three antisymmetric (Dzyaloshinsky–Moriya) exchange parameters, and $\mathbf{S}_1$ and $\mathbf{S}_2$ are effective spins 1/2, with anisotropic $\mathbf{g}_i$ tensors.

The description of the magnetic properties of such systems then requires the determination of nine parameters for the exchange interaction and six parameters for each of the $\mathbf{g}_i$ tensors of the effective spins, i.e., their principal values and orientations. It is evident that such a task cannot be tackled using simple powder measurements but require the use of different techniques, both magnetic and spectroscopic, and the use of single-crystal measurements to obtain the principal directions of the tensors. In the case under study, the $\mathbf{g}_i$ tensors' principal values and orientations could be determined by recording the single-crystal EPR spectra of the diamagnetically substituted $[Ce(dmf)_4(H_2O)_3(\mu\text{-}CN)Co(CN)_5]$ and $[La(dmf)_4(H_2O)_3(\mu\text{-}CN)Fe(CN)_5]$ complexes, which are isostructural with the exchange-coupled derivative. The nine parameters of $\mathbf{D}_{12}$ tensor were then obtained by fitting single-crystal data of both EPR and magnetometry: their combination allowed to determine that the isotropic part of the interaction is AF, with a lower limit estimated as 1.5 cm^{-1}, and that the antisymmetric term, too often neglected, is of the same order of magnitude as the isotropic one [117].

The relative orientations of the three tensors could also be determined by combined fit of EPR and magnetometry data. It is however worth noting that, even after such a detailed experimental study, some unexplained features remained [118]. These were attributed to the presence of low-lying excited states that escape EPR detection, but produce also for the $[Ce(dmf)_4(H_2O)_3(\mu\text{-}CN)Co(CN)_5]$ derivative, a clear rotation of the magnetic anisotropy axis on varying temperature [27]. Even by assuming that only two doublets for Ce(III) and one doublet for Fe(III) are involved, a weak and anisotropic

coupling results in eight populated levels, the energies of which rapidly change with the direction of the applied field: a meaningful fit of the experimental data under this assumption is then unfeasible without the aid of accurate ab initio predictions.

In this respect, a combination of advanced experimental spectroscopic techniques with ab initio calculations has been recently used by Winpenny, Chibotaru, van Slageren, and coworkers to address the problem of the determination of exchange interaction in a Dy(III) dimer, $[hqH_2][Ln_2(hq)_4(NO_3)_3]\cdot MeOH$ (hqH = 8-hydroxyquinoline) where the two Dy(III) centers are characterized by different coordination environments (Fig. 14, *left*) [49].

This results in different properties for the two Dy(III) sites, as calculated by CASSCF: one of the two being predicted to show almost perfect easy axis anisotropy ($g_z^{eff} \approx 20, g_{xy}^{eff} \approx 0$), with an essentially pure $m_J = \pm^{15}/_2$, as ground doublet, and the second one with much more rhombic anisotropic (effective $g_z = 16.42$, $g_y = 1.54$, $g_x = 0.05$) and a close lying (24 cm^{-1}) first excited state. More importantly, the angle between the principal magnetic axes (g_z) of the ground states for the two sites is calculated to be 44 degree by ab initio calculations (Fig. 14). The energy splitting on the second center were also directly measured by magnetic field-dependent FIR absorption spectroscopy which indicated that the ratio of calculated splitting for first and second excited state is correct, but a scaling factor of 1.6 is necessary to reconcile theoretical and experimental results. At the same time, powder EPR spectroscopy on the

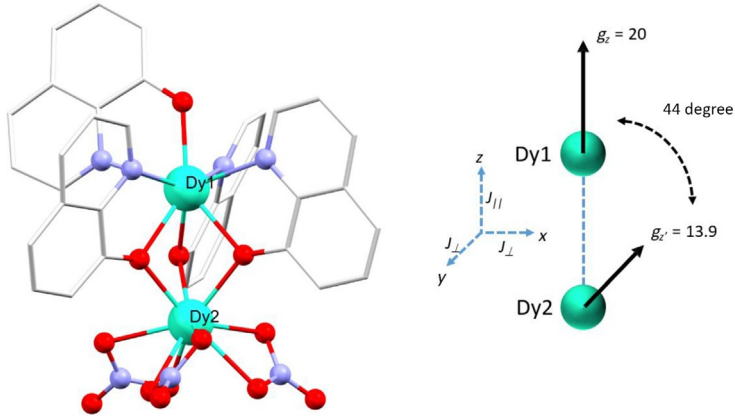

FIG. 14 (*Left*) Molecular structure of $[Ln_2(hq)_4(NO_3)_3]$, hydrogen atoms are omitted for clarity. (*Right*) Schematic of the model used to simulate EPR spectra of $[Ln_2(hq)_4(NO_3)_3]$. The two anisotropic doublet of the Dy centers are noncollinear, and the anisotropic exchange coupling Hamiltonian is expressed in the reference system of Dy1. *Adapted with permission from E. Moreno Pineda, N.F. Chilton, R. Marx, M. Dörfel, D.O. Sells, P. Neugebauer, S.-D. Jiang, D. Collison, J. van Slageren, E.J.L. McInnes, R.E.P. Winpenny, Direct measurement of dysprosium(III)⋯ dysprosium(III) interactions in a single-molecule magnet, Nat. Commun., 5 (2014), © 2014 Macmillan Publishers Ltd.*

Dy(III) doped Lu_2 isostructural complex provided an effective $g_z = 13.9$, the observation of an EPR signal being a confirmation of contribution of different $|m_J>$ to the ground state of this center. With the knowledge of both eigenvalues and eigenvectors of the two Dy(III) centers obtained by experimental and theoretical analysis, the exchange interaction was then evaluated by using two different models. The simplest one was based on Lines model [122], i.e., on the assumption of an isotropic exchange between the spin component of the angular momenta, and was able to reproduce the magnetic data assuming a ferromagnetic exchange between the two centers, but completely failed to provide a reasonable reproduction of the EPR data. Accordingly, the latter were modeled assuming two interacting effective doublets with their relative orientations fixed by ab initio results. In this framework, a simple axially anisotropic exchange interaction, neglecting antisymmetric contribution, was enough to obtain a reasonable reproduction of the experimental data:

$$\mathcal{H} = J_{\perp}\left(\hat{S}_{1x}\hat{S}_{2x} + \hat{S}_{1y}\hat{S}_{2y}\right) + J_{||}\hat{S}_{1z}\hat{S}_{2z} - \mu_B \vec{B} \cdot \left(\hat{\mathbf{S}}_1 \cdot \mathbf{g}_1 + \hat{\mathbf{S}}_2 \cdot \mathbf{g}_2\right) \qquad (13)$$

Also in this case, the best fit provided a ferromagnetic interaction. Interestingly, the anisotropy of the interaction could not be explained by dipolar contribution alone, implying a nonnegligible anisotropic exchange contribution. The accurate determination of the exchange interaction was then used to explain the lack of SMM behavior in this compound: in particular, the presence of many efficient relaxation pathways was traced back to the exchange interaction among noncollinear Dy^{III} centers. This indicates that in polynuclear lanthanide SMMs the magnetic moments of individual spins should be parallel if zero field slow relaxation of the magnetization is sought for, as already suggested by previous investigations on Ln–M–Ln species [123].

Finally, we wish to focus on the only polynuclear lanthanide complex for which, to the best of our knowledge, the exchange interaction has been analyzed in detail, using single-crystal magnetic measurements, high-field EPR (HFEPR), and ab initio calculations. The system under investigation is the archetypal Dy_3 triangular system based on the anion of the o-vanillin (see Fig. 15A), which is characterized by an essentially nonmagnetic ground state [124], but with a paramagnetic excited state which is accessible at high-field/high temperature and shows clear SMM behavior. Earlier reported experiments and ab initio calculations demonstrated that the nonmagnetic ground state originates by magnetic moments of the ground doublets of individual dysprosium ions being located in the plane of the triangle [125,126]. Furthermore, their relative orientation in the plane leads to a so-called toroidal magnetic moment, characterized by two degenerate chiral Kramers doublets with all moments arranged clockwise or anticlockwise.

Notwithstanding the complexity of the molecule, most of the earlier collected experimental data, including single-crystal magnetometry ones, could

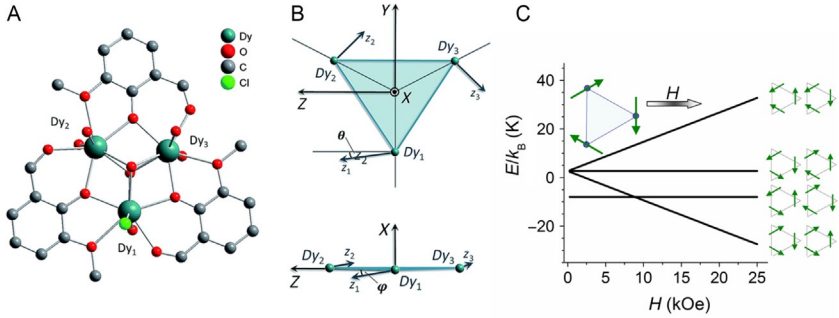

FIG. 15 (A) Molecular structure of Dy_3 (hydrogen atoms omitted for clarity) and (B) schematic views of the orientations of the local anisotropy (*z*-) axes of the ground Kramers doublet of each Dy center, according to results of ab initio calculations. The local *x* axes are taken to be parallel to the molecular *X*-axis. (C) Zeeman splitting of the of Dy_3 levels due to the application of the field in the plane of the *triangle*. *Panel B: Adapted with permission from M. Gysler, F. El Hallak, L. Ungur, R. Marx, M. Hakl, P. Neugebauer, Y. Rechkemmer, Y. Lan, I. Sheikin, M. Orlita, C.E. Anson, A.K. Powell, R. Sessoli, L.F. Chibotaru, J. van Slageren, Multitechnique investigation of Dy3—implications for coupled lanthanide clusters, Chem. Sci. (2016), © The Royal Society of Chemistry. Panel C: Adapted with permission from J. Luzon, K. Bernot, I.J. Hewitt, C.E. Anson, A.K. Powell, R. Sessoli, Spin chirality in a molecular dysprosium triangle: the archetype of the non-collinear Ising model, Phys. Rev. Lett. 100 (2008) 247205, © 2008 The American Physical Society.*

be explained by a very simple model. This considered only effective doublets, purely $m_J = \pm 15/2$ ($g_z = 20$, $g_{xy} = 0$), with all local anisotropy axes assumed to be related by 120° rotations around the axis perpendicular to the triangle plane. The exchange interaction was considered of the Ising type (so that only one parameter is needed to determine it):

$$\mathcal{H} = j \sum_{i,k=1,2,3;\ j>k} \hat{S}_{jz} \cdot \hat{S}_{kz} - \mu_B \vec{B} \cdot \sum_{i=1}^{3} \mathbf{g}_i \cdot \hat{\mathbf{S}}_i \tag{14}$$

A somewhat refined model, able to describe even smaller detail of the magnetization curve, required to consider isotropic exchange interactions, as well as to include $m_J = \pm 13/2$ excited doublets for each of the ions lying 71 cm^{-1} above the ground state in energy. The latter gap was however at odds with the one calculated by CASSCF (about twice larger), which prompted further experimental analysis on this system, including the use of FIR spectroscopy and CTM (down to 50 mK and up to 32 T), while no information could be gained by UV/vis/NIR optical spectroscopy [48]. As discussed earlier, the evaluation of the complete exchange interaction between the CF multiplets would require, even by considering only its first-order expansion, the use of nine exchange parameters per dysprosium pair in the absence of symmetry. If one considers in addition to these, the CF parameters for each center, a complete model would require a huge number of parameters.

Notwithstanding these constraints, it was possible to demonstrate that HFEPR and in-plane cantilever torque measurements can be well simulated by means of the above-mentioned rudimentary model based on Ising spins (Eq. 14), so that they do not provide any further insights in the electronic structure of the systems. On the other hand, FIR spectroscopy and out of plane CTM turned out to be very sensitive to the CF splitting of the individual ions, and to details of the magnetic coupling. The out-of-plane torque measurements were also very sensitive to the exact tilting angles of the local anisotropy axes from the plane of the Dy_3 molecule. On these basis, and using results of ab initio calculations as starting guesses for the investigation of the parameters' space, a large amount of data could be reproduced taking into account an isotropic exchange interaction among the two lowest doublets of all the three dysprosium ions, and a gap between ground and excited doublet in good agreement with results from ab initio calculations. This finally resulted in a very detailed picture of the electronic structure of this polynuclear lanthanide system, confirming that a combination of advanced experimental techniques and ab initio calculations is the only way to arrive at a full understanding of the properties of magnetically coupled lanthanide complexes.

3.2 Effects of the Exchange Coupling on Dynamic Properties

Studies on synthesis, characterization and control of the magnetic properties of exchange-coupled lanthanide-based complexes are not only driven by the interest in fundamental properties of lanthanide molecular complexes. In fact, the presence of a second center exchange coupled to the lanthanide ion can be seen as the source of a small effective field, resulting in suppression of quantum tunneling of the magnetization in zero external applied field. This may lead to effective bistability of the magnetization in zero field, which is the final goal to be reached if these systems are ever to be used for data storage applications.

Studies in this direction have involved families of multiple-decker phthalocyaninato lanthanide complexes, such as triple-decker Dy_2 [127], Tb_2, or quadruple-decker TbCdTb ones [128], as natural extension of the large body of research performed on the corresponding mononuclear double-decker phthalocyaninato complexes [82,129,130]. These studies pointed out that moderate *f–f* interactions, essentially of dipolar origin, suppress the quantum tunneling of magnetization (QTM) in the absence of the external magnetic field; however, faster magnetic relaxation processes are observed for the dinuclear systems compared to the mononuclear one in presence of a moderate applied magnetic field. Based on the calculated Zeeman diagrams using CF parameter adapted from those previously derived using NMR spectroscopy [131], this was attributed to the enhancement in nuclear spin-driven QTM in presence of the external magnetic field.

More detailed studies, involving both single-crystal analysis of the dynamic behavior down to mK region, complemented by ab initio calculations were performed on dinuclear Ln-Schiff base complexes [132]. In one of these systems (Fig. 16A) of formula $[Dy_2ovph_2Cl_2(MeOH)_3]\cdot MeCN$ (where H_2ovph = pyridine-2-carboxylic acid [(2-hydroxy-3-methoxyphenyl) methylene] hydrazide), the metal ions are ferromagnetically coupled and it was shown that quantum tunneling pathways between low-lying exchange multiplets are strongly suppressed at low temperatures, reaching tens of seconds, i.e., three orders of magnitude slower than reported for other Dy_2 systems. Ab initio calculations suggested that this behavior might be attributed to strong axiality of the local **g** tensors, with their easy axis being almost parallel to each other and to the vector connecting the two Dy(III) ions (Fig. 16A). This results in very weak transversal components of the dipolar field induced by the dysprosium ions on each other, thus significantly

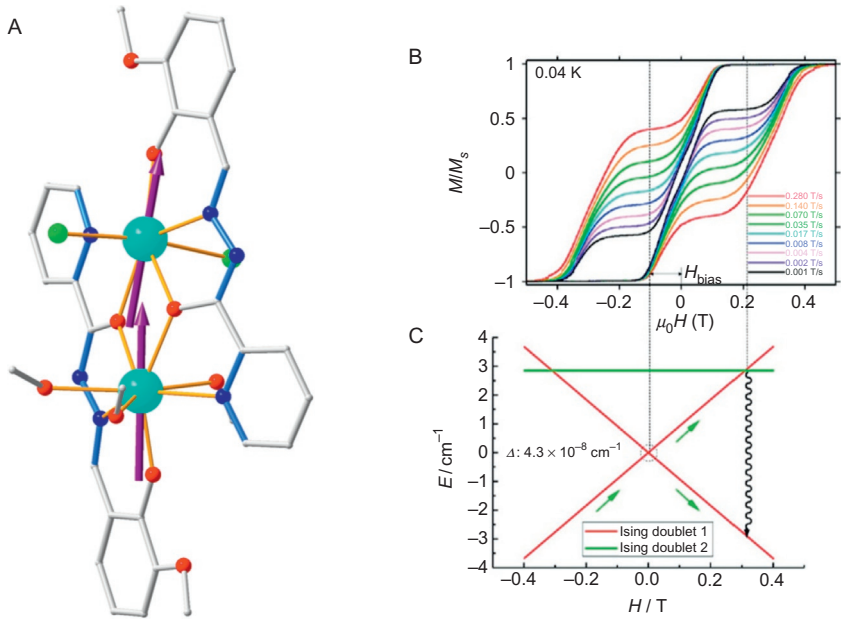

FIG. 16 (A) Molecular structure and calculated orientation of easy axis anisotropy for the two Dy^{III} ions in $[Dy_2ovph_2Cl_2(MeOH)_3]\cdot MeCN$. (B) Hysteresis cycle showing quantum tunneling step in a 0.3 T field, resulting from the ferromagnetic Ising interaction between the two doublets and the corresponding field dependence of energy levels depicted in (C). *Adapted with permission from Y.-N. Guo, G.-F. Xu, W. Wernsdorfer, L. Ungur, Y. Guo, J. Tang, H.-J. Zhang, L.F. Chibotaru, A.K. Powell, strong axiality and Ising exchange interaction suppress zero-field tunneling of magnetization of an asymmetric Dy_2 single-molecule magnet, J. Am. Chem. Soc. 133 (2011) 11948-11951. © 2011 American Chemical Society.*

reducing the efficiency of the tunneling mechanism, which is otherwise often active in concentrated lanthanide-based SMMs. It is worth noting that the calculated dipolar contribution to the exchange coupling provided an estimate of $J_{dip} = 5.36\ cm^{-1}$, assuming an effective $S = 1/2$ for each Dy(III) ion, a value much larger than the pure exchange contribution to the interaction. This interaction provides two low-lying Ising doublets, separated by $2.85\ cm^{-1}$. On applying a field along the easy axis direction of the ground doublet, the energy of the excited one remains essentially unaffected, thus leading to level crossings which are responsible for QTM in an applied field of ca. 0.3 T (Fig. 16).

Other studies on similar systems, involving the use of *4f–4f* interactions to suppress tunneling, were devoted to antiferromagnetically coupled dinuclear Dy(III) molecules, $[Dy_2(valdien)_2(NO_3)_2]$ (H_2valdien = *N1*,*N3*-bis(3-methoxysalicylidene)diethylenetriamine) [133,134]. This showed an "S-shaped" hysteresis with no tunneling in zero field and a large step at $\mu_0 H = 0.3$ T, which was attributed to the antiferromagnetically coupled Dy(III) spins. Indeed, a large step at zero field was observed in hysteresis measurements on the 5% Dy(III)-doped diamagnetic analog Y_2: this indicates that while the slow relaxation of the magnetization is intrinsically linked to the axial nature of the Dy(III) ion, the QTM can be modulated by way of weak interactions which act as bias field on neighboring metal ion within the molecule. In this sense, the observed behavior can be considered as comparable to that previously observed on $\{Mn_4\}_2$ systems where two cluster units are entangled in their slow relaxation of the magnetization [135]. However, in the latter polynuclear systems, the exchange-bias originates mainly from weak intermolecular interactions via hydrogen bonds or dipolar interactions, whereas in Dy_2 systems the interactions are intramolecular rather than intermolecular.

While the use of this exchange-bias approach to reduce the effectiveness of tunneling is applicable even if the *4f–4f* interactions are weak, stronger interactions provide the additional advantage of resulting in a coupled system behaving as a single giant spin. In much the same way as in polynuclear transition metal clusters, relaxation of the magnetization then necessarily occurs via a multistep Orbach process above the ladder, rather than from the lower lying excited states, and competitive processes such as Raman and direct ones are not efficient. At the same time, the tunneling reduction is even more evident. However, as we have seen in previous paragraphs, targeting large coupling in Lanthanide-based complexes is not an easy task at all. In this field, the most spectacular results have been obtained by Long's group, in the family of N_2^{3-} radical-bridged $[\{[(Me_3Si)_2N]_2(THF)Ln\}_2(\mu\text{-}\eta_2\text{:}\eta_2\text{-}N_2)]$ (Ln = Gd(III), Tb(III), Dy(III), Ho(III), Er(III)) complexes (Fig. 17, *left*) [104,136]. The strong AF coupling involving the central radical unit and the two peripheral Ln ions leads to a ferrimagnetic-type arrangement for which the ground state is well isolated from the excited one. Indeed, the magnitude of the coupling is the

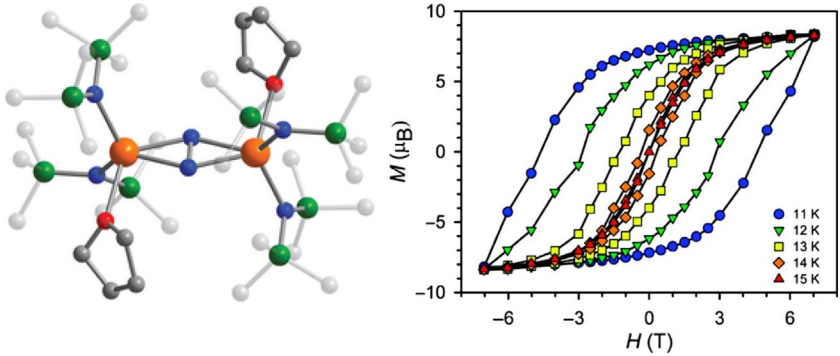

FIG. 17 (*Left*) Molecular structure of $[\{[(Me_3Si)_2N]_2Ln(III)(THF)\}_2(\mu\text{–}\eta^2\text{:}\eta^2\text{–}N_2)]^-$ anion (Ln = Gd, Tb, Dy). (*Right*) Hysteresis cycle of Tb derivative, measured from 11 to 15 K at an average sweep rate of 0.9 mT/s. *Left: Reprinted by permission from J.D. Rinehart, M. Fang, W.J. Evans, J.R. Long, Strong exchange and magnetic blocking in N_2^{3-}-radical-bridged lanthanide complexes, Nature Chem. 3 (2011) 538–542, © 2011 Macmillan Publishers Ltd. Right: Reprinted with permission from J.D. Rinehart, M. Fang, W.J. Evans, J.R. Long, A N_2^{3-} radical-bridged terbium complex exhibiting magnetic hysteresis at 14 K, J. Am. Chem. Soc. 133 (2011) 14236–14239, © 2011 American Chemical Society.*

largest hitherto reported for Ln-based complexes. At the same time, since the two lanthanide ions are related by a center of symmetry, their single-ion anisotropy axes are parallel to each other, thus resulting in both sought-after features required for a SMM: a large spin ground state well isolated from the excited one, and a large easy axis anisotropy. This approach provided two examples of lanthanide-based SMM which are—up to date—the best ones in term of blocking temperatures. Notwithstanding unexceptional effective energy barriers of 177 and 327 K for Dy(III) and Tb(III) derivatives, respectively, the latter exhibits magnetic hysteresis at 14 K (see Fig. 17, *right*) and a 100 s relaxation time at 13.9 K; the Dy derivative was also shown to provide considerable magnetic hysteresis at reasonably slow field sweep rates and $T \approx 7$ K. When compared to mononuclear Ln complexes which often show hysteresis at much lower temperature despite much larger effective barrier, this behavior clearly demonstrates the efficient suppression of competitive relaxation paths (tunneling, Raman, direct) due to the giant spin nature of these systems. Unfortunately, this is, at the moment, a simple proof-of-principle of the possibility of using Ln-radical exchange coupling to produce extremely well-performing SMMs; indeed, their chemical features make these complexes fairly unstable, and not well suited for deposition over surfaces, a must if these systems are to be considered for potential devices.

In this sense, the bipyrimidyl radical dinuclear complexes $[(Cp^*_2Ln)_2(m\text{-}bpym)](BPh_4)$ (where Ln = Gd(III), Tb(III), and Dy(III)) [137], obtained pursuing the same strategy of strong exchange coupling, may provide some

advantage, being much more stable from a chemical point of view. Even for this family a relatively strong AF lanthanide-radical coupling results in a ferrimagnetic-type structure, the two Ln centers being crystallographically equivalent. Both Tb(III) and Dy(III) derivatives turned out to show open magnetic hysteresis cycle at temperatures above that of liquid helium, despite relatively small anisotropy barriers (44(2) and 87.8(3) cm^{-1} for Tb(III) and Dy(III) derivative, respectively). The observation of hysteresis at lower temperature compared to N_2^{3-} radical-bridged complexes is consistent with the lower value of the effective barrier. However, in addition to this difference, for this family, zero-field tunneling is not completely suppressed: this has been tentatively attributed to the lower value of the exchange coupling interaction in this family, compared to N_2^{3-} bridged ones. As a whole, this suggests the need to enhance the strength of the exchange coupling in radical-bridged lanthanide systems to obtain other lanthanide-based SMMs with improved performances. This might in principle be achieved by appropriate synthetic strategies, adding electron-donating or -withdrawing substituents to the bpym ligand and/or exploiting other organic radical bridging ligands. In this sense, this approach provides much room for a relevant contribution from synthetic chemistry, whose potential remains to be fully exploited. Indeed, only Long's group is apparently following this strategy [138,139]: in the tetrapyridylpyrazine-bridged Ln_2 complexes they recently reported SMM behavior only for the mononegative radical anion derivative, as compared to trinegative radical ones, despite the rather similar exchange coupling strength provided by the two species. This was attributed to the larger ligand field strength afforded by the stronger electron donating power in the hard plane of the Ln(III) ions of the trinegative anion compared to the mononegative one. The simultaneous optimization of exchange coupling between the magnetic ions to suppress tunneling and of the CF to generate high anisotropy barriers is mandatory to produce high blocking temperatures in these SMMs but not trivial to realize.

4 CONCLUSION AND OUTLOOK

The magnetic bistability of lanthanide-based molecules, despite the significant improvements of the last years which we outlined in this chapter, has not yet been exploited in applications because the operation temperatures are not competitive with those of inorganic nanostructured materials. On the other hand, the intrinsic quantum nature of molecular spins is well suited for the realization of quantum bits, or qubits, and quantum gates, to be exploited in quantum information technologies [140]. Indeed, inorganic matrices doped with lanthanide ions are already been investigated for this purpose, thanks to their narrow optical transitions, and the interested reader is addressed to another chapter of this Handbooks' series [141].

As discussed in several instances of this chapter, at low temperature molecules containing a single Ln center can often be approximated as a spin doublet; this, with its two levels (spin up and spin down), is the natural realization of a qubit. Pulsed EPR techniques can be used to manipulate the spin system and realize a quantum superposition of the two states. One crucial issue is the lifetime of the quantum state, or coherence time, which must be long enough to allow multiple operations. In this respect, molecular spin systems possess shorter coherence times than other spin-based physical realizations based on defects in solids such as diamond [142] or silicon [143]. Noticeable results about long coherence times [144] and robustness toward temperature [145] have been obtained for coordination complexes of V(IV), thanks to the low spin–orbit coupling of this metal. The use of lanthanide ions, which appears unfavorable from this viewpoint, has however some advantages. Indeed, for lanthanides characterized by long spin–lattice relaxation times, the decoherence time is not limited by short T_1 as recently shown for the Yb(III) complex belonging to the [Ln(trensal)] series already discussed in this chapter [146]. Furthermore one can in principle exploit the photoluminescence for spin detection [147]. In this approach, using lanthanide spin provides an opportunity to bridge microwave and optical domains at the quantum level [148]. In particular, lanthanide-based complexes have been proposed as potential units of hybridized spin–photon states using superconducting cavities in strong-coupling regime, thanks to their large effective g-factor [149,150].

To improve the lifetime of the quantum states, more complex energy level schemes can also be exploited. For instance, avoided level crossings among hyperfine levels gives rise to very robust transitions, so-called, *clock transitions*, that are only weakly affected by gradients or fluctuations of the local magnetic field. A highly symmetric Ho(III) polyoxometallate complex of formula $[Ho(W_5O_{18})_2]^{9-}$ has been investigated by multifrequency pulsed EPR spectroscopy and the possibility to operate at the clock transitions induced by the coupling with $I = 7/2$ of ^{165}Ho has allowed to significantly improve the coherence lifetime [151].

A single qubit has however very little use. Coupling, or rather entanglement, between more qubits is necessary to realize quantum gates [140]. Here molecules present the advantage of a fine tuning of the interaction through chemical design [152]. Using pulsed EPR techniques to address distinct but coupled qubits are actually possible in heterometallic lanthanide containing molecules because of the large variation of the effective g values along the 4*f* series, as recently achieved in a Ce(III)–Er(III) dinuclear complex [153]. This requires however the design of coordination pockets that can selectively accommodate early or late lanthanide ions by exploiting their different ionic radii [154].

Another significant advantage of molecular spin qubits is the possibility to address individual molecules because these preformed units can be easily

organized at the nanoscale. This is a fascinating area of research in molecular magnetism and the reader is addressed to reviews on the topic [18,155].

Worth mentioning are the results obtained on the neutral and evaporable double-decker complex [$TbPc_2$], which has provided the proof-of-principle of electrical detection of single electronic and single nuclear spins [83], as well as the realization of spintronic devices that exploit the interaction between [$LnPc_2$] molecules [156]. The research has been extended to other evaporable molecules like the [Ln(trensal)] series [157] or endohedral fullerene SMMs [158].

Equally fascinating is the possibility to exploit the interaction of the molecules with the substrate to modify the magnetic properties. For instance, the deposition of a submonolayer of [$TbPc_2$] on a magnetic substrate like a Ni film on Cu, enhances the magnetic bistability of the molecules, though the resulting magnetic bistability can no more be considered a single-molecule property but reflects more the bistability of the substrate [159]. While nonmagnetic metals are in general found to enhance fast relaxation of the deposited molecules, the use of a nonmetallic substrate such as Si has been found to increases the magnetic hysteresis of a self-assembled monolayer of prefunctionalized $TbPc_2$ molecules [17]. The use of an insulating thin layer of MgO has recently provided a dramatic increase of the magnetic remanence of [$TbPc_2$] submonolayers [160].

Having demonstrated that a single molecule retains SMM behavior, other questions arise: how relevant is the molecular scaffold and can magnetic bistability be observed on a single atom? After some debated results, it has recently been shown that isolated Ho atoms deposited on a thin insulating film of MgO on Ag(100) surface exhibit magnetic hysteresis up to 30 K [161]. Interestingly, the deposition on a surface realizes the axial coordination required to enhance the CF effects. Moreover the C_{4v} symmetry of the absorption site, combined with the composition of the ground doublet (mainly from $m_J = \pm 7$ and $m_J = \pm 3$) of the Ho atom further reduces the efficiency of tunnel mechanisms of relaxation.

It is obvious that single atoms deposited on surfaces are very labile species with a limited lifetime and need the use of extreme conditions, such as cryogenic temperatures and ultra-high vacuum. Nevertheless, these spectacular results clearly highlight promising directions for molecular magnetism where the versatility of the molecular design can exploit exotic environments that can be realized in hybrid nanostructures.

ACKNOWLEDGMENTS

We have obtained some of the scientific results discussed in this chapter thanks to the contribution of many collaborators to whom we are deeply indebted. A special thank goes to some of them, in particular to Dr. M.E. Boulon, Dr. G. Cucinotta, Dr. E. Lucaccini, Dr. J. Luzon, and Dr. M. Perfetti. Part of our research activity has been funded by the EC through the AdG MolNanoMaS project (No. 267746) and by the Italian MIUR through the project Futuro in Ricerca 2012 (RBFR12RPD1).

ABBREVIATIONS

AF	antiferromagnetic
AOM	angular overlap model
CASSCF	complete active space self-consistent field
CF	crystal field
CTM	cantilever torque magnetometry
DOTA	1,4,7,10-tetraaza-cyclododecane-tetraacetate
EPR	electron paramagnetic resonance
FIR	far infrared
H_3trensal	2,2′,2″-tris(salicylideneimino)triethylamine
HFEPR	high-field electron paramagnetic resonance
PCEM	point-charge electrostatic model
QTM	quantum tunneling of magnetization
REC	radial effective charge
SCM	single-chain magnet
SIM	single-ion magnet
SMM	single-molecule magnet
trensal	see H_3trensal

REFERENCES

[1] O. Kahn, Molecular Magnetism, VCH, Weinheim, 1993.

[2] M. Saint Paul, C. Veyret, Ferromagnetic ordering in an organic compound. Bis(2,2,6,6-tetramethyl-4- piperidinol 1-oxyl) suberate (tanol suberate), Phys. Lett. A 45 (5) (1973) 362–364.

[3] M. Tamura, Y. Nakazawa, D. Shiomi, Y. Nozawa, M. Hosokoshi, M. Ishikawa, M. Takahashi, M. Kinoshita, Bulk ferromagnetism in the β-phase crystal of the p-nitrophenyl nitronyl nitroxide radical, Chem. Phys. Lett. 186 (1991) 401.

[4] J.S. Miller, J.C. Calabrese, H. Rommelmann, S.R. Chittipeddi, J.H. Zhang, W.M. Reiff, A. J. Epstein, Ferromagnetic behavior of $[Fe(C_5Me_5)_2]+.[TCNE]-$. Structural and magnetic characterization of decamethylferrocenium tetracyanoethenide, $[Fe(C_5Me_5)_2]+.[TCNE]-$. MeCN and decamethylferrocenium pentacyanopropenide, $[Fe(C_5Me_5)_2]+.[C_3(CN)_5]-$, J. Am. Chem. Soc. 109 (1987) 769.

[5] O. Kahn, Y. Pei, M. Verdaguer, J.-P. Renard, J. Sletten, Magnetic ordering of manganese(II) copper(II) bimetallic chains; design of a molecular based ferromagnet, J. Am. Chem. Soc. 110 (1988) 782–789.

[6] C. Benelli, D. Gatteschi, Introduction to Molecular Magnetism: From Transition Metals to Lanthanides, John Wiley & Sons, Weinheim, 2015.

[7] D. Gatteschi, R. Sessoli, J. Villain, Molecular Nanomagnets, Oxford University Press, Oxford, 2006.

[8] J.H. Van Vleck, The Theory of Electric and Magnetic Susceptibility, Oxford University Press, Oxford, 1932.

[9] R. Sessoli, D. Gatteschi, A. Caneschi, M.A. Novak, Magnetic bistability in a metal-ion cluster, Nature 365 (1993) 141–143.

[10] C.J. Milios, A. Vinslava, W. Wernsdorfer, S. Moggach, S. Parsons, S.P. Perlepes, G. Christou, E.K. Brechin, A record anisotropy barrier for a single-molecule magnet, J. Am. Chem. Soc. 129 (2007) 2754–2755.
[11] J. Liu, Y.-C. Chen, J.-L. Liu, V. Vieru, L. Ungur, J.-H. Jia, L.F. Chibotaru, Y. Lan, W. Wernsdorfer, S. Gao, X.-M. Chen, M.-L. Tong, A stable pentagonal bipyramidal Dy(III) single-ion magnet with a record magnetization reversal barrier over 1000K, J. Am. Chem. Soc. 138 (2016) 5441–5450.
[12] D.V. Konarev, A.V. Kuzmin, M.A. Faraonov, M. Ishikawa, S.S. Khasanov, Y. Nakano, A. Otsuka, H. Yamochi, G. Saito, R.N. Lyubovskaya, Synthesis, structures, and properties of crystalline salts with radical anions of metal-containing and metal-free phthalocyanines, Chem. Eur. J. 21 (2015) 1014–1028.
[13] R. Marx, F. Moro, M. Dorfel, L. Ungur, M. Waters, S.D. Jiang, M. Orlita, J. Taylor, W. Frey, L.F. Chibotaru, J. van Slageren, Spectroscopic determination of crystal field splittings in lanthanide double deckers, Chem. Sci. 5 (2014) 3287–3293.
[14] N. Ishikawa, M. Sugita, N. Tanaka, T. Ishikawa, S.Y. Koshihara, Y. Kaizu, Upward temperature shift of the intrinsic phase lag of the magnetization of bis(phthalocyaninato) terbium by ligand oxidation creating an S=1/2 spin, Inorg. Chem. 43 (2004) 5498–5500.
[15] S. Takamatsu, T. Ishikawa, S.-y. Koshihara, N. Ishikawa, Significant increase of the barrier energy for magnetization reversal of a single-4f-ionic single-molecule magnet by a longitudinal contraction of the coordination space, Inorg. Chem. 46 (2007) 7250–7252.
[16] M. Gonidec, F. Luis, A. Vilchez, J. Esquena, D.B. Amabilino, J. Veciana, A liquid-crystalline single-molecule magnet with variable magnetic properties, Angew. Chem. Int. Ed. 49 (2010) 1623–1626.
[17] M. Mannini, F. Bertani, C. Tudisco, L. Malavolti, L. Poggini, K. Misztal, D. Menozzi, A. Motta, E. Otero, P. Ohresser, P. Sainctavit, G.G. Condorelli, E. Dalcanale, R. Sessoli, Magnetic behaviour of $TbPc_2$ single-molecule magnets chemically grafted on silicon surface, Nat. Commun. 5 (2014) 4582.
[18] J. Dreiser, Molecular lanthanide single-ion magnets: from bulk to submonolayers, J. Phys. Condens. Matter 27 (2015) 183203.
[19] A. Caneschi, D. Gatteschi, R. Sessoli, P. Rey, Toward molecular magnets—the metal-radical approach, Acc. Chem. Res. 22 (1989) 392–398.
[20] A. Caneschi, D. Gatteschi, N. Lalioti, C. Sangregorio, R. Sessoli, G. Venturi, A. Vindigni, A. Rettori, M.G. Pini, M.A. Novak, Cobalt(II)-nitronyl nitroxide chains as molecular magnetic nanowires, Angew. Chem. Int. Ed. 40 (2001) 1760–1763.
[21] R. Clerac, H. Miyasaka, M. Yamashita, C. Coulon, Evidence for single-chain magnet behavior in a Mn(III)-Ni(II) chain designed with high spin magnetic units: a route to high temperature metastable magnets, J. Am. Chem. Soc. 124 (2002) 12837–12844.
[22] R.J. Glauber, Time-dependent statistic of the Ising model, J. Math. Phys. 4 (1963) 294–307.
[23] L. Bogani, C. Sangregorio, R. Sessoli, D. Gatteschi, Molecular engineering for single-chain-magnet behavior in a one-dimensional dysprosium-nitronyl nitroxide compound, Angew. Chem. Int. Ed. 44 (2005) 5817–5821.
[24] C. Benelli, A. Caneschi, D. Gatteschi, R. Sessoli, Magnetic-ordering in a molecular material containing dysprosium(III) and a nitronyl nitroxide, Adv. Mater. 4 (1992) 504–505.
[25] K.W.H. Stevens, Matrix elements and operator equivalents connected with the magnetic properties of rare earth ions, Proc. Phys. Soc. A 65 (1952) 209.
[26] A. Abragam, B. Bleaney, Electron Paramagnetic Resonance of Transition Ions, Dover, New York, 1986.

[27] L. Sorace, C. Benelli, D. Gatteschi, Lanthanides in molecular magnetism: old tools in a new field, Chem. Soc. Rev. 40 (2011) 3092–3104.
[28] J.D. Rinehart, J.R. Long, Exploiting single-ion anisotropy in the design of f-element single-molecule magnets, Chem. Sci. 2 (2011) 2078–2085.
[29] C. Görller-Walrand, K. Binnemans, Rationalization of Crystal Field Parameters, in: K.A Gschneidner Jr., L. Eyring (Eds.), Handbook on Physics and Chemistry of Rare Earths, vol. 23, Elsevier, Amsterdam, 1996, pp. 221–283, Chapter 155.
[30] L.F. Chibotaru, L. Ungur, Ab initio calculation of anisotropic magnetic properties of complexes. I. Unique definition of pseudospin Hamiltonians and their derivation, J. Chem. Phys. 137 (2012) 064112.
[31] P. Porcher, M. Couto Dos Santos, O. Malta, Relationship between phenomenological crystal field parameters and the crystal structure: the simple overlap model, Phys. Chem. Chem. Phys. 1 (1999) 397–405.
[32] Z. Zolnierek, Crystal field parameters in a modified point charge model, J. Phys. Chem. Solids 45 (1984) 523–528.
[33] J.J. Baldovi, J.J. Borras-Almenar, J.M. Clemente-Juan, E. Coronado, A. Gaita-Arino, Modeling the properties of lanthanoid single-ion magnets using an effective point-charge approach, Dalton Trans. 41 (2012) 13705–13710.
[34] N.F. Chilton, D. Collison, E.J.L. McInnes, R.E.P. Winpenny, A. Soncini, An electrostatic model for the determination of magnetic anisotropy in dysprosium complexes, Nat. Commun. 4 (2013) 2551.
[35] J.J. Baldovi, S. Cardona-Serra, J.M. Clemente-Juan, E. Coronado, A. Gaita-Arino, A. Palii, SIMPRE: a software package to calculate crystal field parameters, energy levels, and magnetic properties on mononuclear lanthanoid complexes based on charge distributions, J. Comput. Chem. 34 (2013) 1961–1967.
[36] J.J. Baldovi, J.M. Clemente-Juan, E. Coronado, A. Gaita-Arino, A. Palii, An updated version of the computational package SIMPRE that uses the standard conventions for Stevens crystal field parameters, J. Comput. Chem. 35 (2014) 1930–1934.
[37] J.J. Baldovi, A. Gaita-Arino, E. Coronado, Modeling the magnetic properties of lanthanide complexes: relationship of the REC parameters with Pauling electronegativity and coordination number, Dalton Trans. 44 (2015) 12535–12538.
[38] N. Ishikawa, M. Sugita, T. Okubo, N. Tanaka, T. Lino, Y. Kaizu, Determination of ligand-field parameters and F-electronic structures of double-decker bis(phthalocyaninato)lanthanide complexes, Inorg. Chem. 42 (2003) 2440–2446.
[39] K. Qian, J.J. Baldovi, S.-D. Jiang, A. Gaita-Arino, Y.-Q. Zhang, J. Overgaard, B.-W. Wang, E. Coronado, S. Gao, Does the thermal evolution of molecular structures critically affect the magnetic anisotropy? Chem. Sci. 6 (2015) 4587–4593.
[40] C.K. Jörgensen, R. Pappalardo, H.H. Schmidtke, Do the "ligand field" parameters in lanthanides represent weak covalent bonding? J. Chem. Phys. 39 (1963) 1422–1430.
[41] B.M. Flanagan, P.V. Bernhardt, E.R. Krausz, S.R. Lüthi, M.J. Riley, Ligand-field analysis of an Er(III) complex with a heptadentate tripodal N_4O_3 ligand, Inorg. Chem. 40 (2001) 5401–5407.
[42] W. Urland, On the ligand-field potential for f electrons in the angular overlap model, Chem. Phys. 14 (1976) 393–401.
[43] M. Kanesato, T. Yokoyama, Synthesis and structural characterization of Ln(III) complexes (Ln=Eu, Gd, Tb, Er, Tm, Lu) of tripodal tris[2-(salicylideneamino)ethyl]amine, Chem. Lett. 28 (1999) 137–138.

[44] B.O. Roos, P.R. Taylor, P.E.M. Siegbahn, A complete active space SCF method (CASSCF) using a density matrix formulated super-CI approach, Chem. Phys. 48 (1980) 157–173.
[45] K. Andersson, P.-A. Malmqvist, B.O. Roos, Second-order perturbation theory with a complete active space self-consistent field reference function, J. Chem. Phys. 96 (1992) 1218–1226.
[46] E. Lucaccini, M. Briganti, M. Perfetti, L. Vendier, J.-P. Costes, F. Totti, R. Sessoli, L. Sorace, Relaxation dynamics and magnetic anisotropy in a low-symmetry Dy^{III} complex, Chem. Eur. J. 22 (2016) 5552–5562.
[47] K.S. Pedersen, L. Ungur, M. Sigrist, A. Sundt, M. Schau-Magnussen, V. Vieru, H. Mutka, S. Rols, H. Weihe, O. Waldmann, L.F. Chibotaru, J. Bendix, J. Dreiser, Modifying the properties of 4f single-ion magnets by peripheral ligand functionalisation, Chem. Sci. 5 (2014) 1650–1660.
[48] M. Gysler, F. El Hallak, L. Ungur, R. Marx, M. Hakl, P. Neugebauer, Y. Rechkemmer, Y. Lan, I. Sheikin, M. Orlita, C.E. Anson, A.K. Powell, R. Sessoli, L.F. Chibotaru, J. van Slageren, Multitechnique investigation of Dy_3—implications for coupled lanthanide clusters, Chem. Sci. 7 (2016) 4347–4354.
[49] E. Moreno Pineda, N.F. Chilton, R. Marx, M. Dörfel, D.O. Sells, P. Neugebauer, S.-D. Jiang, D. Collison, J. van Slageren, E.J.L. McInnes, R.E.P. Winpenny, Direct measurement of dysprosium(III)···dysprosium(III) interactions in a single-molecule magnet, Nat. Commun. 5 (2014) 5243.
[50] S. Ghosh, S. Datta, L. Friend, S. Cardona-Serra, A. Gaita-Arino, E. Coronado, S. Hill, Multi-frequency EPR studies of a mononuclear holmium single-molecule magnet based on the polyoxometalate $[Ho^{III}(W_5O_{18})_2]^{9-}$, Dalton Trans. 41 (2012) 13697–13704.
[51] J.M. Baker, C.A. Hutchison, M.J.M. Leask, P.M. Martineau, M.G. Robinson, Electron paramagnetic resonance, optical and magnetic studies of Tb^{3+} in lanthanide nicotinate dihydrates, Proc. R. Soc. Lond. Ser. A Math. Phys. Eng. Sci. 413 (1987) 515–528.
[52] G. Cucinotta, M. Perfetti, J. Luzon, M. Etienne, P.E. Car, A. Caneschi, G. Calvez, K. Bernot, R. Sessoli, Magnetic anisotropy in a dysprosium/DOTA single-molecule magnet: beyond simple magneto-structural correlations, Angew. Chem. Int. Ed. 51 (2012) 1606–1610.
[53] M.-E. Boulon, G. Cucinotta, J. Luzon, C. Degl'Innocenti, M. Perfetti, K. Bernot, G. Calvez, A. Caneschi, R. Sessoli, Magnetic anisotropy and spin-parity effect along the series of lanthanide complexes with DOTA, Angew. Chem. Int. Ed. 52 (2013) 350–354.
[54] H. Stetter, W. Frank, Complex formation with tetraazacycloalkane-N, N′, N″, N‴-tetraacetic acids as a function of ring size, Angew. Chem. Int. Ed. Eng. 15 (1976) 686.
[55] N. Viola-Villegas, R.P. Doyle, The coordination chemistry of 1,4,7,10-tetraazacyclododecane-N, N′, N″, N‴-tetraacetic acid (H_4DOTA): structural overview and analyses on structure–stability relationships, Coord. Chem. Rev. 253 (2009) 1906–1925.
[56] M. Bottrill, L. Kwok, N.J. Long, Lanthanides in magnetic resonance imaging, Chem. Soc. Rev. 35 (2006) 557–571.
[57] S. Viswanathan, Z. Kovacs, K.N. Green, S.J. Ratnakar, A.D. Sherry, Alternatives to gadolinium-based metal chelates for magnetic resonance imaging, Chem. Rev. 110 (2010) 2960–3018.
[58] L. Vander Elst, A. Roch, P. Gillis, S. Laurent, F. Botteman, J.W.M. Bulte, R.N. Muller, Dy-DTPA derivatives as relaxation agents for very high field MRI: the beneficial effect of slow water exchange on the transverse relaxivities, Magn. Reson. Med. 47 (2002) 1121–1130.

[59] M.E. Boulon, G. Cucinotta, S.S. Liu, S.D. Jiang, L. Ungur, L.F. Chibotaru, S. Gao, R. Sessoli, Angular-resolved magnetometry beyond triclinic crystals: out-of-equilibrium studies of Cp*ErCOT single-molecule magnet, Chem. Eur. J. 19 (2013) 13726–13731.
[60] S. Mitra, Torque magnetometry, Prog. Inorg. Chem. 22 (1977) 309–408.
[61] B.M. Flanagan, P.V. Bernhardt, E.R. Krausz, S.R. Lüthi, M.J. Riley, A ligand-field analysis of the trensal (H_3trensal=2,2′,2″-tris(salicylideneimino)triethylamine) ligand. An application of the angular overlap model to lanthanides, Inorg. Chem. 41 (2002) 5024–5033.
[62] M. Perfetti, E. Lucaccini, L. Sorace, J.P. Costes, R. Sessoli, Determination of magnetic anisotropy in the LnTRENSAL complexes (Ln=Tb, Dy, Er) by torque magnetometry, Inorg. Chem. 54 (2015) 3090–3092.
[63] E. Lucaccini, L. Sorace, M. Perfetti, J.-P. Costes, R. Sessoli, Beyond the anisotropy barrier: slow relaxation of the magnetization in both easy-axis and easy-plane Ln(trensal) complexes, Chem. Commun. 50 (2014) 1648–1651.
[64] M. Perfetti, G. Cucinotta, M.-E. Boulon, F. El Hallak, S. Gao, R. Sessoli, Angular-resolved magnetometry beyond triclinic crystals part II: torque magnetometry of Cp*ErCOT single-molecule magnets, Chem. Eur. J. 20 (2014) 14051–14056.
[65] H. Schumann, R.D. Kohn, F.W. Reier, A. Dietrich, J. Pickardt, Organometallic compounds of the lanthanides. 48. Cyclooctatetraenyl pentamethylcyclopentadienyl derivatives of the rare-earths, Organometallics 8 (1989) 1388–1392.
[66] S.D. Jiang, B.W. Wang, H.L. Sun, Z.M. Wang, S. Gao, An organometallic single-ion magnet, J. Am. Chem. Soc. 133 (2011) 4730–4733.
[67] I. Mihalcea, N. Zill, V. Mereacre, C.E. Anson, A.K. Powell, Spontaneous resolution in homochiral helical [Ln$(nic)_2$(hnic)(NO_3)] coordination polymers constructed from a rigid non-chiral organic ligand, Cryst. Growth Des. 14 (2014) 4729–4734.
[68] I. Mihalcea, M. Perfetti, F. Pineider, L. Tesi, V. Mereacre, F. Wilhelm, A. Rogalev, C.E. Anson, A.K. Powell, R. Sessoli, Spin helicity in chiral lanthanide chains. Inorg. Chem. (2016). http://dx.doi.org/10.1021/acs.inorgchem.6b01010.
[69] G. Wagnière, A. Meier, The influence of a static magnetic field on the absorption coefficient of a chiral molecule, Chem. Phys. Lett. 93 (1982) 78–81.
[70] L.D. Barron, J. Vrbancich, Magneto-chiral birefringence and dichroism, Mol. Phys. 51 (1984) 715–730.
[71] G. Rikken, E. Raupach, Observation of magneto-chiral dichroism, Nature 390 (1997) 493–494.
[72] R. Sessoli, M.-E. Boulon, A. Caneschi, M. Mannini, L. Poggini, F. Wilhelm, A. Rogalev, Strong magneto-chiral dichroism in a paramagnetic molecular helix observed by hard X-rays, Nat. Phys. 11 (2015) 69–74.
[73] D. Gatteschi, R. Sessoli, Quantum tunneling of magnetization and related phenomena in molecular materials, Angew. Chem. Int. Ed. 42 (2003) 268–297.
[74] D.N. Woodruff, R.E.P. Winpenny, R.A. Layfield, Lanthanide single-molecule magnets, Chem. Rev. 113 (2013) 5110–5148.
[75] S.T. Liddle, J. van Slageren, Improving f-element single molecule magnets, Chem. Soc. Rev. 44 (2015) 6655–6669.
[76] S. Demir, I.-R. Jeon, J.R. Long, T.D. Harris, Radical ligand-containing single-molecule magnets, Coord. Chem. Rev. 289–290 (2015) 149–176.
[77] F. Habib, M. Murugesu, Lessons learned from dinuclear lanthanide nano-magnets, Chem. Soc. Rev. 42 (2013) 3278–3288.

[78] H.L.C. Feltham, S. Brooker, Review of purely 4f and mixed-metal nd-4f single-molecule magnets containing only one lanthanide ion, Coord. Chem. Rev. 276 (2014) 1–33.
[79] J. Tang, P. Zhang, Lanthanide Single Molecule Magnets, Springer, Berlin, 2015.
[80] R.A. Layfield, M. Murugesu (Eds.), Lanthanides and Actinides in Molecular Magnetism, Wiley-VCH, Weinheim, 2015.
[81] A. Rossin, G. Giambastiani, M. Peruzzini, R. Sessoli, Amine-templated polymeric lanthanide formates: synthesis, characterization, and applications in luminescence and magnetism, Inorg. Chem. 51 (2012) 6962–6968.
[82] N. Ishikawa, M. Sugita, W. Wernsdorfer, Quantum tunneling of magnetization in lanthanide single-molecule magnets: bis(phthalocyaninato)terbium and bis(phthalocyaninato) dysprosium anions, Angew. Chem. Int. Ed. 44 (2005) 2931–2935.
[83] S. Thiele, F. Balestro, R. Ballou, S. Klyatskaya, M. Ruben, W. Wernsdorfer, Electrically driven nuclear spin resonance in single-molecule magnets, Science 344 (2014) 1135–1138.
[84] R. Vincent, S. Klyatskaya, M. Ruben, W. Wernsdorfer, F. Balestro, Electronic read-out of a single nuclear spin using a molecular spin transistor, Nature 488 (2012) 357–360.
[85] W. Wernsdorfer, A. Caneschi, R. Sessoli, D. Gatteschi, A. Cornia, V. Villar, C. Paulsen, Effects of nuclear spins on the quantum relaxation of the magnetization for the molecular nanomagnet Fe-8, Phys. Rev. Lett. 84 (2000) 2965–2968.
[86] F. Pointillart, K. Bernot, S. Golhen, B. Le Guennic, T. Guizouarn, L. Ouahab, O. Cador, Magnetic memory in an isotopically enriched and magnetically isolated mononuclear dysprosium complex, Angew. Chem. Int. Ed. 54 (2015) 1504–1507.
[87] J.J. Baldovi, S. Cardona-Serra, J.M. Clemente-Juan, E. Coronado, A. Gaita-Arino, A. Palii, Rational design of single-Ion magnets and spin qubits based on mononuclear lanthanoid complexes, Inorg. Chem. 51 (2012) 12565–12574.
[88] M. Gregson, N.F. Chilton, A.-M. Ariciu, F. Tuna, I.F. Crowe, W. Lewis, A.J. Blake, D. Collison, E.J.L. McInnes, R.E.P. Winpenny, S.T. Liddle, A monometallic lanthanide bis(methanediide) single molecule magnet with a large energy barrier and complex spin relaxation behaviour, Chem. Sci. 7 (2016) 155–165.
[89] N.F. Chilton, C.A.P. Goodwin, D.P. Mills, R.E.P. Winpenny, The first near-linear bis(amide) f-block complex: a blueprint for a high temperature single molecule magnet, Chem. Commun. 51 (2015) 101–103.
[90] R. Westerström, J. Dreiser, C. Piamonteze, M. Muntwiler, S. Weyeneth, H. Brune, S. Rusponi, F. Nolting, A. Popov, S. Yang, L. Dunsch, T. Greber, An endohedral single-molecule magnet with long relaxation times: $DySc_2N@C_{80}$, J. Am. Chem. Soc. 134 (2012) 9840–9843.
[91] K.R. Meihaus, J.R. Long, Magnetic blocking at 10 K and a dipolar-mediated avalanche in salts of the bis(η^8-cyclooctatetraenide) complex $[Er(COT)_2]^-$, J. Am. Chem. Soc. 135 (2013) 17952–17957.
[92] A. Bencini, C. Benelli, A. Caneschi, R.L. Carlin, A. Dei, D. Gatteschi, Crystal and molecular structure of and magnetic coupling in two complexes containing gadolinium(III) and copper(II) ions, J. Am. Chem. Soc. 107 (1985) 8128–8136.
[93] C. Benelli, A. Caneschi, D. Gatteschi, O. Guillou, L. Pardi, Magnetic properties of tetranuclear complexes containing exchange coupled Ln_2Cu_2 (Ln=Gd, Dy) species, J. Magn. Magn. Mater. 83 (1990) 522–524.
[94] M. Andruh, I. Ramade, E. Codjovi, O. Guillou, O. Kahn, J.C. Trombe, Crystal-structure and magnetic-properties of $[Ln_2Cu_4]$ hexanuclear clusters (where Ln=trivalent lanthanide)—mechanism of the Gd(III)-Cu(II) magnetic interaction, J. Am. Chem. Soc. 115 (1993) 1822–1829.

[95] J.B. Goodenough, An interpretation of the magnetic properties of the perovskite-type mixed crystals $La_{1-x}Sr_xCoO_{3-\lambda}$ J, Phys. Chem. Solids 6 (1958) 287.
[96] J. Kanamori, Superexchange interaction and symmetry properties of electron orbitals, J. Phys. Chem. Solids 10 (1959) 87.
[97] J. Paulovič, F. Cimpoesu, M. Ferbinteanu, K. Hirao, Mechanism of ferromagnetic coupling in copper(II)-gadolinium(III) complexes, J. Am. Chem. Soc. 126 (2004) 3321–3331.
[98] G. Rajaraman, F. Totti, A. Bencini, A. Caneschi, R. Sessoli, D. Gatteschi, Density functional studies on the exchange interaction of a dinuclear Gd(III)-Cu(II) complex: method assessment, magnetic coupling mechanism and magneto-structural correlations, Dalton Trans. (2009) 3153–3161.
[99] J.P. Costes, F. Dahan, A. Dupuis, Is ferromagnetism an intrinsic property of the Cu^{II}/Gd^{III} couple? 2. Structures and magnetic properties of novel trinuclear complexes with μ-phenolato-μ-oximato (Cu-Ln-Cu) cores (Ln=La, Ce, Gd), Inorg. Chem. 39 (2000) 5994–6000.
[100] J.-P. Costes, F. Dahan, A. Dupuis, J.-P. Laurent, Is ferromagnetism an intrinsic property of the CuII/GdIII couple? 1. Structures and magnetic properties of two novel dinuclear complexes with a μ-phenolato–μ-oximato (Cu, Gd) core, Inorg. Chem. 39 (2000) 169–173.
[101] C. Lescop, D. Luneau, E. Belorizky, P. Fries, M. Guillot, P. Rey, Unprecedented antiferromagnetic metal–ligand interactions in gadolinium–nitroxide derivatives, Inorg. Chem. 38 (1999) 5472–5473.
[102] A. Caneschi, A. Dei, D. Gatteschi, L. Sorace, K. Vostrikova, Antiferromagnetic coupling in a gadolinium(III) semiquinonato complex, Angew. Chem. Int. Ed. 39 (2000) 246–248.
[103] A. Dei, D. Gatteschi, C.A. Massa, L.A. Pardi, S. Poussereau, L. Sorace, Spontaneous symmetry breaking in the formation of a dinuclear gadolinium semiquinonato complex: synthesis, high-field Epr studies, and magnetic properties, Chem. Eur. J. 6 (2000) 4580–4586.
[104] J.D. Rinehart, M. Fang, W.J. Evans, J.R. Long, Strong exchange and magnetic blocking in N_2^{3-}-radical-bridged lanthanide complexes, Nat. Chem. 3 (2011) 538–542.
[105] J.-P. Costes, F. Dahan, A. Dupuis, Influence of anionic ligands (X) on the nature and magnetic properties of dinuclear $LCuGdX_3{\cdot}nH_2O$ complexes (LH_2 standing for tetradentate schiff base ligands deriving from 2-hydroxy-3-methoxybenzaldehyde and X being Cl, N_3C_2, and CF_3COO), Inorg. Chem. 39 (2000) 165–168.
[106] G. Novitchi, W. Wernsdorfer, L.F. Chibotaru, J.-P. Costes, C.E. Anson, A.K. Powell, Supramolecular "double-propeller" dimers of hexanuclear Cu(II)/Ln(III) complexes: a $\{Cu_3Dy_3\}_2$ single-molecule magnet, Angew. Chem. Int. Ed. 48 (2009) 1614–1619.
[107] J. Cirera, E. Ruiz, Exchange coupling in $Cu^{II}Gd^{III}$ dinuclear complexes: a theoretical perspective, C. R. Chimie 11 (2008) 1227–1234.
[108] J.-P. Costes, C. Duhayon, S. Mallet-Ladeira, S. Shova, L. Vendier, Does the sign of the Cu–Gd magnetic interaction depend on the number of atoms in the bridge? Chem. Eur. J. 22 (2016) 2171–2180.
[109] T. Gupta, T. Rajeshkumar, G. Rajaraman, Magnetic exchange in $\{Gd^{III}$-radical$\}$ complexes: method assessment, mechanism of coupling and magneto-structural correlations, Phys. Chem. Chem. Phys. 16 (2014) 14568–14577.
[110] V. Vieru, N. Iwahara, L. Ungur, L.F. Chibotaru, Giant exchange interaction in mixed lanthanides, Sci. Rep. 6 (2016) 24046.
[111] J.-P. Costes, F. Dahan, A. Dupuis, J.-P. Laurent, Nature of the magnetic interaction in the (Cu^{2+}, Ln^{3+}) pairs: an empirical approach based on the comparison between homologous (Cu^{2+}, Ln^{3+}) and ($Ni_{LS}{}^{2+}$, Ln^{3+}) complexes, Chem. Eur. J. 4 (1998) 1616–1620.
[112] M.L. Kahn, C. Mathoniere, O. Kahn, Nature of the interaction between Ln^{III} and Cu^{II} ions in the ladder-type compounds $\{Ln_2[Cu(opba)]_3\}{\cdot}S$ (Ln=lanthanide element; opba=orthophenylenebis(oxamato), S=solvent molecules), Inorg. Chem. 38 (1999) 3692–3697.

[113] M.L. Kahn, J.-P. Sutter, S. Golhen, P. Guionneau, L. Ouahab, O. Kahn, D. Chasseau, Systematic investigation of the nature of the coupling between a Ln(III) ion (Ln=Ce(III) to Dy(III)) and its aminoxyl radical ligands. Structural and magnetic characteristics of a series of $\{Ln(organic\ radical)_2\}$ compounds and the related $\{Ln(nitrone)_2\}$ derivatives, J. Am. Chem. Soc. 122 (2000) 3413–3421.

[114] M.L. Kahn, P. Lecante, M. Verelst, C. Mathonière, O. Kahn, Structural studies and magnetic properties of polymeric ladder-type compounds $\{Ln_2[Ni(opba)]_3\}\cdot S$ (Ln=lanthanide element; opba=o-phenylenebis(oxamato), S=solvent molecules), Chem. Mater. 12 (2000) 3073–3079.

[115] M.L. Kahn, R. Ballou, P. Porcher, O. Kahn, J.-P. Sutter, Analytical determination of the {Ln–aminoxyl radical} exchange interaction taking into account both the ligand-field effect and the spin–orbit coupling of the lanthanide ion ($Ln=Dy^{III}$ and Ho^{III}), Chem. Eur. J. 8 (2002) 525–531.

[116] A. Caneschi, A. Dei, D. Gatteschi, S. Poussereau, L. Sorace, Antiferromagnetic coupling between rare earth ions and semiquinones in a series of 1:1 complexes, Dalton Trans. (2004) 1048–1055.

[117] A. Figuerola, C. Diaz, J. Ribas, V. Tangoulis, J. Granell, F. Lloret, J. Mahía, M. Maestro, Synthesis and characterization of heterodinuclear Ln^{3+}–Fe^{3+} and Ln^{3+}–Co^{3+} complexes, bridged by cyanide ligand (Ln3+=lanthanide ions). Nature of the magnetic interaction in the Ln^{3+}–Fe^{3+} complexes, Inorg. Chem. 42 (2003) 641–649.

[118] L. Sorace, C. Sangregorio, A. Figuerola, C. Benelli, D. Gatteschi, Magnetic interactions and magnetic anisotropy in exchange coupled 4f-3d systems: a case study of a heterodinuclear Ce^{3+}-Fe^{3+} cyanide-bridged complex, Chem. Eur. J. 15 (2009) 1377–1388.

[119] P.M. Levy, Rare-earth-iron exchange interaction in the garnets. I. Hamiltonian for anisotropic exchange interaction, Phys. Rev. 135 (1964) A155–A165.

[120] P.M. Levy, Rare-earth-iron exchange interaction in the garnets. II. Exchange potential for ytterbium, Phys. Rev. 147 (1966) 311–319.

[121] N. Iwahara, L.F. Chibotaru, Exchange interaction between J multiplets, Phys. Rev. B 91 (2015) 174438.

[122] M.E. Lines, Orbital angular momentum in the theory of paramagnetic clusters, J. Chem. Phys. 55 (1971) 2977–2984.

[123] F. Pointillart, K. Bernot, R. Sessoli, D. Gatteschi, Effects of 3d-4f magnetic exchange interactions on the dynamics of the magnetization of Dy^{III}-M^{II}-Dy^{III} trinuclear clusters, Chem. Eur. J. 13 (2007) 1602–1609.

[124] J.K. Tang, I. Hewitt, N.T. Madhu, G. Chastanet, W. Wernsdorfer, C.E. Anson, C. Benelli, R. Sessoli, A.K. Powell, Dysprosium triangles showing single-molecule magnet behavior of thermally excited spin states, Angew. Chem. Int. Ed. 45 (2006) 1729–1733.

[125] L.F. Chibotaru, L. Ungur, A. Soncini, The origin of nonmagnetic kramers doublets in the ground state of dysprosium triangles: evidence for a toroidal magnetic moment, Angew. Chem. Int. Ed. 47 (2008) 4126–4129.

[126] J. Luzon, K. Bernot, I.J. Hewitt, C.E. Anson, A.K. Powell, R. Sessoli, Spin chirality in a molecular dysprosium triangle: the archetype of the noncollinear ising model, Phys. Rev. Lett. 100 (2008) 247205.

[127] K. Katoh, R. Asano, A. Miura, Y. Horii, T. Morita, B.K. Breedlove, M. Yamashita, Effect of f-f interactions on quantum tunnelling of the magnetization: mono- and dinuclear Dy(III) phthalocyaninato triple-decker single-molecule magnets with the same octacoordination environment, Dalton Trans. 43 (2014) 7716–7725.

[128] T. Fukuda, K. Matsumura, N. Ishikawa, Influence of intramolecular f-f interactions on nuclear spin driven quantum tunneling of magnetizations in quadruple-decker phthalocyanine complexes containing two terbium or dysprosium magnetic centers, J. Phys. Chem. A 117 (2013) 10447–10454.
[129] N. Ishikawa, Single molecule magnet with single lanthanide Ion, Polyhedron 26 (2007) 2147–2153.
[130] N. Ishikawa, M. Sugita, T. Ishikawa, S. Koshihara, Y. Kaizu, Lanthanide double-decker complexes functioning as magnets at the single-molecular level, J. Am. Chem. Soc. 125 (2003) 8694–8695.
[131] N. Ishikawa, T. Iino, Y. Kaizu, Determination of ligand-field parameters and f-electronic structures of hetero-dinuclear phthalocyanine complexes with a diamagnetic yttrium(III) and a paramagnetic trivalent lanthanide ion, J. Phys. Chem. A 106 (2002) 9543–9550.
[132] Y.-N. Guo, G.-F. Xu, W. Wernsdorfer, L. Ungur, Y. Guo, J. Tang, H.-J. Zhang, L.F. Chibotaru, A.K. Powell, Strong axiality and ising exchange interaction suppress zero-field tunneling of magnetization of an asymmetric Dy_2 single-molecule magnet, J. Am. Chem. Soc. 133 (2011) 11948–11951.
[133] F. Habib, P.-H. Lin, J. Long, I. Korobkov, W. Wernsdorfer, M. Murugesu, The use of magnetic dilution to elucidate the slow magnetic relaxation effects of a Dy_2 single-molecule magnet, J. Am. Chem. Soc. 133 (2011) 8830–8833.
[134] J. Long, F. Habib, P.H. Lin, I. Korobkov, G. Enright, L. Ungur, W. Wernsdorfer, L.F. Chibotaru, M. Murugesu, Single-molecule magnet behavior for an antiferromagnetically superexchange-coupled dinuclear dysprosium(III) complex, J. Am. Chem. Soc. 133 (2011) 5319–5328.
[135] W. Wernsdorfer, N. Allaga-Alcalde, D.N. Hendrickson, G. Christou, Exchange-biased quantum tunnelling in a supramolecular dimer of single-molecule magnets, Nature 416 (2002) 406–409.
[136] J.D. Rinehart, M. Fang, W.J. Evans, J.R. Long, A N_2^{-3} radical-bridged terbium complex exhibiting magnetic hysteresis at 14K, J. Am. Chem. Soc. 133 (2011) 14236–14239.
[137] S. Demir, J.M. Zadrozny, M. Nippe, J.R. Long, Exchange coupling and magnetic blocking in bipyrimidyl radical-bridged dilanthanide complexes, J. Am. Chem. Soc. 134 (2012) 18546–18549.
[138] S. Demir, M. Nippe, M.I. Gonzalez, J.R. Long, Exchange coupling and magnetic blocking in dilanthanide complexes bridged by the multi-electron redox-active ligand 2,3,5,6-tetra(2-pyridyl)pyrazine, Chem. Sci. 5 (2014) 4701–4711.
[139] K.R. Meihaus, J.F. Corbey, M. Fang, J.W. Ziller, J.R. Long, W.J. Evans, Influence of an inner-sphere K^+ Ion on the magnetic behavior of N_2^{3-} radical-bridged dilanthanide complexes isolated using an external magnetic field, Inorg. Chem. 53 (2014) 3099–3107.
[140] M.A. Nielsen, I.L. Chuang, Quantum Computation and Quantum Information, Cambridge University Press, Cambridge, 2000.
[141] P. Goldner, A. Ferrier, O. Guillot-Noël, Rare earth-doped crystals for quantum information processing, in: J.-C. Bunzli, V.K. Pecharsky (Eds.), Handbook on Physics and Chemistry of Rare Earths, Elsevier, Amsterdam, 2015, pp. 1–78. Chapter 267.
[142] G. Balasubramanian, P. Neumann, D. Twitchen, M. Markham, R. Kolesov, N. Mizuochi, J. Isoya, J. Achard, J. Beck, J. Tissler, V. Jacques, P.R. Hemmer, F. Jelezko, J. Wrachtrup, Ultralong spin coherence time in isotopically engineered diamond, Nat. Mater. 8 (2009) 383–387.

[143] F.A. Zwanenburg, A.S. Dzurak, A. Morello, M.Y. Simmons, L.C.L. Hollenberg, G. Klimeck, S. Rogge, S.N. Coppersmith, M.A. Eriksson, Silicon quantum electronics, Rev. Mod. Phys. 85 (2013) 961–1019.
[144] J.M. Zadrozny, J. Niklas, O.G. Poluektov, D.E. Freedman, Millisecond coherence time in a tunable molecular electronic spin qubit, ACS Cent. Sci. 1 (2015) 488–492.
[145] M. Atzori, L. Tesi, E. Morra, M. Chiesa, L. Sorace, R. Sessoli, Room-temperature quantum coherence and rabi oscillations in vanadyl phthalocyanine: toward multifunctional molecular spin qubits, J. Am. Chem. Soc. 138 (2016) 2154–2157.
[146] K.S. Pedersen, A.-M. Ariciu, S. McAdams, H. Weihe, J. Bendix, F. Tuna, S. Piligkos, Toward molecular 4f single-Ion magnet qubits, J. Am. Chem. Soc. 138 (2016) 5801–5804.
[147] P. Siyushev, K. Xia, R. Reuter, M. Jamali, N. Zhao, N. Yang, C. Duan, N. Kukharchyk, A. D. Wieck, R. Kolesov, J. Wrachtrup, Coherent properties of single rare-earth spin qubits, Nat. Commun. 5 (2014) 3895.
[148] S. Probst, H. Rotzinger, S. Wünsch, P. Jung, M. Jerger, M. Siegel, A.V. Ustinov, P.A. Bushev, Anisotropic rare-earth spin ensemble strongly coupled to a superconducting resonator, Phys. Rev. Lett. 110 (2013) 157001.
[149] M. Jenkins, T. Hümmer, M.J. Martínez-Pérez, J. García-Ripoll, D. Zueco, F. Luis, Coupling single-molecule magnets to quantum circuits, New J. Phys. 15 (2013) 095007.
[150] C. Bonizzoni, A. Ghirri, K. Bader, J. van Slageren, M. Perfetti, L. Sorace, Y. Lan, O. Fuhr, M. Ruben, M. Affronte, Coupling molecular spin centers to microwave planar resonators: towards integration of molecular qubits in quantum circuits, Dalton Trans. (2016), http://dx.doi.org/10.1039/C6DT01953F.
[151] M. Shiddiq, D. Komijani, Y. Duan, A. Gaita-Ariño, E. Coronado, S. Hill, Enhancing coherence in molecular spin qubits via atomic clock transitions, Nature 531 (2016) 348–351.
[152] J. Ferrando-Soria, E.M. Pineda, A. Chiesa, A. Fernandez, S.A. Magee, S. Carretta, P. Santini, I.J. Vitorica-Yrezabal, F. Tuna, G.A. Timco, E.J.L. McInnes, R.E.P. Winpenny, A modular design of molecular qubits to implement universal quantum gates, Nat. Commun. 7 (2016) 11377.
[153] D. Aguila, L.A. Barrios, V. Velasco, O. Roubeau, A. Repolles, P.J. Alonso, J. Sese, S.J. Teat, F. Luis, G. Aromi, Heterodimetallic LnLn′ lanthanide complexes: toward a chemical design of two-qubit molecular spin quantum gates, J. Am. Chem. Soc. 136 (2014) 14215–14222.
[154] G. Aromi, D. Aguila, P. Gamez, F. Luis, O. Roubeau, Design of magnetic coordination complexes for quantum computing, Chem. Soc. Rev. 41 (2012) 537–546.
[155] A. Cornia, M. Mannini, P. Sainctavit, R. Sessoli, Chemical strategies and characterization tools for the organization of single molecule magnets on surfaces, Chem. Soc. Rev. 40 (2011) 3076–3091.
[156] M. Urdampilleta, S. Klyatskaya, J.P. Cleuziou, M. Ruben, W. Wernsdorfer, Supramolecular spin valves, Nat. Mater. 10 (2011) 502–506.
[157] J. Dreiser, C. Wäckerlin, M.E. Ali, C. Piamonteze, F. Donati, A. Singha, K.S. Pedersen, S. Rusponi, J. Bendix, P.M. Oppeneer, T.A. Jung, H. Brune, Exchange interaction of strongly anisotropic tripodal erbium single-ion magnets with metallic surfaces, ACS Nano 8 (2014) 4662–4671.
[158] R. Westerström, A.-C. Uldry, R. Stania, J. Dreiser, C. Piamonteze, M. Muntwiler, F. Matsui, S. Rusponi, H. Brune, S. Yang, A. Popov, B. Büchner, B. Delley, T. Greber, Surface aligned magnetic moments and hysteresis of an endohedral single-molecule magnet on a metal, Phys. Rev. Lett. 114 (2015) 087201.

[159] A. Lodi Rizzini, C. Krull, T. Balashov, J.J. Kavich, A. Mugarza, P.S. Miedema, P.K. - Thakur, V. Sessi, S. Klyatskaya, M. Ruben, S. Stepanow, P. Gambardella, Coupling single molecule magnets to ferromagnetic substrates, Phys. Rev. Lett. 107 (2011) 177205.

[160] C. Wäckerlin, F. Donati, A. Singha, R. Baltic, S. Rusponi, K. Diller, F. Patthey, M. Pivetta, Y. Lan, S. Klyatskaya, M. Ruben, H. Brune, J. Dreiser, Giant hysteresis of single-molecule magnets adsorbed on a nonmagnetic insulator, Adv. Mater. 28 (2016) 5195–5199.

[161] F. Donati, S. Rusponi, S. Stepanow, C. Wäckerlin, A. Singha, L. Persichetti, R. Baltic, K. Diller, F. Patthey, E. Fernandes, J. Dreiser, Ž. Šljivančanin, K. Kummer, C. Nistor, P. Gambardella, H. Brune, Magnetic remanence in single atoms, Science 352 (2016) 318–321.

Chapter 287

Lanthanide Luminescence: From a Mystery to Rationalization, Understanding, and Applications

Jean-Claude G. Bünzli[1]

Institute of Chemical Sciences and Engineering, Swiss Federal Institute of Technology Lausanne (EPFL), Lausanne, Switzerland

Haimen Institute of Science and Technology, Hong Kong Baptist University, Haimen, PR China

[1]*Corresponding author: e-mail: jean-claude.bunzli@epfl.ch*

Chapter Outline

Handbook on the Physics and Chemistry of Rare Earths, Vol. 50. http://dx.doi.org/10.1016/bs.hpcre.2016.08.003

1 INTRODUCTION

A search for lanthanide luminescence and associated terms in bibliographic databases or Web search engines typically returns tens of thousands of articles, pointing to the attractiveness of the field [1]. As a matter of fact, lanthanide luminescence is at the heart of applications as diverse as lighting, telecommunications, security marking, lasers, luminescent molecular thermometers, barcoding, or immunoassays. The subject is fascinating and has always accompanied the development of lanthanide science and technology, from the early discovery of the 4f elements to present high-technology applications. A quick look into market statistics and estimates shows that light-emitting materials (phosphors) and pigments represent the second most important application of rare earths with respect to commercial value of the rare-earth oxides needed for their production (share: about 30%), just behind permanent magnets (about 40%). However, tonnage-wise luminescent materials represent an estimated market share of only about 8% of the total rare earths consumed annually. The large added value of luminescent phosphors, probes, and materials partly explains the enthusiasm research groups are coming up with in looking for new and better materials, in addition to fascination for light emission.

In this perspective essay, we highlight the various facets of light emission by lanthanide compounds with special emphasis on historical developments, understanding the underlying mechanisms, and presentation of leading applications. The topic is vast so that only salient features will be depicted [2]. It is noteworthy that the handbook series has published to date about two dozen of chapters dealing with or including description of light emission by rare-earth inorganic compounds or chelates; they focus on photoluminescence [3–6], laser effect and spectroscopy [7–9], thermoluminescence [10], long-persistent luminescence [11], and photoemission [12–14]. These reviews are sometimes combined with theoretical modeling and/or describe applications such as sensing [15,16], drug delivery [17], luminescent nanomaterials [18], phosphors for light-emitting diodes (LEDs) [19], luminescent thermometry [20], solar energy conversion [21], optical refrigeration [22], or quantum information processing [23]. Furthermore, several chapters are dedicated to the theory of excited states and intensities of f–f transitions [9,24–26].

Before starting, it may be useful to briefly define luminescence. Emission of light by chemical compounds or materials stems from two different mechanisms: (i) incandescence, or black-body emission, which does not depend on the chemical nature of the material but only on its temperature, and (ii) luminescence or "cold light emission" [27] involving quantified energy levels in the sample. Luminescence can be excited in different ways and specific terms are used accordingly. For instance, photoluminescence results when the sample is irradiated with photons; electroluminescence is produced upon excitation of the sample in an electric discharge or in an electric field; cathodoluminescence is

generated when the sample is subjected to an electron flux; chemiluminescence (bioluminescence) arises from the energy released by a chemical (biological) reaction; thermoluminescence is consecutive to heating of the sample, liberating energy trapped in defects; mechanoluminescence is observed upon mechanical stress imposed to the sample.

Regarding nomenclature, "luminescence" is a generic term for quantified emission of light. If the two emitting and receiving levels have the same spin, the process is spin allowed, fast, and is termed "fluorescence." When the emitting level has different spin than the receiving level, then the process is spin forbidden, therefore, much slower, and is called "phosphorescence."

Most trivalent lanthanides ions are luminescent, baring La^{III} and Lu^{III}, and, except for Ce^{III}, the corresponding transitions mainly occur as electronic rearrangement within the 4f shell (f–f transitions). Electric dipole f–f transitions are forbidden by Laporte's selection rule while magnetic-dipole transitions are allowed, but faint. Selection rules are somewhat relaxed by orbital mixing with various functions, due to spin-orbit coupling, vibronic coupling, J-mixing, or mixing with ligand orbitals, but in any case the oscillator strengths remain small. Some Ln^{III} ions are phosphorescent (e.g., Eu^{III}, Tb^{III}), others are fluorescent (e.g., Ho^{III}, Yb^{III}), while many of them are both fluorescent and phosphorescent (e.g., Pr^{III}, Nd^{III}). Interconfigurational, e.g., f↔d and charge-transfer (CT), transitions are allowed. The three types of transitions are discussed in more details in Section 3.2.

2 EARLY APPLICATIONS AND THE DISCOVERY OF RARE-EARTH ELEMENTS

The first two commercial applications of lanthanides were connected to lighting and developed by the Austrian scientist and entrepreneur Carl Auer von Welsbach. The first patent filed by Auer in 1885 described a gas mantle made of a platinum grid coated with a mixture of magnesium oxide (60%), lanthanum oxide (20%), and yttrium oxide (20%); the mantle was very fragile and its emission was greenish so that the company started by Auer in 1887 went bankrupt in 1889. Not discouraged by this initial failure, Auer found that thorium oxide was a better material than magnesium oxide, and in 1891 he was granted a patent for what is known as the Auer mantle (or Auer light): a small cotton bag impregnated with a mixture of 99% thorium nitrate and 1% cerium nitrate; upon contact with the flame, the cotton burns and the nitrates are converted into oxides, yielding a bright white emission. The success was immediate and the mantles and their subsequent improved versions were ubiquitous in gas lighting until the mid-1930s. They can still be bought today; for instance for camping lamps, thorium radioactivity being considered to lie within safe regulatory limits. The second invention is a pyrophoric alloy made of 70% cerium and 30% iron (ferrocerium) that Auer patented in 1903

and used for producing flint stones for various kinds of lighters; this material, called Mischmetal, is still in use today and exists in many different versions, some of them containing rare earths only.

The invention of the spectroscope by Joseph von Fraunhofer in 1814 provided a valuable tool for studying the solar spectrum and for identifying new elements. Robert Bunsen observed sharp emission lines from rare-earth salts in the mid-1860s, and since then many scientists, including Sir William Crookes, turned to this method to detect new elements in several materials, including rare earth-containing minerals. At the beginning of the 20th century, there was a great confusion among specialists about rare-earth elements. Although most of the latter had been chemically separated and identified (at least as their oxides), the study of optical properties, such as absorption spectra, spark spectra in which emission of light is induced by submitting the sample to electric sparks, cathodoluminescence and phosphorescence spectra, generated confusing data. Given the sensitivity of the techniques and the fact that most samples were not of the highest purity, spectroscopists were recording "anomalous" lines and were therefore speculating on the presence of new elements. For instance, Sir William Crookes noted that different yttrium samples would give the same spark spectra, but different phosphorescence spectra, so that he tried to conciliate these two contradictory experiments by the concept of "meta-elements" in which an "element" with a constant spark spectrum is composed of distinct atoms having different phosphorescence spectra, much as elements are made of different isotopes. Thanks to a painstaking detailed investigation by Georges Urbain who purified series of samples until spectroscopic properties became invariant, the "meta-elements" were finally shown to correspond to known lanthanides. The rigorous protocol followed in Urbain's investigation allowed him to discover two new elements, lutetium and hafnium (that he initially called celtium) [28]. Another benefit of this research was the observation that even minute quantities of a luminescent ion such as Eu^{III} embedded into an inorganic matrix (e.g., gadolinium oxide, alumina, calcium oxide) give intense emission lines, while the pure product is often poorly or non luminescent. It was established that the best doping concentration is around 0.5–1%; in a way this may be considered as the start of the research on phosphors that led to the unique Y_2O_3:Eu^{III} red-emitting material still in use today.

However, everything was not yet solved and some doubts remained as to the presence of one or two elements in some samples since diluting a luminescent compound in different matrices gave different spectra. In particular for Eu^{III}, the intensity ratio I(613 nm)/I(593 nm)—in fact $I(^5D_0 \rightarrow {}^7F_2)/I(^5D_0 \rightarrow {}^7F_1)$—would be smaller or larger than 1 depending on the concentration and/or the matrix, a phenomenon that could not be explained. Ln^{III} spectra of solid salts and oxides are mainly composed of sharp and weak lines that were ascribed to intraconfigurational f–f transitions in the 1920s by Bethe, Kramer, and Becquerel, but interpreting them necessitated a detailed and novel theory.

3 UNDERSTANDING RARE-EARTH OPTICAL SPECTRA

3.1 Identifying Electronic Levels and Determining Their Energy

Part of the truth was unveiled by Van Vleck who published a seminal paper in 1937: "The puzzle of rare-earth spectra in solids" [29]. At that time electronic structure and chemical bonding theories were at hand, as well as crystal-field theory put forward by Bethe in 1929 [30]. It was also established that the ground-state electronic configuration of Ln^{III} ions was $[Xe]4f^n$ ($n = 0$–14); note that most divalent ions have the same electronic configuration ($n = 0$–5, Ce–Eu; $n = 6$–11, Tb–Yb) with the exceptions of La and Gd ($[Xe]4f^{N-1}5d^1$, $N = 1$ and 8) as well as Lu ($[Xe]4f^{14}6s^1$).[1] Van Vleck addressed two main issues: (i) assignment of the sharp vs broad lines and (ii) why are the faint lines observed at all? Regarding the first point, sharp lines were referred correctly to intraconfigurational f–f transitions, while broad bands in the Ce^{III} and Yb^{III} spectra were assigned to allowed interconfigurational d–f transitions, which is correct for cerium but not for ytterbium for which d-levels lie at energies larger than 70,000 cm^{-1} (<140 nm) [31]; instead they correspond to charge transfer transitions. Concerning f–f transitions, Van Vleck stated that the most intense ones have electric dipole character, while fainter transitions are magnetic dipole transitions. He postulated that formally forbidden electric dipole transitions are observed because of a "distortion of the electronic motion by crystalline fields." He also established that this "distortion" arises only if the ligand field symmetry is devoid of inversion center; otherwise orbital mixing cannot occur. He also evoked the possibility of these transitions having a quadrupolar character and made a rough estimate of the probabilities for quadrupolar, magnetic dipole, and electric dipole transitions. Equally important, Van Vleck realized that interactions between vibrations and electron motion result in additional "vibronic" lines in the spectra and/or in broadening of some lines. In a way, this contribution can be compared to the order brought in the jungle of known elements by the Periodic Table, and it paved the way for Dieke's electronic level diagrams, crystal field analysis, and Judd–Ofelt theory.

The arduous task of finding, calculating, and assigning energy levels in transition metal-containing compounds was subsequently undertaken in the 1940s, particularly by Racah, and enabled quantitative fits of the ligand-field (LF) sublevels for the entire lanthanide series to be performed thanks to the work of B. G. Wybourne [32]. The first synopsis of the $4f^n$ energy levels of all trivalent lanthanides doped in various crystals and spanning the entire ultraviolet (UV),

1. This is valid for ions in gas phase and for inorganic compounds. Recently, W. Evans' group has demonstrated that all divalent Ln ions can be stabilized in organometallic compounds. Magnetic and spectroscopic data show that Nd, Sm, Eu, Dy, Tm, Yb have $4f^n$ configuration, while La, Pr, Gd, Ho, Er, Lu have $4f^{n-1}5d^1$ electronic structure; Ce and Tb are borderline. See Chapter 293 in this volume. "Expanding the +2 Oxidation State to the Rare-Earth Metals, Uranium, and Thorium in Molecular Complexes" by David H. Woen and William J. Evans.

visible, and NIR spectral ranges was given by G. H. Dieke [33]. The $4f^n$ configurations generate many electronic levels, up to 327 for Gd^{III}, characterized by three quantum numbers, S, L, and J, and further split by weak ligand-field effects, on the order of $10^2\ cm^{-1}$, yielding a multitude of LF sublevels, up to 3436 for Gd^{III}. The number of sublevels for the $4f^{n-1}5d^1$ configurations is far larger, culminating at 37,323 for Tb^{III} for instance as shown in Table 1. From the latter, one sees that these two configurations generate almost 200,000 electronic sublevels for the series of 15 elements, which makes understandable the difficulties encountered in identifying them! But on the other hand, these electronic manifolds offer an unlimited playground to spectroscopists and materials scientists for designing tailored luminescent materials.

TABLE 1 Maximum Number of Electronic Levels, Labels of the Ground Level, And Maximum Number of LF Sublevels for $4f^n$ Electronic Configurations of the Trivalent Lanthanide Ions, As Well As Maximum Number of LF Sublevels of the $4f^{n-1}5d^1$ Configurations [26]

		$4f^n$ Configuration			$4f^{n-1}5d^1$ Configuration
Element	*n*	*Number of* SLJ *Levels*	*Ground Level*	*Number of LF Sublevels*	*Number of LF Sublevels*
La	0	1	$^1S_0$	1	–
Ce	1	2	$^2F_{5/2}$	14	10
Pr	2	13	$^3H_4$	91	231
Nd	3	41	$^4I_{9/2}$	364	1274
Pm	4	107	$^5I_4$	1001	4641
Sm	5	198	$^6H_{5/2}$	2002	12,012
Eu	6	295	$^7F_0$	3003	23,023
Gd	7	327	$^8S_{7/2}$	3432	33,462
Tb	8	295	$^7F_6$	3003	37,323
Dy	9	198	$^6H_{15/2}$	2002	32,032
Ho	10	107	$^5I_8$	1001	21,021
Er	11	41	$^4I_{15/2}$	364	10,374
Tm	12	13	$^3H_6$	91	3731
Yb	13	2	$^2F_{7/2}$	14	924
Lu	14	1	$^1S_0$	1	141
Total	—	1641	—	16,384	180,199

In the 1950s and 1960s a vast effort was made first to correctly identify the energy levels of $4f^n$ trivalent ions, both experimentally and theoretically, and, second, to understand the intensity of the f–f transitions through what is now known as the Judd–Ofelt theory. Energy levels were first identified in doped crystals from absorption and emission spectra, resulting in the publication of Dieke's diagrams that were limited to energies of about 40,000 cm^{-1} [33], and then in solution [6]. Both crystal (or ligand) field [34] and Judd–Ofelt [24,35] theories then provided deep understanding on the splitting of the lines and their intensities. Numerous theoretical and experimental studies have then broadened this knowledge, particularly with respect to extending electronic diagrams first to 50,000 cm^{-1} thanks to calculations and experiments conducted at Argonne National Laboratory (USA). Further extension in the vacuum UV up to 70,000 cm^{-1} was made possible by the availability of cyclotron radiation sources [36]. Furthermore, diagrams for divalent and tetravalent ions have also been established, progresses made in theoretical chemistry allowing for precise calculations of these levels (see Chapter 284, Theory of Rare-Earth Electronic Structure and Spectroscopy by Michael Reid, and Chapter 285, Ab Initio Calculations on Excited States of Lanthanide Containing Materials by Luis Seijo and Zoila Barandiaran, in this volume). This is illustrated in Figs. 1–3 for

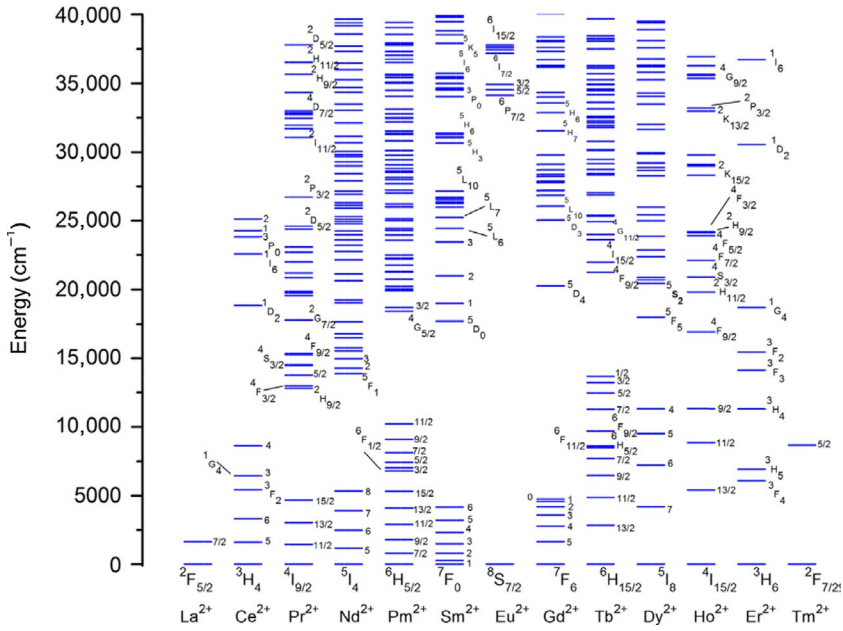

FIG. 1 Calculated energy levels of the divalent lanthanides in the energy range up to 40,000 cm^{-1}. *Reproduced with permission from C.G. Ma, M.G. Brik, D.X. Liu, B. Feng, Y. Tian, A. Suchocki, Energy level schemes of f^N electronic configurations for the di-, tri-, and tetravalent lanthanides and actinides in a free state, J. Lumin. 170 (Pt. 2) (2016) 369–374, © 2016 Elsevier Science B.V.*

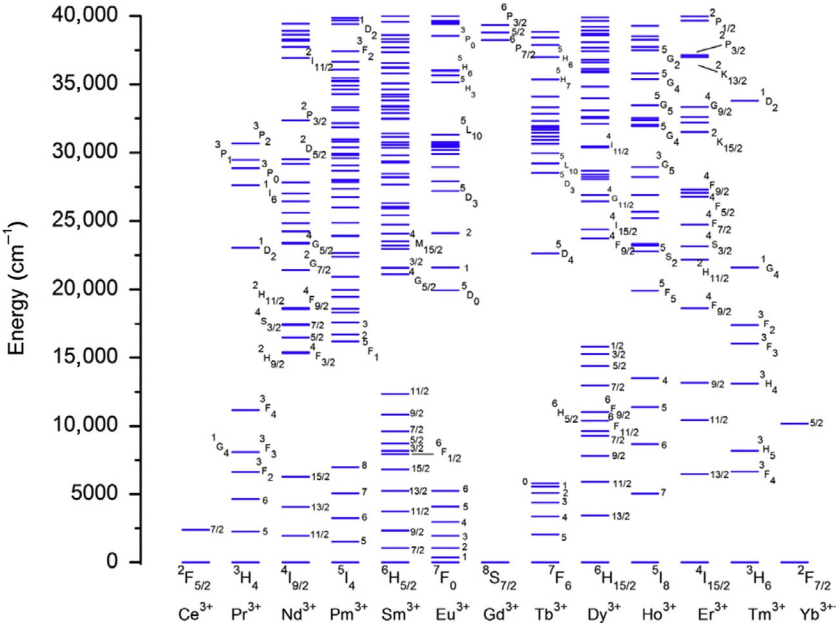

FIG. 2 Calculated energy levels of the trivalent lanthanides in the energy range up to 40,000 cm^{-1}. *Reproduced with permission from C.G. Ma, M.G. Brik, D.X. Liu, B. Feng, Y. Tian, A. Suchocki, Energy level schemes of f^N electronic configurations for the di-, tri-, and tetravalent lanthanides and actinides in a free state, J. Lumin. 170 (Pt. 2) (2016) 369–374, © 2016 Elsevier Science B.V.*

divalent, trivalent, and tetravalent Ln ions, respectively, where levels are plotted up to about 42,500 cm^{-1}. Recent calculations with a fully relativistic first-principles many-electron method performed on $4f^n$ and $4f^{n-1}5d^1$ electronic configurations [26] have allowed further extension of Dieke's diagrams way beyond 100,000 cm^{-1}. Fig. 4 reproduces the levels for $4f^n$ and $4f^{n-1}5d^1$ configurations of the Ln^{III} ions; it clearly points to the lowest levels of the $4f^{n-1}5d^1$ configurations being usually above 50,000 cm^{-1}, making difficult to record the corresponding transition unless vacuum UV instrumentation is at disposal.

3.2 Main Features of Interconfigurational, Intraconfigurational, and Charge-Transfer Transitions in Ln-Containing Luminescent Materials

3.2.1 Laporte's Allowed d↔f Transitions [36,37]

It is to be stressed here that in addition to Laporte's selection rule, the spin rule has to be taken into consideration as well ($\Delta S = 0$) so that only spin-allowed d↔f transitions have sizeable intensity; they are essentially observed for Ce^{III}, Pr^{III}, Tb^{III}, and some Ln^{II} ions (Ln = Sm, Eu, Tm, Yb) since for the other Ln^{III}

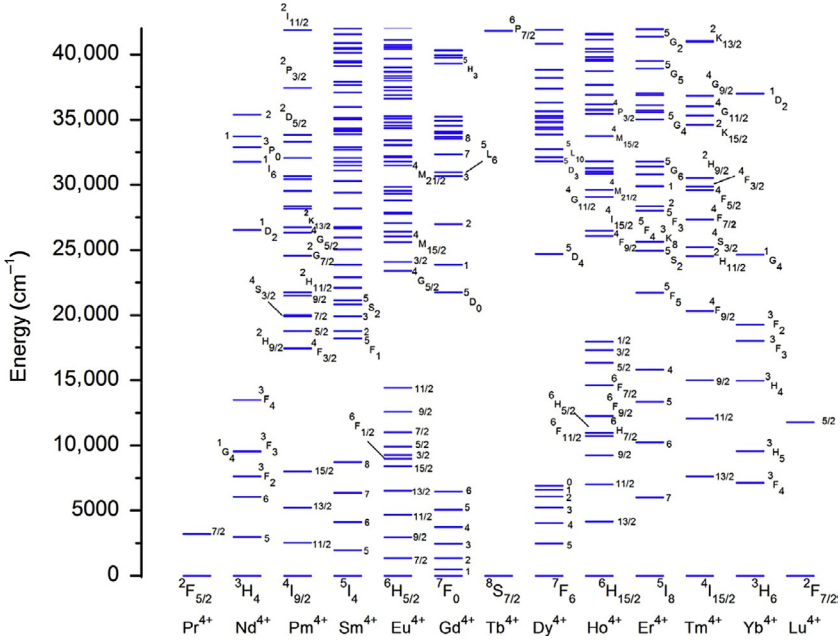

FIG. 3 Calculated energy levels of the tetravalent lanthanides in the energy range up to 42,500 cm^{-1}. *Reproduced with permission from C.G. Ma, M.G. Brik, D.X. Liu, B. Feng, Y. Tian, A. Suchocki, Energy level schemes of f^N electronic configurations for the di-, tri-, and tetravalent lanthanides and actinides in a free state, J. Lumin. 170 (Pt. 2) (2016) 369–374, © 2016 Elsevier Science B.V.*

ions these transitions are often quenched by intersystem crossing to the 4f^n configuration. Spin-forbidden transitions are still observed, but their identification is made difficult in view of their smaller intensity. The d↔f transitions occur at high energy, usually >50,000 cm^{-1} (<200 nm) [31]. They have been documented both theoretically (e.g., calculations in the gas phase by Brewer [38]) and experimentally in several hosts, such as CaF_2, $LiYF_4$, or $Y_3Al_5O_{12}$ (YAG) [39,40]. As an example, energies of the first spin-allowed f→d transition of Ln^{III} ions doped in calcium fluoride are reported in Fig. 5 (top); they correspond to excitation into the ^{2}E levels. For Tb^{III}, this transition occurs at 216 nm (0-phonon component), but less intense bands are seen at longer wavelengths that correspond to spin-forbidden transitions (Fig. 5, bottom). In this figure, HS_1 is the 0-phonon line, while HS_1' is the first vibronic component (475 cm^{-1} assigned to the breathing mode of the fluorides around Tb^{III}). When d-orbitals are implied, the ligand field generated by the surrounding ligands is much larger (10^3–10^4 cm^{-1}) than for f-orbitals. This is exemplified in the energy separation between the low- and high-spin fd states amounting to ≈7900 cm^{-1} [39]. Another consequence of the external nature of d-orbitals lies

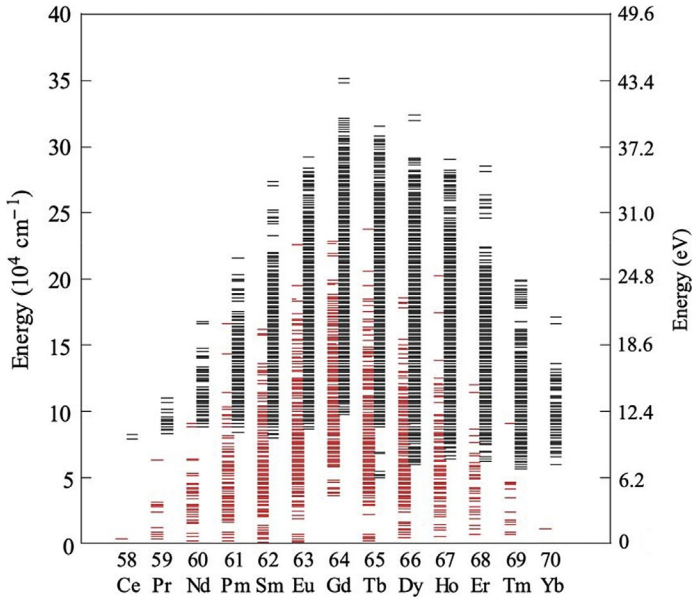

FIG. 4 Complete $4f^n$ (*left*, *red*) and $4f^{n-1}5d^1$ (*right*, *black*) energy diagram for all trivalent Ln ions as calculated by the fully relativistic first-principles many-electron method. Note the *right scale* in eV (1 eV corresponds to 8066 cm^{-1}). *Reproduced with permission from K. Ogasawara, S. Watanabe, H. Toyoshima, M.G. Brik, First-principles calculations of 4f-4f5d transition spectra, in: K.A. Gschneidner Jr., J.-C.G. Bünzli, V.K. Pecharsky (Eds.), Handbook on the Physics and Chemistry of Rare Earths, vol. 37, Elsevier Science B.V., Amsterdam, 2007, pp. 1–59 (Chapter 231), © 2007 Elsevier Science B.V.*

in Stokes shifts being much larger than for f-states, typically between 1000 and 3000 cm^{-1}, as well as in the easy tunability of the energy of d↔f transitions by modifying the nature of the inner coordination sphere of the emitting ions (e.g., by doping in different matrices). A stronger ligand field will induce larger splitting with, as a consequence, the lowest fd state being pushed toward lower energy and the emission wavelength sustaining a red shift.

Owing to their importance for the phosphors used in lighting and displays, d↔f transitions have been thoroughly and systematically studied. The actual position of the lowest fd state with respect to valence and conduction bands is important in this respect since it determines the luminescent properties of the activators (excitation and emission wavelengths, multiphonon relaxation, trapping, and detrapping of charge carriers). A phenomenological equation has been proposed by Dorenbos for estimating its energy with respect to that of Ce^{III}:

$$E(\mathrm{Ln}, A) = 49{,}340\,\mathrm{cm}^{-1} - D(A) + \Delta E^{\mathrm{Ln,Ce}} \tag{1}$$

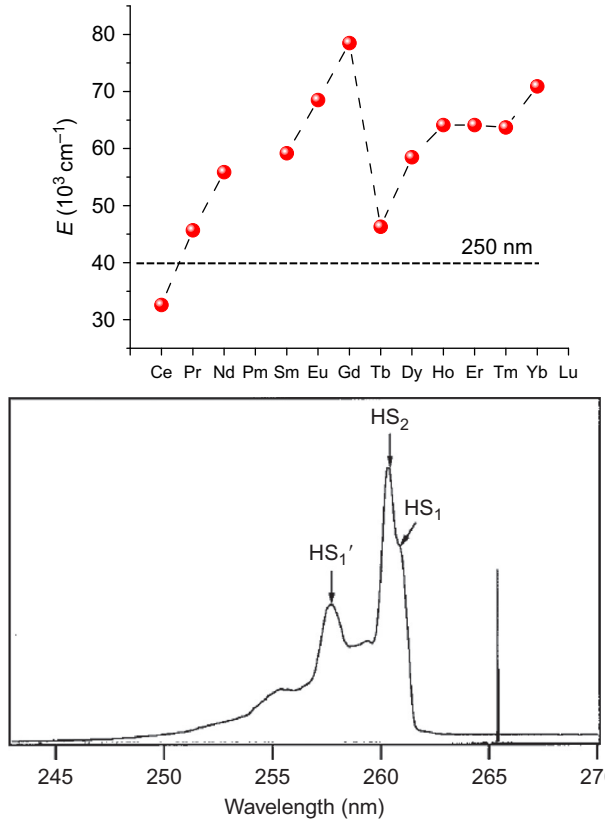

FIG. 5 (*Top*) Energies of the first spin-allowed f→d transitions of Ln^{III} ions doped in CaF_2. (*Bottom*) Excitation spectrum for a CaF_2 crystal doped with 0.1% Tb^{III} recorded monitoring the $^5D_4 \rightarrow {}^7F_5$ transition at 544 nm at 6 K and showing the energy region in which the spin-forbidden transition to the high-spin fd state is observed; the *dotted line* below is the calculated spectrum. Top panel*: Redrawn from P. Dorenbos, f -> d transition energies of divalent lanthanides in inorganic compounds, J. Phys. Condens. Matter 15 (2003) 575–594*. Bottom panel*: Reproduced with permission from L. van Pieterson, M.F. Reid, G.W. Burdick, A. Meijerink, 4f(n)-> 4f(n-1)5d transitions of the heavy lanthanides: experiment and theory, Phys. Rev. B 65 (2002) Art. Nr. 045114, © 2002 The American Physical Society.*

where $E(\mathrm{Ln}, A)$ is the maximum of the lowest f→d band of a Ln^{III} ion lying on a given site of host lattice A. The contribution $D(A)$ is the lowering of the energy of the fd state of Ce^{III} by LF effects (with respect to the free ion value). Finally, $\Delta E^{\mathrm{Ln,Ce}}$ is the energy difference between the lowest df states of a Ln^{III} ion and Ce^{III}, which is host independent. These two parameters are known from the analysis of a large number of materials [41]. More recently, Zych *et al*. proposed to use the energy of the zero-phonon line rather than the peak maximum to more accurately estimate the energies of the df states [42].

3.2.2 Intraconfigurational f–f Transitions [1,43,44]

A transition between two electronic states is achieved thanks to an "operator." Given the nature of light, three main operators may be effective, electric dipoles (EDs), magnetic dipoles (MDs), and electric quadrupoles (EQs). Laporte's parity selection rule implies that states with the same parity cannot be connected by electric dipole transitions; as a consequence, f–f transitions are forbidden by the ED mechanism. However, when lanthanide ions are under the influence of a ligand field, noncentrosymmetric interactions allow the mixing of electronic states of opposite parity into the 4f wavefunctions, which relaxes the selection rules and the transitions become partially allowed; they are called *induced* (or forced) *electric dipole transitions*. Magnetic dipole transitions are allowed, but their intensity is weak; in 4f–4f spectra however they frequently have intensity of the same order of magnitude as induced electric dipole transitions. Quadrupolar transitions are also parity allowed, but they are much weaker than MD transitions so that they are usually not observed or identified. Some induced ED transitions are highly sensitive to minute changes in the Ln^{III} environment and are called *hypersensitive* or sometimes *pseudo-quadrupolar transitions* because they apparently follow the selection rules of EQ transitions.

There are selection rules for each quantum number (ℓ, S, L, J), as well as symmetry-related selection rules. Rules applying to S, L, and J quantum numbers are given in Table 2; for symmetry-related selection rules, please refer to Refs. [34,46].

In 1962, two researchers, B. R. Judd and G.S. Ofelt submitted independently within a month a paper dealing with the same subject: intensities of

TABLE 2 Selection Rules on *S*, *L*, *J* Quantum Numbers for f–d and f–f Transitions [45]

Transition	ΔS	$\lvert\Delta L\rvert$[a]	$\lvert\Delta J\rvert$[b]	Approx. Oscill. Strength[c]
ED (d–f)	0	≤1	≤1	0.01–1
Forced ED (f–f)	0	≤6 (2, 4, 6 if L or $L'=0$)	≤6 (2, 4, 6 if J or $J'=0$)	10^{-4}–10^{-5}
Vibronic (ED, f–f)	Same as forced ED			10^{-7}–10^{-10}
MD (f–f)	0	0	0, ±1	10^{-5}–10^{-6}
EQ (f–f)	0	0, ±1, ±2	0, ±1, ±2	10^{-10}

[a] $L=0 \leftrightarrow L'=0$ *transitions are always forbidden.*
[b] $J=0 \leftrightarrow J'=0$ *transitions are always forbidden.*
[c] *Spin-allowed transitions; spin-forbidden transitions are about 100 times less intense.*

f–f transitions. Now known as Judd–Ofelt (JO) theory, the corresponding model has been established within the frame of the crystal field concept and it provides a simple scheme for reproducing the intensities of f–f absorption spectra. One drawback is that it only takes into account the $4f^n$ electronic configuration, that is, interconfigurational $4f^n$–$4f^{n-1}5d^1$ interactions are neglected. On the other hand, spin-orbit coupling is treated within the frame of the intermediate coupling scheme. The dipole strength in $esu^2\,cm^2$ ($=10^{36}\,D^2$) of an induced ED f–f transition between states ψ and ψ' is given by:

$$D_{\mathrm{ED}} = e^2 \cdot \sum_{\lambda=2,4,6} \Omega_\lambda \cdot \left|\left\langle \Psi \middle\| U^\lambda \middle\| \Psi' \right\rangle\right|^2 \tag{2}$$

in which e is the electric charge of the electron, wavefunctions ψ and ψ' are full intermediate-coupled functions $f^n[SL]J$, U^λ are the irreducible tensor forms of the ED operator, and Ω_λ are the phenomenological Judd–Ofelt parameters, expressed in cm^2. The bracketed expressions in Eq. (2) are dimensionless doubly reduced matrix elements which are insensitive to the metal-ion environment.

JO parameters are adjustable parameters and they are calculated from the absorption spectrum $\varepsilon(\tilde{\nu})$. For an isotropic crystal or a solution, the experimental dipole strength is defined as:

$$D(\exp) = \frac{10^{-36}}{108.9 \cdot \tilde{\nu}_{\mathrm{mean}} \cdot X_{\mathrm{A}}} \cdot \left((2J+1) \cdot \frac{9n}{(n^2+2)^2} \right) \cdot \int \varepsilon(\tilde{\nu}) \mathrm{d}\tilde{\nu} \tag{3}$$

with X_{A} being the fractional population of the initial state while $\tilde{\nu}_{\mathrm{mean}}$ is given by:

$$\tilde{\nu}_{\mathrm{mean}} = \frac{\int \tilde{\nu} \cdot \varepsilon(\tilde{\nu}) \mathrm{d}\tilde{\nu}}{\int \varepsilon(\tilde{\nu}) \mathrm{d}\tilde{\nu}} \tag{4}$$

Finally, $(2J+1)$ is the degeneracy of the initial state and the expression involving the refractive index n is known as Lorentz's local field correction. Calculations of transition probabilities within the frame of JO theory are usually made assuming that all LF sublevels within the ground level are equally populated and that the material under investigation is optically isotropic. The former hypothesis is only reasonable in some cases, e.g., when transitions initiate from nondegenerate states such as $Eu(^7F_0)$. The second assumption is not valid for uniaxial or biaxial crystals, but, of course, holds for solutions.

The phenomenological JO parameters are determined from a fit of Eq. (2) to the experimental values defined by Eq. (3), using adequate matrix elements. The exact procedure is described in details in Refs. [24,35]. In the case of Eu^{III} the procedure is simpler since Ω_2, Ω_4, and Ω_6 can be directly extracted from the dipole strength of the $^5D_2 \leftarrow {}^7F_0$, $^5D_4 \leftarrow {}^7F_0$, and $^5L_6 \leftarrow {}^7F_0$ transitions,

respectively. Extensive tabulations of JO parameters can be found in Ref. [24], while spectra for all Ln^{III} ions are presented in Ref. [6].

The rearrangement consecutive to the promotion of an electron into a 4f orbital of higher energy does not perturb much the binding pattern in the molecules since 4f orbitals do not participate substantially in this binding. As a consequence, the internuclear distances remain almost the same in the excited state, which generates narrow bands and very small Stokes shifts, at least when the Ln ion is excited directly into the f–f transition. Large ligand-induced Stokes shifts are generated when excitation goes through coordinated ligands and/or the matrix into which the emitting ion is imbedded. Selection rules for emission are the same as for absorption. The emission probability is given by Einstein's rates of spontaneous emission A from an initial state $|\Psi_J\rangle$, characterized by a quantum number J, to a final state $|\Psi'_{J'}\rangle$:

$$A\left(\Psi_J, \Psi'_{J'}\right) = k^{\text{rad}} = \frac{1}{\tau^{\text{rad}}} = \frac{64\pi^4\widetilde{\nu}^3}{3h(2J+1)}\left[\frac{n(n^2+2)^2}{9}D_{\text{ED}} + n^3 D_{\text{MD}}\right] \tag{5}$$

where $\widetilde{\nu}$ is the mean energy of the transition defined in Eq. (4), h is Planck's constant, n is the refractive index; D_{ED} is given by Eq. (3) and D_{MD} by Eq. (6):

$$D_{\text{MD}} = \left(\frac{e \cdot h}{4 \cdot \pi \cdot m_e \cdot c}\right)^2 \cdot |\langle \Psi || L + 2S || \Psi' \rangle|^2 \tag{6}$$

The bracketed matrix elements are tabulated and the radiative lifetime can therefore be extracted from the spectral intensity, that is, from Eqs. (2), (5), and (6). Except in few cases, this calculation is not trivial and large errors may occur, including those pertaining to the hypotheses made within Judd–Ofelt theory.

If the absorption spectrum corresponding to an emission spectrum is known, which may be the case when the luminescence transitions terminate onto the ground level, the radiative lifetime can be simply calculated from the following equation where N_A is the Avogadro's number (6.023×10^{23}):

$$\frac{1}{\tau^{\text{rad}}} = 2303 \times \frac{8\pi c n^2 \widetilde{\nu}^2 (2J+1)}{N_A(2J'+1)} \int \varepsilon(\widetilde{\nu}) \mathrm{d}\widetilde{\nu} \tag{7}$$

In the special case of Eu^{III} for which one transition ($^5D_0 \rightarrow {}^7F_1$) has pure magnetic origin, a convenient simplified equation can be derived [47]:

$$A\left(\Psi_J, \Psi'_{J'}\right) = \frac{1}{\tau^{\text{rad}}} = A_{\text{MD},0} \cdot n^3 \left(\frac{I_{\text{tot}}}{I_{\text{MD}}}\right) \tag{8}$$

It is to be stressed that the radiative lifetime depends on the refractive index, on the chemical environment of the emitting ion (bond polarizability), and on the specific emitting level.

3.2.3 Charge Transfer Transitions

Charge transfer transitions play an ambiguous role with respect to lanthanide luminescence. They are essential in sensitizing the luminescence of lanthanide-containing inorganic phosphors, but they can be totally detrimental in other instances, quenching light emission completely. As for d↔f transitions, they are parity allowed and therefore intense. Three main types of charge transfer transitions may be present:

- Ligand-to-metal charge transfer (LMCT) states. During the process, an electron is transferred from the surrounding to the metal ion. As for the 4f–5d transitions, their energies are large so that corresponding transitions are often observed in the UV spectral range. The lowest energies occur for the easily reducible ions, namely, Sm^{III}, Eu^{III}, Tm^{III}, and Yb^{III} as shown in Fig. 6 which displays calculated $2p(O) \rightarrow Ln$ transitions for inorganic phosphors. The LMCT energies, however, depend heavily on the host materials and for Eu^{III}, a transition as low in energy as 31,250 cm^{-1} has been reported for europium azide in water [48]. Covalent contribution to the bonding by organic ligands considerably lowers the energy of the LMCT state in the range 18–25,000 cm^{-1}, and the energy can be modulated by substitution at the coordinating ligands [49]. Mixing of LMCT and 4f states leads to enhanced forced electric dipole transitions. As an example, the very weak $Eu(^5D_0 \leftarrow {}^7F_0)$ absorption with $\varepsilon = 10^{-3}$ M^{-1}-cm^{-1} for the aqua ion $[Eu(H_2O)_9]^{3+}$ at 17,212 cm^{-1} is not only blue shifted to 17,330 cm^{-1} in the binuclear complex with *p*-Bu^t-calix[8]arene H_8L, $[Eu_2(H_2L)(DMF)_5]$, but its absorptivity is enhanced by a factor 5000,

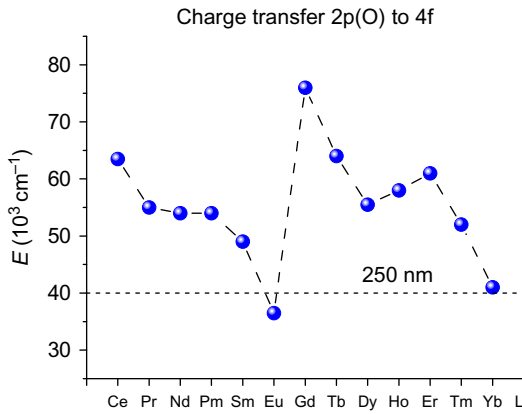

FIG. 6 Calculated energies of the O(2p)-to-Ln^{III} charge transfer states. *Redrawn from T. Kano, Principal phosphor materials and their optical properties: luminescence centers of rare-earth ions, in: S. Shionoya, W.M. Yen (Eds.), Phosphor Handbook, CRC Press Inc., Boca Raton, FL, 1999, pp. 177–200.*

to reach $\varepsilon = 5\ M^{-1}\ cm^{-1}$ [50,51]! This phenomenon is called intensity stealing.

- Metal-to-ligand charge transfer (MLCT) states. These states are commonly observed with d-transition metal ions, but are rarely identified in spectra of lanthanide complexes, except for Ce^{III}, which is easily oxidized into Ce^{IV}.
- Ligand-centered charge transfer states. If the ligand has polarized domains (e.g., push-pull ligand), then charge transfer can occur between them. The states are referred to as intraligand CTs (ILCTs) or intramolecular CTs (ICTs); sometimes more precision is added to point to the origin of the polarization, such as twisted intraligand CT (TICT). Such states are ideal for sensitizing lanthanide luminescence in view of their large absorptivity and, often, of their relatively low energy; moreover the latter can be modulated by modifying substituents decorating organic ligands [52].

In some heterometallic *n*d–4f polynuclear molecular edifices, singlet or triplet MLCTs, LMCTs, or MMCT (metal-to-metal CT) states linked to the d-transition metal moiety may also act as convenient donors for transferring energy on the Ln excited states [53,54].

4 LUMINESCENCE SENSITIZATION AND ITS MODELING

In 1942, S. I. Weissman discovered that lanthanide luminescence could be generated in molecular complexes by excitation into ligand absorption bands [55]. This observation, called *luminescence sensitization* or *antenna effect*, had a major impact on the development of lanthanide-containing luminescent molecules and materials. The brightness of an emissive compound is indeed related to the product of its molar absorption coefficient by the quantum yield:

$$B = \varepsilon(\lambda_{exc}) \times Q \tag{9}$$

The antenna effect allows one to boost the low brightness of Ln ions ($<5\ M^{-1}\ cm^{-1}$) to values up to 10^5–$10^6\ M^{-1}\ cm^{-1}$.

4.1 Energy Transfer Mechanisms

The next point was to unravel the nature of the energy transfer. In 1953, D. L. Dexter extended Th. Förster's dipole–dipole mechanism for energy transfer between fluorescent molecules [56] to forbidden transitions in luminescent solids [57]. He identified several potential mechanisms for energy transfer, each having different distance dependence (Table 3). To get a rough idea of the relative importance of these mechanisms he calculated the number of activator sites that can be excited by a single sensitizer; this estimate is based on a solid having NaCl structure and corresponding site separations. Interestingly, one sees that the electric dipole–quadrupole mechanism is of comparable importance with the exchange mechanism. In activator-doped solids,

TABLE 3 Energy Transfer Mechanisms Between Sensitizer and Activator and Their Distance Dependence

Mechanism	Distance Dependence	Nr Excited Sites
Dipole–dipole (electric)	r_{da}^{-6}	10^3–10^4
Dipole–quadrupole (electric)	r_{da}^{-8}	10^2
Exchange (spin)	$e^{-r_{da}}$	30–40
Quadrupole–quadrupole (electric)	r_{da}^{-10}	n.a.
Electric dipole–magnetic dipole	n.a.	Negligible

experimental distinction between dipole (d) and quadrupole (q) mechanisms can be done by plotting the luminescence intensity of the sensitizer vs the concentration of the activator:

$$\frac{I_0^S}{I^S} \propto c_A^{\alpha/3} \tag{10}$$

with $\alpha = 6$, 8, and 10 for d–d, d–q, and q–q mechanisms, respectively.

This is illustrated in Fig. 7 for the phosphor $NaCaY(PO_4)_2:Eu^{II}(1\%)$, $Mn^{II}(x\%)$ in which Eu^{II} sensitizes the luminescence of divalent manganese. The plot with $\alpha = 6$ is clearly nonlinear, contrary to the plot with $\alpha = 8$, pointing to a major contribution from the dipole–quadrupole mechanism [58].

4.2 Influence of Various Electronic States

The energy transfer process is highly complex. In addition to the various mechanisms that can operate, several energy states may be implied both from the donor and the acceptor. A detailed discussion is out of the scope of this essay so that potential donor states are simply listed below for the case of coordination complexes. For a more detailed discussion, please refer to Ref. [44].

- *Triplet states*. Since these states have long lifetimes, energy transfer can effectively compete with phosphorescence so that they are often invoked as being the main donor states. Therefore, several experimental relationships have been proposed between quantum yields and the energy difference between the 0-phonon component of the triplet state and the emitting level. For Eu^{III} and Tb^{III}, ideal energy gaps are between 2000 and 4000 cm^{-1}. However, this approach is far too simplistic in that it only concentrates on energy transfer, whereas the quantum yield is also affected

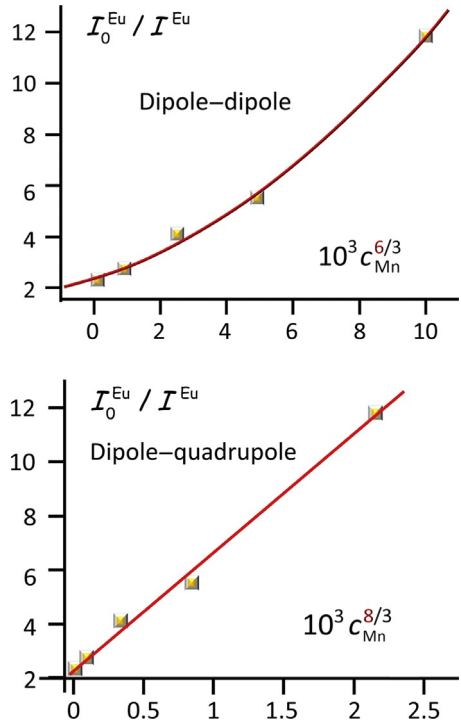

FIG. 7 Plots of emission intensity of the sensitizer (Eu^{II}) vs concentration of the activator (Mn^{II}) in $NaCa(PO_4)_2$:Eu^{II}(1%)Mn^{II}(x%) (x = 1, 3, 5, 7, 10) according to Eq. (10): (*top*) $\alpha = 6$, (*bottom*) $\alpha = 8$. *Redrawn from W.R. Liu, P.C. Lin, A study on luminescence properties and energy transfer mechanism for NaCaY(PO4)2:Eu2+,Mn2+ phosphors for LED applications, Opt. Express 22 (2014) A446–A451.*

by nonradiative deactivation in the coordination sphere (e.g., water coordination). Moreover, the accepting state of the Ln ion is not necessarily the emitting state. Finally, charge transfer states may considerably perturb this simple scheme.

- *Singlet states*. Observation of Ln luminescence upon ligand excitation in some lanthanide chelates despite that the energy of the triplet state was lower than the Ln emitting state prompted M. Kleinerman in 1969 to invoke energy transfer from the singlet state: "Contrary to prevailing notions, it is shown [in this paper] that energy transfer does not require the participation of the lowest triplet level of the chelate" [59]. More recently several examples of singlet-state sensitization have been reported, some involving in fact ^{1}ILCT or ^{1}MLCT states.
- *Charge transfer states*. As mentioned above they may interfere with the energy transfer mechanism, in a positive or negative way. Sometimes they act as simple relays in the energy transfer process [60].

- *Weak interaction*s. These interactions may generate new aggregated species with different electronic levels than the parent moieties. They cannot be neglected, and presently studies on aggregation-induced luminescence are gaining momentum. It is noteworthy that similarly to CT states, aggregation can also trigger emission quenching [61].

In fact, the sensitization process is described by a complex kinetic scheme with numerous rate constants (for each transfer, back transfer has also to be considered). A dominant pathway will emerge only if the corresponding rate constants are the largest. In order to discuss energy transfer in a correct way, the following parameters should be determined: (i) the overall (or external) quantum yield determined upon ligand excitation, Q_{Ln}^{L}; (ii) the intrinsic (or internal) quantum yield measured upon f–f excitation, Q_{Ln}^{Ln}; (iii) the lifetime of the emitting state, τ_{obs}; (iv) the radiative lifetime, τ_{rad}; and (v) the sensitization efficiency, η_{sens}. These parameters are linked by the following equation:

$$\eta_{sens} = \frac{Q_{Ln}^{L}}{Q_{Ln}^{Ln}} = Q_{Ln}^{L} \times \frac{\tau_{rad}}{\tau_{obs}} \tag{11}$$

If Q_{Ln}^{Ln} cannot be determined experimentally, it can be estimated if the lifetimes are known. The radiative lifetime can be calculated from the set of equations (2), (5), and (6) or from Eq. (7) or, for Eu^{III}, from Eq. (8). The only other needed parameter is the refractive index n that can easily be measured. Note that Q_{Ln}^{Ln} reflects the effect of nonradiative deactivations in the Ln surroundings and that it is always larger than, or at most equal to, Q_{Ln}^{L}.

4.3 Modeling the Energy Transfer Process

Theoretical modeling of the energy transfer processes in Ln^{III} complexes with organic ligands has been initially proposed by G. F. de Sá *et al.* [62]. In a first step, the geometry of the complex is optimized within the frame of a semiempirical molecular orbital model; the bonding in lanthanide complexes having essentially an ionic character is simulated with a central potential model, known as the sparkle model. Proper parameterization with Gaussian functions has been achieved by initially reproducing the known structure of several Eu^{III} complexes [62,63], but has been rapidly extended to other lanthanide ions and, presently, parameters are available for the entire series, from La^{III} to Lu^{III} [64].

Energies and transition moments of the ligand excited states are then calculated with the intermediate neglect of differential overlap/single-configuration interaction (INDO/S-CI) method. Despite the purely ionic model used, calculated and experimental electronic spectra are in usually in fairly good agreement. More sophisticated methods for calculating triplet state energies, for instance, ab initio complete active space self-consistent field or time-dependent density functional calculations (TD-DFTs), are also commonly used.

Finally, the quantum yield is calculated taking into account a kinetic model including differential expressions for the transfer rates. The transfer rates, W_{ET}, are expressed within the Fermi theory which assumes the validity of Born–Oppenheimer approximation. The kinetic model simply expresses the population variation of the levels implied within the steady-state approximation:

$$\frac{\partial p_i}{\partial t} = -\sum_{j \neq i} k_{ij} p_i + \sum_{j \neq i} k_{ji} p_j = 0 \tag{12}$$

The system of equations is solved by Runge–Kutta method with adaptive integration steps and the theoretically estimated quantum yield is given by:

$$Q = \frac{A_{tot} \cdot p_j}{\Theta \cdot p_i} \tag{13}$$

here A_{tot} refers to the sum of the radiative and nonradiative rates ($=1/\tau_{obs}$) and Θ is the pumping rate in photons/s. The model requires estimates of some parameters, such as nonradiative decay rates for internal conversion in the Ln^{III} manifolds or the lifetime of the donor state(s) at the temperature at which the transfer occurs, but it nevertheless yields reasonably good results, usually within ±20%. The model has subsequently been improved and the group of R. Freire has produced an open-access computer program for the entire procedure [64].

An example of such a modeling is shown in Fig. 8 for a dimeric Eu^{III} tetrakis(β-diketonate). Little transfer from the singlet state occurs since the

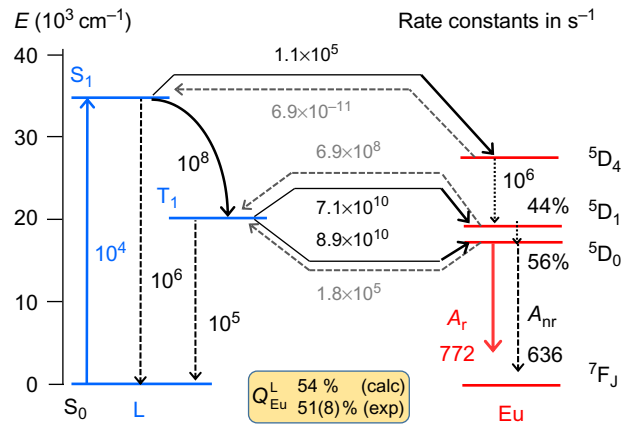

FIG. 8 Calculated rates of transfer and back transfer for a dimeric Eu^{III} tetrakis(β-diketonate). *Adapted from S. Biju, R.O. Freire, Y.K. Eom, R. Scopelliti, J.-C.G. Bünzli, H.K. Kim, A Eu(III) tetrakis(β-diketonate) dimeric complex: photophysical properties, structural elucidation by sparkle/AM1 calculations, and doping into PMMA films and nanowires, Inorg. Chem. 53 (2014) 8407–8417.*

rate constant is one order of magnitude smaller than the fluorescence rate constant and three orders of magnitude smaller than the intersystem crossing rate constant. The rate constants for transfer from the triplet state are very large, and both Eu($^5D_1$) and Eu($^5D_0$) are populated about equally. The calculated quantum yield agrees very well with the experimental one [65].

5 A FIREWORK OF APPLICATIONS

Lanthanide photonics is a burgeoning field because all trivalent lanthanide ions, baring lanthanum and lutetium, behave as ideal wavelength-converting devices with narrow emission bands covering the entire spectral range from UV (Gd) to visible and near-infrared (up to 3 μm). Lifetimes of the excited states tend to be long (ms for phosphorescence, μs for fluorescence) so that luminescence can easily be detected in time-gated mode. In addition, trivalent cerium and some divalent ions, like europium, display broad but widely tunable d–f emission. Selected emission spectra of trivalent lanthanides are shown in Fig. 9, and some applications of lanthanide photonics are briefly outlined below.

5.1 Lasers

Lanthanide ions are ideally suited as active materials for solid-state lasers emitting in the UV, visible, or NIR. One of the most widely used lasers is YAG:Nd^{III} with its mythic line at 1.06 μm, the frequency of which can easily be doubled (532 nm, green; e.g., laser pointers), tripled (355 nm, blue), or quadrupled (266 nm, UV), leading to multi-line lasers for excitation of luminescence spectra. To enhance the yield of YAG:Nd lasers, Cr^{III} or Ce^{III} are often introduced in the garnet as sensitizers. The YAG garnet can be doped

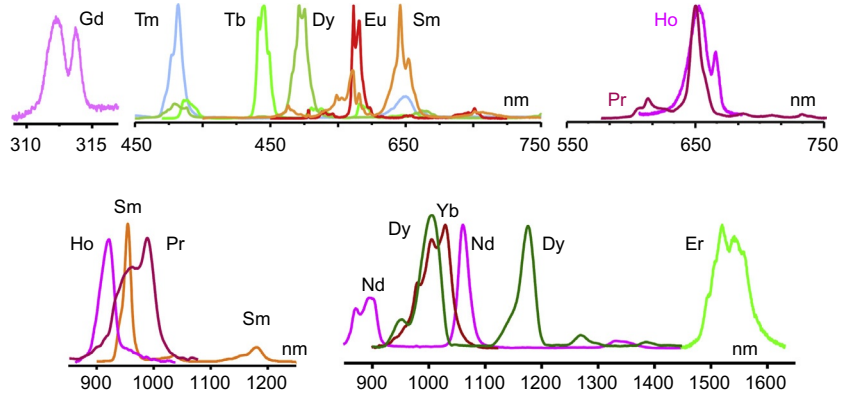

FIG. 9 Emission spectra of selected trivalent lanthanide ions. *Vertical scales* are not comparable.

by several other lanthanide ions, giving rise to devices emitting at 1.03 μm (Yb), 1.93–2.04 μm (Tm), 2.1 μm (Ho, Tm), and 2.94 μm (Er).

Low-power lasers, particularly those emitting at long wavelengths, are central to several medical applications, eye surgery, skin treatment, and dentistry or for monitoring the sugar content in blood. NIR-emitting lasers are one of the major components in telecommunication systems. High-power YAG:Nd lasers are used in manufacturing, while arrays of ultra-high-power Nd-doped phosphate glass lasers provide up to 500 TW power in nuclear fusion experimental facilities in Japan and in the United States.

5.2 Telecommunications

Telecommunications and Internet-providing systems often rely on silica optical fibers, but despite their excellent transparency the signals get attenuated after 50 or 100 km and need amplification. The latter is achieved by erbium-doped fiber amplifiers (EDFAs) that were proposed in 1987. Er^{III} is indeed emitting in the main telecommunication window (C band, 1.5 μm); therefore, silica glasses doped with this ion behave as ideal waveguide amplifiers [66]. The present network of submarine optical fibers is sketched in Fig. 10.

In EDFAs, erbium is excited either at 980 nm, on the $^4I_{11/2}$ level, or at 1480 nm, on a metastable ligand field sublevel of $^4I_{13/2}$. This results in a two-level laser emitting in the range 1530–1550 nm depending on the fine-tuning of the materials into which it is doped. The 980-nm band has higher

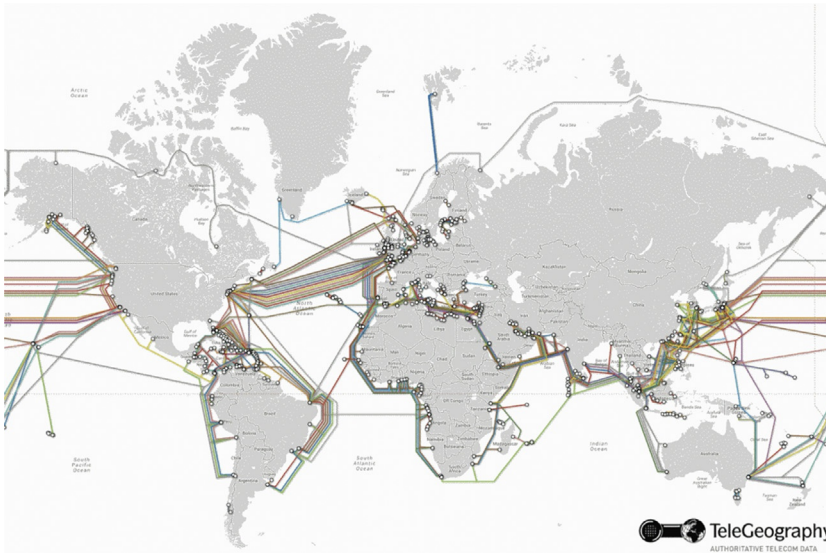

FIG. 10 Submarine cable map 2016. *TeleGeography, http:/www.submarinecablemap.com/ free resource, accessed Aug. 23, 2016.*

absorption cross section, so it is generally used when low-noise performances are required; the transition is narrow and therefore wavelength-stabilized laser sources are needed. The 1480-nm band features a lower absorption cross section but is broader, which makes it ideal for high-power amplifiers. Many EDFAs use a combination of both pump wavelengths.

One of the challenges faced by these systems is the competition with wireless networks. Indeed, the low absorption cross section of Er^{III} f–f transitions and concentration quenching when there are more than 10^{20} Er^{III} ions per cm^{-3} limit the performances of EDFAs. There are several solutions to this problem. The first one is co-doping sensitizers to compensate for the low absorbance of Er^{III} at 980 and 1480 nm; Yb^{III} is particularly adequate for 980-nm pumping since its absorption cross section at that wavelength is about 10 times larger. Moreover, the Yb($^2F_{5/2}$)-excited level efficiently transfers energy onto the resonant Er($^4I_{11/2}$) level that decays faster to the $^4I_{13/2}$ level than back transfer to Yb^{III}. A second solution consists in using hosts different from silica and co-doping high-refractive index components. A third way out is to dope Er^{III} into polymer fibers, for instance, polymethylmethacrylate, with the help of organic fluorinated ligands [3]. The resulting amplifiers have definite technical advantages over silica: better flexibility and larger diameter, allowing optimum coupling to local-scale devices, as well as a much lower pump threshold, up to 660-fold smaller. Presently, much emphasis is put on developing integrated optical devices combining both EDWAs (erbium-doped waveguide amplifiers) and EDWLs (erbium-doped waveguide lasers) on a small 1-mm^2 chip. Optimization of all parameters has led to amplifiers in which the fiber length can be reduced to a few cm thanks to gains up to 935 dB cm^{-1}.

5.3 Lighting

Despite a sharp increase in the number of lighting devices worldwide, the share of electricity devoted to it is continuously decreasing, representing presently only about 12–20% of all electricity used, depending on countries. What is really striking is the prominent role played by rare earths in improving the efficiency of lighting devices (Fig. 11). The historic electric bulb with a very poor efficiency was partly replaced in the 1970s with fluorescent tubes and lamps coated with lanthanide-containing phosphors. The coating was a carefully designed mixture of three phosphors, typically Y_2O_3:Eu^{III} (red emitter), $LaPO_4$:Ce^{III},Tb^{III} (green emitter, Ce^{III} acts as sensitizer), and $BaMgAl_{10}O_{17}$:Eu^{II} (blue emitter). Power efficiency of the luminaires was raised by a factor of 4 compared to incandescent lamps, and the same technology was later introduced in compact fluorescent lamps. These devices contain a small amount of mercury, producing the 254-nm excitation wavelength; when not properly disposed of these lamps cause environmental problems, a reason why their sale is being increasingly banned.

The situation changed in the mid-1990s with the advent of commercial white light-emitting diodes (WLEDs), following the development of GaN

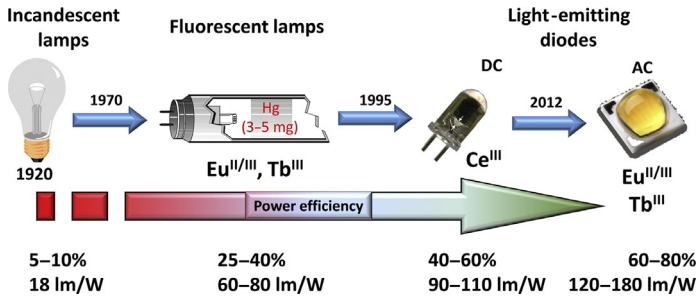

FIG. 11 Impact of rare earths on lighting. Efficiencies are "typical" values, i.e., average of several sources (technology is progressing and numbers keep improving!); luminous efficiency (lm/W) refers to an input electric power of 100 W.

blue LEDs; these devices are much smaller, do not require mercury, and have better lifetime and better efficiency. In the initial design white light was generated by combining the blue emission from (In,Ga)N with the yellow d–f luminescence from $Y_{3-x}Ce_xAl_5O_{12}$ ($0.001 < x < 0.03$, YAG:Ce^{III}, quantum yield >90%), a phosphor that was proposed in 1967 for cathode ray tubes [67]. Initial shortcomings, such as poor color rendering index and high correlated temperature, have since been cured, for instance, by increasing Ce^{III} concentration, co-doping other Ln^{III} ions, or introducing red-emitting Eu^{II} phosphors ($Sr_2Si_5N_8$:Eu^{II}, $CaSiAlN_3$:Eu^{II}).

Following this success, numerous other designs have been investigated, including three-component (RGB) phosphors (e.g., GaN:Ln, Ln = Eu—red, Er—green, and Tm—blue) and careful nanopatterning of the phosphor structure, with the imperative goal of improving brightness. Presently, laboratory luminaires incorporating WLEDs reach brightness in the range 200–250 lm/W. This is a necessity if the general objective of 30% reduction in lighting electricity consumption looked for by most states and international institutions is to be met by 2030. Help toward this goal might come from AC-LEDs introduced in the market in 2012. They are devoid of transformer, which improves their efficiency (claims up to 85% power efficiency has been filed). To compensate the flickering due to alternative electro-excitation, phosphors with long lifetimes (long persistence phosphors) are used that contain $Eu^{II/III}$ and Tb^{III}. It is however presently too early to predict if AC-LEDs are really going to supplant conventional LEDs in view of the large improvements achieved recently in the latter.

5.4 Displays

The phosphors of cathode-ray tube displays commercialized in the mid-1950s were very similar to those of fluorescent tubes. These tubes were then replaced with flat-panel displays based on several different technologies,

liquid crystals, plasma and electroluminescent panels, or, lately, organic LEDs. Except for the latter, most of these panels still work on the RGB principle, and a combination of older and newer RE-containing phosphors makes them shine brightly. The market is evolving rapidly, especially with the spread of smart phones and tablets on one hand and with new emerging technologies sometimes replacing rare-earth phosphors, so that it is difficult to predict the fate of these phosphors, except that it seems that red-emitting Eu^{III} will keep a privileged share in this market.

5.5 Security and Signage

5.5.1 The Tools

The well-defined emission bands of lanthanide luminescence and the possibility of designing fingerprints (or bar codes) by mixing several lanthanides in a probe have prompted its use in security inks, counterfeiting tags, and safety signage, not to mention pressure sensors or luminescent toys.

Several of these applications are based on downshifted luminescence, that is, emission in the visible/NIR following excitation in the UV/visible.

A very important development has been the discovery in 1966 by F. Auzel that anti-Stokes luminescence could be generated by energy transfer between two excited ions leading to upconversion [68]. In this process, two or more long-wavelength photons are combined into a shorter wavelength one. Several mechanisms are operative, in particular, excited-state absorption or energy transfer upconversion with the help of a sensitizer. Corresponding materials are usually inorganic, e.g., the ubiquitous hexagonal $NaYF_4$:Yb(18–20%)Ln (x%), Ln = Er ($x = 2$), Tm ($x = 0.5$). Trivalent erbium emits around 540 (green) and 650 nm (red), while Tm^{III} has emission at 290, 350, 460, 660 (weak), and 800 nm. In order to make these materials more compatible with practical applications, they are commonly used under the form of nanoparticles, the surface of which can be easily derivatized. Upconversion nanoparticles (UCNPs) are now ubiquitous in many applications, including luminescent tags, biosciences, drug delivery, photocatalysis, or solar energy conversion. Quantum yields of upconversion are often low, because the phenomenon is a multiphoton process and this is worsened in UCNPs in view of enhanced nonradiative deactivation due to surface traps and defects that increase with decreasing size. The remedy is to design core-shell UCNPs in which the active core material is coated with a nonluminescent layer of the matrix, passivating surface defects. The field has sustained hefty developments lately that led to remarkable control of the emissive properties. The red-to-green Er^{III} intensity ratio can be tuned by surface modification, adjusting the composition (e.g., by co-doping Mn^{II} or Gd^{III} ions) or the size/structure of the NPs. Increasing the brightness of UCNPs has also been a constant preoccupation, and excellent results have been obtained, by linking UCNPs with silver or

gold islets and taking advantage of plasmon resonances, with enhancement factors reaching 300-fold [69], by modifying their composition [69], by elaborating multi-shell NPs [70], or by 3D-controlled growth [71]. Presently, quantum yields up to several percent are achievable, for instance, with the $LiLuF_4$:Ln system: 5% for Er and 7.6% for Tm [72].

5.5.2 Security Inks

Some of the security features implemented in banknotes rely on lanthanide luminescence. For instance, the orange–red luminescence of euro banknotes under UV excitation clearly arises from a Eu^{III} compound, while the bluish-greenish emission could be due to a Eu^{II} pigment (Fig. 12A). Downshifted luminescence is also used in printing secret documents or counterfeiting tags so that text or pictures can only be revealed under UV illumination [73].

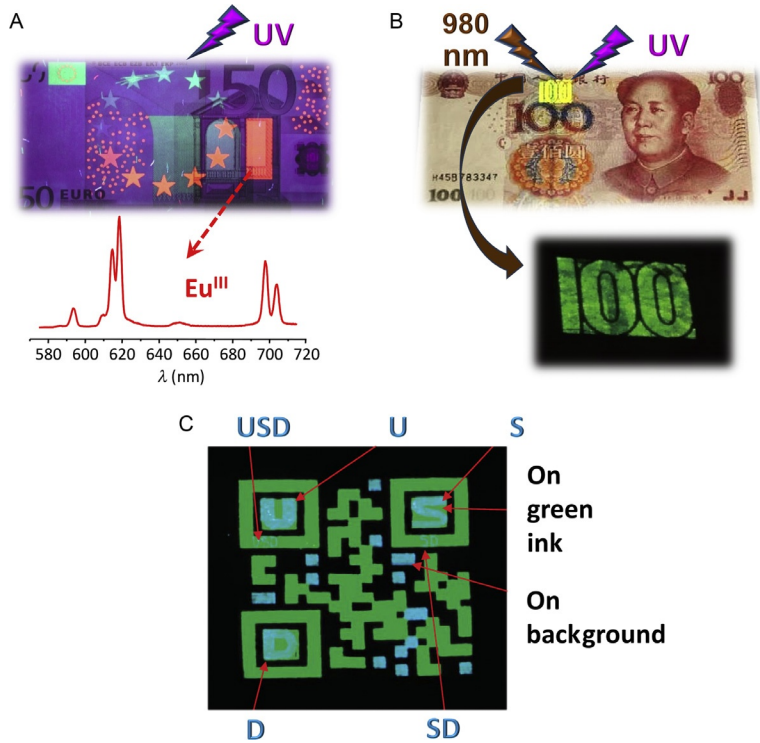

FIG. 12 (A) 50-euro banknote under UV light; (B) 100-yuan banknote under UV and NIR illumination; (C) QR code under 980-nm illumination: emission from $NaYF_4$:Yb(20%),Ln(2%), Ln = Er (*green*, 540 nm), Tm (*blue*, 450–470 nm). *Panel (B): Courtesy of Prof. Liu Xiaogang, NUS, Singapore. Panel (C): Redrawn from J.M. Meruga, W.M. Cross, P.S. May, Q.A. Luu, G.A. Crawford, J.J. Kellar, Security printing of covert quick response codes using upconverting nanoparticle inks, Nanotechnology 23 (2012) Art. Nr. 395201.*

Similarly, banknotes from China include a rectangular spot that emits yellow light under UV excitation. But when this spot is illuminated with 980-nm light, an upconverted green luminescent number is revealed that corresponds to the face value of the banknote (Fig. 12B). Quite spectacular too is the "secret" information that can be embedded into bar codes or quick-response (QR) codes (Fig. 12C) thanks to UCNPs. Similar features are incorporated in identity documents as well as in marking and counterfeiting tags.

5.5.3 Bar Codes for Tagging Commercial Goods

Counterfeiting has emerged as being a major problem for brand marks. Combining several lanthanide ions into one phosphor material leads to designing bar codes or recognition/counterfeiting tags [74]. Several companies are selling rare earth-containing tags for marking batches of various goods as diverse as clothes, airplane fuels, or ammunition. Regarding the latter, explosion transforms the tags into a mixture of rare-earth oxides that retain the same composition as the initial tag, allowing tracing the origin of the ammunition or explosive powder. Similarly, epitaxial growth of hexagonal nanorods encompassing different $NaYF_4$:Yb,Ln phosphors allow designing different RGB combinations for specific nanomarking [75]. Counterfeiting tags take advantage not only of the spectral signature of luminescent lanthanide mixtures but, also, of their different lifetimes.

5.5.4 Safety Signage

Persistent luminescence is the property of some luminescent materials to continue to emit light long after the excitation source is switched off. Zinc sulfide doped with transition metals, for instance, copper and cobalt, has long been used in conjunction with ^{226}Ra as excitation source in luminous paints for watch and clock dials. An important step was achieved in 1994 when it was found that co-doping Eu^{II} and Dy^{III} into strontium aluminate, $SrAl_2O_4$:Eu^{II}, Dy^{III}, resulted in a brighter phosphor that increasingly replaced the historical zinc sulfide materials. Applications as diverse as safety signage (e.g., luminous strips indicating emergency issues) or luminous toys are now standard. Less convincing is road marking (a test has been made in The Netherlands in 2014 with limited success) or energy storage (for solar cells, but the capacity is rather small) [11].

5.6 Life Sciences and Medicine [76–78]

Since the mid-1970s, lanthanide luminescence bioprobes (LLBs) are used in time-resolved luminescent immunoassays, the sensitivity of which is comparable and even better than that of radioactivity-based assays. Applications to bioimaging [78] and drug release [17] have been slower to develop, but they are presently on an upward trend. Both lanthanide complexes and inorganic

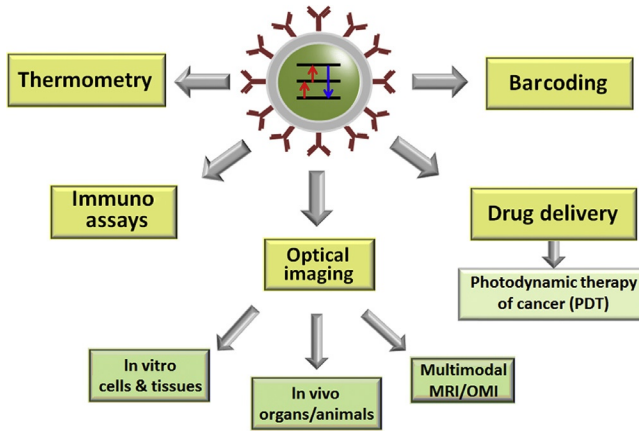

FIG. 13 Applications of UCNPs in biosciences. *Reproduced with permission from J.-C.G. Bünzli, Lanthanide light for biology and medical diagnosis, J. Lumin. 170 (2016) 866–878, © 2016 Elsevier Science B.V.*

compounds (particularly UCNPs) are used, often conjugated to avidin, biotin, monoclonal antibodies, or peptides, to ensure biochemical specificity. Interest is large because several features of lanthanide luminescence are unique, rendering LLBs quite competitive with respect to other conventional probes:

- narrow emission bands and large ligand-induced Stokes shifts
- long lifetimes allowing time-gated detection
- little (complexes with organic ligands) or no (inorganic probes) photobleaching
- easy multiplexing experiments when combining several Ln probes
- possibility of designing NIR–NIR imaging systems [79].

The field has been over-reviewed during the past years, particularly with respect to UCNP-based bioprobes [80] so that we do not elaborate further here, leaving the readers consulting relevant literature entries. As an example though, Fig. 13 sketches the various applications of UCNPs in biosciences. It is noteworthy that recent progresses in Ln-based luminescent thermometry allow for measuring temperature within cells [20]. In addition, lanthanide-based optical encoding materials enable multiplexing of large numbers of samples including assays involving nucleic acids or protein–antibody pairs, as well as multiplexed immunohistochemical staining of cells and tissues (Parallume® technology).

5.7 Scintillators

Radiation detection is important to several fields, including defense, medicine (e.g., PET, CT scans), material testing, environmental hazard monitoring, or

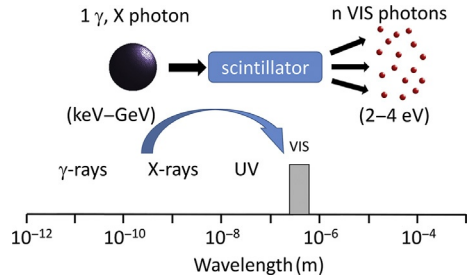

FIG. 14 Wavelength conversion by a scintillator.

security checks at harbors, airports, and borders. It turns out that there is no direct sensitive detector for photons with energy larger than a few keV. A wavelength-converting material is therefore needed (Fig. 14). Earlier scintillator crystals were often made of simple lanthanide salts, such as lanthanum or cerium chloride or bromide, or of calcium fluoride doped with divalent europium. More efficient ones are now at hand, featuring various inorganic matrices such as lutetium silicate, aluminate, or halides doped with Ce^{III} [81]. Present record is held by $Lu_3Al_5O_{12}$:Ce with a yield of 25,000 photons per MeV [82].

5.8 Solar Energy Conversion and Photocatalysis

The role of wavelength-converting lanthanides in solar energy conversion has been the subject of a recent chapter in this series [21]. Converting UV light into visible light improves the yield by 1–2 absolute% in Si-based cells and by 1.5 absolute% in dye-sensitized cells. Converting NIR light is much more difficult since sun illumination has low power density (0.1 W cm^{-2}), resulting in very low upconversion yields; for the time being, improvement around only 0.5 absolute% has been demonstrated. With the progress of nanotechnology, particularly nanopatterning, one may expect that this figure will double or triple in the forthcoming years and that combining downshifting, upconversion, and other effects could lead to a total increase in the yield between 4 and 5 absolute%. Whether implementation of the corresponding wavelength-converting layers will be cost competitive remains to be seen.

Cerium oxide or anatase (TiO_2) doped with Ce^{III} ions is an efficient photocatalyst for water splitting under UV excitation. One goal though is to gain photocatalytic activity under sun illumination alone and UCNPs can help. For instance, Tm-based UCNPs coated with TiO_2 produce UV and blue light under IR solar irradiation that activates TiO_2 photocatalytic properties for air and water purification [83]. Moreover, thermal reduction of ceria in an aerosol reactor illuminated by concentrated solar light promotes the splitting of both water and carbon dioxide, producing syngas that is ultimately transformed into kerosene with solar-to-kerosene yield of 1.7% [84]. These applications are still confined to research laboratories but may develop into economical processes.

Another interesting use of solar irradiation lies in plastics for agriculture that are doped with lanthanide-containing (mainly Eu^{III}) salts or complexes. The resulting emission matches well the photosynthesis efficiency curve, and improvement in crop yields of 10% can be routinely achieved, which is important in view of the growing world population.

6 WHAT IS NEXT?

As for any other rare-earth applications, lanthanide photonics is subject to large market oscillations due to extreme price variations on one hand (caused by geopolitical factors) and to evolving technologies on the other hand. When a technology becomes obsolete, it is replaced by another, more performing one, possibly cheaper, but which does not necessarily need the same amount of rare earth, if any at all. The case of phosphors is quite typical. Present demand for the classical RGB phosphors is plummeting owing to the replacement of compact fluorescent lamps with LEDs, and prices have declined by 60% during the past 2 years. On the other hand, several phosphors for LEDs still contain lanthanides, particularly the red phosphor, though in smaller quantities, and their commercial growth rate is predicted to reach 30% during the next 5 years. Similar phosphors are also provided in all kind of displays, particularly in back lighting of liquid crystal displays. As a consequence, research in this field will continue to be very active, particularly when it comes to nanopatterning in order to better modulate the photophysical properties and to increase the luminance.

Among the fast developing applications are biosensing, bioimaging, and luminescent thermometry. Here, the potential of lanthanide luminescent (bio)probes, including UCNPs, begins only to be explored and deep progresses are predicted. When it comes to UCNPs, present work is concentrating on improving their performances, particularly the quantum yield and luminosity, through clever design of sophisticated nanostructures. Understanding the exact mechanism of energy migration and conversion in these complicated systems will certainly help progressing further. Moreover, a breakthrough has been reached in 2012 for molecular upconversion demonstrated at low temperature in a trinuclear bimetallic Cr–Er–Cr helicate [85]. Molecular upconversion has now been demonstrated to occur at room temperature [86], and this provides another whopping handle to optimize light upconversion by modifying the structure of the ligands.

Solar energy conversion is a stimulating field, and much is needed to succeed in designing commercially viable wavelength-converting layers. But again, materials improvements are at hand, as well as new photonic tricks (photonic crystals, solar concentrators, combination of quantum dots with wavelength-converting layers) that should contribute bringing this field closer to practical use.

New exciting results are presently being found in two futuristic disciplines that have recently been reviewed: optical refrigeration [22] and quantum

information processing, leading to much desired optical computing [23]. These fields need not only materials development but also theoretical modeling, much as energy transfer processes in complexes with organic ligands.

As a conclusion, lanthanide photonics is a science in full development and will provide jewels in many different domains including health sciences, safety procedures, and green energy production. Its future is bright!

ABBREVIATIONS AND SYMBOLS

CT	charge transfer
ED	electric dipole
EDFA	erbium-doped fiber amplifier
EQ	electric quadrupole
HS	high spin
JO	Judd–Ofelt
LED	light-emitting diode
LF	ligand field
LMCT	ligand-to-metal charge transfer
MD	magnetic dipole
MLCT	metal-to-ligand charge transfer
MMCT	metal-to-metal charge transfer
NIR	near-infrared
RGB	red–green–blue
UCNP	upconversion nanoparticle
UV	ultraviolet
WLED	white light-emitting diode
YAG	yttrium aluminum garnet, $Y_3Al_5O_{12}$

REFERENCES

[1] J.-C.G. Bünzli, On the design of highly luminescent lanthanide complexes, Coord. Chem. Rev. 293–294 (2015) 19–47.

[2] J.-C.G. Bünzli, S.V. Eliseeva, Intriguing aspects of lanthanide luminescence, Chem. Sci. 4 (2013) 1939–1949.

[3] I. Hernandez, W.P. Gillin, Organic chromophores-based sensitization of NIR-emitting lanthanides: toward highly efficient halogenated environments, in: J.-C.G. Bünzli, V.K. Pecharsky (Eds.), Handbook on the Physics and Chemistry of Rare Earths, vol. 47, Elsevier Science B.V., Amsterdam, 2015, pp. 1–100. Chapter 269.

[4] S. Comby, J.-C.G. Bünzli, Lanthanide near-infrared luminescence in molecular probes and devices, in: K.A. Gschneidner Jr., J.-C.G. Bünzli, V.K. Pecharsky (Eds.), Handbook on the Physics and Chemistry of Rare Earths, vol. 37, Elsevier Science B.V., Amsterdam, 2007, pp. 217–470. Chapter 235.

[5] N. Sabbatini, M. Guardigli, I. Manet, Antenna effect in encapsulation complexes of lanthanide ions, in: K.A. Gschneidner Jr., L. Eyring (Eds.), Handbook on the Physics and Chemistry of Rare Earths, vol. 23, Elsevier Science B.V., Amsterdam, 1996, pp. 69–120. Chapter 154.

[6] W.T. Carnall, The absorption and fluorescence spectra of rare earth ions in solution, in: K.A. Gschneidner Jr., L. Eyring (Eds.), Handbook on the Physics and Chemistry of Rare Earths, vol. 3, North Holland, Amsterdam, 1979, pp. 171–208. Chapter 24.
[7] F. Auzel, Coherent emission in rare-earth materials, in: K.A. Gschneidner Jr., L. Eyring (Eds.), Handbook on the Physics and Chemistry of Rare Earths, vol. 22, Elsevier Science Publ. B.V., Amsterdam, 1996, pp. 507–606. Chapter 151.
[8] W.M. Yen, Laser spectroscopy, in: K.A. Gschneidner Jr., J.-C.G. Bünzli, V.K. Pecharsky (Eds.), Handbook on the Physics and Chemistry of Rare Earths, vol. 12, Elsevier Science B.V., Amsterdam, 1989, pp. 433–477. Chapter 87.
[9] R. Reisfeld, C.K. Jorgensen, Excited state phenomena in vitreous materials, in: K.A. Gschneidner Jr., L. Eyring (Eds.), Handbook on the Physics and Chemistry of Rare Earths, vol. 9, Elsevier Science Publ. B.V., Amsterdam, 1987, pp. 1–90. Chapter 58.
[10] A. Halperin, Activated thermoluminescence (TL) dosimeters and related radiation detectors, in: K.A. Gschneidner Jr., L. Eyring (Eds.), Handbook on the Physics and Chemistry of Rare Earths, vol. 28, Elsevier B.V., Amsterdam, 2000, pp. 187–309. Chapter 179.
[11] P.F. Smet, K. Van den Eeckhout, O.Q. De Clercq, D. Poelman, Persistent phosphors, in: J.-C.G. Bünzli, V.K. Pecharsky (Eds.), Handbook on the Physics and Chemistry of Rare Earths, vol. 48, Elsevier Science B.V., Amsterdam, 2015, pp. 1–108. Chapter 274.
[12] A.J. Freeman, B.I. Min, M.R. Norman, Local density supercell theory of photoemission and inverse photoemission spectra, in: K.A. Gschneidner Jr., L. Eyring, S. Hüfner (Eds.), Handbook on the Physics and Chemistry of Rare Earths, vol. 10, Elsevier Science Publishers B.V., Amsterdam, 1987, pp. 165–229. Chapter 65.
[13] D.W. Lynch, J.H. Weaver, Photoemission of Ce and its compounds, in: K.A. Gschneidner Jr., L. Eyring, S. Hüfner (Eds.), Handbook on the Physics and Chemistry of Rare Earths, vol. 10, Elsevier B.V., Amsterdam, 1987, pp. 231–300. Chapter 66.
[14] S. Hüfner, Photoemission in chalcogenides, in: K.A. Gschneidner Jr., L. Eyring, S. Hüfner (Eds.), Handbook on the Physics and Chemistry of Rare Earths, vol. 10, Elsevier Science Publishers B.V., Amsterdam, 1987, pp. 301–319. Chapter 67.
[15] S. Shinoda, H. Miyake, H. Tsukube, Molecular recognition and sensing via rare earth complexes, in: K.A. Gschneidner Jr., J.-C.G. Bünzli, V.K. Pecharsky (Eds.), Handbook on the Physics and Chemistry of Rare Earths, vol. 35, Elsevier Science B.V., Amsterdam, 2005, pp. 273–331. Chapter 226.
[16] T. Nishioka, K. Fukui, K. Matsumoto, Lanthanide chelates as luminescent labels in biomedical analyses, in: K.A. Gschneidner Jr., J.-C.G. Bünzli, V.K. Pecharsky (Eds.), Handbook on the Physics and Chemistry of Rare Earths, vol. 37, Elsevier Science B.V., Amsterdam, 2007, pp. 171–216. Chapter 234.
[17] D.C. Rodriguez Burbano, R. Naccache, J.A. Capobianco, Near-IR triggered photon upconversion: imaging, detection, and therapy, in: J.-C.G. Bünzli, V.K. Pecharsky (Eds.), Handbook on the Physics and Chemistry of Rare Earths, vol. 47, Elsevier Science B.V., Amsterdam, 2015, pp. 273–347. Chapter 273.
[18] G.K. Liu, X.Y. Chen, Spectroscopic properties of lanthanides in nanomaterials, in: K.A. Gschneidner Jr., J.-C.G. Bünzli, V.K. Pecharsky (Eds.), Handbook on the Physics and Chemistry of Rare Earths, vol. 37, Elsevier Science B.V., Amsterdam, 2007, pp. 99–169. Chapter 233.
[19] M. Sato, S.W. Kim, Y. Shimomura, T. Hasegawa, K. Toda, G.Y. Adachi, Rare earth-doped phosphors for white light-emitting diodes, in: J.-C.G. Bünzli, V.K. Pecharsky (Eds.), Handbook on the Physics and Chemistry of Rare Earths, vol. 49, Elsevier Science B.V., Amsterdam, 2016, pp. 1–128. Chapter 278.

[20] C.D.S. Brites, A. Millan, L.D. Carlos, Lanthanides in luminescent thermometry, in: J.-C.G. Bünzli, V.K. Pecharsky (Eds.), Handbook on the Physics and Chemistry of Rare Earths, vol. 49, Elsevier Science B.V., Amsterdam, 2016, pp. 339–427. Chapter 281.
[21] J.-C.G. Bünzli, A.-S. Chauvin, Lanthanides in solar energy conversion, in: J.-C.G. Bünzli, V. K. Pecharsky (Eds.), Handbook on the Physics and Chemistry of Rare Earths, vol. 44, Elsevier Science B.V., Amsterdam, 2014, pp. 169–281. Chapter 261.
[22] M.P. Hehlen, M. Sheik-Bahae, R.I. Epstein, Solid-state optical refrigeration, in: J.-C.G.Bünzli, V.K. Pecharsky (Eds.), Handbook on the Physics and Chemistry of Rare Earths, vol. 45, Elsevier Science B.V., Amsterdam, 2014, pp. 179–260. Chapter 265.
[23] P. Goldner, A. Ferrier, O. Guillot-Noël, Rare-earth doped crystal for quantum information processing, in: J.-C.G. Bünzli, V.K. Pecharsky (Eds.), Handbook on the Physics and Chemistry of Rare Earths, vol. 46, Elsevier Science B.V., Amsterdam, 2015, pp. 1–78. Chapter 267.
[24] C. Görller-Walrand, K. Binnemans, Spectral intensities of f-f transitions, in: K.A. Gschneidner Jr., L. Eyring (Eds.), Handbook on the Physics and Chemistry of Rare Earths, vol. 25, Elsevier Science B.V., Amsterdam, 1998, pp. 101–264. Chapter 167.
[25] M. Dolg, H. Stoll, Electronic structure calculations for molecules containing lanthanide atoms, in: K.A. Gschneidner Jr., E.M. Eyring (Eds.), Handbook on the Physics and Chemistry of Rare Earths, vol. 22, Elsevier Science B.V., Amsterdam, 1996, pp. 607–720. Chapter 152.
[26] K. Ogasawara, S. Watanabe, H. Toyoshima, M.G. Brik, First-principles calculations of 4f-4f5d transition spectra, in: K.A. Gschneidner Jr., J.-C.G. Bünzli, V.K. Pecharsky (Eds.), Handbook on the Physics and Chemistry of Rare Earths, vol. 37, Elsevier Science B.V., Amsterdam, 2007, pp. 1–59. Chapter 231.
[27] E.N. Harvey, A History of Luminescence. From the Earliest Times Until 1900, American Philosophical Society, Philadelphia, 1957.
[28] G. Urbain, Twenty-five years of research on the yttrium earths, Chem. Rev. 1 (1924) 143–185.
[29] J.H. Van Vleck, The puzzle of rare-earth spectra in solids, J. Phys. Chem. 41 (1937) 67–80.
[30] H. Bethe, Termaufspaltung in Kristallen, Ann. Phys. 395 (1929) 133–208.
[31] P. Dorenbos, The 4f to 4f5d transitions of the trivalent lanthanides in halogenides and chalcogenides, J. Lumin. 91 (2000) 91–106.
[32] B.G. Wybourne, Spectroscopic Properties of Rare Earths, Wiley Interscience, New York, 1965.
[33] G.H. Dieke, Spectra and Energy Levels of Rare Earth Ions in Crystals, Interscience Publishers, New York, 1968.
[34] C. Görller-Walrand, K. Binnemans, Rationalization of crystal field parameterization, in: K. A. Gschneidner Jr., L. Eyring (Eds.), Handbook on the Physics and Chemistry of Rare Earths, vol. 23, Elsevier Science B.V., Amsterdam, 1996, pp. 121–283. Chapter 155.
[35] B.M. Walsh, Judd Ofelt theory: principles and practices, in: B. Di Bartolo, O. Forte (Eds.), Advances in Spectroscopy for Lasers and Sensing, Springer Verlag, Berlin, 2006, pp. 403–433.
[36] A. Meijerink, R.T. Wegh, VUV spectroscopy of lanthanides: extending the horizon, Mater. Sci. Forum 315–317 (1999) 11–26.
[37] L. van Pieterson, M.F. Reid, R.T. Wegh, A. Meijerink, 4f(n) <-> 4f(n-1)5d transitions of the trivalent lanthanides: experiment and theory, J. Lumin. 94 (2001) 79–83.
[38] L. Brewer, Systematics of the properties of the lanthanides, in: S.P. Sinha (Ed.), Systematics and the Properties of the Lanthanides, Springer Verlag, Berlin, 1983, pp. 17–69.

[39] L. van Pieterson, M.F. Reid, G.W. Burdick, A. Meijerink, 4f(n)->4f(n-1)5d transitions of the heavy lanthanides: experiment and theory, Phys. Rev. B 65 (2002). Art. Nr. 045114-1–045114-13.
[40] L. van Pieterson, M.F. Reid, R.T. Wegh, S. Soverna, A. Meijerink, 4f(n)->4f(n-1)5d transitions of the light lanthanides: experiment and theory, Phys. Rev. B 65 (2002). Art. Nr. 045113-1–045113-16.
[41] P. Dorenbos, Predictability of 5d level positions of the triply ionized lanthanides in halogenides and chalcogenides, J. Lumin. 87–89 (2000) 970–972.
[42] A. Zych, J. Ogieglo, C. Ronda, D.C. de Mello, A. Meijerink, Analysis of the shift of zero-phonon lines for f-d luminescence of lanthanides in relation to the Dorenbos model, J. Lumin. 134 (2013) 174–179.
[43] J.-C.G. Bünzli, S.V. Eliseeva, Basics of lanthanide photophysics, in: O.S. Wolfbeis, M. Hof (Eds.), Lanthanide Luminescence: Photophysical, Analytical and Biological Aspects, Springer Series on Fluorescence, vol. 7, Springer Verlag, Berlin, 2011, pp. 1–45.
[44] J.-C.G. Bünzli, S.V. Eliseeva, Photophysics of lanthanoid coordination compounds, in: V. W.-W. Yam (Ed.), Comprehensive Inorganic Chemistry II, Elsevier B.V., Amsterdam, 2013, pp. 339–398.
[45] P.A. Tanner, Some misconceptions concerning the electronic spectra of tri-positive europium and cerium, Chem. Soc. Rev. 42 (2013) 5090–5101.
[46] J.-C.G. Bünzli, Luminescent probes, in: J.-C.G. Bünzli, G.R. Choppin (Eds.), Lanthanide Probes in Life, Chemical and Earth Sciences. Theory and Practice, Elsevier Science Publ. B.V., Amsterdam, 1989, pp. 219–293
[47] M.H.V. Werts, R.T.F. Jukes, J.W. Verhoeven, The emission spectrum and the radiative lifetime of Eu^{3+} in luminescent lanthanide complexes, Phys. Chem. Chem. Phys. 4 (2002) 1542–1548.
[48] H. Kunkely, A. Vogler, Photolysis of aqueous europium(III) azide complexes: formation of europium(II) induced by ligand-to-metal charge transfer excitation, Inorg. Chem. Commun. 8 (2005) 117–118.
[49] L.D. Carlos, J.A. Fernandes, R.A.S. Ferreira, O.L. Malta, I.S. Goncalves, P. Ribeiro-Claro, Emission quantum yield of a europium(III) tris-beta-diketonate complex bearing a 1,4-diaza-1,3-butadiene: comparison with theoretical prediction, Chem. Phys. Lett. 413 (2005) 22–24.
[50] J.-C.G. Bünzli, P. Froidevaux, J.M. Harrowfield, Photophysical properties of lanthanide dinuclear complexes with p-tert-butylcalix[8]arene, Inorg. Chem. 32 (1993) 3306–3311.
[51] J.-C.G. Bünzli, F. Ihringer, Photophysical properties of lanthanide dinuclear complexes with p-nitro-calix[8]arene, Inorg. Chim. Acta 246 (1996) 195–205.
[52] A. D'Aleo, F. Pointillart, L. Ouahab, C. Andraud, O. Maury, Charge transfer excited states sensitization of lanthanide emitting from the visible to the near-infra-red, Coord. Chem. Rev. 256 (2012) 1604–1620.
[53] F.F. Chen, Z.Q. Chen, Z.Q. Bian, C.H. Huang, Sensitized luminescence from lanthanides in d-f bimetallic complexes, Coord. Chem. Rev. 254 (2010) 991–1010.
[54] M.D. Ward, Mechanisms of sensitization of lanthanide(III)-based luminescence in transition metal/lanthanide and anthracene/lanthanide dyads, Coord. Chem. Rev. 254 (2010) 2634–2642.
[55] S.I. Weissman, Intramolecular energy transfer. The luminescence of complexes of europium (β-diketonate complexes), J. Chem. Phys. 10 (1942) 214–217.
[56] Th. Förster, Zwischenmolekulare Energiewanderung und Fluoreszenz, Ann. Phys. 2 (1948) 55–75.
[57] D.L. Dexter, A theory of sensitized luminescence in solids, J. Chem. Phys. 21 (1953) 836–850.

[58] W.R. Liu, P.C. Lin, A study on luminescence properties and energy transfer mechanism for NaCaY(PO4)2:Eu2+, Mn2+ phosphors for LED applications, Opt. Express 22 (2014) A446–A451.
[59] M. Kleinerman, Energy migration in lanthanide chelates, J. Chem. Phys. 51 (1969) 2370–2381.
[60] L.N. Puntus, K.A. Lyssenko, I. Pekareva, J.-C.G. Bünzli, Intermolecular interactions as actors in energy transfer processes in lanthanide complexes with 2,2'-bipyridine, J. Phys. Chem. B 113 (2009) 9265–9277.
[61] Y. Zhang, P.C. Jiao, H.B. Xu, M.J. Tang, X.P. Yang, S. Huang, J.G. Deng, Switchable sensitizers stepwise lighting up lanthanide emissions, Sci. Rep. 5 (2015). Art. Nr. 9335-1–9335-5.
[62] G.F. de Sá, O.L. Malta, C.D. Donega, A.M. Simas, R.L. Longo, P.A. Santa-Cruz, E.F. da Silva, Spectroscopic properties and design of highly luminescent lanthanide coordination complexes, Coord. Chem. Rev. 196 (2000) 165–195. review.
[63] G.B. Rocha, R.O. Freire, N.B. Da Costa, G.F. de Sá, A.M. Simas, Sparkle model for AM1 calculation of lanthanide complexes: improved parameters for europium, Inorg. Chem. 43 (2004) 2346–2354.
[64] M.A.M. Filho, J.D.L. Dutra, H.L.B. Cavalcanti, G.B. Rocha, A.M. Simas, R.O. Freire, RM1 model for the prediction of geometries of complexes of the trications of Eu, Gd, and Tb, J. Chem. Theory Comput. 10 (2014) 3031–3037.
[65] S. Biju, R.O. Freire, Y.K. Eom, R. Scopelliti, J.-C.G. Bünzli, H.K. Kim, A Eu(III) tetrakis (b-diketonate) dimeric complex: photophysical properties, structural elucidation by sparkle/AM1 calculations, and doping into PMMA films and nanowires, Inorg. Chem. 53 (2014) 8407–8417.
[66] S.V. Eliseeva, J.-C.G. Bünzli, Rare earths: jewels for functional materials of the future, New J. Chem. 35 (2011) 1165–1176.
[67] V. Tucureanu, A. Matei, A.M. Avram, Synthesis and characterization of YAG:Ce phosphors for white LEDs, Opto-Electron. Rev. 23 (2015) 239–251.
[68] F. Auzel, Upconversion and anti-stokes processes with f and d ions in solids, Chem. Rev. 104 (2004) 139–173.
[69] S.Y. Han, R.R. Deng, X.J. Xie, X.G. Liu, Enhancing luminescence in lanthanide-doped upconversion nanoparticles, Angew. Chem. Int. Ed. 53 (2014) 11702–11715.
[70] H.L. Wen, H. Zhu, X. Chen, T.F. Hung, B.L. Wang, G.Y. Zhu, S.F. Yu, F. Wang, Upconverting near-infrared light through energy management in core-shell-shell nanoparticles, Angew. Chem. Int. Ed. 52 (2013) 13419–13423.
[71] D. Liu, X. Xu, Y. Du, X. Qin, Y. Zhang, C. Ma, S. Wen, W. Ren, E.M. Goldys, J.A. Piper, S. Dou, X. Liu, D. Jin, Three-dimensional controlled growth of monodisperse sub-50 nm heterogeneous nanocrystals, Nat. Commun. 7 (2016). Art. Nr. 10254-1–10254-8.
[72] P. Huang, W. Zheng, S.Y. Zhou, D.T. Tu, Z. Chen, H.M. Zhu, R.F. Li, E. Ma, M.D. Huang, X.Y. Chen, Lanthanide-doped LiLuF4 upconversion nanoprobes for the detection of disease biomarkers, Angew. Chem. Int. Ed. 53 (2014) 1252–1257.
[73] J. Andres, R.D. Hersch, J.E. Moser, A.S. Chauvin, A new anti-counterfeiting feature relying on invisible luminescent full color images printed with lanthanide-based inks, Adv. Funct. Mater. 24 (2014) 5029–5036.
[74] O. Guillou, C. Daiguebonne, G. Calvez, K. Bernot, A long journey in lanthanide chemistry: from fundamental crystallogenesis studies to commercial anticounterfeiting taggants, Acc. Chem. Res. 49 (2016) 844–856.
[75] Y. Zhang, L. Zhang, R. Deng, J. Tian, Y. Zong, D. Jin, X. Liu, Multicolor barcoding in a single upconversion crystal, J. Am. Chem. Soc. 136 (2014) 4893–4896.

[76] J.-C.G. Bünzli, Lanthanide luminescence for biomedical analyses and imaging, Chem. Rev. 110 (2010) 2729–2755.
[77] J.-C.G. Bünzli, Lanthanide light for biology and medical diagnosis, J. Lumin. 170 (2016) 866–878.
[78] J.-C.G. Bünzli, Luminescence bioimaging with lanthanide complexes, in: A. de Bettencourt-Dias (Ed.), Luminescence in Lanthanide Coordination Compounds and Nanomaterials, Wiley-Blackwell, Oxford, 2014, pp. 125–197.
[79] E. Hemmer, N. Venkatachalam, H. Hyodo, A. Hattori, Y. Ebina, H. Kishimoto, K. Soga, Upconverting and NIR emitting rare earth based nanostructures for NIR-bioimaging, Nanoscale 5 (2013) 11339–11361.
[80] Z. Chen, W. Zheng, P. Huang, D. Tu, S. Zhou, M. Huang, X. Chen, Lanthanide-doped luminescent nano-bioprobes for the detection of tumor markers, Nanoscale 7 (2015) 4274–4290.
[81] M. Nikl, A. Yoshikawa, Recent R&D trends in inorganic single-crystal scintillator materials for radiation detection, Adv. Opt. Mater. 3 (2015) 463–481.
[82] S. Liu, J.A. Mares, X. Feng, A. Vedda, M. Fasoli, Y. Shi, H. Kou, A. Beitlerova, L. Wu, C. D'Ambrosio, Y. Pan, M. Nikl, Towards bright and fast Lu3Al5O12:Ce, Mg optical ceramics scintillators, Adv. Opt. Mater. 4 (2016) 731–739.
[83] X. Guo, W. Di, C. Chen, C. Liu, X. Wang, W. Qin, Enhanced near-infrared photocatalysis of NaYF4:Yb, Tm/CdS/TiO2 composites, Dalton Trans. 43 (2014) 1048–1054.
[84] J.R. Scheffe, M. Welte, A. Steinfeld, Thermal reduction of ceria within an aerosol reactor for H_2O and CO_2 splitting, Ind. Eng. Chem. Res. 53 (2014) 2175–2182.
[85] J.F. Lemonnier, L. Babel, L. Guenee, P. Mukherjee, D.H. Waldeck, S.V. Eliseeva, S. Petoud, C. Piguet, Perfluorinated aromatic spacers for sensitizing europium(III) centers in dinuclear oligomers: better than the best by chemical design? Angew. Chem. Int. Ed. 51 (2012) 11302–11305.
[86] A. Nonat, C.F. Chan, T. Liu, C. Platas-Iglesias, Z. Liu, W.T. Wong, W.K. Wong, K.L. Wong, L.J. Charbonniere, Room temperature molecular up conversion in solution, Nat. Commun. 7 (2016). Art. Nr. 111978-1–111978-8.

Chapter 288

Thermoelectric Properties of Zintl Antimonides

Nasrin Kazem and Susan M. Kauzlarich[1]
University of California, Davis, CA, United States
[1]*Corresponding author: e-mail: smkauzlarich@ucdavis.edu*

Chapter Outline

1 BACKGROUND

The ever-increasing worldwide demand for energy not only requires more sources of energy but also calls for a much greater versatility in generation of electricity. Reliance upon and escalation of the use of fossil fuels only strengthens concerns about climate changes due to increased emission of greenhouse gases such as CO_2 into the atmosphere. High reliability, long-time durability, scalability, along with the environmentally friendly performances of thermoelectric (TE) materials make them one of the promising areas of study in energy conversion and generation technologies.

TE materials can play important roles both in primary energy generation by utilizing heat sources such as solar or geothermal energy and also in energy conservation by harvesting waste heat such as that produced by automotive engines or nuclear power plants [1,2]. As TE energy generation is a carbon neutral process that produces no emissions, TEs have even been considered as a possible way to alleviate the climate crisis [3–6]. However, the extent of its impact (if any) on climate change remains the subject of debate [7,8].

Handbook on the Physics and Chemistry of Rare Earths, Vol. 50. http://dx.doi.org/10.1016/bs.hpcre.2016.05.003

Recently, considerable effort has been devoted to direct conversion of solar radiation into electricity by concentrated solar thermoelectric generator and solar photovoltaic–thermoelectric hybrid systems [9]. Moreover, substantial advancements have been made in the conversion of waste heat from a combustion engine into electricity in automobiles by TE generators [2,10]. Yet, the low efficiency of TE materials is a challenging problem for large-scale applications. To achieve high efficiencies, many research groups worldwide are working to develop materials with high TE figures of merit, zT. zT is defined by Eq. (1) where α is the Seebeck coefficient, ρ is the electrical resistivity, κ is the thermal conductivity, and T is the temperature. zT is a dimensionless quantity that is used to estimate the performance of TE materials to convert heat to electricity.

$$zT = \frac{\alpha^2 T}{\rho\kappa} \tag{1}$$

To describe the fundamental challenges in increasing the zT value of a material, a brief review of the TE effect is required. The TE phenomenon can be simply described by a series of thermocouples, where one n-type and one p-type semiconducting material are connected, Fig. 1, top. When a temperature gradient is applied to a thermocouple, the charge carriers (electrons in n-type leg and holes in p-type leg) move from the hot side to the cold side. As a result, an electrical potential is created between the ends of the legs. By connecting these thermocouples electrically in series, acting like a small battery, this electrical potential can be augmented to generate a large voltage,

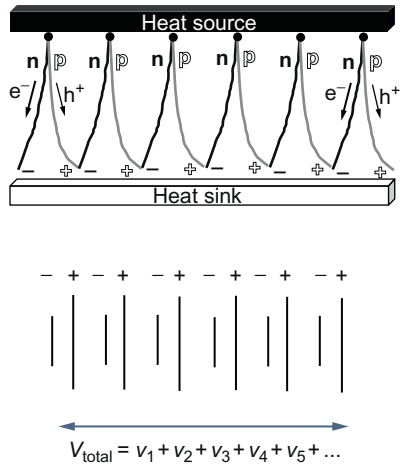

FIG. 1 The simplest thermoelectric module can be imagined as the thermocouples connected electrically in series and thermally in parallel resulting in a Seebeck voltage produced between the legs of thermocouple, top, so each thermocouple acts like a battery, bottom, then the total voltage will be the sum of all the voltages produced by each thermocouple.

Fig. 1, bottom. The magnitude of the electrical voltage depends on the applied temperature gradient and the fundamental properties of the material and is called the Seebeck coefficient, α, Eq. (2):

$$\Delta V = \alpha \Delta T \tag{2}$$

The thermocouple's constituent materials must be poor conductors of heat to maintain the temperature gradient, otherwise the electrical voltage will be negligible. To create a large voltage, given a temperature gradient, a material with large Seebeck coefficient is required. From a parabolic band structure model, the Seebeck coefficient can be given by Eq. (3) [11] where n is the carrier concentration and m^* is the effective mass of the carrier.

$$\alpha = \frac{8\pi^2 k_b^2}{3eh^2} m^* T \left(\frac{\pi}{3n}\right)^{2/3} \tag{3}$$

At the same time, these thermocouples will be part of an electrical circuit to generate electricity, so they must be made of a material with low electrical resistivity. The electrical resistivity, ρ, is a function of the carrier concentration, n, the mobility, μ, and the elementary charge of the carrier (electrons or holes), e, Eq. (4).

$$\rho = \frac{1}{ne\mu} \tag{4}$$

A fundamental challenge as a result of the opposing dependency of ρ and thermal conductivity, κ, on charge carrier concentration is apparent. Moreover, the aforementioned thermal conductivity can be described mainly as a combination of the lattice contribution, κ_l, the electronic contribution, κ_e. Lattice thermal conductivity is the only physical property in the zT equation that is independent of the electronic properties and is only controlled by the structure. However, the electronic contribution is inversely proportional to electrical resistivity, ρ, according to the Wiedemann–Franz law, Eq. (5):

$$\kappa = \kappa_l + \kappa_e; \kappa_e = \frac{LT}{\rho} = Lne\mu T, \text{ where } L = \frac{\pi^2 k_b^2}{3e^2} \tag{5}$$

As a result of the optimization of all the transport properties with respect to the charge carrier concentration, efficient TE materials are found among the narrow band gap semiconductors with the charge carrier concentrations in the range of 10^{19}–10^{21} cm^{-3} [5,12]. To create a large Seebeck coefficient, materials in each leg must contain only one type of charge carrier. Intrinsic semiconductors which create both electrons and holes as a result of thermal excitation are not good candidates for possessing efficient TE properties. Extrinsic semiconductors (heavily doped semiconductors) are the best candidates as they generally contain only one type of charge carrier. In order for a TE module to have a high efficiency, in addition to a high zT, the module should be operated over a large temperature gradient as the overall efficiency

of a TE device, η, is limited by the Carnot efficiency, Eq. (6), where T_C is the cold-side temperature, T_H the hot-side temperature. zT in this equation stands for the average value given by $\frac{T_H + T_C}{2}$.

$$\eta = \left(\frac{T_H - T_C}{T_H}\right)\left(\frac{\sqrt{1+zT}-1}{\sqrt{1+zT}+T_C/T_H}\right) \tag{6}$$

By having a large temperature gradient, there will be a continuous gradual change in temperature in each leg. However, as mentioned already, the transport properties are temperature dependent and a single material cannot act as an efficient TE generator over a broad range of temperatures. To overcome this problem, different materials can be segmented so that each material has $zT \sim 1$ for the corresponding temperature in the TE device. Therefore, p-type and n-type legs are made by segmenting the efficient p-type and n-type TEs, respectively, to make segmented power generators [13], Fig. 2. Selecting compatible materials becomes an important concern as the interfaces can result in significant scattering of the carriers and energy losses. Compatible materials can be identified by the compatibility factor, s, which provides a simple means of identifying materials that have similar current densities, Eq. (7) [14]:

$$s = \frac{\sqrt{1+zT}-1}{\alpha T} \tag{7}$$

For almost half a century, only three families of compounds all having $zT \sim 1$ in their corresponding temperature range have been employed for TE applications: for near room temperatures, Bi_2Te_3; for intermediate temperatures, PbTe; and for high temperatures, SiGe; Fig. 3 [7,15]. However, TE

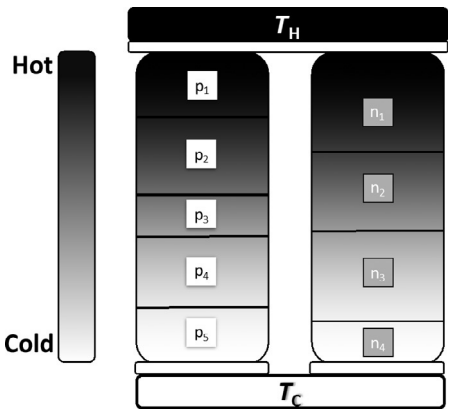

FIG. 2 Segmented power generator thermoelectric made of combined p-type and n-type efficient materials for the exposed temperatures.

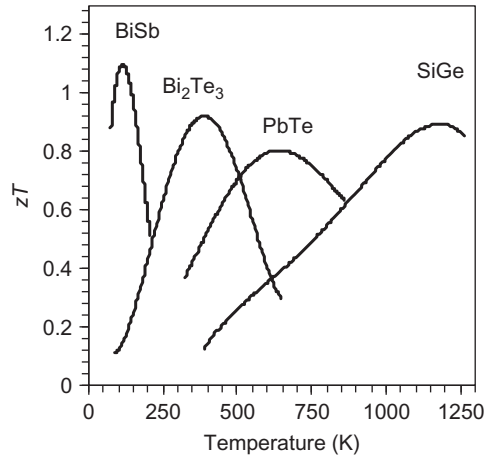

FIG. 3 Thermoelectric figure of merit as a function of temperature for several n-type materials that dominated the field of thermoelectrics in 1992 are shown. *Adapted from C.B. Vining, The thermoelectric limit zt∼1: fact or artifact, in: K.R. Rao (Ed.), XI International Conference on Thermoelectrics, University of Texas at Arlington, Arlington, Texas (1992).*

materials need to achieve a $zT \sim 3$ to reach ∼40% Carnot efficiency, see Fig. 4, in order to be competitive with the modern mechanical power generators [7]. Although a new generation of bulk materials show zT values of 1.6–1.7 at approximately 700–800 K [16], we are still far away from the desired zT value of 3, so the development of novel materials remains a formidable challenge [7].

As discussed earlier, high Seebeck coefficients, high electrical, and low thermal conductivities are desirable in order to increase zT value. TE studies mainly focus on engineering existing materials to reduce their thermal conductivities in order to enhance efficiency. Different materials processing such as nanotechnology and thin-film fabrication techniques as well as alloying methods can be applied to decrease lattice thermal conductivity. These processes can be effective, if the size-scale of the features is comparable with the mean free paths of the major phonon modes involved in lattice thermal conductivities [17]. TE figure of merit values have been significantly increased by nanostructuring of known TE materials. Among all of them, p-type thin-film Bi_2Te_3/Sb_2Te_3 superlattices and $PbSe_{0.98}Te_{0.02}/PbTe$ quantum-dot superlattices, with zT of ∼2.4 at room temperature and $zT \sim 3.6$ at 580 K, respectively, have had the best reported zT values for more than a decade [18,19]. Although high efficiencies can be achieved by the nanotechnology techniques, it remains challenging to preserve the transport properties of the nanosized motifs during materials consolidation for large-scale applications. Although there is no theoretical limit for achieving zT values in excess of 3 in bulk materials, it seems that there is no clear

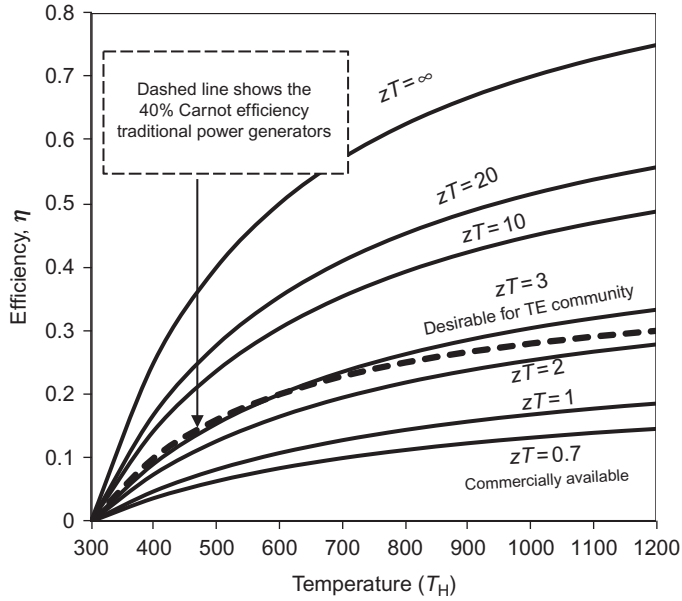

FIG. 4 Thermoelectric efficiency as a function of hot-side temperature for different zT values, the cold side is assumed as 300 K. Commercial thermoelectrics can provide efficiencies lower than 15% in the temperature range of 300–1000 K. *The graph is adapted from C.B. Vining, An inconvenient truth about thermoelectrics, Nat. Mater. 8 (2009) 83–85.*

candidate among known materials in which such values can be achieved. In the case of low thermal conductivity materials, enhancement of the power factor, $\frac{\alpha^2}{\rho}$, can be the focus of study and optimization. Zintl compounds, see Section 2, are one of the best candidates to provide narrow bandgap semiconductors with characteristically low lattice thermal conductivities. Moreover, similar to the low-dimensional materials in which physical transport properties can be tuned separately, the two types of bonding in Zintl phases, ionic and covalent, provide two avenues for tuning the properties [12].

This review emphasizes new single-phase bulk Zintl materials with consideration of the crystal structure, chemistry, and tuning of transport properties. In this short perspective, we present a few of the most recent compounds belonging to a subclass of Zintl bulk materials studied for TE applications over the last decade. These materials are ternary rare-earth (R) transition metal (TM) Zintl antimonide (RTMSb) phases where R = Eu or Yb and TM = Mn, Zn, or Cd. These materials have been studied for TE applications in the form of pressed pellets through consolidating polycrystalline bulk materials. More comprehensive reviews on TE materials are well covered in several articles and books [5,7,8,12,15,16,19–21].

2 ZINTL PHASES

Zintl phases are a subclass of intermetallic compounds that are traditionally defined as made from electropositive and electronegative main group metals [22]. It is conventionally assumed that the electrons are donated from the electropositive metals to the more electronegative elements similar to ionic salt-like compounds, but in many cases, the total number of electrons is not sufficient to satisfy the octet rule for the more electronegative elements. As a result, the electronegative elements complete a filled valence electron configuration through covalent bonding by making anionic networks. This description considers the electropositive elements as charge-balancing "spectators" that fill the cavities made in the anionic networks. In contrast to the traditional description of Zintl phases, various nonclassical Zintl compounds, called polar intermetallic phases, can be formed via integration of transition and rare-earth metals replacing the more electropositive main group and alkali or alkaline earth elements, respectively [22,23]. These TM- or rare-earth metal-containing phases can be described as Zintl compounds, showing that Zintl phases are not limited to elemental compositions with large electronegativity differences. As a result, a wide variety of materials with bonding/electronic structure between that of insulators and metals is possible.

This flexibility of Zintl structures enables the engineering of the band gap in this family to optimize the electronic properties. Moreover, regardless of the valence-precise satisfaction in Zintl compounds, they can be favorably doped by either isovalent or aliovalent elements to coarsely or finely tune the charge carrier concentration to reach to the regime of high zT values. This region is found for heavily doped semiconductors with n between 10^{19} and 10^{20} carriers/cm^3. There is usually a solubility window in which the carrier concentration can be tuned by the dopant. Some Zintl phases are flexible in terms of accepting large dopant concentrations, whereas others are not and phase separation occurs. For example, $Yb_{14}AlSb_{11}$ is an extrinsic semiconductor with $n_H \sim 10^{19}$ h$^+$/cm^3 showing a high structural flexibility as Al^{3+} sites can be completely substituted by Mn^{2+} to generate a heavily doped semiconductor with $n_H \sim 10^{21}$ h$^+$/cm^3 providing a rich chemistry for tuning the transport properties [24].

Zintl phases form a large family of inorganic compounds with many different crystal structures and compositions; however, only a small fraction of them has been studied for their TE properties. In a simple electron counting scheme, it is assumed that cations in Zintl phases mainly control the charge carrier concentrations; for example, in AZn_2Sb_2 (A = Ca, Eu, Yb) [25,26], and $Eu_{1-x}Yb_xCd_2Sb_2$ [14] charge carrier concentrations were shown to be tuned by the cation. Recent research in this area, on the other hand, points to subtle differences in vacancies and bonding as contributing to the changes in carrier concentration. Moreover, the covalent bonding in the anionic network in Zintl compounds are effective for charge transport, for example, in

$YbCd_{2-x}Zn_xSb_2$, as Sb and Zn provide similar electronegativities and the character of the Sb–Zn bonds provides higher charge carrier mobilities than the Cd–Zn analogs [27].

2.1 $A_{11}B_6X_{12}$: $Sr_{11}Cd_6Sb_{12}$ Structure Type (*C*2/*m*)

Two of the most recent TE studies on novel Zintl phases examined the $Eu_{11}Cd_6Sb_{12}$ and $Eu_{11}Zn_6Sb_{12}$ compounds [28], the only rare-earth metal-containing ternary intermetallics adopting the $Sr_{11}Cd_6Sb_{12}$ structure type [29]; their generic chemical formula can be described as $A_{11}B_6X_{12}$ [30,31]. This structure can be described as infinite, one-dimensional columns of stacked two edge-fused pentagons. The crystal structure of the $Sr_{11}Cd_6Sb_{12}$ structure type is defined by the space group *C*2/*m* (no. 12) having 15 crystallographically unique atomic positions comprised of six (each) Sr and Sb and three Cd sites. The crystal structure of $Eu_{11}TM_6Sb_{12}$ projected along the *b*-axis is shown in Fig. 5. Infinite $[TM_6Sb_{12}]^{22-}$ double-pentagon channels running along the *b*-axis involve a covalent network of vertex-sharing $TMSb_4$ tetrahedra that are separated by Eu^{2+} cations. The structure can be described based on the Zintl formalism as the valence-precise compound of $(Eu^{2+})_{11}[(4b\text{-}TM^{2-})_6(1b\text{-}Sb^{2-})_2(2b\text{-}Sb^{1-})_6(3b\text{-}Sb^0)_4]$ by assigning three-bonded Sb atoms (3b-Sb), two-bonded Sb atoms (2b-Sb), and one-bonded Sb atoms (1b-Sb) as Sb^0, Sb^{1-}, and Sb^{2-}, respectively.

The chemical and physical flexibility of the $Eu_{11}Cd_6Sb_{12}$ structure using the pnictogen, and TM sites for alloying, and their TE properties can be examined. So far, $Eu_{11}Cd_6Sb_{12-x}As_x$ [31] and $Eu_{11}Cd_{6-x}Zn_xSb_{12}$ [30] solid solutions have been studied for their possible TE applications by our group. Solid solutions of the $Eu_{11}Cd_6Sb_{12}$ and $Eu_{11}Zn_6Sb_{12}$ Zintl compounds have a solubility gap and feature specific site substitution [30,31]. This site

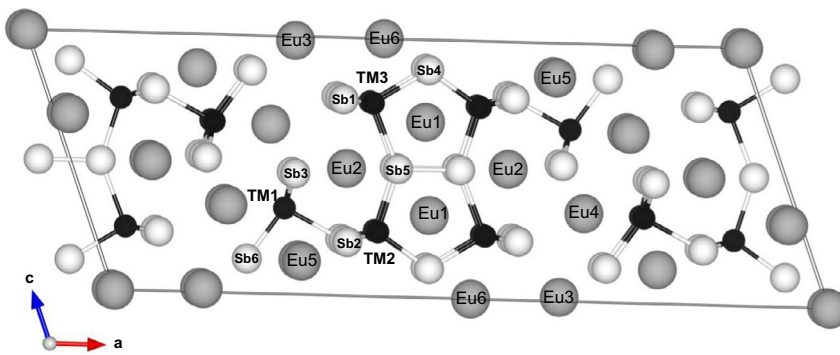

FIG. 5 A view of the crystal structure of $Eu_{11}TM_6Sb_{12}$ showing all the 15 unique crystallographic positions. Eu, TM, and Sb atoms are designated by *gray*, *black*, and *white spheres*, respectively.

specificity as opposed to random substitutions is referred to as the coloring phenomenon [32]. Arsenic (As) selects the Sb2 site (see Fig. 5) as the highest percentage for substituting, and the solid solution terminates when the total As concentration exceeds 35% As. The highest arsenic containing composition detected in $Eu_{11}Cd_6Sb_{12-x}As_x$ is $Eu_{11}Cd_6Sb_{7.76}As_{4.24(6)}$ from reaction of $x_{syn}=3$ [31]. Zn also shows distinct coloring since the Cd3 site systematically shows lower occupancy factors for Zn and also displays a solubility gap at $1.2 \leq x \leq 4.3$. High-temperature TE studies of these phases are limited up to ~600°C, above which antimony begins to sublime.

The transport properties measurements on $Eu_{11}Cd_6Sb_{12}$ showed exceptionally low lattice thermal conductivities from room temperature to 775 K: $0.78-0.49$ W/mK, and high p-type Seebeck coefficient: from +118 to 153 μV/K similar to the state-of-the-art TEs [31,33]. However, its high electrical resistivity of 6.8–12.8 mΩ cm results in low zT values (zT reaches 0.23 at 774 K), Fig. 6. In the case of the As substitution to form $Eu_{11}Cd_6Sb_{12-x}As_x$, the goal was to increase the Seebeck coefficients by opening the band gap. However, the addition of As introduces lattice defects that result in high charge carrier concentration, Fig. 6, which reduces the Seebeck coefficient and results in lower zT values, Fig. 7. Theoretical calculations on $Eu_{11}Cd_6Sb_{12-x}As_x$ show that the energy gap does not open at the Fermi level by As substitution at the Sb sites unless it substitutes on the Sb4 site. This is consistent with the experimental Hall measurements; a sharp drop in Hall mobilities occurs at $x>2$ as the Sb4 site begins to become populated by As atoms in $Eu_{11}Cd_6Sb_{12-x}As_x$ when $x \geq 2$, Fig. 6. Theoretical calculations on $Eu_{11}Cd_6Sb_{12}$ also show that the classic Zintl formalism does not describe the bonding in this compound as mixing of Eu1 and Sb4 orbitals is observed in vicinity of the Fermi level, contrasting with the expected ionic interactions between the cation (Eu) and the anionic network described by Zintl concept. This suggests that these compounds are better described as polar intermetallic Zintl compounds [12].

The TM site was also targeted for alloying in the $Eu_{11}Cd_{6-x}Zn_xSb_{12}$ study [30]. In order to keep the Eu–Sb framework chemically untouched as their interactions were found to be important, Zn was substituted for Cd. The smaller Zn (1.20 Å) substitution at Cd (1.40 Å) sites shows similar occupation factors for Cd1 and Cd2 sites whereas Cd3 site systematically shows lower Zn occupancy. It has been suggested the larger Cd can stabilize the structure better than the solid solution with Zn as the larger TM can provide the better orbital overlap with Sb5 atoms involved in the only homoatomic bonding in this compound; Sb5–Sb5 bond. Zn substitution causes the Eu1–Sb4 bond to become shorter, so a higher orbital overlap of Eu1–Sb4 is expected to provide for higher mobility. Although no large change in carrier concentration is expected by isovalent substitution of Cd^{2+} sites by Zn^{2+} [31], Hall measurements show higher carrier concentration for the solid

solutions compared to the end members, Fig. 6. This inconsistency has been attributed to the size incompatibility of Zn^{2+} and Cd^{2+} that alters the equilibrium defect concentration as observed in AZn_2Sb_2 [26,34]. The Seebeck coefficients of the $Eu_{11}Cd_{6-x}Zn_xSb_{12}$ solid solutions with significant charge carrier concentration ($x = 1$ and 4.4) are lower than the end member. However, $Eu_{11}Cd_{4.5}Zn_{1.5}Sb_{12}$ solid solution with low charge carrier concentration becomes a better TE material when compared to the end members as a result

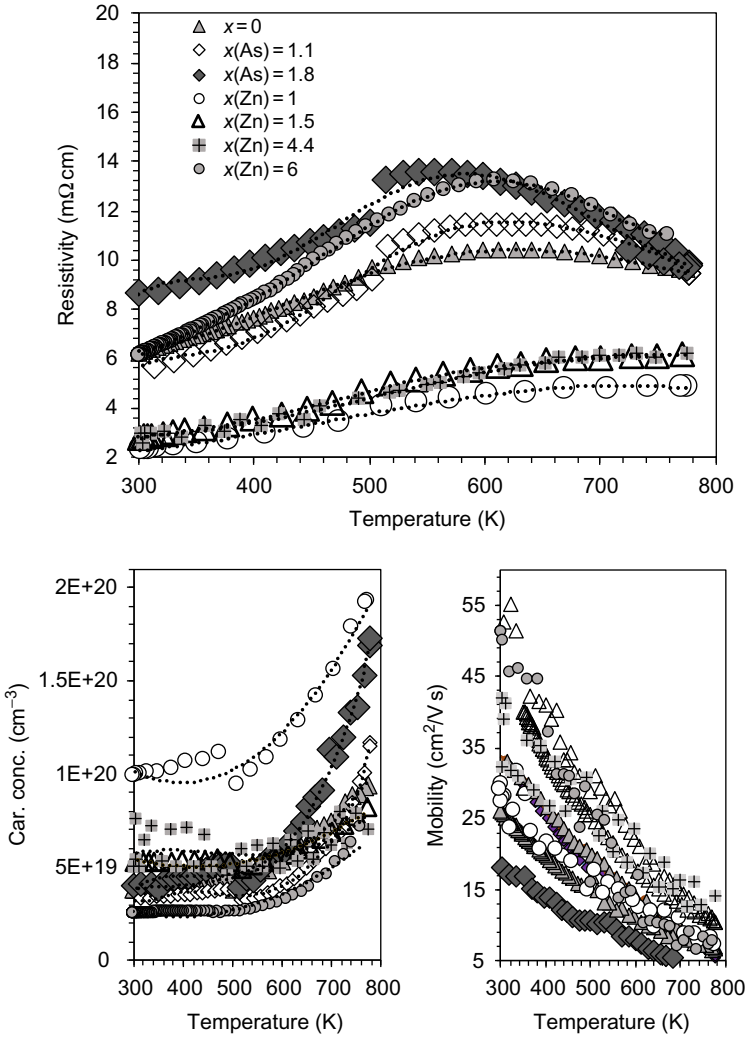

FIG. 6 Resistivity and Hall carrier concentration and Hall mobility of $Eu_{11}Cd_6Sb_{12-x}As_x$, and $Eu_{11}Cd_{6-x}Zn_xSb_{12}$ solid solutions are shown.

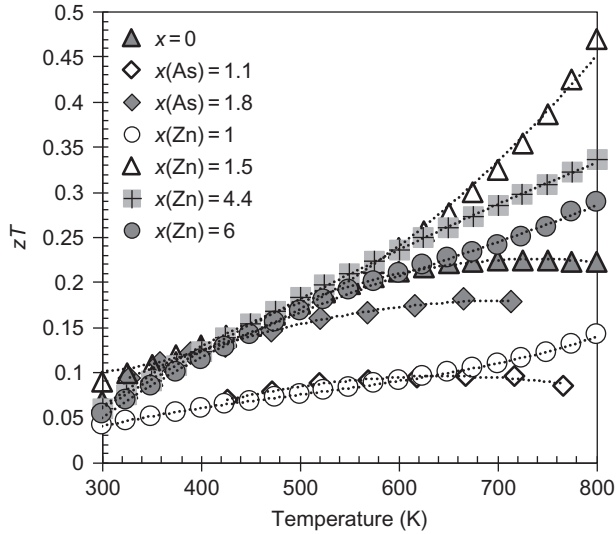

FIG. 7 High-temperature thermoelectric figures of merit of derivatives of $Eu_{11}Cd_6Sb_{12}$ ($x=0$), $Eu_{11}Cd_6Sb_{12-x}As_x$ ($x=1.1$, 1.8), and $Eu_{11}Cd_{6-x}Zn_xSb_{11}$ ($x=1$, 1.5, 4.4, 6).

of both improved resistivity and Seebeck coefficient; zT value has been improved by ~250%, from 0.2 to 0.5 at ~800 K, Fig. 7.

It has been experimentally [30,31] and theoretically [35] shown that, in $Eu_{11}Cd_6Sb_{12}$ derivatives, if the Eu1–Sb4 orbital overlap is conserved, the high mobility for holes can be assured. By using smaller TM atoms, while the Eu–Sb framework is chemically undisturbed, the Eu1–Sb4 overlap may be enhanced to improve the charge carrier mobility. The TM atom should be similar in size to prevent the introduction of defects to the structure thereby affecting the charge carrier concentrations and as a result the electronic properties. So, the choice of atom type for the TM site can tune both the mobility and the charge carrier concentration to modify the power factor in $Eu_{11}(Cd/Zn)_{6-x}TM_xSb_{12}$. We suggest the substitution of slightly smaller Co^{2+} at Zn^{2+} tetrahedral sites in $Eu_{11}Zn_6Sb_{12}$ to reach the high mobility with no significant change in the charge carrier concentrations and effective masses as a result of the similar ionic radii of Zn^{2+} and Co^{2+}. Therefore, the unwanted defects possibly may be avoided while a better orbital overlap of Eu1–Sb4 is offered. So, the high Seebeck coefficient in $Eu_{11}Zn_6Sb_{12}$ should be preserved, as the charge carrier concentration is unchanged while the lower resistivities are attained through higher mobilities.

2.2 $A_9B_{4+x}X_9$: $Ca_9Mn_{4+x}Bi_9$ Structure Type (*Pbam*)

The recent discovery of extremely low thermal conductivity ($\kappa_L < 0.4\,W/mK$), and high zT ($zT=0.7$ at 950 K) in $Yb_9Mn_{4.2}Sb_9$ [36] shows the promise of Zintl

phases for good TE performance. $Yb_9Mn_{4.2}Sb_9$ crystallizes in the $Ca_9Mn_4Bi_9$ structure type (Pearson code oP44) where the additional interstitial site of the so-called TM3 position (4g Wyckoff site) is partially occupied by Mn. The generic expression for this structure type can be written as $A_9TM_{4+x}Pn_9$ and can be referred to as the "9-4-9" family of compounds. Many members of this family $A_9TM_{4+x}Pn_9$ (A = Ca, Sr, Yb, Eu; TM = Mn, Zn, Cd; Pn = As, Sb, Bi) belong to this interstitially stabilized structure resulting in non-stoichiometric compositions [37–42]. In Fig. 8, the crystal structure of the fully interstitially filled $A_9TM_4Sb_9$ (9-4-9) resulting in a stoichiometric $A_9TM_4B_2Sb_9$ (9-6-9) composition where B stands for the interstitial atom has been demonstrated. Aside from the extent of the occupation at the interstitial site, the interstitial atom type has also been investigated. Recently, the flexibility of this structure has been shown by incorporating Group 11 metals (TM = Cu, Ag, and Au) in the Cd–Sb framework of $Eu_9Cd_{4-x}TM_{2+x-y}\square_ySb_9$ compounds [38]. The flexibility of this structure type is demonstrated as regardless of the different covalent radii of Cu (1.22 Å), Ag (1.36 Å), and Au (1.30 Å) [43], they all show very similar fractional occupation of ~50% at the interstitial position while also showing different level of tendency to mix at the TM1 site. There has been no evidence of the presence of Group 11 atoms at TM2.

The bonding in the 9-4-9 family can be described based on conventional electron counting as a valence-imprecise Zintl compound $(Eu^{2+})_9[(Cd^{2+})_4(Sb^{-3})_9]$ as $[Cd_4Sb_9]^{19-}$ anionic network requires 19 electrons

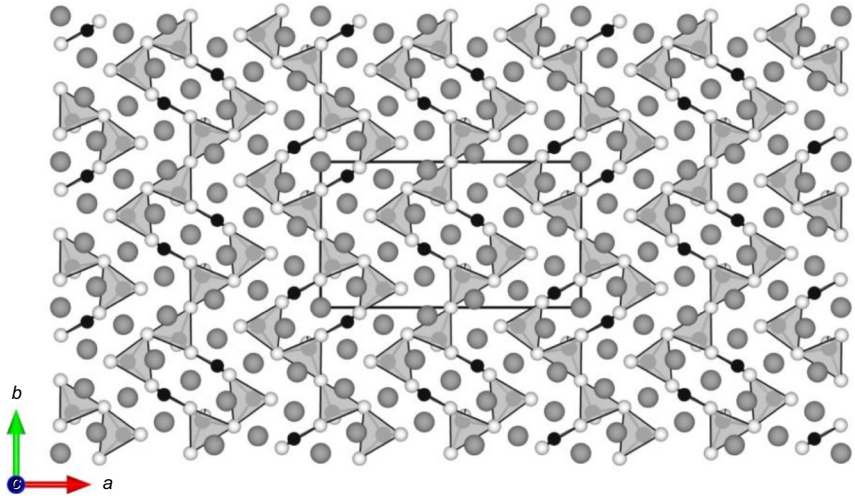

FIG. 8 A view of crystal structure projected in the *c* direction of an interstitially filled $A_9TM_4Sb_9$ (9-4-9) resulting in a hypothetical $A_9TM_4B_2Sb_9$ (9-6-9) where B stands for interstitial atom. Corner-shared tetrahedral units of $TMSb_4$ are making one-dimensional $[Cd_4Sb_9]^{19-}$ ribbon-like chains that are running parallel to *c* direction become connected in *b* direction by B atoms. A, B, TM, and Sb ions are designed as *large gray*, *black*, *small gray* (inside the tetrahedral), and *white spheres*, respectively.

while only 18 electrons are provided by Eu^{2+}. So, generally, the interstitial sites of the 9-4-9 family are populated to overcome its electron deficiency. This hypothesis is supported by the theoretical calculations; the Fermi level locates at a pseudogap for the interstitially stabilized compounds such as $Eu_9Cd_{3.7}$ $Cu_{1.5}Sb_9$ and $Sr_9Cd_{4.5}Sb_9$. If the interstitial atoms are divalent atoms such as Mn, Zn, and Cd, the occupational factor of the interstitial sites will be 25%, and if it is a monovalent atom such as Cu, Ag, or Au, the occupational factor will be 50% to supply one additional electron per formula unit. The variation in the occupation at the interstitial sites and also in the occupation of the divalent TM sites in the anionic frame by monovalent atoms classifies these compounds as high extrinsic carrier concentration semiconductors.

The 9-4-9 family of compounds shows an effective combination of phonon-glass electron-crystal (PGEC) properties due to their low total thermal conductivities combined by low electrical resistivities. In order to describe such an exceptional combination, either very low lattice thermal conductivities to avoid unprecedentedly low Lorenz numbers in bulk materials or very low Lorenz numbers to avoid negative lattice thermal conductivities at high temperatures need to be considered. In a recent work, low Lorenz numbers have been considered as the key factor leading to low total thermal conductivities in this family of compounds [44]. However, the low Lorenz numbers have not been experimentally verified due to unavailability of experimental methods for Lorenz number measurements of low mobility charge carrier compounds. Assuming the Sommerfeld–Lorenz number (free electron model), $L_0 = 2.45 \times 10^8$ WΩ/K^2—an appropriate L for metals and degenerate semiconductors, which is being used in the literature for most of the Zintl metallic and degenerate semiconductor compounds at room temperature—9-4-9 compounds can be ranked with respect to the state-of-the-art known PGEC examples of materials for TE applications as shown in Table 1. We used a simple multiplication of resistivity times lattice thermal conductivity ($\rho \times \kappa_l$) as a ranking term to show which of them minimizes this value, thereby maximizing the PGEC property. We emphasize that k_l for all the compounds in Table 1 is from the subtraction of the electronic contribution given by the Wiedemann–Franz law, $\kappa_e = L_0 T/\rho$, from the total thermal conductivity, where $L_0 = 2.45 \times 10^8$ WΩ/K^2 and $T = 300$K. As listed in Table 1, all of the studied 9-4-9 phases offer very low values for the $\rho \times \kappa_l$ term. $Eu_9Cd_{3.82}Au_{1.24}Sb_9$ with ρ of 0.43 mΩ cm and κ_l of 0.29 W/(mK) clearly stands out compared to the best-known PGEC compounds that inevitably show small electrical resistivity and thermal conductivity values.

$Gd_{117}Co_{56}Sn_{112}$ with κ_l of 0.28 W/(mK) and ρ of 0.52 mΩ cm at room temperature which has one of the lowest ever reported lattice thermal conductivity for a nonglassy bulk solid and the best reported PGEC example is placed in the second rank due to its higher electrical resistivity compared to $Eu_9Cd_{3.82}Au_{1.24}Sb_9$. $Eu_9Cd_{4-x}CM_{2+x-y}\square_ySb_9$ (TM = Zn, Cu, and Au) are

TABLE 1 Estimated Lattice Thermal Conductivities (κ_L), Using the Lorentz Factor from Free Electron Model Limit to Calculate κ_e, Electrical Resistivity (ρ), and ($\rho \times \kappa_l$) Values at 300 K of $Eu_9Cd_{4-x}TM_{2+x-y\square y}Sb_9$ Compounds Compared to Some of the State-of-the-Art Known PGEC Materials

Compound	κ_L (W/(mK))	ρ (10^{-5} Ω m)	($\rho \times \kappa_l$) (10^{-5} Ω/W/K)
$(Bi/Sb)_2Te_3$ [45] (nanocrystalline)	0.6	0.794	0.4764
$Ba_{0.08}La_{0.05}Yb_{0.04}Co_4Sb_{12}$ [46]	1.16	0.417	0.4837
$Yb_{14}MnSb_{11}$ [33]	0.55	2	1.100
$Gd_{117}Co_{56}Sn_{112}$ [47]	0.28	0.52	0.146
Ag_9TlTe_5 [48]	0.23	130	29.90
$Ba_8Au_{16}P_{30}$ [49]	0.18	1.7	0.306
$Eu_9Cd_{3.67}Cu_{1.50}Sb_9$ [44]	0.46	0.55	0.253
$Eu_9Cd_{3.75}Ag_{1.42}Sb_9$ [44]	0.55	0.88	0.484
$Eu_9Cd_{3.82}Au_{1.24}Sb_9$ [44]	0.29	0.43	0.125
$Yb_9Mn_{4.2}Sb_9$ [36]	0.45	3.2	1.440
$Yb_9Zn_{4.2}Sb_9$ [50]	0.9	0.27	0.270

even superior to the recently reported clathrate phase, $Ba_8Au_{16}P_{30}$, with extremely low lattice thermal conductivity of 0.18 W/(mK) and low electrical resistivity of 1.7 mΩ cm at room temperature [49].

Theory and experiment have shown that the structural complexity of the materials is clearly the vital factor in determining low lattice thermal conductivities. This trend was beautifully shown by Toberer *et al.* [20] by relating the κ_l and the primitive cell volume (V), as a representative for the complexity of a system in many Zintl phases. It is shown that lattice thermal conductivity is inversely related to the primitive cell volume, $\kappa_L = aV^{-1} + \kappa_{min}$ [20], see top graph in Fig. 9. This shows that even for a very large unit cell, there is a nonzero lattice thermal conductivity of κ_{min}. Compounds like $Ba_8Au_{16}P_{30}$ and $Gd_{117}Co_{56}Sn_{112}$ with 216 and 285 atoms per primitive unit cell and large primitive unit cell volumes of ~4440 and 6858 Å^3, respectively, can be considered as a good approximation for the lower limit of the thermal conductivity according to the relation mentioned above. In a similar approach, Toberer *et al.* used number of atoms in the primitive unit cell as the complexity representative [51], see bottom graph in Fig. 9. As the number of atoms in the

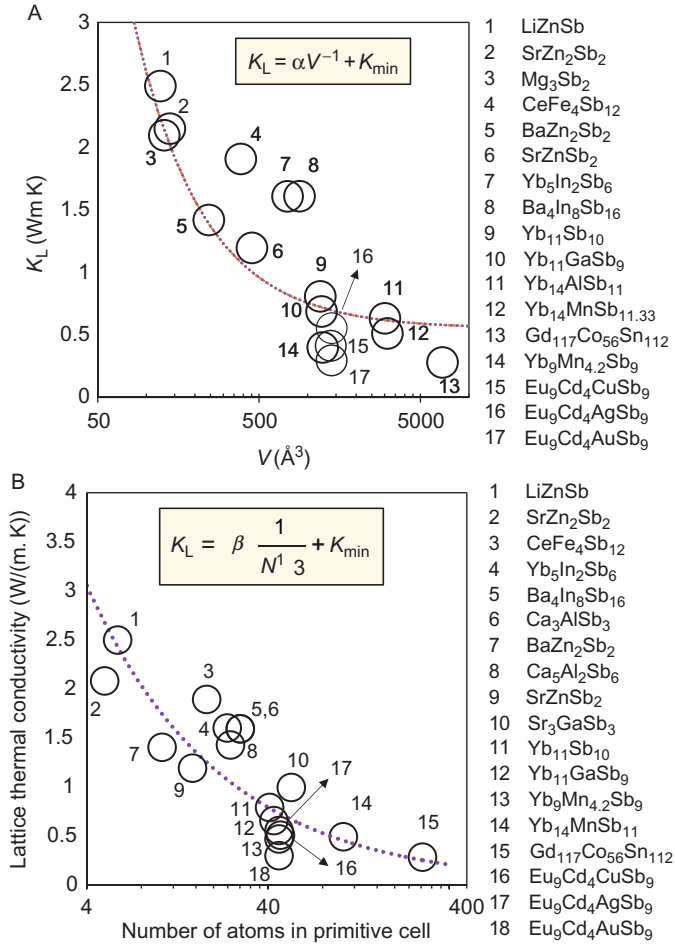

FIG. 9 (A) Graph representing the estimated lattice thermal conductivity for a variety of Zintl antimonides at 300 K by subtracting the electronic thermal conductivity contribution, assuming a free electron Lorenz number, from the total thermal conductivity. The *dashed line* is according to the proposed equation by Toberer *et al.* [20], shown in the box, which displays the inverse dependence of the lattice thermal conductivity on the primitive cell volume. (B) In the same approach, the lattice thermal conductivity for a variety of Zintl antimonides at 300 K are related to the number of atoms in their primitive unit cell. Similarly, the *dashed line* is according to the proposed equation by Toberer *et al.* [51], shown in the box, which demonstrates the inverse dependence of the lattice thermal conductivity on the number of atoms in the primitive unit cell. $Eu_9Cd_{3.67}Cu_{1.50}Sb_9$ [44], $Eu_9Cd_{3.75}Ag_{1.42}Sb_9$ [44], $Eu_9Cd_{3.82}Au_{1.24}Sb_9$ [44], LiZnSb [52], $SrZn_2Sb_2$ [53], Mg_3Sb_2 [54], $CeFe_4Sb_{12}$ [5], $Yb_5In_2Sb_6$ [55], $Ba_4In_8Sb_{16}$ [56], Ca_3AlSb_3 [57], $BaZn_2Sb_2$ [58], $Ca_5Al_2Sb_6$ [59], $SrZnSb_2$ [53], Sr_3GaSb_3 [60], $Yb_{11}Sb_{10}$ [61], $Yb_{11}GaSb_9$ [62], $Yb_9Mn_{4.2}Sb_9$ [36], $Yb_{14}MnSb_{11}$ [33], and $Gd_{117}Co_{56}Sn_{112}$ [47]. *Adapted from E.S. Toberer, A.F. May, G.J. Snyder, Zintl chemistry for designing high efficiency thermoelectric materials, Chem. Mater. 22 (2009) 624–634.*

primitive cell (N) increases, κ_L decreases, because $\kappa_L \propto \frac{1}{N^{1/3}}$. However, $Eu_9Cd_{3.82}Au_{1.24}Sb_9$ compound with ~46 atoms per primitive unit cell and a volume of ~1400 Å^3 which are only ~15% and ~20% of the number of atoms and the volume of primitive unit cell of $Gd_{117}Co_{56}Sn_{112}$ [47], respectively, produces lattice thermal conductivity very similar to $Gd_{117}Co_{56}Sn_{112}$, see Fig. 9.

This brings an enormous optimism to the area of thermoelectricity by suggesting that a perfect PGEC can be achieved through modest systems with smaller unit cells and number of atoms in the unit cells and that extraordinary complexity is not necessity to approach a perfect PGEC compound highly essential for TE applications. It is shown that the 9-4-9 family of compounds is amorphous to phonons while providing the high electron mobility as a result of low effective mass. In the case of $Eu_9Cd_{4-x}TM_{2+x-y}\square_ySb_9$ compounds (TM = Group 11 metals), the disorder at the interstitial position and also Cd1 site (mixed occupancy) may be an important factor in reducing the phonon mean free path significantly. This extremely low lattice thermal conductivity is common in 9-4-9 family members as $Yb_9Mn_{4.2}Sb_9$ and $Yb_9Zn_{4.2}Sb_9$ compounds also show very low lattice thermal conductivities of 0.39 and 0.43 W/mK at room temperature, respectively [36,50]. Although $Yb_9Mn_{4.2}Sb_9$ shows a fairly high zT for a bulk material, only two other members of the 9-4-9 family, $Yb_9Mn_{4.2-x}Zn_xSb_9$ and $Eu_9Cd_{4-x}TM_{2+x-y}\square_ySb_9$, have been studied so far. These two compounds become too metallic because of defects, and the low electrical resistivity lowers the Seebeck coefficients. As a result of the overly high charge carrier concentrations, low zT values of ~0.18 and ~0.32 at 975 and 750 K are obtained for $Yb_9Zn_{4.2}Sb_9$ and $Eu_9Cd_{3.75}Ag_{1.42}Sb_9$, respectively. However, the single parabolic band model predicts zT of >0.9 [50] for an optimized charge carrier system in the Zn system at the optimized charge carrier of $n_H = 4 \times 10^{19}$ h$^+$/cm^3 which can be obtained by substitution of a more electropositive cation element such as Ca.

2.3 AB_2X_2: $CaAl_2Si_2$ Structure Type ($P\bar{3}m$)

AB_2X_2 compounds with $CaAl_2Si_2$ crystal structure crystallize in a trigonal space group of $P\bar{3}m$ which is a layered crystal structure with a monolayer A cations between $[B_2X_2]^{2-}$ layers. $[B_2X_2]^{2-}$ layers are made by B–X tetrahedral corner sharing with a high degree of covalent bonding extended in the *ab* plane and are perpendicular to the *c*-axis, Fig. 10. So far, $YbZn_2Sb_2$ [27,63], $YbMn_2Sb_2$ [64,65], $YbCd_2Sb_2$ [27], and $EuZn_2Sb_2$ [66] (and their corresponding solid solutions) are the only rare-earth Zintl antimonides with $CaAl_2Si_2$ crystal structure [67] type that has been studied for possible TE applications. $CaAl_2Si_2$ rare-earth Zintl antimonide phases show a high flexibility for chemical substitution and alloying at the rare earth and TM sites (no pnictogen site alloying has been reported yet) since they can preserve the parent trigonal structure at any stoichiometry. As a result, the required

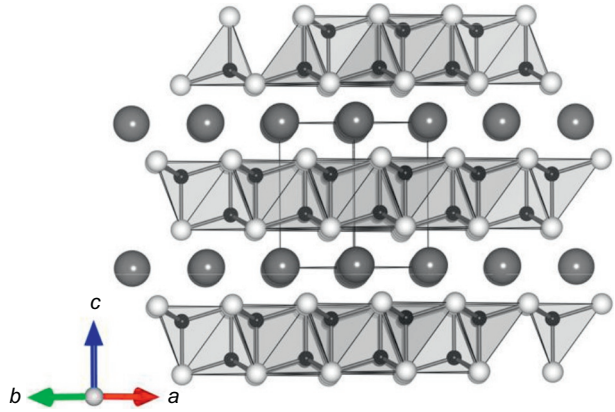

FIG. 10 Structure of AB_2X_2 compound with $CaAl_2Si_2$ crystal structure is shown. It contains the layers of $[B_2X_2]^{2-}$ formed by tetrahedral edge sharing of BX_4 units extended in the *ab* plane separated by a layer of A atoms (A, B, and X atoms are *large gray*, *small black*, and *white spheres*, respectively), and the unit cell is outlined.

tunability of electronic properties becomes readily achievable in this family of compounds.

$EuZn_2Sb_2$ and $YbCd_2Sb_2$, show high zT values of 0.9 [27,66] at 700 K, respectively, which is mainly due to low electrical resistivity of these compounds. The $CaAl_2Si_2$ rare-earth Zintl antimonide compounds such as $YbZn_2Sb_2$ [14,63], $EuZn_2Sb_2$ [66], $EuMg_2Bi_2$ [68], and $YbMg_2Bi_2$ [68] systematically show higher charge carrier mobilities compared to their main group analogs such as $CaZn_2Sb_2$ [25,69], $SrZn_2Sb_2$ [70], and $CaMg_2Bi_2$ [68]. The interesting mobility trend in AB_2X_2 compounds could not be rationalized by the band effective masses as the theoretical calculations resulted in very similar effective masses for all the members. Thus, the differences in mobilities were attributed to the scattering mechanisms due to the presence of the secondary phases or grain boundaries. However, Hall measurements on $CaMn_2Sb_2$, $YbZn_2Sb_2$, and $EuZn_2Sb_2$ single crystals confirmed that these trends in mobility and charge carrier concentrations are inherent to the materials and the possible impurity effects were eliminated [25]. So, the explanation of the mobility in the AB_2X_2 compounds still remains as a challenge. Moreover, the dependency of the carrier concentrations on the cation electronegativity is observed; the more electronegative the element, the lower the hole carrier concentration. This dependency was initially justified by the different extent of electron donation of the cations to the anionic network [71], so the more electropositive main group donates more electrons and results in low hole concentration. However, this justification has been revisited by Toberer *et al.* [26], who showed that this partial electron donation cannot be the source of the observed trend as the electronegativity cannot change the number of states and, as a result, the carrier concentration. They proposed that

the heavily doped semiconducting behavior in this class of compounds is related to hole production resulting from A-site vacancies. The extent of the vacancy formation depends on the energy required to form a vacancy that increases by making the compounds more ionic; as a result, fewer vacancies are expected when A is a main group metal than the rare-earth metal in AB_2X_2 compounds.

Alloying isoelectronic species in AB_2X_2 compounds controls the extent of the vacancy creation, and the charge carrier concentration can be altered subsequently. Various solid solutions such as $Yb_{1-x}Ca_xZn_2Sb_2$ [71], $Yb_{1-x}Ca_xCd_2Sb_2$ [72], $Eu_{1-x}Yb_xCd_2Sb_2$ [14], $YbZn_{2-x}Mn_xSb_2$ [65], and $YbCd_{2-x}Zn_xSb_2$ [27] have been studied with the goal of tuning the transport properties. These efforts have successfully resulted in reaching zT values >0.95 for $Yb_{0.6}Ca_{0.4}Cd_2Sb_2$ and $Yb_{0.75}Eu_{0.25}Cd_2Sb_2$ solid solutions and zT values >1.2 for $YbCd_{1.6}Zn_{0.4}Sb_2$ at $\sim$700 K.

All of the AB_2X_2 compounds show very low thermal conductivities between $\sim$1 and 3 W/mK, and zT enhancement has been accomplished by maximizing the power factors. These solid solutions produced by isovalent elemental substitutions typically retain carrier concentrations of $\sim 1–10 \times 10^{19}$ carriers/cm^3 which are considered as the optimized carrier concentrations for most good TE materials. The concurrent high mobility in rare-earth-containing materials (327 and 159 cm^2/V s for $YbCd_2Sb_2$ and $EuCd_2Sb_2$, respectively) [14] makes rare-earth-containing AB_2X_2 compounds a promising structure type for TE studies.

2.4 A_2BX_2: Yb_2CdSb_2 Structure Type ($Cmc2_1$)

A_2BX_2 intermetallic compounds can mainly adopt two crystal structure types, namely Yb_2CdSb_2 and Ca_2CdSb_2 which are closely related [73]. In this review, we only focus on the A_2BX_2 intermetallics with Yb_2CdSb_2 crystal structure type. These compounds crystallize in the noncentrosymmetric orthorhombic space group $Cmc2_1$ (No. 36, $Z=4$) containing five independent crystallographic sites of two A, two X, and one B atoms. This structure can be described as a two dimensional $[BX_2]^{4-}$ polyanionic layer extended in *ac* plane as a result of corner sharing of the BX_4 tetrahedra, Fig. 11. "A" atoms occupy the space between the adjacent polyanionic layers. The structure can be rationalized as a charge-balanced Zintl phase by the Zintl–Klemm concept as $[A^{2+}]_2[Cd^{2+}][Sb^{3-}]_2$.

Various Zintl compounds with Yb_2CdSb_2 structure type have been synthesized; most belong to the more electronegative pnictogen analogs such as Ca_2CdP_2 [74], α-Ca_2CdAs_2 [75], Sr_2CdAs_2 [74], Ba_2CdAs_2 [74], and Eu_2CdAs_2 [74]. The only A_2BX_2 rare-earth antimonide compound (A = Yb or Eu; and X = Sb) with Yb_2CdSb_2 crystal structure is Yb_2CdSb_2 itself; Eu_2CdSb_2 does not exist and only its solid solutions such as $Sr_{2-x}Eu_xCdSb_2$, $Ba_{2-x}Eu_xCdSb_2$, $Eu_{2-x}Yb_xCdSb_2$ [76] can preserve the Yb_2CdSb_2 crystal structure in incomplete phase widths which all show distinct coloring mostly

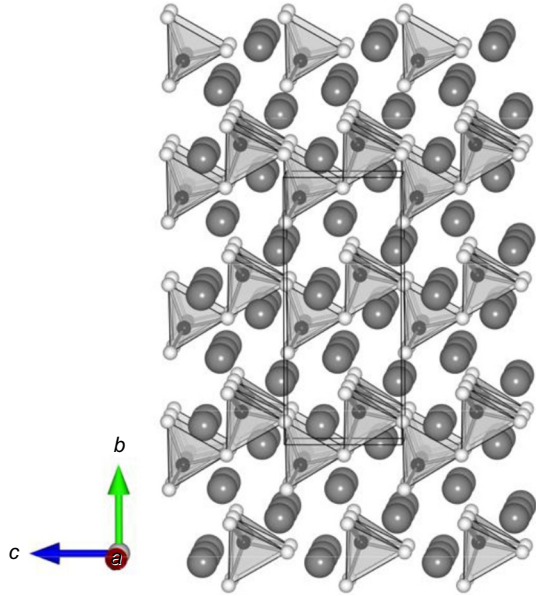

FIG. 11 Structure of A_2BX_2 compound with Yb_2CdSb_2 crystal structure type ($Cmc2_1$), viewed down the *a*-axis. A, B, and X atoms are *large gray*, *small black* (center of tetrahedral), and *white spheres*, respectively. The BX_4 units are shown by transparent tetrahedra, and the unit cell is outlined.

related to the atomic sizes. The richest Eu-containing A_2BX_2 compound is $Eu_{1.6}Yb_{0.4}CdSb_2$ [76].

A_2BX_2 compounds are interesting for TE applications due to the narrow gap semiconducting properties predicted by their electronic band structures [74]. Although the TE properties calculations of α-Ca_2CdAs_2 compounds in this family show promising results [75], following a relatively recent discovery of Yb_2CdSb_2 crystal structure type in 2007 [73], TE properties have not been measured for any of the members. Theoretical calculations suggest a bandgap of 0.96 eV and a relatively high zT value of ∼0.8 at 800 K with the Seebeck coefficient, electrical conductivity, and thermal conductivity of 266 μV/K, 2.8 $(\Omega ms)^{-1}$, and 2.1 W/(mK), respectively, in α-Ca_2CdAs_2 [75]. The low-temperature transport properties measurements for $Eu_{2-x}Yb_xCdSb_2$ also show relatively high Seebeck coefficient and low electrical resistivity values of 220 μV/K and 2.25 mΩ cm, suggesting a very high power factor value of 20.93 μW/(cm K^2) for Yb_2CdSb_2 at room temperature. This is higher than the power factor of $Yb_{0.6}Ca_{0.4}Cd_2Sb_2$ which is ∼13 μW/(cm K^2) at 700 K giving rise to $zT \sim 1$ and is comparable with the power factor of 19.5 of $YbCd_{1.6}Zn_{0.4}Sb_2$ at 700 K with $zT > 1.2$ [76]. Assuming low thermal conductivity, which is typical in Zintl compounds, interesting TE properties are expected in other A_2BX_2 intermetallics compounds.

2.5 $A_{14}BX_{11}$: $Ca_{14}AlSb_{11}$ Structure Type ($I4_1/acd$)

$Yb_{14}MnSb_{11}$ and its derivatives have shown the most promising results to date among bulk Zintl materials for the highest temperature applications. Radioisotope thermal generators for space and terrestrial applications have been designed and developed by the Space and Defense Power Systems programs for over 50 years [77–79]. Plutonium-238 provides the heat through its decay process for the hot side of the TE couple to induce direct current electricity flow. The hot-side temperature requires materials that are stable to 1200 K. While these devices have proven to be highly effective in applications where solar photovoltaics is not an option, new materials for breakthrough TE couples that produce electricity more efficiently than current state of the art are needed. As new multielement-containing materials with high zT are discovered, the potential for further increases in efficiency can be realized. The p-type Zintl phase, $Yb_{14}MnSb_{11}$, has been an important component for increasing efficiencies to 15% for advanced power generation devices at the Jet Propulsions Laboratory [80–83]. This is a significant accomplishment and more than doubles the current radioisotope TE generator efficiency [33,80].

$Yb_{14}MnSb_{11}$ was first reported by Chan *et al.* [84] and crystallizes in the $Ca_{14}AlSb_{11}$ structure type (Fig. 12) [85]. The tetragonal crystal structure is defined by the space group $I4_1/acd$ (no. 142) having nine unique crystallographic positions. With a general formula of $A_{14}MPn_{11}$ (A = Ca, Sr, Ba, Eu, Yb; M = Nb, Mn, Zn, Cd, Al, Ga, In; Pn = P, As, Sb, Bi), there is a large chemical variety possible for the structure type; the combinations reported to date are shown in Table 2. In general, all of these compounds consist of $14A^{2+}$ cations, a MPn_4^{9-} anion, a Pn_3^{7-} linear chain, and four Pn^{3-} anions. The tetrahedral and linear units are alternately stacked along the c-axis, and the linear unit is rotated 90 degree with respect to the previous linear unit. In the case of $Ca_{14}AlSb_{11}$, the compound is valence-precise as Al is formally 3+ and Pn_3^{7-} is considered as a hypervalent valence-precise anion [99]. This is the only Zintl phase described in this review that consists of distinct anionic units rather than the extended anionic networks [99–101].

$Yb_{14}MnSb_{11}$ is ferromagnetic, with the Mn moments ordering below 56 K through a Ruderman–Kittel–Kasuya–Yosida (RKKY) interaction, where the mobile charge carries couple the localized spins [84]. Initial magnetic measurements suggested Mn to be in the 3+ state with Yb in the 2+ state [102]; X-ray magnetic circular dichroism confirmed Yb as Yb^{2+} and showed Mn to be Mn^{2+} with a parallel hole localized on the Sb in the tetrahedron [103].

$Yb_{14}MnSb_{11}$ is an excellent high temperature p-type TE material [33,80]. According to Zintl electron counting, it is one electron deficient when M = Mn, as Mn is present as Mn^{2+} [100,103,104]. In part, the high zT for this compound can be attributed to its low thermal conductivity, due to the heavy

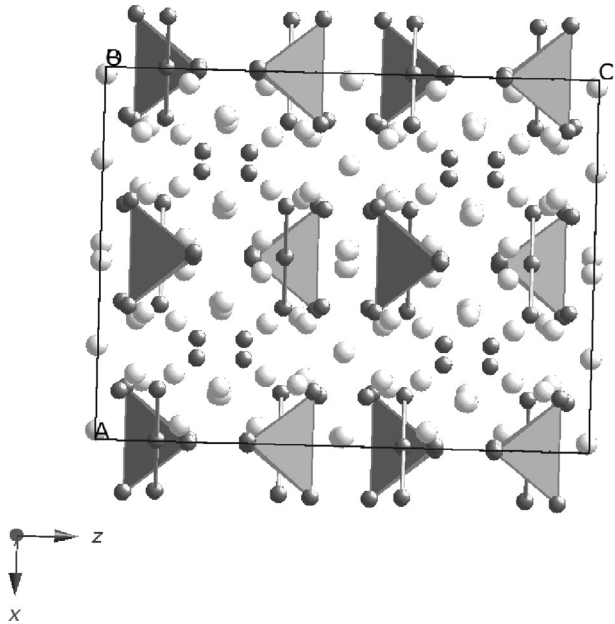

FIG. 12 A projection along the *b*-axis of the structure of $Yb_{14}MnSb_{11}$ with Yb in *white*, Mn are not shown in the center of the tetrahedra, and Sb in *dark gray*.

atoms and the complex structure described earlier [105]. While the electronic properties of $Yb_{14}MnSb_{11}$ are also favorable, they can be further improved [24,106,107]. The carrier concentration of $Yb_{14}MnSb_{11}$ is too high to achieve optimal zT, and the thermopower (α^2/ρ) can be enhanced by reducing the carrier concentration.

The ideal Zintl composition is reflected in the first compound prepared with this structure type, $Ca_{14}AlSb_{11}$ [85]. Since the publication of this structure type, a number of TM-containing analogs have been reported with M = Mn, Zn, Cd, and Nb [89,92–94,97,98,108–111]. Within these compositions, the TM oxidation state is variable with Mn, Zn, Cd being 2+ and Nb being 5+. These oxidation states lead to a compound that is one electron deficient, in the case of M = Mn, and more complex structures for M = Zn, Cd, and Nb [92–94]. In the case of Nb, it has only been reported for two compounds to date: $Sr_{14-x}NbAs_{11}$ and $Eu_{14-x}NbAs_{11}$ [94]. The +5 oxidation state of Nb leads to a defect in the cation site (one less 2+ cation in the formula), providing a valence-precise compound, $A_{13}NbAs_{11}$ (A = Sr, Eu). Both of the 2+ rare-earth elements, Eu and Yb, also form this structure type [84,102,112–115]. Aside from the group 13 elements, Mg also substitutes on the M site [116].

Solid solutions of $Yb_{14}MnSb_{11}$ have been recently prepared in order to increase the TE figure of merit of this p-type high temperature material [33].

TABLE 2 Elemental Compositions for $A_{14}MPn_{11}$ Reported to Date

		A				
		Ca	*Sr*	*Ba*	*Eu*	*Yb*
Pn	P	M = Mn [86] M = Ga [87]	–	–	M = Mn [88]	–
	As	M = Mn [89] M = Ga [90,91]	M = Mn [89] M = Ga [91] M = Cd [92] M = Nb [93]	M = Mn [89]	M = Mn [88] M = Cd [92] M = Nb [93]	–
	Sb	M = Mn [89] M = Zn [94] M = Cd [94] M = Al [95]	M = Mn [89] M = Al [95] M = Zn [94] M = Cd [92,94]	M = Mn [89] M = Al [95]	M = Mn [96] M = In [96] M = Cd [92]	M = Mn [84] M = Zn [97]
	Bi	M = Mn [98]	M = Mn [98]	M = Mn [98]	M = Mn [96] M = In [96]	M = Mn [84]

Solid solutions of La [107,117], Ce [118], Pr and Sm [119], Gd [120], Tm [121,122], and Lu [123] substitution for Yb, Al [24] and Zn [124] for Mn, and Ge [125] and Te [126] for Sb substitution have been reported with an emphasis on controlling carrier concentration in this structure type, although their magnetic properties are also of interest [118]. The maximum amount of each R substituted for Yb was determined to be 0.7 for La, 0.6 for Ce, and 0.5 for Tm [117,118,121]. However, it is likely that these are slightly overestimated as it appears that the nominal $x \sim 0.4$ is the average maximum solubility for the entire R series, $Yb_{14-x}R_xMnSb_{11}$ [127]. In the case of Ce, site preferences are apparent where Ce initially occupies the Yb2 site and when $x \geq 0.3$, it also substitutes on Yb4 [118]. These sites have the largest volume as indicated by Hirshfeld surface analysis of chemical bonding [128].

Low-temperature magnetization vs applied magnetic field data of samples with Ce substitution indicate that the Ce^{3+} moment does not participate in the ferromagnetic ordering of the material [118]. Temperature-dependent magnetization data for La^{3+}, Tm^{3+}, and Ce^{3+} substitutions show a decrease in the magnetic ordering temperature, which is attributed to the reduction in carrier concentration resulting in an increase in the effective magnetic moment of the material. This is due to the additional electron introduced by substituting a 3+ cation for a 2+ cation filling the hole associated with the $MnSb_4$ tetrahedron and thereby reducing the screening of the 3d electron. Changing carrier concentration is not the only method for improving TE properties; when Zn is substituted for Mn, there is a decrease in electrical resistivity due to a reduction in carrier scattering from the magnetic moments on Mn [124]. It has also been shown that applying pressure to $Yb_{14}MnSb_{11}$ can increase the Seebeck coefficient and resistivity, causing a net improvement in zT [129]. Various solid solutions reported to date and their relevant TE properties are provided in Table 3.

3 CONCLUDING REMARKS

As discussed in this review, substantial progress in chemistry of Zintl compounds targeting improved TE performance has been achieved during the last 15 years. At least one structure type, namely A_2BX_2, can be expected to have some potential but TE properties have not yet been reported. Importantly, all materials have been studied for TE application in the form of pressed pellets obtained through consolidation of bulk polycrystalline materials. Zintl phases with antimony typically show a high structural flexibility that provides numerous opportunities for substitutional alloying on the cation, TM, and Sb sites. In some cases, however, for example, $Eu_{11}Cd_{6-x}Zn_xSb_{12}$ where both end members have the same crystal structure, an immiscibility gap can develop and the solid solution terminates, thus naturally limiting chemical tuning options. Moreover, in many cases, the alloyed element is not randomly distributed in the structure as a result of a coloring

TABLE 3 Various Solid Solutions and Their Relevant Thermoelectric Data at 1000 K for $Yb_{14-x}A_xMn_{1-y}B_ySb_{11-z}X_z$

	A = Ca [130]	A = La [107]	A = Tm [122]	B = Zn [124]	B = Al [24]	X = Te [126]
x, *y*, *z*	1, 0, 0	0.4, 0, 0	0.4, 0, 0	0, 0.4, 0	0, 0.6, 0	0, 0, 0.07
cc ($\times 10^{20}$ cm^3)	–	6	9	–	–	
μ ($cm^2/V^1/s^1$)	–	4	–	–	–	
k (W/mK)	0.8	0.6	1	0.9	0.7	0.75
ρ (mΩ cm)	5	7.5	6	3.5		6
α (μV/K)	180	200	200	175		190
zT	0.7	1	0.7	0.8	0.9	0.8

phenomenon. This has been observed in $Eu_{11}Cd_6Sb_{12-x}As_x$, $Eu_{11-x}Yb_xCd_6Sb_{12}$, $Eu_9Cd_4CMSb_9$, and $Yb_{14-x}RE_xMnSb_{11}$ solid solutions.

New bulk Zintl materials with $zT > 1.0$ over both intermediate and high temperatures have been synthesized during the past decade. These include $YbCd_{1.6}Zn_{0.4}Sb_2$ with zT of 1.2 at ~700 K [27], and $Yb_{14}Mn_{0.4}Al_{0.6}Sb_{11}$ with zT of 1.3 at ~1200 K [106]. None of these materials have been further improved/optimized by engineering/nanotechnology/superlattice fabrications. This leaves significant potential for further development of Zintl phase-based TE materials in the future. Although TE research has made significant progress during a short period of time, the desired optimal structure to achieve ideal PGEC properties remains elusive and the search for new systems will undoubtedly result in even greater advances.

ACKNOWLEDGMENTS

Many of the results reported in this perspective review have been generously supported by the National Science Foundation (NSF DMR-1405973) and by the Nuclear Energy University Program (NEUP). S.M.K. thanks Jason Grebenkemper for the paragraph concerning $Yb_{14}MnSb_{11}$ which is adapted from his dissertation.

REFERENCES

[1] J.R. Sootsman, D.Y. Chung, M.G. Kanatzidis, New and old concepts in thermoelectric materials, Angew. Chem. Int. Ed. 48 (2009) 8616–8639.
[2] K. Salzgeber, P. Prenninger, A. Grytsiv, P. Rogl, E. Bauer, Skutterudites: thermoelectric materials for automotive applications? J. Electron. Mater. 39 (2010) 2074–2078.
[3] T.M. Terry, T. Xinfeng, Z. Qingjie, X. Wenjie, et al., Solar thermoelectrics: direct solar thermal energy conversion, in: D.S. David, D. Cahen (Eds.), Fundamentals of Materials for Energy and Environmental Sustainability, Cambridge University Press, Cambridge, 2011.
[4] L.E. Bell, Cooling, heating, generating power, and recovering waste heat with thermoelectric systems, Science 321 (2008) 1457–1461.
[5] G.J. Snyder, E.S. Toberer, Complex thermoelectric materials, Nat. Mater. 7 (2008) 105–114.
[6] G.W. Crabtree, N.S. Lewis, Solar energy conversion, Phys. Today 60 (2007) 37–42. print edition.
[7] C.B. Vining, ZT ~ 3.5: fifteen years of progress and things to come, in: European Conference on Thermoelectrics, 2007.
[8] C.B. Vining, An inconvenient truth about thermoelectrics, Nat. Mater. 8 (2009) 83–85.
[9] D. Kraemer, B. Poudel, H.-P. Feng, J.C. Caylor, B. Yu, X. Yan, Y. Ma, X. Wang, D. Wang, A. Muto, K. McEnaney, M. Chiesa, Z. Ren, G. Chen, High-performance flat-panel solar thermoelectric generators with high thermal concentration, Nat. Mater. 10 (2011) 532–538.
[10] S. Kumar, S. Heister, X. Xu, J. Salvador, G. Meisner, Thermoelectric generators for automotive waste heat recovery systems part I: numerical modeling and baseline model analysis, J. Electron. Mater. 42 (2013) 665–674.
[11] M. Cutler, J. Leavy, R. Fitzpatrick, Electronic transport in semimetallic cerium sulfide, Phys. Rev. 133 (1964) A1143.
[12] S.M. Kauzlarich, S.R. Brown, G. Jeffrey Snyder, Zintl phases for thermoelectric devices, Dalton Trans. (2007) 2099–2107.

[13] P.H. Ngan, D.V. Christensen, G.J. Snyder, L.T. Hung, S. Linderoth, N.V. Nong, N. Pryds, Towards high efficiency segmented thermoelectric unicouples, Phys. Status Solidi A 211 (2014) 9–17.
[14] H. Zhang, L. Fang, M.-B. Tang, Z.Y. Man, H.H. Chen, X.X. Yang, M. Baitinger, Y. Grin, J.-T. Zhao, Thermoelectric properties of $Yb_xEu_{1-x}Cd_2Sb_2$, J. Chem. Phys. 133 (2010) 194701.
[15] Z.-G. Chen, G. Han, L. Yang, L. Cheng, J. Zou, Nanostructured thermoelectric materials: current research and future challenge, Prog. Nat. Sci. 22 (2012) 535–549.
[16] L. Kong, T. Li, H. Hng, F. Boey, T. Zhang, S. Li, Waste thermal energy harvesting (I): thermoelectric effect, in: Waste Energy Harvesting, Springer, Berlin Heidelberg, 2014, pp. 263–403.
[17] K. Biswas, J. He, I.D. Blum, C.-I. Wu, T.P. Hogan, D.N. Seidman, V.P. Dravid, M.G. Kanatzidis, High-performance bulk thermoelectrics with all-scale hierarchical architectures, Nature 489 (2012) 414–418.
[18] R. Venkatasubramanian, E. Siivola, T. Colpitts, B. O'Quinn, Thin-film thermoelectric devices with high room-temperature figures of merit, Nature 413 (2001) 597–602.
[19] T.C. Harman, M.P. Walsh, B.E. LaForge, G.W. Turner, Nanostructured thermoelectric materials, J. Electron. Mater. 34 (2005) L19–L22.
[20] E.S. Toberer, A.F. May, G.J. Snyder, Zintl chemistry for designing high efficiency thermoelectric materials, Chem. Mater. 22 (2009) 624–634.
[21] T.M. Tritt, M.A. Subramanian, Thermoelectric materials, phenomena, and applications: a bird's eye view, MRS Bull. 31 (2006) 188–198.
[22] R. Nesper, The Zintl-Klemm concept—a historical survey, Z. Anorg. Allg. Chem. 640 (2014) 2639–2648.
[23] R. Nesper, Bonding patterns in intermetallic compounds, Angew. Chem. Int. Ed. Engl. 30 (1991) 789–817.
[24] C.A. Cox, E.S. Toberer, A.A. Levchenko, S.R. Brown, G.J. Snyder, A. Navrotsky, S.M. Kauzlarich, Structure, heat capacity, and high-temperature thermal properties of $Yb_{14}Mn_{1-x}Al_xSb_{11}$, Chem. Mater. 21 (2009) 1354–1360.
[25] A.F. May, M.A. McGuire, J. Ma, O. Delaire, A. Huq, R. Custelcean, Properties of single crystalline AZn_2Sb_2 (A = Ca, Eu, Yb), J. Appl. Phys. 111 (2012) 033708.
[26] E.S. Toberer, A.F. May, B.C. Melot, E. Flage-Larsen, G.J. Snyder, Electronic structure and transport in thermoelectric compounds AZn_2Sb_2 (A = Sr, Ca, Yb, Eu), Dalton Trans. 39 (2010) 1046–1054.
[27] X.-J. Wang, M.-B. Tang, H.-H. Chen, X.-X. Yang, J.-T. Zhao, U. Burkhardt, Y. Grin, Synthesis and high thermoelectric efficiency of Zintl phase $YbCd_{2-x}Zn_xSb_2$, Appl. Phys. Lett. 94 (2009) 092106.
[28] B. Saparov, S. Bobev, A. Ozbay, E.R. Nowak, Synthesis, structure and physical properties of the new Zintl phases $Eu_{11}Zn_6Sb_{12}$ and $Eu_{11}Cd6Sb_{12}$, J. Solid State Chem. 181 (2008) 2690–2696.
[29] S.-M. Park, S.-J. Kim, $Sr_{11}Cd_6Sb_{12}$: a new Zintl compound with infinite chains of pentagonal tubes, J. Solid State Chem. 177 (2004) 3418–3422.
[30] N. Kazem, A. Hurtado, F. Sui, S. Ohno, A. Zevalkink, J.G. Snyder, S.M. Kauzlarich, High temperature thermoelectric properties of the solid-solution Zintl phase $Eu_{11}Cd_{6-x}Zn_xSb_{12}$, Chem. Mater. 27 (2015) 4413–4421.
[31] N. Kazem, W. Xie, S. Ohno, A. Zevalkink, G.J. Miller, G.J. Snyder, S.M. Kauzlarich, High-temperature thermoelectric properties of the solid–solution Zintl phase $Eu_{11}Cd_6Sb_{12-x}As_x$ ($x < 3$), Chem. Mater. 26 (2014) 1393–1403.
[32] G.J. Miller, The "coloring problem" in solids: how it affects structure, composition and properties, Eur. J. Inorg. Chem. 1998 (1998) 523–536.

[33] S.R. Brown, S.M. Kauzlarich, F. Gascoin, G.J. Snyder, $Yb_{14}MnSb_{11}$: new high efficiency thermoelectric material for power generation, Chem. Mater. 18 (2006) 1873–1877.

[34] G.S. Pomrehn, A. Zevalkink, W.G. Zeier, A. van de Walle, G.J. Snyder, Defect-controlled electronic properties in AZn_2Sb_2 Zintl phases, Angew. Chem. 126 (2014) 3490–3494.

[35] S.-Q. Xia, S. Bobev, Are $Ba_{11}Cd_6Sb_{12}$ and $Sr_{11}Cd_6Sb_{12}$ Zintl phases or not? A density-functional theory study, J. Comput. Chem. 29 (2008) 2125–2133.

[36] S.K. Bux, A. Zevalkink, O. Janka, D. Uhl, S. Kauzlarich, J.G. Snyder, J.-P. Fleurial, Glass-like lattice thermal conductivity and high thermoelectric efficiency in $Yb_9Mn_{4.2}Sb_9$, J. Mater. Chem. A 2 (2014) 215–220.

[37] S. Bobev, J.D. Thompson, J.L. Sarrao, M.M. Olmstead, H. Hope, S.M. Kauzlarich, Probing the limits of the Zintl concept: structure and bonding in rare-earth and alkaline-earth zinc-antimonides $Yb_9Zn_{4+x}Sb_9$ and $Ca_9Zn_{4.5}Sb_9$, Inorg. Chem. 43 (2004) 5044–5052.

[38] N. Kazem, A. Hurtado, B. Klobes, R.P. Hermann, S.M. Kauzlarich, $Eu_9Cd_{4-x}CM_{2+x-y}\square_ySb_9$: $Ca_9Mn_4Bi_9$-type structure stuffed with coinage metals (Cu, Ag, and Au) and the challenges with classical valence theory in describing these possible Zintl phases, Inorg. Chem. 54 (2015) 850–859.

[39] S.-Q. Xia, S. Bobev, New manganese-bearing antimonides and bismuthides with complex structures. synthesis, structural characterization, and electronic properties of $Yb_9Mn_{4+x}Pn_9$ (Pn = Sb or Bi), Chem. Mater. 22 (2010) 840–850.

[40] S.-J. Kim, J. Salvador, D. Bilc, S.D. Mahanti, M.G. Kanatzidis, $Yb_9Zn_4Bi_9$: extension of the Zintl concept to the mixed-valent spectator cations, J. Am. Chem. Soc. 123 (2001) 12704–12705.

[41] S.-q. Xia, S. Bobev, Interplay between size and electronic effects in determining the homogeneity range of the $A_9Zn_{4+x}Pn_9$ and $A_9Cd_{4+x}Pn_9$ phases ($0 \le x \le 0.5$), A = Ca, Sr, Yb, Eu; Pn = Sb, Bi, J. Am. Chem. Soc. 129 (2007) 10011–10018.

[42] X.-C. Liu, Z. Wu, S.-Q. Xia, X.-T. Tao, S. Bobev, Structural variability versus structural flexibility. a case study of $Eu_9Cd_{4+x}Sb_9$ and $Ca_9Mn_{4+x}Sb_9$ ($x \approx 1/2$), Inorg. Chem. 54 (2015) 947–955.

[43] M. Mantina, R. Valero, C.J. Cramer, D.G. Truhlar, Atomic radii of the elements, in: W.M. Haynes (Ed.), CRC Handbook of Chemistry and Physics, 94th ed., CRC Press, London, 2013.

[44] N. Kazem, J.V. Zaikina, S. Ohno, G.J. Snyder, S.M. Kauzlarich, Coinage-metal-stuffed $Eu_9Cd_4Sb_9$: metallic compounds with anomalous low thermal conductivities, Chem. Mater. 27 (2015) 7508–7519.

[45] B. Poudel, Q. Hao, Y. Ma, Y. Lan, A. Minnich, B. Yu, X. Yan, D. Wang, A. Muto, D. Vashaee, X. Chen, J. Liu, M.S. Dresselhaus, G. Chen, Z. Ren, High-thermoelectric performance of nanostructured bismuth antimony telluride bulk alloys, Science 320 (2008) 634–638.

[46] X. Shi, J. Yang, J.R. Salvador, M. Chi, J.Y. Cho, H. Wang, S. Bai, J. Yang, W. Zhang, L. Chen, Multiple-filled skutterudites: high thermoelectric figure of merit through separately optimizing electrical and thermal transports, J. Am. Chem. Soc. 133 (2011) 7837–7846.

[47] D.C. Schmitt, N. Haldolaarachchige, Y. Xiong, D.P. Young, R. Jin, J.Y. Chan, Probing the lower limit of lattice thermal conductivity in an ordered extended solid: $Gd_{117}Co_{56}Sn_{112}$, a phonon glass–electron crystal system, J. Am. Chem. Soc. 134 (2012) 5965–5973.

[48] K. Kurosaki, A. Kosuga, H. Muta, M. Uno, S. Yamanaka, Ag_9TlTe_5: a high-performance thermoelectric bulk material with extremely low thermal conductivity, Appl. Phys. Lett. 87 (2005) 061919.

[49] J. Fulmer, O.I. Lebedev, V.V. Roddatis, D.C. Kaseman, S. Sen, J.-A. Dolyniuk, K. Lee, A. V. Olenev, K. Kovnir, Clathrate $Ba_8Au_{16}P_{30}$: the "Gold Standard" for lattice thermal conductivity, J. Am. Chem. Soc. 135 (2013) 12313–12323.

[50] S. Ohno, A. Zevalkink, Y. Takagiwa, S.K. Bux, G.J. Snyder, Thermoelectric properties of the $Yb_9Mn_{4.2-x}Zn_xSb_9$ solid solutions, J. Mater. Chem. A 2 (2014) 7478–7483.

[51] E.S. Toberer, A. Zevalkink, G.J. Snyder, Phonon engineering through crystal chemistry, J. Mater. Chem. 21 (2011) 15843–15852.

[52] G.K.H. Madsen, Automated search for new thermoelectric materials: the case of LiZnSb, J. Am. Chem. Soc. 128 (2006) 12140–12146.

[53] A.F. May, E.S. Toberer, G.J. Snyder, Transport properties of the layered Zintl compound $SrZnSb_2$, J. Appl. Phys. 106 (2009) 013706.

[54] C.L. Condron, S.M. Kauzlarich, F. Gascoin, G.J. Snyder, Thermoelectric properties and microstructure of Mg_3Sb_2, J. Solid State Chem. 179 (2006) 2252–2257.

[55] S.-J. Kim, J.R. Ireland, C.R. Kannewurf, M.G. Kanatzidis, $Yb_5In_2Sb_6$: a new rare earth Zintl phase with a narrow band gap, J. Solid State Chem. 155 (2000) 55–61.

[56] S.-J. Kim, S. Hu, C. Uher, M.G. Kanatzidis, $Ba_4In_8Sb_{16}$: thermoelectric properties of a new layered Zintl phase with infinite zigzag Sb chains and pentagonal tubes, Chem. Mater. 11 (1999) 3154–3159.

[57] A. Zevalkink, G.S. Pomrehn, Y. Takagiwa, J. Swallow, G. Snyder, Thermoelectric properties and electronic structure of the Zintl phases Sr_3AlSb_3, Chem. Sus. Chem. 6 (12) (2013) 2316–2321.

[58] X.-J. Wang, M.-B. Tang, J.-T. Zhao, H.-H. Chen, X.-X. Yang, Thermoelectric properties and electronic structure of Zintl compound $BaZn_2Sb_2$, Appl. Phys. Lett. 90 (2007) 232107-1–232107-3.

[59] E.S. Toberer, A. Zevalkink, N. Crisosto, G.J. Snyder, The Zintl compound $Ca_5Al_2Sb_6$ for low-cost thermoelectric power generation, Adv. Funct. Mater. 20 (2010) 4375–4380.

[60] A. Zevalkink, W.G. Zeier, G. Pomrehn, E. Schechtel, W. Tremel, G.J. Snyder, Thermoelectric properties of Sr_3GaSb_3—a chain-forming Zintl compound, Energy Environ. Sci. 5 (2012) 9121–9128.

[61] S.R. Brown, S.M. Kauzlarich, F. Gascoin, G. Jeffrey Snyder, High-temperature thermoelectric studies of $A_{11}Sb_{10}$ (A=Yb, Ca), J. Solid State Chem. 180 (2007) 1414–1420.

[62] T. Yi, C.A. Cox, E.S. Toberer, G.J. Snyder, S.M. Kauzlarich, High-temperature transport properties of the Zintl phases $Yb_{11}GaSb_9$ and $Yb_{11}InSb_9$, Chem. Mater. 22 (2009) 935–941.

[63] O.Y. Zelinska, A.V. Tkachuk, A.P. Grosvenor, A. Mar, Structure and physical properties of $YbZn_2Sb_2$ and $YbCd_2Sb_2$, Chem. Met. Alloys 1 (2008) 204–209.

[64] A.V. Morozkin, O. Isnard, P. Henry, S. Granovsky, R. Nirmala, P. Manfrinetti, Synthesis and magnetic structure of the YbMn2Sb2 compound, J. Alloys Compd. 420 (2006) 34–36.

[65] T.J. Zhu, C. Yu, J. He, S.N. Zhang, X.B. Zhao, T. Tritt, Thermoelectric properties of Zintl compound $YbZn_2Sb_2$ with Mn substitution in anionic framework, J. Electron. Mater. 38 (2009) 1068–1071.

[66] H. Zhang, J.-T. Zhao, Y. Grin, X.-J. Wang, M.-B. Tang, Z.-Y. Man, H.-H. Chen, X.-X. Yang, A new type of thermoelectric material, $EuZn_2Sb_2$, J. Chem. Phys. 129 (2008) 164713.

[67] C. Zheng, R. Hoffmann, R. Nesper, H.G. Von Schnering, Site preferences and bond length differences in $CaAl_2Si_2$-type Zintl compounds, J. Am. Chem. Soc. 108 (1986) 1876–1884.

[68] A.F. May, M.A. McGuire, D.J. Singh, R. Custelcean, G.E. Jellison Jr., Structure and properties of single crystalline $CaMg_2Bi_2$, $EuMg_2Bi_2$, and $YbMg_2Bi_2$, Inorg. Chem. 50 (2011) 11127–11133.

[69] D. Stark, G.N. Snyder, The synthesis of CaZn2Sb2 and its thermoelectric properties, in: Thermoelectrics, 2002. Proceedings ICT '02. Twenty-First International Conference on 25–29 August, 2002, pp. 181–184.

[70] H. Zhang, M.-B. Tang, W. Schnelle, M. Baitinger, Z.-Y. Man, H.-H. Chen, X.-X. Yang, J.-T. Zhao, Y. Grin, Thermoelectric properties of polycrystalline $SrZn_2Sb_2$ prepared by spark plasma sintering, J. Electron. Mater. 39 (2010) 1772–1776.

[71] F. Gascoin, S. Ottensmann, D. Stark, S.M. Haïle, G.J. Snyder, Zintl phases as thermoelectric materials: tuned transport properties of the compounds $Ca_xYb_{1-x}Zn_2Sb_2$, Adv. Funct. Mater. 15 (2005) 1860–1864.

[72] Q. Cao, M. Tang, G. Ma, H. Chen, X. Yang, J. Zhao, Transport properties of Zintl phase $Yb_{1-x}Ca_xCd_2Sb_2$ at low temperature, J. Rare Earths 28 (2010) 403–406.

[73] S.-q. Xia, S. Bobev, Cation−anion interactions as structure directing factors: structure and bonding of Ca_2CdSb_2 and Yb_2CdSb_2, J. Am. Chem. Soc. 129 (2007) 4049–4057.

[74] J. Wang, M. Yang, M.-Y. Pan, S.-Q. Xia, X.-T. Tao, H. He, G. Darone, S. Bobev, Synthesis, crystal and electronic structures, and properties of the new pnictide semiconductors A_2CdPn_2 (A = Ca, Sr, Ba, Eu; Pn = P, As), Inorg. Chem. 50 (2011) 8020–8027.

[75] W. Khan, J. Minar, Theoretical study on optical and thermoelectric properties of the direct band gap α/β Ca_2CdAs_2 pnictide semiconductors, RSC Adv. 4 (2014) 46791–46799.

[76] B. Saparov, M. Saito, S. Bobev, Syntheses, and crystal and electronic structures of the new Zintl phases Na_2ACdSb_2 and K_2ACdSb_2 (A=Ca, Sr, Ba, Eu, Yb): structural relationship with Yb_2CdSb_2 and the solid solutions $Sr_{2-x}A_xCdSb_2$, $Ba_{2-x}A_xCdSb_2$ and $Eu_{2-x}Yb_xCdSb_2$, J. Solid State Chem. 184 (2011) 432–440.

[77] S.B. Riffat, X. Ma, Thermoelectrics: a review of present and potential applications, Appl. Therm. Eng. 23 (2003) 913–935.

[78] S. LeBlanc, Thermoelectric generators: linking material properties and systems engineering for waste heat recovery applications, Sustain. Mater. Technol. 1 (2014) 26–35.

[79] J. Yang, T. Caillat, Thermoelectric materials for space and automotive power generation, MRS Bull. 31 (2006) 224–229.

[80] J.H. Grebenkemper, Y. Hu, D. Barrett, P. Gogna, C.-K. Huang, S.K. Bux, S.M. Kauzlarich, High temperature thermoelectric properties of $Yb_{14}MnSb_{11}$ prepared from reaction of MnSb with the elements, Chem. Mater. 27 (2015) 5791–5798.

[81] F. Jean-Pierre, B. Sabah, C. Thierry, Engineering of novel thermoelectric materials and devices for next generation, long life, 20% efficient space power systems, in: 11th International Energy Conversion Engineering Conference, American Institute of Aeronautics and Astronautics, 2013.

[82] E. Brandon, T. Caillat, J.-P. Fleurial, R. Ewell, B. Li, S. Firdosy, J.-A. Paik, G. Nakatsukasa, C.-K. Huang, B. Nesmith, Development of new high temperature power generating couples for the Advanced Thermoelectric Converter (ATEC), in: 40th International Conference on Environmental Systems, 2010. p. 7004.

[83] T. Caillat, S. Firdosy, B. Li, V. Ravi, J.-A. Paik, G. Nakatsukasa, C.-K. Huang, D. Uhl, N. Keyawa, J. Chase, J.-P. Fleurial, Progress status of the development of high-efficiency segmented thermoelectric couples, in: 11th International Energy Conversion Engineering Conference, AIAA 2013, San Jose, CA, 2013. p. 3928 (+6).

[84] J.Y. Chan, M.M. Olmstead, S.M. Kauzlarich, D.J. Webb, Structure and ferromagnetism of the rare-earth zintl compounds: $Yb_{14}MnSb_{11}$ and $Yb_{14}MnBi_{11}$, Chem. Mater. 10 (1998) 3583–3588.

[85] G. Cordier, H. Schäfer, M. Stelter, Darstellung und Struktur der Verbindung $Ca_{14}AlSb_{11}$, Z. Anorg. Allg. Chem. 519 (1984) 183–188.

[86] H. Kim, S.M. Kauzlarich, Structure and magnetic properties of $Ca_{14}MnP_{11}$, J. Solid State Chem. 178 (2005) 1935–1939.

[87] J.T. Vaughey, J.D. Corbett, Synthesis and structure of $Ca_{14}GaP_{11}$ with the new hypervalent P_3^{7-} anion. Matrix effects within the family of isostructural alkaline-earth metal pnictides, Chem. Mater. 8 (1996) 671–675.

[88] A.C. Payne, M.M. Olmstead, S.M. Kauzlarich, D.J. Webb, Structure, magnetism, and magnetoresistance of the compounds $Eu_{14}MnAs_{11}$ and $Eu_{14}MnP_{11}$, Chem. Mater. 13 (2001) 1398–1406.

[89] A. Rehr, T.Y. Kuromoto, S.M. Kauzlarich, J. Delcastillo, D.J. Webb, Structure and properties of the transition-metal Zintl compounds $A_{14}MnPn_{11}$ (A=Ca, Sr, Ba Pn=As, Sb), Chem. Mater. 6 (1994) 93–99.

[90] S.M. Kauzlarich, M.M. Thomas, D.A. Odink, M.M. Olmstead, $Ca_{14}GaAs_{11}$: a new compound containing discrete $GaAs_4$ tetrahedra and a hypervalent As_3 polyatomic unit, J. Am. Chem. Soc. 113 (1991) 7205–7208.

[91] S. Kauzlarich, T.Y. Kuromoto, Exploring the structure and bonding of the Zintl compounds: $A_{14}GaAs_{11}$ (A=Ca, Sr), Croat. Chem. Acta 64 (1991) 343–352.

[92] J.P.A. Makongo, G.M. Darone, S.-Q. Xia, S. Bobev, Non-stoichiometric compositions arising from synergistic electronic and size effects. Synthesis, crystal chemistry and electronic properties of $A_{14}Cd_{1+x}Pn_{11}$ compounds ($0 \le x \le 0.3$; A=Sr, Eu; Pn=As, Sb), J. Mater. Chem. C 3 (2015) 10388–10400.

[93] K. Vidyasagar, W. Honle, H.G. von Schnering, $Sr_{13}NbAs_{11}$ and $Eu_{13}NbAs_{11}$—defect variants of the $Ca_{14}AlSb_{11}$ structure with asymmetric $[As_3]^{7-}$ anions, Z. Anorg. Allg. Chem. 622 (1996) 518–524.

[94] D.M. Young, C.C. Torardi, M.M. Olmstead, S.M. Kauzlarich, Exploring the limits of the Zintl concept for the $A_{14}MPn_{11}$ structure type with M=Zn, Cd, Chem. Mater. 7 (1995) 93–101.

[95] S.L. Brock, L.J. Weston, M.M. Olmstead, S.M. Kauzlarich, Synthesis, structure, and properties of $A_{14}AlSb_{11}$ (A=Ca, Sr, Ba), J. Solid State Chem. 107 (1993) 513–523.

[96] J.Y. Chan, M.E. Wang, A. Rehr, S.M. Kauzlarich, D.J. Webb, Synthesis, structure, and magnetic properties of the rare-earth Zintl compounds $Eu_{14}MnPn_{11}$ and $Eu_{14}InPn_{11}$ (Pn=Sb, Bi), Chem. Mater. 9 (1997) 2131–2138.

[97] I. Fisher, S. Bud'ko, C. Song, P. Canfield, T. Ozawa, S. Kauzlarich, $Yb_{14}ZnSb_{11}$: charge balance in Zintl compounds as a route to intermediate Yb valence, Phys. Rev. Lett. 85 (2000) 1120–1123.

[98] T.Y. Kuromoto, S.M. Kauzlarich, D.J. Webb, Structure and properties of the transition-metal zintl compounds: $A_{14}MnBi_{11}$ (A=Ca, Sr, Ba), Chem. Mater. 4 (1992) 435–440.

[99] R.F. Gallup, C.Y. Fong, S.M. Kauzlarich, Bonding properties of $Ca_{14}GaAs_{11}$—a compound containing discrete $GaAs_4$ tetrahedra and a hypervalent As_3 polyatomic unit, Inorg. Chem. 31 (1992) 115–118.

[100] D. Sánchez-Portal, R.M. Martin, S.M. Kauzlarich, W.E. Pickett, Bonding, moment formation, and magnetic interactions in $Ca_{14}MnBi_{11}$ and $Ba_{14}MnBi_{11}$, Phys. Rev. B 65 (2002) 144414.

[101] H. Kleinke, New bulk materials for thermoelectric power generation: clathrates and complex antimonides, Chem. Mater. 22 (2010) 604–611.

[102] I.R. Fisher, T.A. Wiener, S.L. Bud'ko, P.C. Canfield, J.Y. Chan, S.M. Kauzlarich, Thermodynamic and transport properties of single-crystal $Yb_{14}MnSb_{11}$, Phys. Rev. B Condens. Matter Mater. Phys. 59 (1999) 13829–13834.

[103] A.P. Holm, S.M. Kauzlarich, S.A. Morton, G.D. Waddill, W.E. Pickett, J.G. Tobin, XMCD characterization of the ferromagnetic state of $Yb_{14}MnSb_{11}$, J. Am. Chem. Soc. 124 (2002) 9894–9898.

[104] A.P. Holm, T.C. Ozawa, S.M. Kauzlarich, S.A. Morton, G.D. Waddill, J.G. Tobin, X-ray photoelectron spectroscopy studies of $Yb_{14}MnSb_{11}$ and $Yb_{14}ZnSb_{11}$, J. Solid State Chem. 178 (2005) 262–269.

[105] A. Möchel, I. Sergueev, H.C. Wille, F. Juranyi, H. Schober, W. Schweika, S.R. Brown, S. M. Kauzlarich, R.P. Hermann, Lattice dynamics in the thermoelectric Zintl compound $Yb_{14}MnSb_{11}$, Phys. Rev. B 84 (2011) 184303.

[106] E.S. Toberer, C.A. Cox, S.R. Brown, T. Ikeda, A.F. May, S.M. Kauzlarich, G.J. Snyder, Traversing the metal-insulator transition in a Zintl phase: rational enhancement of thermoelectric efficiency in $Yb_{14}Mn_{1-x}Al_xSb_{11}$, Adv. Funct. Mater. 18 (2008) 2795–2800.

[107] E.S. Toberer, S.R. Brown, T. Ikeda, S.M. Kauzlarich, G. Jeffrey Snyder, High thermoelectric efficiency in lanthanum doped $Yb_{14}MnSb_{11}$, Appl. Phys. Lett. 93 (2008) 062110.

[108] S.M. Kauzlarich, T.Y. Kuromoto, M.M. Olmstead, Preparation and structure of a new ternary transition-metal Zintl compound containing high spin Mn(III)Bi_4 tetrahedra, J. Am. Chem. Soc. 111 (1989) 8041–8042.

[109] T.Y. Kuromoto, S.M. Kauzlarich, D.J. Webb, A novel ferromagnet—$Ca_{14}MnBi_{11}$, Mol. Cryst. Liq. Cryst. 181 (1990) 349–357.

[110] D.J. Webb, T.Y. Kuromoto, S.M. Kauzlarich, New ternary magnets (Ca, Sr, Ba)$_{14}MnBi_{11}$, J. Magn. Magn. Mater. 98 (1991) 71–75.

[111] D.J. Webb, T.Y. Kuromoto, S.M. Kauzlarich, Some new ternary ferromagnets, J. Appl. Phys. 69 (1991) 4825.

[112] J.Y. Chan, M.E. Wang, A. Rehr, S.M. Kauzlarich, D.J. Webb, Synthesis, structure, and magnetic properties of the rare-earth Zintl compounds $Eu_{14}MnPn_{11}$ and $Eu_{14}InPn_{11}$ (Pn = Sb, Bi), Chem. Mater. 9 (1997) 2131–2138.

[113] J.Y. Chan, S.M. Kauzlarich, P. Klavins, R.N. Shelton, D.J. Webb, Colossal negative magnetoresistance in an antiferromagnet, Phys. Rev. B 57 (1998) 8103–8106.

[114] A.C. Payne, M.M. Olmstead, S.M. Kauzlarich, D.J. Webb, Structure, magnetism, and magnetoresistance of the compounds $Eu_{14}MnAs_{11}$ and $Eu_{14}MnP_{11}$, Chem. Mater. 13 (2001) 1398–1406.

[115] S.M. Kauzlarich, A.C. Payne, D.J. Webb, Magnetism and magnetotransport properties of transition metal Zintl isotypes, in: J.S. Miller, M. Drillon (Eds.), Magnetism: Molecules to Materials III, Wiley-VCH, Weinham, 2002, pp. 37–62.

[116] Y.F. Hu, J. Wang, A. Kawamura, K. Kovnir, S.M. Kauzlarich, $Yb_{14}MgSb_{11}$ and $Ca_{14}MgSb_{11}$—new Mg-containing Zintl compounds and their structures, bonding, and thermoelectric properties, Chem. Mater. 27 (2015) 343–351.

[117] B. Sales, P. Khalifah, T. Enck, E. Nagler, R. Sykora, R. Jin, D. Mandrus, Kondo lattice behavior in the ordered dilute magnetic semiconductor $Yb_{14-x}La_xMnSb_{11}$, Phys. Rev. B 72 (2005) 205207-1–205207-5.

[118] J.H. Grebenkemper, S.M. Kauzlarich, Magnetic and structural effects of partial Ce substitution in $Yb_{14}MnSb_{11}$, APL Mater. 3 (2015) 041503.

[119] Y.F. Hu, S.K. Bux, J.H. Grebenkemper, S.M. Kauzlarich, The effect of light rare earth element substitution in $Yb_{14}MnSb_{11}$ on thermoelectric properties, J. Mater. Chem. C 3 (2015) 10566–10573.

[120] J.Y. Chan, S.M. Kauzlarich, P. Klavins, J.-Z. Liu, R.N. Shelton, D.J. Webb, Synthesis, magnetic properties, and colossol magnetoresistance of $Eu_{13.97}Gd_{0.03}MnSb_{11}$, Phys. Rev. B 61 (2000) 459–463.

[121] J.H. Roudebush, J. Grebenkemper, Y. Hu, N. Kazem, M.N. Abdusalyamova, S.M. Kauzlarich, $Yb_{14-x}Tm_xMnSb_{11}$ ($0<x<0.5$): structure and magnetic properties, J. Solid State Chem. 211 (2014) 206–211.

[122] C.A. Uvarov, M.N. Abdusalyamova, F. Makhmudov, K. Star, J.P. Fleurial, S.M. Kauzlarich, The effect of Tm substitution on the thermoelectric performance of $Yb_{14}MnSb_{11}$, Sci. Adv. Mater. 3 (2011) 652–658.

[123] C. Yu, Y. Chen, H. Xie, G.J. Snyder, C. Fu, J. Xu, X. Zhao, T. Zhu, Improved thermoelectric properties in Lu-doped $Yb_{14}MnSb_{11}$ Zintl compounds, Appl. Phys. Express. 5 (2012) 031801.

[124] S.R. Brown, E.S. Toberer, T. Ikeda, C.A. Cox, F. Gascoin, S.M. Kauzlarich, G.J. Snyder, Improved thermoelectric performance in $Yb_{14}Mn_{1-x}Zn_xSb_{11}$ by the reduction of spin-disorder scattering, Chem. Mater. 20 (2008) 3412–3419.

[125] J.F. Rauscher, C.A. Cox, T. Yi, C.M. Beavers, P. Klavins, E.S. Toberer, G.J. Snyder, S.M. Kauzlarich, Synthesis, structure, magnetism, and high temperature thermoelectric properties of Ge doped $Yb_{14}MnSb_{11}$, Dalton Trans. 39 (2010) 1055.

[126] T. Yi, M.N. Abdusalyamova, F. Makhmudov, S.M. Kauzlarich, Magnetic and transport properties of Te doped $Yb_{14}MnSb_{11}$, J. Mater. Chem. 22 (2012) 14378–14384.

[127] I.G. Vasilyeva, R.E. Nikolaev, M.N. Abdusaljamova, S.M. Kauzlarich, Thermochemistry study and improved thermal stability of $Yb_{14}MnSb_{11}$ alloyed by Ln^{3+} (La-Lu), J. Mater. Chem. C 4 (2016) 3342–3348.

[128] S. Kastbjerg, C.A. Uvarov, S.M. Kauzlarich, E. Nishibori, M.A. Spackman, B.B. Iversen, Multi-temperature synchrotron powder X-ray diffraction study and Hirshfeld surface analysis of chemical bonding in the thermoelectric Zintl phase $Yb_{14}MnSb_{11}$, Chem. Mater. 23 (2011) 3723–3730.

[129] A. Akrap, N. Barisic, L. Forro, D. Mandrus, B.C. Sales, High-pressure resistivity and thermoelectric power in $Yb_{14}MnSb_{11}$, Phys. Rev. B 76 (2007) 085203.

[130] C.A. Cox, S.R. Brown, G.J. Snyder, S.M. Kauzlarich, Effect of Ca doping on the thermoelectric performance of $Yb_{14}MnSb_{11}$, J. Electron. Mater. 39 (2010) 1373–1375.

Chapter 289

Ceria-Based Materials in Catalysis: Historical Perspective and Future Trends

Eleonora Aneggi, Marta Boaro, Sara Colussi, Carla de Leitenburg and Alessandro Trovarelli[1]

Università di Udine, Udine, Italy

[1]*Corresponding author: e-mail: alessandro.trovarelli@uniud.it*

Chapter Outline

1 INTRODUCTION

Rare earth elements are increasingly being used for a growing number of applications in research and industry; high-technology (electronics, medical science, energy) and manufacturing in chemical industry are at the forefront of these applications [1,2]. They differ from transition metals due to the peculiar position of the 4f orbitals that are shielded from the environment by 4d, 5s, and 5p electrons, contributing to their unique properties. Cerium is the first element of the lanthanide group to possess 4f electrons, and this property is responsible for its powerful redox behavior when cycling between the smaller Ce^{4+} ion and the larger Ce^{3+}. When combined with oxygen, it forms a series of nonstoichiometric CeO_x compositions (with $1.5 < x < 2$) characterized by adopting the face-centered cubic (fcc) fluorite lattice; fully

Handbook on the Physics and Chemistry of Rare Earths, Vol. 50. http://dx.doi.org/10.1016/bs.hpcre.2016.05.002

oxidized, stoichiometric ceria (CeO_2) is the upper limiting composition; it consists of a cubic closed-packed array of metal atoms with all tetrahedral holes filed by oxygen atoms. The removal/uptake of oxygen from the fluorite lattice is fully reversible, and it confers to the material its fascinating and unique properties in the broad field of materials for catalysis [3–10] and in several other more or less related applications which go from solid oxide fuel cells [11–13], where ceria increases the activity of the anode for the electrochemical oxidation, to materials for protections [14], antioxidant agents [15], solar cells [16,17], optical films [18], gas sensors [19], and polishing powders [20]. Scientists at Ford Motor Company in 1976 first reported about the unique oxygen storage/release properties of ceria in automotive catalysis [21,22]; the ability of ceria to assist CO/NO reduction in three-way catalysts (TWCs) is still unsurpassed, and several generation of ceria-based materials have been made available through the years, like ceria–zirconia solid solutions, that have become one of the major players in catalysis and that set the standard in present after-treatment technologies [23]. The wide success of ceria-based materials in catalysis is also documented by the huge number of articles and reviews appearing each year and by the regular gathering of the catalysis community in specific events focused on the use of ceria in catalysis [24]. The properties of ceria nanoparticles can be modified by using several strategies; these have been developed and finalized in the last 20 years. An easy and efficient way to tailor the redox and stability behavior of ceria comes from the simple use of dopants [25,26]; Zr-doping represents the best and more important example in this regard. More recently, the modification of crystal shape and size [27–30] or the creation of metal–ceria core–shell structures with atomic scale accuracy [31,32] offered powerful tools to tailor the catalytic behavior of cerium oxide. The success of these approaches goes in parallel to the understanding of ceria properties from a surface science perspective, which is slowly reducing the gap between real and model catalysts [33]. A prerequisite to the successful design of ceria-based catalytic materials with improved activity is also a more adequate description of adsorption and reaction steps. Recent advances in theory and computational simulation techniques have become an integral part of the overall approach and the atomistic understanding of the catalyst structure and of the elementary catalytic steps from this point of view has enormously increased in the last decades [34–37]. This approach has also allowed to better understand the specific and mutual interaction between ceria and active metal phase and to prepare catalyst with new functionalities by engineering the ceria–metal interface at the nanoscale level, to better support catalytic reaction [38–40].

In this review we want to highlight some historical and more recent issues regarding the application of ceria-based materials in catalysis and trying to see how the tremendous growth and knowledge experienced within ceria-based materials in the last years can contribute to imagine future developments.

2 STRUCTURAL PROPERTIES OF CERIUM DIOXIDE

Cerium metal is thermodynamically unstable in presence of oxygen and forms oxides showing the oxidation states of +3 and +4 [41]. The capability of being progressively reduced from CeO_2 to Ce_2O_3 brings to the formation of oxides with intermediate composition, depending on the oxygen partial pressure [42]. This ability leads to the formation of a wide number of crystalline phases whose structure and properties are strongly correlated. The most important of these oxides is CeO_2; as shown in Fig. 1 [43] the CeO_2 crystal structure presents a face-centered unit cell (fcc) with space group $Fm\bar{3}m$ ($a = 0.541134(12)$ nm, JCPDS 34-394), where Ce cations are bonded to eight nearest equivalent oxygen atoms, while the O anions are tetrahedrally bonded to four Ce nearest neighbors. It is possible to represent the structure by means of a ccp array of cerium with oxygen atoms filling the tetrahedral holes.

Starting from a fluorite-type structure with oxygen in a tetrahedral site (Ce_4O), the removal of O^{2-} from the lattice produces vacancies (anion-vacant sites indicated as □) with the formation of defects and the progressive reduction of Ce^{4+} to Ce^{3+}:

$$4Ce^{4+} + O^{2-} \rightarrow 2Ce^{4+} + 2Ce^{3+} + \square + 0.5O_2 \quad (1)$$

The phase diagram of the reduced CeO_{2-x} species has been extensively studied: at high temperature a continuum of oxygen-deficient CeO_{2-x}-type oxides is formed; the so-called *α phase* with composition $0 < x < 0.286$ and a random distribution of oxygen vacancies [44–46]. The effect of oxygen

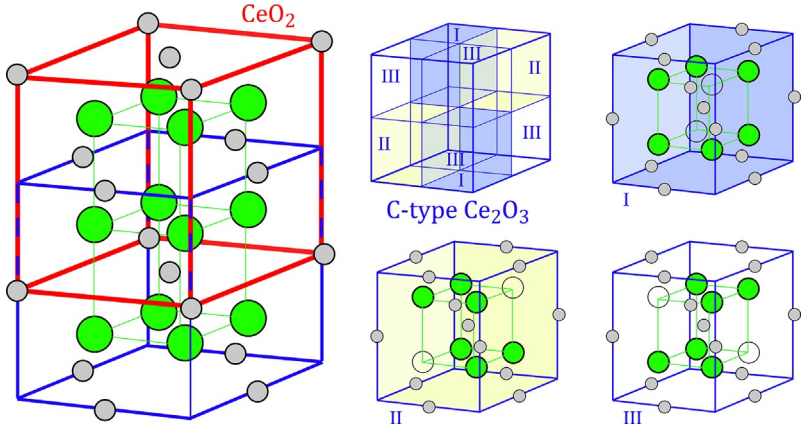

FIG. 1 On the *left*, fcc CeO_2 unit cell structure (*thick line*). On the *right*, the unit cell of Ce_2O_3 bcc C-type sesquioxide as a combination of fluorite-like unit cell octants. The different disposition of oxygen vacancies is evidenced in I, II, and III structures. The relation between CeO_2 structure and Ce_2O_3 octant (*thin line*) is shown on the *left*. *Adapted from S. Tsunekawa, R. Sivamohan, S. Ito, A. Kasuya, T. Fukuda, Structural study on monosize CeO_{2-x} nano-particles, Nanostruct. Mater. 11 (1999) 141–147.*

partial pressure on the lattice constant has been observed and shows the CeO_{2-x} unit cell expansion with the increase of the amount of oxide ion vacancies in the range of 973–1273 K [47,48]. The unit cell parameter increases with the oxygen vacancies according to the presence of higher concentration of Ce^{3+} that exhibits a ionic radius larger than Ce^{4+} (1.14 Å vs 0.97 Å [49]).

The removal of oxygen atoms leads to an increase of defect concentration that, at low temperature, causes the formation of a series of discrete compounds Ce_nO_{2n-2m} whose composition is still a subject of discussion due to the complexity of phase relations. The superstructures modeling of these anion-deficient, intermediate higher oxides has been proposed by Kang and Eyring, starting from fcc sublattices [50]. A number of crystalline phases of suboxides are formed at temperatures less than around 700 K and have been characterized with X-ray or neutron diffraction, electron microscopy [51], and specific heat [52] studies. The anion vacancies are long-range ordered within the lattice, forming, under appropriate conditions, organized fluorite-related superstructures. Compounds of stoichiometry like $Ce_{11}O_{20}$, Ce_9O_{16}, and Ce_7O_{12} have been characterized and critically examined [53,54]. Despite the change of space group for the unit cell due to the presence of oxygen vacancies in CeO_{2-x}, Ce and O maintain an fcc close-packed symmetry at least with $0 < x < 0.286$ [42]. For higher reduction degree the limiting structure for fluorite-based Ce_2O_3 is body-centered cubic (bcc)-type C or bixbyte (space group *Ia3*) with a very large unit cell with 32 Ce atoms and 48 O atoms where every Ce ion is coordinated to six oxygen atoms. The conversion from the fluorite-type structure to the C-type one does not require a crystal structure change, because the C-type structure is formally brought about by a combination of three kinds of fluorite-like unit cells (octant types I, II, and III, Fig. 1) with two body diagonals ordered vacancies and the unit cell parameter two times as large as the original fluorite one [43].

The thermodynamically stable form of the fully reduced cerium oxide, A-type hexagonal Ce_2O_3, has a hexagonal structure (space group $P\bar{3}ml$) [55] and Ce cations are seven times O coordinated (four closer). However, in the intermediate compositions of CeO_{2-x} with $0 < x < 0.5$, the structure is based on a fluorite lattice with Ce retaining near fcc-like positions and O vacancies either randomly distributed or ordered depending on composition and temperature.

The open fluorite structure of ceria can tolerate a high level of atomic disorder/defects, and their organization has a key role in the properties of the material. Defects can be introduced in ceria either by reduction or by doping. In the first case the presence of vacancies and electrons results in a large contribution to electronic conductivity, while extrinsic defects are due to the presence of aliovalent dopants or impurities and play a key role on the properties of these materials in many applications such as catalysis (oxygen storage capability, OSC) [56–59] and fuel cell [60–62].

3 AUTO-EXHAUST CATALYSTS

The most important application of cerium in catalysis is certainly the use of CeO_2 in the so-called TWCs for the simultaneous removal of CO, NO, and hydrocarbons from gasoline engines exhaust. The application dates back to the late 1970s and from that time it has been continuously implemented to reach a high level of efficiency. The catalyst consists of noble metals (Pt, Rh, and Pd) deposited on an alumina-based washcoat anchored to a ceramic or metallic substrate. Modification of the washcoat through the use of promoters like cerium dioxide allows increasing the simultaneous conversion of the three pollutants. This occurs thanks to the oxygen buffering/storage capacity of CeO_2 (OSC) which is reduced under rich-mixture and oxidized when composition turns lean, according to the following reactions:

$$CeO_2 \rightarrow CeO_{2-x} + 0.5xO_2 \tag{2}$$

$$CeO_2 + xCO \rightarrow CeO_{2-x} + xCO_2 \tag{3}$$

$$CeO_{2-x} + 0.5xO_2 \rightarrow CeO_2 \tag{4}$$

$$CeO_{2-x} + xNO \rightarrow CeO_2 + 0.5xN_2 \tag{5}$$

Reduction and oxidation of ceria under this environment occur in an easy fashion through continuous formation and filling of oxygen vacancies while maintaining the structural integrity of the fluorite ceria lattice. The overall effect of cerium dioxide is that of reducing the departure of the mixture composition far from the stoichiometric point increasing the efficiency of conversion near the stoichiometric point, Fig. 2.

In addition to this effect, the presence of ceria in the TWC formulations was shown to induce several other benefits through its interaction with metals,

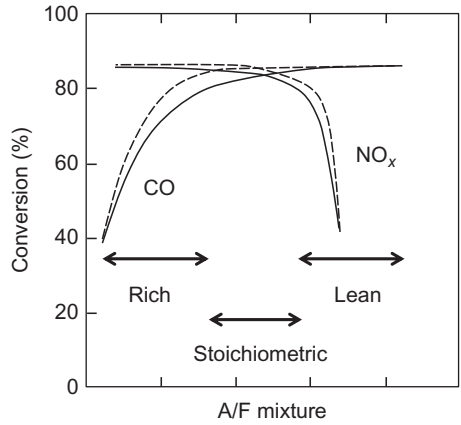

FIG. 2 TWC window showing the effect of ceria (*dotted line*) in CO and NO conversion near stoichiometric point; A/F is the air-to-fuel ratio.

like the stabilization of metal dispersion and the promotion of side reaction through interfacial metal/ceria contact sites [8]. One of the major drawbacks in the use of CeO_2 in TWCs is due to its poor thermal stability under reaction conditions; the exposure of CeO_2 at high temperature, in fact, strongly affects its surface area which drops at very low values, thus affecting low temperature redox activity [63]. This is clearly seen by monitoring the reduction of ceria with different surface areas under hydrogen through temperature-programmed reduction (TPR) [64]. A strong effort was therefore directed toward finding a way to improve the catalytic properties of ceria in this application; this has been done mainly through doping of the CeO_2 by substitution of lattice Ce ions with Zr (and/or other rare earth elements) with formation of solid solutions [26].

Ceria–zirconia is one of the main components of current new generation of TWCs [23,26]. It has gradually replaced pure cerium oxide whose characteristics were not adequate to sustain the high degree of conversion and the thermal resistance required to meet the more severe regulations in terms of emissions of CO, NO_x, and hydrocarbons. Compared to ceria, ceria–zirconia shows a higher thermal resistance and a higher reduction efficiency of the redox couple Ce^{4+}–Ce^{3+}, with a higher oxygen buffer/storage capacity. By monitoring the reduction of CeO_2 in ceria–zirconia solid solutions according to the following reaction:

$$Ce_xZr_{1-x}O_2 + \delta H_2 = Ce_xZr_{1-x}O_2 + \delta H_2O + \delta V_o \tag{6}$$

it is shown that the value of δ varies with composition x and is almost independent of surface area, Fig. 3 [65].

The promotion of reduction is attributed to the enhanced oxygen mobility of solid solutions compared to the pure oxides [6]. With evolution of TWCs performances during cold start, request for more thermally stable carriers led to several strategies for implementing thermal stability of ceria–zirconia and resulting OSC. Doping of ceria–zirconia with rare earth elements like La, Nd, Pr, Y, and Sm resulted in a better thermal stability and overall oxygen storage capacity [66–68]. Also, playing with Ce/Zr composition and mixing with other components can help in this regard [69]. Additional benefits to the final properties of ceria-based carriers for TWCs come from the development of novel synthetic and manufacturing approaches [70] that allowed further increase of thermal stability up to 1100°C. Overall, in the last 20 years, the doping of CeO_2 with Zr and other rare earth elements and the development of novel synthetic strategies have brought to a tremendous increase of thermal stability and redox properties (Fig. 4) which confirmed the superior behavior of ceria–zirconia in this application.

The fundamental understanding of the way of operation of these promoters revealed that the mechanism is far from being completely understood; however, it has stimulated a great amount of work that highlighted the utility of ceria in several other applications [4]. In addition to the use of doped ceria

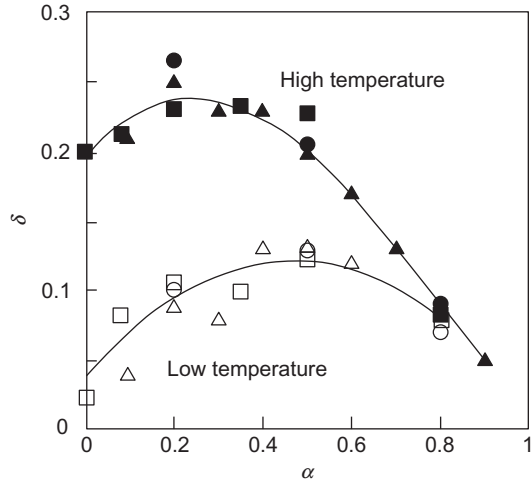

FIG. 3 Reduction degree (δ) at low and high temperature against composition (α) in a series of $Ce_\alpha Zr_{1-\alpha}O_2$ solid solutions with different surface areas (△, low surface area; ○, medium surface area; □, high surface area samples). *Adapted from A. Trovarelli, C. de Leitenburg, G. Dolcetti, Designing better cerium-based oxidation catalysts, ChemTech 27 (1997) 32–37.*

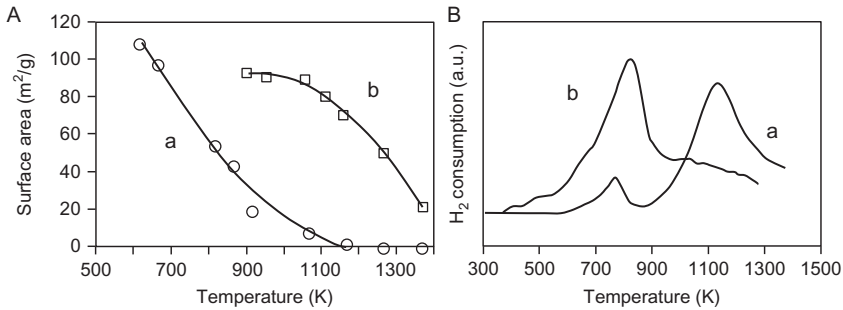

FIG. 4 Surface area (A) and extent of reduction (B) against temperature of a sample of CeO_2 (a) and $Ce_{0.8}Zr_{0.2}O_2$ (b).

in TWC technology, the potential use of CeO_2 in the development of robust catalysts for treatment of diesel engines has also been investigated in the last years. In this regard, ceria has shown great potential in the formulation of catalysts for carbon soot combustion [71,72], as an additive in lean NO_x-trapping materials [73] and also in combination with ZrO_2 as potential ingredient in selective catalytic reduction formulations [74].

4 ROLE OF CERIA–METAL INTERFACE IN CATALYSIS

A direct consequence of the use of ceria as the key component of TWCs was the flourishing of several studies investigating the catalytic properties induced

by the contact at the ceria–metal interface. At first, because the research was carried out in the field of automotive catalysts, it involved mainly noble metals (Pt, Rh, Pd) and the coupled reactions of CO oxidation and NO reduction [75–77]. On these systems CO was supposed to react with lattice oxygen from ceria in the presence of the noble metal, leaving a reduced ceria site for NO adsorption. Within this frame, many researchers described the modifications of the catalytic behavior of noble metals in the presence of cerium oxide in both reducing and oxidizing conditions, and already from the early studies the key role of the metal–ceria interface was envisaged [8]. The phenomena taking place on metal–ceria catalysts in many cases were distinguished from the strong metal–support interaction (SMSI) described by Tauster et al. [78]: the authors did not observe the typical blocking of the metal active sites due to the decoration by oxide particles as in the SMSI effect, but suggested instead a different kind of metal–ceria relationship occurring mainly at the interface [79,80]. The nature of this interaction was investigated in several studies that opened new perspectives on the role of the interface and led to a series of substantial observations: (i) the ceria–metal interface was identified as the preferential site for oxygen exchange; (ii) the formation of oxygen vacancies was associated with reduced ceria sites in the vicinity of metal particles; and (iii) these modifications occurring at the interface were pointed out as being responsible for the high catalytic activity recorded on these systems (ie, they were recognized as the active sites).

From these first results onward, the research on ceria-based catalysts almost always involved the interface as one of the primary subjects, directly or indirectly. In the past, in most of the works the role of the interface was studied as a consequence of other phenomena or as a complementary explanation for the observed reaction mechanisms. A significant example of an "indirect" study is the water–gas shift reaction (WGSR) on metal–ceria systems: the previous knowledge on the role of the interface allowed to hypothesize an interfacial, bifunctional reaction mechanism in which CO is adsorbed on the noble metal and oxidized by oxygen transfer from ceria, which in turn is reoxidized by water [81]. The same redox mechanism in the water–gas shift was proposed also for Cu- and Ni-based catalysts [82]. The spreading of the research on WGSR due to the growing interest in fuel cell applications led to a series of fundamental works on Au–ceria systems [57,83,84] and to the identification of a different mechanism involving the presence of formate species on reduced ceria surface [85].

All these results proved that the ceria–metal interface is the preferential site of complex interactions, not depending on the type of metal, that in general include the formation of defects on ceria lattice and modifications in the electronic state of the metal particles involved, causing the easy activation of reagent molecules.

Also other studies on different reactions have evidenced the occurrence of oxygen transfer phenomena and of formation of active ionic centers with

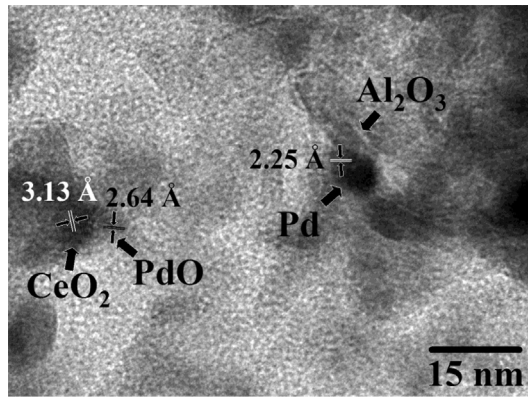

FIG. 5 HRTEM image of a $Pd/CeO_2/Al_2O_3$ catalyst showing the oxidation of only PdO particles at the ceria interface. *Reprinted with permission from S. Colussi, A. Trovarelli, G. Groppi, J. Llorca, The effect of CeO_2 on the dynamics of Pd-PdO transformation over Pd/Al_2O_3 combustion catalysts, Catal. Commun. 8 (2007) 1263–1266, © 2007 Elsevier.*

subsequent molecular activation at the metal–ceria interface [86–89]. Recently, the unique properties of the interface have made it attractive also in novel research fields such as photocatalytic degradation of volatile organic compounds [90] and water splitting [91]. In all these works, the common feature can be identified in the presence of a relevant amount of Ce^{3+} due to the reactivity of ceria lattice oxygen triggered by the proximity with metal nanoparticles. This property turns out to be fundamental also for tuning the metal oxidation states in catalytic systems experiencing redox cycles, in particular for copper [92,93] and palladium [94,95]. For the latter, it has been shown that the contact between Pd and CeO_2 particles on an alumina support favors the high temperature Pd reoxidation to PdO in oxidative atmosphere, confirming the key role of the metal–ceria interface in the oxygen transfer processes (Fig. 5) [96].

Due to the great relevance of the metal–ceria interface emerging from several different applications, a number of experiments aimed at a direct study of interfacial properties and effects have been designed in the past [39,97], and the research in this direction is still ongoing, often involving CO oxidation as a model reaction. Thanks to the novel approaches, it has been possible to demonstrate experimentally the role of the interfacial atoms not only in model systems [98] but also under real operating conditions [38]. In particular, it has been shown that atoms at the perimeter and corners of metal nanoparticles on ceria are the active sites for CO oxidation (Fig. 6), irrespective of the metal, thus giving a definitive proof of the role of the metal–ceria interface on catalytic activity [38].

Further insights into the metal–ceria interaction taking place at the interface have been gained through the tailoring of the so-called inverse catalysts,

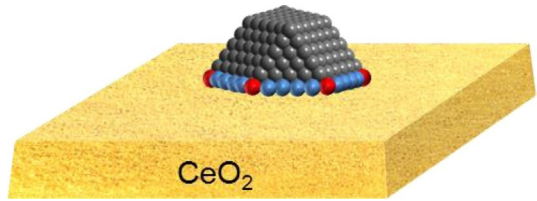

FIG. 6 Active metal atoms for CO oxidation on ceria surface.

in which the oxide (ceria) is supported on the metal [59,99]. These systems provide additional evidences of the interfacial activity involving molecular dissociation on ceria oxygen vacancies followed by the other reaction steps at the metal–ceria boundary.

With the development of advanced characterization techniques, able to follow in situ and/or *operando* behavior of the materials involved, a direct, systematic investigation of the properties of the ceria–metal interface has been carried out [100–102]. This has contributed to proving some fundamental points: (i) the synergy between metal and O vacancy, with the metal facilitating the formation of O vacancies on CeO_2; (ii) the key role of interfacial sites in the formation of reaction intermediates, thus explaining the substantial different behavior between the metal–ceria systems and the metal or ceria alone; and (iii) the presence of short-lived Ce^{3+} under transient reaction conditions that constitute a fundamental species in CO oxidation mechanism.

Despite these advancements, a still controversial issue of ceria–metal interaction is the mechanism responsible for the formation of oxygen vacancies at the ceria–metal interface. Some authors have reported the occurrence of geometrical and strain effects [103], while in other works the electronic interactions between CeO_2 and the metal are indicated as the key parameter for the formation of active sites [40,104]. The presence of both effects, with one prevailing on the other under different experimental conditions, is the most likely to occur [105], but in order to clarify this point further research work is needed. Moreover, since most of the work in the field is carried out on single crystals or thin films, often in ultrahigh vacuum, it is desirable for the future to develop experimental protocols that can deal with more realistic conditions. Another crucial aspect that has received lots of attention but still deserves further investigation is the influence of ceria morphology on the interface properties and, consequently, on the catalytic activity. The combination of photoelectron spectroscopy characterization with density functional theory calculations has tried to shed some light on this issue, demonstrating a remarkable effect of ceria structure on ceria–metal interactions [40,106] as already observed in many experimental works [107]. What remains quite obscure is the nature of this effect: for example, for Cu/CeO_2 system the morphology is supposed to influence the electron transfer from CuO to CeO_2 [106], while for Pt/CeO_2 this seems not to be the case and the ceria structure

is reported to affect only the oxygen transfer from ceria to Pt [40]. The different types of metal might play a role in this discrepancy; nevertheless in this respect there is still matter for research, as evidenced by the same authors.

All these new findings have increased the awareness and understanding of the role of ceria–metal interface in catalysis, and have driven the efforts toward the design of novel, more active catalytic systems able to exploit these unique properties. In the last decade, many researchers addressed the engineering of new metal–ceria catalytic formulations, with a particular attention to the configuration in which the metal is somehow encapsulated inside ceria or surrounded by a ceria shell [108–110]. This kind of assembly appears to be very effective in enhancing the contact between the metal and ceria, thus improving their interfacial properties. The latest efforts in the optimization of ceria–metal interaction at the interface try to exploit the reactivity of different ceria planes that have been shown to have a strong influence on the adhesion and morphology of supported metal nanoparticles and, consequently, on their catalytic activity [111]. In this respect, it is important to highlight that the exposure of different ceria facets can promote or inhibit the lattice oxygen mobility, thus having a paramount relevance for the metal–ceria properties at the interface.

5 SHAPE AND FACE MATTER

Catalytic properties of oxide catalysts are very sensitive to crystal morphologies and exposed surfaces; therefore, fine-tuning of nanocrystal shape and faces has been actively pursued in order to seek and optimize the desired surface atomic environment. Recently, several studies have addressed the development of robust synthetic approach to the preparation of shape/face-controlled CeO_2-based nanostructures and the investigation of their catalytic properties. The shape of CeO_2 nanoparticles is generally dominated by an octahedron or truncated octahedron geometry defined by the (111) and (111)/(100) facets, respectively (see Fig. 7).

The extent and nature of truncation is a function of the particle size and the thermal history of the sample; high temperature calcination, for example, favors the formation of irregular metastable truncated octahedral structure with a higher ratio of reactive 100 facets. By adopting appropriate synthetic approaches [30], CeO_2 particles with cube- and rod-like morphologies can be prepared. CeO_2 nanocubes expose predominantly the (100) planes, while surface characteristics of nanorods are more complex and shapes of these particles may result from terminations on different specific crystallographic planes [112–115]. More detailed high-resolution transmission electron microscopy (HRTEM) and 3D electron tomography studies suggest that various geometrical shapes can be associated to nanocubes [113,116]; in particular the extension of edges and corners (respectively, (110) and (111) facet dominated) can significantly modify the surface area associated with the

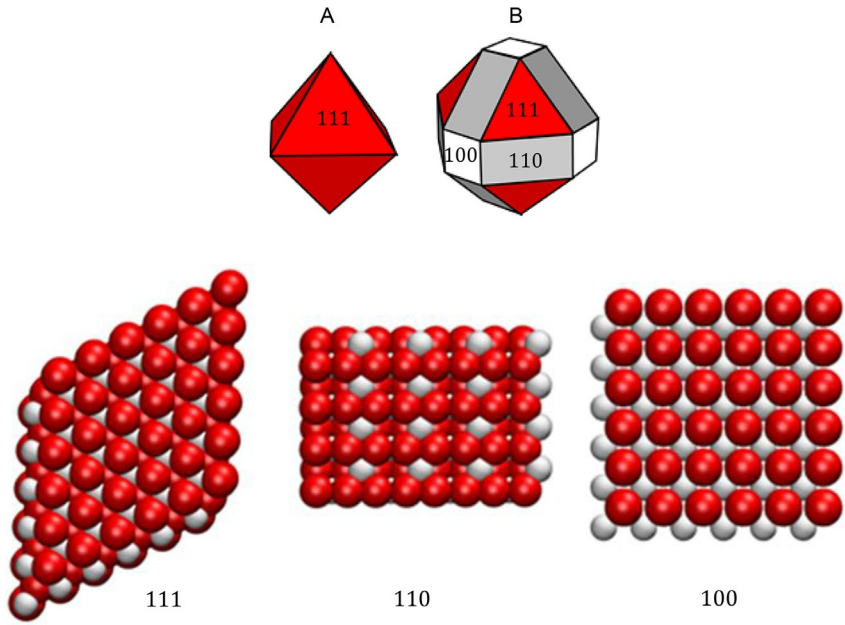

FIG. 7 CeO_2 octahedron (A) and truncated octahedron (B) geometry. Below, CeO_2 facets: (111), (110), and (100).

different planes exposed. In addition to the different surfaces exposed in edge and corners, surface nanofaceting can also affect the overall surface characteristics of nanoceria, with implication in face-selective catalysis.

Li et al. [117] in 2005 first compared activity of traditional CeO_2 nanoparticles (CeO_2-NP) with that of CeO_2 nanorods, showing that, irrespective of surface area, rods were three times more active than CeO_2-NP in CO oxidation. This was later shown in several other investigations using different shapes [118,119]. The reasons behind this enhancement were correlated to the lower formation energies of oxygen vacancies in rods and cubes, and to the nature and amount of defect sites compared to traditional CeO_2-NP that expose preferentially the (111) family planes. The enhancement of CO oxidation rate was also observed over traditional polycrystalline CeO_2-NP exposed to aging treatment in order to increase the amount of (100) surface termination [120].

One of the consequences of the surface structure sensitivity to the formation of oxygen vacancies is that the shape of ceria nanoparticles also influences its reduction and oxygen storage properties [30,121] (Table 1).

For example, the reduction degree of ceria (x in CeO_{2-x}), calculated by integrating the TPR profiles, shows that a higher degree of reduction is obtained over nanorods and nanocubes compared to ceria nanopolyhedra

TABLE 1 OSC Values and Degree of Reduction for CeO_2 Nanopolyhedra (CeO_2-NP), Nanorods (CeO_2-NR), and Nanocubes (CeO_2-NC) (Elaboration of Literature Results)

CeO_2-NP	CeO_2-NR	CeO_2-NC	Ref.
OSC (μmol O/m^2)			
5.1	9.1	10.6	[30][a]
0.2	0.3	0.3	[121][b]
0.9	9.9	11.2	[122][c]
Degree of reduction (x in CeO_{2-x})			
0.18	0.22	0.25	[122][d]
0.25	0.28	/	[123][e]
0.02	0.07	0.03	[124][f]

[a]*Calculated by oxygen pulse injection method after reduction by H_2/Ar at 400°C for 2 h.*
[b]*Calculated in a fixed bed flow microreactor at 400°C in CO/He atmosphere.*
[c]*Calculated by TGA experiments in Ar/H_2 atmosphere at 400°C for 30 min.*
[d]*Calculated by integrating the TPR profiles until 800°C.*
[e]*Calculated by integrating the TPR profiles until 880°C.*
[f]*Calculated by isothermal H_2 reduction profiles at 500°C for 1 h.*

[122–124]. The enhancement of reduction characteristics of ceria in nanoshapes also positively affects the properties of ceria in carbon soot oxidation [122]. On the opposite, hydrogenation reaction is hindered over ceria cubes compared to traditional ceria nanoparticles, and this is attributed to the different oxygen vacancy chemistry of the (100) and (111) facets [29]. In contrast to oxidations, hydrogenation reactions over CeO_2 are favored over low-vacancy surfaces, owing to the role of oxygen in stabilizing reactive intermediate species. This will in principle enable the determination of structure/performance relationships in ceria-based catalysts by the control of crystal face and its morphology.

Due to very interesting results obtained on ceria catalysts, several investigations were carried out on metal supported on ceria nanoshapes. The (100) and (110) dominant surface structures were also shown to affect the catalytic properties of Rh supported on ceria nanorods (CeO_2-NR) in ethanol-reforming reaction [125] and of Pd-loaded 1D ceria in WGSR [126], while loading Au nanoparticles onto CeO_2 nanorods remarkably improves aqueous methyl orange photodegradation [127] and dramatically enhances CO oxidation [123], CO preferential oxidation in a H_2-rich gas (CO-PROX) [128], and WGSR [129]. Recent works also show the significant support-morphology-

dependent catalytic activity for ceria nanocubes, nanorods, and nanopolyhedra modified with Ru nanoparticles toward CO_2 methanation [121], with CuO in N_2O decomposition reaction [130] and with Pt for WGSR [131] and CO oxidation [132].

In all the above examples, with the only exception of Ru nanoparticles for CO_2 methanation, CeO_2 nanorods have demonstrated lower activation energy and higher activity/reaction rate compared to modified CeO_2 nanocubes and nanopolyhedra. The better activity of metal supported on ceria NRs has been attributed to the favorable creation of highly dispersed metal clusters and to the synergic effects arising from the strong metal–support interaction between the metal nanoclusters and the more reactive surfaces of nanorods [123,130,131]. In the case of Ru nanoparticles, the high activity of ceria nanocubes for CO_2 methanation was attributed to the higher concentration of oxygen vacancies formed over Ru-NCs.

In summary, the catalytic behavior of ceria in several reactions can be efficiently modulated and enhanced working at a nanoscale level. The catalytic activity could be significantly improved by the design of ceria catalysts with controlled morphologies that expose specific crystallographic surfaces while maintaining high surface area. The selectivity and activity of a structure sensitive reaction can be selectively modified by selection of appropriate catalyst morphology. The control of the shape and size of nanocrystals is therefore of the utmost importance for the rational design of superior ceria-based heterogeneous catalysts.

6 CERIA IN ENERGY APPLICATIONS AND TECHNOLOGIES

Currently, a large portion of the research on ceria and related materials focuses on applications for the production and storage of energy. There are three main fields of development within this area: (i) the use of ceria for the production of hydrogen and fuels from fossil and renewable resources via conventional catalytic approaches or alternative methods; (ii) ceria-based devices for the production and storage of energy; and (iii) production of hydrogen via photocatalytic and/or photoelectrocatalytic processes.

It is well known that the oxygen storage capacity and electronic properties of ceria can be modified by means of various approaches (selection of dopants, methods of synthesis, thermal treatment). Recent developments have led to the general consensus that a careful control of structure and morphology at the nanoscale is pivotal to obtaining advanced ceria-based catalysts. In the following section we will review the importance of this aspect in the development of materials and systems for energy applications. Moreover we will discuss the applications of this class of materials in the above fields with the aim of summarizing the progress made and highlighting the future scenarios for research and development.

6.1 Ceria for the Production of Hydrogen and Fuels from Fossil and Renewable Resources

In the field of applications for the production of energy, ceria has certainly gained a prominent role in the production of hydrogen via reforming of both hydrocarbons and renewable sources (biomasses and alcohols) [133]. There are numerous studies concerning the development of metal-supported catalysts with cerium-based oxides as support for the production of syngas from hydrocarbons [134] and for hydrogen purification by means of the WGSR and by preferential oxidation of carbon monoxide (PROX). Many metals have been investigated in the literature; in the case of steam and dry reforming reactions, the metals used are often Ni, Co, or Ru and their alloys [135], while Au, Pt, and Cu are used in the case of the WGSR [136] and PROX reactions [137]. Here we will focus on highlighting the main characteristics of these catalysts and the issues that still need to be further addressed.

In these processes, the interaction between metal and support plays a central role in determining the catalytic activity. Many studies have focused on the identification of the active sites and on determining the parameters that contribute to their deactivation [138]. In many cases, the reaction takes place at the metal/support interface involving Me–O–Ce units and implies spillover of oxygen from the support to the metal [107]. The choice of operating conditions is also a critical aspect in the investigation of such systems since the nature of the metal/support interface and the distribution of active sites strongly depend on the atmosphere to which they are exposed [135,138].

In order to maximize the interaction between metal and support, implementation of hierarchical assemblies based on specific units such as core–shell or nanostructure substrates (in the form of rods or cubes) has proven effective [139,140]; however, the stability and durability of such assemblies under the actual conditions of the process are rarely assessed [141]. In the effort to produce green-H_2 from renewable sources, steam reforming of alcohols such as ethanol and methanol has become an increasingly attractive process [142]. In this case the use of nanostructured ceria, specifically in the form of rods, increases H_2 selectivity in several systems such as Cu/CeO_2, Rh/CeO_2, and Au/CeO_2 [139,140].

In all carbon-fuel reforming processes the use of ceria-based catalysts is beneficial in preventing the catalyst from deactivating because of coke formation; this thanks to the OSC properties of these materials. The latter aspect is crucial especially when Ni is used as the metal catalyst because of its high cracking activity [143]. In case of Ni supported catalysts ceria morphology plays a significant role in improving the activity. The comparative catalytic activity and coke resistance are examined in carbon dioxide reforming of methane over Ni/CeO_2 nanorods and nanopolyhedra (NP) [144]. The Ni/CeO_2-NR catalysts display excellent catalytic activity and higher coke resistance compared with the Ni/CeO_2-NP, and this is attributed to a strong

metal/support interaction effect and to the abundance of oxygen vacancies in the (110) and (100) planes.

In the process of methane dry reforming ($CH_4 + CO_2 \leftrightarrows 2H_2$ and 2CO) the modulation of the acid/basic properties of ceria–supports also becomes a key factor in CO_2 activation. Differences in morphology and nanostructures [145] as well as the presence of other rare earth elements or alkaline-earth metals such as La, Pr, or Ca and Ba can contribute to modify the surface properties of ceria so that it may enhance its CO_2 adsorption capability [146].

It is worth noting that H_2O and CO_2 are always present in reforming processes, and a better understanding of their interaction with ceria and ceria-based materials is crucial. In the literature there are interesting theoretical models that address the issue of water adsorption in relation to the type of ceria surfaces [147,148], while, to our knowledge, no experimental studies have been reported yet. Differences in the associative and dissociative adsorption energy of water were calculated, predicting that water dissociation for the (110) surface is barrierless [149]. A preferential adsorption of water on specific facets may lead to a different reactivity of associated nanostructures; however, further investigations are necessary to define precise correlations and mechanisms in the H_2 production/purification processes.

A deeper understanding of how water and carbon dioxide interact with the support would provide insight into the mechanism of reactions and therefore help devise a new generation of nanostructured and multifunctional catalysts which can find applications also in other strategic processes of industrial chemistry.

The reactivity of water with ceria has been recently investigated in the reaction of water splitting through thermochemical redox cycles (TWSR) [150,151]. This process, associated with solar concentrators technology, makes it possible to produce hydrogen and synthetic fuels without emitting greenhouse gases into the atmosphere [152]. In thermochemical water splitting reaction (TWSR), ceria is reduced in inert atmosphere or in air at high temperature (higher than 1800°C) releasing oxygen; it is then rapidly oxidized with water or carbon dioxide with the simultaneous production of hydrogen and/or carbon monoxide at intermediate temperatures (500–900°C).

The use of ceria rather than other traditionally employed materials (hematite and zinc oxide) allows for direct production of pure H_2 without additional purification steps and yields of up to 16% [153]. This is an encouraging value compared to the state of the art of other emerging solar water/CO_2-splitting technologies (ie, photocatalysis, photoelectrocatalysis) [154]. It should be pointed out that achieving such yields requires reactors and plants where an efficient management of the involved heat flows may be implemented. In this regard there are several fluid dynamics simulations and mathematical models based on ceria's thermodynamic properties [155], which have made the construction of suitable industrial prototypes possible [156,157]. A scheme of the demonstrative plant installed at EHT Zürich Center is given in Fig. 8.

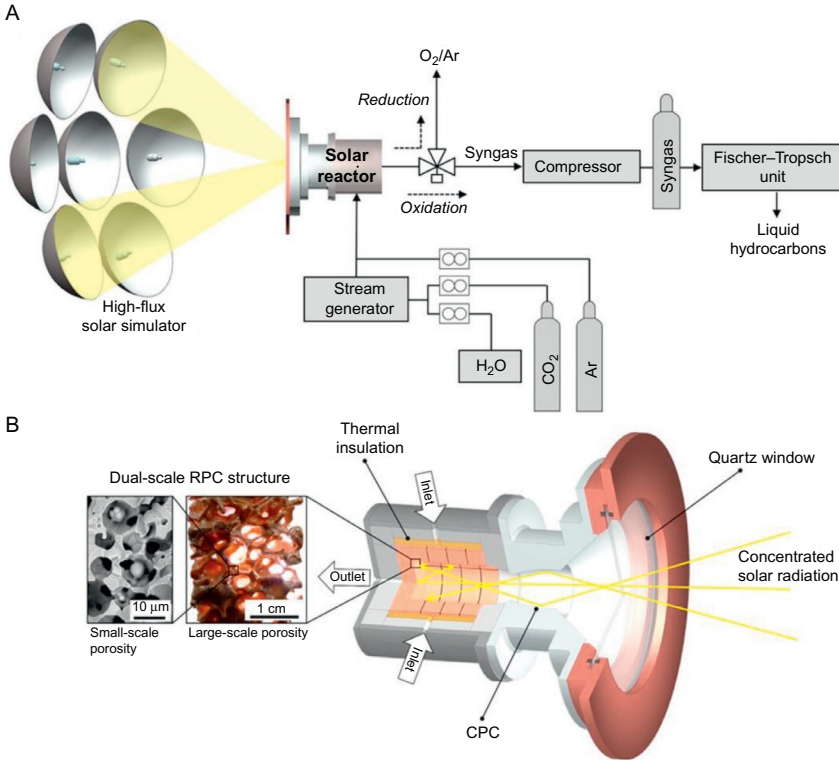

FIG. 8 (A) Schematic of the experimental setup, featuring the main system components of the production chain to solar kerosene from H_2O and CO_2 via the ceria-based thermochemical redox cycle. (B) Schematic of the solar reactor configuration. The cavity receiver contains a reticulated porous ceramic structure, made from ceria, with dual-scale porosity in the millimeter and micrometer scale. *Reprinted from D. Marxer, P. Furler, J. Scheffe, H. Geerlings, C. Falter, V. Batteiger, A. Sizmann, A. Steinfeld, Demonstration of the entire production chain to renewable kerosene via solar thermochemical splitting of H_2O and CO_2, Energy Fuels (2015) 3241–3250, with permission, © 2015 American Chemical Society.*

These systems are geared toward the creation of high surface area 3D structures characterized by a reticular framework designed to favor reagent–support interactions and to increase thermal and mechanical stress resistance [158] (the compounds are subjected to drastic heat treatments and exposure to different reaction atmospheres).

One of the drawbacks of ceria is that its reduction occurs at above 1800°C, a temperature at which it starts to sublimate. Keeping in mind that an increase in the degree of reduction inherently leads to an improvement in the oxidation step and consequently to greater hydrogen productivity, the strategy adopted has been to implement materials with high OSC properties and which are reducible at lower temperatures when compared to ceria. This strategy implies the insertion of alio and/or isovalent ions into the ceria lattice [151,152].

Similarly to what observed for the TWC technology, ceria and zirconia solid solutions have proved to be materials with improved TWSR activity in comparison to ceria alone [159]. These materials are easily reducible at temperatures ranging from 1300°C to 1500°C and can be rapidly oxidized at temperatures between 600°C and 900°C.

While there are many studies investigating the effects of changes in the stoichiometry of the oxides assuming structural homogeneity of the materials, only a few studies instead highlight the existence of correlations between structural properties and water splitting activity [160], despite the fact that different synthesis approaches of these materials, thermal treatments, and redox cycles could affect the bulk and surface properties resulting in segregation phenomena and structural reorganization.

Recently, zirconium-rich compositions have been tested in water splitting and showed reactivity similar to that of ceria-rich compositions. Indeed this occurs due to modifications undergone during the prolonged reduction in nitrogen at high temperatures and over several redox cycles [161]. These transformations lead to the segregation of ceria-rich phases on the surface and to the formation of a zirconium-rich oxynitride phase (see Fig. 9).

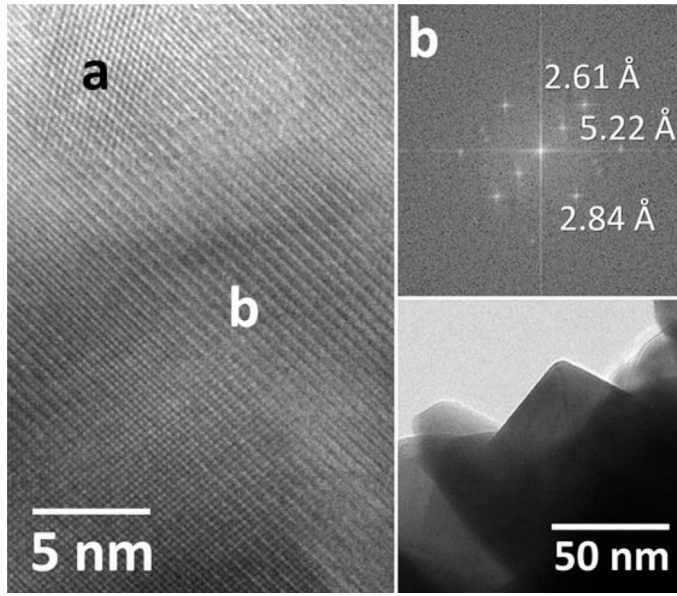

FIG. 9 HRTEM images of $Ce_{0.15}Zr_{0.85}O_2$ treated in N_2 flow at 1300°C for 4 h, with area labeled *a* belonging to cubic ceria–zirconia while area labeled *b* belonging to zirconia oxynitride superstructure. In the *inset* the lattice fringes of the Fourier transform image of area *b* proper of Zr_2ON_2 structure doped with cerium is shown. *Reproduced with permission from A. Pappacena, M. Boaro, L. Armelao, J. Llorca, A. Trovarelli, Water splitting reaction on $Ce_{0.15}Zr_{0.85}O_2$ driven by surface heterogeneity, Catal. Sci. Technol. (2016) 399–403, © 2016 The Royal Society of Chemistry.*

The synergistic interaction of these phases is supposed to be responsible for the enhanced performance. This result shows that controlling the structure and composition of materials at the nanoscale is of great interest for the creation of catalysts with enhanced properties.

6.2 Ceria-Based Devices for the Production and Storage of Energy

In the last 15 years, ceria has been investigated and used as a component in solid oxide fuel cells (SOFCs). Traditional zirconia-based SOFCs operate at high temperatures (900–1000°C); this causes problems with the stability and compatibility of the components and therefore with durability of the stacks. The short lifespan of these devices is keeping SOFC technology from rapidly entering the market. Therefore, one research challenge currently lies in the development of intermediate-temperature solid oxide fuel cells (IT-SOFCs).

Ceria-based materials represent an attractive option to develop IT-SOFC since they possess high ionic conductivity at low temperatures ranging from 600°C to 800°C.

A critical review of the use of ceria-based materials as electrolytes and as electrodes has been recently given by Chatzichristodoulou et al. [162]. Below, we will summarize some of the points highlighted in their work and will illustrate some of the results obtained in our laboratory with the aim to stress on the importance of nanoceria properties for further advancements.

Ceria as an electrolyte is an ionic–electronic conductor, ie, a conductor in which charge transport is due to both oxygen anions and electrons depending on the operating conditions. The common electrolytes are gadolinium- and samarium-doped ceria (SDC); commercial use of these materials as electrolytes is problematic given that under certain operating conditions the electronic current leaks can be significant and compromise cell efficiency. Moreover, ceria reduction leads to the expansion of its lattice, which may negatively affect the cell mechanical resistance. To date, only Ceres Power Ltd., Crawly, UK, is developing SOFCs with ceria-based electrolytes, while various companies are producing SOFCs with zirconia-based electrolytes.

In the recent years it has been demonstrated that the ionic conductivity of conventional ceria electrolytes can be increased by codoping the ceria materials with other rare earth elements, achieving outstanding results using neodymium [163]. Further advances have been reported using two-phase electrolyte nanocomposites. In these systems, doped ceria is combined with carbonates, hydroxides, sulfates, halides, or oxides, and its ionic conductivity exceeds those of single-phase doped ceria by up to 10 orders of magnitude [139].

Low temperature ceramic fuel cells with such composite electrolytes reach excellent performances. Fig. 10 shows the cross section microstructure (A and B) and voltage/power–current density curves (C) of a cell made with

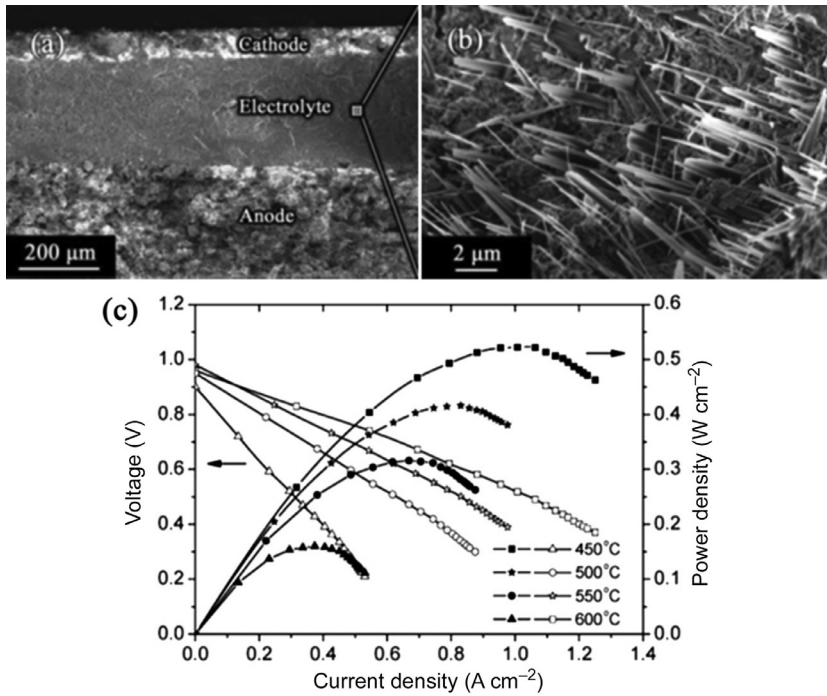

FIG. 10 (A) and (B) SEM images of single SOFC with doped ceria nanowire-carbonate electrolyte and (C) the corresponding electrochemical performance. *Reprinted with permission from L.D. Fan, C.Y. Wang, M.M. Chen, B. Zhu, Recent development of ceria based (nano)composite materials for low temperature ceramic fuel cells and electrolyte-free fuel cells, J. Power Sources 234 (2013) 154-174, © 2013 Elsevier.*

an SDC nanowire-carbonate composite electrolyte. In this case, the carbonate phase helps to stabilize the one-dimension nanowire structure at the operating SOFC conditions. Nanowire orientation/alignment allows obtaining large and continuous interfaces, which contributes to increase ionic conductivity and fuel cell performance (522 mW cm^2 at 600°C with an electrolyte thickness of 200 μm).

It is suggested that the ionic conductivity of these composites is ruled by the interfacial phenomena occurring among the phases [11]. Full understanding of the transport mechanism in these systems would be relevant also for the development of functional materials for other advanced applications such as water electrolysis to H_2 production and CO_2 separation.

More promising is the use of ceria as a component in fuel cell electrodes. At the cathode side ceria-doped materials are used to form an additional protective dense layer which would hinder the formation of the $SrZrO_3$ and La_2Zr_2O insulating phases due to the interaction between cathode catalysts (ie, $La_{1-x}Sr_xMnO_3$ (LSM), $La_{1-x}Sr_xCoO_3$, $La_{1-x}Sr_xFe_{1-y}Co_yO_3$) and the

zirconia-based electrolytes [164]. On the other hand, the last decade has seen great developments in the use of ceria also as part of the anode, especially, in the form of a nanosized material. It has been demonstrated that the integration of ceria permits the use of carbon-based fuels thanks to its resistance to carbon deposition; moreover it increases tolerance to sulfur poisoning [12]. Recent results show also that ceria is inherently active toward hydrogen electrooxidation [165]. Despite these recent results, the electroconductivity of ceria-based oxides is too low to allow their use as a single material. Metal–ceria composites are used to overcome this drawback; alternatively, ceria has been infiltrated into an electronic-conductive ceramic, such $SrTiO_3$ or in a yttria-stabilized zirconia (YSZ) porous scaffold to create a multicomponent electrode. In the latter case ceria is infiltrated together with copper or another metal that works as electronic conductor and/or cocatalyst [166].

The infiltration technique is similar to the wet-impregnation method used to prepare catalysts in heterogeneous catalysis and allows a dispersion of ceria in the form of nanometric particles that alter the surface chemistry of the porous backbone. Therefore, this approach allows one to prepare electrodes of various compositions and morphologies [167]. Recently Sn/CeO_2 has been shown to be a promising composition for IT-SOFC anodes thanks to the self-structuring of tin and ceria in SnO_x@Sn/CeO_2 nanoparticles [168]. These particles are characterized by a core–shell structure where a thin layer of amorphous tin oxide stabilizes molten tin nanoparticles over ceria. This occurs through an interfacial redox communication between ceria and tin, likely involving a transfer of oxygen from ceria to the metal and electrons from metal to ceria (see Fig. 11).

The particular layout was proven to increase the electronic and ionic conductivity of the electrode, thus enhancing cell performance. Similarly, Pd@CeO_2 core–shell particles layered on a YSZ anode were proven to significantly increase the performance in SOFC when compared to bare Pd NPs.

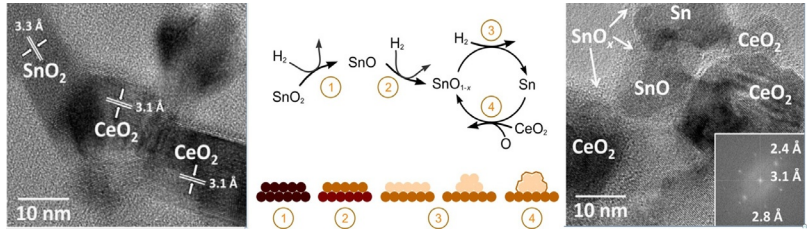

FIG. 11 Mechanism of formation of SnO_x@Sn molten nanoparticles on CeO_2 in H_2 atmosphere at high temperature. (1) Homogeneous tin(IV) oxide film; (2) reduction to tin(II) oxide and further reduction to a tin suboxide; (3) further reduction, formation of molten metallic tin, and coalescence of the molten metal; (4) oxygen transfer from ceria and surface reoxidation of the molten tin nanoparticles. HRTEM images of SnO_2 and CeO_2 particle distribution before (*left*) and after (*right*) reduction. *Reprinted with permission from L. Bardini, A. Pappacena, M. Dominguez-Escalante, J. Llorca, M. Boaro, Structural and electrocatalytic properties of molten core Sn@SnOx nanoparticles on ceria, Appl. Catal. B Environ. (2016), © 2016 Elsevier.*

The above examples highlight the importance of understanding the nature of metal/ceria/electrolyte interfaces and the mechanisms of interaction among components in this kind of electrodes. The high electrochemical activity of infiltrated ceria materials might be related to the formation of peculiar nanostructured assemblies, as above exemplified, or to the interface energy between ceria and the backbone phase, having ceria nanocrystals facets of different activities. It is worth underlining that structural characterization of the impregnated phases is usually performed ex situ on "as prepared" or tested catalysts and the working structure remains unknown. One of the future challenges in this field is the development of in situ analysis able to demonstrate the existence of specific nanostructures under operating conditions and their correlation with cell performance.

Ceria can be infiltrated alone or with other dopants (Sm, Gd, Zr, La) to form a solid solution. The use of a ceria–zirconia solid solution is expected to lead to greater performance than ceria alone when tested in hydrogen or methane; one would also expect Sm- and Gd-doped materials to achieve lower activity with respect to pure ceria. This is not always the case, as CeO_2–ZrO_2 solid solutions perform very similarly to ceria and sometimes worse [169]. By contrast, promising performance has been reported with Ni–SDC anodes with methane as a fuel [170]. These results show that comparing the catalytic performance of ceria-based materials in heterogeneous catalysis with the electrocatalytic performance of the same materials in SOFC anodes, based on the properties of the materials involved, can be questionable. How ceria contributes to improve cell performance is still to be clarified; likely the electrochemical process implies the release of lattice oxygen anions from the ceria phase, thus involving oxygen storage capacity of ceria. However, it must bear in mind that ceria-based materials would be in a reduced state when operating in a hydrocarbon or hydrogen environment in an SOFC. Moreover the degree of fuel conversion and corresponding changes in gas composition induce changes in the mixed transport properties of doped ceria. All these features will peculiarly affect the surface chemistry and (electro)oxidation mechanisms.

Ceria has also been used to implement polymeric membrane fuel cell electrodes operating with ethanol. The CeO_2 is added as cosupport on a Pt/C electrode and contributes to a remarkable decrease of the onset oxidation potential of ethanol [171]. Today, the interaction between ceria and carbon supports is of growing interest also for the development of supercapacitors. Ceria has a high theoretical capacitance of 560 Fg^{-1} and in this application, morphology and size of CeO_2 were designated to increase electronic conductivity and to obtain a good capacitive characteristic. Recently, a capacitance of 644 Fg^{-1} in carbon-supported CeO_2 nanorods has been reported and a CeO_2 nanoparticles/graphene composite has been demonstrated to be a potential electrode for supercapacitors, which encourages further use of ceria for energy storage applications [172].

6.3 Ceria for the Production of Hydrogen via Photocatalytic and/or Photoelectrocatalytic Processes

Bulk CeO_2 is not considered a photoactive material since its band gap is generally attributed to a charge-transfer $O_{2p} \rightarrow Ce_{4f}$ transition; however, ceria nanoparticles showed a photovoltaic response related to the morphology and nanostructure of the constituent particles [140]. For example, Corma et al. [17] prepared a hierarchically structured mesoporous material by self-assembly of 5-nm CeO_2 pretreated nanoparticles. The material possesses large pore volumes, high surface areas, and marked thermal stability. It also exhibits a photovoltaic response, which is directly derived from the nanometric particle size because traditional CeO_2 does not show this response.

Photocatalytic behavior of CeO_2 is mainly focused on its oxidizing properties [140], while its reducing properties have been explored only recently. CeO_2 nanoparticles have been utilized to construct an artificial photosynthesis system for the reduction of CO_2 to methanol based on a metalloenzyme (nitrogen-doped graphene Cu(II) complex, Fig. 12).

In this case, CeO_2 serves as light harvester and the photovoltaic activity seems to be related to the presence of a high number of defects and vacancies and the copresence of Ce(IV) and Ce(III) cations in the nanostructured material [173]. Suitable heterojunctions for H_2 production through water photolysis were also reported.

CeO_2 nanoshaped materials have also been used in photocatalytic hydrogen production. Oriented hexagonal CeO_2 nanorods with (100) planes as the main exposed surfaces were directly grown on Ti substrates via a simple template-free electrochemical method [174]. The photocatalytic activity of CeO_2-NRs was studied in water splitting reaction and compared with that of commercial CeO_2, CdS, and TiO_2. It was observed that the activity of CeO_2-NRs depends on the sacrificial agent used and usually is higher than those of commercial CeO_2.

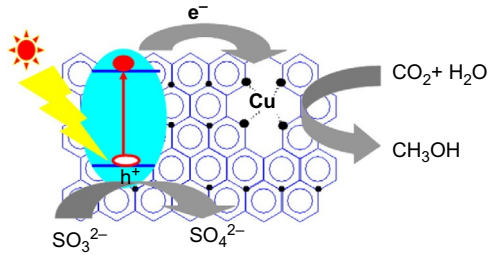

FIG. 12 Photocatalytic reduction of CO_2 to methanol. "●" denotes N atoms on the graphene-frame. *Reprinted with permission from S.-Q. Liu, S.-S. Zhou, Z.-G. Chen, C.-B. Liu, F. Chen, Z.-Y. Wu, An artificial photosynthesis system based on CeO_2 as light harvester and N-doped graphene Cu(II) complex as artificial metalloenzyme for CO_2 reduction to methanol fuel, Catal. Commun. 73 (2016) 7–11, © 2016 Elsevier.*

Summarizing, we have shown that in all these applications, it is important to develop multiphase materials with appropriate structural nanofeatures rather than compositionally homogeneous materials. The presence of mixed phases, indeed, determines the formation of highly active interfaces characterized by the presence of metastable nanostructures in dynamic equilibrium with the reaction atmosphere. It is also clear that, in such applications, nanostructured ceria has several advantages over similar microcrystalline materials. The high density of surface defects in nanostructured materials provides a large number of active sites for various surface interactions and surface exchange processes. All these features need to be further explored to better understand the origin of their electric and catalytic properties and to develop more efficient systems and devices.

7 CONCLUSIVE REMARKS

Overall, in the last 40 years, ceria has changed from an almost unknown oxide of the rare earth family to one of the most important ingredients in several well-established and emerging applications. The use of ceria in the automotive area has accompanied this evolution with enormous achievements; first of all the stabilization of the surface area of CeO_2 against thermal treatment that has contributed to the progress in this field, allowing the development of the last generation of TWCs. In addition to the stabilizing effect, the introduction of Zr and other dopants opened the way also to the increase of redox and oxygen storage properties which are at the basis of modern TWCs. Redox properties of ceria are being increasingly investigated for many other emerging applications, which go from the thermochemical water splitting reaction to the use of ceria to influence the antioxidant properties in biological systems. All these applications, which work under very different conditions, benefit from the presence of CeO_2 surfaces in either liquid or gaseous environment. The growth in these areas has been possible thanks to the progress made in the use of new characterizing tools which enabled near-atomic characterization of the surface of ceria under more realistic conditions. This, in parallel with the development of modeling skills, has increased the understanding of surface chemistry of ceria and its predictive power, compared to the early phenomenological approaches. Computational and modeling studies, surface chemistry, novel synthesis approach, and the development of new strategies for creating active metal/ceria interfaces at the nanoscale are necessary ingredients for the improvement of our knowledge on these systems and for the creation of more active and robust ceria-based catalysts. This can happen not only in the area of energy and environment but also in the more traditional chemical sector where ceria-based materials might be ready to start another journey.

ABBREVIATIONS

bcc	body-centered cubic
CeO_2-NP	ceria nanoparticles or nanopolyhedra
CeO_2-NR	ceria nanorods
fcc	face-centered cubic
HRTEM	high-resolution transmission electron microscope
IT-SOFC	intermediate-temperature solid oxide fuel cell
OSC	oxygen storage capability
PROX	preferential oxidation
SDC	samarium-doped ceria
SMSI	strong metal–support interaction
SOFC	solid oxide fuel cell
TPR	temperature-programmed reduction
TWC	three-way catalyst
TWSR	thermochemical water splitting reaction
WGSR	water–gas shift reaction

REFERENCES

[1] C. Bouzigues, T. Gacoin, A. Alexandrou, Biological applications of rare-earth based nanoparticles, ACS Nano 5 (2011) 8488–8505.
[2] M. Bettinelli, L. Carlos, X. Liu, Lanthanide-doped upconversion nanoparticles, Phys. Today 68 (2015) 38–44.
[3] A. Trovarelli, P. Fornasiero, Catalysis by Ceria and Related Materials, in: second ed., Imperial College Press, London, 2013, p. 888.
[4] R.J. Gorte, Ceria in catalysis: from automotive applications to the water gas shift reaction, AICHE J. 56 (2010) 1126–1135.
[5] L. Vivier, D. Duprez, Ceria-based solid catalysts for organic chemistry, ChemSusChem 3 (2010) 654–678.
[6] E. Aneggi, M. Boaro, C. de Leitenburg, G. Dolcetti, A. Trovarelli, Insights into the redox properties of ceria-based oxides and their implications in catalysis, J. Alloys Compd. 408 (2006) 1096–1102.
[7] J. Kaspar, P. Fornasiero, M. Graziani, Use of CeO_2-based oxides in the three-way catalysis, Catal. Today 50 (1999) 285–298.
[8] A. Trovarelli, Catalytic properties of ceria and CeO_2-containing materials, Catal. Rev. Sci. Eng. 38 (1996) 439–520.
[9] J.H. Wang, H. Chen, Z.C. Hu, M.F. Yao, Y.D. Li, A review on the Pd-based three-way catalyst, Catal. Rev. Sci. Eng. 57 (2015) 79–144.
[10] A. Trovarelli, C. de Leitenburg, M. Boaro, G. Dolcetti, The utilization of ceria in industrial catalysis, Catal. Today 50 (1999) 353–367.
[11] L.D. Fan, C.Y. Wang, M.M. Chen, B. Zhu, Recent development of ceria-based (nano)composite materials for low temperature ceramic fuel cells and electrolyte-free fuel cells, J. Power Sources 234 (2013) 154–174.

[12] X.M. Ge, S.H. Chan, Q.L. Liu, Q. Sun, Solid oxide fuel cell anode materials for direct hydrocarbon utilization, Adv. Energy Mater. 2 (2012) 1156–1181.
[13] A. Atkinson, S. Barnett, R.J. Gorte, J.T.S. Irvine, A.J. McEvoy, M. Mogensen, S.C. Singhal, J. Vohs, Advanced anodes for high-temperature fuel cells, Nat. Mater. 3 (2004) 17–27.
[14] C.E. Castano, M.J. O'Keefe, W.G. Fahrenholtz, Cerium-based oxide coatings, Curr. Opinion Solid State Mater. Sci. 19 (2015) 69–76.
[15] C. Xu, X.G. Qu, Cerium oxide nanoparticle: a remarkably versatile rare earth nanomaterial for biological applications, NPG Asia Mater. 6 (2014) 1–16.
[16] W.C. Chueh, C. Falter, M. Abbott, D. Scipio, P. Furler, S.M. Haile, A. Steinfeld, High-flux solar-driven thermochemical dissociation of CO_2 and H_2O using nonstoichiometric ceria, Science 330 (2010) 1797–1801.
[17] A. Corma, P. Atienzar, H. Garcia, J.Y. Chane-Ching, Hierarchically mesostructured doped CeO_2 with potential for solar-cell use, Nat. Mater. 3 (2004) 394–397.
[18] P. Patsalas, S. Logothetidis, C. Metaxa, Optical performance of nanocrystalline transparent ceria films, Appl. Phys. Lett. 81 (2002) 466–468.
[19] P. Jasinski, T. Suzuki, H.U. Anderson, Nanocrystalline undoped ceria oxygen sensor, Sens. Actuators B Chem. 95 (2003) 73–77.
[20] S.H. Lee, Z.Y. Lu, S.V. Babu, E. Matijevic, Chemical mechanical polishing of thermal oxide films using silica particles coated with ceria, J. Mater. Res. 17 (2002) 2744–2749.
[21] H.S. Gandhi, G.W. Graham, R.W. McCabe, Automotive exhaust catalysis, J. Catal. 216 (2003) 433–442.
[22] H.S. Ghandi, A.G. Piken, M. Shelef, R.G. Delosh, Laboratory evaluation of three-way catalysts, 1976, pp. 901–912. SAE Paper, 76021.
[23] J. Kaspar, P. Fornasiero, N. Hickey, Automotive catalytic converters: current status and some perspectives, Catal. Today 77 (2003) 419–449.
[24] Fundamentals and applications of cerium dioxide in Catalysis, Udine (Italy) July 11–14, 2014; CeO_2-based materials in catalysis and electrochemistry. Rauischholzhausen, Giessen (Germany) July 27–30, 2015; Advances in Ceria Based Catalysis: Structural, Electronic and Chemical Properties Tailored for Chemical Conversion, 250th American Chemical Society Fall National Meeting, Boston (MA, USA) August 16–19, 2015; Fundamentals and applications of cerium dioxide in Catalysis 2, Beijing (China), June 30 July 2, 2016.
[25] W. Liu, M. Flytzani-Stephanopoulos, Total oxidation of carbon-monoxide and methane over transition metal-fluorite oxide composite catalysts. 1. Catalyst composition and activity, J. Catal. 153 (1995) 304–316.
[26] P. Fornasiero, R. Dimonte, G.R. Rao, J. Kaspar, S. Meriani, A. Trovarelli, M. Graziani, Rh-loaded CeO_2-ZrO_2 solid-solutions as highly efficient oxygen exchangers—dependence of the reduction behavior and the oxygen storage capacity on the structural properties, J. Catal. 151 (1995) 168–177.
[27] Z.-A. Qiao, Z. Wu, S. Dai, Shape-controlled ceria-based nanostructures for catalysis applications, ChemSusChem 6 (2013) 1821–1833.
[28] K. Zhou, Y. Li, Catalysis based on nanocrystals with well-defined facets, Angew. Chem. Int. Ed. 51 (2012) 602–613.
[29] G. Vile, S. Colussi, F. Krumeich, A. Trovarelli, J. Perez-Ramirez, Opposite face sensitivity of CeO_2 in hydrogenation and oxidation catalysis, Angew. Chem. Int. Ed. 53 (2014) 12069–12072.
[30] H.X. Mai, L.D. Sun, Y.W. Zhang, R. Si, W. Feng, H.P. Zhang, H.C. Liu, C.H. Yan, Shape-selective synthesis and oxygen storage behavior of ceria nanopolyhedra, nanorods, and nanocubes, J. Phys. Chem. B 109 (2005) 24380–24385.

[31] M. Cargnello, N.L. Wieder, T. Montini, R.J. Gorte, P. Fornasiero, Synthesis of dispersible Pd@CeO_2 core-shell nanostructures by self-assembly, J. Am. Chem. Soc. 132 (2010) 1402–1409.
[32] J. Qi, J. Chen, G. Li, S. Li, Y. Gao, Z. Tang, Facile synthesis of core-shell Au@CeO_2 nanocomposites with remarkably enhanced catalytic activity for CO oxidation, Energy Environ. Sci. 5 (2012) 8937–8941.
[33] D.R. Mullins, The surface chemistry of cerium oxide, Surf. Sci. Rep. 70 (2015) 42–85.
[34] J. Paier, C. Penschke, J. Sauer, Oxygen defects and surface chemistry of ceria: quantum chemical studies compared to experiment, Chem. Rev. 113 (2013) 3949–3985.
[35] M.V. Ganduglia-Pirovano, A. Hofmann, J. Sauer, Oxygen vacancies in transition metal and rare earth oxides: current state of understanding and remaining challenges, Surf. Sci. Rep. 62 (2007) 219–270.
[36] J.C. Conesa, Computer modeling of surfaces and defects on cerium dioxide, Surf. Sci. 339 (1995) 337–352.
[37] S. Fabris, G. Vicario, G. Balducci, S. de Gironcoli, S. Baroni, Electronic and atomistic structures of clean and reduced ceria surfaces, J. Phys. Chem. B 109 (2005) 22860–22867.
[38] M. Cargnello, V.V.T. Doan-Nguyen, T.R. Gordon, R.E. Diaz, E.A. Stach, R.J. Gorte, P. Fornasiero, C.B. Murray, Control of metal nanocrystal size reveals metal-support interface role for ceria catalysts, Science 341 (2013) 771–773.
[39] G.S. Zafiris, R.J. Gorte, Evidence for low-temperature oxygen migration from ceria to Rh, J. Catal. 139 (1993) 561–567.
[40] G.N. Vayssilov, Y. Lykhach, A. Migani, T. Staudt, G.P. Petrova, N. Tsud, T. Skala, A. Bruix, F. Illas, K.C. Prince, V. Matolin, K.M. Neyman, J. Libuda, Support nanostructure boosts oxygen transfer to catalytically active platinum nanoparticles, Nat. Mater. 10 (2011) 310–315.
[41] L.R. Morss, Comparative thermochemical and oxidation-reduction properties of lanthanides and actinides, in: K.A. Gschneidner, L. Eyring, G.R. Chopping, G.H. Lander (Eds.), Handbook of the Physics and Chemistry of Rare Earths, Elsevier Science, New York, 1994, pp. 239–291.
[42] A. Trovarelli, Structural properties and nonstoichiometric behavior of CeO_2, in: A. Trovarelli (Ed.), Catalysis by Ceria and Related Materials, Imperial College Press, London, 2002, pp. 15–50.
[43] S. Tsunekawa, R. Sivamohan, S. Ito, A. Kasuya, T. Fukuda, Structural study on monosize CeO_{2-x} nano-particles, Nanostruct. Mater. 11 (1999) 141–147.
[44] D.J.M. Bevan, J. Kordis, Mixed oxides of the type MO_2 (fluorite)—M_2O_3—I oxygen dissociation pressures and phase relationships in the system CeO_2-Ce_2O_3 at high temperatures, J. Inorg. Nucl. Chem. 26 (1964) 1509–1523.
[45] J. Campserveux, P. Gerdanian, Etude thermodynamique de l'oxyde CeO_{2-x} pour $1.5 < OCe < 2$, J. Solid State Chem. 23 (1978) 73–92.
[46] R.J. Panlener, R.N. Blumenthal, J.E. Garnier, A thermodynamic study of nonstoichiometric cerium dioxide, J. Phys. Chem. Solid 36 (1975) 1213–1222.
[47] S.R. Wang, M. Katsuki, T. Hashimoto, M. Dokiya, Expansion behavior of $Ce_{1-y}Gd_yO_{2.0-0.5y-\delta}$ under various oxygen partial pressures evaluated by HTXRD, J. Electrochem. Soc. 150 (2003) A952–A958.
[48] M. Mogensen, N.M. Sammes, G.A. Tompsett, Physical, chemical and electrochemical properties of pure and doped ceria, Solid State Ion. 129 (2000) 63–94.
[49] R. Shannon, Revised effective ionic radii and systematic studies of interatomic distances in halides and chalcogenides, Acta Crystallogr. A 32 (1976) 751–767.

[50] Z. Kang, L. Eyring, The structural basis of the fluorite-related rare earth higher oxides, Aust. J. Chem. 49 (1996) 981–996.
[51] M. Yashima, Crystal and electronic structures, structural disorder, phase transformation and phase diagram of ceria–zirconia and ceria-based materials, in: P. Fornasiero, A. Trovarelli (Eds.), Catalysis by Ceria and Related Materials, Imperial College Press, London, 2013, pp. 1–45.
[52] R. Körner, M. Ricken, J. Nölting, I. Riess, Phase transformations in reduced ceria: determination by thermal expansion measurements, J. Solid State Chem. 78 (1989) 136–147.
[53] E.A. Kümmerle, G. Heger, The structures of C–$Ce_2O_{3+\delta}$, Ce_7O_{12}, and $Ce_{11}O_{20}$, J. Solid State Chem. 147 (1999) 485–500.
[54] M. Zinkevich, D. Djurovic, F. Aldinger, Thermodynamic modelling of the cerium-oxygen system, Solid State Ion. 177 (2006) 989–1001.
[55] H. Bärnighausen, G. Schiller, The crystal structure of A-Ce_2O_3, J. Less-Common Met. 110 (1985) 385–390.
[56] M.S. Dresselhaus, I.L. Thomas, Alternative energy technologies, Nature 414 (2001) 332–337.
[57] Q. Fu, H. Saltsburg, M. Flytzani-Stephanopoulos, Active nonmetallic Au and Pt species on ceria-based water-gas shift catalysts, Science 301 (2003) 935–938.
[58] G.A. Deluga, J.R. Salge, L.D. Schmidt, X.E. Verykios, Renewable hydrogen from ethanol by autothermal reforming, Science 303 (2004) 993–997.
[59] J.A. Rodriguez, S. Ma, P. Liu, J. Hrbek, J. Evans, M. Perez, Activity of CeOx and TiOx nanoparticles grown on Au(111) in the water-gas shift reaction, Science 318 (2007) 1757–1760.
[60] S.D. Park, J.M. Vohs, R.J. Gorte, Direct oxidation of hydrocarbons in a solid-oxide fuel cell, Nature 404 (2000) 265–267.
[61] B.C.H. Steele, A. Heinzel, Materials for fuel-cell technologies, Nature 414 (2001) 345–352.
[62] J.A. Kilner, M. Burriel, Materials for intermediate-temperature solid-oxide fuel cells, Annu. Rev. Mater. Res. 44 (44) (2014) 365–393.
[63] V. Perrichon, A. Laachir, S. Abouarnadasse, O. Touret, G. Blanchard, Thermal-stability of a high-surface area ceria under reducing atmosphere, Appl. Catal. A Gen. 129 (1995) 69–82.
[64] F. Giordano, A. Trovarelli, C. de Leitenburg, M. Giona, A model for the temperature-programmed reduction of low and high surface area ceria, J. Catal. 193 (2000) 273–282.
[65] A. Trovarelli, C. de Leitenburg, G. Dolcetti, Designing better cerium-based oxidation catalysts, ChemTech 27 (1997) 32–37.
[66] E. Rohart, O. Larcher, S. Deutsch, C. Hedouin, H. Aimin, F. Fajardie, M. Allain, P. -Macaudiere, From Zr-rich to Ce-rich: thermal stability of OSC materials on the whole range of composition, Top. Catal. 30–31 (2004) 417–423.
[67] P. Vidmar, P. Fornasiero, J. Kaspar, G. Gubitosa, M. Graziani, Effects of trivalent dopants on the redox properties of $Ce_{0.6}Zr_{0.4}O_2$ mixed oxide, J. Catal. 171 (1997) 160–168.
[68] A. Trovarelli, Structural and oxygen storage/release properties of CeO_2-based solid solutions, Comments Inorg. Chem. 20 (1999) 263–284.
[69] J.C. Hernandez-Garrido, S. Desinan, R. Di Monte, E. Fonda, P.A. Midgley, J.J. Calvino, J. Kaspar, Self-assembly of one-pot synthesized $Ce_xZr_{1-x}O_2$-$BaOnAl_2O_3$ nanocomposites promoted by site-selective doping of alumina with barium, J. Mater. Chem. A 1 (2013) 3645–3651.
[70] B. Zhao, G.F. Li, C.H. Ge, Q.Y. Wang, R.X. Zhou, Preparation of $Ce_{0.67}Zr_{0.33}O_2$ mixed oxides as supports of improved Pd-only three-way catalysts, Appl. Catal. B Environ. 96 (2010) 338–349.

[71] A. Bueno-Lopez, Diesel soot combustion ceria catalysts, Appl. Catal. B Environ. 146 (2014) 1–11.
[72] E. Aneggi, C. de Leitenburg, A. Trovarelli, Ceria-based formulations for catalysts for diesel soot combustion, in: A. Trovarelli, P. Fornasiero (Eds.), Catalysis by Ceria and Related Materials, second ed., vol. 12, Imperial College Press, London, 2013, pp. 565–621.
[73] B. Pereda-Ayo, U. De La Torre, M.P. Gonzalez-Marcos, J.R. Gonzalez-Velasco, Influence of ceria loading on the NOx storage and reduction performance of model Pt-Ba/Al2O3 NSR catalyst, Catal. Today 241 (2015) 133–142.
[74] F. Can, S. Berland, S. Royer, X. Courtois, D. Duprez, Composition-dependent performance of $Ce_xZr_{1-x}O_2$ mixed-oxide-supported WO_3 catalysts for the NOx storage reduction-selective catalytic reduction coupled process, ACS Catal. 3 (2013) 1120–1132.
[75] S.H. Oh, Effects of cerium addition on the CO-NO reaction kinetics over alumina-supported rhodium catalysts, J. Catal. 124 (1990) 477–487.
[76] P. Lööf, B. Kasemo, L. Björnkvist, S. Andersson, A. Frestad, Tpd and Xps studies of CO and NO on highly dispersed Pt+Rh automotive exhaust catalysts: evidence for noble metal-ceria interaction, in: A. Crucq (Ed.), Studies in Surface Science and Catalysis, Elsevier, Amsterdam (NL), 1991, pp. 253–274.
[77] H. Cordatos, R.J. Gorte, CO, NO, and H_2 adsorption on ceria-supported Pd, J. Catal. 159 (1996) 112–118.
[78] S.J. Tauster, S.C. Fung, R.L. Garten, Strong metal-support interactions. Group 8 noble metals supported on TiO_2, J. Am. Chem. Soc. 100 (1978) 170–175.
[79] P. Meriaudeau, J.F. Dutel, M. Dufaux, C. Naccache, Further investigation on metal-support interaction: TiO_2, CeO_2, SiO_2 supported platinum catalysts, in: B. Imelik et al., (Ed.), Studies in Surface Science and Catalysis, Elsevier, Amsterdam (NL), 1982, pp. 95–104.
[80] S. Bernal, J.J. Calvino, M.A. Cauqui, G.A. Cifredo, A. Jobacho, J.M. Rodriguezizquierdo, Metal-support interaction phenomena in rhodium ceria and rhodium titania catalysts—comparative-study by high-resolution transmission electron-spectroscopy, Appl. Catal. A Gen. 99 (1993) 1–8.
[81] T. Bunluesin, R.J. Gorte, G.W. Graham, Studies of the water-gas-shift reaction on ceria-supported Pt, Pd, and Rh: implications for oxygen-storage properties, Appl. Catal. B Environ. 15 (1998) 107–114.
[82] Y. Li, Q. Fu, M. Flytzani-Stephanopoulos, Low-temperature water-gas shift reaction over Cu- and Ni-loaded cerium oxide catalysts, Appl. Catal. B Environ. 27 (2000) 179–191.
[83] Q. Fu, A. Weber, M. Flytzani-Stephanopoulos, Nanostructured Au-CeO_2 catalysts for low-temperature water-gas shift, Catal. Lett. 77 (2001) 87–95.
[84] D. Andreeva, V. Idakiev, T. Tabakova, L. Ilieva, P. Falaras, A. Bourlinos, A. Travlos, Low-temperature water-gas shift reaction over Au/CeO_2 catalysts, Catal. Today 72 (2002) 51–57.
[85] G. Jacobs, L. Williams, U. Graham, G.A. Thomas, D.E. Sparks, B.H. Davis, Low temperature water-gas shift: in situ DRIFTS-reaction study of ceria surface area on the evolution of formates on Pt/CeO_2 fuel processing catalysts for fuel cell applications, Appl. Catal. A Gen. 252 (2003) 107–118.
[86] R. Wang, H.Y. Xu, X.B. Liu, Q.J. Ge, W.Z. Li, Role of redox couples of $Rh^0/Rh^{\delta+}$ and Ce^{4+}/Ce^{3+} in CH_4/CO_2 reforming over Rh-CeO_2/Al_2O_3 catalyst, Appl. Catal. A Gen. 305 (2006) 204–210.
[87] K.-I. Shimizu, H. Kawachi, A. Satsuma, Study of active sites and mechanism for soot oxidation by silver-loaded ceria catalyst, Appl. Catal. B Environ. 96 (2010) 169–175.

[88] J. Graciani, K. Mudiyanselage, F. Xu, A.E. Baber, J. Evans, S.D. Senanayake, D.J. Stacchiola, P. Liu, J. Hrbek, J.F. Sanz, J.A. Rodriguez, Highly active copper-ceria and copper-ceria-titania catalysts for methanol synthesis from CO_2, Science 345 (2014) 546–550.

[89] G. Grzybek, P. Stelmachowski, S. Gudyka, P. Indyka, Z. Sojka, N. Guillen-Hurtado, V. Rico-Perez, A. Bueno-Lopez, A. Kotarba, Strong dispersion effect of cobalt spinel active phase spread over ceria for catalytic N_2O decomposition: the role of the interface periphery, Appl. Catal. B Environ. 180 (2016) 622–629.

[90] M.J. Munoz-Batista, M. Natividad Gomez-Cerezo, A. Kubacka, D. Tudela, M. Fernandez-Garcia, Role of interface contact in CeO_2-TiO_2 photocatalytic composite materials, ACS Catal. 4 (2014) 63–72.

[91] S. Kundu, J. Ciston, S.D. Senanayake, D.A. Arena, E. Fujita, D. Stacchiola, L. Barrio, R.M. Navarro, J.L.G. Fierro, J.A. Rodriguez, Exploring the structural and electronic properties of Pt/Ceria-modified TiO_2 and its photocatalytic activity for water splitting under visible light, J. Phys. Chem. C 116 (2012) 14062–14070.

[92] X.L. Tang, B.C. Zhang, Y. Li, Y.D. Xu, Q. Xin, W.J. Shen, CuO/CeO_2 catalysts: redox features and catalytic behaviors, Appl. Catal. A Gen. 288 (2005) 116–125.

[93] Y. Nagai, K. Dohmae, Y.F. Nishimura, H. Kato, H. Hirata, N. Takahashi, Operando XAFS study of catalytic NO reduction over Cu/CeO_2: the effect of copper-ceria interaction under periodic operation, Phys. Chem. Chem. Phys. 15 (2013) 8461–8465.

[94] A. Iglesias-Juez, A. Martinez-Arias, M. Fernandez-Garcia, Metal-promoter interface in Pd/(Ce, Zr)O-x/Al2O3 catalysts: effect of thermal aging, J. Catal. 221 (2004) 148–161.

[95] M. Cargnello, J.J.D. Jaen, J.C.H. Garrido, K. Bakhmutsky, T. Montini, J.J.C. Gamez, R.J. Gorte, P. Fornasiero, Exceptional activity for methane combustion over modular $Pd@CeO_2$ subunits on functionalized Al_2O_3, Science 337 (2012) 713–717.

[96] S. Colussi, A. Trovarelli, G. Groppi, J. Llorca, The effect of CeO_2 on the dynamics of Pd-PdO transformation over Pd/Al_2O_3 combustion catalysts, Catal. Commun. 8 (2007) 1263–1266.

[97] S. Salasc, V. Perrichon, M. Primet, M. Chevrier, N. Mouaddib-Moral, Oxygen titration of spill-over hydrogen in ceria and ceria-alumina supported platinum-rhodium catalysts: application to the determination of the ceria surface in contact with metal, J. Catal. 189 (2000) 401–409.

[98] D.J. Stacchiola, Tuning the properties of copper-based catalysts based on molecular in situ studies of model systems, Acc. Chem. Res. 48 (2015) 2151–2158.

[99] S.D. Senanayake, D. Stacchiola, J.A. Rodriguez, Unique properties of ceria nanoparticles supported on metals: novel inverse ceria/copper catalysts for CO oxidation and the water-gas shift reaction, Acc. Chem. Res. 46 (2013) 1702–1711.

[100] X. Wang, J.A. Rodriguez, J.C. Hanson, D. Gamarra, A. Martínez-Arias, M. Fernández-García, In situ studies of the active sites for the water gas shift reaction over Cu−CeO2 catalysts: complex interaction between metallic copper and oxygen vacancies of ceria, J. Phys. Chem. B 110 (2006) 428–434.

[101] K. Mudiyanselage, S.D. Senanayake, L. Feria, S. Kundu, A.E. Baber, J. Graciani, A.B. Vidal, S. Agnoli, J. Evans, R. Chang, S. Axnanda, Z. Liu, J.F. Sanz, P. Liu, J.A. Rodriguez, D.J. Stacchiola, Importance of the metal-oxide interface in catalysis: in situ studies of the water-gas shift reaction by ambient-pressure X-ray photoelectron Spectroscopy, Angew. Chem. Int. Ed. 52 (2013) 5101–5105.

[102] R. Kopelent, J.A. van Bokhoven, J. Szlachetko, J. Edebeli, C. Paun, M. Nachtegaal, O.V. Safonova, Catalytically active and spectator Ce^{3+} in ceria-supported metal catalysts, Angew. Chem. Int. Ed. 54 (2015) 8728–8731.

[103] C. Castellarin-Cudia, S. Surnev, G. Schneider, R. Podlucky, M.G. Ramsey, F.P. Netzer, Strain-induced formation of arrays of catalytically active sites at the metal-oxide interface, Surf. Sci. 554 (2004) L120–L126.

[104] M. Lopez-Haro, J.M. Cies, S. Trasobares, J.A. Perez-Omil, J.J. Delgado, S. Bernal, P. Bayle-Guillemaud, O. Stephan, K. Yoshida, E.D. Boyes, P.L. Gai, J.J. Calvino, Imaging nanostructural modifications induced by electronic metal-support interaction effects at Au parallel to cerium-based oxide nanointerfaces, ACS Nano 6 (2012) 6812–6820.

[105] B. Liu, J. Liu, T. Li, Z. Zhao, X.Q. Gong, Y. Chen, A.J. Duan, G.Y. Jiang, Y.C. Wei, Interfacial effects of CeO_2-supported Pd nanorod in catalytic CO oxidation: a theoretical study, J. Phys. Chem. C 119 (2015) 12923–12934.

[106] M. Monte, G. Munuera, D. Costa, J.C. Conesa, A. Martinez-Arias, Near-ambient XPS characterization of interfacial copper species in ceria-supported copper catalysts, Phys. Chem. Chem. Phys. 17 (2015) 29995–30004.

[107] A. Kubacka, A. Martinez-Arias, M. Fernandez-Garcia, Role of the interface in base-metal ceria-based catalysts for hydrogen purification and production processes, ChemCatChem 7 (2015) 3614–3624.

[108] C.M.Y. Yeung, K.M.K. Yu, Q.J. Fu, D. Thompsett, M.I. Petch, S.C. Tsang, Engineering Pt in ceria for a maximum metal-support interaction in catalysis, J. Am. Chem. Soc. 127 (2005) 18010–18011.

[109] C. Wen, Y. Zhu, Y.C. Ye, S.R. Zhang, F. Cheng, Y. Liu, P. Wang, F. Tao, Water-gas shift reaction on metal nanoclusters encapsulated in mesoporous ceria studied with ambient-pressure X-ray photoelectron spectroscopy, ACS Nano 6 (2012) 9305–9313.

[110] E.T. Saw, U. Oemar, M.L. Ang, K. Hidajat, S. Kawi, Highly active and stable bimetallic nickel-copper core-ceria shell catalyst for high-temperature water-gas shift reaction, ChemCatChem 7 (2015) 3358–3367.

[111] Y.Y. Lin, Z.L. Wu, J.G. Wen, K.L. Ding, X.Y. Yang, K.R. Poeppelmeier, L.D. Marks, Adhesion and atomic structures of gold on ceria nanostructures: the role of surface structure and oxidation state of ceria supports, Nano Lett. 15 (2015) 5375–5381.

[112] S. Agarwal, L. Lefferts, B.L. Mojet, D.A. Ligthart, E.J. Hensen, D.R. Mitchell, W.J. Erasmus, B.G. Anderson, E.J. Olivier, J.H. Neethling, A.K. Datye, Exposed surfaces on shape-controlled ceria nanoparticles revealed through AC-TEM and water–gas shift reactivity, ChemSusChem 6 (2013) 1898–1906.

[113] I. Florea, C. Feral-Martin, J. Majimel, D. Ihiawakrim, C. Hirlimann, O. Ersen, Three-dimensional tomographic analyses of CeO_2 nanoparticles, Cryst. Growth Des. 13 (2013) 1110–1121.

[114] S. Agarwal, X. Zhu, E.J.M. Hensen, B.L. Mojet, L. Lefferts, Surface-dependence of defect chemistry of nanostructured ceria, J. Phys. Chem. C 119 (2015) 12423–12433.

[115] N. Ta, J.J. Liu, S. Chenna, P.A. Crozier, Y. Li, A. Chen, W. Shen, Stabilized gold nanoparticles on ceria nanorods by strong interfacial anchoring, J. Am. Chem. Soc. 134 (2012) 20585–20588.

[116] Y.Y. Lin, Z.L. Wu, J.G. Wen, K.R. Poeppelmeier, L.D. Marks, Imaging the atomic surface structures of CeO_2 nanoparticles, Nano Lett. 14 (2014) 191–196.

[117] K.B. Zhou, X. Wang, X.M. Sun, Q. Peng, Y.D. Li, Enhanced catalytic activity of ceria nanorods from well-defined reactive crystal planes, J. Catal. 229 (2005) 206–212.

[118] Z.L. Wu, M.J. Li, S.H. Overbury, On the structure dependence of CO oxidation over CeO_2 nanocrystals with well-defined surface planes, J. Catal. 285 (2012) 61–73.

[119] Tana, M. Zhang, J. Li, H. Li, Y. Li, W. Shen, Morphology-dependent redox and catalytic properties of CeO2 nanostructures: nanowires, nanorods and nanoparticles, Catal. Today 148 (2009) 179–183.

[120] E. Aneggi, J. Llorca, M. Boaro, A. Trovarelli, Surface-structure sensitivity of CO oxidation over polycrystalline ceria powders, J. Catal. 234 (2005) 88–95.
[121] F. Wang, C.M. Li, X.Y. Zhang, M. Wei, D.G. Evans, X. Duan, Catalytic behavior of supported Ru nanoparticles on the {100}, {110}, and {111} facet of CeO_2, J. Catal. 329 (2015) 177–186.
[122] E. Aneggi, D. Wiater, C. de Leitenburg, J. Llorca, A. Trovarelli, Shape-dependent activity of ceria in soot combustion, ACS Catal. 4 (2014) 172–181.
[123] X.S. Huang, H. Sun, L.C. Wang, Y.M. Liu, K.N. Fan, Y. Cao, Morphology effects of nanoscale ceria on the activity of Au/CeO_2 catalysts for low-temperature CO oxidation, Appl. Catal. B Environ. 90 (2009) 224–232.
[124] Y.X. Gao, R.T. Li, S.L. Chen, L.F. Luo, T. Cao, W.X. Huang, Morphology-dependent interplay of reduction behaviors, oxygen vacancies and hydroxyl reactivity of CeO_2 nanocrystals, Phys. Chem. Chem. Phys. 17 (2015) 31862–31871.
[125] W.I. Hsiao, Y.S. Lin, Y.C. Chen, C.S. Lee, The effect of the morphology of nanocrystalline CeO_2 on ethanol reforming, Chem. Phys. Lett. 441 (2007) 294–299.
[126] W.Q. Han, W. Wen, J.C. Hanson, X.W. Teng, N. Marinkovic, J.A. Rodriguez, One-dimensional ceria as catalyst for the low-temperature water-gas shift reaction, J. Phys. Chem. C 113 (2009) 21949–21955.
[127] W.Y. Lei, T.T. Zhang, L. Gu, P. Liu, J.A. Rodriguez, G. Liu, M.H. Liu, Surface-structure sensitivity of CeO_2 nanocrystals in photocatalysis and enhancing the reactivity with nanogold, ACS Catal. 5 (2015) 4385–4393.
[128] G.Q. Yi, H.W. Yang, B.D. Li, H.Q. Lin, K. Tanaka, Y.Z. Yuan, Preferential CO oxidation in a H_2-rich gas by Au/CeO_2 catalysts nanoscale CeO_2 shape effect and mechanism aspect, Catal. Today 157 (2010) 83–88.
[129] R. Si, M. Flytzani-Stephanopoulos, Shape and crystal-plane effects of nanoscale ceria on the activity of Au-CeO_2 catalysts for the water-gas shift reaction, Angew. Chem. Int. Ed. 47 (2008) 2884–2887.
[130] M. Zabilskiy, P. Djinovic, E. Tchernychova, O.P. Tkachenko, L.M. Kustov, A. Pintar, Nanoshaped CuO/CeO_2 materials: effect of the exposed ceria surfaces on catalytic activity in N_2O decomposition reaction, ACS Catal. 5 (2015) 5357–5365.
[131] Z.J. Mei, Y. Li, M.H. Fan, L. Zhao, J. Zhao, Effect of the interactions between Pt species and ceria on Pt/ceria catalysts for water gas shift: the XPS studies, Chem. Eng. J. 259 (2015) 293–302.
[132] N. Singhania, E.A. Anumol, N. Ravishankar, G. Madras, Influence of CeO_2 morphology on the catalytic activity of CeO_2-Pt hybrids for CO oxidation, Dalton Trans. 42 (2013) 15343–15354.
[133] P.K. Cheekatamarla, C.M. Finnerty, Reforming catalysts for hydrogen generation in fuel cell applications, J. Power Sources 160 (2006) 490–499.
[134] G. Nahar, V. Dupont, Hydrogen production from simple alkanes and oxygenated hydrocarbons over ceria-zirconia supported catalysts: review, Renew. Sustain. Energy Rev. 32 (2014) 777–796.
[135] M. Usman, W.M. Daud, H.F. Abbas, Dry reforming of methane: influence of process parameters—a review, Renew. Sustain. Energy Rev. 45 (2015) 710–744.
[136] C. Ratnasamy, J.P. Wagner, Water gas shift catalysis, Catal. Rev. Sci. Eng. 51 (2009) 325–440.
[137] N. Bion, F. Epron, M. Moreno, F. Marino, D. Duprez, Preferential oxidation of carbon monoxide in the presence of hydrogen (PROX) over noble metals and transition metal oxides: advantages and drawbacks, Top. Catal. 51 (2008) 76–88.

[138] M.G. Castaño, T.R. Reina, S. Ivanova, M.A. Centeno, J.A. Odriozola, Pt vs. Au in water-gas shift reaction, J. Catal. 314 (2014) 1–9.
[139] M. Melchionna, P. Fornasiero, The role of ceria-based nanostructured materials in energy applications, Mater. Today 17 (2014) 349–357.
[140] C.W. Sun, H. Li, L.Q. Chen, Nanostructured ceria-based materials: synthesis, properties, and applications, Energy Environ. Sci. 5 (2012) 8475–8505.
[141] L. Adijanto, A. Sampath, A.S. Yu, M. Cargnello, P. Fornasiero, R.J. Gorte, J.M. Vohs, Synthesis and stability of Pd@CeO_2 core-shell catalyst films in solid oxide fuel cell anodes, ACS Catal. 3 (2013) 1801–1809.
[142] T.F. Hou, S.Y. Zhang, Y.D. Chen, D.Z. Wang, W.J. Cal, Hydrogen production from ethanol reforming: catalysts and reaction mechanism, Renew. Sustain. Energy Rev. 44 (2015) 132–148.
[143] S. Ahmed, A. Aitani, F. Rahman, A. Al-Dawood, F. Al-Muhaish, Decomposition of hydrocarbons to hydrogen and carbon, Appl. Catal. A Gen. 359 (2009) 1–24.
[144] X.J. Du, D.S. Zhang, L.Y. Shi, R.H. Gao, J.P. Zhang, Morphology dependence of catalytic properties of Ni/CeO_2 nanostructures for carbon dioxide reforming of methane, J. Phys. Chem. C 116 (2012) 10009–10016.
[145] Z.L. Wu, A.K.P. Mann, M.J. Li, S.H. Overbury, Spectroscopic investigation of surface-dependent acid base property of ceria nanoshapes, J. Phys. Chem. C 119 (2015) 7340–7350.
[146] D. Pakhare, J. Spivey, A review of dry (CO_2) reforming of methane over noble metal catalysts, Chem. Soc. Rev. 43 (2014) 7813–7837.
[147] M. Fronzi, S. Piccinin, B. Delley, E. Traversa, C. Stampfl, Water adsorption on the stoichiometric and reduced CeO_2(111) surface: a first-principles investigation, Phys. Chem. Chem. Phys. 11 (2009) 9188–9199.
[148] S. Fuente, M.M. Branda, F. Illas, Role of step sites on water dissociation on stoichiometric ceria surfaces, Theor. Chem. Accounts 131 (2012) 1190–1192.
[149] M. Molinari, S.C. Parker, D.C. Sayle, M.S. Islam, Water adsorption and its effect on the stability of low index stoichiometric and reduced surfaces of ceria, J. Phys. Chem. C 116 (2012) 7073–7082.
[150] S. Abanades, G. Flamant, Thermochemical hydrogen production from a two-step solar-driven water-splitting cycle based on cerium oxides, Sol. Energy 80 (2006) 1611–1623.
[151] J.R. Scheffe, A. Steinfeld, Oxygen exchange materials for solar thermochemical splitting of H_2O and CO_2: a review, Mater. Today 17 (2014) 341–348.
[152] D. Yadav, R. Banerjee, A review of solar thermochemical processes, Renew. Sustain. Energy Rev. 54 (2016) 497–532.
[153] W.C. Chueh, S.M. Haile, A thermochemical study of ceria: exploiting an old material for new modes of energy conversion and CO_2 mitigation, Philos. Trans. R. Soc. 368 (2010) 3269–3294.
[154] F. Yilmaz, M. Tolga Balta, R. Selbaş, A review of solar based hydrogen production methods, Renew. Sustain. Energy Rev. 56 (2016) 171–178.
[155] J. Lapp, J.H. Davidson, W. Lipinski, Efficiency of two-step solar thermochemical non-stoichiometric redox cycles with heat recovery, Energy 37 (2012) 591–600.
[156] D. Marxer, P. Furler, J. Scheffe, H. Geerlings, C. Falter, V. Batteiger, A. Sizmann, A. Steinfeld, Demonstration of the entire production chain to renewable kerosene via solar thermochemical splitting of H_2O and CO_2, Energy Fuel (2015) 3241–3250.
[157] H. Kaneko, T. Miura, A. Fuse, H. Ishihara, S. Taku, H. Fukuzumi, Y. Naganuma, Y. Tamaura, Rotary-type solar reactor for solar hydrogen production with two-step water splitting process, Energy Fuel 21 (2007) 2287–2293.

[158] P. Furler, J. Scheffe, M. Gorbar, L. Moes, U. Vogt, A. Steinfeld, Solar thermo-chemical CO_2 splitting utilizing a reticulated porous ceria redox system, Energy Fuel 26 (2012) 7051–7059.

[159] A. Le Gal, S. Abanades, G. Flamant, CO_2 and H_2O splitting for thermochemical production of solar fuels using nonstoichiometric ceria and ceria/Zirconia solid solutions, Energy Fuel 25 (2011) 4836–4845.

[160] N.D. Petkovich, S.G. Rudisill, L.J. Venstrom, D.B. Boman, J.H. Davidson, A. Stein, Control of heterogeneity in nanostructured $Ce_{1-x}Zr_xO_2$ binary oxides for enhanced thermal stability and water splitting activity, J. Phys. Chem. 115 (2011) 21022–21033.

[161] A. Pappacena, M. Boaro, L. Armelao, J. Llorca, A. Trovarelli, Water splitting reaction on $Ce_{0.15}Zr_{0.85}O_2$ driven by surface heterogeneity, Catal. Sci. Technol. 6 (2016) 399–403.

[162] C. Chatzichristodoulou, P.T. Blennow, M. Sogaard, P.V. Hendrikens, M.B. Mogenesen, Ceria and its use in solid oxide cells and oxygen membranes, in: A. Trovarelli, P. Fornasiero (Eds.), Catalysis by Ceria and Related Materials, Imperial College Press, London, 2013, pp. 623–782.

[163] L. Ma, K. Zhao, B.-H. Kim, Q. Li, J. Huang, Electrochemical performance of solid oxide fuel cells with Sm, Nd co-doped $Ce_{0.85}(Sm_xNd_{1-x})_{0.15}O_{2-\delta}$ electrolyte, Ceram. Int. 41 (2015) 6391–6397.

[164] C. Sun, R. Hui, J. Roller, Cathode materials for solid oxide fuel cells: a review, J. Solid State Electrochem. 14 (2010) 1125–1144.

[165] W.C. Chueh, Y. Hao, W.J. Jung, S.M. Haile, High electrochemical activity of the oxide phase in model ceria–Pt and ceria–Ni composite anodes, Nat. Mater. 11 (2011) 155–161.

[166] R.J. Gorte, J.M. Vohs, Nanostructured anodes for solid oxide fuel cells, Curr. Opin. Colloid Interface Sci. 14 (2009) 236–244.

[167] Z.B. Liu, B.B. Liu, D. Ding, M.F. Liu, F.L. Chen, C.R. Xia, Fabrication and modification of solid oxide fuel cell anodes via wet impregnation/infiltration technique, J. Power Sources 237 (2013) 243–259.

[168] L. Bardini, A. Pappacena, M. Dominguez-Escalante, J. Llorca, M. Boaro, Structural and electrocatalytic properties of molten core Sn@SnOx nanoparticles on ceria. Appl. Catal. B Environ. 197 (2016), in press. http://dx.doi.org/10.1016/j.apcatb.2016.02.050.

[169] K.Y. Ahn, H.P. He, J.M. Vohs, R.J. Gorte, Enhanced thermal stability of SOFC anodes made with CeO_2-ZrO_2 solutions, Electrochem. Solid-State Lett. 8 (2005) A414–A417.

[170] J.B. Wang, H.C. Jang, T.J. Huang, Study of Ni-samaria-doped ceria anode for direct oxidation of methane in solid oxide fuel cells, J. Power Sources 122 (2003) 122–131.

[171] V. Bambagioni, C. Bianchini, Y.X. Chen, J. Filippi, P. Fornasiero, M. Innocenti, A. Lavacchi, A. Marchionni, W. Oberhauser, F. Vizza, Energy efficiency enhancement of ethanol electrooxidation on Pd-CeO_2/C in passive and active polymer electrolyte-membrane fuel cells, ChemSusChem 5 (2012) 1266–1273.

[172] J.C. Yu, K.F. Chen, X. Chen, H. Wang, D.F. Xue, Applying cerium to high performance supercapacitors, Materials Focus 4 (2015) 81–83.

[173] S.-Q. Liu, S.-S. Zhou, Z.-G. Chen, C.-B. Liu, F. Chen, Z.-Y. Wu, An artificial photosynthesis system based on CeO2 as light harvester and N-doped graphene Cu(II) complex as artificial metalloenzyme for CO2 reduction to methanol fuel, Catal. Commun. 73 (2016) 7–11.

[174] X.H. Lu, T. Zhai, H.N. Cui, J.Y. Shi, S.L. Xie, Y.Y. Huang, C.L. Liang, Y.X. Tong, Redox cycles promoting photocatalytic hydrogen evolution of CeO_2 nanorods, J. Mater. Chem. 21 (2011) 5569–5572.

Chapter 290

Lanthanide Metal-Organic Frameworks for Luminescent Applications

Yuanjing Cui*, Jun Zhang*, Banglin Chen*,†,1 and Guodong Qian*,1
*State Key Laboratory of Silicon Materials, Cyrus Tang Center for Sensor Materials and Applications, School of Materials Science and Engineering, Zhejiang University, Hangzhou, China
†University of Texas at San Antonio, San Antonio, TX, United States
1Corresponding authors: e-mail: banglin.chen@utsa.edu; gdqian@zju.edu.cn

Chapter Outline

1 INTRODUCTION

Metal-organic frameworks (MOFs) are an intriguing class of inorganic–organic hybrid materials belonging to the larger group of coordination polymers that consist of metal ions or metal-containing clusters connected to multidentate organic ligands via metal coordination bonds [1–4]. MOFs generally exhibit microporous character and the pore sizes can be tuned from several angstroms to several nanometers. The extraordinarily high porosity and wide range of pore sizes of MOFs make them attractive for scientific and industrial applications as new porous materials. Compared with conventional inorganic porous materials, such as zeolites and mesoporous silica, one of the most

Handbook on the Physics and Chemistry of Rare Earths, Vol. 50. http://dx.doi.org/10.1016/bs.hpcre.2016.04.001

intriguing advantages of MOFs is their easy design and structural flexibility. The nearly limitless choices of metal ions and organic linkers make it possible to construct an enormous amount of new MOFs with diverse structures, topologies, and porosity. Furthermore, the mild conditions usually employed for their synthesis allow for the functionalization of their building blocks, and thus the rational design of novel materials [5–8]. In fact, a large numbers of MOFs have been synthesized up to now that exhibit significantly high surface area, up to 7000 m^2/g, tunable pore sizes through the interplay of both organic and inorganic components with the pore sizes ranging from 3 to 100 Å, and the lowest framework density down to 0.13 g/cm^3. These unique features have enabled MOFs to be very promising materials for potential applications in many diverse areas, such as gas storage, gas capture, separations, chemical catalysis, luminescence, magnetism, and drug delivery [9–64]. For example, a MOF methane fuel tank has already been implemented in test vehicles; while a few MOFs have been targeted for the industrially very important separation of small hydrocarbons such as acetylene, ethylene, and ethane [46–48].

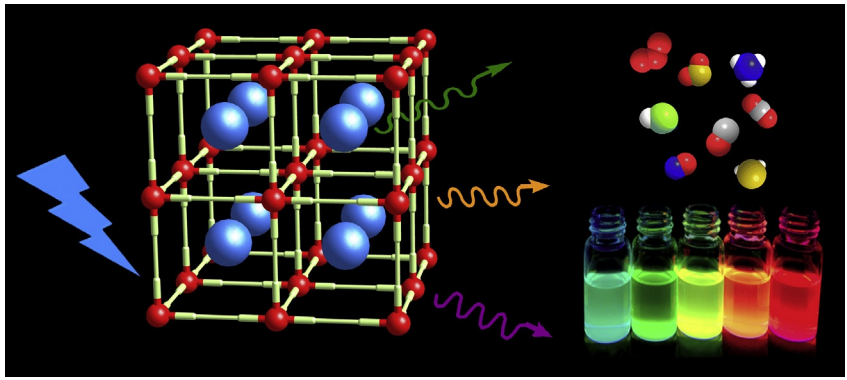

Recently, the development of luminescent functional MOFs has attracted more scientific interest [49–98]. In fact, the luminescence of MOFs cannot only be generated from the metal ions/clusters and organic linkers but can also be tuned by the interplay/interactions among these building components. The intrinsic permanent porosity in a large number of MOFs further enables the encapsulation of guest fluorescent species and thus produces additional luminescence. Furthermore, the periodical location of light-emissive metal ions and organic ligands as well as the confinement of guests within pores can effectively prevent aggregation-induced luminescence quenching.

As one special type of luminescent MOF materials, the lanthanide MOFs provide the bright promise to develop various types of luminescent applications due to their unique luminescence properties such as high luminescence quantum yield, long-lived emission, large ligand-induced Stokes shifts, and

characteristically sharp line emissions [65–67]. In addition, the luminescent intensity of lanthanide ions is very sensitive to structural details of the coordination environment, thereby providing an effective platform for chemical sensing. The lanthanide MOFs potentially can also provide other attractive characteristics, such as permanent porosity and nanoscale processability, generating different functionalities from these molecular lanthanide complexes. These intrinsic luminescent features of lanthanides together with the unique advantages of MOFs offer excellent prospects for designing novel luminescent materials with enhanced targeted functionalities and high added values for specific applications.

Different from the transition-metal ions, lanthanide ions tend to adopt high coordination numbers and flexible coordination geometry. The high coordination numbers and connectivities facilitate stabilizing the frameworks if all these coordination sites are utilized and bridged by organic linkers. Based on hard and soft acid–base considerations, the lanthanides have affinity for relatively hard oxygen-containing linkers over other functional groups. Up to now, a number of lanthanide MOFs with various dimensionality and topologies have been constructed based on multidentate ligands with oxygen or with mixed oxygen–nitrogen atoms [65–67]. Among the published reports, and besides the presentation of fundamental aspects such as their syntheses and luminescent properties, functional applications of luminescent lanthanide MOFs are increasingly being addressed during recent years. In this chapter, we review the latest developments in lanthanide MOFs and their applications in sensing, light-emitting devices, and biomedicine. In addition, we highlight some strategies for effectively improving their luminescent properties for functional applications.

2 THE STATUS AND ADVANTAGES OF LANTHANIDE MOFs

Lanthanide elements have atomic numbers ranging from 57 to 71 with electronic configurations of neutral atoms being $[Xe]4f^n6s^2$ or $[Xe]4f^{n-1}5d^16s^2$. Because the 4f shells of lanthanide elements are unfilled, the electronic configurations $[Xe]4f^n$ ($n = 0$–14) of trivalent lanthanide ions generate a rich variety of electronic energy levels, resulting in the fascinating luminescent properties. With the exception of La^{3+} and Lu^{3+}, all lanthanide ions can generate luminescent f–f emissions from ultraviolet (UV) to visible and near-infrared (NIR) ranges. The Eu^{3+}, Tb^{3+}, Sm^{3+}, and Tm^{3+} ions emit red, green, orange, and blue light, respectively, while the Yb^{3+}, Nd^{3+}, and Er^{3+} ions display the well-known NIR luminescence [99–104].

Lanthanide MOFs have some advantages over the conventional inorganic and organic luminescent materials. Firstly, the richness of lanthanide ions/clusters as the nodes and a large number of organic chromophores as the linkers to construct lanthanide MOFs have endowed grand promise to generate a large amount of new luminescent materials. In addition, the highly ordered

MOF structures may systematically control luminescent properties, especially the mutual separation of lanthanide ions induced by carefully tailored ligands in lanthanide MOFs prevent self-quenching of luminescence. Secondly, because the 4f electrons of lanthanide ions are well shielded from the external interactions by the outer $5s^2$ and $5p^6$ shells, the 4f–4f transitions are Laporte forbidden, resulting in the long-lived narrow and characteristic emissions. Such narrow lanthanide-based luminescence can improve the color purity of solid-state light materials and devices. Thirdly, the isostructural behavior of lanthanide MOFs may allow for the incorporation of different lanthanide ions into the same host material. By doping two or more lanthanide ions into mixed-lanthanide MOFs, multiple luminescent centers and tunable luminescence can be successfully achieved, which are very useful for developing ratiometric luminescent sensors and white-light-emitting materials. Fourthly, the permanent porosities of lanthanide MOFs allow them to reversibly take up and release guest substrates and result in sensing properties of the hosts with differential luminescence recognition. Incorporation of analytes into the pores of lanthanide MOFs can lead to the interactions between the linkers/lanthanides and the analytes. These interactions may facilitate or disrupt the energy transfer process by modifying the energy transfer ability of the bound ligands and/or providing a new path for the energy transfer from the analytes to the lanthanide ions, enabling lanthanide MOFs as useful luminescent probes. Furthermore, their high surface areas make the lanthanide MOFs useful preconcentrators for increasing the analyte concentrations to levels high above those in the surrounding atmosphere, thus leading to much smaller detection levels than otherwise available.

Although the lanthanide ions suffer from weak light absorption due to the forbidden f–f transitions, this problem can be overcome in MOFs by coupling organic linkers that can participate in energy transfer processes, known as "luminescence sensitization" or "antenna effect" [99–102]. The mechanism of antenna sensitization within lanthanide MOFs is comprised of three steps: light is absorbed by the organic ligands around the lanthanide ions; energy is transferred to the lanthanide ions from organic ligands, and then the luminescence is generated from the lanthanide ions. One of the main energy migration paths, particularly for the visible-emitting ions Eu^{3+} and Tb^{3+}, is ligand-centered absorptions followed by intersystem crossing $S_1 \rightarrow T_1$, $T_1 \rightarrow Ln^{3+}$ transfer, and lanthanide-centered emission. In lanthanide MOFs, the following conditions have to be fulfilled to generate efficient lanthanide-centered luminescence:

(1) The intersystem crossing yield of the antenna linkers should be high, although the lanthanide ion can enhance the intersystem crossing yield via an external heavy atom effect.
(2) The linkers should have matching triplet state energy levels for resonance levels of the lanthanide ion. If the energy difference between donor and

acceptor is too small a thermally activated energy back transfer can occur, whereas large energy differences may lead to slower energy transfer rates. The energy of the triplet state must be elaborately tuned to maximize the transfer and minimize the back transfer.

(3) The antenna linkers should have a high absorption coefficient, in order to obtain high luminescence intensities.

(4) The antenna linkers should be in close proximity to the lanthanide ion, because the energy transfer process is strongly distance dependent.

3 LANTHANIDE MOFs FOR LUMINESCENT SENSING

The combination of inherent porosity and unique luminescent properties has enabled lanthanide MOFs to be a very promising type of sensing materials. As mentioned earlier, the luminescent properties of lanthanide MOFs are very sensitive to their structural characteristics, coordination environment of lanthanide ions, as well as the interactions of either ligands or lanthanide ions with analytes, which have provided a solid rationale for developing luminescent sensing platforms. The high surface area and permanent porosity suggest the potential to effectively concentrate analytes at higher levels within the MOFs, and thereby improve the sensitivity. In principle, the porous MOF architecture provides remarkable selectivity over other sensor materials. The tunable pore sizes enable the selective accommodation of analytes, while functional sites such as open metal sites and Lewis acidic and basic sites for their differential interactions with analytes will certainly further enhance the sensing selectivity of MOF sensors.

3.1 Functional Sites Within Lanthanide MOFs for Highly Selective Sensing

Incorporation of functional sites including open metal sites, Lewis acidic sites, and Lewis basic pyridyl sites within porous lanthanide MOFs is the key for highly selective luminescence sensing. By immobilizing the free Lewis base sites within porous lanthanide MOFs as sensing sites, Chen and Qian have developed a new way of sensing Cu^{2+} [68]. Exploiting the preferential binding of lanthanide ions to carboxylate oxygen atoms over pyridyl nitrogen atoms, a lanthanide MOF $Eu(PDC)_{1.5}$ (PDC = pyridine-3,5-dicarboxylate) was synthesized. In this MOF, Eu^{3+} ions are bridged by PDC organic linkers to form a three-dimensional rod packing structure. Each europium atom is coordinated by six oxygen atoms from the carboxylate groups of PDC, and capped by one distorted DMF molecule. The MOF $Eu(PDC)_{1.5}$ is porous and the basic Lewis sites line the interior of the channels, which may be emptied of DMF and water molecules by heating at 200°C. The desolvated MOF $Eu(PDC)_{1.5}$ was immersed in DMF solutions containing different metal ions, such as Na^+, K^+, Mg^{2+}, Ca^{2+}, Mn^{2+}, Co^{2+}, Cu^{2+}, Zn^{2+}, and Cd^{2+} ions, to form

metal-ion incorporated samples for luminescence studies. Only Cu^{2+} can quench the lanthanide emission significantly (Fig. 1), whereas alkali metal ions and alkaline earth metal ions have a negligible effect on the luminescence intensity. It is speculated that the binding of the pyridyl nitrogen atoms to Cu^{2+} reduces the antenna efficiency of the PDC organic linkers to amplify the f–f transitions of Eu^{3+}, resulting in quenching of the luminescence. These results indicate that the free Lewis base sites within porous lanthanide MOFs are expected to play very important roles for their selective sensing of small Lewis acidic molecules and metal ions.

Considering that the open metal sites play very important roles in highly selective gas separation and storage because they favorably interact with gas molecules, Chen and Qian have illustrated this strategy by achieving highly selective luminescent sensing of small molecules using a porous lanthanide MOF [69], Eu(BTC) (BTC = 1,3,5-benzenetricarboxylate), which is isostructural with MOF-76 ($[Tb(BTC)(H_2O)]\cdot 3(H_2O)0.5DMF$). The MOF has 1D channels of about 6.6×6.6 Å^2 along the *c*-axis (Fig. 2), enabling the reversible uptake and release of some solvent molecules such as DMF, CH_3CN, $CHCl_3$, 2-propanol, 1-propanol, methanol, THF, ethanol, and acetone. The Eu^{3+} open metal sites were generated by removal of free and terminal water molecules after simple calcination of Eu(BTC) at 140°C under vacuum for 24 h. The luminescence intensity of activated Eu(BTC) is largely dependent on the solvent molecules in which it was immersed, particularly in the case of DMF and acetone, which exhibits the most significant enhancing and quenching effects, respectively. It is suggested that the binding interaction of the open metal sites with guest solvent molecules definitely plays an

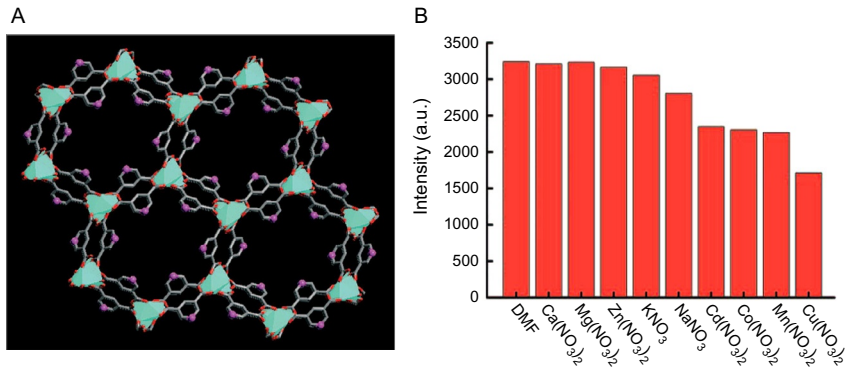

FIG. 1 (A) Crystal structure of $Eu(PDC)_{1.5}$, viewed along the *a*-axis indicating immobilized Lewis basic pyridyl sites oriented toward pore centers. (B) Comparison of the luminescence intensity of dehydrated MOF $Eu(PDC)_{1.5}$ incorporating different metal ions in 10 mM DMF solutions of $M(NO_3)_x$. *Reprinted with permission from B. Chen, L. Wang, Y. Xiao, F.R. Fronczek, M. Xue, Y. Cui, G. Qian, A luminescent metal-organic framework with lewis basic pyridyl sites for the sensing of metal ions, Angew. Chem. Int. Ed. 48 (2009) 500–503, © 2009, John Wiley & Sons Ltd.*

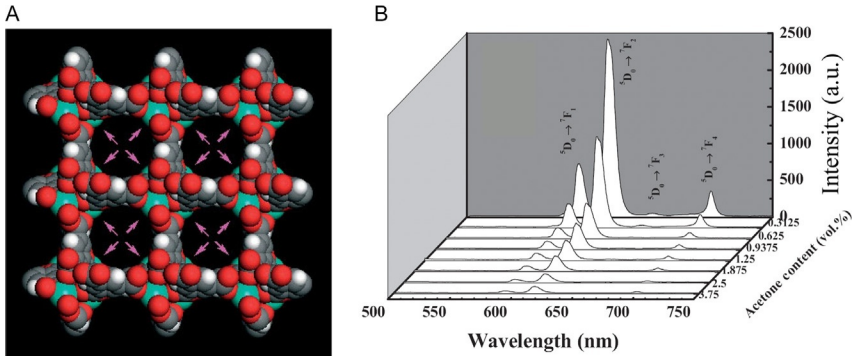

FIG. 2 (A) X-ray crystal structure of the MOF Eu(BTC) viewed along the *c*-axis. (B) The PL spectra of 1-propanol emulsion of Eu(BTC) in the presence of various contents of acetone. *Reprinted with permission from B. Chen, Y. Yang, F. Zapata, G. Lin, G. Qian, E.B. Lobkovsky, Luminescent open metal sites within a metal-organic framework for sensing small molecules, Adv. Mater. 19 (2007) 1693–1696, © 2007, John Wiley & Sons Ltd.*

important role, and the weakly coordinated 1-propanol molecules on the Eu^{3+} sites can be gradually replaced by DMF and acetone molecules, leading to luminescence enhancement and quenching, respectively.

Similar to the above sensing of small molecules in liquid phase, the luminescent properties of lanthanide MOFs can also be perturbed by gases, thereby providing an effective means for sensing of gases. Song et al. reported a lanthanide MOF, $[Eu_2L_3(H_2O)_4]\cdot 3DMF$ (L = 2′,5′-bis(methoxymethyl)-[1,1′:4′,1″-terphenyl]-4,4″-dicarboxylate), for sensing DMF vapor [70]. The water-exchanged MOF displays a weak luminescence under UV irradiation, while exhibiting more than eightfold emission enhancement after incubation under DMF vapor (Fig. 3). This DMF-triggered turn-on luminescence was rationalized by the DMF–ligand interactions that presumably shift the excited state energy level of the ligand and thus facilitates the ligand–lanthanide energy transfer process. The response rate of this MOF sensor is quite fast, with 95% of turn-on and -off achieved within a few minutes and 10–20 s, respectively. This example points to the potential of building lanthanide-based turn-on luminescent MOF sensors by proper functional ligand design, targeting analytes through ligand–analyte interactions.

Another possible method for selective sensing is the utilization of specific chemical interactions of the analyte with the MOF internal surface, for example, through hydrogen bonding interactions. To induce the hydrogen bonding interactions between MOFs and anions, Chen et al. have reported a novel lanthanide MOF, [Tb(BTC)·G] (G = guest solvent with O–H groups) [71]. The luminescence intensity of the [MOF Tb(BTC)·methanol] is significantly enhanced when incorporated into methanol solutions of Br^-, Cl^-, F^-, SO_4^{2-}, and CO_3^{2-} anions. In particular, the luminescence intensity of the fluoride-incorporated [Tb(BTC)·methanol] MOF is about four times stronger than that

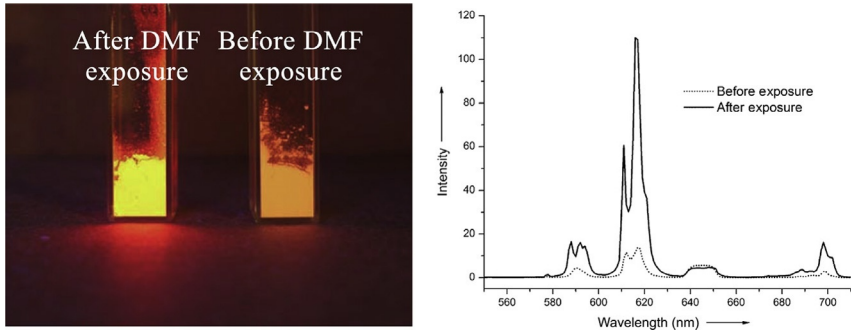

FIG. 3 Photograph (*left*) and emission spectra (*right*) of $Eu_2L_3(H_2O)_4$ (L = 2′,5′-bis(methoxymethyl)-[1,1′:4′,1″-terphenyl]-4,4″-dicarboxylate) before and after exposure to DMF vapor. *Reprinted with permission from Y. Li, S. Zhang, D. Song, A luminescent metal-organic framework as a turn-on sensor for DMF vapor, Angew. Chem. Int. Ed. 52 (2013) 710–713, © 2013, John Wiley & Sons Ltd.*

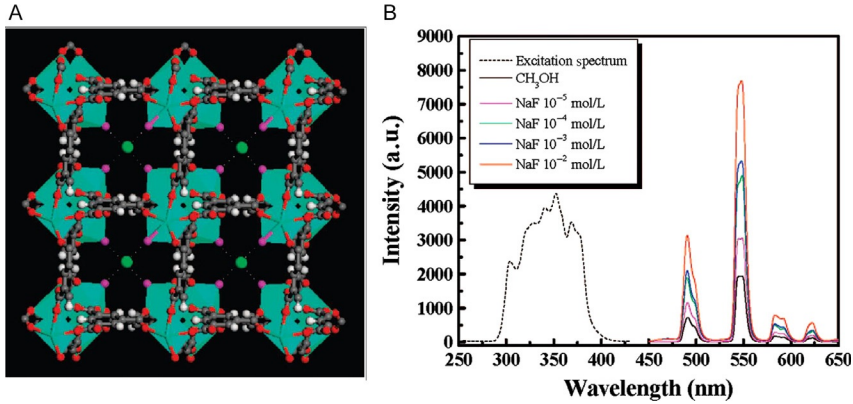

FIG. 4 (A) Single crystal X-ray structure of Tb(BTC) activated in methanol-containing NaF; fluoride anions (*green*) lie at the *center* of the channel, enabling hydrogen–bond interaction with terminal methanol molecules. (B) Excitation (*dotted*) and PL spectra (*solid*) of Tb(BTC) solid activated in methanol containing different concentrations of NaF (excited and monitored at 353 and 548 nm, respectively). *Reprinted with permission from B. Chen, L. Wang, F. Zapata, G. Qian, E.B. Lobkovsky, A luminescent microporous metal-organic framework for the recognition and sensing of anions, J. Am. Chem. Soc. 130 (2008) 6718–6719. © 2008, American Chemical Society.*

of the parent MOF, suggesting its potential for the sensing of fluoride anion. Because the F^- anion is involved in very strong hydrogen bonding interactions with the terminal methanol molecules, the O–H bond stretching vibration is restricted, thus reducing its quenching effect. As a result, the addition of F^- can significantly enhance the luminescence intensity of Tb^{3+} (Fig. 4).

3.2 Dual-Emitting Lanthanide MOFs for Self-Referencing Luminescence Sensing

Up to now, most examples of luminescent sensing are based on changes in the intensity of one transition. Changes in luminescence intensity are easy to be detected, however, intensity-based luminescence sensing is often susceptible to errors due to changes in probe concentration, excitation power, or detection efficiency. Indeed, even if all the experimental conditions, such as similar concentration of luminescence centers, excitation wavelength, and light source power are kept constant during the measurements, the absorption, and scatter cross section may vary from sample to sample. Thus, the comparison of the emission of different samples based on the detected intensity may lead to erroneous conclusions. Although the measurements of quantum yields and/or lifetime are neither affected by the intensity of the excitation source nor by the probe concentration, they require a relatively long experimental time and computational treatment. The utilizing of the ratio between the intensity of two transitions of the same luminescent material, instead of only one transition, can overcome the main drawbacks of the intensity-based measurements of only one transition. Ratiometric luminescent sensors enable analysis independent of the sample concentration and of the drifts of the optoelectronic system such as lamp and detectors.

Doping different lanthanide ions into isostructural MOF materials to construct mixed-lanthanide MOFs is an effective strategy for tuning luminescent properties [83]. The mixed-lanthanide MOFs can generate simultaneous emission of different lanthanide ions using one excitation wavelength. Furthermore, the luminescence intensity and the quantum efficiency will be increased due to the elimination or decrease of concentration quenching effect. In the resultant mixed-lanthanide MOFs, any desired lanthanide composition and ratio can be obtained in a predictable and reproducible fashion by controlling the stoichiometry of the reactants, thus opening a convenient pathway to design dual-emitting MOFs for ratiometric luminescence sensing.

In 2012, Qian et al. have demonstrated the first ratiometric luminescent MOF thermometer based on a Eu^{3+}/Tb^{3+} mixed-MOF, $Eu_{0.0069}Tb_{0.9931}$-DMBDC (DMBDC = 2,5-dimethoxy-1,4-benzenedicarboxylate) [84], which is isostructural to the parent MOFs Tb-DMBDC and Eu-DMBDC. Due to the strong sensitizing ability of ligand DMBDC, the lanthanide MOFs Tb-DMBDC and Eu-DMBDC exhibit the characteristic green emission of Tb^{3+} and red emission of Eu^{3+} ions, respectively. Besides being sensitized by the ligand DMBDC, Eu^{3+} ions in the mixed-MOF $Eu_{0.0069}Tb_{0.9931}$-DMBDC are also sensitized by Tb^{3+} ions through intermetallic energy transfer. Upon excitation at 381 nm, the MOF $Eu_{0.0069}Tb_{0.9931}$-DMBDC simultaneously shows the $^5D_4 \rightarrow {}^7F_J$ ($J = 6$, 5, 4, and 3) transitions of Tb^{3+} and the $^5D_0 \rightarrow {}^7F_J$ ($J = 1$, 2, 3, and 4) transitions of Eu^{3+}.

As expected, the luminescent intensity of Tb-DMBDC and Eu-DMBDC gradually decreases as the temperature increases from 10 to 300 K, due to the thermal activation of nonradiative decay. However, the Eu^{3+}/Tb^{3+} mixed-MOF $Eu_{0.0069}Tb_{0.9931}$-DMBDC exhibits a significantly different temperature-dependent luminescence behavior. The emission intensity of the Tb^{3+} ions in $Eu_{0.0069}Tb_{0.9931}$-DMBDC decreases, while that of the Eu^{3+} increases with temperature (Fig. 5). At 10 K, the emission bands at 613 nm (Eu^{3+}) and 545 nm (Tb^{3+}) have comparable intensity, whereas at 300 K, the emission of Eu^{3+} almost dominates the whole spectrum despite the very low content of Eu^{3+} in $Eu_{0.0069}Tb_{0.9931}$-DMBDC. This is attributed to the temperature-dependent energy-transfer probability. Therefore, an enhanced energy transfer from Tb^{3+} to Eu^{3+} is achieved with increasing temperature by phonon-assisted Förster energy transfer mechanism, as evidenced by luminescent lifetime measurements. The fact that the temperature can be linearly related to the emission intensity ratio (I_{Tb}/I_{Eu}) of the $^5D_4 \rightarrow {}^7F_5$ (Tb^{3+}, 545 nm) to $^5D_0 \rightarrow {}^7F_2$ (Eu^{3+}, 613 nm) transitions from 50 to 200 K indicates that the $Eu_{0.0069}Tb_{0.9931}$-DMBDC MOF is able to measure the temperature in this range with a maximum relative sensitivity (S_m) of 1.15% K^{-1}, and no further calibration of luminescence intensity is required. Additionally, when the temperature increases from 10 to 300 K, the $Eu_{0.0069}Tb_{0.9931}$-DMBDC MOF displays tunable luminescence colors from green–yellow to red, which can be directly observed by the naked eye. This feature allows visualizing the temperature change instantly and straightforwardly.

By varying the molar ratios of the metal salts and using the same synthetic method as for the parent MOFs, two other isostructural mixed-MOFs $Eu_{0.0011}Tb_{0.9989}$-DMBDC and $Eu_{0.0046}Tb_{0.9954}$-DMBDC were obtained. These

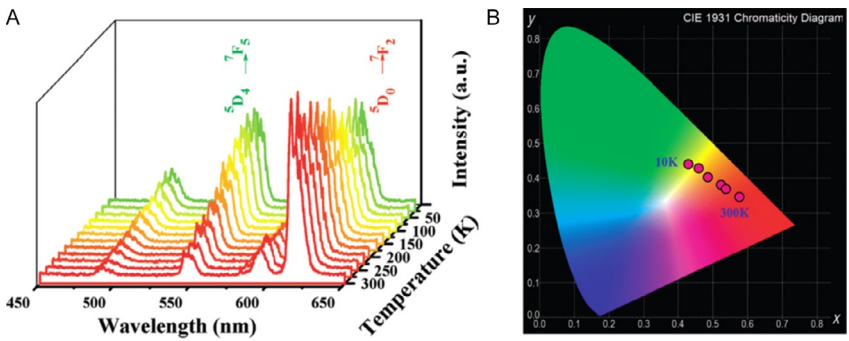

FIG. 5 (A) Emission spectra of $Eu_{0.0069}Tb_{0.9931}$-DMBDC recorded between 10 and 300 K. (B) CIE chromaticity diagram showing the luminescence color of $Eu_{0.0069}Tb_{0.9931}$-DMBDC at different temperatures. *Reprinted with permission from Y. Cui, H. Xu, Y. Yue, Z. Guo, J. Yu, Z. Chen, J. Gao, Y. Yang, G. Qian, B. Chen, A luminescent mixed-lanthanide metal-organic framework thermometer, J. Am. Chem. Soc. 134 (2012) 3979–3982. © 2012, American Chemical Society.*

MOFs exhibit similar temperature-dependent luminescence behaviors and permit the temperature measurement with a S_m of 0.613% K^{-1} and 0.526% K^{-1} at 200 K, respectively. Such mixed-lanthanide MOFs featuring different temperature-dependent lanthanide-centered luminescence behaviors within the same material are excellent materials for self-referencing luminescent temperature sensors.

To further enhance the sensitivity and tune the response range of the luminescent thermometers, two other Eu^{3+}/Tb^{3+} mixed-MOFs, $Tb_xEu_{1-x}PIA$ (H_2PIA = 5-(pyridin-4-yl)isophthalic acid; x = 0.01, 0.05, 0.10, 0.20, 0.50, and 0.80) and $Tb_{0.957}Eu_{0.043}cpda$ (H_3cpda = 5-(4-carboxyphenyl)-2,6-pyridinedicarboxylic acid), with ligands having higher triplet state energy were designed and developed [85,86]. In principle, the triplet state energy levels (T_1) of the organic ligands can tune the energy transfer rate from ligands to lanthanide ions, k_1^{Eu} and k_1^{Tb} and the energy back transfer rate from the $^5D_0$ level of Eu^{3+} to T_1, k_{-1}^{Eu} and $^5D_4$ level of Tb^{3+} to T_1, k_{-1}^{Tb}, which subsequently affects the probabilities of the radiative U of the $^5D_0 \rightarrow {}^7F_J$ transitions of $Eu^{3+}\left(k_{DF}^{Eu}\right)$ and of the $^5D_4 \rightarrow {}^7F_J$ transitions of $Tb^{3+}\left(k_{DF}^{Tb}\right)$. The temperature-dependent luminescence behaviors of the Eu^{3+} and Tb^{3+} can be modulated by selecting different organic ligands with different triplet excited state energies, thus maximizing the sensitivity and optimizing the response range. For example, the MOF thermometer $Tb_{0.9}Eu_{0.1}PIA$ shows a higher relative sensitivity of 3.27% K^{-1} compared to $Eu_{0.0069}Tb_{0.9931}$-DMBDC because the ligand PIA^{2-} exhibits higher triplet state energy of 26,455 cm^{-1} compared to 23,306 cm^{-1}.

Similar ratiometric temperature sensing was demonstrated by Hasegawa et al. using a mixed MOF, $[Tb_{0.99}Eu_{0.01}(hfa)_3(dpbp)]_n$ (hfa = hexafluoro acetylacetonato, dpbp = 4,4′-bis(diphenylphosphoryl) biphenyl) in the range of 200–500 K [88]. The MOF exhibits temperature-dependent emission. The emission intensity at 543 nm decreases dramatically with increasing temperature. In contrast, the emission intensity at 613 nm increases slightly. This MOF exhibits brilliant green, yellow, orange, and red photoluminescence (PL) under UV irradiation at 250, 300, 350, and 400 K, respectively.

Rocha et al. also demonstrated that nanoparticles of the MOF $Tb_{0.99}Eu_{0.01}(BDC)_{1.5}(H_2O)_2$ (BDC = 1,4-benzenedicarboxylate) work as ratiometric luminescent nanothermometers in the physiological temperature range (300–320 K) [89]. The nanoparticles were prepared by a reverse microemulsion method and had average length and diameter of 300 and 30 nm, respectively. Aqueous suspensions of the nano-MOF displays an emission quantum yield of 0.23 under excitation at 320 nm and relative sensitivity of 0.37% K^{-1} at 318 K, suggesting the possibility of using nano-MOFs to measure physiological temperatures.

NIR excited NIR luminescent MOFs are very useful for practical temperature sensing in biological systems because the generated NIR emission has high penetration depth in biotissues and no competing fluorescence from

biomatrices. Qian et al. synthesized a NIR-pumped mixed-lanthanide MOF $Nd_{0.577}Yb_{0.423}BDC\text{-}F_4$ ($H_2BDC\text{-}F_4$ = 2,3,5,6-tetrafluoro-1,4-benzenedicarboxylic acid) [90]. Under excitation at 808 nm, this MOF displays the characteristic emission of both Nd^{3+} and Yb^{3+} ions, ascribed to efficient energy transfer from Nd^{3+} to Yb^{3+}. The intensity ratio of the $^4F_{3/2} \rightarrow {}^4I_{11/2}$ (Nd^{3+}, 1060 nm) and $^2F_{5/2} \rightarrow {}^7F_{7/2}$ (Yb^{3+}, 980 nm) transitions shows excellent linear relationship with temperature in the range of 293–313 K, which can be potentially applied as a luminescent thermometer for biological sensing.

Recently, Shi et al. reported a mixed-lanthanide MOF, $Eu_{0.5}Tb_{1.5}(FDA)_3$ (H_2FDA = furan-2,5-dicarboxylic acid), as a self-referencing luminescent probe for mixtures of glycol and 1,4-dioxane in a large volume ratio range [91]. 1,4-Dioxane is an important industrial solvent and is widely used in the synthesis of dyes, oils, waxes, resins, cellulosic esters, cellulosic ethers, and polyvinyl polymers. The condensation reaction of glycol has been considered as being the most economic and reasonable preparation route for 1,4-dioxane. When the volume ratio of glycol/1,4-dioxane varies from 0 to 1, the luminescence intensities of both Eu^{3+} and Tb^{3+} in $Eu_2(FDA)_3$ and $Tb_2(FDA)_3$ gradually increase. However, the $Eu_{0.5}Tb_{1.5}(FDA)_3$ MOF exhibits a very unusual volume ratio-dependent luminescence: the emission intensity of the Tb^{3+} ions in $Eu_{0.5}Tb_{1.5}(FDA)_3$ decreases, and that of Eu^{3+} increases as the volume ratio increases (Fig. 6).

Although such mixed-lanthanide MOF approach is quite attractive for developing ratiometric luminescent sensors, this strategy is limited to the available luminescence emissions of the mixed-lanthanide MOFs. For example, Eu^{3+} and Tb^{3+} ions in Eu^{3+}/Tb^{3+} mixed-MOFs usually generate main characteristic red and green emission with emission wavelengths of about 615 and 545 nm, respectively. Encapsulating organic fluorescent dyes into the porous lanthanide MOFs to form MOF ⊃ dye composites can readily add another luminescence band with variable emission color to the original transitions of lanthanide ions. Furthermore, the energy transfer between guest dyes and lanthanide ions can be elaborately tuned by inclusion of appropriate organic dyes through the spectral overlap between their emission spectrum and the absorption spectra of lanthanide ions.

Qian et al. therefore proposed a conceptually different approach for ratiometric luminescent sensing and demonstrated it using a MOF ZJU-88 ⊃ perylene as proof of concept [92]. This dye-encapsulated MOF was synthesized by adding a solution of perylene in DMF into the growth solution of the lanthanide MOF $[Eu_2(QPTCA)(NO_3)_2(DMF)_4]\cdot(CH_3CH_2OH)_3$ (ZJU-88) (QCTPA=1,1′:4′,1″:4″,1‴-quaterphenyl-3,3‴,5,5‴-tetracarboxylate). The ZJU-88 ⊃ perylene MOF is isostructural to the parent MOF and has particle sizes in the range of 0.2–1 μm. As expected, the ZJU-88 ⊃ perylene MOF features a red emission of Eu^{3+} at 615 nm and an appended blue emission around 473 nm from the perylene dyes. Interestingly, the luminescence intensity at 473 nm substantially decreases, while the intensity of the $^5D_0 \rightarrow {}^7F_2$ transition

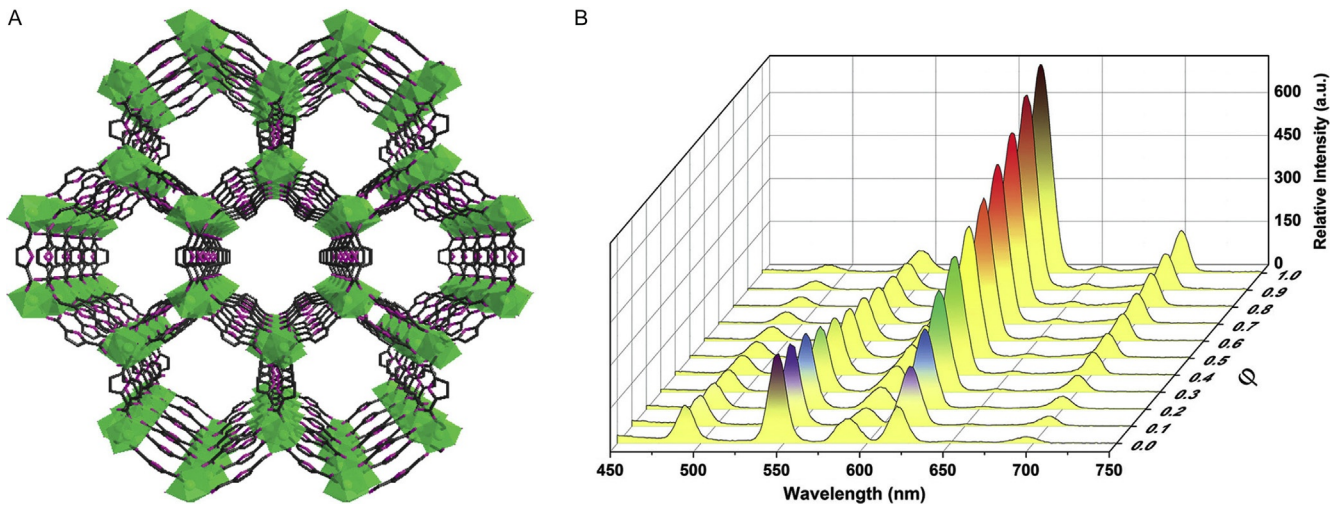

FIG. 6 (A) 3D framework with honeycomb-type channels along the *a*-axis. (B) Emission spectra of $Eu_{0.5}Tb_{1.5}(FDA)_3$ recorded for volume ratios of 1,4-dioxane/glycol ranging from 0 to 1, under excitation at 300 nm. *Reprinted with permission from J. Zhou, H. Li, H. Zhang, W. Shi, P. Cheng, A bimetallic lanthanide metal-organic material as a self-calibrating color-gradient luminescent sensor, Adv. Mater. 27 (2015) 7072–7077. © 2015, John Wiley & Sons Ltd.*

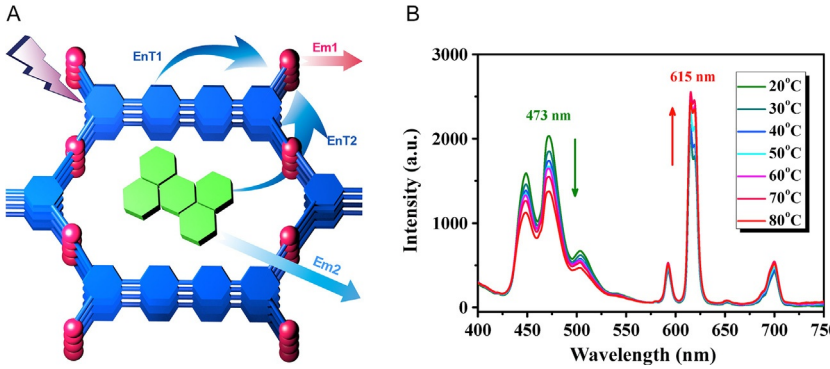

FIG. 7 (A) Schematic representation of dual-emitting ZJU-88⊃perylene (*EnT*: energy transfer, *Em*: emission). (B) Emission spectra of ZJU-88⊃perylene recorded from 20 to 80°C, excited at 388 nm. *Reprinted with permission from Y. Cui, R. Song, J. Yu, M. Liu, Z. Wang, C. Wu, Y. Yang, B. Chen, G. Qian, Dual-emitting MOF⊃dye composite for ratiometric temperature sensing, Adv. Mater. 27 (2015) 1420–1425. © 2015, John Wiley & Sons Ltd.*

of Eu^{3+} at 615 nm increases with increasing temperature, from 20 to 80°C (Fig. 7). This temperature-dependent luminescence behavior is significantly different from those of perylene solution and ZJU-88 alone and is attributed to the energy transfer from perylene dyes to Eu^{3+} ions. More importantly, the luminescence intensity ratios between Eu^{3+} and perylene emission in ZJU-88⊃perylene correlate linearly very well with the temperature in the range 20–80°C. This makes the ZJU-88⊃perylene MOF a novel ratiometric thermometer for physiological temperature sensing with a maximum relative sensitivity of $1.28\%\,K^{-1}$.

4 LANTHANIDE MOFs FOR WHITE-LIGHT-EMITTING DEVICES

White-light-emitting materials and devices have attracted significant attention due to their broad applications in displays and lighting. High-quality white-light illumination requires a source with the Commission Internationale de l'Éclairage (CIE) coordinates (0.333, 0.333), with correlated color temperature (CCT) between 2500 and 6500 K, and color rendering index (CRI) above 80. Emission from organic or inorganic luminescent materials can only cover part of the visible spectrum. To overcome this limitation, various architectures of devices combining the primary color (red, blue, and green) emission from different compounds have been suggested.

In lanthanide MOFs, besides the characteristic f–f emission of lanthanide ions, broad emission bands ascribed to organic linkers can sometimes be

observed due to incomplete energy transfer from the ligand to the lanthanide ions. In principle, white-light-emitting materials can be obtained by tuning the relative amount of these emission components. Considering that the Eu^{3+} and Tb^{3+} ions are two of the most important luminescent components displaying strong red and green emissions, respectively, whereas the organic linker H_2PDA can produce blue emission, Qian et al. synthesized a new two-dimensional lanthanide MOF, $La_2(PDA)_3(H_2O)_5$ (ZJU-1) (PDA = pyridine-2,6-dicarboxylate), that exhibited a blue emission at 408 nm attributed to the emissive organic PDA linkers [93]. Compared with luminescence of the free ligand, the ZJU-1 MOF exhibits much enhanced blue light emission and slight red shifts, which was attributed to the increase in rigidity of the PDA^{2-} ligands after coordinating to La^{3+} ions. Doping of a small amount of Tb^{3+} and Eu^{3+} led to the formation of isostructural ZJU-1:Tb^{3+} and ZJU-1:Eu^{3+}, providing additional green (543 nm) and red (614 nm) emissions, respectively. As expected, when the amount of Tb^{3+}/Eu^{3+} doped into ZJU-1 increases, the corresponding emissions increase gradually, while emission intensities from PDA^{2-} ligand basically keeps unchanged, thus combination of the emission from PDA^{2-} ligand and those from f–f transitions of Tb^{3+}/Eu^{3+} can readily generate colors tunable from blue to blue–green, green–yellow, blue–red, and red. Therefore, a white-light-emitting MOFs ZJU-1:Tb^{3+}, Eu^{3+} can be realized by tuning the molar amount of Tb^{3+} and Eu^{3+} in the host framework. The optimized white-light-emitting MOFs, ZJU-1:1.0% Tb^{3+}, 2.0% Eu^{3+} and ZJU-1:1.5% Tb^{3+}, 2.0% Eu^{3+} exhibit CIE coordinates of (0.3269, 0.3123) and (0.3109, 0.3332), respectively, which are both very close to the coordinate for pure white light (Fig. 8).

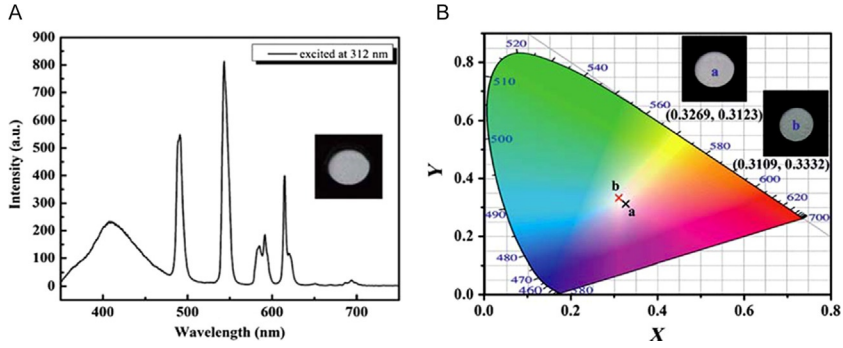

FIG. 8 (A) Emission spectrum of ZJU-1:1.0% Tb^{3+}, 2.0% Eu^{3+} upon excitation at 312 nm. (B) CIE chromaticity diagram for the ZJU-1:x% Tb^{3+}, y% Eu^{3+} excited at 312 nm: (A) $x = 1.0$, $y = 2.0$ and (B) $x = 1.5$, $y = 2.0$. The *insets* are the optical photographs of the MOFs excited at 312 nm. *Reprinted with permission from X. Rao, Q. Huang, X. Yang, Y. Cui, Y. Yang, C. Wu, B. Chen, G. Qian, Color tunable and white light emitting Tb^{3+} and Eu^{3+} doped lanthanide metal-organic framework materials, J. Mater. Chem. 22 (2012) 3210–3214. © 2012, The Royal Society of Chemistry.*

Liu et al. reported a 4d–4f mixed MOF $[EuAg_3(3\text{-}TPyMNTB)_2(H_2O)(MeCN)](ClO_4)_6{\cdot}4MeCN$ (3-TPyMNTB = tris((pyridin-3-ylmethyl)-benzoimidazol-2-ylmethyl)amine) for direct white-light emission from a single crystal [94]. There are two kinds of transitions in the emission spectrum of this MOF: one is the characteristic Eu^{3+} sharp emissions and the other is a broad emission centered around 510 nm arising from the ligand 3-TPyMNTB. However, in the Eu-3-TPyMNTB MOF, the ligand emission can barely be observed, so it is reasonable to assume that the Ag^+ ions can resensitize the ligand, which results in the two peak emission in Eu-Ag_3-TPyMNTB. It was found that, when excited at different wavelengths, the MOF shows an overall white-light emission, enabling a potential approach to regulate the white-light property by means of such dual-emissive single-phase compound.

Another possible method for white-light emission was reported by Yan et al. using lanthanide organic–inorganic hybrids materials [95]. They encapsulated the Eu^{3+} ion in MOF-253 (Al(OH)(bpydc)) using postsynthetic method, and then introduced this modified MOF-253 into an organic polymer by monomer functionalization, which eventually led to a transparent hybrid material, MOF-PEMA (PEMA = poly(ethylmethacrylate)). Under excitation at 395 nm, the emission spectrum of MOF-PEMA is constituted by a broad band from MOF-253 (550 nm) and a narrow band from the Eu^{3+} ion (614 nm). Since the luminescence of PEMA is very weak, the luminescence spectrum of MOF-PEMA only depends on the added MOF-based hybrid material. Furthermore, MOF-PEMA was assembled on a near-UV GaN chip to form a white LED with tunable color temperature and high CRI. It is noteworthy that the white light from the MOF-PEMA LED could be adjusted from warm shade to natural white by altering the content of MOF in the polymer.

Nenoff et al. reported the intrinsic broad band direct white-light emission originating from a single component MOF, which was synthesized based on an indium complex, $[In_3(BTB)_2(ox)_3]_n$ (BTB = 1,3,5-tris(4-carboxyphenyl) benzene, ox = oxalate) [96]. Interestingly, the material already emitted a white light owing to the broad band emission over the entire visible light region. In order to improve the intrinsic color properties such as CRI, CCT, and chromaticity to meet the requirements for solid-state lighting, the authors introduced a narrow band, red emission component into this system via Eu^{3+} doping. The simple mixing of Eu^{3+} into the reaction solution of the indium compound successfully led to the formation of a mixed-metal framework. By increasing the Eu^{3+} concentration to 10%, the CRI and CCT shifted closer to the set target of CRI ~ 90 and CCT ~ 3200 K. When the sample is excited at 350, 360, 380, and 394 nm, the coordinates are (0.369, 0.301), (0.309, 0.298), (0.285, 0.309), and (0.304, 0.343), respectively, which closely approach the targeted values (Fig. 9). This result provides a new path for the rational design of alternative materials for white-light emission.

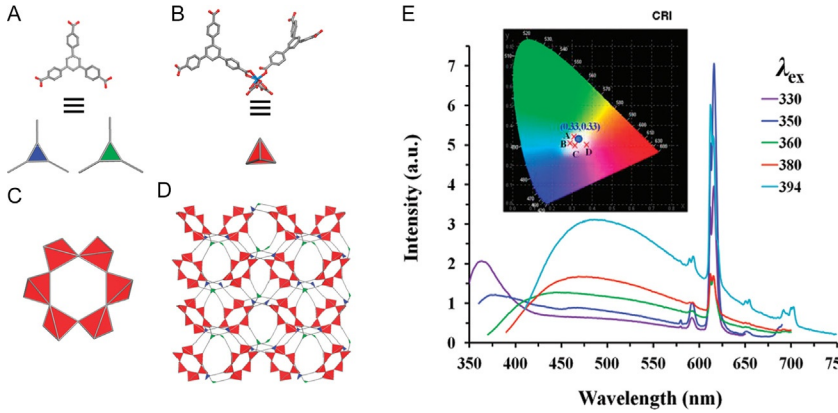

FIG. 9 Molecular building blocks in MOF $[In_3(BTB)_2(ox)_3]_n$, corresponding to (A) two topologically distinct three-connected nodes and (B) a four-connected node; (C) corner sharing tetrahedra forming a 6-member ring; and (D) topological representation of single net in $[In_3(BTB)_2(ox)_3]_n$; (E) emission spectra of 10% Eu doped $[In_3(BTB)_2(ox)_3]_n$ when excited between 330 and 380 nm; (*inset*) 1931 CIE chromaticity diagram highlighting corresponding chromaticity coordinates (A–D) approaching targeted values. *Reprinted with permission from D.F. Sava, L.E. Rohwer, M.A. Rodriguez, T.M. Nenoff, Intrinsic broad-band white-light emission by a tuned, corrugated metal-organic framework, J. Am. Chem. Soc. 134 (2012) 3983–3986. © 2012, American Chemical Society.*

5 BIOMEDICAL APPLICATIONS OF LANTHANIDE MOFs

Recently, the use of nanoscale lanthanide MOFs for biological and biomedical applications has attracted increasing attention [105–109]. The interest for these functional materials relies on the combination of the chemical or biofunctional behavior of MOFs and the unique luminescence properties of lanthanide ions, such as high photostability, long decay rates, large ligand-induced Stokes shifts, and narrow emission bands. Besides their luminescent characteristics, lanthanide MOFs can possess paramagnetic properties which help to increase the relaxation rate of water protons in the tissues being imaged, making them useful as contrast agents in magnetic resonance imaging (MRI).

Multimodal imaging is a new imaging technique which combines more than one imaging modality, such as X-ray, nuclear, ultrasound, computed tomography, MRI, and optical imaging. Multimodal imaging is becoming more popular because of its improved sensitivity, high resolution, and morphological visualization. In particular, the combination of optical imaging and MRI allies the sensitivity of the luminescent component with the high degree of spatial resolution of MRI. Lin et al. synthesized nanorods of the $Gd(BDC)_{1.5}(H_2O)_2$ MOF through a reverse microemulsion method, which allowed the control of the morphologies and sizes by alteration of the water–surfactant ratio in the microemulsion system [97]. These nanomaterials

display large longitudinal relaxivity (R_1) of 35.8 mM^{-1} s^{-1} and transverse relaxivity (R_2) of 55.6 mM^{-1} s^{-1} on a per Gd^{3+} basis and extraordinarily large R_1 of 1.6×10^7 mM^{-1} s^{-1} and R_2 of 2.5×10^7 mM^{-1} s^{-1} on a per nanoparticle basis. The level of R_1 is unprecedented and at least an order of magnitude higher than those of Gd^{3+}-containing liposomes which have been shown to be effective target-specific MRI contrast agents for cancer and cardiovascular disease. In addition, the analogues $Gd_{0.95}(BDC)_{1.5}(H_2O)_2{:}Eu_{0.05}$ and $Gd_{0.95}(BDC)_{1.5}(H_2O)_2{:}Tb_{0.05}$ were also synthesized. Ethanol suspensions of these materials are highly luminescent upon UV excitation with characteristic red and green luminescence from Eu^{3+} and Tb^{3+}, respectively, suggesting that they can be used as potential contrast agents for multimodal imaging.

Centre et al. reported a NIR-emitting nanoscale MOF, Yb-PVDC-3 (PVDC = phenylenevinylene dicarboxylate), for NIR imaging in living cells [98,110]. This MOF exhibits Yb^{3+} luminescence centered at 970 nm and PVDC emission at 445 nm, upon excitation of the PVDC sensitizer in both water and 0.1 M HEPES buffer (pH 7.3) environments. Besides, the stability and cytotoxicity results show that this MOF is a promising biological probe for in vivo applications. Furthermore, this probe was tested on human cancer and mouse cells in a NIR microscopy experimental setup. Visible PVDC and NIR Yb^{3+} emission signals were both monitored in the same field and the difference between these two signals results from the discrimination of the NIR signal from the visible autofluorescence arising from the biological material (Fig. 10).

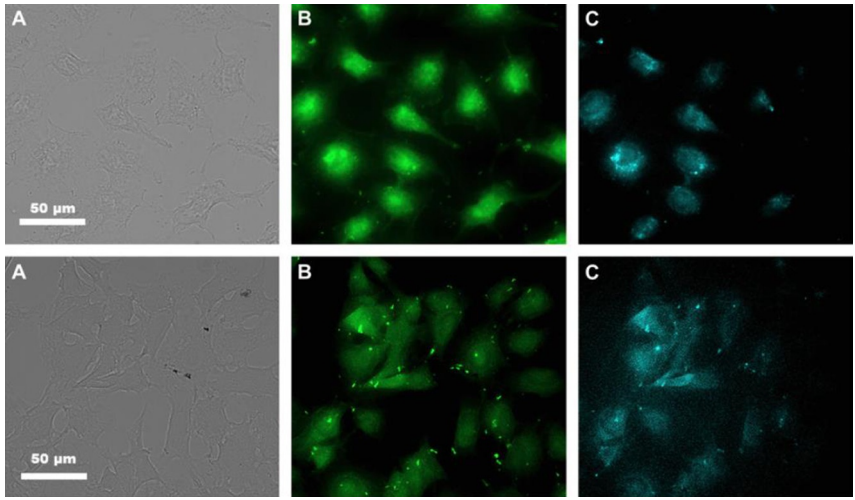

FIG. 10 Visible and NIR microscopy images of nano-Yb-PVDC-3 in human cancer (*upper*) and mouse (*lower*) cells ($\lambda_{ex} = 340$ nm). Bright-field (A), H_2-PVDC emission ($\lambda_{ex} = 377$ nm, $\lambda_{em} = 445$ nm) (B), and Yb^{3+} emission ($\lambda_{ex} = 377$ nm, λ_{em} = long pass 770 nm) (C) images. *Reprinted with permission from A. Foucault-Collet, K.A. Gogick, K.A. White, S. Villette, A. Pallier, G. Collet, C. Kieda, T. Li, S.J. Geib, N.L. Rosi, S. Petoud, Lanthanide near infrared imaging in living cells with Yb^{3+} nano metal organic frameworks, Proc. Natl. Acad. Sci. USA 110 (2013) 17199–17204. © 2013, National Academy of Sciences of the United States of America.*

6 CONCLUSION AND OUTLOOK

In the past decades, the growing research interest of chemists, physicists, and materials scientists has greatly accelerated the development of luminescent lanthanide MOFs, and some novel applications including luminescent sensors and light-emitting materials have been demonstrated. In this chapter, the recent research on the design and construction of lanthanide MOFs, as well as their applications in the fields of luminescent sensing, lighting, and biomedicine have been summarized.

The design of lanthanide MOFs is still a key issue with respect to the control or prediction of the final network architecture in view of the high coordination flexibility and the lack of preferential geometries of lanthanide ions. The molecular building block (MBB) approach developed by Eddaoudi et al. is one of the breakthroughs in the construction of lanthanide MOFs [111–113]. This approach indicates that some lanthanide-containing secondary building units can indeed be utilized to construct lanthanide MOFs with desired framework topologies and thus can assist chemists and material scientists to rationally implement desired luminescent properties in these MOFs. Additionally, the organic linkers not only play a role as the building blocks for the coordination networks, but also act as efficient sensitizers for the lanthanide ions via the "antenna effect," thus the deliberate selection and design of organic linkers are very important to ensure the absorbed energy can be efficiently transferred to the lanthanide ions.

The ability to rationally incorporate functional sites such as open metal sites and Lewis basic pyridyl sites in the pores of the molecular frameworks has promoted porous lanthanide MOFs as very promising sensors for selective sensing of small molecules, cations, and anions. In fact, some practically useful MOFs with functional sites for gas storage, separation, and heterogeneous catalysis have been realized at laboratory scale, with the input of industrial partners. Some of these promising MOFs for luminescent sensing applications will certainly be implemented in the near future in commercial analytical systems.

The mixed-lanthanide MOFs approach has opened a new strategy for designing dual-emitting MOFs for ratiometric luminescent sensing. In most of the luminescent MOFs so far, the sensing functionality is based on the intensity change of one transition. The simple, yet more sophisticated ratiometric sensing approach makes luminescent sensing independent of the concentration of the sample and of the drifts in the optoelectronic system, including excitation source and detectors, thus overcoming the main drawbacks of the intensity-based measurements of only one transition.

In conclusion, lanthanide MOFs are very promising luminescent materials for sensing, white-light-emitting, and biomedicine. We can anticipate that with continued focus on the design and development of new lanthanide MOFs as well as collaboration among chemists, materials scientists, biomedical scientists, and bioengineers, luminescent lanthanide MOFs have a bright future for practical applications.

ACKNOWLEDGMENTS

This work was supported by the National Natural Science Foundation of China (Nos. 51272229, 51272231, 51472217, and 51432001) and Zhejiang Provincial Natural Science Foundation of China (Nos. LR13E020001 and LZ15E020001).

ACRONYMS AND ABBREVIATIONS

BDC	1,4-benzenedicarboxylate
BTB	1,3,5-tris(4-carboxyphenyl)benzene
BTC	1,3,5-benzenetricarboxylate
CCT	correlated color temperature
CIE	Commission Internationale de l'Éclairage
cpda	5-(4-carboxyphenyl)-2,6-pyridinedicarboxylate
CRI	color rendering index
DMBDC	2,5-dimethoxy-1,4-benzenedicarboxylate
FDA	furan-2,5-dicarboxylate
MBB	molecular building block
MOFs	metal-organic frameworks
MRI	magnetic resonance imaging
NIR	near-infrared
ox	oxalic acid
PDA	pyridine-2,6-dicarboxylate
PDC	pyridine-3,5-dicarboxylate
PEMA	poly(ethylmethacrylate)
PIA	5-(pyridin-4-yl)isophthalate
PL	photoluminescence
PVDC	phenylenevinylene dicarboxylate
TPyMNTB	tris((pyridin-3-ylmethyl)-benzoimidazol-2-ylmethyl)amine

REFERENCES

[1] H.-C. Zhou, J.R. Long, O.M. Yaghi, Introduction to metal-organic frameworks, Chem. Rev. 112 (2012) 673–674.

[2] Y. He, B. Li, M. O'Keeffe, B. Chen, Multifunctional metal-organic frameworks constructed from meta-benzenedicarboxylate units, Chem. Soc. Rev. 43 (2014) 5618–5656.

[3] J.P. Zhang, P.Q. Liao, H.L. Zhou, R.B. Lin, X.M. Chen, Single-crystal X-ray diffraction studies on structural transformations of porous coordination polymers, Chem. Soc. Rev. 43 (2014) 5789–5814.

[4] T.R. Cook, Y.R. Zheng, P.J. Stang, Metal-organic frameworks and self-assembled supramolecular coordination complexes: comparing and contrasting the design, synthesis, and functionality of metal-organic materials, Chem. Rev. 113 (2013) 734–777.

[5] X. Kong, H. Deng, F. Yan, J. Kim, J.A. Swisher, B. Smit, O.M. Yaghi, J.A. Reimer, Mapping of functional groups in metal-organic frameworks, Science 341 (2013) 882–885.

[6] H. Furukawa, K.E. Cordova, M. O'Keeffe, O.M. Yaghi, The chemistry and applications of metal-organic frameworks, Science 341 (2013) 1230444.
[7] W. Lu, Z. Wei, Z.Y. Gu, T.F. Liu, J. Park, J. Tian, M. Zhang, Q. Zhang, T. Gentle Iii, M. Bosch, H.C. Zhou, Tuning the structure and function of metal-organic frameworks via linker design, Chem. Soc. Rev. 43 (2014) 5561–5593.
[8] D. Zhao, D.J. Timmons, D. Yuan, H.-C. Zhou, Tuning the topology and functionality of metal-organic frameworks by ligand design, Acc. Chem. Res. 44 (2011) 123–133.
[9] C. He, D. Liu, W. Lin, Nanomedicine applications of hybrid nanomaterials built from metal–ligand coordination bonds: nanoscale metal-organic frameworks and nanoscale coordination polymers, Chem. Rev. 115 (2015) 11079–11108.
[10] M.D. Allendorf, C.A. Bauer, R.K. Bhakta, R.J.T. Houk, Luminescent metal-organic frameworks, Chem. Soc. Rev. 38 (2009) 1330–1352.
[11] Y. Cui, Y. Yue, G. Qian, B. Chen, Luminescent functional metal-organic frameworks, Chem. Rev. 112 (2012) 1126–1162.
[12] R.C. Huxford, J. Della Rocca, W. Lin, Metal-organic frameworks as potential drug carriers, Curr. Opin. Chem. Biol. 14 (2010) 262–268.
[13] M.L. Foo, R. Matsuda, S. Kitagawa, Functional hybrid porous coordination polymers, Chem. Mater. 26 (2014) 310–322.
[14] A.A. Talin, A. Centrone, A.C. Ford, M.E. Foster, V. Stavila, P. Haney, R.A. Kinney, V. Szalai, F. El Gabaly, H.P. Yoon, F. Leonard, M.D. Allendorf, Tunable electrical conductivity in metal-organic framework thin-film devices, Science 343 (2014) 66–69.
[15] Q.L. Zhu, Q. Xu, Metal-organic framework composites, Chem. Soc. Rev. 43 (2014) 5468–5512.
[16] Y. He, W. Zhou, G. Qian, B. Chen, Methane storage in metal-organic frameworks, Chem. Soc. Rev. 43 (2014) 5657–5678.
[17] Y. Han, J.R. Li, Y. Xie, G. Guo, Substitution reactions in metal-organic frameworks and metal-organic polyhedra, Chem. Soc. Rev. 43 (2014) 5952–5981.
[18] J.D. Evans, C.J. Sumby, C.J. Doonan, Post-synthetic metalation of metal-organic frameworks, Chem. Soc. Rev. 43 (2014) 5933–5951.
[19] S. Furukawa, J. Reboul, S. Diring, K. Sumida, S. Kitagawa, Structuring of metal-organic frameworks at the mesoscopic/macroscopic scale, Chem. Soc. Rev. 43 (2014) 5700–5734.
[20] P. Falcaro, R. Ricco, C.M. Doherty, K. Liang, A.J. Hill, M.J. Styles, MOF positioning technology and device fabrication, Chem. Soc. Rev. 43 (2014) 5513–5560.
[21] V. Stavila, A.A. Talin, M.D. Allendorf, MOF-based electronic and opto-electronic devices, Chem. Soc. Rev. 43 (2014) 5994–6010.
[22] S. Qiu, M. Xue, G. Zhu, Metal-organic framework membranes: from synthesis to separation application, Chem. Soc. Rev. 43 (2014) 6116–6140.
[23] M.P. Suh, H.J. Park, T.K. Prasad, D.-W. Lim, Hydrogen storage in metal-organic frameworks, Chem. Rev. 112 (2012) 782–835.
[24] S.C. Xiang, Z. Zhang, C.G. Zhao, K. Hong, X. Zhao, D.R. Ding, M.H. Xie, C.D. Wu, M. C. Das, R. Gill, K.M. Thomas, B. Chen, Rationally tuned micropores within enantiopure metal-organic frameworks for highly selective separation of acetylene and ethylene, Nat. Commun. 2 (2011) 204.
[25] B. Li, H.M. Wen, H. Wang, H. Wu, M. Tyagi, T. Yildirim, W. Zhou, B. Chen, A porous metal-organic framework with dynamic pyrimidine groups exhibiting record high methane storage working capacity, J. Am. Chem. Soc. 136 (2014) 6207–6210.
[26] H. Wu, Q. Gong, D.H. Olson, J. Li, Commensurate adsorption of hydrocarbons and alcohols in microporous metal-organic frameworks, Chem. Rev. 112 (2012) 836–868.

[27] K. Sumida, D.L. Rogow, J.A. Mason, T.M. McDonald, E.D. Bloch, Z.R. Herm, T.-H. Bae, J.R. Long, Carbon dioxide capture in metal-organic frameworks, Chem. Rev. 112 (2012) 724–781.
[28] B. Chen, S. Xiang, G. Qian, Metal-organic frameworks with functional pores for recognition of small molecules, Acc. Chem. Res. 43 (2010) 1115–1124.
[29] E. Barea, C. Montoro, J.A. Navarro, Toxic gas removal-metal-organic frameworks for the capture and degradation of toxic gases and vapours, Chem. Soc. Rev. 43 (2014) 5419–5430.
[30] C.K. Brozek, M. Dinca, Cation exchange at the secondary building units of metal-organic frameworks, Chem. Soc. Rev. 43 (2014) 5456–5467.
[31] A. Dhakshinamoorthy, H. Garcia, Metal-organic frameworks as solid catalysts for the synthesis of nitrogen-containing heterocycles, Chem. Soc. Rev. 43 (2014) 5750–5765.
[32] W.Y. Gao, M. Chrzanowski, S. Ma, Metal-metalloporphyrin frameworks: a resurging class of functional materials, Chem. Soc. Rev. 43 (2014) 5841–5866.
[33] G. Férey, C. Serre, T. Devic, G. Maurin, H. Jobic, P.L. Llewellyn, G. De Weireld, A. Vimont, M. Daturi, J.-S. Chang, Why hybrid porous solids capture greenhouse gases? Chem. Soc. Rev. 40 (2011) 550.
[34] J.-R. Li, J. Sculley, H.-C. Zhou, Metal-organic frameworks for separations, Chem. Rev. 112 (2012) 869–932.
[35] H.-L. Jiang, Q. Xu, Porous metal-organic frameworks as platforms for functional applications, Chem. Commun. 47 (2011) 3351–3370.
[36] S. Xiang, Y. He, Z. Zhang, H. Wu, W. Zhou, R. Krishna, B. Chen, Microporous metal-organic framework with potential for carbon dioxide capture at ambient conditions, Nat. Commun. 3 (2012) 954.
[37] M. Yoon, R. Srirambalaji, K. Kim, Homochiral metal-organic frameworks for asymmetric heterogeneous catalysis, Chem. Rev. 112 (2012) 1196–1231.
[38] Y. He, W. Zhou, T. Yildirim, B. Chen, A series of metal-organic frameworks with high methane uptake and an empirical equation for predicting methane storage capacity, Energy Environ. Sci. 6 (2013) 2735.
[39] Y. Cui, F. Zhu, B. Chen, G. Qian, Metal-organic frameworks for luminescence thermometry, Chem. Commun. 51 (2015) 7420–7431.
[40] P. Horcajada, R. Gref, T. Baati, P.K. Allan, G. Maurin, P. Couvreur, G. Férey, R.E. Morris, C. Serre, Metal-organic frameworks in biomedicine, Chem. Rev. 112 (2012) 1232–1268.
[41] H. Deng, S. Grunder, K.E. Cordova, C. Valente, H. Furukawa, M. Hmadeh, F. Gandara, A. C. Whalley, Z. Liu, S. Asahina, H. Kazumori, M. O'Keeffe, O. Terasaki, J.F. Stoddart, O. M. Yaghi, Large-pore apertures in a series of metal-organic frameworks, Science 336 (2012) 1018–1023.
[42] K. Liang, C. Carbonell, M.J. Styles, R. Ricco, J. Cui, J.J. Richardson, D. Maspoch, F. Caruso, P. Falcaro, Biomimetic replication of microscopic metal-organic framework patterns using printed protein patterns, Adv. Mater. 27 (2015) 7293–7298.
[43] H. Sato, W. Kosaka, R. Matsuda, A. Hori, Y. Hijikata, R.V. Belosludov, S. Sakaki, M. Takata, S. Kitagawa, Self-accelerating CO sorption in a soft nanoporous crystal, Science 343 (2014) 167–170.
[44] G.K. Shimizu, J.M. Taylor, S. Kim, Chemistry. Proton conduction with metal-organic frameworks, Science 341 (2013) 354–355.
[45] T.L. Hu, H. Wang, B. Li, R. Krishna, H. Wu, W. Zhou, Y. Zhao, Y. Han, X. Wang, W. Zhu, Z. Yao, S. Xiang, B. Chen, Microporous metal-organic framework with dual functionalities for highly efficient removal of acetylene from ethylene/acetylene mixtures, Nat. Commun. 6 (2015) 7328.

[46] Y. He, R. Krishna, B. Chen, Metal-organic frameworks with potential for energy-efficient adsorptive separation of light hydrocarbons, Energy Environ. Sci. 5 (2012) 9107.
[47] E.D. Bloch, W.L. Queen, R. Krishna, J.M. Zadrozny, C.M. Brown, J.R. Long, Hydrocarbon separations in a metal-organic framework with open iron(II) coordination sites, Science 335 (2012) 1606–1610.
[48] Y. He, S. Xiang, Z. Zhang, S. Xiong, F.R. Fronczek, R. Krishna, M. O'Keeffe, B. Chen, A microporous lanthanide-tricarboxylate framework with the potential for purification of natural gas, Chem. Commun. 48 (2012) 10856–10858.
[49] Z. Hu, B.J. Deibert, J. Li, Luminescent metal-organic frameworks for chemical sensing and explosive detection, Chem. Soc. Rev. 43 (2014) 5815–5840.
[50] Q. Yao, A. Bermejo Gómez, J. Su, V. Pascanu, Y. Yun, H. Zheng, H. Chen, L. Liu, H.N. Abdelhamid, B. Martín-Matute, X. Zou, Series of highly stable isoreticular lanthanide metal-organic frameworks with expanding pore size and tunable luminescent properties, Chem. Mater. 27 (2015) 5332–5339.
[51] C.Y. Sun, X.L. Wang, X. Zhang, C. Qin, P. Li, Z.M. Su, D.X. Zhu, G.G. Shan, K.Z. Shao, H. Wu, J. Li, Efficient and tunable white-light emission of metal-organic frameworks by iridium-complex encapsulation, Nat. Commun. 4 (2013) 2717.
[52] J. Yu, Y. Cui, C.D. Wu, Y. Yang, B. Chen, G. Qian, Two-photon responsive metal-organic framework, J. Am. Chem. Soc. 137 (2015) 4026–4029.
[53] Y. Cui, T. Song, J. Yu, Y. Yang, Z. Wang, G. Qian, Dye encapsulated metal-organic framework for warm-white LED with high color-rendering index, Adv. Funct. Mater. 25 (2015) 4796–4802.
[54] J. Yu, Y. Cui, H. Xu, Y. Yang, Z. Wang, B. Chen, G. Qian, Confinement of pyridinium hemicyanine dye within an anionic metal-organic framework for two-photon-pumped lasing, Nat. Commun. 4 (2013) 2719.
[55] D. Buso, J. Jasieniak, M.D.H. Lay, P. Schiavuta, P. Scopece, J. Laird, H. Amenitsch, A.J. Hill, P. Falcaro, Highly luminescent metal-organic frameworks through quantum dot doping, Small 8 (2012) 80–88.
[56] J. An, C.M. Shade, D.A. Chengelis-Czegan, S. Petoud, N.L. Rosi, Zinc-adeninate metal-organic framework for aqueous encapsulation and sensitization of near-infrared and visible emitting lanthanide cations, J. Am. Chem. Soc. 133 (2011) 1220–1223.
[57] J. Yu, Y. Cui, C. Wu, Y. Yang, Z. Wang, M. O'Keeffe, B. Chen, G. Qian, Second-order nonlinear optical activity induced by ordered dipolar chromophores confined in the pores of an anionic metal-organic framework, Angew. Chem. Int. Ed. 51 (2012) 10542–10545.
[58] G. Lu, S. Li, Z. Guo, O.K. Farha, B.G. Hauser, X. Qi, Y. Wang, X. Wang, S. Han, X. Liu, J.S. DuChene, H. Zhang, Q. Zhang, X. Chen, J. Ma, S.C. Loo, W.D. Wei, Y. Yang, J.T. Hupp, F. Huo, Imparting functionality to a metal-organic framework material by controlled nanoparticle encapsulation, Nat. Chem. 4 (2012) 310–316.
[59] N. Yanai, K. Kitayama, Y. Hijikata, H. Sato, R. Matsuda, Y. Kubota, M. Takata, M. Mizuno, T. Uemura, S. Kitagawa, Gas detection by structural variations of fluorescent guest molecules in a flexible porous coordination polymer, Nat. Mater. 10 (2011) 787–793.
[60] X.-Z. Song, S.-Y. Song, S.-N. Zhao, Z.-M. Hao, M. Zhu, X. Meng, L.-L. Wu, H.-J. Zhang, Single-crystal-to-single-crystal transformation of a Europium(III) metal-organic framework producing a multi-responsive luminescent sensor, Adv. Funct. Mater. 24 (2014) 4034–4041.
[61] Y. Guo, X. Feng, T. Han, S. Wang, Z. Lin, Y. Dong, B. Wang, Tuning the luminescence of metal-organic frameworks for detection of energetic heterocyclic compounds, J. Am. Chem. Soc. 136 (2014) 15485–15488.

[62] M.J. Dong, M. Zhao, S. Ou, C. Zou, C.D. Wu, A luminescent dye@MOF platform: emission fingerprint relationships of volatile organic molecules, Angew. Chem. Int. Ed. 53 (2014) 1575–1579.
[63] Z. Dou, J. Yu, Y. Cui, Y. Yang, Z. Wang, D. Yang, G. Qian, Luminescent metal-organic framework films as highly sensitive and fast-response oxygen sensors, J. Am. Chem. Soc. 136 (2014) 5527–5530.
[64] S.S. Nagarkar, B. Joarder, A.K. Chaudhari, S. Mukherjee, S.K. Ghosh, Highly selective detection of nitro explosives by a luminescent metal-organic framework, Angew. Chem. Int. Ed. 52 (2013) 2881–2885.
[65] Y. Cui, B. Chen, G. Qian, Lanthanide metal-organic frameworks for luminescent sensing and light-emitting applications, Coord. Chem. Rev. 273–274 (2014) 76–86.
[66] J. Rocha, L.D. Carlos, F.A.A. Paz, D. Ananias, Luminescent multifunctional lanthanides-based metal-organic frameworks, Chem. Soc. Rev. 40 (2011) 926–940.
[67] B. Li, H.-M. Wen, Y. Cui, G. Qian, B. Chen, Multifunctional lanthanide coordination polymers, Prog. Polym. Sci. 48 (2015) 40–84.
[68] B. Chen, L. Wang, Y. Xiao, F.R. Fronczek, M. Xue, Y. Cui, G. Qian, A luminescent metal-organic framework with lewis basic pyridyl sites for the sensing of metal ions, Angew. Chem. Int. Ed. 48 (2009) 500–503.
[69] B. Chen, Y. Yang, F. Zapata, G. Lin, G. Qian, E.B. Lobkovsky, Luminescent open metal sites within a metal-organic framework for sensing small molecules, Adv. Mater. 19 (2007) 1693–1696.
[70] Y. Li, S. Zhang, D. Song, A luminescent metal-organic framework as a turn-on sensor for DMF vapor, Angew. Chem. Int. Ed. 52 (2013) 710–713.
[71] B. Chen, L. Wang, F. Zapata, G. Qian, E.B. Lobkovsky, A luminescent microporous metal-organic framework for the recognition and sensing of anions, J. Am. Chem. Soc. 130 (2008) 6718–6719.
[72] Y. Xiao, L. Wang, Y. Cui, B. Chen, F. Zapata, G. Qian, Molecular sensing with lanthanide luminescence in a 3D porous metal-organic framework, J. Alloys Compd. 484 (2009) 601–604.
[73] B. Chen, Y. Yang, F. Zapata, G. Qian, Y. Luo, J. Zhang, E.B. Lobkovsky, Enhanced near-infrared–luminescence in an erbium tetrafluoroterephthalate framework, Inorg. Chem. 45 (2006) 8882–8886.
[74] H. Xu, F. Liu, Y. Cui, B. Chen, G. Qian, A luminescent nanoscale metal-organic framework for sensing of nitroaromatic explosives, Chem. Commun. 47 (2011) 3153–3155.
[75] H. Xu, X. Rao, J. Gao, J. Yu, Z. Wang, Z. Dou, Y. Cui, Y. Yang, B. Chen, G. Qian, A luminescent nanoscale metal-organic framework with controllable morphologies for spore detection, Chem. Commun. 48 (2012) 7377–7379.
[76] Y. Takashima, V.M. Martinez, S. Furukawa, M. Kondo, S. Shimomura, H. Uehara, M. Nakahama, K. Sugimoto, S. Kitagawa, Molecular decoding using luminescence from an entangled porous framework, Nat. Commun. 2 (2011) 168.
[77] W. Zhang, J. Yu, Y. Cui, X. Rao, Y. Yang, G. Qian, Synthesis, structures and luminescent properties of two coordination polymers based on 5-(4-carboxyphenyl)-2,6-pyr-idinedicarboxylic acid, Z. Anorg. Allg. Chem. 639 (2013) 430–434.
[78] W. Zhang, J. Yu, Y. Cui, X. Rao, Y. Yang, G. Qian, Assembly and tunable luminescence of lanthanide-organic frameworks constructed from 4-(3,5-dicarboxyphenyl)pyridine-2,6-dicarboxylate ligand, J. Alloys Compd. 551 (2013) 616–620.
[79] N.B. Shustova, B.D. McCarthy, M. Dinca, Turn-on fluorescence in tetraphenylethylene-based metal-organic frameworks: an alternative to aggregation-induced emission, J. Am. Chem. Soc. 133 (2011) 20126–20129.

[80] N.B. Shustova, T.C. Ong, A.F. Cozzolino, V.K. Michaelis, R.G. Griffin, M. Dinca, Phenyl ring dynamics in a tetraphenylethylene-bridged metal-organic framework: implications for the mechanism of aggregation-induced emission, J. Am. Chem. Soc. 134 (2012) 15061–15070.
[81] Y. Xiao, Y. Cui, Q. Zheng, S. Xiang, G. Qian, B. Chen, A microporous luminescent metal-organic framework for highly selective and sensitive sensing of Cu2+ in aqueous solution, Chem. Commun. 46 (2010) 5503–5505.
[82] Z. Guo, H. Xu, S. Su, J. Cai, S. Dang, S. Xiang, G. Qian, H. Zhang, M. O'Keeffe, B. Chen, A robust near infrared luminescent ytterbium metal-organic framework for sensing of small molecules, Chem. Commun. 47 (2011) 5551–5553.
[83] P. Falcaro, S. Furukawa, Doping light emitters into metal-organic frameworks, Angew. Chem. Int. Ed. 51 (2012) 8431–8433.
[84] Y. Cui, H. Xu, Y. Yue, Z. Guo, J. Yu, Z. Chen, J. Gao, Y. Yang, G. Qian, B. Chen, A luminescent mixed-lanthanide metal-organic framework thermometer, J. Am. Chem. Soc. 134 (2012) 3979–3982.
[85] X. Rao, T. Song, J. Gao, Y. Cui, Y. Yang, C. Wu, B. Chen, G. Qian, A highly sensitive mixed lanthanide metal-organic framework self-calibrated luminescent thermometer, J. Am. Chem. Soc. 135 (2013) 15559–15564.
[86] Y. Cui, W. Zou, R. Song, J. Yu, W. Zhang, Y. Yang, G. Qian, A ratiometric and colorimetric luminescent thermometer over a wide temperature range based on a lanthanide coordination polymer, Chem. Commun. 50 (2014) 719–721.
[87] D. Zhao, X. Rao, J. Yu, Y. Cui, Y. Yang, G. Qian, Design and synthesis of an MOF thermometer with high sensitivity in the physiological temperature range, Inorg. Chem. 54 (2015) 11193–11199.
[88] K. Miyata, Y. Konno, T. Nakanishi, A. Kobayashi, M. Kato, K. Fushimi, Y. Hasegawa, Chameleon luminophore for sensing temperatures: control of metal-to-metal and energy back transfer in lanthanide coordination polymers, Angew. Chem. Int. Ed. 52 (2013) 6413–6416.
[89] A. Cadiau, C.D. Brites, P.M. Costa, R.A. Ferreira, J. Rocha, L.D. Carlos, Ratiometric nanothermometer based on an emissive $ln(^{3+})$-organic framework, ACS Nano 7 (2013) 7213–7218.
[90] X. Lian, D. Zhao, Y. Cui, Y. Yang, G. Qian, A near infrared luminescent metal-organic framework for temperature sensing in the physiological range, Chem. Commun. 51 (2015) 17676–17679.
[91] J. Zhou, H. Li, H. Zhang, W. Shi, P. Cheng, A bimetallic lanthanide metal-organic material as a self-calibrating color-gradient luminescent sensor, Adv. Mater. 27 (2015) 7072–7077.
[92] Y. Cui, R. Song, J. Yu, M. Liu, Z. Wang, C. Wu, Y. Yang, B. Chen, G. Qian, Dual-emitting MOF⊃dye composite for ratiometric temperature sensing, Adv. Mater. 27 (2015) 1420–1425.
[93] X. Rao, Q. Huang, X. Yang, Y. Cui, Y. Yang, C. Wu, B. Chen, G. Qian, Color tunable and white light emitting Tb^{3+} and Eu^{3+} doped lanthanide metal-organic framework materials, J. Mater. Chem. 22 (2012) 3210–3214.
[94] Y. Liu, M. Pan, Q.-Y. Yang, L. Fu, K. Li, S.-C. Wei, C.-Y. Su, Dual-emission from a single-phase Eu–Ag metal-organic framework: an alternative way to get white-light phosphor, Chem. Mater. 24 (2012) 1954–1960.
[95] Y. Lu, B. Yan, Lanthanide organic–inorganic hybrids based on functionalized metal-organic frameworks (MOFs) for a near-UV white LED, Chem. Commun. 50 (2014) 15443–15446.

[96] D.F. Sava, L.E. Rohwer, M.A. Rodriguez, T.M. Nenoff, Intrinsic broad-band white-light emission by a tuned, corrugated metal-organic framework, J. Am. Chem. Soc. 134 (2012) 3983–3986.
[97] W.J. Rieter, K.M.L. Taylor, H. An, W. Lin, W. Lin, Nanoscale metal-organic frameworks as potential multimodal contrast enhancing agents, J. Am. Chem. Soc. 128 (2006) 9024–9025.
[98] A. Foucault-Collet, K.A. Gogick, K.A. White, S. Villette, A. Pallier, G. Collet, C. Kieda, T. Li, S.J. Geib, N.L. Rosi, S. Petoud, Lanthanide near infrared imaging in living cells with Yb^{3+} nano metal organic frameworks, Proc. Natl. Acad. Sci. U. S. A. 110 (2013) 17199–17204.
[99] S.V. Eliseeva, J.-C.G. Bünzli, Lanthanide luminescence for functional materials and bio-sciences, Chem. Soc. Rev. 39 (2010) 189–227.
[100] L.D. Carlos, R.A.S. Ferreira, V. de Zea Bermudez, B. Julián-López, P. Escribano, Progress on lanthanide-based organic–inorganic hybrid phosphors, Chem. Soc. Rev. 40 (2011) 536–549.
[101] J.-C.G. Bünzli, C. Piguet, Lanthanide-containing molecular and supramolecular polymetallic functional assemblies, Chem. Rev. 102 (2002) 1897–1928.
[102] J.-C.G. Bünzli, Lanthanide luminescence for biomedical analyses and imaging, Chem. Rev. 110 (2010) 2729–2755.
[103] K. Binnemans, Lanthanide-based luminescent hybrid materials, Chem. Rev. 109 (2009) 4283–4374.
[104] E.G. Moore, A.P.S. Samuel, K.N. Raymond, From antenna to assay: lessons learned in lanthanide luminescence, Acc. Chem. Res. 42 (2009) 542–552.
[105] A. Carné, C. Carbonell, I. Imaz, D. Maspoch, Nanoscale metal-organic materials, Chem. Soc. Rev. 40 (2011) 291–305.
[106] E.L. Que, D.W. Domaille, C.J. Chang, Metals in neurobiology: probing their chemistry and biology with molecular imaging, Chem. Rev. 108 (2008) 1517–1549.
[107] K.M.L. Taylor-Pashow, J.D. Rocca, Z. Xie, S. Tran, W. Lin, Postsynthetic modifications of iron-carboxylate nanoscale metal-organic frameworks for imaging and drug delivery, J. Am. Chem. Soc. 131 (2009) 14261–14263.
[108] K.M.L. Taylor, W.J. Rieter, W. Lin, Manganese-based nanoscale metal-organic frameworks for magnetic resonance imaging, J. Am. Chem. Soc. 130 (2008) 14358–14359.
[109] K.M.L. Taylor, A. Jin, W. Lin, Surfactant-assisted synthesis of nanoscale gadolinium metal-organic frameworks for potential multimodal imaging, Angew. Chem. Int. Ed. 47 (2008) 7722–7725.
[110] K.A. White, D.A. Chengelis, M. Zeller, S.J. Geib, J. Szakos, S. Petoud, N.L. Rosi, Near-infrared emitting ytterbium metal-organic frameworks with tunable excitation properties, Chem. Commun. 45 (2009) 4506.
[111] V. Guillerm, D. Kim, J.F. Eubank, R. Luebke, X. Liu, K. Adil, M.S. Lah, M. Eddaoudi, A supermolecular building approach for the design and construction of metal-organic frameworks, Chem. Soc. Rev. 43 (2014) 6141–6172.
[112] D.X. Xue, A.J. Cairns, Y. Belmabkhout, L. Wojtas, Y. Liu, M.H. Alkordi, M. Eddaoudi, Tunable rare-earth fcu-MOFs: a platform for systematic enhancement of CO_2 adsorption energetics and uptake, J. Am. Chem. Soc. 135 (2013) 7660–7667.
[113] D.-X. Xue, Y. Belmabkhout, O. Shekhah, H. Jiang, K. Adil, A.J. Cairns, M. Eddaoudi, Tunable rare earth fcu-MOF platform: access to adsorption kinetics driven gas/vapor separations via pore size contraction, J. Am. Chem. Soc. 137 (2015) 5034–5040.

Chapter 291

Rare Earth Coordination Chemistry in Action: Exploring the Optical and Magnetic Properties of the Lanthanides in Bioscience While Challenging Current Theories

David Parker[1]
Durham University, Durham, United Kingdom
[1]*Corresponding author: e-mail: david.parker@dur.ac.uk*

Chapter Outline

Handbook on the Physics and Chemistry of Rare Earths, Vol. 50. http://dx.doi.org/10.1016/bs.hpcre.2016.03.004

1 BACKGROUND: A PERSONAL HISTORICAL PERSPECTIVE

In the 1980s, two emerging areas in healthcare stimulated the development of new chemistry involving kinetically inert rare earth complexes. The first involved the creation of low MW complexes of Gd(III), to serve as contrast agents for the field of magnetic resonance imaging (MRI). Nowadays 40% of all MRI scans use a Gd contrast agent to assist the radiographer, typically at a dose of 0.1 mmol/kg body weight (ca. 5 g).

The second area required coordination complexes of radioactive rare earth ions, to be used for targeted imaging and therapy. Several common challenges were posed in each case, notably in making complexes that were kinetically stable, with respect to premature release of the metal ion in vivo. Since 2001, radioimmunotherapy has formed part of the therapeutic portfolio to combat cancer in the clinic. The complex design features that emanated from this work now guide the selection of rare earth coordination complexes that can be used safely in vivo and in cellulo.

1.1 Radioimmunotherapy with ^{90}Y Conjugates

In the early 1980s, the challenge of creating a targeted therapeutic agent, based on a monoclonal antibody labeled with a cytotoxic radioisotope, was first mooted. The antibody vector targets a cell-surface glycoprotein that is overexpressed on tumor cells, and the radioisotope can be selected to possess sufficient energy and penetration to deliver a local cytotoxic dose of radiation. A key objective was to develop a protein conjugate modified with a chelating ligand and radiolabeled with a long-range β-emitting isotope, such as ^{90}Y ($t_{1/2} = 2.64$ days). Yttrium is a rare earth element with a very similar coordination chemistry to the later lanthanide(III) ions in solution. Two key features were apparent. First, the radiolabeled complex needed to be kinetically stable with respect to premature dissociation of the ^{90}Y, on the timescale of the half-life of the protein conjugate in the body—estimated to be of the order of 18–24 h for such systems. Second, a chelating ligand was required that could be linked to the antibody easily and which coordinated the ^{90}Y rapidly and selectively, in the radiolabeling step. In this second aspect, the forward rate of metal ion association needed to be fast and also chemoselective, as the nanomolar concentration of the ^{90}Y isotope was often significantly lower than the concentration of impurities in solution, typically zinc, calcium, and copper ions. The work of Desreux [1,2] suggested that the ligands of choice for this task were macrocyclic ligands based on a 12-membered core structure, ie, those based on 1,4,7,10-tetraazacyclododecane-1,4,7,10-tetraacetate "DOTA" and its analogues. These ligands not only formed the most stable complexes, in terms of their thermodynamic stability constant, but also were more kinetically inert than acyclic analogues, with respect to the rate of loss of the metal ion from

the metal complex. The requirement for high kinetic stability and fast rates of radiolabeling (310 K, pH 6.5) guided the work in Durham from the outset [3].

In this period, other workers who were addressing this issue [4,5] started by using yttrium-labeled conjugates involving acyclic DTPA-monoamide ligands. In biodistribution studies, they noted rather large amounts of the metal ion deposited in the liver and bone of experimental animals given these radiolabeled antibody conjugates. Such profiles limited the radioactive dose that could be given, lowering the therapeutic efficacy, as premature loss of the ^{90}Y label leads to the onset of myelosuppression (ie, suppression of the immune system) as a result of buildup of ^{90}Y label in the bone, giving rise to proximate irradiation of the radiosensitive bone marrow.

The premise that superior complexes would be based on the macrocyclic DOTA ligand rather than "DTPA-based" approaches was followed independently by the groups of Gansow/Brechbiel and Meares [6,7]. The approach that was adopted to test the suitability of ligands for this purpose was to track the fate of a radiolabel with time in experimental animals, examining the biodistribution of the radiolabeled complex or conjugate, typically in non-tumor- and tumor-bearing mice. Premature loss of the ^{90}Y label in vivo was characterized by buildup of the radioactivity in the bone and in the liver; such behavior is typical of weakly coordinated lanthanide(III) species, eg, the acetate or citrate salts of a lanthanide(III) aqua ion, followed by very slow clearance from these organs [8].

In preliminary work the efficacy of a chelating agent was screened by assessing its forward rate of association with the ligand (pH 6 and 37°C) and its stability in vitro and in vivo, as defined by its rate of release of the metal ion and retention of radiolabeled metal (^{90}Y, ^{153}Gd) in the skeleton and liver of mice. Complexes with the macrocyclic ligands based on DOTA were superior to acyclic ligands, based on DTPA, in terms of their stability with respect to dissociation [9]. More recently, antibodies targeted to cell-surface antigens and labeled with other rare earth radioisotopes (^{177}Lu and ^{166}Ho) have been intensively studied, often using ligands closely related to the pioneering work with DOTA [10].

1.2 Gadolinium(III) Complexes as Contrast Agents for MRI

The work that was going on to develop gadolinium contrast agents for use in MRI had obvious analogies with the development of radiolabeled therapeutic antibodies, notably in the criteria for ligand design and selection. Weakly bound Gd^{3+} species, eg, the chloride, acetate, or citrate salts, administered in vivo give rise to a series of toxic effects [11]. The "free" gadolinium ion has been shown to affect the reticuloendothelial system adversely and may cause undesirable hematological effects. In addition, liver necrosis may occur [12], and skin lesions can develop [13].

Most work focussed on modified DTPA systems and on derivatives of DOTA. In addition, new macrocyclic ligands with aza-phosphinates were developed, which formed kinetically stable complexes with gadolinium [14,15]. Radiolabeled complexes of the long-lived isotope ^{153}Gd (γ, $t_{1/2}$ = 242 days) were used to track the fate of the gadolinium in vivo. Indeed, the measured rate of dissociation of the complex (studied in vitro using ^{153}Gd-labeled complex or ^{13}C-labeled ligand for nuclear magnetic resonance (NMR) analyses) showed a very strong correlation with the in vivo stability profile. A hypothesis was put forward that linked the observed in vivo behavior to the sensitivity of the complex to acid-catalyzed dissociation; complexes that were more resistant to acid-catalyzed dissociation gave rise to the lowest amounts of ^{153}Gd in the bone and liver of experimental animals. Similar observations were deduced independently by Tweedle [16] in their analyses of the kinetic stability of various macrocyclic Gd complexes and certain acyclic complexes of gadolinium, and the link to the premature dissociation of free Gd, manifested by the deposition and retention of Gd in the bone and liver. Through this work, the relative instability of Gd(III) and Y(III) complexes of DTPA- and DTPA-diamide complexes, compared to macrocyclic DOTA-based systems, was clearly evident. Indeed, it was stated at that time: "It is generally accepted that the complexes of Gd and Y with macrocyclic ligands are more kinetically stable in vivo than DTPA-based ligands, and should therefore avert any long term, ie, chronic, rather than acute toxicity problems" [15].

The EC/European Science Foundation COST Chemistry Action Groups actively studied lanthanide coordination chemistry from 1990 to 2012, Actions D1/D8, D18/D38 examining metal complexes for diagnosis and therapy over this period. In May 2007 at Eindhoven, a special session was devoted to assess the links between the recently discovered, debilitating disease, nephrogenic systemic fibrosis (NSF) and the stability of certain gadolinium contrast agents. Speakers included Brücher (Debrecen, Hungary), Schmidt-Willich (Schering, Berlin), and Toth (Orleans) among others. The following statement was agreed by each participant and released in May 2007 on the European Science Foundation (ESF) COST Chemistry website. This statement preceded revised guidance issued by the FDA in 2009 and in Dec. 2010, warning radiographers about the use of contrast agents in patients with slow renal clearance, such as those on dialysis, in which the acyclic DTPA-based systems were contraindicated in such patients, http://www.fda.gov/drugs/drugsafety/ucm223966.htm (accessed 11.02.2016).

> *Given the prevalence of nephrogenic systemic fibrosis in patients who have been administered either Omniscan® or Optimark®, the fact that such patients were often proven to be acidotic or renally insufficient and that for some of these patients gadolinium retention in the body has been unequivocally established, the condition may be linked to the known relative kinetic instability of these 'Gd-DTPA-diamide' complexes to acid promoted dissociation, leading to retention of Gd in the skeleton, liver and/or kidney. The ESF-COST Chemistry D38*

Action group supports Regulatory Agencies statements recommending that Omniscan® and Optimark® should not be given to patients with severe renal impairment. Preferred contrast agents are those which are more kinetically inert with respect to any pathway leading to premature gadolinium dissociation, e.g., the macrocyclic based agent Dotarem, [Gd(DOTA)(H_2O)]$^-$.

In July 2015, the FDA reported a further safety communication, detailing the need to evaluate the risks associated with findings of Gd in the brain: mostly, levels are negligible but it is plausible that cases that emerge are likely to be linked to the repeated use of the less kinetically stable complexes called Omniscan and Optimark, ie, the acyclic, DTPA-diamide complexes of gadolinium (http://www.fda.gov/Drugs/DrugSafety/ucm455386.htm).

1.3 Ligand Design for Lanthanide(III) Complexes Used In Vivo

In devising a kinetically stable lanthanide complex, there are various design criteria for clinical use that were apparent to certain practising coordination chemists in the 1980s, and guided ligand design in these systems.

1.3.1 Ligand Denticity

The ligand must possess seven or eight donor atoms that can bind simultaneously to the approximately spherical Gd ion, leaving space for one or two water molecules to coordinate to the Gd center. The metal-bound waters are required, as the role of the Gd ion is to catalyze the rate of relaxation of the bulk water signal, leading to an increase in the observed water proton signal intensity in a standard (T1 weighted) MRI experiment. Normally, one bound water per Gd is sufficient for this purpose, as long as it is in fast exchange with bulk water molecules. Complexes with two coordinated waters possess lower kinetic and thermodynamic stability with respect to loss of Gd. In fact, no di-aqua Gd complexes have been approved for clinical use.

1.3.2 Ligand Constitution

The donor atoms should be oxygen or nitrogen, to maximize the affinity of the ligand for the positively charged, hard Ln^{3+} ion. The presence of a negatively charged oxygen atom is preferable, as the electrostatic interaction between it and the Gd^{3+} ion is stronger than between Gd and a neutral oxygen, such as an amide carbonyl oxygen (two amide carbonyl donors occur in DTPA-BMA in "Omniscan®") or an alcohol oxygen (one alcohol oxygen occurs in hydroxypropyl-DO3A, the ligand in "ProHance®") (Fig. 1).

This effect is apparent in comparing the relative stability of the [Gd(DTPA)(H_2O)]$^{2-}$ ("Magnevist®": five negatively charged oxygens) vs DTPA-BMA (three negatively charged oxygens and two neutral oxygens), for which the log K_{ML} thermodynamic stability constants are 22.2 and 16.8, respectively [17].

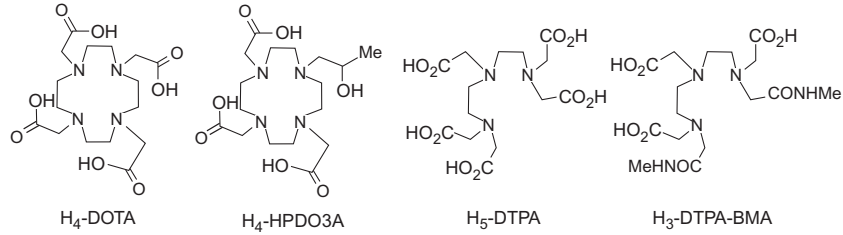

FIG. 1 Ligand structures used in Gd(III) contrast agents for MRI.

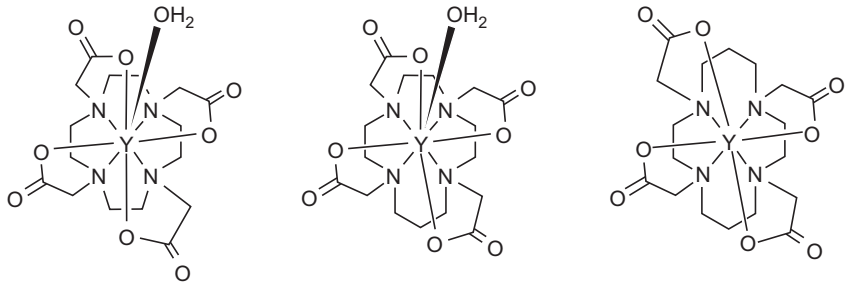

FIG. 2 Thermodynamic stability (298 K, $I = 0.1$ M) of yttrium(III) complexes [3].

1.3.3 Ligand Conformation

The ligand should bind the Gd in a manner that does not lead to the creation of strain in the complex. As Gd(III) and the lanthanide(III) ions can be considered as spherical ions to a first approximation, with relatively small ligand field energies (100–1000 cm^{-1}), they have no preferred geometries that are imposed on the ligand, in contrast to d-block systems. Rather, minimization of the energy of the complex is determined by the constitution of the ligand and the conformation it adopts. These ideas explain the preference for formation of five-membered chelate rings in the lanthanide complex [18]. Such five-membered chelate rings are formed between adjacent donor atoms and the relatively large lanthanide ion, eg, LnNCCN and LnNCCO, and are of lower energy than analogous six-membered chelate rings, LnNCCCN in metal complexes with total coordination numbers of greater than 4/5. The links between chelate ring size and complex stability were first expounded by Irving [19]. Thus, in the series of macrocyclic tetraacetate ligands based on DOTA (12-ring), TRITA (13-ring), and TETA (14-ring), the thermodynamic binding constants log K to Y^{3+} follow the order: log $K_{ML} = 24.9$, 19.1, 16.3 [3], reflecting the added strain from the presence of zero, one, and two six-membered chelate rings (Fig. 2).

1.3.4 Ligand Conformational Flexibility and Degree of Preorganization

The degree of conformational rigidity of the ligand in the metal complex can have a significant influence on the rates of metal complex formation and dissociation. For example, in the slowest step of a metal complex dissociation pathway, a nitrogen atom is often protonated and the energy barrier to this change can be related to the ease with which the ligand is able to change its shape (conformation) to allow this to occur. The more flexible the ligand, the lower this energy barrier and the faster the rate of this process. One way of restricting ligand motion, in this context, is to add a substituent next to the ligand donor atom, such as a simple alkyl group. This thinking is evident in the work of Gansow [6], examining various substituted DTPA derivatives and assessing the rate of loss of yttrium as a function of time. The substituted complex lost yttrium more slowly than the unsubstituted DTPA complex, examining acid-catalyzed dissociation. The effect is also seen in the size of the overall thermodynamic stability constant: $[Gd(EOB\text{-}DTPA)(H_2O)]^{2-}$—with an ethoxybenzyl substituent off the carbon backbone—has a log K value that is one unit higher than $[Gd(DTPA)(H_2O)]^{2-}$. Similarly, the log K value for $[Gd(HPDO3A)(H_2O)]$ (ProHance®) is 1.6 units higher than the hydroxyethyl analogue $[Gd(HEDO3A)(H_2O)]$, which lacks a methyl group next to the ligating oxygen atom [20].

The principle of microscopic reversibility forewarns that slow rates of dissociation may be correlated with slow association rates, for the more rigid ligand systems. The rate-limiting step in metal association will relate to the deformation of the ligand as the proton is removed. Somewhere, a balance needs to be struck if ambient temperature radiolabeling is to be carried out on a protein conjugate. The introduction of such alkyl or aralkyl substituents to DTPA ligands (as in BOPTA, the ligand in "MultiHance®," or EOB-DTPA, the ligand in "Primovist®"-formerly termed "Eovist") leads to increased complex stability, with respect to dissociation, compared to DTPA itself or related ligands without such C-substituents in the chelate rings of the complex.

Finally, the "macrocyclic effect" needs to be considered. This effect is also related to enhanced rigidification of any ligand system by restricting its conformational motion. Such thinking was at the forefront of science in the 1980s. In 1987, the Nobel Prize for Chemistry was awarded to Cram, Lehn, and Pedersen for their work with various cyclic compounds that possessed unique stability and reactivity profiles. This work embraced the idea of the enhanced thermodynamic and kinetic stability of the complexes of macrocyclic ligands compared with acyclic analogues. Such behavior was ascribed to their slow rates of dissociation that, in turn, was linked to ideas of their higher degree of conformational rigidity. Indeed, the enhanced stability of complexes of macrocyclic ligands is apparent in a whole variety of publications and papers from that era. Thus, the greater thermodynamic stability of the complex of Gd with DOTA compared with DTPA (log K_{ML} values are

25.3 vs 22.2, respectively) can be rationalized, notwithstanding the larger number of charged oxygens binding Gd in the DTPA complex.

1.4 In Vitro Methods to Assess Kinetic Stability

A rate constant, k, can be defined reflecting the sensitivity of a metal complex to a given dissociation pathway. The mechanism by which metal complexes dissociate in aqueous solution is most likely to involve acid catalysis. In acidic solution, metal complexes exchange the metal ion for protons and the metal ion is released from the ligand. The observed rate of dissociation is the sum of a series of terms involving various rate constants defining mechanistically viable processes. Such dissociation kinetics can be related to a simplified rate equation, Eq. (1), where k_{obs} is the measured rate constant for the dissociation reaction, k_d is the intrinsic rate constant for dissociation of the complex (very slow), and k_{H^+} and $k_{M^{2+}}$ are second-order rate constants describing the sensitivity of the complex to acid or metal ion catalyzed dissociation:

$$k_{obs} = k_d + k_{H^+}[H^+] + k_{M^{2+}}[M^{2+}] \quad (1)$$

The values of the second-order rate constant k_{H^+} have been measured (298 K under "pseudo-first-order conditions") by examining the change in the rate of dissociation of the complex with increasing acid concentration (Table 1).

Such an analysis does not allow for the increased rate that may arise from additional participation of a metal ion-assisted dissociation route, involving, say zinc. Translating such data to an in vivo system must be considered cautiously; for example, it takes no account of any reassociation of the released

TABLE 1 Acid-Catalyzed Dissociation Kinetics of Selected Gadolinium Complexes

Complex	k_{H+} (M^{-1}/s)
$[Gd\text{-}DOTA(H_2O)]^-$	2.5×10^{-5} (3.2×10^{-5})[a]
$[Gd\text{-}HPDO3A(H_2O)]$	6.4×10^{-4}
$[Gd\text{-}DTPA(H_2O)]^{2-}$	120×10^{-4}
$[Gd\text{-}DTPA\text{-}BMA(H_2O)]$	$>700\times10^{-4}$ (a lower limit)

[a]*The value in parentheses is from Pulukoddy et al. [15], at 310 K; Toth et al.[21] report this value at 298 K as 2.5×10^{-5} M^{-1}/s; other data are taken from Caravan et al. [17] where there is a transcriptional error on the Gd-DTPA-BMA half-life data in Table 11 which is stated to be 0.16 h at pH 1; this value in fact refers to Gd-DTPA, and for Gd-DTPA-BMA, $t_{1/2}$ (the time taken for the complex concentration to fall to half of its initial value) is less than 2 min at pH 1. For Gd-DOTA, $t_{1/2}$ is 78 h (25°C) under these conditions and for Gd-DTPA-BMEA (ie, Optimark), the value is quoted within the same range as for Gd-DTPA-BMA [22].*

Gd ion with the liberated protonated ligand. This reverse process is likely to be slow in vivo (slowing as pH drops), as there are competing anions in solution, eg, citrate (0.13 mM), phosphate (0.9 mM), and bicarbonate (25 mM) that form complexes or insoluble salts with gadolinium that are less reactive to substitution by a higher affinity ligand, thereby reducing the rate of reassociation. Furthermore, the endogenous metal ions Ca^{2+} (ca. 1 mM) and to a lesser extent Zn^{2+} can bind the ligand quickly at ambient pH. The concentration of zinc ions in serum is in the micromolar range, and it is bound to albumin with a K_d value of 10 nM.

The metal ion decomplexation step in vivo is more likely to be irreversible than reversible. Following dissociation, the local concentration of free Gd and of the protonated ligand is immediately reduced, by diffusion of each species away from each other and the immediate dilution into a rapidly flowing system with a total volume of about 5 L—the human bloodstream. This dilution process slows down the rate of the reaction that leads to reassociation of the complex, as the rate of this step is a function of the concentration of each reacting species, ie, the ligand and a "kinetically active" metal ion species.

2 CRITICAL ASSESSMENT OF THE THEORETICAL BACKGROUND

The paramagnetic lanthanide(III) ions possess unique ground and excited state properties that have led to numerous applications in analysis, imaging science, and the biosciences. Two main areas of research have been pursued: in magnetic resonance based on fast relaxation processes and large dipolar shifts, and in optical phenomena, associated with the sharp emission spectra and long-lived lifetimes characterizing the parity-forbidden f–f transitions.

2.1 Theories of Magnetic Anisotropy: A Reflection

In the early days of FT-NMR, Williams was exploring the uses of lanthanide(III) ions to aid spectral simplification and assist in the structural analysis of biomolecules, based on the shift and relaxation properties induced by the presence of a proximate paramagnetic ion. Bleaney, his colleague at Oxford, developed a theory of magnetic anisotropy accounting for the pseudocontact shift (PCS) that arises from electron-nuclear dipolar coupling.

The PCS (δ_p) is defined with respect to the nature of the lanthanide ion, the geometric coordinates, the ligand field, and the absolute temperature:

$$\delta_p(r,\theta,\phi) = \frac{1}{12\pi r^3}\left[\chi_{ax}\left(3\cos^2\theta - 1\right) + \frac{3}{2}\chi_{rh}\sin^2\theta\cos 2\phi\right]$$

$$\delta_p(x,y,z) = \frac{1}{12\pi r^3}\left[\chi_{ax}\frac{2z^2 - x^2 - y^2}{r^2} + \frac{3}{2}\chi_{rh}\frac{x^2 - y^2}{r^2}\right] \quad (2)$$

where $\{r, \theta, \phi\}$ are spherical coordinates of the observed nucleus, χ_{ax} is the axiality of the electron magnetic susceptibility tensor, and χ_{rh} is its rhombicity. The coordinate system is aligned to the eigensystem of the susceptibility tensor, with the electron located at the origin. These equations are usually expressed (Eq. 3) with reference to the principal magnetic axes system, highlighting the strong directional dependence of the PCS, and its link to the Bleaney constant, C_J (Eq. 4):

$$\delta_p = \frac{C_J \mu_B^2}{60\,(kT)^2}\left[\frac{(3\cos^2\theta - 1)B_0^2}{r^3} + \frac{(\sin^2\theta\cos^2\phi)B_2^2}{r^3}\right] \tag{3}$$

$$C_J = g^2 J(J+1)(2J-1)(2J+3)\langle J|\alpha|J\rangle \tag{4}$$

where C_J is characteristic of the Ln(III) ion, θ and ϕ are the angles between the nucleus under consideration and the principal magnetic axis of the lanthanide ion, g is the Landé factor, and μ_B is the Bohr magneton (BM). The B parameters are second-order ligand field terms, determined primarily by local symmetry and donor atom polarizability.

Several assumptions need to be assessed in considering the validity of this theory. First, it is assumed that the ligand field splitting is much less than kT ($205\ cm^{-1}$ at 298 K). However, the value of B_0^2 varies between 80 and $1500\ cm^{-1}$, and for most coordination complexes, it is more than two times kT. The contribution of higher order crystal field terms, that play a very important role in determining the overall ligand field, especially in low symmetry systems, is not considered. Second, the electron is assumed to be a point charge at the coordinate origin, with instantaneous relaxation. This is not true. Inspection of f electron density probability functions suggests that a distributed model is more appropriate. This approach has been put forward [23] in an important step where a partial differential equation for the PCS was developed.

Furthermore, models of f electron distributions reveal how certain ions (eg, Eu, Yb, Tm, and Er) have a prolate f electron density distribution, while others (eg, Ce, Pr, Tb, Dy) are oblate. Such behavior correlates qualitatively with the differing sense of shift, incorporated in the Bleaney constant, C_J (Fig. 3).

Third, in an isostructural series of complexes it is assumed that the position of the principal magnetic axis does not change, as the lanthanide ion varies. Sessoli [24] has demonstrated that the principal (easy) axis of magnetization in $[Ln(DOTA)(H_2O)]^-$ changes the position as the Ln series is traversed. For the Dy complex, it moves by 90 degrees according to whether there is a water molecule bound at the axial site and it rotates by 90 degrees across the series from Tb to Yb, aligning approximately with the molecular C_4 axis only for ions with a prolate f electron distribution, ie, Yb,

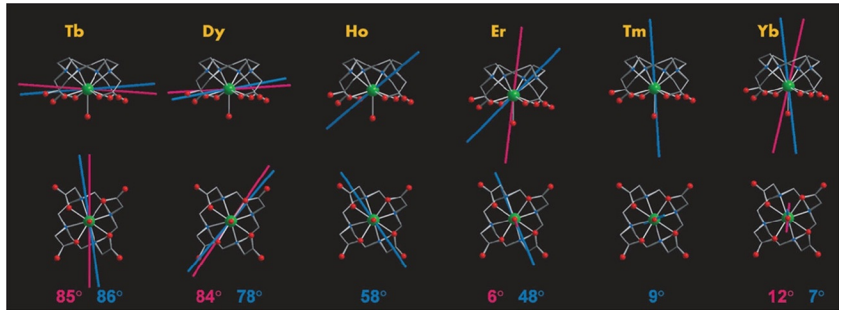

FIG. 3 Variation of the position of the easy axis of magnetization in $[Ln(DOTA)(H_2O)]^-$ complexes (*pink*—experimental; *blue*—calculated). *Reproduced with permission from Boulon, M.-F., Cucinotta, G., Luzon, J., Degl'Innocenti, C., Perfetti, M., Bernot, K., Calvez, G., Ceneschi, A., Sessoli, R., 2013. Magnetic anisotropy and spin-parity effect along the series of lanthanide complexes with DOTA. Angew. Chem. Int. Ed. Engl. 52, 350–354. © 2013 Wiley.*

Tm, and Eu. Finally, in devising the Bleaney constants (C_J), it is implicitly assumed that J is a good quantum number that defines the spin–orbit coupling. However, adoption of the Russell–Saunders coupling scheme is an approximation. Indeed, values of spin–orbit coupling energies (typically of the order of 650–1800 cm^{-1}) are not much bigger than the overall ligand field splitting terms in many complexes where the ligand field is large.

These limitations have been emphasized in recent work examining a dozen series of isostructural lanthanide complexes [25,26] where it was also shown that the second-order ligand field term B_0^2 does not correlate well with the observed dipolar shifts. It is the directional dependence (anisotropy) of the magnetic susceptibility tensor that matters most, and the relative size of the mutually orthogonal components is sensitively dependent upon the nature (polarizability) of the ligand, as well as the nature of the lanthanide ion. Thus, eight- vs nine-coordinate systems give rise to vastly different dipolar shifts, and even for closely related ligand systems in common symmetry ($[Ln(L^{1-3})]$; Fig. 4), variations in ligand donor polarizability perturb the relative size of the magnetic susceptibility components differentially, for one lanthanide ion over another.

Furthermore, in nine-coordinate systems the PCS is exquisitely sensitive to the nature of an axial donor in numerous mono-capped square-antiprismatic systems [27–29]. For example, replacing a coordinated water molecule by dimethylsulfoxide (DMSO) or dimethylformamide (DMF) in Eu and Yb tetra-amide complexes, eg, $[LnL^{4,5}]^{3+}$, results in shifts of reporter ligand proton resonances of 30 and 75 ppm, respectively. Indeed, replacement of water by fluoride actually inverts the sense of the paramagnetic shift. In each case, the relative size of the mutually orthogonal components of the magnetic susceptibility tensor is varying considerably; in the limiting case, the position of

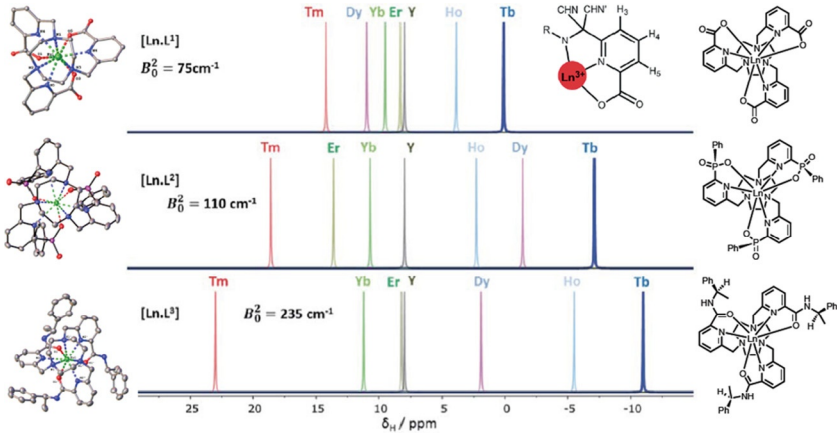

FIG. 4 Illustration of the chemical shift behavior of the pyridyl H^3 resonance in three related C_3-symmetric complexes (295 K, 9.4 T); Bleaney C_J values: Tb(−89), Dy(−100), Ho(−39), Er(+33), Tm(+55), and Yb(+22) do not correlate well with this shift behavior. *Adapted from Funk, A.M., Harvey, P., Finney, K.-L.N.A., Kenwright, A.M., Neil, E.R., Parker, D., Rogers, N.J., Senanayake, P.K., 2015a. Critical analysis of the limitations of Bleaney's theory of magnetic anisotropy in lanthanide coordination complexes. Chem. Sci. 6, 1655–1663.*

the principal axis switches (Fig. 5), as may occur with lanthanide ion permutation in a common complex [24].

Such conclusions condemn Bleaney's theory to the grave; it has outlived its usefulness despite heroic efforts to adapt it. The work also calls for a more cautious approach when using PCS information from lanthanide(III) labels in proteins to aid NMR structural assignments, particularly when varying the lanthanide ion. The approach taken by Kuprov [23] may be favored in future, if it can be coupled with greater physical insight into our understanding of the magnetic susceptibility tensor, and its relationship to the nature of the lanthanide ion and the ligand symmetry, constitution, and conformation.

2.2 Challenging Relaxation Theory

For lanthanide complexes, spin relaxation theory is usually considered using perturbative treatments based on Bloch–Redfield–Wangsness (BRW) theory. The longitudinal paramagnetic relaxation depends upon rotational and conformational modulation of the electron-nuclear dipolar interaction, Eq. (5):

$$R_1 = \frac{2}{15}\left(\frac{\mu_0}{4\pi}\right)^2 \frac{\gamma_N^2 \mu_{\text{eff}}^2}{r^6}\left[\frac{7\tau_{R+e}}{1+\omega_e^2\tau_{R+e}^2} + \frac{3\tau_{R+e}}{1+\omega_N^2\tau_{R+e}^2}\right] + \frac{2}{5}\left(\frac{\mu_0}{4\pi}\right)^2 \frac{\omega_N^2 \mu_{\text{eff}}^4}{(3kT)^2 r^6} \frac{3\tau_R}{1+\omega_N^2\tau_R^2}$$

$$\mu_{\text{eff}}^2 = g_e^2 \mu_B^2 \left\langle \hat{S}^2 \right\rangle \qquad \tau_{R+e} = \left(\tau_R^{-1} + T_{1e}^{-1}\right)^{-1} \tag{5}$$

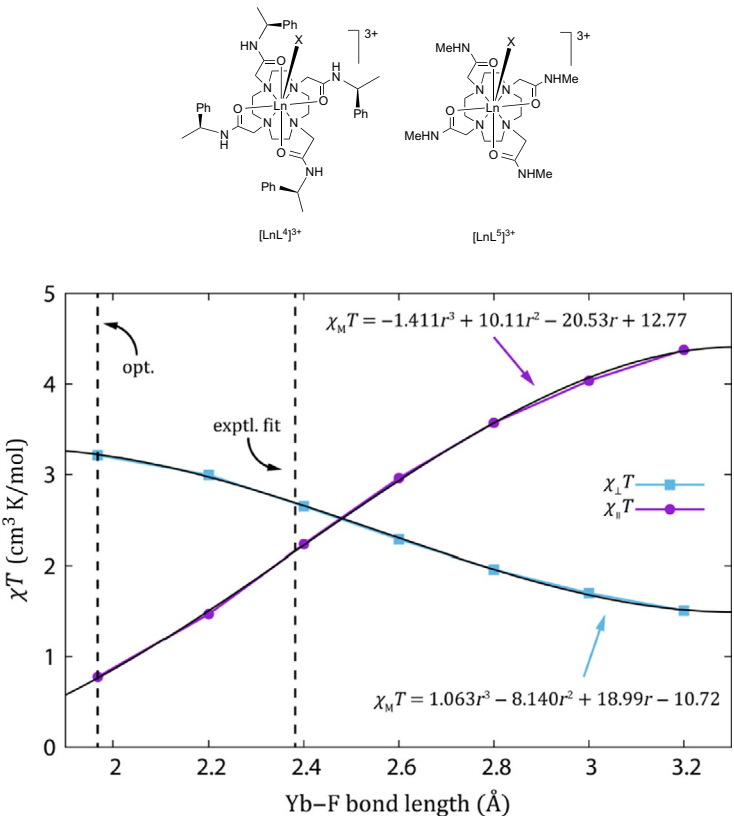

FIG. 5 Calculated magnetic anisotropy tensor in $[YbL^5]^{3+}$ showing the variation in the principal components with the axial Yb–F length: when *X* is varied, the size of the orthogonal components of the magnetic anisotropy tensor changes dramatically. *Reproduced with permission from Blackburn, O.A., Chilton, N.F., Keller, K., Tait, C.E., Myers, W.K., McInnes, E.J.L., Kenwright, A.M., Beer, P.D., Timmel, C.R., Faulkner, S., 2015. Spectroscopic and crystal field consequences of fluoride binding by [Yb-DTMA]$^{3+}$ in aqueous solution. Angew. Chem. Int. Ed. Engl. 54, 10783–10786. © 2015, Wiley.*

where μ_0 is the vacuum permeability, g_N is the gyromagnetic ratio of the nucleus, g_{Ln} is the Landé factor of the fundamental multiplet J of the free Ln^{3+} ion, μ_B is the BM, r is the electron–nuclear distance, τ_r is the rotational correlation time, ω_N is the nuclear Larmor frequency, ω_e is the electron Larmor frequency, and T_{1e} is the longitudinal relaxation time of the electron spin. In the second part of Eq. (5), the dependence of R_1 on $(\mu_{eff})^4$ and $(\omega_N)^2$ (Curie term) becomes more significant at high magnetic fields, especially for ions with larger values of μ_{eff}, such as Dy and Ho. At such high fields, the relaxation rates for the later Ln^{3+} ions echo the μ_{eff} sequence:

Dy/Ho > Tb > Er > Tm > Yb. At fields of below 3 T, the value of T_{1e} primarily determines relaxation.

A key problem with the BRW theory is that the perturbation theory assumptions are often violated for the electron. Knowledge of a large number of empirical parameters is also required that can be tricky to prove independently, eg, T_{1e}, τ_R, and the true value of μ_{eff}. The electronic relaxation time, T_{1e}, with values between 0.1 and 1 ps, has been shown to be a function of the nature of both the lanthanide ion and the transient ligand field induced by solvent collision. Highly symmetric systems exhibited a direct dependence of T_{1e} [78] on the second-order ligand field term, B_0^2. At the imaging fields encountered in clinical scanners (1.5–3 T), it is T_{1e} that should be given consideration (Fig. 6; [78]) in selecting (non-Gd) paramagnetic probes for use in vivo.

Yet, the same concerns that undermine our belief in Bleaney's theory of magnetic anisotropy apply here: is J a good enough quantum number when the ligand field is large and comparable in energy to the spin–orbit coupling? Also, can we trust the use of "free-ion" magnetic susceptibility values? Moreover, why does this theory assume that the rotational correlation time is isotropic, when observed nuclei usually have motion that is not coupled to the rotation of the whole molecule. And, why is only the size of the magnetic susceptibility considered and not its anisotropy? The effect of the anisotropy of the magnetic susceptibility on relaxation has been considered theoretically, leading to a modification of Eq. (5) [30], but very few examples of the

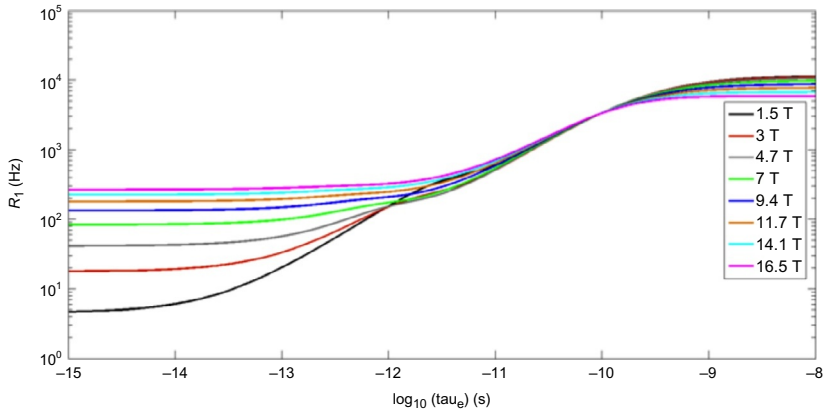

FIG. 6 Simulated variation of relaxation rate, R_1, with T_{1e} for a ^{19}F lanthanide relaxation probe (μ_{eff} = 10 BM, 295 K, τ_r = 250 ps, r = 6 Å). *Adapted from Funk, A.M., Fries, P.H., Harvey, P., Kenwright, A.M., Parker, D., 2013. Experimental measurement and theoretical assessment of fast lanthanide electronic relaxation in solution with four series of isostructural complexes, J. Phys. Chem. A 117, 905–917.*

application of this analysis have been reported, although the limitations have been noted [28,31].

Recalling that electron density clouds for the maximum $|m_J|$ projections are prolate for Yb, Tm, Er, and Eu and oblate for Ce, Tb, Pr, Dy, Nd, and Ho, ligand electron density on the molecular z-axis has been suggested to destabilize maximum $|m_J|$ for the former ions and stabilize them for the latter [32]. Therefore, it is expected that magnetic moments for Ln(III) ions in coordination complexes must vary with the coordination environment, especially when ligand field splittings are large. Such effects have been reported [33] for the LnOBr series; for example, ligand field splittings rise to over 1300 cm^{-1} and values of μ_{eff} for HoOBr are 11% lower than the "free-ion" value.

Measurements of the proton NMR paramagnetic relaxation rates for several series of isostructural lanthanide(III) complexes have been undertaken [25,26] over six magnetic fields in the range of 1–16.5 T. Values for T_{1e} and the magnetic susceptibility, μ_{eff}, were estimated, assuming BRW theory. Anomalous relaxation rate profiles were obtained, notably for erbium and thulium complexes of low symmetry in eight-coordinate complexes (Fig. 7), when

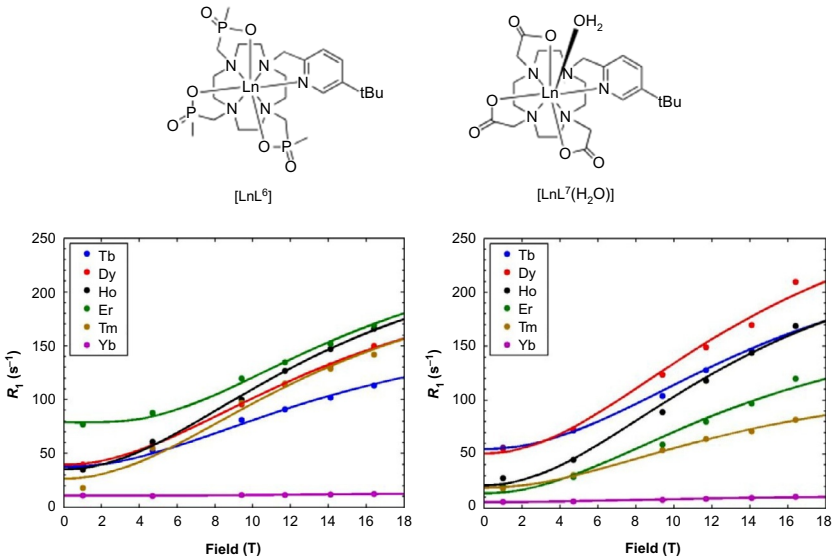

FIG. 7 ^{1}H NMR relaxation rates (R_1 (s^{-1})) for the ^{t}Bu resonances in [LnL^6] (*left* at −75 ppm) and [$Ln(L^7)(H_2O)$] (−20.5 ppm, *right*) as a function of magnetic field, showing the fits of BRW theory (line) to the experimental data points (295 K, D_2O); this analysis requires low values of μ_{eff} for Tb, Dy (8.81 and 9.47) and high values for Tm (9.51). Typical "free-ion" values: Tb, 9.8; Dy, 10.5; Tm, 7.7 BM. *Adapted from Funk, A.M., Finney, K.-L.N.A., Fox, M.A., Harvey, P., Rogers, N.J., Senanayake, P.K., Kenwright, A.M., Parker, D., 2015b. Challenging lanthanide relaxation theory: erbium and thulium complexes that show NMR relaxation rates faster than dysprosium and terbium analogues. Phys. Chem. Chem. Phys. 17, 16507–16511.*

the nine-coordinate systems behaved more classically. Such behavior challenges the validity of BRW theory. The importance of this work lies in its relationship to the development of PARASHIFT probes for imaging in vivo (^{1}H-PARASHIFT probes; [34]: see Section 4.2), wherein the fast relaxation rate of the observed reporter resonance (eg, a *t*-butyl group) allows much faster data acquisition in MRI and MR spectral imaging in vivo, provided that the observed signal is >15,000 Hz from the water and fat signals.

2.3 Future Perspective on Theories of Lanthanide Optical Spectroscopy

Ever since Sir George Stokes examined "dispersive reflection" from Eu(II)- and Yb(II)-doped samples of fluorite (ie, CaF_2 samples from Weardale in the North-East of England), in his original studies that led him to coin the term "fluorescence," rare earth compounds and materials have played a preeminent role in display materials and emissive probe systems. The theories that are currently used to rationalize the experimental data from emission and absorption experiments have not had a significant impact on the broader community of f-element scientists. The most well known of these is Judd–Ofelt theory, but it remains rather intractable and opaque and mostly considers transition energies and lifetimes rather than oscillator strengths. It is rarely applied by practising experimental scientists.

Of greater benefit, to coordination chemists at least, have been analyses based on symmetry considerations and the ligand polarization model [35–37]. For example, the hypersensitive transitions often monitored in Eu emission spectroscopy ($\Delta J = 2$ or 4) are known to be sensitive to ligand perturbation, notably in the polarizability of the ligand donors, such as axial donor perturbation in Eu emission spectra of $[EuL^{4,5}]^{3+}$. The ligand polarization model explains this behavior in terms of electric-quadrupole transitions gaining electric dipole (ED) strength via a coupling mechanism, involving the quadrupole on the Ln^{3+} ion with induced dipoles on the ligand. The induced dipoles on the ligand are created by direct coupling to the ED components of the radiation field. Therefore, ED strength in 4f–4f transitions can be traced to ligand dipolar polarizabilities and to the directional dependence of these polarizabilities.

In any radiation field, the ED and magnetic dipole (MD) components are mutually orthogonal. Therefore, it is appropriate to consider the anisotropy of the electric susceptibility tensor in optical spectroscopy, just as we examine the magnetic susceptibility tensor and its directional dependence to assess behavior in a magnetic field. Such an approach is used to rationalize the nonlinear optical behavior of compounds and materials. Therefore, the anisotropy of ligand dipolar polarizability will play a key role in rationalizing emission intensity changes, which are often critical in monitoring a change in the lanthanide coordination environment.

Two examples in lanthanide complexes of C_3 or C_4 symmetry offer scope for reflection. In the series of nine-coordinate complexes based on triazacyclononane (Fig. 4, $[LnL^{1-3}]$), the ligand field splitting is small (B_0^2 for Eu: 70–230 cm^{-1}) and so are the ^1H NMR PCSs. In contrast, the relative intensity of the $\Delta J = 2$ transition in the Eu(III) complexes around 620 nm is very high, being highest for the carboxylate system with the smallest PCSs. On the other hand, in the C_4 symmetric series of complexes based on 12-N_4 (eg, $[Ln(DOTA)(H_2O)]^-$ and its amide derivatives, $[LnL^{4,5}(S)]^{3+}$), the ligand field is much larger and is particularly sensitive to the nature of the axial donor (S) and its polarizability [27,29]. PCSs Values are very large for a hard donor such as water, whereas with more polarizable, axial oxygen donors (DMSO, DMF, HMPA), the PCS dramatically reduces and the relative intensity of the $\Delta J = 2$ manifold increases by nearly 5, over the MD-allowed $\Delta J = 1$ transition. Evidently, the orthogonality of the electric and magnetic susceptibility tensors may be manifesting itself, and the relative magnitude of their principal components may be varying in concert.

Such empirical thinking suggests that a unified theory could be contemplated in the future, addressing the role of the electric and magnetic susceptibility tensors in their interaction with a given lanthanide(III) system, for the appropriate electromagnetic radiation field. Such an approach, emulating Maxwell's approach in the 19th century, to electromagnetism is perhaps long overdue [28].

3 LANTHANIDE EMISSION IN ACTION

The wealth of applications harnessing the brightness of lanthanide emission continues to grow. The beautiful pure "red" and "green" emission profiles from the $^5D_0$ (17,200 cm^{-1}) and $^5D_4$ (20,400 cm^{-1}) excited states of europium and terbium, respectively, may yet find further application in security printing [38]. For example, the printing on paper of red and green inks can be undertaken with mixtures of $[Ln(dpa)_3]^{3-}$ complexes (dpa = pyridine-2,6-dicarboxylate) yet is only visualized under UV illumination (280 nm). In this context, blue emission from a lanthanide source with a high overall quantum yield remains a challenge, both in the solid and in the solution states. In a solid-state lattice, the allowed f–d transition from the excited Eu(II) ion usually gives rise to a deep blue color. It remains difficult to stabilize the f^7 ion, Eu(II), in a coordination complex in aqueous solution [39,40], with respect to one electron oxidation, although neutral [222]-cryptands have been known for over 30 years to stabilize this oxidation state with respect to Eu^{3+}, by a size-matching effect and the absence of a Coulombic interaction that favors Eu^{3+} binding.

Blue emission from the $^1G_4$ Tm^{3+} excited state (21,350 cm^{-1}) in the solid-state is restricted by the very low absorbance of the Laporte-forbidden f–f transitions [41]. In a coordination complex in solution, it is rather sensitive

to quenching by energy matched XH (X = N, O, and C) oscillators. However, promising photophysical properties (λ_{exc} 306 nm, $\varepsilon = 25{,}000\ M^{-1}/cm$, $\tau = 4.6$ ms, $\phi = 0.12\%$) have been reported for sensitized visible emission from the per-deuterated system $[TmL^8]^-$ [42], notwithstanding the complexity of the emission processes that characterize the excited state chemistry of thulium(III) [43,44].

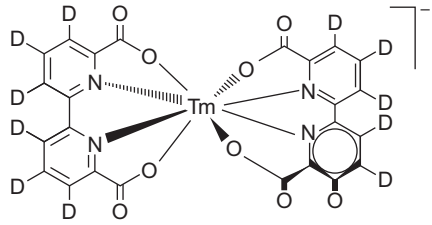

$[TmL^8]^-$

It should be noted that this complex is still three orders of magnitude less bright ($B(\lambda) = \varepsilon(\lambda)\phi$) than the brightest Eu or Tb complexes in water [45–47] that can be excited over the range 337–365 nm.

3.1 In Vitro Analyses

A plethora of analytical applications has been reported [48], wherein selective and reversible binding of an ion, most often an electron-rich or anionic species, to a Eu or Tb complex in aqueous solution is signaled by modulation of the lanthanide emission intensity profile, lifetime, or circular polarization [49]. Two main classes can be considered, involving perturbation either of the ligand singlet or triplet excited states, or the metal excited state itself. In the latter case, this process often involves a change in the metal coordination environment—and hence ligand field, for example, by reversible formation of a ternary complex [50]. Selectivity for the target anion is achieved via variation of the charge and steric demand at the metal center (Fig. 8; [51]) and has allowed ratiometric analyses to be undertaken in complex biofluids, such as seminal fluid where the citrate concentration has been determined in hundreds of human samples [52].

In complexes with electron-poor sensitizing ligands, reducing agents like ascorbate, catecholate, and urate can form exciplexes with the triplet excited state, leading to quenching of the metal-based emission and a reduction in its lifetime. This process was shown to occur for terbium complexes with

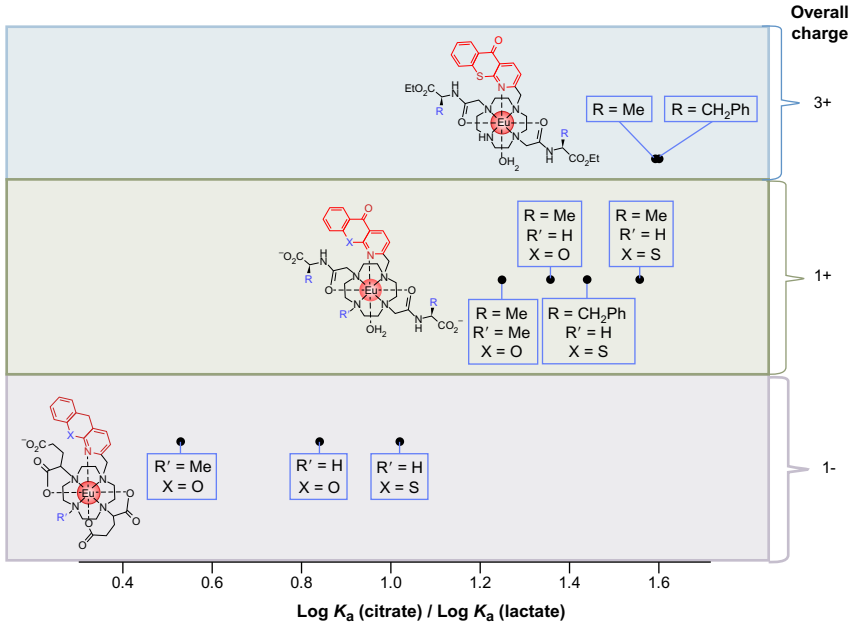

FIG. 8 Comparative binding affinities for citrate and lactate allowing identification of Eu(III) complexes in analyses of biofluids [51]. *Reproduced with permission from Heffern, M.C., Matosziuk, L.M., Meade, T.J., 2014. Lanthanide probes for bioresponsive imaging. Chem. Rev. 114, 4496–4539. © ACS.*

azaxanthone [Ln(L^7)(H_2O)] and tetra-azatriphenylene chromophores [LnL^8], but not for their Eu analogues [53].

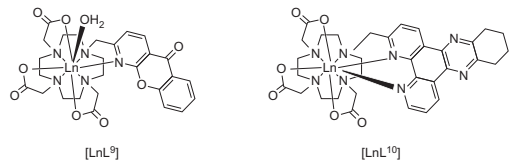

The exciplex possesses a lower excited state energy and allows back-energy transfer to occur from the Tb ion to the sensitizer, thereby reducing the lifetime of the Tb $^5D_4$ excited state. Direct quenching of the lanthanide excited state by these electron-rich species does not occur and was proven by examining behavior following direct population of the Ln excited state using laser excitation at 457 nm ($^7F_0$–$^5D_2$) for Eu and 488 nm ($^7F_6$–$^5D_4$) for Tb [54].

Calibration of the spectral response uses the ratio of red/green light emission (eg, 620–545 nm bands) or modulation of the terbium lifetime. The analytical method works well to determine urate concentrations in complex biofluid samples, such as urine or serum.

3.2 In Cellulo Studies

Over the past 15 years, metal coordination complexes have emerged as a new class of emissive probes for imaging studies. Lanthanide complexes that are resistant to excited quenching processes constitute a diverse class of emissive stains and probes for cell imaging [55–58,60]; New et al., 2010. Typically, complexes localized within cells are excited at 355 or 365 nm, although future confocal microscope systems may use a laser-driven white light source, which permits excitation up to 375 or 380 nm. Such excitation wavelengths require the use of pulsed excitation to limit the UV exposure of the sample and impose strict limitations to the nature of the integral sensitizing moiety. It should possess an absorption wavelength that matches the laser/LED excitation source and a small singlet–triplet energy gap or possess a strong internal charge transfer transition to aid efficient energy transfer from the chromophore to the lanthanide ion [59].

An expression (Eq. 6) has been introduced for the observed brightness, B', of a luminescent complex in a time-gated spectroscopy or microscopy experiment in cellulo, following pulsed excitation at a wavelength, λ:

$$B'(\lambda, c) = \eta\varepsilon\phi \int e^{-kt}\, dt \tag{6}$$

where c is the complex loading concentration, λ is the applied excitation wavelength, and η is a cellular accumulation constant, reflecting the internal complex concentration. The integral has limits ($t_{acq}+t_d$) and t_d, in which k is the emission decay rate constant, t_{acq} is the spectroscopic integration time or microscopy acquisition time, and t_d is the delay time following pulsed excitation [55].

The majority of lanthanide(III) complexes *examined so far* are taken into cells by macropinocytosis, involving cell-surface recognition of a hydrophobic moiety [60,61]. This nonspecific uptake process can be suppressed by introducing anionic sulfonate groups on the periphery of the ligand. With several amphipathic systems, cell-localization profiles have been determined empirically in a range of different cell types. Thus, the tris-sugar derivative, [EuL^{11}], which is as bright as red fluorescent protein, localizes selectively to mitochondria and, unlike MitoTracker Green, can be used for longer term live cell imaging studies without killing the cell or co-staining lipid droplets ([46,55]; Fig. 9).

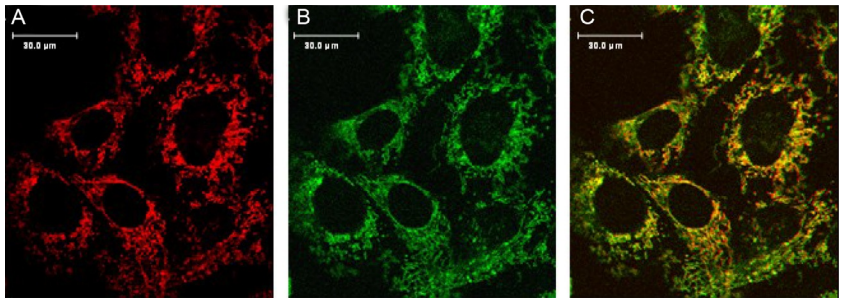

FIG. 9 Confocal microscopy images showing: (A) mitochondrial localization of [EuL^{11}] of NIH-3T3 cells (1 h, 18 µM, λ_{exc} 355 nm, λ_{em} 605–720 nm); (B) MitoTracker Green (λ_{exc} 488 nm, λ_{em} 500–530 nm); (C) RGB merged image showing colocalization ($P = 0.95$). *Adapted from Butler, S.J., Lamarque, L., Pal, R., Parker, D., 2014. EuroTracker dyes: highly emissive europium complexes as alternative organelle stains for live cell imaging. Chem. Sci. 5, 1750–1755.*

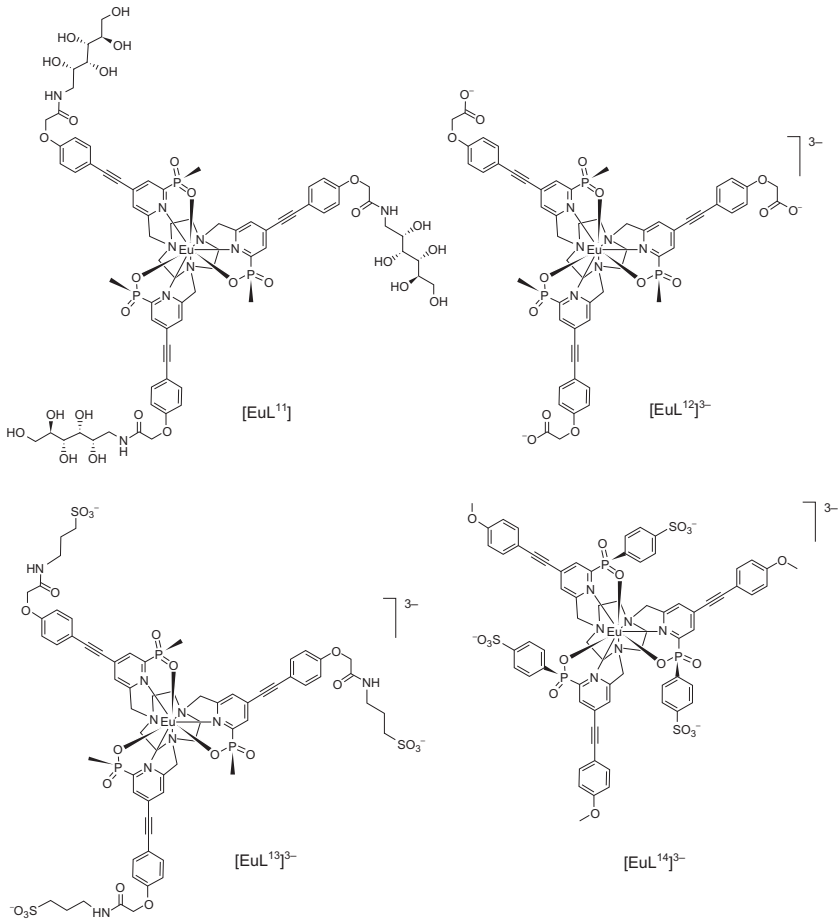

On the other hand, the anionic analogue, $[EuL^{12}]^{3-}$, localizes to the lysosomes and the tris-sulfonates, $[EuL^{13}]^{3-}$ and $[EuL^{14}]^{3-}$, show no cell uptake under live cell imaging conditions [45]. The absence of nonspecific cell-surface binding and uptake allows such sulfonated systems to be used in conjugates designed to tag or bind to a certain cell-surface receptor, or to be conjugated to an appropriate vector for internalization by a specific pathway. Responsive ratiometric probes localizing to particular compartments have been created that measure pH [62–64] and bicarbonate [63,64] in the mitochondrial region.

3.3 Prospects and Limitations of Optical Imaging In Vivo

Future live cell imaging work is likely to examine the development of further organelle-specific stains, aided by the conjugation of targeting vectors that give rise to unique localization profiles. Provided that due care is taken not to perturb the membrane permeability of the cell system under study, nor change the cell's ability to proliferate, differentiate, and function, eg, by assessing mitochondrial redox and esterase activity [60], then additional luminescent responsive probes are likely to be created. These probes should function reversibly for live cell imaging, rather than undergo irreversible transformations that render them simple dosimeters, for which calibration uncertainty negates true utility. Additionally, the breadth of applications of FRET-based assays both examining cell-surface and intracellular receptors will continue to grow. Such systems, often using a bright Eu or Tb donor and a strongly absorbing cyanine dye as the acceptor, were developed in the 1970s and 1980s at the beginning of work with time-resolved measurements and continue to be refined notably for high-throughput assays in vitro and to study protein–protein interactions within cells [65].

Further examples using longer-lived metal-based probes may become more common if the manufacturers of microscopes start to use broader range laser excitation sources rather than the He/Ne, argon, and solid-state laser sources that traditionally cover the visible spectral range. The advantages of higher resolution microscopy are yet to be fully realized, but the discovery of low-cost systems, such as "phase-modulated nanoscopy" [66] that breaks the diffraction limit and allows a twofold increase in resolution, ie, down to 70 nm, for 355 nm excitation, represents an important advance. Coupled with the use of time-gated imaging for the new ranges of d block (Ir, Pt, Re), Eu and Tb probes, and stains, with pulsed excitation over the range 355–450 nm, the use of time-gated imaging systems should become more widespread.

Optical imaging agents have rather limited scope in clinical practice because of their short penetration depth in tissue, caused by light scattering and endogenous absorption. Even when using two-photon excitation, requiring expensive high-powered lasers and examining the near-IR region of 710–980 nm (eg, using Yb complexes), depths of only 1 or 2 cm can be

probed. However, specific applications may emerge, eg, in image-guided surgery where oxygen-sensitive probes may help the surgeon to define regions of hypoxia, and in many applications that involve the largest organ of the body—the skin.

4 LANTHANIDE SHIFT AND RELAXATION PROBES

In the 1970s, magnetic resonance spectroscopy was vying with MRI for commercial exploitation of the NMR experiment that had been discovered 25 years earlier. The advent of stable gradient magnetic fields and wide-bore magnets, coupled with the remarkable differences in relaxation times of water in different tissue types, meant that MRI became and remains pre-eminent in clinical imaging. Image contrast was further enhanced by the use of Gd-based contrast agents (vide supra), whose development—at a commercial level—has stalled, despite the opportunities that exist for better targeted and higher relaxivity agents. Economic factors are the main issue in this regard, as well as the need to prove that acute or chronic toxicities are minimized.

The frontier of MRI contrast agent design involves creation of functionalized agents that target specific aspects of cellular or physiological properties of the disease under investigation. Agents which bind to various targets, such as collagen in fibrotic scar tissue [67] or the endothelial wall [68], have been developed. These agents, however, rely on indirect detection via changes in water relaxation rates (R_1, R_2, or R_2^*) through conventional gadolinium contrast agents or iron oxide particles, rather than detecting the contrast molecule directly.

The main reason why magnetic resonance spectroscopy imaging (MRSI) has not been used more widely, despite an inherently richer information content, can be traced to the intrinsically low sensitivity of the NMR experiment. The net magnetization that determines signal strength at 7 T represents only a 0.002% population difference in nuclear spin states. In MRI, the abundant water signal is examined: all other potential endogenous analytes are present at much lower concentrations, typically in the millimolar range. If the probe itself is to be detected, toxicity limitations for lanthanide(III) complexes mean that the injected dose should not exceed 0.3 mmol/kg bodyweight.

Increased sensitivity in any NMR experiment follows if you use higher field (proportional to $B^{3/2}$) or if you can significantly increase the rate of signal intensity acquisition, by enhancing the relaxation rate of the observed signal, without unduly compromising its linewidth. Hyperpolarization methods offer a very promising future in this respect, for selected bioactive species (eg, lactate, pyruvate, bicarbonate for indirect pH imaging), albeit over relatively short imaging timescales. The other main avenues of research activity, embracing paramagnetic lanthanide complexes, involve methods based on chemical exchange by saturation transfer, again involving the bulk water signal (PARACEST) or involving the direct observation of a resonance (eg, a CF_3 for ^{19}F imaging [69] or ^{t}Bu group for ^1H MRI) engineered into the ligand

structure and close in space to the paramagnetic center. A strongly shifted and fast-relaxing signal is thereby created (PARASHIFT) [34,70–72].

4.1 Using Lanthanide Probes: PARACEST and PARASHIFT Complexes

Paramagnetic complexes of Yb and Eu have found use in the development of PARACEST agents [73]. Chemical exchange by saturation transfer (CEST) methods are indirect, measuring a change in the bulk (tissue) water signal as a result of saturation of a frequency shifted proton that is undergoing chemical exchange between the tracer of interest and the bulk water itself. The frequency shift in PARACEST is due to induced chemical shifts arising from the presence of the Yb(III) or Eu(III) ion, often involving a ligand secondary amide proton in a coordinated amide carbonyl group. With these PARACEST agents, a major limitation remains the need to determine absolute concentration for many classes of molecules, due to the indirect nature of the detection, and the high powers that are needed to saturate the signal. While several agents have been evaluated for sensitivity to physiological parameters in vitro, relatively few have been demonstrated in vivo and, in most cases, direct injection into the tissue of interest and/or a high injected dose (ca. 2 mmol/kg) is required to obtain high local tissue concentrations [74,75].

In the PARASHIFT experiment [34], the observed ligand resonance is 5–7 Å from the paramagnetic center and relaxes two orders of magnitude faster. For ^{1}H imaging in vivo, the signal should be shifted by more than 15 kHz from the water and fat signals, to allow fast gradient-echo pulse sequences to be used with short echo and delay times [71,77]. Signal intensity gains over diamagnetic controls are in the range 10- to 25-fold, bringing direct probe imaging into the submillimolar range. By observing ^{t}Bu probe resonances, sensitivity is enhanced to the 0.1 mmol/kg regime. Thus, at a field of 7 T with the Dy complex, $[DyL^{15}]^{-}$ (0.05 mmol/kg injected), the signal at −61 ppm for the probe can be imaged simultaneously with structural MRI scans, observing the water signal: this is dual imaging exemplified. It offers an alternative to PET-MRI, with the advantage that the shift of the observed resonance can be made to report on environmental factors, such as pH and temperature (Fig. 10; [72]).

4.2 Future Perspectives for MRI and MRSI

Targeted Gd contrast agents and PARACEST/PARASHIFT agents should allow greater sensitivity and enhance spatial discrimination. Cheap and effective vectors are needed, and the merits of targeting endogenous proteins [67] or abundant cell-surface receptors have been expounded [76]. In the latter case, if the probe is bound reversibly, such as a conjugate of a competitive antagonist, and does not get internalized, the risks associated with prolonged retention are minimized.

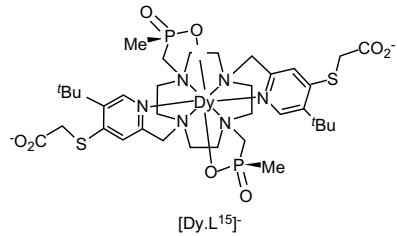

[Dy.L[15]]-

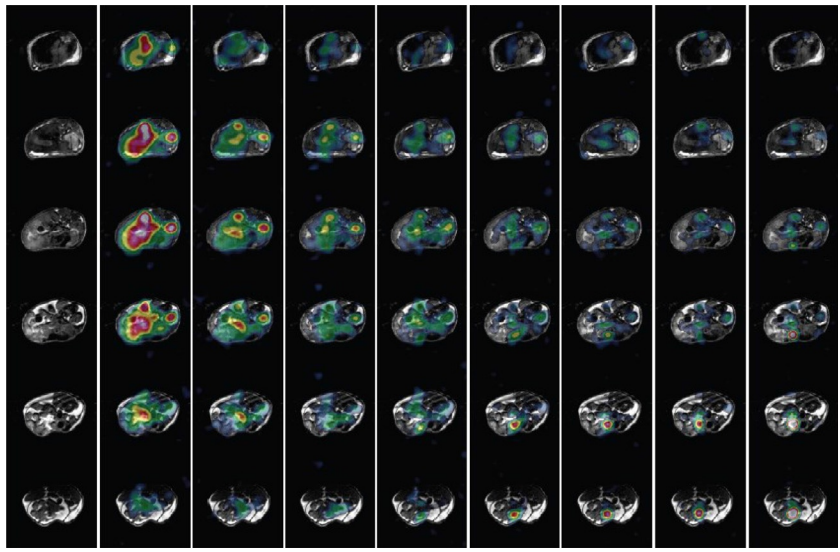

FIG. 10 PARASHIFT dual MR imaging with $[DyL^{15}]^-$ showing the time-dependent(*left* to *right*, ca. 60 s intervals) clearance via the liver and kidneys following tail vein injection of 0.05 mmol/kg. *Adapted from Senanayake, P.K., Rogers, N.J., Finney, K.-L.N.A., Harvey, P., Funk, A.M., Wilson, J.I., O'Hogain, D., Maxwell, R., Parker, D., Blamire, A.M., 2016. A new paramagnetically shifted imaging probe for MRI. Magn. Reson. Med. http://dx.doi.org/10.1002/mrm.26185. [Epub ahead of print].*

In PARASHIFT systems, the selection of the lanthanide ion determines the magnitude of the PARASHIFT, with Dy, Er, and Tm complexes arguably offering most scope, while retaining fast relaxation. Recent work suggests that although these shifts and relaxation rates cannot be predicted by current theory [25,26], the acquisition of large data sets for isostructural systems has allowed shifts to be predicted semi-empirically. Coinjection of PARASHIFT agents with different functional properties (eg, pH, T), or with different Ln ions selected to produce shifts in different regions of the spectrum, could permit monitoring of multiple processes in vivo by appropriate selection of bandwidth and resonant frequency. A further possibility is to regard these complexes as "building blocks" for higher order assemblies. Most simply, conjugation of multiple copies of a single structure to a larger molecule can

be envisaged as a way to regulate biodynamics and enhance detection sensitivity [69]. In addition, linking structures based on a common ligand but with different PARASHIFTs engineered via selection of different lanthanide ions or reporter group distances creates multifunctional probes. An example might be the creation of dual probes with distinguishable signals that are physiologically sensitive and insensitive to provide an internally referenced scan intensity. Such dual or multiprobe systems have the added advantage that the biodynamics for each group is guaranteed to be identical [72].

Finally, it is likely that the acquisition of additional sets of shift and relaxation data, coupled with detailed measurements of lanthanide EPR and magnetic susceptibility, will allow better theories/probe design strategies to be developed. We need to establish structure/property relationships that help us grasp how the electric and magnetic susceptibility tensors determine the magneto-optical phenomena we observe.

ABBREVIATIONS

BM	Bohr magneton
BMA	bis(carboxymethyl)amide
BOPTA	benic acid
BRW	Bloch–Redfield–Wangsness
COST	European Cooperation in Science and Technology
DMF	dimethylformamide
DMSO	dimethylsulfoxide
DO3A	1,4,7,10-tetraazacyclododecane-1,4,7-triacetate
DOTA	1,4,7,10-tetraazacyclododecane-1,4,7,10-tetraacetate
DTPA	diethylenetriamine pentaacetate
EC	European Commission
ED	electric dipole
EOB	ethoxybenzyl
EPR	electron paramagnetic resonance
ESF	European Science Foundation
FDA	United States Food and Drug Administration
FRET	Förster resonant energy transfer
HMPA	hexamethylphosphoramide
LED	light-emitting diode
MD	magnetic dipole
MRI	magnetic resonance imaging
MRSI	magnetic resonance spectroscopy imaging
MW	molecular weight
NMR	nuclear magnetic resonance
NSF	nephrogenic systemic fibrosis
PARACEST	paramagnetic chemical exchange saturation transfer
PARASHIFT	paramagnetic shift

PCS	pseudocontact shift
$t_{1/2}$	radioactive or kinetic half -live
TETA	1,4,8,11-tetraazacyclotetradecane-1,4,8,11-tetraacetate
TRITA	1,4,8,11-tetraazacyclotridecane-1,4,8,11-tetraacetate

REFERENCES

[1] J.F. Desreux, Nuclear magnetic resonance spectroscopy of lanthanide complexes with a tetraacetic tetraaza macrocycle. Unusual conformation properties, Inorg. Chem. 19 (1980) 1319–1324.

[2] M. Spirlet, J.F. Desreux, M.F. Loncin, Crystal and molecular structure of sodium aquo-(1,4,7,10-tetraazacyclododecane-1,4,7,10-tetraacetato)-europate(III) tetrahydrate, Na +(EuDOTA·H_2O)$^-$·4H_2O, and its relevance to NMR studies of the conformational behavior of the lanthanide complexes formed by the macrocylic ligand DOTA, Inorg. Chem. 23 (1984) 359–365.

[3] J.P.L. Cox, K.J. Jankowski, R. Kataky, D. Parker, N.R.A. Beeley, B.A. Boyce, M.A.W. Eaton, K. Millar, A.T. Millican, A. Harrison, C. Walker, Synthesis of a kinetically stable yttrium-90 labelled macrocycle antibody conjugate, J. Chem. Soc., Chem. Commun. (1989) 797–798.

[4] W.T. Anderson-Berg, R.A. Squire, M. Strand, Specific radioimmunotherapy using ^{90}Y-labeled monoclonal antibody in erythroleukemic mice, Cancer Res. 47 (1987) 1905–1912.

[5] D.J. Hnatowich, M. Chinol, D.A. Siebecker, M. Gionet, T. Griffin, P.W. Doherty, R. Hunter, K.R. Kase, Patient biodistribution of intraperitoneally administered yttrium-90-labeled antibody, J. Nucl. Med. 29 (1988) 1428–1435.

[6] T.J. McMurry, C.G. Pippin, C. Wu, K.A. Deal, M.W. Brechbiel, O.A. Gansow, Physical parameters and biological stability of yttrium(III) diethylenetriaminepentaacetic acid derivative conjugates, J. Nucl. Med. 41 (1998) 3546–3549.

[7] M.K. Moi, C.F. Meares, S. DeNardo, The peptide way to macrocyclic bifunctional chelating agents, J. Am. Chem. Soc. 110 (1988) 626–627.

[8] A. Harrison, C. Walker, J.P.L. Cox, K.J. Jankowski, D. Parker, J. Sansom, M.A.W. Eaton, N. R.A. Beeley, A.T. Millican, The in-vivo release of ^{90}Y from cyclic and acyclic ligand antibody conjugates, Nucl. Med. Biol. 18 (1991) 469–476.

[9] D. Parker, Towards clinical applications of synthetic macrocycles: from diagnosis to therapy, Chem. Soc. Rev. 19 (1990) 271–291.

[10] C. Seidl, C. Zockler, R. Beck, L. Quintinilla-Martinez, F. Bruchertseifer, R. Senekowitsche-Schmidtke, ^{177}Lu-immunotherapy of experimental peritoneal carcinomatosis shows comparable effectiveness to ^{213}Bi-immunotherapy, but causes toxicity not observed with ^{213}Bi, Eur. J. Nucl. Med. Mol. Imaging 38 (2011) 312–322.

[11] T.J. Haley, K.A. Gschneider, L. Eyring (Eds.), Handbook of the Physics and Chemistry of Rare Earths, vol. 4, Elsevier, Amsterdam, 1979, pp. 5553–5585.

[12] M.L. Rose, B.U. Bradford, D.R. Germolec, M. Lin, H. Tsukamoto, R.G. Thurman, Gadolinium chloride-induced hepatocyte proliferation is prevented by antibodies to tumor necrosis factor alpha, Toxicol. Appl. Pharmacol. 170 (2001) 39–45.

[13] H.C. Hodge, H.S. Sterner, Tabulation of toxicity classes, Am. Ind. Hyg. Assoc. Q. 10 (1943) 93–96.

[14] K. Pulukoddy, T.J. Norman, D. Parker, L. Royle, A. Harrison, Stable anionic, neutral, and cationic complexes of gadolinium with functionalised amino-phosphinic acid macrocyclic ligands, J. Chem. Soc. Chem. Commun. (1992) 1441–1443.

[15] P.K. Pulukoddy, T.J. Norman, D. Parker, L. Royle, C.J. Broan, Synthesis of charged and uncharged complexes of gadolinium and yttrium with cyclic polyaza-phosphinic acid ligands for in vivo applications, J. Chem. Soc., Perkin Trans. 2 (1993) 605–620.
[16] P. Wedeking, K. Kumar, M.F. Tweedle, Reaction of gadolinium chelates with endogenously available ions, Magn. Reson. Imaging 10 (1992) 641–648.
[17] P. Caravan, J. Ellison, T.J. McMurry, R.B. Lauffer, Gadolinium(III) chelates as MRI contrast agents: structure, dynamics, and applications, Chem. Rev. 99 (1999) 2293–2352.
[18] R.D. Hancock, Macrocycles and their selectivity for metal ions on the basis of size, Pure Appl. Chem. 58 (1986) 1445–1452.
[19] H.M.N. Irving, R.J.P. Williams, The stability of transition-metal complexes, J. Chem. Soc. (1954) 3192–3210.
[20] E. Brucher, Kinetic stabilities of gadolinium(III) chelates used as MRI contrast agents, Top. Curr. Chem. 221 (2002) 103–122.
[21] E. Toth, E. Brucher, I. Lazar, I. Toth, Kinetics of formation and dissociation of lanthanide(III) dota complexes, Inorg. Chem. 33 (18) (1994) 4070–4076.
[22] N.F. Rofsky, A.D. Sherry, R.E. Lenkinski, Nephrogenic systemic fibrosis: a chemical perspective, Radiology 247 (2008) 608–612.
[23] G.T.P. Charnock, I. Kuprov, A partial differential equation for pseudocontact shift, Phys. Chem. Chem. Phys. 16 (2014) 20184–20189.
[24] M.-F. Boulon, G. Cucinotta, J. Luzon, C. Degl'Innocenti, M. Perfetti, K. Bernot, G. Calvez, A. Ceneschi, R. Sessoli, Magnetic anisotropy and spin-parity effect along the series of lanthanide complexes with DOTA, Angew. Chem. Int. Ed. Engl. 52 (2013) 350–354.
[25] A.M. Funk, P. Harvey, K.-L.N.A. Finney, A.M. Kenwright, E.R. Neil, D. Parker, N.J. Rogers, P.K. Senanayake, Critical analysis of the limitations of Bleaney's theory of magnetic anisotropy in lanthanide coordination complexes, Chem. Sci. 6 (2015) 1655–1663.
[26] A.M. Funk, K.-L.N.A. Finney, M.A. Fox, P. Harvey, N.J. Rogers, P.K. Senanayake, A.M. Kenwright, D. Parker, Challenging lanthanide relaxation theory: erbium and thulium complexes that show NMR relaxation rates faster than dysprosium and terbium analogues, Phys. Chem. Chem. Phys. 17 (2015) 16507–16511.
[27] O.A. Blackburn, N.F. Chilton, K. Keller, C.E. Tait, W.K. Myers, E.J.L. McInnes, A.M. Kenwright, P.D. Beer, C.R. Timmel, S. Faulkner, Spectroscopic and crystal field consequences of fluoride binding by $[Yb\text{-}DTMA]^{3+}$ in aqueous solution, Angew. Chem. Int. Ed. Engl. 54 (2015) 10783–10786.
[28] O.A. Blackburn, R.M. Edkins, S. Faulkner, A.M. Kenwright, D. Parker, N.J. Rogers, S. Shuvaev, Electromagnetic susceptibility anisotropy and its importance for paramagnetic NMR and optical spectroscopy in lanthanide coordination chemistry, Dalton Trans. 45 (2016) 6782–6800.
[29] R.S. Dickins, J.I. Bruce, D. Parker, D.J. Tozer, Correlation of optical and ^{1}H NMR spectral information with coordination variation for axially symmetric europium and ytterbium(III) complexes: importance of axial donor polarisability in determining affinity and ligand field, Dalton Trans. (2003) 1264–1271.
[30] A.J. Vega, D. Fiat, Nuclear relaxation processes of paramagnetic complexes. The slow motion case, Mol. Phys. 31 (1976) 347–355.
[31] N.J. Rogers, K.-L.N.A. Finney, D. Parker, P.K. Senanayake, Another challenge to paramagnetic relaxation theory: a study of paramagnetic proton NMR relaxation in closely related series of pyridine-derivatised dysprosium complexes, Phys. Chem. Chem. Phys. 18 (2016) 4370–4375.

[32] J.D. Rinehart, J.R. Long, Exploiting single-ion anisotropy in the design of f-element single-molecule magnets, Chem. Sci. 2 (2011) 2078–2085.
[33] J. Holsa, M. Lastusaari, J. Niittykoski, R.S. Puche, Interplay between crystal structure and magnetic susceptibility of tetragonal ROBr, Phys. Chem. Chem. Phys. 4 (2002) 3091–3098.
[34] P. Harvey, A.M. Blamire, J.I. Wilson, K.-L.N.A. Finney, A.M. Funk, P.K. Senanayake, D. Parker, Moving the goal posts: enhancing the sensitivity of PARASHIFT proton magnetic resonance imaging and spectroscopy, Chem. Sci. 4 (2013) 4251–4258.
[35] S.F. Mason, The ligand polarization model for the spectra of metal complexes, Struct. Bond. (Berlin) 39 (1980) 43–79.
[36] S.F. Mason, R.D. Peacock, B. Stewart, Ligand polarisability contributions to the hypersensitive transitions of the trivalent lanthanides, Mol. Phys. 30 (1975) 1829–1841.
[37] M.F. Reid, F.S. Richardson, Anisotropic ligand polarizability contributions to lanthanide 4f-4f intensity parameters, Chem. Phys. Lett. 95 (1983) 501–507.
[38] J. Andres, R.D. Hirsch, J.-E. Moser, A.-S. Chauvin, A new anti-counterfeiting feature relying on invisible luminescent full colour images printed with lanthanide-based inks, Adv. Mater. 24 (2014) 5029–5036.
[39] J. Garcia, M.J. Allen, Developments in the coordination chemistry of europium(II), Eur. J. Inorg. Chem. (2012) 4550–4563.
[40] A.N.W. Kuda-Wedagedara, C. Wang, P.D. Martin, M.J. Allen, Aqueous Eu(II)-containing complex with bright yellow luminescence, J. Am. Chem. Soc. 137 (2015) 4960–4963.
[41] W.T. Carnall, in: K.A. Gschneidner Jr., L. Eyring (Eds.), Handbook on the Physics and Chemistry of Rare Earths, vol. 3, North Holland, Amsterdam, The Netherlands, 1979, p. 172.
[42] J. Wahsner, M. Seitz, Perdeuterated 2,2′-bipyridine-6,6′-dicarboxylate: an extremely efficient sensitizer for thulium luminescence in solution, Inorg. Chem. 52 (2013) 13301–13303.
[43] O.A. Blackburn, M. Tropiano, T.J. Sørensen, J. Thom, A. Beeby, L.M. Bushby, D. Parker, L.S. Natrajan, S. Faulkner, Luminescence and up-conversion from thulium (III) species in solution, Phys. Chem. Chem. Phys. 14 (2012) 13378–13384.
[44] N. Wartenberg, O. Raccurt, E. Bourgeat-Lami, D. Imbert, M. Mazzanti, Multicolour optical coding from a series of luminescent lanthanide complexes with a unique antenna, Chem. Eur. J. 19 (2013) 3477–3482.
[45] M. Delbianco, V. Sadovnikova, E. Bourrier, L. Lamarque, G. Mathis, D. Parker, J.M. Zwier, Bright, highly water soluble triazacyclononane europium complexes to detect ligand binding with time-resolved FRET microscopy, Angew. Chem. Int. Ed. Engl. 53 (2014) 10718–10722.
[46] J.W. Walton, A. Bourdolle, S.J. Butler, M. Soulie, M. Delbianco, B.K. McMahon, R. Pal, H. -Puschmann, J.M. Zwier, L. Lamarque, O. Maury, C. Andraud, D. Parker, Very bright europium complexes that stain cellular mitochondria, Chem. Commun. 49 (2013) 1600–1602.
[47] J. Xu, T.M. Corneillie, E.G. Moore, G.-L. Law, N.G. Butlin, K.N. Raymond, Octadentate cages of Tb(III) 2-hydroxyisophthalamides: a new standard for luminescent lanthanide labels, J. Am. Chem. Soc. 133 (2011) 19900–19910.
[48] M.C. Heffern, L.M. Matosziuk, T.J. Meade, Lanthanide probes for bioresponsive imaging, Chem. Rev. 114 (2014) 4496–4539.
[49] R. Carr, N.H. Evans, D. Parker, Lanthanide complexes as chiral probes exploiting circularly polarised luminescence, Chem. Soc. Rev. 41 (2012) 7673–7686.
[50] S.J. Butler, D. Parker, Anion binding in water at lanthanide centres: from structure and selectivity to signalling and sensing, Chem. Soc. Rev. 42 (2013) 1652–1666.

[51] R. Pal, L. Costello, D. Parker, A europium luminescence assay of lactate and citrate in biological fluids, Org. Biomol. Chem. 7 (2009) 1525–1528.
[52] R. Pal, A. Beeby, D. Parker, Rapid and accurate analysis of citrate in low-volume seminal fluid samples using a time-gated and ratiometric measurement of europium luminescence, J. Pharmaceut. Biomed. Anal. 56 (2011) 352–358.
[53] R.A. Poole, F. Kielar, S.L. Richardson, P.A. Stenson, D. Parker, A ratiometric and non-enzymatic luminescence assay for uric acid: differential quenching of lanthanide excited states by anti-oxidants, Chem. Commun. (2006) 4084–4086.
[54] G.-L. Law, D. Parker, S.L. Richardson, K.-L. Wong, The mechanism of quenching of the lanthanide excited state for optical probes using sensitised emission, Dalton Trans. (2009) 8481–8484.
[55] S.J. Butler, L. Lamarque, R. Pal, D. Parker, EuroTracker dyes: highly emissive europium complexes as alternative organelle stains for live cell imaging, Chem. Sci. 5 (2014) 1750–1755.
[56] A.S. Chauvin, S. Comby, B. Song, C.D.B. Vandevvver, F. Thomas, J.-C.G. Bunzli, A polyoxyethylene-substituted bimetallic europium helicate for luminescent staining of living cells, Chem. Eur. J. 13 (2007) 9515–9526.
[57] E. Deiters, B. Song, A.-S. Chauvin, C.D.B. Vandevyver, F. Gumy, J.-C.G. Bunzli, Luminescent bimetallic lanthanide bioprobes for cellular imaging with excitation in the visible-light range, Chem. Eur. J. 15 (2009) 885–900.
[58] R.A. Poole, G. Bobba, M.J. Cann, J.-C. Frias, D. Parker, R.D. Peacock, Synthesis and characterisation of highly emissive and kinetically stable chiral lanthanide complexes suitable for usage in cellulo, Org. Biomol. Chem. 66 (2005) 1013–1024.
[59] M. Soulie, F. Latzko, E. Bourrier, V. Placide, S.J. Butler, R. Pal, J.W. Walton, P.L. Baldeck, B. Le Guennic, C. Andraud, J.M. Zwier, L. Lamarque, D. Parker, O. Maury, Comparative analysis of conjugated alkynyl chromophore-triazacyclononane ligands for sensitized emission of europium and terbium, Chem. Eur. J. 20 (2014) 8636–8646.
[60] E.J. New, D. Parker, D.G. Smith, J.W. Walton, Development of responsive lanthanide probes for cellular applications, Curr. Opin. Chem. Biol. 14 (2010) 238–246.
[61] E.J. New, A. Congreve, D. Parker, Definition of the uptake mechanism and sub-cellular localisation profile of emissive lanthanide complexes as cellular optical probes, Chem. Sci. 1 (2010) 111–117.
[62] B.K. McMahon, R. Pal, D. Parker, A bright and responsive europium probe for determination of pH change within the endoplasmic reticulum, Chem. Commun. 49 (2013) 5363–5365.
[63] D.G. Smith, R. Pal, D. Parker, Measuring equilibrium bicarbonate concentrations directly in cellular mitochondria and in human serum using europium/terbium emission intensity ratios, Chem. Eur. J. 18 (2012) 11604–11613.
[64] D.G. Smith, B.K. McMahon, R. Pal, Live cell imaging of lysosomal pH changes with responsive ratiometric lanthanide probes, Chem. Commun. 48 (2012) 8520–8522.
[65] J.M. Zwier, H. Bazin, L. Lamarque, G. Mathis, Luminescent lanthanide cryptates: from the bench to the bedside, Inorg. Chem. 53 (2014) 1854–1866.
[66] R. Pal, Phase modulation nanoscopy: a simple approach to enhanced optical resolution, Faraday Discuss. 177 (2015) 507–515.
[67] P. Caravan, Y. Yang, R. Zachariah, A. Schmitt, M. Mino-Kenudson, H.H. Chen, D.E. Sosnovik, G. Dai, B.C. Fuchs, M. Lanuti, Molecular magnetic resonance imaging of pulmonary fibrosis in mice, Am. J. Respir. Cell Mol. Biol. 49 (2013) 1120–1126.

[68] S. Serres, M.S. Soto, A. Hamilton, M.A. McAteer, W.S. Carbonell, M.D. Robson, O. Ansorge, A. Khrapitchev, C. Bristow, L. Balathason, T. Weissensteiner, D.C. Anthony, R.P. Choudhury, R.J. Muschel, N.R. Sibson, Molecular MRI enables early and sensitive detection of brain metastases, PNAS 109 (2012) 6674–6679.

[69] E. De Luca, P. Harvey, K.H. Chalmers, A. Mishra, D. Parker, P.K. Senanayake, J.I. Wilson, M. Botta, M. Fekete, A.M. Blamire, Characterisation and evaluation of paramagnetic fluorine labelled glycol chitosan conjugates for ^{19}F and ^{1}H magnetic resonance imaging, J. Biol. Inorg. Chem. 19 (2014) 215–227.

[70] K.H. Chalmers, E. De Luca, N.H.M. Hogg, A.M. Kenwright, I. Kuprov, J.I. Wilson, M. Botta, A.M. Blamire, D. Parker, Paramagnetic fluorine labelled lanthanide complexes as probes for 19-F magnetic resonance imaging and spectroscopy, Chem. Eur. J. 16 (2010) 134–148.

[71] K.H. Chalmers, A.M. Kenwright, D. Parker, A.M. Blamire, ^{19}F-lanthanide complexes with increased sensitivity for ^{19}F-MRI: optimization of the MR acquisition, Magn. Reson. Med. 66 (2011) 931–936.

[72] P.K. Senanayake, N.J. Rogers, K.-L.N.A. Finney, P. Harvey, A.M. Funk, J.I. Wilson, D. O'Hogain, R. Maxwell, D. Parker, A.M. Blamire, A new paramagnetically shifted imaging probe for MRI. Magn. Reson. Med. (2016). http://dx.doi.org/10.1002/mrm.26185. [Epub ahead of print.

[73] S.R. Zhang, M. Merritt, D.E. Woessner, R.E. Lenkinski, A.D. Sherry, PARACEST agents: modulating MRI contrast via water proton exchange, Acc. Chem. Res. 36 (2003) 783–790.

[74] G.S. Liu, Y.G. Li, V.R. Sheth, M.D. Pagel, Imaging in vivo extracellular pH with a single paramagnetic chemical exchange saturation transfer magnetic resonance imaging contrast agent, Mol. Imaging 11 (2012) 47–57.

[75] N. McVicar, A.X. Li, M. Suchy, R.A.H.E. Hudson, R.S. Menon, R. Bartha, Simultaneous in vivo pH and temperature mapping using a PARACEST-MRI contrast agent, Magn. Reson. Med. 70 (2013) 1016–1025.

[76] N. Sim, D. Parker, Critical design features for the targeted molecular imaging of cell surface receptors, Chem. Soc. Rev. 44 (2015) 2122–2134.

[77] R. Schmidt, N. Nippe, K. Strobel, M. Masthoff, O. Reifschneider, D.D. Castelli, C. Holtke, S. Aime, U. Karst, C. Sunderkotter, C. Bremer, C. Faber, Highly shifted proton MR imaging: cell tracking by using direct detection of paramagnetic compounds, Radiology 272 (2014) 785–795.

[78] A.M. Funk, P.H. Fries, P. Harvey, A.M. Kenwright, D. Parker, Experimental measurement and theoretical assessment of fast lanthanide electronic relaxation in solution with four series of isostructural complexes, J. Phys. Chem. A 117 (2013) 905–917.

Chapter 292

Lanthanide Nanoparticles: Promising Candidates for Magnetic Resonance Imaging Contrast Enhancement

Xiao-Yu Zheng, Lin-Dong Li, Ling-Dong Sun and Chun-Hua Yan[1]
Beijing National Laboratory for Molecular Sciences, State Key Laboratory of Rare Earth Materials Chemistry and Applications, PKU-HKU Joint Laboratory in Rare Earth Materials and Bioinorganic Chemistry, College of Chemistry and Molecular Engineering, Peking University, Beijing, China
[1]*Corresponding author: e-mail: yan@pku.edu.cn*

Chapter Outline

1 INTRODUCTION

In the early 1970s, chemist P.C. Lauterbur and coworkers successfully transformed nuclear magnetic resonance (NMR) signals into cross-sectional images, which was the earliest rudiment of magnetic resonance imaging (MRI) [1]. With subsequent continuous improvement, MRI has become one of the most widely used imaging techniques in bioimaging due to its distinctive advantages, including noninvasive detection, superb spatial resolution, outstanding capacity of differentiating soft tissues, and the avoidance of

Handbook on the Physics and Chemistry of Rare Earths, Vol. 50. http://dx.doi.org/10.1016/bs.hpcre.2016.05.001

radiation damage [2–4]. However, owing to the low sensitivity of MRI, the obtained images may have insufficient contrast, which hampers practical applications. To gain additional contrast and improve diagnostic accuracy, a number of exogenous contrast agents (CAs) have been developed and utilized in MRI examinations [5]. It is reported that approximately 35% of clinical MRI scans in the United States in 2010 employed MRI CAs, indicating their popularity and significance [6].

The production of MRI signal is based on the resonance and relaxation properties of nuclei (eg, ^{1}H) under magnetic field, and through spatially encoding, the signal can be transformed into image. The signal intensity difference between each pixel and voxel is referred to as contrast. In principle, the obtained signal intensity is related to local proton density, longitudinal (T_1) and transverse (T_2) relaxation times, water diffusion rates, chemical shifts, and pulse sequences [7]. The local proton density and relaxation times strongly rely on the proton environment, resulting in intrinsic contrast between various biological tissues. However, the difference between normal and nearby abnormal tissues is usually subtle, leading to low intrinsic contrast. The addition of CAs can enlarge the image contrast through altering the relaxation times of nearby protons. The capacity of a CA to change relaxation time is evaluated by its relaxivity (r_1 and r_2), which is defined as the change in relaxation rate ($1/T_1$ and $1/T_2$, respectively) normalized to the concentration of metal ions. From the viewpoint of applications, the CAs are commonly classified into two groups according to their r_2 to r_1 ratio (r_2/r_1). T_1 CAs, also known as positive CAs, refer to those with low r_2/r_1 values, for which the T_1 shortening effect is dominant and improves signal intensity. In contrast, T_2 CAs, also known as negative CAs, refer to those with high r_2/r_1 values, for which the T_2 shortening effect is dominant and reduces signal intensity. Notably, the rule does not always apply; in some cases, T_1 CAs can also cause a significant reduction in signal intensity while T_2 CAs do not necessarily reduce T_1. The function of CAs depends on the practical imaging sequence as well as the magnetic field strength.

Currently, paramagnetic Gd-chelates are commonly used as T_1 CAs, while superparamagnetic materials such as iron-oxide nanoparticles (NPs) act as T_2 CAs. The employment of paramagnetic agents dates back to the early 1980s, when Carr and coworkers applied Gd-diethylenetriaminepentaacetate (DTPA) (Fig. 1), a paramagnetic Gd-chelate, to enhance the lesion in the region of cerebral capillary breakdown, demonstrating the diagnostic potential of paramagnetic agents [8]. Superparamagnetic iron oxide (SPIO) NPs also emerged in 1980s, which was the first nanoparticulate MRI CAs [9]. During the past decades, great efforts have been made in the exploration of novel MRI CAs with better performance, and diverse contrast enhancing materials based on macromolecular systems and nanosystems as well as responsive, chemical exchange saturation transfer, and hyperpolarization agents have been developed [10–13]. Among them, lanthanide (Ln) NPs, exploiting the unique properties

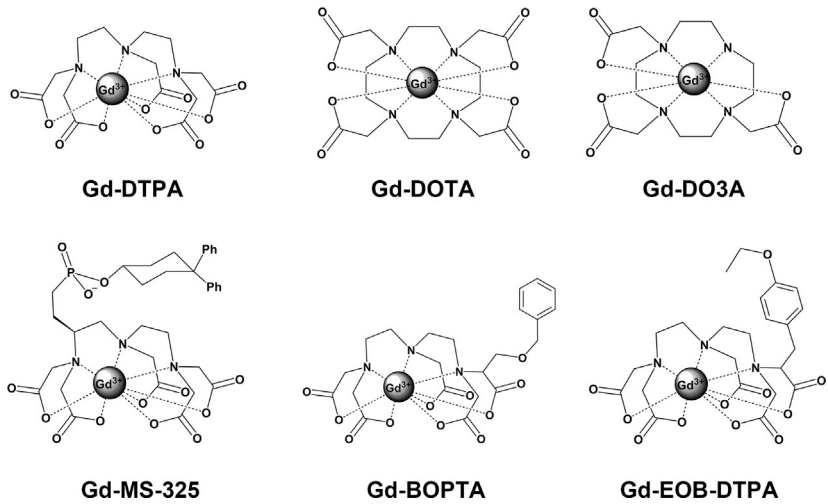

FIG. 1 Schematic representation of commercially available and clinical Gd^{3+}-based contrast agents: Gd-DTPA, Gd-DOTA, Gd-DO3A, Gd-MS-325, Gd-BOPTA, and Gd-EOB-DTPA.

of the 4f electronic configurations and the nanosize-effect, have attracted great attention and are regarded as promising candidates for MRI contrast enhancement [14–16]. The magnetic moment, magnetic susceptibility, and electronic relaxation time of Ln ions are mainly determined by their respective electronic configuration (Table 1). Typically, symmetric electronic ground state ($^8S_{7/2}$) and negligible net orbital momentum of Gd^{3+} endow it with weak spin–orbit coupling and thus long electronic relaxation time, therefore Gd^{3+} can efficiently reduce both T_1 and T_2 relaxation times thanks to its large number of unpaired electrons [5,17]. Other paramagnetic trivalent lanthanide ions (Ln^{3+}), especially Tb^{3+}, Dy^{3+}, Ho^{3+}, and Er^{3+}, have shorter electronic relaxation time (around 4–5 orders of magnitude shorter than Gd^{3+}) due to their asymmetric electronic ground states, but large magnetic moments and susceptibilities, which make them useful in shortening proton relaxation time as well [18,19]. With the development of nanoscience and nanotechnology, Ln NPs have been extensively developed, showing distinctive properties from both small molecules and bulk materials. Here we will discuss the requirements for Ln NPs to be used as MRI CAs, and the challenges for potential applications.

2 GD-BASED NPs FOR T_1-WEIGHTED MRI CONTRAST ENHANCEMENT

2.1 Contrast Enhancing Mechanism

Knowledge of the basic mechanism underlying the proton relaxation process is essential for the following discussion and will be briefly introduced (Fig. 2).

TABLE 1 Physical Parameters for Ln(III) Ions: Atomic Number, Electronic Configuration, Ground State, g Value, Experimental Room Temperature χT Value, K-Edge Energy, and X-ray Mass Attenuation Coefficient at 100 keV

Ln (III)	Atomic Number (Z)	Configuration	Ground State	g_J	χT (emu mol^{-1} K)	K-Edge Energy (keV)	X-ray Mass Attenuation Coefficient (cm^2 g^{-1})
La	57	f^0	$^1S_0$		0	38.9	2.32
Ce	58	f^1	$^2F_{5/2}$	6/7	0.66–0.78	40.4	2.44
Pr	59	f^2	$^3H_4$	4/5	1.45–1.62	42.0	2.59
Nd	60	f^3	$^4I_{9/2}$	8/11	1.45–1.53	43.6	2.69
Pm	61	f^4	$^5I_4$	3/5	1.05	45.2	2.84
Sm	62	f^5	$^6H_{5/2}$	2/7	0.32	46.8	2.90
Eu	63	f^6	$^7F_0$	0	1.53	48.5	3.04
Gd	64	f^7	$^8S_{7/2}$	2	7.61–7.8	50.2	3.11
Tb	65	f^8	$^7F_6$	3/2	11.76–12.01	52.0	3.25
Dy	66	f^9	$^6H_{15/2}$	4/3	13.01–14.05	53.8	3.36
Ho	67	f^{10}	$^5I_8$	5/4	13.26–13.78	55.6	3.49
Er	68	f^{11}	$^4I_{15/2}$	6/5	11.05–11.28	57.5	3.63
Tm	69	f^{12}	$^3H_6$	7/6	7.03	59.4	3.78
Yb	70	f^{13}	$^2F_{7/2}$	8/7	2.53	61.3	3.88
Lu	71	f^{14}	$^1S_0$		0	63.3	4.03

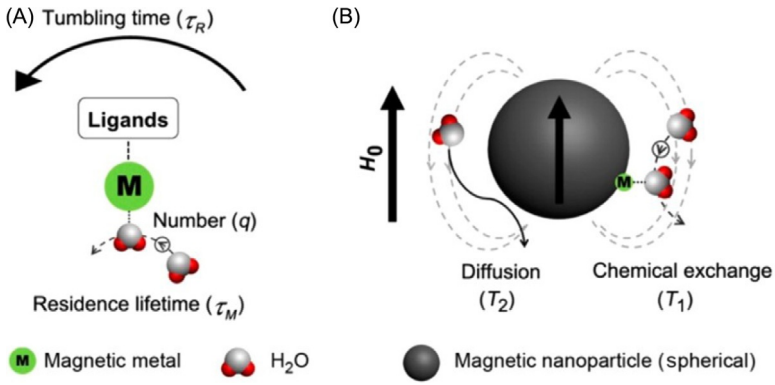

FIG. 2 Schematic illustrations of proton phenomena in magnetic systems relating to T_1 and T_2 relaxations. (A) Paramagnetic metal complex system (typically Gd-chelate) and several key parameters determining T_1 relaxation of protons: rotation correlation time (τ_R), mean residence time of bound water molecules (τ_M), and the number of directly bound water molecules per metal ion (q), while the magnetic gradient field around paramagnetic center is neglected. (B) Phenomena of proton interaction with a spherical magnetic nanoparticle system: chemical exchange with surfacial magnetic metals related to T_1 contrast enhancement and water molecular diffusion related to T_2 contrast enhancement. *Reprinted with permission from J. Zhou, Z.G. Lu, G.G. Shan, S.H. Wang, Y. Liao, Gadolinium complex and phosphorescent probe-modified $NaDyF_4$ nanorods for T_1- and T_2-weighted MRI/CT/phosphorescence multimodality imaging, Biomaterials 35 (2014), 368–377; L. Zhou, X. Zheng, Z. Gu, W. Yin, X. Zhang, L. Ruan, Y. Yang, Z. Hu, Y. Zhao, Mesoporous $NaYbF_4$@$NaGdF_4$ core-shell up-conversion nanoparticles for targeted drug delivery and multimodal imaging, Biomaterials 35 (2014), 7666–7678. Copyright 2014 American Chemical Society.*

Previous reviews can be referred to for detailed information [5,18,20]. The Solomon–Bloembergen–Morgan (SBM) equations are commonly used to describe the relaxation process. For paramagnetic agents, the contribution to longitudinal relaxivity can be divided into two parts: inner- (IS) and outer-sphere (OS) contributions. The IS contribution comes from the interaction of the metal ion with directly bound water molecules, while the OS contribution comes from the water molecules bonded to the ligands and the diffusion of nearby water molecules in the bulk. The IS contribution to relaxivity (R_1^{IS}) is governed by Eq. (1), where P_M is the molar ratio of metal ions, q is the number of directly bound water molecules per metal ion, T_{1M} is the longitudinal relaxation time of bound water proton, and τ_M is the mean residence time of bound water molecules.

$$R_1^{IS} = \frac{qP_M}{(T_{1M} + \tau_M)} \tag{1}$$

T_{1M} can be expressed by Eqs. (2) and (3), which involve a series of constants (K), the distance between the metal ion and bound water protons (r_H), the

Larmor frequencies of proton (ω_H) and electron (ω_S), the rotation correlation time (τ_R), and the longitudinal electronic relaxation time (T_{1e}).

$$\frac{1}{T_{1M}} = \frac{K_1}{r_H^6}\left[\frac{3\tau_c}{1+\omega_H^2\tau_c^2} + \frac{7\tau_c}{1+\omega_S^2\tau_c^2}\right] + K_2\left[\frac{\tau_e}{1+\omega_S^2\tau_c^2}\right] \tag{2}$$

$$\frac{1}{\tau_c} = \frac{1}{\tau_R} + \frac{1}{\tau_M} + \frac{1}{T_{1e}} \tag{3}$$

$$\frac{1}{\tau_e} = \frac{1}{\tau_M} + \frac{1}{T_{1e}} \tag{4}$$

τ_R can be estimated from several parameters, including the radius of the molecule (r), the viscosity of the solution (η), Boltzmann constant (k), and the temperature (T), according to the equation $\tau_R = 4\pi r^3\eta/3kT$ for spherical molecules. The OS contribution, however, has received less attention compared to IS contribution, and is fairly complicated to quantify. The fraction of OS contribution to relaxation enhancement varies in different situations. For complexes with a large number of bound water molecules or long rotational tumbling times (eg, macromolecular complexes), the IS contribution is quite large, while the OS contribution becomes dominant for complexes with a small number of bound water molecules, especially when $q = 0$. Taken together, the relaxivity of an MRI CA is controlled simultaneously by structural, dynamic, and electronic parameters, including molecular dimension, number of coordinated water molecules, hydrogen-bond acceptor (or donor) groups of ligands, overall electric charge, and hydrophilic (or hydrophobic) property. Furthermore, the environmental conditions, such as temperature, the pH of the aqueous solution, and the applied field strength, strongly influence the relaxivity as well.

2.2 Gd-Chelates

Although free Gd^{3+} ions in aqueous media show relatively high r_1 value, they cannot be directly used in ionic form for in vivo imaging. Due to its ionic radius similar to Ca^{2+} ion, Gd^{3+} ion has a high affinity for Ca^{2+} ion channels, and as a result, free Gd^{3+} ions may accumulate in undesirable tissues such as bones, liver, or spleen, and induce potential toxicity [21–23]. To cope with the safety concern and prevent potential accumulation, stable chelation is commonly required to provide appropriate biodistribution and safety profiles. Until now, a large number of Gd-chelates, with Gd-DTPA as a representative, have been extensively explored, and a handful of them have been approved for clinical applications. Unfortunately, chelates have several drawbacks as CAs. For instance, the strong chelating ligands greatly reduce the number of coordinated sites for water molecules in comparison to free Gd^{3+}, leading to a low relaxivity. In addition, each chelate has only one Gd^{3+} ion, resulting in a low local concentration. Also, chelates with small molecular size usually

have short blood circulation time and can be rapidly excreted through renal pathways into urine. Moreover, limited by the short molecular chain, multifunctional applications based on conventional chelating ligands are quite impractical.

To overcome these disadvantages, various strategies have been proposed to optimize the behaviors of Gd-chelates, which commonly involve the design of new chelating ligands (Fig. 1). Specifically, to maximize the r_1 value, the key parameters controlling relaxivity including q, τ_R, and τ_M are mainly focused on. For instance, by removing one acetate group from Gd-1,4,7,10-tetraazacyclododecane-1,4,7,10-tetraacetate (DOTA), an extra coordination position can be obtained (ie, an increase in q), leading to an increased r_1 value from 4.3 mM^{-1} s^{-1} (Gd-DOTA) to 6.2 mM^{-1} s^{-1} (Gd-1,4,7,10-tetraazacyclododecane-1,4,7-triacetate amide (DO3A)) [21]. However, the tailoring of q usually necessitates a change in the chelate structure and is often limited by the requirement of high thermodynamic stability. Since longer τ_R will bring higher r_1 value according to the SBM equations, one can slow down the reorientation of the chelates through increasing molecular size or binding to a larger structure. This strategy has been used, and gadofosveset trisodium (MS-325), a low-molecular-weight complex, is a typical example, which can reversely bind to human serum albumin through covalent coupling, thereby lengthening its τ_R. Beyond that, multiple Gd-chelates can be attached to a scaffold, such as polymers, dendrimers, and NPs, forming a multimeric system with both higher payload of Gd and longer τ_R than the parent molecules [24–26]. Due to its significant influence on relaxivity, the modulation of τ_R has also become an important route to design biologically responsive MRI CAs [6,10]. Furthermore, by tuning the steric hindrance and overall charge of chelates, the water exchange process (ie, τ_M) can be effectively altered, which is also an important parameter in the design of novel agents, especially for those with slow tumbling. In addition to the improvement of relaxivity, the modulation of pharmacokinetics and biodistribution can also be realized through ligand design [22]. For instance, the highly hydrophilic DTPA endows Gd-DTPA with an extracellular biodistribution and a rapid renal excretion. When more lipophilic groups are grafted on DTPA, the complex can be partially eliminated by biliary pathways, as in the case of Gd-ethoxybenzyl-diethylenetriaminepentaacetate (EOB-DTPA) (gadoxetate) and Gd-benzyloxy-diethylenetriaminepentaacetate (BOPTA) (gadobenate), while interaction with albumin will lead to lengthened blood circulation time, as in the case of MS-325.

2.3 Gd-Based NPs

By virtue of the fascinating features of NPs, incorporation of Gd^{3+} into crystalline nanostructures has emerged as a promising route to develop novel MRI CAs, either by encompassing Gd^{3+} ions into inorganic nanostructures or by using crystalline Gd-containing compounds as the host matrix. To date,

various inorganic nanostructures doped with Gd^{3+} ions have been investigated for their proton relaxation enhancing effect, including CaF_2 [27], hydroxyapatite [29], carbon nanomaterials (such as carbon nanotubes, carbon nanodots, and gadofullerene) [30–32], semiconductor nanocrystals (such as CdSe, CdTe, ZnO, ZnS, and TiO_2) [33–37], and other Ln^{3+}-based NPs [14,38]. Here we only focus on crystalline Gd-based NPs and pay particular attention to their evolution in the past decade.

Generally speaking, nanoparticulate MRI CAs can be described as core–shell structures, in which the paramagnetic centers are located in the inorganic core region and hydrophilic molecules coated as shell on the surface render the NPs water-dispersible and biocompatible. In addition, functional groups can also be anchored on the surface to realize multifunctional applications. Similar to the chelating effect, the NPs hamper dissociation of Gd^{3+} ions by keeping them into their rigid crystal structure, which greatly settles the safety concern, especially in combination with the help of surface-chelating ligands. A well-known feature of NPs is that each particle contains a large amount of Gd^{3+} ions, resulting in a high local concentration, which is of great significance for ultrasensitive detection. Moreover, the size of NPs generally ranges from several to dozens of nanometers, which is larger than low-molecular-weight chelates. As mentioned earlier, τ_R increases with molecular size, and thus NPs with longer τ_R are expected to bring improved relaxation enhancement. Furthermore, the controllable dimension, shape, composition, and surface properties of NPs afford more feasibility to tuning the image contrast, pharmacokinetics, biodistribution, and excretion profiles than conventional small chelates [39,40]. Moreover, when doped with fluorescent centers or modified by judicious surface engineering, the NPs can act as multifunctional platforms for extended applications, such as multimodal imaging, active targeting, environmental response, and drug delivery, which is beneficial for clinical diagnosis and biomedical research.

2.3.1 Composition of Inorganic Core

In contrast to SPIO NPs which emerged in 1980s, the study of physicochemical and proton relaxation enhancing properties of Gd-based NPs did not appear until 2003, when McDonald and coworkers investigated Gd_2O_3 NPs with a diameter of 20–40 nm for the first time [41]. From then on, investigations on Gd-based NPs have been rapidly expanding, including oxides, fluorides, hydroxides, oxysalts, and several other compounds.

2.3.1.1 Gadolinium Oxides

Among various compositions, Gd_2O_3 has been the subject of most investigations due to the strong affinity of Gd to oxygen and the easy synthesis in air. The polyol route is a typical method for synthesizing Gd_2O_3 NPs, where diverse polyol agents function as capping agents and solvents [42–44].

Meanwhile, additional protective agents can be used for improving the colloidal dispersity and stability. Despite easy synthesis, the polyol route usually suffers from low production yield and lengthy dialysis time, which is essential for separating the product from free Gd^{3+} ions. A polyol-free route was reported by Uvdal and coworkers, and the obtained Gd_2O_3 NPs (4–5 nm) showed an efficient proton relaxation enhancing ability with r_1 value of 6.9 mM^{-1} s^{-1} and r_2 value of 7.9 mM^{-1} s^{-1} [45]. Thermal decomposition method is also a widely used route for preparing Gd_2O_3 NPs, and high boiling point organic molecules as capping agents and solvents are usually adopted. However, to cope with the demand of subsequent bioapplications, further surface modification is necessary. For example, Colvin and coworkers prepared a class of Gd_2O_3 nanoplates with a diameter ranging from 2 to 22 nm by thermal decomposition method [46]. By efficient surface modification with either an oleic acid bilayer or an octylamine-modified polyacrylic acid (PAA) polymer layer, the nanoplates achieved a good water dispersity and large MRI contrast enhancement, with r_1 value as high as 47.2 mM^{-1} s^{-1} at 1.41 T (Fig. 3).

In contrast to the direct synthesis of Gd_2O_3 NPs, template-directed method affords more flexibility for finely controlling the morphology of the nanostructures. Zhou and coworkers first prepared size-tunable $Gd_2O(CO_3)_2 \cdot H_2O$ NPs using a hydrothermal method with glycerol as capping agent, and then obtained Gd_2O_3 NPs by calcination [47]. Hollow and porous Gd_2O_3

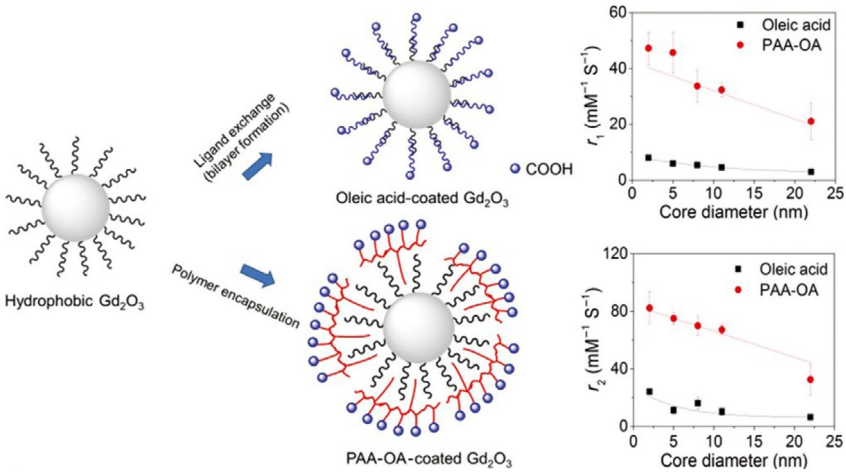

FIG. 3 (*Left*) Schematic illustration of the phase transfer method of ligand exchange for Gd_2O_3 nanoparticles using oleic acid and of polymer encapsulation using PAA–OA. (*Right*) Plots of r_1 and r_2 values vs the core diameters for two surface coatings. *Reprinted with permission from M. Cho, R. Sethi, J.S. Ananta narayanan, S.S. Lee, D.N. Benoit, N. Taheri, P. Decuzzi, V.L. Colvin, Gadolinium oxide nanoplates with high longitudinal relaxivity for magnetic resonance imaging, Nanoscale 6 (2014), 13637–13645. Copyright 2014 Royal Society of Chemistry.*

nanospheres can be obtained by using sacrificial templates, which are typically carbon-based materials. Yeh and coworkers used biological gelatin particles as templates and prepared Gd_2O_3 nanospheres with an average size below 200 nm [48]. Zhao and coworkers prepared hollow Ln^{3+}-doped Gd_2O_3 nanospheres using hydrothermal carbon spheres as templates [49]. To prepare ligand-free NPs, Li and coworkers used laser ablation in liquid (LAL) method to obtain monoclinic Gd_2O_3 NPs with a mean diameter of 7.1 nm, which showed a relatively large r_1 value of 5.53 $mM^{-1}\ s^{-1}$ [50]. As a top-down method, LAL generates nearly no waste and higher product purity compared to traditional precipitation and decomposition methods.

2.3.1.2 Gadolinium Fluorides

Fluorides are well known for their lower phonon energy, which makes them better host matrixes for luminescent centers than oxides. Thus, the gadolinium fluorides including binary fluoride (GdF_3) and complex fluorides (typically $NaGdF_4$) have attracted much attention regarding their potential multifunctional applications. Mimun and coworkers employed trifluoroacetates as precursors to synthesize Nd-doped GdF_3 NPs with a diameter of 5.5 ± 2.2 nm, and after coating with hydrophilic polymers, the obtained NPs showed efficient near-infrared (NIR) to NIR down-shifting luminescent and T_1 relaxation enhancing properties (0.1481 $mM^{-1}\ s^{-1}$ at 7 T) [51]. Similarly, Chen and coworkers synthesized Ln^{3+}-doped GdF_3 NPs and applied them in T_1-weighted MRI (1.44 $mM^{-1}s^{-1}$ at 9.4 T) and time-resolved photoluminescent biodetection [52]. Botta and coworkers used a milder coprecipitation method to synthesize small-sized GdF_3 NPs (2.2–2.3 nm), where citrate was applied to limit the particle size and then improve the water dispersity of the NPs [53]. The obtained NPs in aqueous solution were systematically investigated for their relaxation enhancing behaviors under different magnetic fields, and the surfacial Gd^{3+} ions were found to have a dominant contribution to the relaxation enhancement. Prosser and coworkers used a similar coprecipitation method and synthesized GdF_3 NPs and GdF_3/LaF_3-mixed NPs coated with citrate and 2-aminoethyl phosphate, respectively [54]. The mass relaxivities of citrate-coated GdF_3 NPs were measured, showing a r_1 value of $7.4 \pm 0.2\ s^{-1}\ (mg/mL)^{-1}$ at 1.5 T and $8.8 \pm 0.2\ s^{-1}\ (mg/mL)^{-1}$ at 3 T.

Controllable synthesis of ultrasmall hexagonal-phase $NaGdF_4$ NPs with tunable size below 10 nm were reported by van Veggel and coworkers, and their size-dependent relaxation enhancing performance was investigated after a ligand-exchange process [55]. Shi and coworkers synthesized ultrasmall $NaGdF_4$ nanodots modified with polyethylene glycol (PEG) [56]. To further reduce the possibility of leakage of Gd^{3+} ions, they anchored DTPA on the surface to capture the released Gd^{3+} ions. The as-prepared nanodots exhibited a high r_1 value of 8.93 $mM^{-1}\ s^{-1}$ at 3 T, and were successfully applied in MR angiography and atherosclerotic plaque imaging (Fig. 4). Due to the extremely small size, the nanodots can be excreted through urine, greatly reducing the

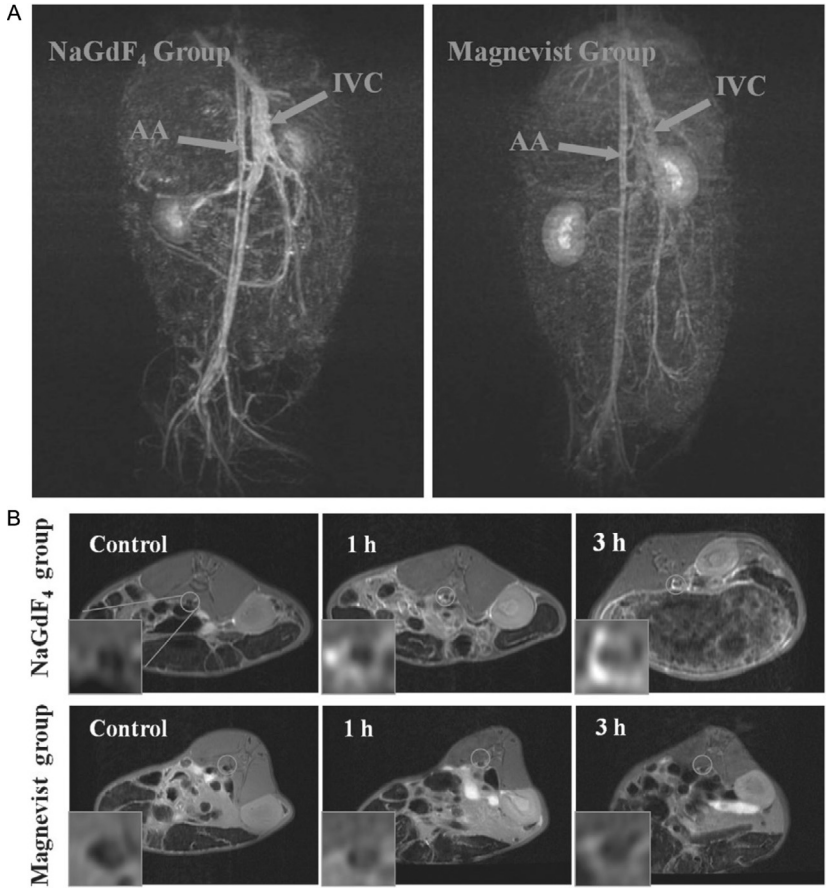

FIG. 4 (A) MR angiography of rabbits within 3 min after injection with $NaGdF_4$ nanodots or Magnevist® at the same dosage (13 mg Gd/kg): abdominal aorta (AA) and inferior vena cava (IVC). (B) Transversal cross-sectional MR images of rabbits' atherosclerotic plaques after injection with $NaGdF_4$ nanodots or Magnevist® for varied time periods at the same dosage (13 mg Gd/kg). *Reprinted with permission from H. Xing, S. Zhang, W. Bu, X. Zheng, L. Wang, Q. Xiao, D. Ni, J. Zhang, L. Zhou, W. Peng, K. Zhao, Y. Hua, J. Shi, Ultrasmall $NaGdF_4$ nanodots for efficient MR angiography and atherosclerotic plaque imaging, Adv. Mater. 26 (2014), 3867–3872. Copyright 2014 Wiley-VCH Verlag GmbH & Co. KGaA.*

accumulation in body. Also, by doping luminescent Ln^{3+} ions into the matrix, gadolinium fluoride NPs can also be used for optical imaging. Chen and coworkers synthesized polyethylenimine-coated Ln^{3+}-doped $KGdF_4$ NPs with solvothermal method and demonstrated that these NPs can be used as MRI CAs ($r_1 = 5.86\ mM^{-1}\ s^{-1}$ at 9.4 T) as well as sensitive time-resolved FRET bioprobes [57].

2.3.1.3 Gadolinium Oxysalts

Suzuki and coworkers reported the synthesis of dextran-coated rod-like $GdPO_4$ NPs with the size of their major and minor axes amounting to 20–30 and 6–15 nm, respectively [58]. The $GdPO_4$ nanorods showed relatively high r_1 (13.9 mM^{-1} s^{-1}) and r_2 values (15.0 mM^{-1} s^{-1}) at 0.47 T and achieved effective MRI on tumors in rabbit with only 1/10 of the clinically dosage for Gd-DPTA [59]. Zhao and coworkers synthesized $GdPO_4$ nanorods as well with a length of up to ~100 nm and a diameter of ~10 nm, with a r_1 value of 2.08 mM^{-1} s^{-1} at 4.7 T [60].

Ln^{3+}-doped $GdVO_4$ nanosheets with a thickness of ~5 nm and a width of ~150 nm were synthesized by Li and coworkers via solvothermal reaction [61]. The nanosheets exhibited strong fluorescence and a high r_1 value of 37.8 $mM^{-1}s^{-1}$ at 0.5 T after replacing the surface oleates by hydrophilic PAA. Lin and coworkers fabricated hollow and porous $GdVO_4$:Dy nanospheres using $Gd(OH)CO_3$:Dy as sacrificial template, which combined fluorescence, T_1 relaxation enhancement (0.3716 $mM^{-1}s^{-1}$ at 0.5 T), and drug delivery capability [62]. Eu-doped $GdVO_4$ NPs synthesized by Alexandrou and coworkers were used as luminescent probes, T_1 CAs, and oxidant sensors [63].

$Gd(IO_3)_3 \cdot 2H_2O$ NPs were synthesized with a one-pot precipitation method by Lee and coworkers, which exhibited relatively high r_1 (52.3 $mM^{-1}s^{-1}$) and r_2 (63.4 $mM^{-1}s^{-1}$) values at 1.5 T, and good X-ray attenuation properties due to the presence of gadolinium and iodine elements [64]. The remarkable relaxivities of $Gd(IO_3)_3 \cdot 2H_2O$ were likely related to hydrated water molecules, since the water molecules directly bound to Gd^{3+} ions in the crystal lattice may interact intensely with the Gd^{3+} ion. In contrast, for other anhydrous Gd-based NPs the distance between water molecules and Gd^{3+} ions may be larger, leading to a less-efficient interaction.

Li and coworkers used the reverse microemulsion method to synthesize $Gd_2(CO_3)_3$:Tb NPs with a quasi-spherical structure and a narrow size distribution [65]. After coating the NPs with a thin silica layer, the r_1 value was measured to be 1.625 $mM^{-1}s^{-1}$ at 0.5 T. PAA-coated $Gd(OH)CO_3 \cdot 2H_2O$ NPs with a size of 2.3 ± 0.1 nm were reported by Kong and coworkers, showing a r_1 value of 34.8 $mM^{-1}s^{-1}$ and a r_2/r_1 ratio of 1.17 [66]. A hybrid nanomaterial, $Gd_2O(CO_3)_2 \cdot H_2O$/silica/Au, was fabricated by Yeh and coworkers, which can be used for T_1-weighted MRI and photothermal therapy [67]. A similar composition, $Gd_2O(CO_3)_2 \cdot H_2O$, was reported by Zhao and coworkers, which showed size-dependent MRI contrast enhancing property with diameters ranging from 10 to 280 nm [68].

2.3.1.4 Other Gadolinium Compounds

Eu^{3+}-doped GdS NPs (8 nm) were synthesized with a sonochemistry method by Park and coworkers [69]. The obtained NPs combined photoluminescence and MRI contrast enhancing properties with high relaxivities at 4.7 T

(13.48 and 24.53 $mM^{-1}s^{-1}$ for r_1 and r_2, respectively). Gossuin and coworkers studied the NMR relaxometric properties of rod-like $Gd(OH)_3$ NPs with a length of 150 nm, and the relaxivities were determined to be 4.03 and 8.0 $mM^{-1}s^{-1}$ for r_1 and r_2, respectively [70]. Yuan and coworkers synthesized $Gd(OH)_3$ nanorods with an average length and diameter of 100 and 15 nm, respectively, which showed a r_1 value of 12.3 $mM^{-1}s^{-1}$ at 1.5 T [71].

A class of anionic clays consisting of positively charged hydroxide layers of Gd^{3+} ions, with a general composition of $Gd_2(OH)_5X \cdot nH_2O$ (X = anions), have been investigated for their MRI contrast enhancing properties. For instance, Ghanotakis and coworkers synthesized $Gd_2(OH)_5NO_3$ nanosheets by the aqueous coprecipitation method, which showed a r_1 value of 0.24 ± 0.03 $mM^{-1}s^{-1}$ at 1.5 T [72]. Byeon and coworkers synthesized ultrathin $[Gd_2(OH)_5(H_2O)_x]Cl$ nanosheets with lateral sizes of 120 ± 30 nm, and the relaxivities were 2.20 $mM^{-1}s^{-1}$ for r_1 and 6.92 $mM^{-1}s^{-1}$ for r_2 [73].

2.3.1.5 Discussion on Composition

Although various compositions have been investigated, few studies referred to the composition effect on proton relaxation, ie, comparison of different compositions. Which type of composition or crystal structure is most suitable for enhancing proton relaxation still remains an unanswered question. Longitudinal electronic relaxation time (T_{1e}) is one of the key parameters determining relaxivity. The selection of Gd^{3+} ion instead of other Ln^{3+} ions for T_1 relaxation mainly stems from its long T_{1e} value, since longer T_{1e} commonly yields higher r_1 value. Despite the lack of comprehensive theory for the electronic spin relaxation of metal ions in solution, a general relationship has been proposed which states that an increase in transient zero-field splitting will lead to shorter T_{1e} value and reduced relaxivity [5]. For chelates, the microenvironment of Gd^{3+} ion strongly correlates with the chelating ligand, which then may affect T_{1e}. Structurally, Gd-based NPs can be regarded as analogues of chelates, since each Gd^{3+} ion in the crystal lattice is surrounded by several anions. As a result, the T_{1e} of Gd^{3+} ions in crystalline structures is very likely to be influenced by the crystal symmetry, coordination number, adjacent atom species, and distance between Gd^{3+} ions and anions. Besides T_{1e} of Gd^{3+} ions, the surface configuration of NPs, the surface density of Gd^{3+} ions and the possible dangling bonds, are dependent on the crystal structure as well. Consequently, the distance between Gd^{3+} ions and water molecules (ie, r_H) and the residence of water molecules on the NP surface (ie, τ_M) will also be influenced. The selection of suitable composition is a prerequisite when designing novel high-performance MRI CAs. Before that, a comprehensive understanding of composition effect on relaxation is necessary. This field has been overlooked for a long time, and is worthy of more attention. Beyond the relaxation property, other relevant factors including the thermodynamic stability and complexity of synthesis, should be taken into account as well for the composition of Gd-based particles.

2.3.2 Size of the Inorganic Core

A prominent feature of Gd-based NPs is that the Gd^{3+} ions share different coordination environments, while in chelates the chemical environments of Gd^{3+} ions are identical. Within a NP, only part of the Gd^{3+} ions are exposed on the surface, while the remaining ones are encompassed inside. Obviously, the inner Gd^{3+} ions have no direct contact with water molecules, and only dipolar interaction (depending on distance) makes a contribution to relaxation enhancement [5]. However, because of the relatively large distance to water molecules, the contribution of inner Gd^{3+} ions is usually insignificant according to Eqs. (2)–(4). To differentiate the contributions of surface and inner Gd^{3+} ions for enhancing proton relaxation, a comparative study was reported by Shi and coworkers using a rare earth fluoride core–shell structure as a model [28]. As shown in Fig. 5, a nearly 100% loss of r_1 value was observed after burying Gd^{3+} ions deeply (>4 nm) by a Gd-free layer, while a new Gd-containing layer leads to the recovery of r_1. This phenomenon implied that the surfacial Gd^{3+} ions have a dominant contribution to relaxation enhancing while the innermost Gd^{3+} ions contribute far less.

Given the important role of surfacial Gd^{3+} ions on relaxation, an effective strategy to improve the relaxivity is to increase the surface-to-volume ratio (S/V) of Gd-based NPs. For isotropic (0D) particles, the S/V ratio is directly determined by their size, and the smaller the particle size, the higher the S/V ratio. The dependence of r_1 upon size has been well investigated. As reported by van Veggel and coworkers, the r_1 value of $NaGdF_4$ NPs per Gd^{3+} ion was found to increase from 3.0 to 7.2 $mM^{-1}s^{-1}$ with the particle size decreasing from 8.0 to 2.5 nm (Fig. 6), indicating that surfacial Gd^{3+} ions are the major contributors to the relaxivity enhancement [55]. Further discussion involving concentration, mass concentration of NPs, and r_1 value per unit surface area revealed that the surfacial Gd^{3+} ions of larger NPs affect the relaxivity more strongly than those of smaller NPs, probably due to the increased τ_R as the size increases. Similarly, Talham and coworkers found the r_1 value of $Eu_{0.2}Gd_{0.8}PO_4 \cdot H_2O$ NPs increasing with the particle size [74]. However, the r_1 value of Gd-based NPs sometimes shows a nonmonotonic behavior with respect to the particle size, and an optimal particle size may exist, as evidenced by Rahman and coworkers [75]. These authors synthesized Gd_2O_3 NPs with size ranging from 1.5 to 194.0 nm, among which the 2.3-nm-sized NPs showed the highest r_1 value. Lee and coworkers proposed that the surfacial Gd^{3+} ions of Gd_2O_3 NPs can cooperatively interact with the water protons, and for NPs smaller than 1 nm, the cooperation effect will no longer occur [76]. Combining the cooperation of surfacial Gd^{3+} ions and S/V ratio, the optimal range for r_1 is suggested to be 1–2.5 nm. The optimal size may vary for different systems. For $NaGdF_4$ NPs synthesized by Gao and coworkers, the 15 nm NPs (5.7 $mM^{-1}\ s^{-1}$) showed lower r_1 value than 5 nm- (6.2 $mM^{-1}\ s^{-1}$) and 20 nm- (8.78 $mM^{-1}\ s^{-1}$) NPs (Fig. 7) [77]. A qualitative explanation for this size-related effect was proposed in that with the size decreasing, the S/V ratio

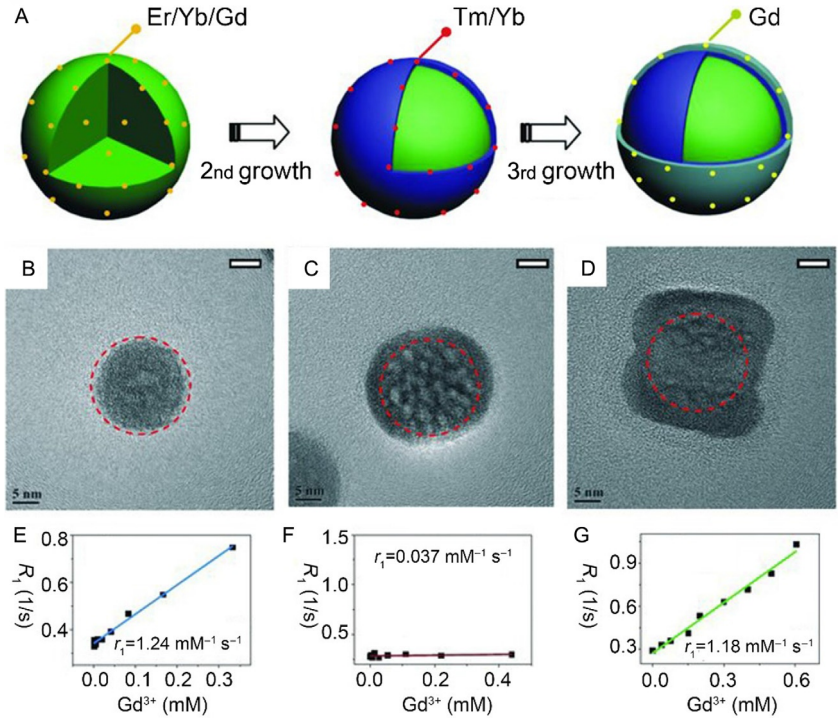

FIG. 5 Schematic illustration (A) and corresponding TEM images (B)-(D) of multishell growth of lanthanide nanoparticles. $NaYF_4$:Yb, Er, Gd was coated with $NaYF_4$:Yb, Tm as the first shell, and $NaGdF_4$ as the second shell. All nanoparticles were transferred into water by a silica shell with nearly the same thickness of ca. 10 nm, demonstrating the negative lattice shielding effect (E)-(G). *Reproduced with permission from F. Chen, W. Bu, S. Zhang, X. Liu, J. Liu, H. Xing, Q. Xiao, L. Zhou, W. Peng, L. Wang, J. Shi, Positive and negative lattice shielding effects co-existing in Gd(III) ion doped bifunctional upconversion nanoprobes, Adv. Funct. Mater. 21 (2011), 4285–4294; F. Chen, P. Huang, Y.J. Zhu, J. Wu, C.L. Zhang, D.X. Cui, The photoluminescence, drug delivery and imaging properties of multifunctional Eu^{3+}/Gd^{3+} dual-doped hydroxyapatite nanorods, Biomaterials 32 (2011), 9031–9039. Copyright 2011 Wiley-VCH Verlag GmbH & Co. KGaA.*

increases while the τ_R decreases. In summary, the particle size dependence of r_1 value involves more than one parameter influencing relaxation, including S/V ratio and τ_R, and further systematic investigation is necessary for deeper understanding.

2.3.3 Shape of Inorganic Core

The shape of NP is also a crucial factor determining the performance of MRI CAs. Generally, the NPs can be divided into 0D (such as nanospheres, nanocubes, and nanopolyhedrons), one-dimensional (1D) (such as nanowires and nanorods), and two-dimensional (2D) structures (nanoplates and nanosheets).

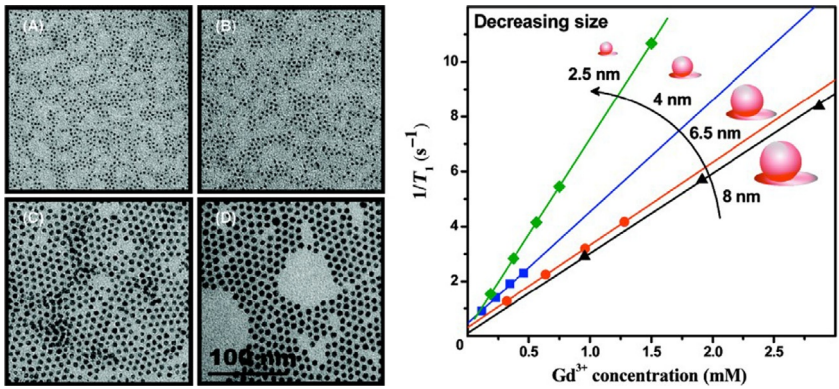

FIG. 6 (*Left*) TEM images of oleate-stabilized $NaGdF_4$ nanoparticles with sizes of (A) 2.5, (B) 4.0, (C) 6.5, and (D) 8.0 nm. (*Right*) T_1 ionic relaxivity plot for $NaGdF_4$ nanoparticles of different sizes after transfer into water (at 1.5 T). *Reprinted with permission from N.J.J. Johnson, W. Oakden, G.J. Stanisz, R.S. Prosser, F.C.J.M. van Veggel, Size-tunable, ultrasmall $NaGdF_4$ nanoparticles: insights into their T_1 MRI contrast enhancement, Chem. Mater. 23 (2011), 3714–3722. Copyright 2011 American Chemical Society.*

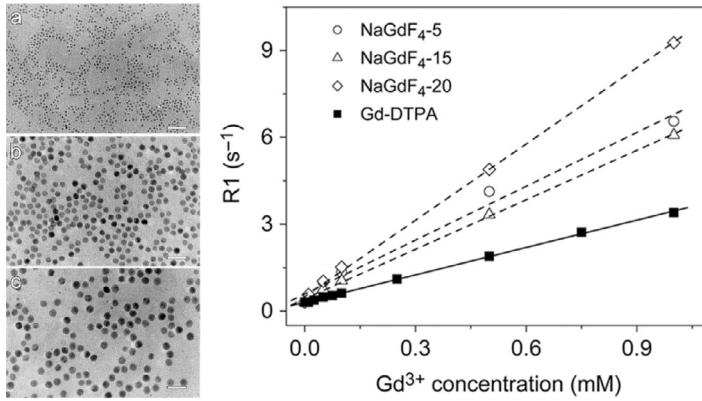

FIG. 7 (*Left*) TEM images of oleate-stabilized $NaGdF_4$ NPs with sizes of (A) 5.4, (B) 15.1, and (C) 19.8 nm. (*Right*) T_1 ionic relaxivity plot for Gd-DTPA and $NaGdF_4$ NPs of different sizes after transfer into water (at 3 T). *Reprinted with permission from Y. Hou, R. Qiao, F. Fang, X. Wang, C. Dong, K. Liu, C. Liu, Z. Liu, H. Lei, F. Wang, M. Gao, $NaGdF_4$ nanoparticle-based molecular probes for magnetic resonance imaging of intraperitoneal tumor xenografts in vivo, ACS Nano 7 (2012), 330–338. Copyright 2012 American Chemical Society.*

The 1D and 2D structures can be considered as the product of elongating 0D nanostructures in one or two dimensions, which can originate from an anisotropic crystal structure and selective adsorption of surface capping agents on exposed crystal facets. As an example, during the synthesis of GdF_3 nanowires reported by Jin and coworkers, small-sized quasi-spherical

GdF_3 nanocrystals were formed at the beginning [78], and the capping ligands selectively anchored onto the surface, facilitating the oriented attachment along the specific crystal planes with no (or less) capping agents. After transfer into water, the obtained GdF_3 nanowires showed a high r_1 value of 15.0 $mM^{-1}s^{-1}$ at 7 T, which was attributed to the large length in one dimension.

The Gd-based 0D nanostructures are most commonly reported as MRI CAs, while anisotropic 1D and 2D nanostructures are relatively rare. The 1D rod-like nanostructure has been observed in some gadolinium compounds, including GdF_3 nanowires [78], $GdPO_4$ nanorods [58,60], $Gd(OH)_3$ nanorods [70], Gd_2O_3 nanorods [79], and rod-like $NaDyF_4/NaGdF_4$ core–shell structure [80], while the 2D nanostructures of Gd_2O_3 and $GdVO_4$ have been reported [46,61]. The superiority of anisotropic nanostructures compared to 0D ones for relaxation enhancement is that through rational design simultaneous improvement of S/V and τ_R can be achieved. As discussed earlier for 0D NPs, the τ_R value is lengthened with increasing particle size, counteracting the reduced S/V ratio. By contrast, the variation trend of S/V and τ_R for anisotropic nanostructures can be consistent. Through finely tuning the shape of NPs, relaxivity can be improved to a large extent.

2.3.4 Surface Coating Layer

To cope with the demand of bioapplications, it is essential for the NPs to be water-dispersible and biocompatible. Diverse strategies for surface modification and various capping agents have been exploited [81,82]. Similar to the size and shape of the inorganic core, the surface capping agents also strongly affect proton relaxation. On one hand, the OS contribution directly comes from the interaction between ligands and water molecules, such as hydrogen bonding. On the other hand, several key parameters determining relaxation will be influenced by the surface coating. For instance, the hydrodynamic radius of NPs will change with different surface coating, and thus the τ_R value varies with different surfacial ligands. The residence time of bound water molecules (ie, τ_M) and the distance between surfacial Gd^{3+} ions and water molecules (ie, r_H) are also believed to correlate with the surface coating.

A handful of studies have evidenced the important role of surfacial ligands on relaxation. Ultrasmall Gd_2O_3 NPs synthesized by Ding and coworkers were modified by either ligand exchange with polyvinylpyrrolidone or bilayer coating with hexadecyl trimethylammonium bromide [83]. The latter showed much higher r_1 value (12.1 $mM^{-1}s^{-1}$) than the former (0.54 $mM^{-1}s^{-1}$), which was attributed to the prevention of water molecules from contacting the surfacial Gd^{3+} ions due to the long hydrophobic chains. Lee and coworkers investigated the ligand-size-dependent relaxivities of Gd_2O_3 NPs, and they found that both r_1 and r_2 values decrease with ligand size increasing from D-glucuronic acid to PEG diacid-250 to PEG diacid-600 (Fig. 8) [84]. The proposed possible reason was that shorter ligands allow easier access of water

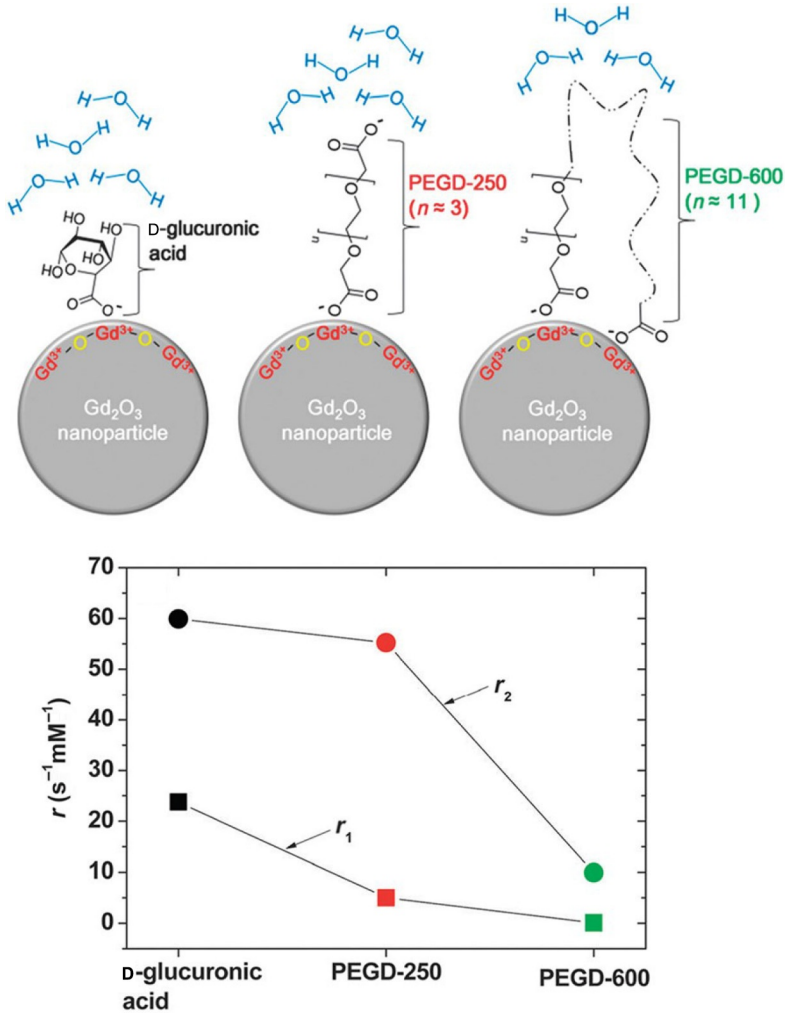

FIG. 8 (*Upper*) Schematic illustrations of ultrasmall Gd_2O_3 NPs with surface coating structures (D-glucuronic acid, PEGD-250, and PEGD-600). (*Lower*) Plots of r_1 and r_2 values depending on the ligand species (at 1.5 T). *Reprinted with permission from C.R. Kim, J.S. Baeck, Y. Chang, J.E. Bae, K.S. Chae, G.H. Lee, Ligand-size dependent water proton relaxivities in ultrasmall gadolinium oxide nanoparticles and in vivo T_1 MR images in a 1.5 T MR field, Phys. Chem. Chem. Phys. 16 (2014), 19866–19873. Copyright 2014 Royal Society of Chemistry.*

molecules to the surfacial Gd^{3+} ions while longer ligands may hinder the free accessibility of water. Ligand-free Gd_2O_3 NPs were studied by Li and coworkers, which exhibited a r_1 value of 5.53 $mM^{-1}s^{-1}$ [50]. They attributed the increased r_1 compared to ligand-coated NPs to the fairly close distance between surface Gd^{3+} ions and water protons.

3 LN NPs FOR T_2-WEIGHTED MRI CONTRAST ENHANCEMENT

3.1 Gd-Based NPs

Most Gd-based NPs show low r_2/r_1 values and T_1 relaxation enhancement is dominant. However, due to the relatively high magnetic moment of the metal ion, Gd-based NPs sometimes may exhibit more prominent T_2 relaxation enhancement. For instance, mesoporous Eu-doped GdF_3 NPs with a size of ~85 nm showed a high r_2/r_1 value of ~5 at 1.5 T (1.22 and 6.08 $mM^{-1}s^{-1}$ for r_1 and r_2, respectively) [85]. Also, D-glucuronic acid-coated ultrasmall Gd_2O_3 NPs showed a r_2/r_1 value of 6.4 at 1.5 T (4.25 and 27.11 $mM^{-1}s^{-1}$ for r_1 and r_2, respectively) [86]. Moreover, Gd-doped upconversion nanophosphors synthesized by Prasad and coworkers showed a high r_2/r_1 value of ~62 at 9.4 T [87]. The Gd_2O_3 tripodal nanoplates reported by Murray and coworkers showed r_2/r_1 values of 99.3 and 217 at 9.4 and 14.1 T, respectively [88]. Higher r_2/r_1 values were reported by Speghini and coworkers, which were ~452 and ~790 for Yb^{3+}/Er^{3+} and Yb^{3+}/Tm^{3+} codoped GdF_3 NPs, respectively [89]. Despite the above cases which demonstrated the potential of Gd-based NPs for T_2 relaxation enhancement, Gd^{3+} ion was primarily investigated for T_1 relaxation enhancement because its magnetic moment is still lower that other trivalent Ln^{3+} ions.

3.2 Other Ln^{3+}-Based NPs

All Ln^{3+} ions have unpaired electrons, exhibiting paramagnetic properties, except La^{3+} and Lu^{3+} which have empty and full 4f shell. On one hand, the anisotropic 4f electron ground state of Ln^{3+} ions (other than Gd^{3+}) give rise to a short electronic relaxation time (T_{1e}) on the order of 10^{-13} s, leading to a minor contribution to T_1 relaxation, according to the SBM theory [18]. On the other hand, these paramagnetic Ln^{3+} ions, especially Tb^{3+} (9.72 μB), Dy^{3+} (10.63 μB), Ho^{3+} (10.60 μB), and Er^{3+} (9.59 μB), own large magnetic moments and thus are most efficient T_2 MRI CAs. The r_2 relaxation enhancement of paramagnetic agents primarily come from the dephasing of magnetic moments of protons under an inhomogeneous field created by these agents, which can be interpreted by OS interaction. Generally, this process is mainly related to the diffusion of water molecules and the difference in Larmor frequency ($\triangle\omega$) between water protons located at the particle surface and those at infinity [90,91]. The diffusion correlation time (τ_D) can be described as $\tau_D = r^2/D$, where r is the radius of the NP and D is the diffusion constant. The static correlation time ($1/\triangle\omega$) is dependent on the magnetic properties of the particle, and also related indirectly to particle size, since particle size determines the total magnetic moment. The r_2 value of paramagnetic particles has several formulations involving τ_D and $\triangle\omega$ with respect to different regimes. For small size particles, the r_2 value is proportional to τ_D and the square of $\triangle\omega$, while for larger ones, the r_2 value may be solely dependent on $\triangle\omega$ [19].

The relationship between r_2 value and particle size for paramagnetic agents has been reported. The r_2 values of dextran-coated Dy_2O_3 NPs with different sizes were investigated by Peters and coworkers, and the optimal r_2 value appeared to vary between 70 nm at 7 T ($r_2 \approx 190\ mM^{-1}\ s^{-1}$) and 600 nm at 17.6 T ($r_2 \approx 675\ mM^{-1}\ s^{-1}$) [91]. van Veggel and coworkers systematically investigated the size dependence of r_2 value of $NaDyF_4$ NPs with the size ranging from 5 to 20 nm (Fig. 9A and B) [92]. With the size

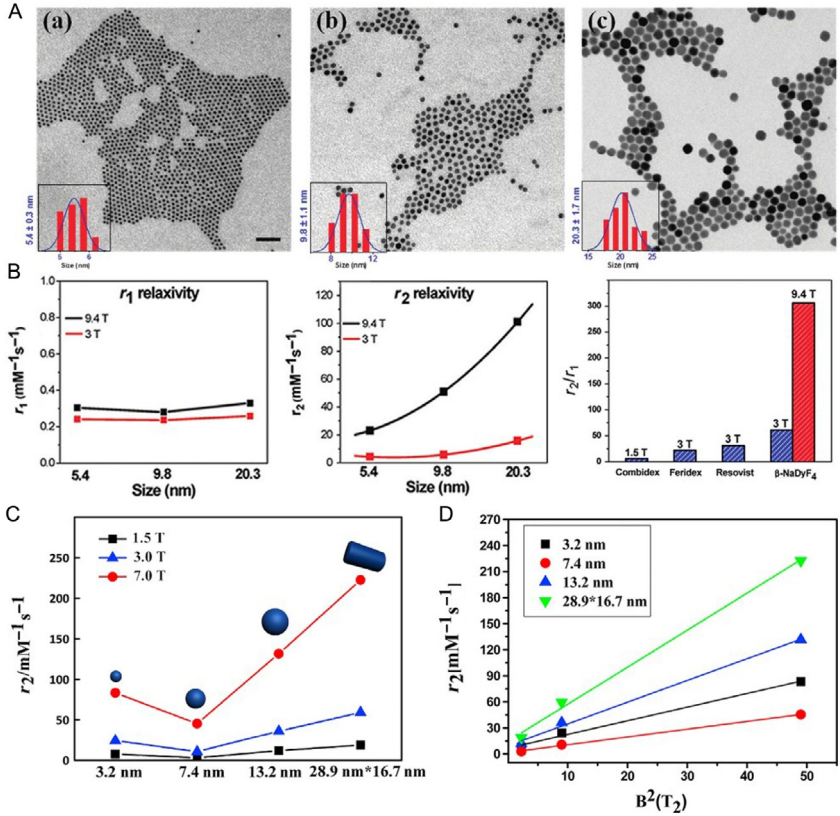

FIG. 9 (A) TEM images of oleate-stabilized $NaDyF_4$ nanoparticles with sizes of (a) 5.4 ± 0.3, (b) 9.8 ± 1.1, and (c) 20.3 ± 1.7 nm. (B) Plots of r_1 and r_2 values of $NaDyF_4$ nanoparticles after transfer into water depending on the size and magnetic field, and comparison of r_2/r_1 values between the commercial T_2 CAs and the 20.3 nm $NaDyF_4$ nanoparticles. (C and D) Plots of r_2 values of $NaHoF_4$ nanoparticles depending on the size and magnetic field. *Panels (A and B): Reprinted with permission from G.K. Das, N.J.J. Johnson, J. Cramen, B. Blasiak, P. Latta, B. Tomanek, F.C.J.M. van Veggel, $NaDyF_4$ nanoparticles as T_2 contrast agents for ultrahigh field magnetic resonance imaging, J. Phys. Chem. Lett. 3 (2012), 524–529. Copyright 2012 American Chemical Society. Panels (C and D): Reprinted with permission from D. Ni, J. Zhang, W. Bu, C. Zhang, Z. Yao, H. Xing, J. Wang, F. Duan, Y. Liu, W. Fan, X. Feng, J. Shi, PEGylated $NaHoF_4$ nanoparticles as contrast agents for both X-ray computed tomography and ultra-high field magnetic resonance imaging, Biomaterials 76 (2016), 218–225. Copyright 2016 Elsevier B.V.*

increasing, the r_2 value increased from 32 mM^{-1} s^{-1} for 5.4 nm to 101 mM^{-1} s^{-1} for 20.3 nm at 9.4 T. Shi and coworkers studied the relaxation mechanisms of $NaHoF_4$ NPs with different sizes both experimentally and theoretically [90]. They found a nonmonotonic correlation between particle size and r_2 value, that is the r_2 value increases remarkably as the size increases from 7.4 to 289.9 nm, the smallest NPs (3 nm) being an exception (Fig. 9C and D). This phenomenon can be interpreted by separating dipolar and Curie contributions. Curie contribution was proposed to be dominant when the particle size is smaller than 7 nm, and the dipolar contribution should be taken into account as well when the size increases to 13 nm and above.

The most attractive feature of paramagnetic Ln^{3+}-based NPs is their field strength-dependent r_2 values, which also distinguishes them from another large class of T_2 MRI CAs, iron-oxide NPs. The present trend of MRI development is toward ultrahigh magnetic field strength (>3 T), owing to the improved signal-to-noise ratio and spatial and temporal resolution [93–95]. However, both Gd- and iron oxide-based agents show reduced efficacies under ultrahigh field. For Gd-based chelates, the optimal field strength is below 1 T, and the r_1 value is significantly reduced at 3 T [94,96]. Also, the magnetization of iron-oxide NPs will be saturated at around 1.5 T, and thus no improvement of r_2 value is expected with the increase of field strength [97,98]. In contrast, paramagnetic Ln^{3+} ions are far from magnetization saturation in practical examinations. For instance, Dy_2O_3 NPs did not reach magnetization saturation even at extremely high field (up to 30 T) [91]. As a result, with the field strength increasing, the magnetization of Ln^{3+}-based NPs as well as the r_2 value would continuously increase. Peters and coworkers found that the r_2 value of Ln (Nd, Dy, Er, and Yb) oxide NPs is proportional to the field strength and the square of effective magnetic moment [99]. Similarly, Gossuin and coworkers observed a quadratic increase for paramagnetic Ln^{3+}-based NPs, including Dy_2O_3, Tb_4O_7, $Er_4O(OH)_9NO_3$, and $Ho_4O(OH)_9NO_3$ [100]. Although T_2 relaxation enhancing properties of paramagnetic Ln^{3+}-based agents may be not comparable with those of iron-oxide NPs under low magnetic field, they hold great potential for ultrahigh field MRI.

4 LN NPs FOR MULTIMODE IMAGING

Every imaging modality inevitably has its own limitations. The concept of dual-mode or multimode imaging has therefore been proposed to overcome the shortcomings of single imaging modality [101–103]. A typical example is presented in Fig. 10. Development of multimode imaging is of great significance but is highly challenging. On the technical level, the challenge mainly arises from simultaneous (or consecutive) acquisition of individual imaging components and then from appropriate data registration and fusion in a single image file [104]. Up to now, a handful of preclinical machines have been established to cope with the demand of combining different imaging modalities, such as MRI/CT, MRI/positron emission tomography (PET), or even

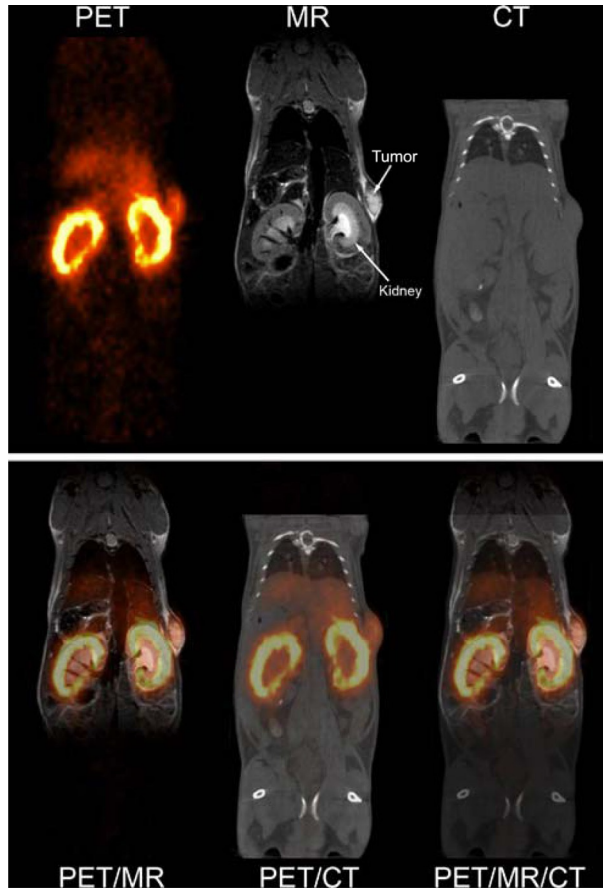

FIG. 10 Single-modality PET, MR, and CT images (*upper row*) and fused images (*lower row*) of a mouse injected with a ^{64}Cu labeled monoclonal antibody. The fused images combined their respective advantages: PET image clearly depicts the high antibody clearance through the kidneys and a low tracer uptake in the tumor, while MR and CT images provide high-resolution morphological information. Notably, MR image shows higher soft tissue contrast than CT image. *Reprinted with permission from H.F. Wehrl, M.S. Judenhofer, S. Wiehr, B.J. Pichler, Pre-clinical PET/MR: technological advances and new perspectives in biomedical research, Eur. J. Nucl. Med. Mol. Imaging 36 (2009) 56–68. Copyright 2009 Springer Science + Business Media.*

PET/MRI/CT. On the material level, attention is paid to the development of novel imaging probes integrating diverse functions. One common strategy of constructing multimode imaging probe is through the coupling of different functional building blocks forming nanohybrids. However, the complicated procedure and possible detachment/dissociation may become the main limitations. In fact, due to the unique intrinsic properties of Ln elements, it is easier to incorporate various functions into a single Ln NP.

4.1 T_1 and T_2 Dual-Mode MRI

The combination of T_1- and T_2-weighted MRI can effectively eliminate artifacts and differentiate the T_2-weighted MR signal induced by agents from the background, greatly improving diagnostic accuracy [105,106]. All of the MRI CAs will intrinsically show T_1 and T_2 relaxation enhancement, however to a different extent. As we discussed earlier, Gd^{3+}-based and other Ln^{3+}-based NPs commonly show prominent T_1 and T_2 relaxation enhancement, respectively. The design of novel CAs with both large T_1 and T_2 relaxation enhancement is challenging. A promising strategy for fabricating T_1 and T_2 dual-mode MRI CAs relies on associating two traditional T_1 and T_2 CAs, such as modifying T_1 material (eg, Gd-chelates) on the surface of T_2 material (eg, iron oxide or $NaDyF_4$ NPs) [106–108]. For instance, Lee and coworkers synthesized MnO-coated Gd_2O_3 NPs with the r_1 and r_2 value of 12.8 and 26.6 $mM^{-1}\ s^{-1}$ at 3 T, respectively [109]. Tan and coworkers synthesized $NaDyF_4$:Yb@$NaGdF_4$:Yb,Er NPs which can offer excellent dark T_2-weighted contrast as well as tunable bright and dark T_1-weighted contrast [80]. Similarly, Anker and coworkers reported Fe_3O_4@$NaGdF_4$ NPs [110]. With respect to the undesired quenching of T_1 effect due to the direct contact between T_1 and T_2 materials, a "magnetically decoupled" core–shell structure was designed by Cheon and coworkers, which comprised $Gd_2O(CO_3)_2$ as T_1 material, $MnFe_2O_4$ as T_2 material, and SiO_2 as the separating layer [105]. By controlling the thickness of the separating layer, the T_1 and T_2 effect can be well tuned. This design can be extended to other similar compositions and applied to perform the "AND logic gate" algorithm (Fig. 11) [111]. Gao and coworkers suggested the effect of induced magnetic field on T_1 material depends on their spatial location [112]. They synthesized Gd-embedded iron-oxide NPs and investigated the synergistic enhancement of T_1 and T_2 relaxation. On one hand, the embedded T_1 material was actually exposed to an increased field, leading to an enhanced T_1 effect. On the other hand, the magnetic moment of Gd^{3+} induced a local magnetic field, and thus enhanced the T_2 relaxation. This design route was further verified by Ye and coworkers [113]. More recently, Gao and coworkers engineered the relaxometric properties of core–shell structured $NaDyF_4$@$NaREF_4$@$NaGdF_4$:Yb,Er (RE = Gd^{3+}, Er^{3+}, or Y^{3+}) NPs by tailoring the chemical spacer layer [114]. They found the r_1 value of NPs varying from 0.50 to 1.82 $mM^{-1}\ s^{-1}$ from Gd^{3+} to Er^{3+} to Y^{3+}, and attributed this tendency to the decrease of electron cloud distortion ability of RE^{3+} which strongly mediates the interaction between electron clouds of Dy^{3+} in the core and Gd^{3+} in the shell.

4.2 Combining MRI and Optical Imaging

Optical imaging with high detection sensitivity and spatial resolution can provide supplementary information to MRI. Thanks to their similar chemical

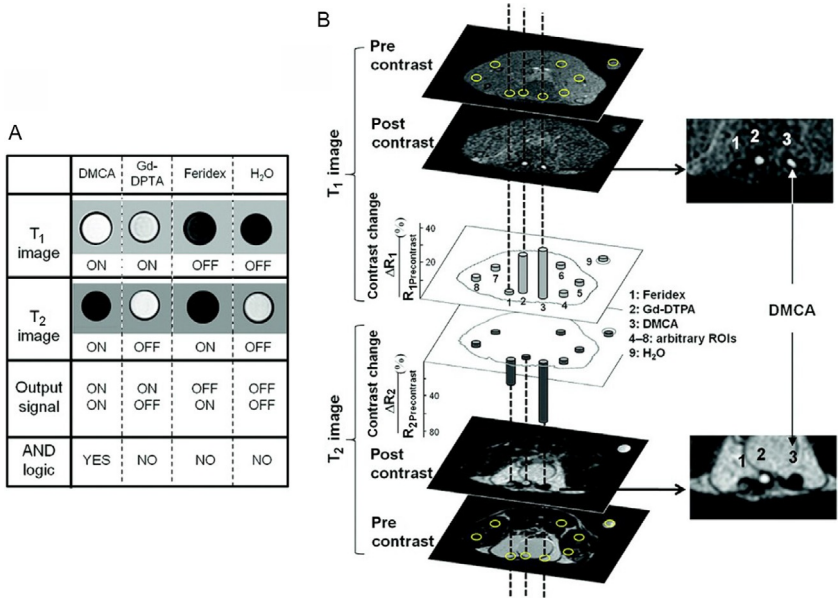

FIG. 11 (A) T_1- and T_2-weighted MR images of $MnFe_2O_4@SiO_2@Gd_2O(CO_3)_2$ (DMCA), Feridex, Gd-DTPA, and water. Only DMCA exhibited the "ON" state in both T_1- and T_2-weighted images to give its AND logic. (B) T_1- and T_2-weighted transverse MR images of a mouse where 1 mm diameter tubes containing DMCA, Feridex, and Gd-DTPA were implanted near the abdomen. Only DMCA exhibited simultaneously high signal in both T_1- and T_2-weighted MR images to satisfy the "ON" output for AND logic. *Reprinted with permission from E.S. Choi, J.Y. Park, M.J. Baek, W. Xu, K. Kattel, J.H. Kim, J.J. Lee, Y. Chang, T.J. Kim, J.E. Bae, K.S. Chae, K.J. Suh, G.H. Lee, Water-soluble ultra-small manganese oxide surface doped gadolinium oxide (Gd_2O_3@MnO) nanoparticles for MRI contrast agent, Eur. J. Inorg. Chem. 2010 (2010), 4555–4560; J.S. Choi, J.H. Lee, T.H. Shin, H.T. Song, E.Y. Kim, J. Cheon, Self-confirming "AND" logic nanoparticles for fault-free MRI, J. Am. Chem. Soc. 132 (2010), 11015–11017. Copyright 2010 American Chemical Society.*

properties and ionic radii, different Ln ions with either magnetic or luminescent properties can be easily doped into a single NP forming MRI and optical dual-mode imaging nanoprobes. Luminescent Ln^{3+} ions exhibit outstanding advantages, including excellent photostability, sharp-band emissions, and long luminescence lifetimes [14,115]. Besides traditional down-shifting process, the Ln^{3+} ions are able to realize upconversion luminescence (UCL), which involves the absorption of low-energy photons and emitting of high-energy photons [116]. The Gd^{3+} ion emits in the UV, around 310 nm, upon UV-excitation so that it can be applied as matrix for other luminescent ions such as Eu^{3+}, Tb^{3+}, Tm^{3+}, and Er^{3+}, which are the most widely used luminescent centers [117]. Owing to the small absorption cross-section of Ln^{3+} ions, sensitizers can be introduced to enlarge the absorption, such as Yb^{3+} and Nd^{3+} ions [118,119]. For instance, Gao and coworkers prepared $NaGdF_4$:Yb,Er NPs for MRI/UCL dual-mode tumor imaging, where Gd ions generate T_1-weighted

MRI signal and Yb^{3+}–Er^{3+} pairs generate UCL signal [120]. $NaYF_4$:Yb,Er, Gd@$NaGdF_4$ NPs were prepared by Shi and coworkers and further modified with Angiopep-2 molecules which can actively bind to both blood–brain barrier and glioblastoma cells [121]. They revealed the great potential of these NPs in preoperative diagnosing and intraoperative positioning of brain tumors from the MRI and UCL imaging results.

4.3 Combining MRI and X-ray Computed Tomography

X-ray computed tomography (CT) is also a clinically used diagnostic technique with noninvasive detection, deep penetration in biological tissues, and facile imaging process. The contrast in CT comes from the different X-ray attenuation coefficients of various tissues [122,123]. However, the difference between soft tissues is usually subtle, and exogenous substances, namely CT CAs, are required to afford additional contrast. CT CAs generate the contrast directly by themselves contrary to MRI CAs which do not generate MR signal by themselves. Iodinated agents are currently used as CT CAs in clinical practice, and many heavy elements have been explored for their potential for CT contrast enhancement. Due to their large atomic numbers and X-ray attenuation coefficients (Table 1), Ln elements have also been reported as promising candidates for CT CAs, including La, Gd, Dy, Yb, and Lu. With incorporation of T_1 relaxation enhancing and X-ray attenuation ability, various Gd-based NPs have been investigated for MRI and CT dual-mode imaging, such as Gd_2O_3 [124], GdF_3 [125], $NaGdF_4$ [126,127], $GdVO_4$ [128], and $Gd(IO_3)_3{\cdot}H_2O$ [64]. Similarly, other paramagnetic Ln ions, such as Dy^{3+}, Ho^{3+}, and Tb^{3+}, can be used to simultaneously enhance T_2-weighted MRI and CT contrast as well [90,108,129,130].

4.4 Combining MRI and PET/SPECT

PET and single-photon emission computed tomography (SPECT) are two highly sensitive imaging techniques based on radioactive isotopes, by which a detectable signal can be obtained with only a picomolar concentration of radiotracers [131,132]. Therefore, PET and SPECT are adequate techniques for monitoring the physiological processes at molecular level, which is difficult to realize with MRI. Combination of MRI and PET/SPECT enables the simultaneous acquisition of anatomical and physiological information [133–135]. For instance, Li and coworkers labeled ^{18}F on rare earth NPs through a facile reaction between surface rare earth ions and fluoride ions [136]. The obtained ^{18}F-labeled $NaYF_4$ NPs codoped with Gd^{3+}, Yb^{3+}, and Er^{3+} can be used for PET, MRI, and UCL multimode imaging. Similarly, by introducing Gd^{3+} ions with a cation exchange method, they prepared ^{18}F-Gd-$NaYF_4$:Yb,Er NPs with multimode imaging capability [137]. Ln radioisotopes, such as ^{153}Pm, ^{166}Dy, ^{166}Ho, and ^{175}Yb can be used for SPECT imaging. Due to the similar atomic radii and chemical properties, Ln radioisotopes can be readily doped into Ln-based matrixes or postlabeled on the

surface by cation exchange, forming radioactive nanoprobes. For instance, Li and coworkers labeled ^{153}Sm on $Gd(OH)_3$ nanorods to track their circulation and biodistribution in body after intravenous injection [138]. They also prepared ^{153}Sm-$NaLuF_4$:Yb,Tm@$NaGdF_4$ core–shell-structured NPs for MRI/UCL/CT/SPECT four-mode imaging [139].

5 PERSPECTIVE

The emergence of Gd-chelates as MRI CAs greatly facilitates clinical diagnosis and biomedical research. With deepened understanding on imaging mechanism and improved nanotechnology, Ln NPs are evolving as promising alternatives to traditional chelates. To further promote the development of Ln NPs for MRI and related applications, some issues worthy of attention are outlined below.

(1) The present design of Gd-based NPs relies on traditional relaxation mechanism, which was initially proposed for Gd-chelates. Despite the reasonable understanding of contrast enhancing results for a handful of NPs, the mechanism behind Gd-based NPs is still not fully elucidated and requires more research efforts, since Gd-based nanoparticulate systems have distinct chemical, geometric, and magnetic properties compared with chelates. For instance, the influence of crystal structure, exposed NP surface, and impurity-induced change in magnetic environment on relaxation enhancement remains unknown.

(2) Similar to contrast enhancing properties, the circulation, biodistribution, and toxicity of nanomaterials are also strongly dependent on the composition, size, shape, and surface status of the NPs, which means that the design of novel MRI CAs should balance the requirements of contrast enhancing performance and in vivo behaviors [40,140,141]. The biosafety of nanomaterials is a prerequisite before practical applications, but in most published reports the evaluation of biosafety of Ln NPs is relatively rudimentary and superficial [142–144]. Therefore, comprehensive and long-term investigation on the biosafety of Ln NPs is needed.

(3) Last but not least, scalable and reproducible preparation is necessary for the translation of nanomaterials from lab to market. Due to the nanometric size of the particles, a minor change in the characteristics of NPs (including composition, size, shape, and surface status) may result in appreciable difference in their performance. Moreover, accurate characterization is also a challenge especially for small-sized NPs.

Overall, given the exciting advances that have been attained, more progress of Ln NPs in the field of MRI is underway and expected to yield prominent results. We hope this essay will be helpful for the design and fabrication of novel high-performance Ln-based MRI CAs, and we are looking forward to their practical applications in clinical practice in the future.

ABBREVIATIONS

BOPTA	benzyloxy-diethylenetriaminepentaacetate
CA	contrast agent
CT	X-ray computed tomography
DO3A	1,4,7,10-tetraazacyclododecane-1,4,7-triacetate amide
DOTA	1,4,7,10-tetraazacyclododecane-1,4,7,10-tetraacetate
DTPA	diethylenetriaminepentaacetate
EOB-DTPA	ethoxybenzyl-diethylenetriaminepentaacetate
IS	inner sphere
LAL	laser ablation in liquid
PET	positron emission tomography
SBM	Solomon–Bloembergen–Morgan
SPECT	single-photon emission computed tomography
SPIO	superparamagnetic iron oxide
S/V	surface to volume
UCL	upconversion luminescence
0D	isotropic
1D	one-dimensional
2D	two-dimensional

REFERENCES

[1] P.C. Lauterbur, Image formation by induced local interactions: examples employing nuclear magnetic resonance, Nature 242 (1973) 190–191.

[2] M. Bottrill, L.K. Nicholas, N.J. Long, Lanthanides in magnetic resonance imaging, Chem. Soc. Rev. 35 (2006) 557–571.

[3] Y.K. Peng, S.C.E. Tsang, P.T. Chou, Chemical design of nanoprobes for T_1-weighted magnetic resonance imaging, Mater. Today (2015). http://dx.doi.org/10.1016/j.mattod.2015.11.006.

[4] R. Weissleder, M.J. Pittet, Imaging in the era of molecular oncology, Nature 452 (2008) 580–589.

[5] P. Caravan, J.J. Ellison, T.J. McMurry, R.B. Lauffer, Gadolinium(III) chelates as MRI contrast agents: structure, dynamics, and applications, Chem. Rev. 99 (1999) 2293–2352.

[6] D.V. Hingorani, A.S. Bernstein, M.D. Pagel, A review of responsive MRI contrast agents: 2005-2014, Contrast Media Mol. Imaging 10 (2015) 245–265.

[7] N. Lee, T. Hyeon, Designed synthesis of uniformly sized iron oxide nanoparticles for efficient magnetic resonance imaging contrast agents, Chem. Soc. Rev. 41 (2012) 2575–2589.

[8] D.H. Carr, J. Brown, G.M. Bydder, H.J. Weinmann, U. Speck, D.J. Thomas, I.R. Young, Intravenous chelated gadolinium as a contrast agent in NMR imaging of cerebral tumours, Lancet 323 (1984) 484–486.

[9] M.H.M. Dias, P.C. Lauterbur, Ferromagnetic particles as contrast agents for magnetic resonance imaging of liver and spleen, Magnet. Reson. Med. 3 (1986) 328–330.

[10] G.L. Davies, I. Kramberger, J.J. Davis, Environmentally responsive MRI contrast agents, Chem. Commun. 49 (2013) 9704–9721.

[11] E. Terreno, D.D. Castelli, S. Aime, Encoding the frequency dependence in MRI contrast media: the emerging class of CEST agents, Contrast Media Mol. Imaging 5 (2010) 78–98.

[12] A.J.L. Villaraza, A. Bumb, M.W. Brechbiel, Macromolecules, dendrimers, and nanomaterials in magnetic resonance imaging: the interplay between size, function, and pharmacokinetics, Chem. Rev. 110 (2010) 2921–2959.
[13] S. Viswanathan, Z. Kovacs, K.N. Green, S.J. Ratnakar, A.D. Sherry, Alternatives to gadolinium-based metal chelates for magnetic resonance imaging, Chem. Rev. 110 (2010) 2960–3018.
[14] H. Dong, S.R. Du, X.Y. Zheng, G.M. Lyu, L.D. Sun, L.D. Li, P.Z. Zhang, C. Zhang, C. H. Yan, Lanthanide nanoparticles: from design toward bioimaging and therapy, Chem. Rev. 115 (2015) 10725–10815.
[15] Z. Gao, T. Ma, E. Zhao, D. Docter, W. Yang, R.H. Stauber, M. Gao, Small is smarter: nano MRI contrast agents—advantages and recent achievements, Small 12 (2015) 556–576.
[16] D. Zhu, F. Liu, L. Ma, D. Liu, Z. Wang, Nanoparticle-based systems for T_1-weighted magnetic resonance imaging contrast agents, Int. J. Mol. Sci. 14 (2013) 10591–10607.
[17] S. Aime, M. Botta, E. Terreno, Gd(III)-based contrast agents for MRI, in: R. van Eldik, C. D. Hubbard (Eds.), Advances in Inorganic Chemistry, Elsevier, San Diego, USA, 2005.
[18] S. Aime, M. Fasano, E. Terreno, Lanthanide(III) chelates for NMR biomedical applications, Chem. Soc. Rev. 27 (1998) 19–29.
[19] M. Norek, J.A. Peters, MRI contrast agents based on dysprosium or holmium, Prog. Nucl. Magn. Reson. Spectrosc. 59 (2011) 64–82.
[20] E. Boros, E.M. Gale, P. Caravan, MR imaging probes: design and applications, Dalton Trans. 44 (2015) 4804–4818.
[21] L.M. De León-Rodríguez, A.F. Martins, M.C. Pinho, N.M. Rofsky, A.D. Sherry, Basic MR relaxation mechanisms and contrast agent design, J. Magn. Reson. Imaging 42 (2015) 545–565.
[22] C. Geraldes, S. Laurent, Classification and basic properties of contrast agents for magnetic resonance imaging, Contrast Media Mol. Imaging 4 (2009) 1–23.
[23] P.J. Klemm, W.C. Floyd, D.E. Smiles, J.M.J. Frechet, K.N. Raymond, Improving T_1 and T_2 magnetic resonance imaging contrast agents through the conjugation of an esteramide dendrimer to high-water-coordination Gd(III) hydroxypyridinone complexes, Contrast Media Mol. Imaging 7 (2012) 95–99.
[24] M. Botta, L. Tei, Relaxivity enhancement in macromolecular and nanosized Gd^{III}-based MRI contrast agents, Eur. J. Inorg. Chem. 2012 (2012) 1945–1960.
[25] Y. Liu, N. Zhang, Gadolinium loaded nanoparticles in theranostic magnetic resonance imaging, Biomaterials 33 (2012) 5363–5375.
[26] J.A. Peters, K. Djanashvili, Lanthanide loaded zeolites, clays, and mesoporous silica materials as MRI probes, Eur. J. Inorg. Chem. 2012 (2012) 1961–1974.
[27] I.X. Cantarelli, M. Pedroni, F. Piccinelli, P. Marzola, F. Boschi, G. Conti, A. Sbarbati, P. Bernardi, E. Mosconi, L. Perbellini, L. Marongiu, M. Donini, S. Dusi, L. Sorace, C. Innocenti, E. Fantechi, C. Sangregorio, A. Speghini, Multifunctional nanoprobes based on upconverting lanthanide doped CaF_2: towards biocompatible materials for biomedical imaging, Biomater. Sci. 2 (2014) 1158–1171.
[28] F. Chen, W. Bu, S. Zhang, X. Liu, J. Liu, H. Xing, Q. Xiao, L. Zhou, W. Peng, L. Wang, J. Shi, Positive and negative lattice shielding effects co-existing in Gd(III) ion doped bifunctional upconversion nanoprobes, Adv. Funct. Mater. 21 (2011) 4285–4294.
[29] F. Chen, P. Huang, Y.J. Zhu, J. Wu, C.L. Zhang, D.X. Cui, The photoluminescence, drug delivery and imaging properties of multifunctional Eu^{3+}/Gd^{3+} dual-doped hydroxyapatite nanorods, Biomaterials 32 (2011) 9031–9039.

[30] H. Chen, G.D. Wang, W. Tang, T. Todd, Z. Zhen, C. Tsang, K. Hekmatyar, T. Cowger, R. B. Hubbard, W. Zhang, J. Stickney, B. Shen, J. Xie, Gd-encapsulated carbonaceous dots with efficient renal clearance for magnetic resonance imaging, Adv. Mater. 26 (2014) 6761–6766.
[31] P.P. Fatouros, M.D. Shultz, Metallofullerenes: a new class of MRI agents and more? Nanomedicine 8 (2013) 1853–1864.
[32] Q. Ma, M. Jebb, M.F. Tweedle, L.J. Wilson, The gadonanotubes: structural origin of their high-performance MRI contrast agent behavior, J. Mater. Chem. B 1 (2013) 5791–5797.
[33] P. Chandran, A. Sasidharan, A. Ashokan, D. Menon, S. Nair, M. Koyakutty, Highly biocompatible TiO_2:Gd^{3+} nano-contrast agent with enhanced longitudinal relaxivity for targeted cancer imaging, Nanoscale 3 (2011) 4150–4161.
[34] I.F. Li, C.S. Yeh, Synthesis of Gd doped CdSe nanoparticles for potential optical and MR imaging applications, J. Mater. Chem. 20 (2010) 2079–2081.
[35] X. Wei, W. Wang, K. Chen, Preparation and characterization of ZnS:Tb, Gd and ZnS:Er, Yb,Gd nanoparticles for bimodal magnetic-fluorescent imaging, Dalton Trans. 42 (2013) 1752–1759.
[36] Q. Yin, X. Jin, G. Yang, C. Jiang, Z. Song, G. Sun, Biocompatible folate-modified Gd^{3+}/Yb^{3+}-doped ZnO nanoparticles for dual modal MRI/CT imaging, RSC Adv. 4 (2014) 53561–53569.
[37] F. Zhang, T.T. Sun, Y. Zhang, Q. Li, C. Chai, L. Lu, W. Shen, J. Yang, X.W. He, Y.K. Zhang, W.Y. Li, Facile synthesis of functional gadolinium-doped CdTe quantum dots for tumor-targeted fluorescence and magnetic resonance dual-modality imaging, J. Mater. Chem. B 2 (2014) 7201–7209.
[38] H.B. Na, T. Hyeon, Nanostructured T1 MRI contrast agents, J. Mater. Chem. 19 (2009) 6267–6273.
[39] M. Longmire, P.L. Choyke, H. Kobayashi, Clearance properties of nano-sized particles and molecules as imaging agents: considerations and caveats, Nanomedicine 3 (2008) 703–717.
[40] M. Yu, J. Zheng, Clearance pathways and tumor targeting of imaging nanoparticles, ACS Nano 9 (2015) 6655–6674.
[41] M.A. McDonald, K.L. Watkin, Small particulate gadolinium oxide and gadolinium oxide albumin microspheres as multimodal contrast and therapeutic agents, Invest. Radiol. 38 (2003) 305–310.
[42] M. Ahrén, L.a. Selegård, A. Klasson, F. Söderlind, N. Abrikossova, C. Skoglund, T.R. Bengtsson, M. Engström, P.O. Käll, K. Uvdal, Synthesis and characterization of PEGylated Gd_2O_3 nanoparticles for MRI contrast enhancement, Langmuir 26 (2010) 5753–5762.
[43] F. Marc-André, M.P. Rodrigo Jr., S. Fredrik, A. Klasson, E. Maria, V. Teodor, K. Per-Olof, U. Kajsa, Polyethylene glycol-covered ultra-small Gd_2O_3 nanoparticles for positive contrast at 1.5 T magnetic resonance clinical scanning, Nanotechnology 18 (2007) 395501.
[44] M.A. McDonald, K.L. Watkin, Investigations into the physicochemical properties of dextran small particulate gadolinium oxide nanoparticles, Acad. Radiol. 13 (2006) 421–427.
[45] M. Ahrén, L. Selegård, F. Söderlind, M. Linares, J. Kauczor, P. Norman, P.O. Käll, K. Uvdal, A simple polyol-free synthesis route to Gd_2O_3 nanoparticles for MRI applications: an experimental and theoretical study, J. Nanopart. Res. 14 (2012) 1006.
[46] M. Cho, R. Sethi, J.S. Ananta narayanan, S.S. Lee, D.N. Benoit, N. Taheri, P. Decuzzi, V. L. Colvin, Gadolinium oxide nanoplates with high longitudinal relaxivity for magnetic resonance imaging, Nanoscale 6 (2014) 13637–13645.

[47] L. Zhou, Z. Gu, X. Liu, W. Yin, G. Tian, L. Yan, S. Jin, W. Ren, G. Xing, W. Li, X. Chang, Z. Hu, Y. Zhao, Size-tunable synthesis of lanthanide-doped Gd_2O_3 nanoparticles and their applications for optical and magnetic resonance imaging, J. Mater. Chem. 22 (2012) 966–974.
[48] C.C. Huang, T.Y. Liu, C.H. Su, Y.W. Lo, J.H. Chen, C.S. Yeh, Superparamagnetic hollow and paramagnetic porous Gd_2O_3 particles, Chem. Mater. 20 (2008) 3840–3848.
[49] G. Tian, Z.J. Gu, X.X. Liu, L.J. Zhou, W.Y. Yin, L. Yan, S. Jin, W.L. Ren, G.M. Xing, S. J. Li, Y.L. Zhao, Facile fabrication of rare-earth-doped Gd_2O_3 hollow spheres with upconversion luminescence, magnetic resonance, and drug delivery properties, J. Phys. Chem. C 115 (2011) 23790–23796.
[50] N. Luo, X. Tian, C. Yang, J. Xiao, W. Hu, D. Chen, L. Li, Ligand-free gadolinium oxide for in vivo T_1-weighted magnetic resonance imaging, Phys. Chem. Chem. Phys. 15 (2013) 12235–12240.
[51] L.C. Mimun, G. Ajithkumar, M. Pokhrel, B.G. Yust, Z.G. Elliott, F. Pedraza, A. Dhanale, L. Tang, A.L. Lin, V.P. Dravid, D.K. Sardar, Bimodal imaging using neodymium doped gadolinium fluoride nanocrystals with near-infrared to near-infrared downconversion luminescence and magnetic resonance properties, J. Mater. Chem. B 1 (2013) 5702–5710.
[52] Q. Ju, Y. Liu, D. Tu, H. Zhu, R. Li, X. Chen, Lanthanide-doped multicolor GdF_3 nanocrystals for time-resolved photoluminescent biodetection, Chem. Eur. J. 17 (2011) 8549–8554.
[53] F. Carniato, K. Thangavel, L. Tei, M. Botta, Structure and dynamics of the hydration shells of citrate-coated GdF_3 nanoparticles, J. Mater. Chem. B 1 (2013) 2442–2446.
[54] F. Evanics, P.R. Diamente, F.C.J.M. van Veggel, G.J. Stanisz, R.S. Prosser, Water-soluble GdF_3 and GdF_3/LaF_3 nanoparticles-physical characterization and NMR relaxation properties, Chem. Mater. 18 (2006) 2499–2505.
[55] N.J.J. Johnson, W. Oakden, G.J. Stanisz, R.S. Prosser, F.C.J.M. van Veggel, Size-tunable, ultrasmall $NaGdF_4$ nanoparticles: insights into their T_1 MRI contrast enhancement, Chem. Mater. 23 (2011) 3714–3722.
[56] H. Xing, S. Zhang, W. Bu, X. Zheng, L. Wang, Q. Xiao, D. Ni, J. Zhang, L. Zhou, W. Peng, K. Zhao, Y. Hua, J. Shi, Ultrasmall $NaGdF_4$ nanodots for efficient MR angiography and atherosclerotic plaque imaging, Adv. Mater. 26 (2014) 3867–3872.
[57] Q. Ju, D.T. Tu, Y.S. Liu, R.F. Li, H.M. Zhu, J.C. Chen, Z. Chen, M.D. Huang, X.Y. Chen, Amine-functionalized lanthanide-doped $KGdF_4$ nanocrystals as potential optical/magnetic multimodal bioprobes, J. Am. Chem. Soc. 134 (2012) 1323–1330.
[58] H. Hifumi, S. Yamaoka, A. Tanimoto, D. Citterio, K. Suzuki, Gadolinium-based hybrid nanoparticles as a positive MR contrast agent, J. Am. Chem. Soc. 128 (2006) 15090–15091.
[59] H. Hifumi, S. Yamaoka, A. Tanimoto, T. Akatsu, Y. Shindo, A. Honda, D. Citterio, K. Oka, S. Kuribayashi, K. Suzuki, Dextran coated gadolinium phosphate nanoparticles for magnetic resonance tumor imaging, J. Mater. Chem. 19 (2009) 6393–6399.
[60] W. Ren, G. Tian, L. Zhou, W. Yin, L. Yan, S. Jin, Y. Zu, S. Li, Z. Gu, Y. Zhao, Lanthanide ion-doped $GdPO_4$ nanorods with dual-modal bio-optical and magnetic resonance imaging properties, Nanoscale 4 (2012) 3754–3760.
[61] H. Hu, S. Liu, D. Li, M. Wang, R. Moats, H. Shan, P.S. Conti, Z. Li, The synthesis of lanthanide-doped $GdVO_4$ ultrathin nanosheets with great optical and paramagnetic properties for FRET biodetection and in vivo MR imaging, J. Mater. Chem. B 2 (2014) 3998–4007.
[62] X.J. Kang, D.M. Yang, P.A. Ma, Y.L. Dai, M.M. Shang, D.L. Geng, Z.Y. Cheng, J. Lin, Fabrication of hollow and porous structured $GdVO_4:Dy^{3+}$ nanospheres as anticancer drug carrier and MRI contrast agent, Langmuir 29 (2013) 1286–1294.

[63] M. Abdesselem, M. Schoeffel, I. Maurin, R. Ramodiharilafy, G. Autret, O. Clément, P.L. Tharaux, J.P. Boilot, T. Gacoin, C. Bouzigues, A. Alexandrou, Multifunctional rare-earth vanadate nanoparticles: luminescent labels, oxidant sensors, and MRI contrast agents, ACS Nano 8 (2014) 11126–11137.

[64] E.J. Lee, W.C. Heo, J.W. Park, Y. Chang, J.E. Bae, K.S. Chae, T.J. Kim, J.A. Park, G. H. Lee, D-glucuronic acid coated $Gd(IO_3)_3 \cdot 2H_2O$ nanomaterial as a potential T_1 MRI-CT dual contrast agent, Eur. J. Inorg. Chem. 2013 (2013) 2858–2866.

[65] Y. Wu, X. Xu, Q. Tang, Y. Li, A new type of silica-coated $Gd_2(CO_3)_3$:Tb nanoparticle as a bifunctional agent for magnetic resonance imaging and fluorescent imaging, Nanotechnology 23 (2012) 20.

[66] G. Liang, L. Cao, H. Chen, Z. Zhang, S. Zhang, S. Yu, X. Shen, J. Kong, Ultrasmall gadolinium hydrated carbonate nanoparticle: an advanced T_1 MRI contrast agent with large longitudinal relaxivity, J. Mater. Chem. B 1 (2013) 629–638.

[67] K.W. Hu, F.Y. Jiang, C.H. Su, C.S. Yeh, Fabrication of $Gd_2O(CO_3)_2$-H_2O/silica/gold hybrid particles as a bifunctional agent for MR imaging and photothermal destruction of cancer cells, J. Mater. Chem. 19 (2009) 2147–2153.

[68] L. Zhou, W. Yin, W. Ren, Z. Gu, W. Li, S. Jin, L. Yan, G. Tian, Z. Hu, Y. Zhao, Controllable synthesis of $Gd_2O(CO_3)_2 \cdot H_2O$@silica-FITC nanoparticles with size-dependent optical and magnetic resonance imaging properties, New J. Chem. 36 (2012) 2599–2606.

[69] J. Jung, M.A. Kim, J.H. Cho, S.J. Lee, I. Yang, J. Cho, S.K. Kim, C. Lee, J.K. Park, Europium-doped gadolinium sulfide nanoparticles as a dual-mode imaging agent for T_1-weighted MR and photoluminescence imaging, Biomaterials 33 (2012) 5865–5874.

[70] Y. Gossuin, A. Hocq, Q.L. Vuong, S. Disch, R.P. Hermann, P. Gillis, Physico-chemical and NMR relaxometric characterization of gadolinium hydroxide and dysprosium oxide nanoparticles, Nanotechnology 19 (2008) 475102.

[71] S. Huang, J. Liu, D. Liu, Q. Yuan, Facile and large-scale synthesis of $Gd(OH)_3$ nanorods for MR imaging with low toxicity, New J. Chem. 36 (2012) 1335–1338.

[72] V.S. Perera, L.D. Yang, J. Hao, G. Chen, B.O. Erokwu, C.A. Flask, P.Y. Zavalij, J.P. Basilion, S.D. Huang, Biocompatible nanoparticles of $KGd(H_2O)_2Fe(CN)_6 \cdot H_2O$ with extremely high T_1-weighted relaxivity owing to two water molecules directly bound to the Gd(III) center, Langmuir 30 (2014) 12018–12026.

[73] B.I. Lee, K.S. Lee, J.H. Lee, I.S. Lee, S.H. Byeon, Synthesis of colloidal aqueous suspensions of a layered gadolinium hydroxide: a potential MRI contrast agent, Dalton Trans. (2009) 2490–2495.

[74] Y.C. Li, T. Chen, W.H. Tan, D.R. Talham, Size-dependent MRI relaxivity and dual imaging with $Eu_{0.2}Gd_{0.8}PO_4 \cdot H_2O$ nanoparticles, Langmuir 30 (2014) 5873–5879.

[75] A.T.M.A. Rahman, P. Majewski, K. Vasilev, Gd_2O_3 nanoparticles: size-dependent nuclear magnetic resonance, Contrast Media Mol. Imaging 8 (2013) 92–95.

[76] J.Y. Park, M.J. Baek, E.S. Choi, S. Woo, J.H. Kim, T.J. Kim, J.C. Jung, K.S. Chae, Y. Chang, G.H. Lee, Paramagnetic ultrasmall gadolinium oxide nanoparticles as advanced T_1 MRI contrast agent: account for large longitudinal relaxivity, optimal particle diameter, and in vivo T_1 MR images, ACS Nano 3 (2009) 3663–3669.

[77] Y. Hou, R. Qiao, F. Fang, X. Wang, C. Dong, K. Liu, C. Liu, Z. Liu, H. Lei, F. Wang, M. Gao, $NaGdF_4$ nanoparticle-based molecular probes for magnetic resonance imaging of intraperitoneal tumor xenografts in vivo, ACS Nano 7 (2012) 330–338.

[78] Y. Tian, H.Y. Yang, K. Li, X. Jin, Monodispersed ultrathin GdF_3 nanowires: oriented attachment, luminescence, and relaxivity for MRI contrast agents, J. Mater. Chem. 22 (2012) 22510–22516.

[79] G.K. Das, B.C. Heng, S.C. Ng, T. White, J.S.C. Loo, L. D'Silva, P. Padmanabhan, K.K. Bhakoo, S.T. Selvan, T.T.Y. Tan, Gadolinium oxide ultranarrow nanorods as multimodal contrast agents for optical and magnetic resonance imaging, Langmuir 26 (2010) 8959–8965.

[80] Y. Zhang, G.K. Das, V. Vijayaragavan, Q.C. Xu, P. Padmanabhan, K.K. Bhakoo, S.T. Selvan, T.T.Y. Tan, "Smart" theranostic lanthanide nanoprobes with simultaneous up-conversion fluorescence and tunable T_1-T_2 magnetic resonance imaging contrast and near-infrared activated photodynamic therapy, Nanoscale 6 (2014) 12609–12617.

[81] G.Y. Chen, H.L. Qiu, P.N. Prasad, X.Y. Chen, Upconversion nanoparticles: design, nanochemistry, and applications in theranostics, Chem. Rev. 114 (2014) 5161–5214.

[82] S.L. Gai, C.X. Li, P.P. Yang, J. Lin, Recent progress in rare earth micro/nanocrystals: soft chemical synthesis, luminescent properties, and biomedical applications, Chem. Rev. 114 (2014) 2343–2389.

[83] J. Fang, P. Chandrasekharan, X.L. Liu, Y. Yang, Y.B. Lv, C.T. Yang, J. Ding, Manipulating the surface coating of ultra-small Gd_2O_3 nanoparticles for improved T_1-weighted MR imaging, Biomaterials 35 (2014) 1636–1642.

[84] C.R. Kim, J.S. Baeck, Y. Chang, J.E. Bae, K.S. Chae, G.H. Lee, Ligand-size dependent water proton relaxivities in ultrasmall gadolinium oxide nanoparticles and in vivo T_1 MR images in a 1.5 T MR field, Phys. Chem. Chem. Phys. 16 (2014) 19866–19873.

[85] S. Rodriguez–Liviano, N.O. Nunez, S. Rivera–Fernandez, J.M. de la Fuente, M. Ocana, Ionic liquid mediated synthesis and surface modification of multifunctional mesoporous Eu:GdF3 nanoparticles for biomedical applications, Langmuir 29 (2013) 3411–3418.

[86] K. Kattel, J.Y. Park, W. Xu, H.G. Kim, E.J. Lee, B.A. Bony, W.C. Heo, J.J. Lee, S. Jin, J.S. Baeck, Y. Chang, T.J. Kim, J.E. Bae, K.S. Chae, G.H. Lee, A facile synthesis, in vitro and in vivo MR studies of d-glucuronic acid-coated ultrasmall Ln_2O_3 (Ln = Eu, Gd, Dy, Ho, and Er) nanoparticles as a new potential MRI contrast agent, ACS Appl. Mater. Interfaces 3 (2011) 3325–3334.

[87] R. Kumar, M. Nyk, T.Y. Ohulchanskyy, C.A. Flask, P.N. Prasad, Combined optical and MR bioimaging using rare earth ion doped $NaYF_4$ nanocrystals, Adv. Funct. Mater. 19 (2009) 853–859.

[88] T. Paik, T.R. Gordon, A.M. Prantner, H. Yun, C.B. Murray, Designing tripodal and triangular gadolinium oxide nanoplates and self-assembled nanofibrils as potential multimodal bioimaging probes, ACS Nano 7 (2013) 2850–2859.

[89] T. Passuello, M. Pedroni, F. Piccinelli, S. Polizzi, P. Marzola, S. Tambalo, G. Conti, D. Benati, F. Vetrone, M. Bettinelli, A. Speghini, PEG-capped, lanthanide doped GdF_3 nanoparticles: luminescent and T_2 contrast agents for optical and MRI multimodal imaging, Nanoscale 4 (2012) 7682–7689.

[90] D. Ni, J. Zhang, W. Bu, C. Zhang, Z. Yao, H. Xing, J. Wang, F. Duan, Y. Liu, W. Fan, X. Feng, J. Shi, PEGylated $NaHoF_4$ nanoparticles as contrast agents for both X-ray computed tomography and ultra-high field magnetic resonance imaging, Biomaterials 76 (2016) 218–225.

[91] M. Norek, E. Kampert, U. Zeitler, J.A. Peters, Tuning of the size of Dy_2O_3 nanoparticles for optimal performance as an MRI contrast agent, J. Am. Chem. Soc. 130 (2008) 5335–5340.

[92] G.K. Das, N.J.J. Johnson, J. Cramen, B. Blasiak, P. Latta, B. Tomanek, F.C.J.M. van Veggel, $NaDyF_4$ nanoparticles as T_2 contrast agents for ultrahigh field magnetic resonance imaging, J. Phys. Chem. Lett. 3 (2012) 524–529.

[93] N. Blow, How to get ahead in imaging, Nature 458 (2009) 925–930.

[94] P. Fries, J.N. Morelli, F. Lux, O. Tillement, G. Schneider, A. Buecker, The issues and tentative solutions for contrast-enhanced magnetic resonance imaging at ultra-high field strength, Wiley Interdiscip. Rev. Nanomed. Nanobiotechnol. 6 (2014) 559–573.
[95] T. Nakada, Clinical application of high and ultra high-field MRI, Brain Dev. 29 (2007) 325–335.
[96] P. Caravan, C.T. Farrar, L. Frullano, R. Uppal, Influence of molecular parameters and increasing magnetic field strength on relaxivity of gadolinium- and manganese-based T_1 contrast agents, Contrast Media Mol. Imaging 4 (2009) 89–100.
[97] C. Corot, P. Robert, J.M. Idée, M. Port, Recent advances in iron oxide nanocrystal technology for medical imaging, Adv. Drug Deliv. Rev. 58 (2006) 1471–1504.
[98] M. Rohrer, H. Bauer, J. Mintorovitch, M. Requardt, H.J. Weinmann, Comparison of magnetic properties of MRI contrast media solutions at different magnetic field strengths, Invest. Radiol. 40 (2005) 715–724.
[99] M. Norek, G.A. Pereira, C.F.G.C. Geraldes, A. Denkova, W.Z. Zhou, J.A. Peters, NMR transversal relaxivity of suspensions of lanthanide oxide nanoparticles, J. Phys. Chem. C 111 (2007) 10240–10246.
[100] Q.L. Vuong, S. Van Doorslaer, J.L. Bridot, C. Argante, G. Alejandro, R. Hermann, S. Disch, C. Mattea, S. Stapf, Y. Gossuin, Paramagnetic nanoparticles as potential MRI contrast agents: characterization, NMR relaxation, simulations and theory, Magn. Reson. Mater. Phys. 25 (2012) 467–478.
[101] W.Y. Huang, J.J. Davis, Multimodality and nanoparticles in medical imaging, Dalton Trans. 40 (2011) 6087–6103.
[102] J. Key, J.F. Leary, Nanoparticles for multimodal in vivo imaging in nanomedicine, Int. J. Nanomed. 9 (2014) 711–726.
[103] J. Zhou, Z. Liu, F. Li, Upconversion nanophosphors for small-animal imaging, Chem. Soc. Rev. 41 (2012) 1323–1349.
[104] G.C. Kagadis, G. Loudos, K. Katsanos, S.G. Langer, G.C. Nikiforidis, In vivo small animal imaging: current status and future prospects, Med. Phys. 37 (2010) 6421–6442.
[105] J.S. Choi, J.H. Lee, T.H. Shin, H.T. Song, E.Y. Kim, J. Cheon, Self-confirming "AND" logic nanoparticles for fault-free MRI, J. Am. Chem. Soc. 132 (2010) 11015–11017.
[106] H. Yang, Y. Zhuang, Y. Sun, A. Dai, X. Shi, D. Wu, F. Li, H. Hu, S. Yang, Targeted dual-contrast T_1- and T_2-weighted magnetic resonance imaging of tumors using multifunctional gadolinium-labeled superparamagnetic iron oxide nanoparticles, Biomaterials 32 (2011) 4584–4593.
[107] W. Zhao, H. Huang, Y. Sun, X. Zhang, Y. Li, J. Wang, T_1-weighted and T_2-weighted MRI probe based on Gd-DTPA surface conjugated SPIO nanomicelles, RSC Adv. 5 (2015) 97675–97680.
[108] J. Zhou, Z.G. Lu, G.G. Shan, S.H. Wang, Y. Liao, Gadolinium complex and phosphorescent probe-modified $NaDyF_4$ nanorods for T_1- and T_2-weighted MRI/CT/phosphorescence multimodality imaging, Biomaterials 35 (2014) 368–377.
[109] E.S. Choi, J.Y. Park, M.J. Baek, W. Xu, K. Kattel, J.H. Kim, J.J. Lee, Y. Chang, T.J. Kim, J.E. Bae, K.S. Chae, K.J. Suh, G.H. Lee, Water-soluble ultra-small manganese oxide surface doped gadolinium oxide (Gd_2O_3@MnO) nanoparticles for MRI contrast agent, Eur. J. Inorg. Chem. 2010 (2010) 4555–4560.
[110] H. Chen, B. Qi, T. Moore, D.C. Colvin, T. Crawford, J.C. Gore, F. Alexis, O.T. Mefford, J. N. Anker, Synthesis of brightly PEGylated luminescent magnetic upconversion nanophosphors for deep tissue and dual MRI imaging, Small 10 (2014) 160–168.

[111] T.H. Shin, J.S. Choi, S. Yun, I.S. Kim, H.T. Song, Y. Kim, K.I. Park, J. Cheon, T_1 and T_2 dual-mode MRI contrast agent for enhancing accuracy by engineered nanomaterials, ACS Nano 8 (2014) 3393–3401.

[112] Z. Zhou, D. Huang, J. Bao, Q. Chen, G. Liu, Z. Chen, X. Chen, J. Gao, A synergistically enhanced T_1–T_2 dual-modal contrast agent, Adv. Mater. 24 (2012) 6223–6228.

[113] N. Xiao, W. Gu, H. Wang, Y. Deng, X. Shi, L. Ye, T_1–T_2 dual-modal MRI of brain gliomas using PEGylated Gd-doped iron oxide nanoparticles, J. Colloid Interface Sci. 417 (2014) 159–165.

[114] J. Huang, Y. Hou, C. Liu, L. Jing, T. Ma, X. Sun, M. Gao, Chemical spacer design for engineering the relaxometric properties of core–shell structured rare earth nanoparticles, Chem. Mater. 27 (2015) 7918–7925.

[115] G. Wang, Q. Peng, Y. Li, Lanthanide-doped nanocrystals: synthesis, optical-magnetic properties, and applications, Acc. Chem. Res. 44 (2011) 322–332.

[116] H. Dong, L.D. Sun, C.H. Yan, Basic understanding of the lanthanide related upconversion emissions, Nanoscale 5 (2013) 5703–5714.

[117] L.D. Sun, H. Dong, P.Z. Zhang, C.H. Yan, Upconversion of rare earth nanomaterials, in: M.A. Johnson, T.J. Martinez (Eds.), Annual Review of Physical Chemistry, Annual Reviews, USA, 2015.

[118] H. Dong, L.D. Sun, C.H. Yan, Energy transfer in lanthanide upconversion studies for extended optical applications, Chem. Soc. Rev. 44 (2015) 1608–1634.

[119] L.D. Sun, Y.F. Wang, C.H. Yan, Paradigms and challenges for bioapplication of rare earth upconversion luminescent nanoparticles: small size and tunable emission/excitation spectra, Acc. Chem. Res. 47 (2014) 1001–1009.

[120] C. Liu, Z. Gao, J. Zeng, Y. Hou, F. Fang, Y. Li, R. Qiao, L. Shen, H. Lei, W. Yang, M. Gao, Magnetic/upconversion fluorescent NaGdF4:Yb, Er nanoparticle-based dual-modal molecular probes for imaging tiny tumors in vivo, ACS Nano 7 (2013) 7227–7240.

[121] D. Ni, J. Zhang, W. Bu, H. Xing, F. Han, Q. Xiao, Z. Yao, F. Chen, Q. He, J. Liu, S. Zhang, W. Fan, L. Zhou, W. Peng, J. Shi, Dual-targeting upconversion nanoprobes across the blood–brain barrier for magnetic resonance/fluorescence imaging of intracranial glioblastoma, ACS Nano 8 (2014) 1231–1242.

[122] N. Lee, S.H. Choi, T. Hyeon, Nano-sized CT contrast agents, Adv. Mater. 25 (2013) 2641–2660.

[123] Y. Liu, K. Ai, L. Lu, Nanoparticulate X-ray computed tomography contrast agents: from design validation to in vivo applications, Acc. Chem. Res. 45 (2012) 1817–1827.

[124] M.W. Ahmad, W. Xu, S.J. Kim, J.S. Baeck, Y. Chang, J.E. Bae, K.S. Chae, J.A. Park, T. J. Kim, G.H. Lee, Potential dual imaging nanoparticle: Gd_2O_3 nanoparticle, Sci. Rep. 5 (2015) 8549.

[125] X.Y. Zheng, L.D. Sun, T. Zheng, H. Dong, Y. Li, Y.F. Wang, C.H. Yan, PAA-capped GdF_3 nanoplates as dual-mode MRI and CT contrast agents, Sci. Bull. 60 (2015) 1092–1100.

[126] E.N.M. Cheung, R.D.A. Alvares, W. Oakden, R. Chaudhary, M.L. Hill, J. Pichaandi, G.C. H. Mo, C. Yip, P.M. Macdonald, G.J. Stanisz, F.C.J.M. van Veggel, R.S. Prosser, Polymer-stabilized lanthanide fluoride nanoparticle aggregates as contrast agents for magnetic resonance imaging and computed tomography, Chem. Mater. 22 (2010) 4728–4739.

[127] L. Zhou, X. Zheng, Z. Gu, W. Yin, X. Zhang, L. Ruan, Y. Yang, Z. Hu, Y. Zhao, Mesoporous $NaYbF_4$@$NaGdF_4$ core-shell up-conversion nanoparticles for targeted drug delivery and multimodal imaging, Biomaterials 35 (2014) 7666–7678.

[128] K. Dong, E. Ju, J. Liu, X. Han, J. Ren, X. Qu, Ultrasmall biomolecule-anchored hybrid $GdVO_4$ nanophosphors as a metabolizable multimodal bioimaging contrast agent, Nanoscale 6 (2014) 12042–12049.
[129] X. Jin, F. Fang, J. Liu, C. Jiang, X. Han, Z. Song, J. Chen, G. Sun, H. Lei, L. Lu, An ultrasmall and metabolizable PEGylated $NaGdF_4$:Dy nanoprobe for high-performance T_1/T_2-weighted MR and CT multimodal imaging, Nanoscale 7 (2015) 15680–15688.
[130] X. Zheng, Y. Wang, L. Sun, N. Chen, L. Li, S. Shi, S. Malaisamy, C. Yan, TbF_3 nanoparticles as dual-mode contrast agents for ultrahigh field magnetic resonance imaging and X-ray computed tomography, Nano Res. 9 (2016) 1135–1147.
[131] C.S. Cutler, C.J. Smith, G.J. Ehrhardt, T.T. Tyler, S.S. Jurisson, E. Deutsch, Current and potential therapeutic uses of lanthanide radioisotopes, Cancer Biother. Radio. 15 (2000) 531–545.
[132] L. Zhu, K. Ploessl, H.F. Kung, Multifunctional rare-earth vanadate nanoparticles: luminescent labels, oxidant sensors, and MRI contrast agents, Chem. Soc. Rev. 43 (2014) 6683–6691.
[133] R.T.M. de Rosales, Potential clinical applications of bimodal PET-MRI or SPECT-MRI agents, J. Labelled Compd. Rad. 57 (2014) 298–303.
[134] E. Gianolio, L. Maciocco, D. Imperio, G.B. Giovenzana, F. Simonelli, K. Abbas, G. Bisi, S. Aime, Dual MRI-SPECT agent for pH-mapping, Chem. Commun. 47 (2011) 1539–1541.
[135] R. Misri, K. Saatchi, U.O. Hafeli, Nanoprobes for hybrid SPECT/MR molecular imaging, Nanomedicine 7 (2012) 719–733.
[136] J. Zhou, M. Yu, Y. Sun, X. Zhang, X. Zhu, Z. Wu, D. Wu, F. Li, Fluorine-18-labeled $Gd^{3+}/Yb^{3+}/Er^{3+}$ co-doped $NaYF_4$ nanophosphors for multimodality PET/MR/UCL imaging, Biomaterials 32 (2011) 1148–1156.
[137] Q. Liu, Y. Sun, C. Li, J. Zhou, C. Li, T. Yang, X. Zhang, T. Yi, D. Wu, F. Li, ^{18}F-labeled magnetic-upconversion nanophosphors via rare-earth cation-assisted ligand assembly, ACS Nano 5 (2011) 3146–3157.
[138] Y. Yang, Y. Sun, Y. Liu, J. Peng, Y. Wu, Y. Zhang, W. Feng, F. Li, Long-term in vivo biodistribution and toxicity of $Gd(OH)_3$ nanorods, Biomaterials 34 (2013) 508–515.
[139] Y. Sun, X. Zhu, J. Peng, F. Li, Core–shell lanthanide upconversion nanophosphors as four-modal probes for tumor angiogenesis imaging, ACS Nano 7 (2013) 11290–11300.
[140] E.B. Ehlerding, F. Chen, W. Cai, Biodegradable and renal clearable inorganic nanoparticles, Adv. Sci. 3 (2016) 1500223.
[141] C. Liu, Y. Hou, M. Gao, Are rare-earth nanoparticles suitable for in vivo applications? Adv. Mater. 26 (2014) 6922–6932.
[142] A. Gnach, T. Lipinski, A. Bednarkiewicz, J. Rybka, J.A. Capobianco, Upconverting nanoparticles: assessing the toxicity, Chem. Soc. Rev. 44 (2015) 1561–1584.
[143] S. Sharifi, S. Behzadi, S. Laurent, M. Laird Forrest, P. Stroeve, M. Mahmoudi, Toxicity of nanomaterials, Chem. Soc. Rev. 41 (2012) 2323–2343.
[144] Y. Sun, W. Feng, P. Yang, C. Huang, F. Li, The biosafety of lanthanide upconversion nanomaterials, Chem. Soc. Rev. 44 (2015) 1509–1525.

Chapter 293

Expanding the +2 Oxidation State of the Rare-Earth Metals, Uranium, and Thorium in Molecular Complexes

David H. Woen and William J. Evans[1]
University of California, Irvine, CA, United States
[1]*Corresponding author: e-mail: wevans@uci.edu*

Chapter Outline

Handbook on the Physics and Chemistry of Rare Earths, Vol. 50. http://dx.doi.org/10.1016/bs.hpcre.2016.08.002

1 INTRODUCTION

This chapter describes recent developments in the low oxidation state chemistry of the rare-earth elements since the publication in 2010 of Chapter 246 in this Handbook on the Physics and Chemistry of Rare Earths series on "The Molecular Chemistry of the Rare-Earth Elements in Uncommon Low-Valent States" by Nief [1]. Ordinarily, there would be no need for a new chapter on this topic so soon after this last publication. However, the landscape of low oxidation states in the rare-earth metal series has changed dramatically between 2011 and 2016 and a new chapter focused on developments in this area and their implications is warranted. Expansion of the +2 oxidation state chemistry of uranium and thorium is also described in this chapter because recent advances with these actinide metals are closely related to the rare-earth metal chemistry.

This chapter is presented in the order of the chronological development of these results and starts with a background section that describes the current level of knowledge prior to the discoveries of the new oxidation states. A section is included toward the end of the chapter on earlier literature that contains information that now can be seen as relevant to these discoveries. Hopefully, presenting these results in this historical context and adding a retrospective on prior literature will be useful in stimulating the examination of the current literature to make the next generation of discoveries.

2 BACKGROUND

2.1 Eu^{2+}, Yb^{2+}, and Sm^{2+} Complexes

For many years, the oxidation state chemistry of the rare-earth elements in molecules was thought to be quite simple: the +3 oxidation state was the most stable for all the members and the only other oxidation states accessible in solution were Ce^{4+}, Eu^{2+}, Yb^{2+}, and Sm^{2+} [1–6]. The +3 oxidation state was the most stable because it represented an optimal balance of energy according to Born–Haber analyses [7]. Effectively, the balance between the amount of energy needed to ionize three electrons from these metals and the stabilization energy (e.g., lattice energy) in the product from electrostatic interactions with the +3 ion was better for +3 than for other oxidation states. The optimum +3 oxidation state was found for all the metals in the series because the number of 4f electrons involved, i.e., the $4f^n$ electron configuration, had little effect on the chemistry due to the limited radial extension of the 4f orbitals [8].

Eu^{2+}, Yb^{2+}, and Sm^{2+} were identified early in the history of recorded rare-earth metal chemistry starting in 1906 [5,9–13] and were regarded for the next

90 years as the only +2 ions accessible in solution for the lanthanides [2]. Their existence was explained on the basis of their half-filled ($4f^7$), filled ($4f^{14}$), and approaching half-filled ($4f^6$) shell electron configurations, respectively. The quantum mechanical stabilization of these electron configurations did not override the stability of the +3 ions for these elements, i.e., Eu^{2+}, Yb^{2+}, and Sm^{2+} are all reducing agents, but it did allow the +2 ions to exist in solution.

The experimental standard reduction potentials for a $4f^n$ Ln^{3+} to $4f^{n+1}$ Ln^{2+} process for these three ions, −0.35, −1.15, and −1.55 V vs standard hydrogen electrode (SHE), respectively, Table 1 [3,4,14–22], reflected the greater stability of a half-filled shell over a filled shell and the least stabilization for Sm^{2+}, which only approached one of these favored electron configurations. This order of reduction potentials was also consistent with the fact that europium and ytterbium are the only lanthanides that give up just two electrons to the

TABLE 1 Estimated Ln^{3+}/Ln^{2+} Reduction Potentials (±0.2 V vs SHE) of Yttrium and the Lanthanides Based on Experimental and Spectroscopic Data [3,4,14–22]

Ln	Potential
Eu	−0.35
Yb	−1.15
Sm	−1.55
Tm	−2.3
Dy	−2.5
Nd	−2.6
Pm	−2.6
Lu	−2.72
Pr	−2.7
Y	−2.8
Ho	−2.9
Er	−3.1
La	−3.1
Ce	−3.2
Tb	−3.7
Gd	−3.9

electron sea in the metallic state and form +2 ions in the metal. The rest of the lanthanides form +3 ions in the metallic state. As a result, the density, melting points, enthalpies of sublimation, and metallic radii of Eu and Yb do not follow the periodic trends of the rest of the lanthanides series [23,24]. This affects all of the thermodynamic properties of these two elements. Since Eu and Yb are +2 in the metal, Eu^{2+} and Yb^{2+} were expected to be accessible ions in compounds. In contrast, compounds containing Sm^{2+} ions were regarded as unusual since samarium was known to be Sm^{3+} in the metal. Hence, Sm^{2+} was considered to define the furthest boundary of available +2 rare-earth metal chemistry. The reaction chemistry of these three ions also matched these standard redox values with Sm^{2+} being less stable, i.e., more reducing, than Yb^{2+}, which is a stronger reductant than Eu^{2+}. Since the calculated Ln^{3+}/Ln^{2+} reduction potentials in Table 1 [3,4,14] for all the other lanthanides were much more negative, it was believed that they would reduce solvents rather than exist in solution. The failed attempts to isolate complexes of these other +2 ions in solution were consistent with this idea for many years. However, it should be remembered that the conditions of standard reduction potentials rarely match those of actual reactions and redox potentials in specific reactions can vary significantly.

An important aspect in analyzing the new data in this chapter involves one of the structural characteristics of Eu^{2+}, Yb^{2+}, and Sm^{2+} complexes, namely that bond distances in their complexes could be estimated from analogous complexes of Ln^{3+} ions. Addition of the difference in generalized ionic radii between Ln^{2+} and Ln^{3+} ions to the distance in a +3 complex is a good predictor of the distance in a +2 complex [25–27]. This difference was typically as large as 0.16–0.19 Å for Eu^{2+}, Yb^{2+}, and Sm^{2+}. For example, the metal–(C_5Me_5 ring centroid) distances of $4f^6$ Sm^{2+} $(C_5Me_5)_2Sm(THF)_2$ [28] and its Ln^{3+} analog, i.e., $4f^5$ Sm^{3+} $[(C_5Me_5)_2Sm(THF)_2]^{1+}$ [29], are 2.42 and 2.60 Å, respectively. This is an increase of 0.18 Å for the Ln^{2+} complex. A regular relationship between ionic radius and bond distance is known from lanthanide to lanthanide [30,31] and also occurs between +2 and +3 oxidation states. This is consistent with the ionic nature of these complexes arising from the limited radial extension of the 4f orbitals [8].

2.2 Tm^{2+}, Dy^{2+}, and Nd^{2+} Complexes

Although Eu^{2+}, Yb^{2+}, and Sm^{2+} were the only known +2 lanthanide ions for many years, three additional Ln^{2+} ions subsequently were found in the solid state: Tm^{2+}, Dy^{2+}, and Nd^{2+} [2,5,13,32,33]. The $4f^4$ Nd^{2+} ion was identified in 1959 [34,35], $4f^{13}$ Tm^{2+} in 1960 [36], and $4f^{10}$ Dy^{2+} in 1966 [37]. These ions were found in compounds such as metal dihalides, LnX_2 (X = halide), that were synthesized by heating a 1:2 ratio of the elements to high temperature in tantalum crucibles. These compounds were salt-like $(Ln^{2+})(X^{1-})_2$ species analogous to SrX_2 and $PbCl_2$ [13,32,33]. The identification of these

Tm^{2+}, Dy^{2+}, and Nd^{2+} ions was also consistent with the calculated reduction potentials in Table 1 in that these were the next most likely lanthanide ions to exist in a +2 oxidation state.

Compounds with LnX_2 formulas were subsequently identified for other lanthanides, specifically for Ln = La, Ce, Pr, and Gd. However, they were found to be best described as $4f^n$ Ln^{3+} complexes with an electron in a delocalized band in the solid-state lattice formed by 5d orbitals, i.e., $(Ln^{3+})(X^{1-})_2(e^{1-})$ [5,13,32,33]. These compounds were black insoluble materials that were either metallic or semiconducting depending on the band gap associated with the delocalized electrons [38]. The isolation of these Ln^{3+} LnX_2 compounds suggested that even under the extreme reducing conditions of their preparation, a $4f^n$ Ln^{3+} ion with a delocalized electron in the lattice was preferable to a $4f^{n+1}$ Ln^{2+} ion. These compounds were taken as further evidence that only Eu, Yb, Sm, Tm, Dy, and Nd would form isolable compounds of +2 ions.

The discovery of molecular examples of Tm^{2+}, Dy^{2+}, and Nd^{2+} accessible in solution is described in detail in Chapter 246 [1] and in a review by Bochkarev [39], so it will only be summarized here. Initially, these three ions were only reported in solution as transient species observed by fleeting intense colors [1,17,39–43]. These colors were thought to arise from Laporte allowed transitions from the 4f ground state to 5d orbitals [44,45] that had energies around 20,000–30,000 cm^{-1} according to atomic spectra of the Ln^{2+} ions [46–48]. The bleaching of this intense color was consistent with conversion to Ln^{3+} species that are pale in color since the electric dipole components of 4f–4f transitions are Laporte forbidden and the limited radial extension of the 4f orbitals minimizes orbital mixing that could relax the selection rule. Since the 5d orbitals for Ln^{3+} ions, except for Ce^{3+}, are typically around 40,000–50,000 cm^{-1} above the 4f ground state [46–48], the 4f–5d transitions are out of the visible region. The transient nature of the colors of these three ions was consistent with the expected limited stability of these species in solution and their capacity to decompose solvents due to their very negative calculated reduction potentials, Table 1.

As pointed out by Nief in his review [1], reports of Tm^{2+} being stable in THF were in the literature as early as 1983 [43] along with an isolated compound formulated as TmI_2(18-crown-6) [49]. However, definitive X-ray crystallographic data were not obtained to substantiate the claim.

In 1997–2000, the situation changed significantly when Bochkarev and coworkers discovered syntheses of solvated diiodides of Tm^{2+}, Dy^{2+}, and Nd^{2+} that could be characterized by X-ray crystallography [39,50–53], Scheme 1. These results demonstrated that Tm^{2+}, Dy^{2+}, and Nd^{2+} could be obtained in molecular species in solution. This subsequently led to an extensive effort to characterize the solution chemistry of these ions as described in Chapter 246 [1]. As in the case of Eu^{2+}, Yb^{2+}, and Sm^{2+}, the chemistry of Tm^{2+}, Dy^{2+}, and Nd^{2+} followed the calculated potentials

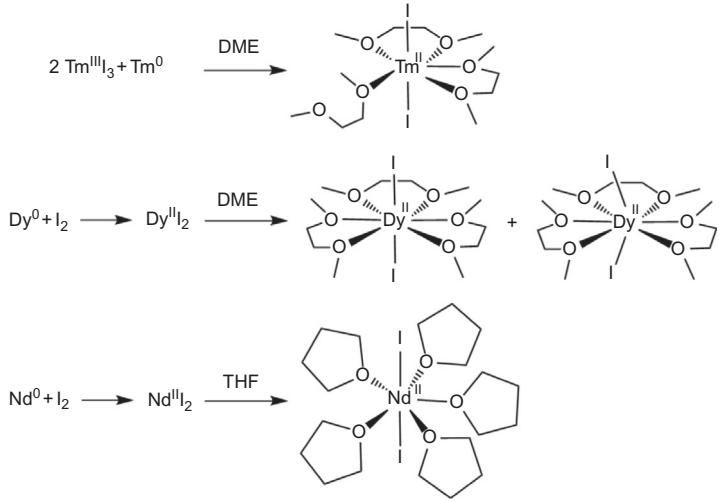

SCHEME 1 Syntheses of $TmI_2(DME)_3$, $DyI_2(DME)_3$, and $NdI_2(THF)_5$.

given in Table 1, i.e., Nd^{2+} is more reducing than Dy^{2+}, which is more reducing than Tm^{2+}, and all three are more reactive than Sm^{2+}. This was further evidence that led to confidence in the reduction potentials listed in Table 1.

2.3 Ln^{3+}/Ln^{2+} Reduction Potentials

It should be pointed out that reduction potentials in Table 1 are not the only literature estimates for the lanthanides. The values listed in Table 1 in the reviews by Morss [3,4] originated from a correlation developed by Nugent and coworkers [14,15] that related the experimental redox potentials known for Eu^{2+}, Yb^{2+}, and Sm^{2+} to the predicted values for the other ions in Table 1. The relationship involved effective nuclear charge, Racah crystal field parameters, spin–orbit coupling parameters, and f–d absorption energies for the Ln^{3+} ions [14,15]. The estimated error of these calculated values was ± 0.2 V. The 1976 Morss review [3] also contained two other series of calculated redox potentials that were based on thermodynamic cycles [16]. These are shown in Table 2. Each of these series had a slightly different ordering for the elements beyond Nd, but, in general, each showed that all the other Ln^{2+} ions would be much more reducing than the traditional six divalent ions, Eu^{2+}, Yb^{2+}, Sm^{2+}, Tm^{2+}, Dy^{2+}, and Nd^{2+}.

A rather different set of redox potentials was also in the literature from Mikheev, Kamenskaya, and coworkers [17–21], Table 2. These potentials were based on correlations obtained from molten salt chemistry. Although these values matched the order for the first six elements in Table 1, the potentials for Er, La, Ce, Tb, and Gd were less negative than the other predictions. None of the estimates for these metals were more negative than

TABLE 2 Estimated Ln^{3+}/Ln^{2+} Reduction Potentials (V vs SHE) Based on Thermodynamic [3,16] and Molten Salt Data [17–21] Listed in the Order of Table 1

Ln	Thermodynamic Estimate [3]	Thermodynamic Estimate [16]	Molten Salt Data [17–21]
Eu	−0.35	−0.35	−0.34
Yb	−1.04	−1.1	−1.18
Sm	−1.57	−1.5	−1.50
Tm	−2.27	−1.57	−2.22
Dy	−2.42	−2.6	−2.56
Nd	−2.62	−2.8	−2.62
Pm	−2.67	−2.5	−2.44
Lu			−2.72
Pr	−3.03	−3.0	−2.84
Ho	−2.80	−2.9	−2.79
Er	−2.96	−3.0	−2.87
La	−3.74	−3.8	−2.94
Ce	−3.76	−3.5	−2.92
Tb	−3.47	−3.5	−2.83
Gd	−3.82	−3.6	−2.85

−2.95 V vs SHE compared to values of −3.1 to −3.9 V vs SHE in Table 1. Error limits were estimated to be ±0.01–0.08 V. Although the connection between these molten salt data and solution data was unclear [4], this also showed that Eu, Yb, Sm, Tm, Dy, and Nd had the most accessible Ln^{2+} ions.

Although the various estimates of Ln^{3+}/Ln^{2+} reduction potentials did not agree beyond the first six traditional Ln^{2+} ions [22], they all led to the belief that the +2 ions of La, Ce, Pr, Gd, Tb, Ho, Er, and Lu would be too reactive to isolate in molecular species. It was expected that Ln^{2+} ions of these metals would only be accessible transiently under special conditions. Such species had been reported in gas-phase atomic spectra [47,54], in ion cyclotron resonance studies [55–58], in spectroscopic studies of Ln^{3+} ions doped into CaF_2 and treated with gamma radiation [59], and in electrochemical experiments in molten salts [17–21,60,61] and THF [62]. However, these ions were not expected to be accessible in soluble, crystallographically characterizable molecular complexes.

3 REDUCTION OF DINITROGEN

3.1 Reduction of N_2 by Tm^{2+}, Dy^{2+}, and Nd^{2+} Complexes

An integral part of the discovery of new oxidation states for the lanthanides described in this chapter involves dinitrogen reduction chemistry and the lanthanide diiodides of Tm, Dy, and Nd discussed above. Attempts to make amide, aryloxide, and cyclopentadienide derivatives of the molecular diiodides of Tm^{2+}, Dy^{2+}, and Nd^{2+} led to the reduction of dinitrogen rather than the synthesis of new Ln^{2+} complexes [63–66]. This was surprising since the only previous examples of lanthanide-based reduction of dinitrogen involved rather special complexes.

The first example of lanthanide-based dinitrogen reduction was observed with Sm^{2+} in the bent metallocene complex, $(C_5Me_5)_2Sm$, Scheme 2 [67]. In this case, the Sm^{2+} complex was barely able to reduce dinitrogen and formed an equilibrium mixture from which both $(C_5Me_5)_2Sm$ and $[(C_5Me_5)_2Sm]_2(\mu\text{-}\eta^2\text{:}\eta^2\text{-}N_2)$ could be cocrystallized.

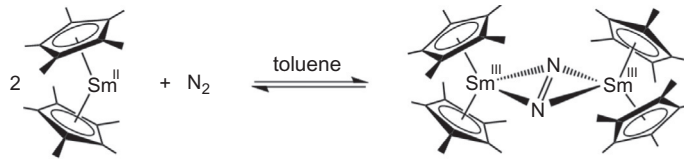

SCHEME 2 Reduction of N_2 by Sm^{2+}.

Subsequent examples with samarium involved chelating octaethylporphyrinogen and dipyrrolide ligands and resulted in complicated polymetallic structures containing two to four samarium atoms and as many as six lithium ions [68–71]. Reduced dinitrogen complexes were also obtained from sodium naphthalenide and octaethylporphyrinogen complexes of Pr and Nd [72], which suggested that these chelating porphyrinogen ligands were especially effective in this type of reaction.

The range of lanthanide-based dinitrogen reduction chemistry expanded greatly when the synthesis of new Ln^{2+} complexes was attempted by addition of reagents such as KC_5Me_5 [63], $KC_5H_4SiMe_3$ [63], $KC_5H_3(SiMe_3)_2$ [63,64], $NaN(SiMe_3)_2$ [65], and $KOC_6H_3{}^tBu_2$ [65,66] to TmI_2, DyI_2, and NdI_2. These reactions did not lead to substitution of the iodides and new Ln^{2+} complexes, but instead generated complexes of $(N{=}N)^{2-}$ [63–66], Scheme 3, and $(N_2)^{3-}$ [66] with a broad range of common ligands.

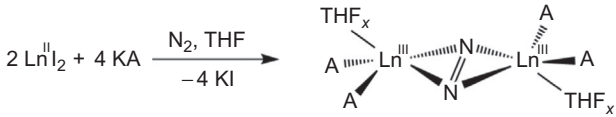

Ln = Tm, Dy, Nd

A = C_5Me_5, $C_5H_4SiMe_3$, $C_5H_3(SiMe_3)_2$, $N(SiMe_3)_2$, $OC_6H_3{}^tBu_2$-2,6; x = 0–1

SCHEME 3 Reduction of N_2 to $(N{=}N)^{2-}$ by Tm^{2+}, Dy^{2+}, and Nd^{2+}.

In retrospect, since Sm^{2+} can reduce N_2 [67], Scheme 2, and the Tm^{2+}, Dy^{2+}, and Nd^{2+} ions are more reducing than Sm^{2+}, Table 1, this may not seem surprising. However, it was not obvious at the time that the reactions in Scheme 3 should occur, since the Scheme 2 reaction involved only an equilibrium with an unusually bent metallocene complex and the porphyrinogen- and dipyrrolide-based dinitrogen reduction reactions involved special types of chelating ligands [68–72].

The results in Scheme 3 provided another likely explanation for the "instability" of the Tm^{2+}, Dy^{2+}, and Nd^{2+} ions in solution: dinitrogen is not an inert atmosphere for these species. It is likely that in some of the early attempts to make complexes of these ions, the fleeting colors described in the literature arose because the Ln^{2+} complexes were reducing N_2 to make pale-colored Ln^{3+} complexes of $(N{=}N)^{2-}$!

3.2 Reduction of N_2 by LnA_3/M Methods

The pathway to new Ln^{2+} ions developed further through attempts to synthesize the new reduced dinitrogen complexes shown in Scheme 3 by alternative, more facile means. Since the LnI_2 complexes are stable under N_2, it was postulated that the dinitrogen reduction in Scheme 3 occurred through "LnA_2" or "$KLnA_3$" intermediates in which anion A was an amide, aryloxide, or cyclopentadienide anion. It seemed possible that these "LnA_2" or "$KLnA_3$" intermediates could be formed by reduction of a Ln^{3+} precursor, i.e., LnA_3, by alkali metal reduction, Scheme 4.

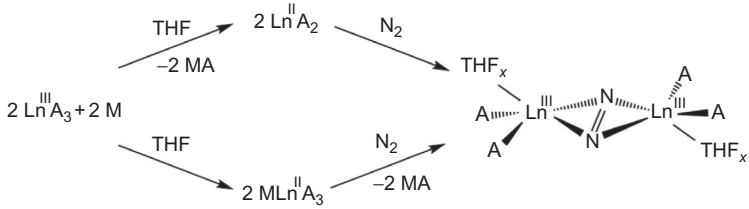

Ln = Sc, Y, La, Ce, Pr, Nd, Gd, Tb, Dy, Ho, Er, Tm, Lu
A = $N(SiMe_3)_2$, $OC_6H_3{}^tBu_2$-2,6, C_5Me_5, C_5Me_4H, $C_5H_2{}^tBu_3$
M = K, KC_8, Na; x = 0–2

SCHEME 4 Reduction of N_2 to $(N{=}N)^{2-}$ by the LnA_3/M reaction.

The approach in Scheme 4 was an established route to Ln^{2+} complexes [73] as shown in 1969 by the reduction of $(C_5H_5)_3Sm$ with K to make the insoluble $[(C_5H_5)_2Sm(THF)_x]_n$ complex, Scheme 5 [74]. Since the LnA_3 precursors are prepared readily from $LnCl_3$, and the preparation of DyI_2 and NdI_2 requires

$$(C_5H_5)_3Sm^{III} \xrightarrow[-KC_5H_5]{K,\ THF} [(C_5H_5)_2Sm^{II}(THF)_x]_n$$

SCHEME 5 $(C_5H_5)_3Sm$/K reaction to form a Sm^{2+} complex.

temperatures of 500°C and a quartz furnace to prepare the compounds from the elements in a melt of LnI_2 [51,75], reduction of LnA_3 precursors would be a less difficult route to the "Ln^{2+}" intermediates.

Since the LnA_3 amides with $A = N(SiMe_3)_2$ were readily available from $LnCl_3$ [76], the synthesis of reduced dinitrogen complexes by reduction of Ln $[N(SiMe_3)_2]_3$ with alkali metals under N_2 was attempted. Success was achieved with Ln = Tm, Dy, and Nd, using potassium, potassium graphite, and sodium, and this provided a much more facile route to the $(N{=}N)^{2-}$ complexes, such as $\{[(Me_3Si)_2N]_2(THF)Ln\}_2(\mu\text{-}\eta^2{:}\eta^2\text{-}N_2)$, Scheme 6 (Ln = Tm, Dy, Nd) [77].

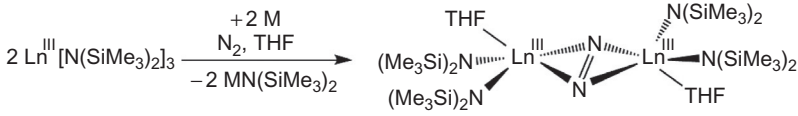

SCHEME 6 $Ln[N(SiMe_3)_2]_3$/M reduction of N_2 to $(N{=}N)^{2-}$.

Although the reduced dinitrogen complexes could be obtained by this route, no dark transient colors appropriate for a "$Ln[N(SiMe_3)_2]_2$" [78] or "$KLn[N(SiMe_3)_2]_3$" [79,80] intermediate were observed [77]. To examine the viability of a Ln^{2+} intermediate, an analogous reaction with holmium, a metal for which a Ln^{2+} ion was not known in solution, was attempted. Holmium was chosen since it is similar in size and reduction potential to Dy and Tm. Surprisingly, the reaction of $Ho[N(SiMe_3)_2]_3$ with potassium graphite under N_2 also made a reduced dinitrogen complex, $\{[(Me_3Si)_2N]_2(THF)\text{-}Ho\}_2(\mu\text{-}\eta^2{:}\eta^2\text{-}N_2)$, Scheme 6 (Ln = Ho) [77]. Other lanthanide metals were examined and crystallographically characterizable reduced dinitrogen complexes were obtained in the $Ln[N(SiMe_3)_2]_3$/M reaction with Ln = Er, Tb, Gd, Y, and Lu according to Scheme 6 with M = K, KC_8, and Na [81].

Similar reactions appeared to occur with Ln = La, Ce, and Pr in Scheme 6, but crystallographically characterizable $\{[(Me_3Si)_2N]_2(THF)Ln\}_2(\mu\text{-}\eta^2{:}\eta^2\text{-}N_2)$ complexes were not obtained with these larger metals. To determine if this was only a problem of crystallization with these large metals, reductions of a different trivalent system with larger ligands were explored. Reduction of $(C_5Me_4H)_3Ln$ with K under N_2 with Ln = La, Ce, and Pr provided crystals of $[(C_5Me_4H)_2(THF)Ln]_2(\mu\text{-}\eta^2{:}\eta^2\text{-}N_2)$ according to Scheme 7 [82,83]. This confirmed that this type of dinitrogen reduction reaction could be accomplished with these larger metals as well.

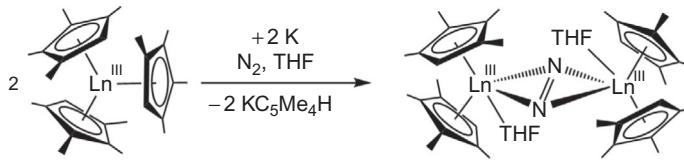

SCHEME 7 $(C_5Me_4H)_3Ln$/K reduction of N_2 to $(N{=}N)^{2-}$.

Reactions of the type shown in Schemes 6 and 7 proved to be quite general [77,81–93]. Since the mechanism of the reaction and the intermediacy of Ln^{2+} species were unknown, this type of reaction was simply called LnA_3/M (A = anion; M = alkali metal) as a way to designate this reduction technique. This was not a new reaction type, since reduction of LnA_3 with alkali metals had been studied as early as the days of Wöhler [13,73,94] and had been used to make complexes of Ln^{2+} as shown in Scheme 5 [74]. These LnA_3/M reactions were also successful with heteroleptic LnA_2A' precursors, Scheme 8 [83,85,88–91]. This method proved to be useful in preparing numerous examples of reduced dinitrogen complexes of the rare-earth metals.

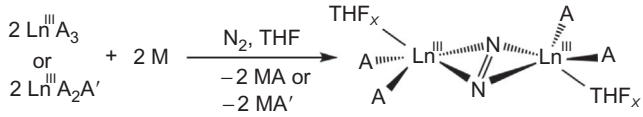

Ln = Sc, Y, La, Ce, Pr, Nd, Gd, Tb, Dy, Ho, Er, Tm, Lu
A = $N(SiMe_3)_2$, $OC_6H_3{}^tBu_2$-2,6, C_5Me_5, C_5Me_4H, $C_5H_4SiMe_3$, $C_5H_2{}^tBu_3$
A′ = BPh_4, I, H; M = K, KC_8, Na; x = 0–2

SCHEME 8 The generality of the LnA_3/M and LnA_2A'/M reductions of N_2 to $(N{=}N)^{2-}$.

Although it was conceivable that these LnA_3/M and LnA_2A'/M reactions could occur via Ln^{2+} intermediates for Ln = Tm, Dy, Nd, there was no spectroscopic evidence for such species. On the basis of the redox potentials in Table 1, Ln^{2+} intermediates were also possible for Pr, Y, Ho, and Lu, but Ln^{2+} intermediates for Ln = Er, La, Ce, Tb, and Gd seemed much less likely since these metals had calculated reduction potentials of −3.1 to −3.9 V vs SHE according to Table 1. These reactions should not be possible with potassium, which has a K^+/K reduction potential of −2.9 V vs SHE. Interestingly, the alternative set of molten salt redox potentials published by Mikheev and Kamenskaya, Table 2 [17–21], for these metals were between −2.79 and −2.94 V vs SHE. This would make reduction to Ln^{2+} in the range accessible with potassium. However, since these dinitrogen reduction reactions could also be accomplished with sodium (Na^+/Na −2.7 V vs SHE), a Ln^{2+} pathway seemed less likely. As noted above, the conditions of these standard reduction potentials generally do not match those of actual reactions such that redox potentials in specific reactions can vary significantly from these values. Various mechanisms which did not involve Ln^{2+} ions of these metals were considered, but as stated in Chapter 246 of this Handbook, "the mechanism is unsettled" [1].

The mechanism of the $Ln[N(SiMe_3)_2]_3/K$ reaction was probed by conducting reactions under argon in attempts to isolate Ln^{2+} complexes such as "$Ln[N(SiMe_3)_2]_2$" [78] or "$KLn[N(SiMe_3)_2]_3$" [79,80]. This proved

difficult. The only isolated product was typically just the starting material, $Ln[N(SiMe_3)_2]_3$. However, by careful choice of conditions, an EPR spectrum consistent with a complex of Y^{2+} was obtained from a $Y[N(SiMe_3)_2]_3/K$ reaction at −35°C, Fig. 1 [93]. A two-line hyperfine pattern with $g = 1.976$ and $A = 110$ G was observed at room temperature that was consistent with $4d^1$ Y^{2+} due to the 100% naturally abundant ^{89}Y nucleus, which has a nuclear spin of 1/2.

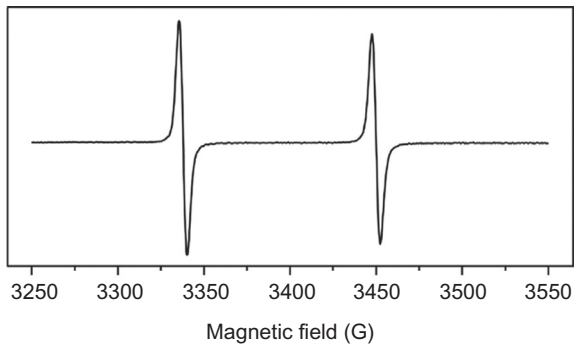

FIG. 1 EPR spectrum in THF of a transient Y^{2+} species from the reduction of $Y[N(SiMe_3)_2]_3$ by potassium. *Adapted with permission from M. Fang, D.S. Lee, J.W. Ziller, R.J. Doedens, J.E. Bates, F. Furche, W.J. Evans, Synthesis of the $(N_2)^{3-}$ radical from Y^{2+} and its protonolysis reactivity to form $(N_2H_2)^{2-}$ via the $Y[N(SiMe_3)_2]_3/KC_8$ reduction system, J. Am. Chem. Soc. 133 (2011) 3784–3787, © 2011, American Chemical Society.*

4 La^{2+} AND Ce^{2+} COMPLEXES

LnA_3/M reactions were also conducted by Lappert and coworkers starting in 1995 [95–103], not to find new routes to reduced dinitrogen complexes as described in Section 3, but rather to synthesize complexes of Ce^{2+} and Nd^{2+} along the traditional lines shown in Scheme 5 for Sm^{2+}. The cerium and neodymium ions were targets because of earlier reports in the literature of a single example of a Ce^{2+} complex, $[K(monoglyme)]_2[(C_8H_8)_2Ce]$, in 1976 [104] and one Nd^{2+} complex, $[K(THF)_n][(C_5Me_5)_2NdCl_2]$, in 1990 [105,106]. Neither of these complexes was characterized by X-ray crystallography. As will be described in this section, Lappert's studies provided more information about reductive rare-earth metal chemistry in a variety of ways.

4.1 Dimethoxyethane Cleavage Reactions

When the LnA_3/M reactions were conducted with $A = C_5H_3(SiMe_3)_2$ (Cp″), M = Li, and Ln = Ce and Nd in the presence of dimethoxyethane, $MeOCH_2CH_2OMe$ (DME), cleavage of the ether solvent was observed. Ln^{3+} methoxide products $[Cp''_2Ln(\mu\text{-}OMe)]_2$, Scheme 9, and $Cp''_2Ln(\mu\text{-}OMe)_2M(DME)$ were obtained [95]. These Ln^{3+} methoxide products

were attributed to the decomposition of DME by transient $[M(DME)_n]$-$[Cp''_3Ln]$ or Cp''_2Ln intermediates. This was consistent with the reduction potentials in Table 1 and the idea that Ln^{2+} complexes of these metals were too reducing to survive in solvent. No evidence of the intermediates was observed in these cases.

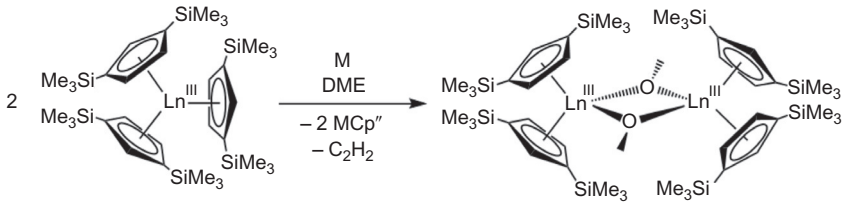

SCHEME 9 Cleavage of $MeOCH_2CH_2OMe$ (DME) in Cp''_3Ln/K reactions.

This Ce and Nd research was extended to La with K as the reducing agent and a similar methoxide product was identified. However, in the Ln = La version of this reaction, an EPR spectrum of a dark blue intermediate was obtainable. The solution displayed two eight-line patterns, Fig. 2 [97], at $g = 1.969(8)$ and $1.971(8)$, with different hyperfine coupling constants, $A = 136$ and 146 gauss, respectively, that were much larger than earlier reports of A values of La^{3+} complexes of radical ligands [107]. Since La has a nuclear spin of 7/2, this was consistent with La^{2+} in solution. Later studies showed four different species in solution [99].

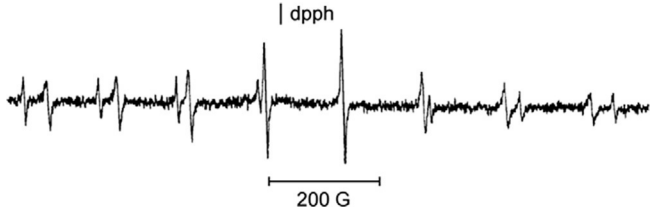

FIG. 2 EPR spectrum at 295K of transient La^{2+} species formed from Cp''_3La/K reactions. *Adapted with permission from M.C. Cassani, M.F. Lappert, F. Laschi, First identification by EPR spectra of lanthanum(II) organometallic intermediates (and $E_{½}$ for $La^{3+} \rightarrow La^{2+}$) in the C–O bond activation of dimethoxyethane, Chem. Commun. (1997) 1563–1564, © 1997, Royal Society of Chemistry.*

4.2 Arene Reduction Reactions

Studies of Cp''_3Ln reduction in the presence of arenes led to reduced arene complexes. Reduction with excess potassium in C_6H_6 formed the monometallic Ln^{3+} $(C_6H_6)^{2-}$ complexes, $[K(18\text{-crown-}6)][(C_6H_6)LnCp''_2]$ (Ln = La, Ce, Pr, Nd), Scheme 10 [96,99].

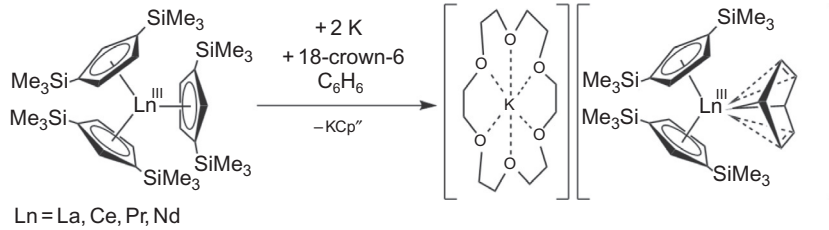

SCHEME 10 Formation of $(C_6H_6)^{2-}$ complexes from Cp''_3Ln/K reactions.

Extension of this reaction chemistry from the silyl-substituted $[C_5H_3(SiMe_3)_2]^{1-}$ ligand to the carbon analog, $[C_5H_3(CMe_3)_2]^{1-}$ $[Cp^{tt} = C_5H_3(CMe_3)_2]$, gave less stable species. However, in a small variation from Scheme 10 with 1.5 equivalents of K rather than a large excess, a bimetallic complex of formula $\left[K(18\text{-crown-6}]\left[\left(Cp^{tt}_2La\right)_2(C_6H_6)\right]\right.$ was obtained, Scheme 11 [98].

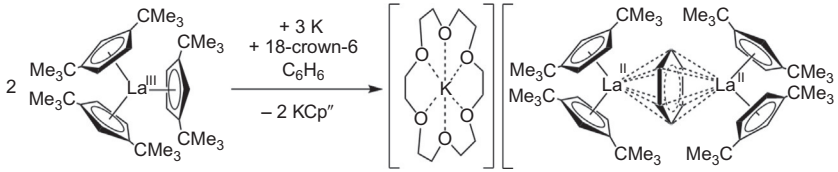

SCHEME 11 Formation of a $(C_6H_6)^{1-}$ complex from a Cp^{tt}_3La/K reaction.

This compound was postulated to be a La^{2+} complex of a $(C_6H_6)^{1-}$ bridging ligand rather than a La^{3+} complex of $(C_6H_6)^{3-}$. Similar reactions with the silyl analogs, Cp''_3Ln (Ln = La, Ce), in toluene were reported to form $(C_6H_5CH_3)^{1-}$ complexes although good structural data were not obtained [98,100]. The known difficulty in assigning oxidation states in bridging arene systems [108–116] and the disorder in the crystal structure complicated the assignments until unambiguous examples of La^{2+} were found as described in the next section. In a further variation with $(C_5H_4SiMe_2{}^tBu)_3Ln$ precursors in toluene, a tris(cyclopentadienyl) Ln^{3+} hydride product, $[K(18\text{-crown-6})(\text{toluene})_2]\{[(C_5H_4SiMe_2{}^tBu)_3Ln]_2(\mu\text{-H})\}$, with a potassium 18-crown-6 cation with two toluene ligands was found, Scheme 12 [100].

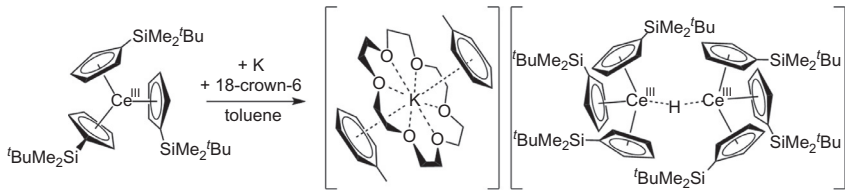

SCHEME 12 Formation of a hydride complex from a $(C_5H_4SiMe_2{}^tBu)_3Ce/K$ reaction.

4.3 An Unambiguous La^{2+} Complex

In 2008, further studies of the reduction of Cp''_3La, in diethyl ether with 18-crown-6 and in THF with 2.2.2-cryptand, provided crystal structures of reduced complexes free of redox-ambiguous ligands. Charge balance was consistent with the existence of La^{2+} ions in the molecular complexes, [K(18-crown-6)(OEt$_2$)][Cp''_3La] and [K(2.2.2-cryptand)][Cp''_3La], Scheme 13 [102]. A cerium complex was also crystallized that contained an extra Ce^{3+} Cp''_3Ce unit in addition to the Ce^{2+} $\left(Cp''_3Ce\right)^{1-}$ anion, Scheme 13.

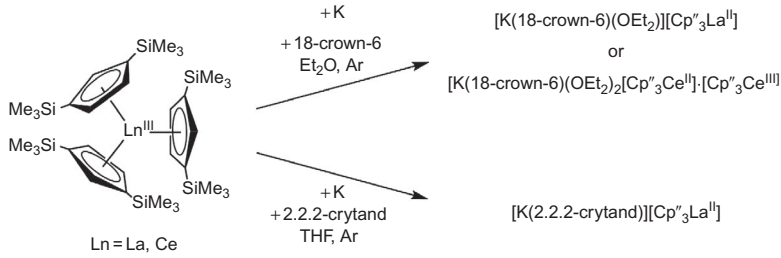

SCHEME 13 Formation of La^{2+} and Ce^{2+} complexes from Cp''_3Ln/K reactions.

Since crystallographic disorder had complicated the structural analysis of [K(18-crown-6)][($Cp''_2^{tt}La$)$_2$(C_6H_6)] described above, the lanthanum structures in Scheme 13 provided the first chance to assess bond distances in an unequivocal La^{2+} complex. The structure of the $\left(Cp''_3La\right)^{1-}$ anion was unusual in that the 2.632 Å La–(ring centroid) distance was only slightly longer than the analogous length in the Ln^{3+} complex, Cp''_3La, 2.600 Å [102]. This was significantly different than the 0.16–0.19 Å differences that were previously observed between $4f^n$ Ln^{3+} and $4f^{n+1}$ Ln^{2+} complexes as described in Section 2.1 and led to skepticism about the presence of La^{2+}.

The small difference in bond distance from La^{3+} to La^{2+} was rationalized in the following way: because lanthanum was the first element in the lanthanide series where the 4f and 5d orbital energies are similar [46–48,54,117], La^{2+} was assigned to be a $5d^1$ ion not a $4f^1$ ion [102]. Since transition metal complexes do not show such a large change in radius with oxidation state as the lanthanides [102], this small difference in distances was reasonable for a $5d^1$ ion. For example, Cp_2TiCl_2 [118] and [$Cp_2Ti(\mu\text{-}Cl)]_2$ [119] have average Ti–C(Cp) bond lengths of 2.370 and 2.350 Å, respectively. Similarly, Cp_4Zr [120] and Cp_3Zr [121] both have the same average Zr–C(Cp) bond length of 2.58 Å. The $5d^1$ configuration was also consistent with the EPR spectrum for this complex.

5 AN Y^{2+} COMPLEX

The isolation of an Y^{2+} complex arose by comparison of the data in Sections 3 and 4. The LnA_3/M reactions in Section 3 consistently gave reduced dinitrogen complexes, $[A_2Ln(THF)]_2(\mu\text{-}\eta^2\text{:}\eta^2\text{-}N_2)$, Scheme 8, possibly through Ln^{2+} intermediates. However, no N_2 reduction was reported for the isolated La^{2+} complex $[K(18\text{-crown-}6)(OEt_2)][Cp''_3La]$ [102]. After Professor Lappert's retirement, an attempt to prepare this complex independently was made to determine if it would reduce dinitrogen [122]. It was found that $[K(18\text{-crown-}6)(OEt_2)][Cp''_3La]$ did not reduce dinitrogen. Moreover, as shown in Scheme 14, this La^{2+} complex could even be prepared under N_2 by an LnA_3/M reaction [122]. This seemed strange because of all the LnA_3/M reactions in Section 3.2 that led to reduced dinitrogen products. In addition, reduction of a different tris(cyclopentadienyl)*lanthanum* complex, namely, $La(C_5Me_4H)_3$, with potassium graphite (KC_8) in a LnA_3/M reaction provided a reduced dinitrogen complex, $[(C_5Me_4H)_2(THF)La]_2(\mu\text{-}\eta^2\text{:}\eta^2\text{-}N_2)$ [82,83], Scheme 7. A lanthanum complex of $(N{=}N)^{2-}$ could also be made by reduction of the La^{3+} complex, $(C_5Me_5)_2La(\mu\text{-}Ph)_2BPh_2$, in a LnA_2A'/M reaction [82], Scheme 14.

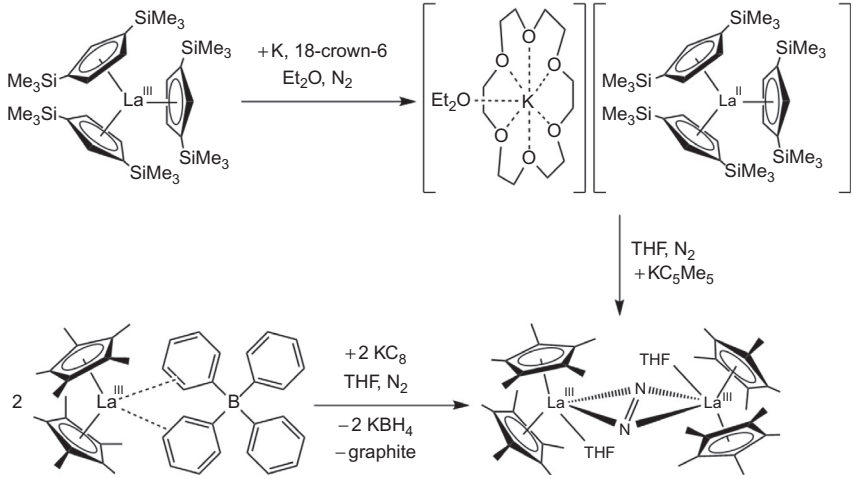

SCHEME 14 Ligand dependence of the reactivity of lanthanum complexes with N_2.

Clearly the substitution of the cyclopentadienyl rings made a big difference in reactivity in terms of reduction of dinitrogen vs formation of a La^{2+} complex. To probe this further, KC_5Me_5 was added to $[K(18\text{-crown-}6)(OEt_2)][Cp''_3La]$ and it was found that the $(N{=}N)^{2-}$ complex $[(C_5Me_5)_2(THF)La]_2(\mu\text{-}\eta^2\text{:}\eta^2\text{-}N_2)$ was formed, Scheme 14 [122]. In this reaction, a La^{2+} ion reduces N_2, but only in the presence of $(C_5Me_5)^{1-}$ ligands.

These results indicated that some ligands, e.g., $[N(SiMe_3)_2]^{1-}$, $(C_5Me_5)^{1-}$, and $(C_5Me_4H)^{1-}$, were good for N_2 reduction, while others, e.g., $[C_5H_3(SiMe_3)_2]^{1-}$, were better for isolating Ln^{2+} complexes.

This suggested that the $Ln[N(SiMe_3)_2]_3/K$ reduction system that gave the EPR spectrum for Y^{2+}, Fig. 1 [93], should be revisited with the Lappert silylcyclopentadienyl ligand, $[C_5H_3(SiMe_3)_2]^{1-}$ (Cp″) [95–103,123]. As this project was developing and $(C_5H_4SiMe_3)^{1-}$ (Cp′) was synthesized as the precursor to Cp″, it was decided to try the reaction with Cp'_3Y rather than with Cp''_3Y. This "shortcut" proved to be an excellent decision since subsequent attempts to make $\left(Cp''_3Ln\right)^{1-}$ complexes of the smaller lanthanides later in the series gave much less stable complexes [124].

Examination of a LnA_3/M reaction with A = Cp′ allowed the isolation of the first crystallographically characterizable complex of Y^{2+}, [K(18-crown-6)][Cp'_3Y], Scheme 15 (Ln = Y) [122]. The complex had an intense dark color and a two-line $g = 1.991$ EPR spectrum similar to Fig. 1 of the $Y[N(SiMe_3)_2]_3/K$ reaction product [93], but with $A = 36.6$ G. The difference between Y–(ring centroid) distances for the Y^{2+} and Y^{3+} complexes, 0.031 Å, was small like that in the La^{2+} case [102]. However, since Y^{2+} is necessarily a $4d^1$ ion and not a $4f^n$ system, this was consistent with small changes in distances between ions with d electron configurations in different oxidation states [102,118–121].

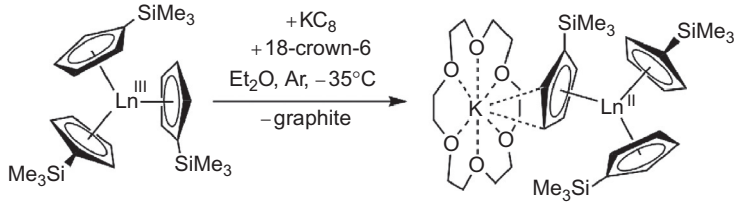

SCHEME 15 Formation of Ln^{2+} complexes from Cp'_3Ln/K reactions in the presence of 18-crown-6.

6 Ho^{2+} AND Er^{2+} COMPLEXES

The crystallographic identification of the first molecular complex of Y^{2+} did not immediately imply that this oxidation state would be available to all the lanthanide metals. Complexes of $4f^0$ Y^{3+} are similar to those of the late $4f^n$ Ln^{3+} lanthanide ions because yttrium has a similar size to those metals and Ln^{3+} chemistry is not affected by the $4f^n$ electron configuration due to the limited radial extension of the 4f orbitals. This similarity would not apply to the $4d^1$ Y^{2+} ion. The $5d^1$ configuration postulated for La^{2+} was expected to be possible only at the beginning of the lanthanide series where 4f and 5d orbitals are close in energy [46–48,54,117]. Hence, the decision to examine the yttrium chemistry in Scheme 15 with holmium was a severe test of the

similarity of yttrium to the late lanthanides and there was no particular expectation that analogous chemistry would be observed.

However, examination of the reaction in Scheme 15 with Ln = Ho produced an analogous complex, [K(18-crown-6)][Cp'_3Ho], the first crystallographically characterizable example of a Ho^{2+} complex [125]. The holmium complex was isomorphous with the yttrium compound [122] and again a small difference, 0.032 Å, was observed between the Ln–(ring centroid) distances of this Ho^{2+} complex and its Ho^{3+} analog, Cp'_3Ho. This was unusual because reduction of $4f^{10}$ Ho^{3+} would be expected to form $4f^{11}$ Ho^{2+} and this ion would be expected to be 0.16–0.19 Å larger than $4f^{10}$ Ho^{3+}. A surprising result was also found via Scheme 15 with Ln = Er: an analogous [K(18-crown-6)][Cp'_3Er] complex could be crystallographically defined even though the calculated Er^{3+}/Er^{2+} reduction potential of −3.1 V vs SHE, Table 1, was more negative than the −2.9 V value for K^+/K. Again the difference in bond distances between this first Er^{2+} complex and its Er^{3+} analog, Cp'_3Er, was small, 0.030 Å [125].

The discovery of the three new oxidation states for Y, Ho, and Er in Scheme 15 may look simple in retrospect. However, it should be realized that these results were possible because all of the chemical manipulations were done at −40°C or below using Schlenk techniques [122,125]. In each case, the Cp'_3Ln starting material, potassium graphite, and 18-crown-6 were placed in a Schlenk flask fitted with an inverted low-temperature Schlenk filter funnel and a receiving flask. The flask containing the starting materials was cooled in an acetonitrile slush bath (−40 to −45°C) and the reaction occurred upon vacuum transfer of Et_2O onto the reagents. After the reaction was over, the apparatus was inverted into a Dewar containing an acetonitrile slush bath so the graphite could be filtered at low temperature. The cold filtrate was pulled into the receiver flask chilled in an acetonitrile slush bath and the filter was detached. The product was crystallized by concentrating the solution by removal of Et_2O, addition of pentane, and cooling to −78°C. Hence, these complexes were not likely to be found by conducting reactions at ambient temperature.

7 Pr^{2+}, Gd^{2+}, Tb^{2+}, AND Lu^{2+} COMPLEXES

Once complexes of Ho^{2+} and Er^{2+} were identified, it was of interest to see if this applied to all the metals in the lanthanide series. The tedious Schlenk preparation of these complexes was replaced by a new method that involved a flash reduction column that allowed the low-temperature reaction to be performed completely in a glovebox [125]. In this method, a concentrated solution of Cp'_3Ln and 18-crown-6 in Et_2O was chilled to −35°C in the glovebox freezer. A $1 \times 10\ cm^2$ chromatography column with a filter frit at the bottom was packed with potassium graphite and chilled to −35°C in the glovebox freezer. Passing the Et_2O solution through the column at the proper rate produced a concentrated solution of product below the filter frit which was collected in a chilled flask placed in a bath of cold hexane chilled to

–35°C in the glovebox freezer. This allowed the complexes to be prepared in a much shorter time and immediately put into the glovebox freezer for crystallization.

When this new flash reduction technique was used for a Cp'_3Tb/K reaction, the first example of a Tb^{2+} complex was obtained, Scheme 16 [126]. The terbium reaction differed from those in Scheme 15 in that the countercation was not $[K(18\text{-crown-6})]^{1+}$. In the terbium case, the product had an inverse cyclopentadienyl sandwich cation, $\{[K(18\text{-crown-6})]_2(\mu\text{-}Cp')\}^{1+}$, that was not located close to the $\left(Cp'_3Tb\right)^{1-}$ anion (Scheme 16).

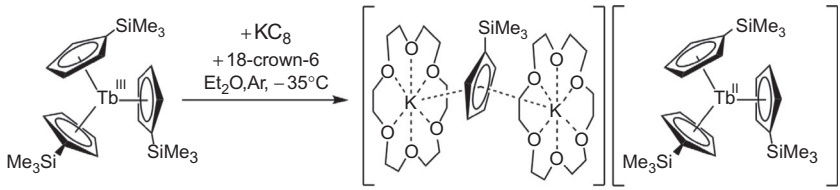

SCHEME 16 Synthesis of a Tb^{2+} complex.

The terbium crystal structure was important in that it demonstrated that $[K(18\text{-crown-6})]^{1+}$ was not essential for isolating these new Ln^{2+} complexes. Consequently, an alternative reagent for chelating potassium was examined, namely the 2.2.2-cryptand employed earlier by Lappert, Scheme 13 [102]. Using this cryptand with the flash reduction technique led to new examples of Y^{2+}, Ho^{2+}, Er^{2+}, and Tb^{2+} complexes, $[K(2.2.2\text{-cryptand})][Cp'_3Ln]$, Scheme 17 [126]. Moreover, it was found that these new compounds were not as temperature sensitive as the $[K(18\text{-crown-6})][Cp'_3Ln]$ complexes in Scheme 15 and the syntheses could be run at room temperature if the flash reduction was carried out very quickly.

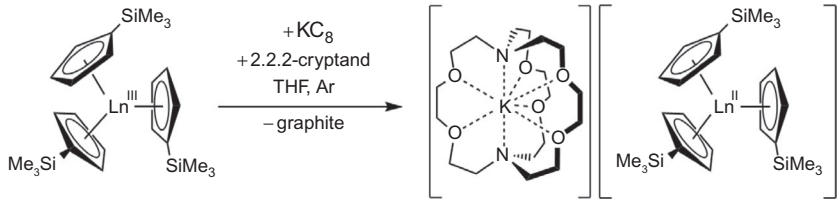

SCHEME 17 Formation of Ln^{2+} complexes from Cp'_3Ln/K reactions in the presence of 2.2.2-cryptand.

Using the flash reduction method with 2.2.2-cryptand, the number of new Ln^{2+} complexes was extended to Pr^{2+}, Gd^{2+}, and Lu^{2+} according to Scheme 17 [126]. This demonstrated, for the first time, that Ln^{2+} ions were accessible in soluble, crystalline molecular complexes for *all* the lanthanides except Pm, which was not investigated because of its radioactivity.

Comparisons of the Ln–(ring centroid) distances in the structures of the Cp'_3Ln precursors and the $(Cp'_3Ln)^{1-}$ complexes for Pr^{2+}, Gd^{2+}, Tb^{2+}, and Lu^{2+} also showed small differences between the Ln^{3+} and Ln^{2+} complexes as had been observed with La, Y, Ho, and Er [126]. In the case of Lu, an EPR spectrum with $g = 1.974$ consistent with Lu^{2+} was obtainable, Fig. 3 (97.4% abundant ^{175}Lu has $I = 7/2$).

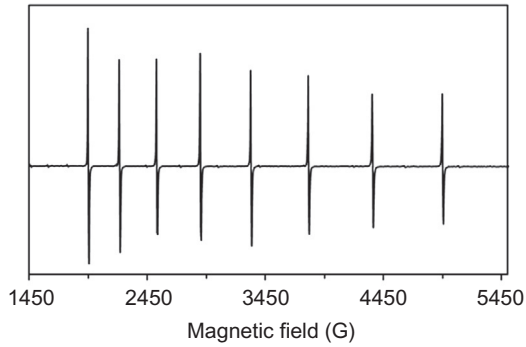

FIG. 3 EPR spectrum of [K(2.2.2-cryptand)][Cp'_3Lu] in THF. *Adapted with permission from M.R. MacDonald, J.E. Bates, J.W. Ziller, F. Furche, W.J. Evans, Completing the series of +2 ions for the lanthanide elements: synthesis of molecular complexes of Pr^{2+}, Gd^{2+}, Tb^{2+}, and Lu^{2+}, J. Am. Chem. Soc. 135 (2013) 9857–9868, © 2013, American Chemical Society.*

8 UV–VISIBLE SPECTRA AND DFT ANALYSIS OF Y^{2+}, PR^{2+}, GD^{2+}, TB^{2+}, HO^{2+}, ER^{2+}, AND LU^{2+} IN $(CP'_3LN)^{1-}$ COMPLEXES

The UV–visible spectra for the [K(2.2.2-cryptand)][Cp'_3Ln] complexes for all the new ions described above, Fig. 4, match those of the $4d^1$ Y^{2+} complex and the Lu^{2+} complex, which must be a $5d^1$ ion since Lu^{3+} is $4f^{14}$ [126]. Each spectrum has broad absorptions typical of transition metal species and is very different from the line-like spectra of $4f^n$ Ln^{3+} complexes.

Density functional theory (DFT) studies by Furche and coworkers provided an explanation for the UV–visible spectra as well as for the small differences in the Ln–(ring centroid) distances between the Ln^{3+} and Ln^{2+} complexes. DFT studies revealed that the lowest unoccupied molecular orbital (LUMO) of the Cp'_3Ln precursors and the highest occupied molecular orbital (HOMO) of the $(Cp'_3Ln)^{1-}$ products were d_{z^2} orbitals, Fig. 5 [125,126]. Although this was normal for $4d^1$ Y^{2+}, it was unexpected for the other Ln^{2+} ions. Hence, the d_{z^2} HOMO for Ho^{2+} shown in Fig. 5 was not expected since a traditional $4f^n$ to $4f^{n+1}$ reduction for $4f^{10}$ Ho^{3+} should form a $4f^{11}$ ion. These results indicated that the reduction of the $4f^n$ Ln^{3+} cyclopentadienyl complexes generated $4f^n5d^1$ Ln^{2+} products and not the expected traditional $4f^{n+1}$ Ln^{2+} ions.

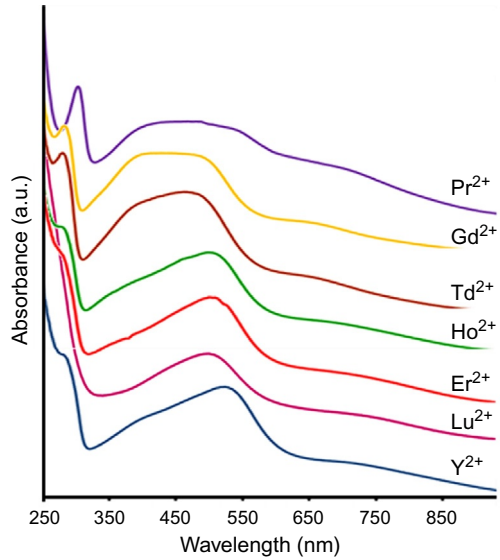

FIG. 4 UV–visible spectra of [K(2.2.2-cryptand)][Cp'_3Ln] (Ln = Pr, Gd, Tb, Ho, Er, Lu, Y) in THF at room temperature. *Adapted with permission from M.R. MacDonald, J.E. Bates, J.W. Ziller, F. Furche, W.J. Evans, Completing the series of +2 ions for the lanthanide elements: synthesis of molecular complexes of Pr^{2+}, Gd^{2+}, Tb^{2+}, and Lu^{2+}, J. Am. Chem. Soc. 135 (2013) 9857–9868, © 2013, American Chemical Society.*

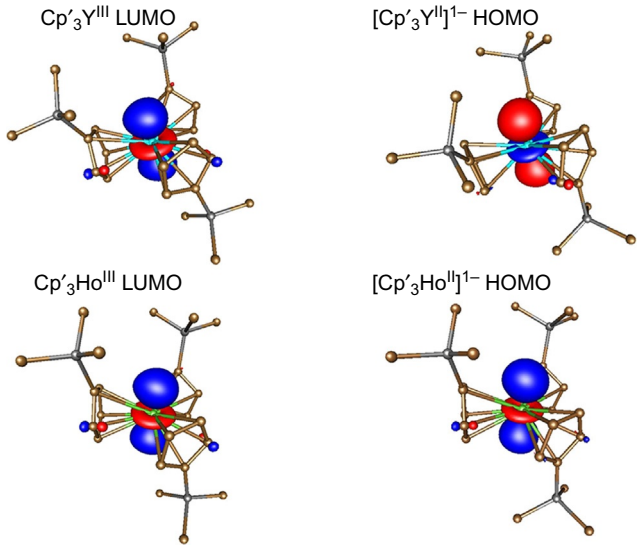

FIG. 5 Contour plots of the LUMOs of Cp'_3Ln (Ln = Y, Ho) and HOMOs of $\left(Cp'_3Ln\right)^{1-}$ anions of [K(2.2.2-cryptand)][Cp'_3Ln] (Ln = Y, Ho). *Adapted with permission from M.R. MacDonald, J.E. Bates, M.E. Fieser, J.W. Ziller, F. Furche, W.J. Evans, Expanding rare-earth oxidation state chemistry to molecular complexes of holmium(II) and erbium(II), J. Am. Chem. Soc. 134 (2012) 8420–8423, © 2012, American Chemical Society.*

The DFT assignments of $4f^n5d^1$ for the new Ln^{2+} ions not only explained the UV–visible spectra in Fig. 4, but they also rationalized the small difference in bond distance between the Ln^{2+} and parent Ln^{3+} complexes. As described in Section 4.3, transition metal complexes do not show such a large change in radius with oxidation state as the lanthanides [102,118–121]. The small differences could be explained by the addition of an electron to a 5d orbital instead of a 4f orbital upon reduction.

Population of the $5d_{z^2}$ orbital in these tris(cyclopentadienyl) complexes could be rationalized on the basis of numerous previous theoretical studies of Cp_3M complexes [127–130,121,131]. The ligand field created by three cyclopentadienyl ligands gives the splitting diagram in Fig. 6. Evidently with a single low-lying d_{z^2} orbital in this 2 over 2 over 1 pattern, the $5d_{z^2}$ is low enough in energy that it can be populated instead of a 4f orbital in the $\left(Cp'_3Ln\right)^{1-}$ complexes.

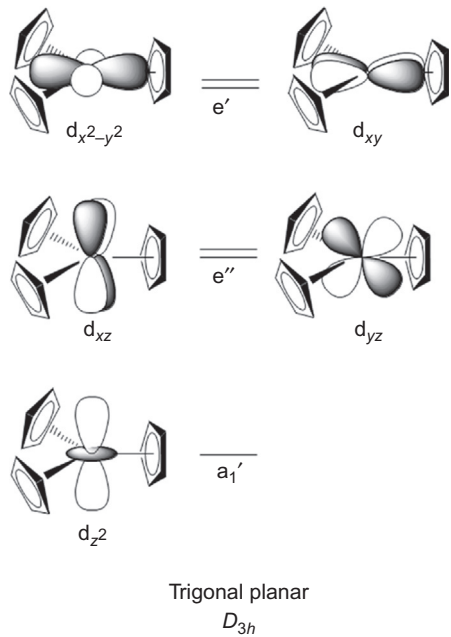

FIG. 6 Splitting diagram caused by the ligand field of three cyclopentadienyl ligands.

9 A SURPRISE WITH DY^{2+} AND ND^{2+} IN $(CP'_3LN)^{1-}$ COMPLEXES

Following the discovery of the new ions discussed above, it appeared that there were two types of Ln^{2+} ions in the lanthanide series. The traditional six ions, Eu^{2+}, Yb^{2+}, Sm^{2+}, Tm^{2+}, Dy^{2+}, and Nd^{2+}, were obtained by reduction

of $4f^n$ Ln^{3+} ions to make $4f^{n+1}$ Ln^{2+} ions. For the rest of the metals in the lanthanide series, reduction of the $4f^n$ Ln^{3+} ions generated $4f^n5d^1$ ions. This dichotomy matched previously observed solid-state results: Eu, Yb, Sm, Tm, Dy, and Nd formed $Ln^{2+}(I^{1-})_2$ salts, whereas reduction of La, Ce, Pr, and Gd in solid-state reactions gave $4f^n$ Ln^{3+} ions with the extra electron delocalized throughout the lattice in a band comprised of 5d orbitals, i.e., $Ln^{3+}(I^{1-})_2(e^{1-})$ [5,13,32,33,132]. In this sense, the new $(Cp_3Ln)^{1-}$ complexes are molecular examples of the LnX_2 solid-state compounds except that the added electron resides in a 5d orbital on the metal. It is interesting to note that these molecular $4f^n5d^1$ $\left(Cp'_3Ln\right)^{1-}$ analogs of the $Ln^{3+}(I^{1-})_2(e^{1-})$ solids are obtainable with Tb, Ho, Er, and Lu as well as with La, Ce, Pr, and Gd.

Although this grouping of Ln^{2+} ions seemed self-consistent, a direct comparison of the two types of ions had not been made using the same set of molecular complexes. The structural and spectroscopic data collected on the new ions, Pr^{2+}, Gd^{2+}, Ho^{2+}, Y^{2+}, Er^{2+}, Tb^{2+}, and Lu^{2+}, in Scheme 17 involved $\left(Cp'_3Ln\right)^{1-}$ complexes, whereas data on complexes of the traditional six ions, Eu^{2+}, Yb^{2+}, Sm^{2+}, Tm^{2+} Dy^{2+}, and Nd^{2+}, were available only for complexes with other ligand sets. To make a direct comparison, Cp'_3Ln and $\left(Cp'_3Ln\right)^{1-}$ complexes of the traditional six metals were prepared [133]. In addition, Cp'_3Ln and $\left(Cp'_3Ln\right)^{1-}$ complexes of La and Ce were synthesized since La^{2+} and Ce^{2+} were only known with Cp″, Scheme 13 [102].

This synthetic effort provided the first comparison of structural data on both Ln^{3+} and Ln^{2+} ions for all the lanthanides (except radioactive Pm) in the same coordination environment, namely that of three Cp′ ligands, as summarized in Table 3 [133]. The data on Cp'_3Ln and $\left(Cp'_3Ln\right)^{1-}$ complexes of La and Ce were similar to the other new ions discussed above as well as Lappert's result with Cp″ [102] in that the difference in Ln–(ring centroid) distances between complexes of the +2 and +3 ions was small. This is consistent with $5d^1$ and $4f^15d^1$ configurations for the $\left(Cp'_3Ln\right)^{1-}$ complexes of La^{2+} and Ce^{2+}, respectively.

It was expected that the pairs of distances for the +2 and +3 ion complexes of the other six elements, Eu, Yb, Sm, Tm, Dy, and Nd, would show large differences as observed in the past for other classes of complexes of these metals (Section 2.1). This was the case for the $\left(Cp'_3Ln\right)^{1-}$ complexes of Eu^{2+}, Yb^{2+}, Sm^{2+}, and Tm^{2+}, which showed these much larger differences, 0.123–0.156 Å, compared to their Cp'_3Ln Ln^{3+} analogs. Surprisingly, however, this was not observed for Dy^{2+} and Nd^{2+}. The bond distances in $\left(Cp'_3Dy\right)^{1-}$ and $\left(Cp'_3Nd\right)^{1-}$ were only slightly larger than those in the Ln^{3+} Cp'_3Ln analogs, 0.036 and 0.030 Å, respectively. This suggested that Dy^{2+} and Nd^{2+} are $4f^n5d^1$ ions in this tris(cyclopentadienyl) coordination environment rather than $4f^{n+1}$ ions. Fig. 7 shows this graphically [133].

Examination of the UV–visible spectra of $\left(Cp'_3Dy\right)^{1-}$ and $\left(Cp'_3Nd\right)^{1-}$ supported this assessment. The spectra were more like those in Fig. 4 than those of the Eu^{2+}, Yb^{2+}, Sm^{2+}, and Tm^{2+} complexes, Fig. 8 [133]. Hence, it

TABLE 3 Comparison of Metal Ligand Distances in Ln^{2+} and Ln^{3+} Complexes in the Same Coordination Environment: Ln–(ring centroid) Distances for Ln^{3+} Cp'_3Ln Complexes, for Ln^{2+} $(Cp'_3Ln)^{1-}$ Complexes, and the Difference Between Them

	Cp'_3Ln Metal–(Ring Centroid) Distances (Å)	$(Cp'_3Ln)^{1-}$ Metal–(Ring Centroid) Distances (Å)	Difference in Metal–(Ring Centroid) Distances (Å)	
Ln	*Ln^{3+}*	*Ln^{2+}*	*New Ln^{2+} Ions*	*Traditional Ln^{2+} Ions*
La	2.559	2.586	0.027	
Ce	2.529	2.558	0.029	
Pr	2.508	2.535	0.027	
Nd	2.489	2.519		0.030
Sm	2.459	2.608		0.149
Eu	2.451	2.607		0.156
Gd	2.437	2.468	0.031	
Tb	2.423	2.454	0.031	
Dy	2.407	2.443		0.036
Y	2.405	2.436	0.031	
Ho	2.394	2.426	0.032	
Er	2.386	2.416	0.030	
Tm	2.379	2.502		0.123
Yb	2.365	2.508		0.143
Lu	2.361	2.392	0.031	

appears that the electronic ground state of complexes of Dy^{2+} and Nd^{2+} depends on the ligand environment. In $(Cp'_3Ln)^{1-}$, these ions are $4f^95d^1$ and $4f^35d^1$, respectively; in previously examined examples they are reported as $4f^{10}$ and $4f^4$, respectively. This demonstrated for the first time in molecular rare-earth metal chemistry that the electronic ground state of a complex could be varied by the ligand environment [133].

DFT calculations on the $(Cp'_3Ln)^{1-}$ complexes of Dy^{2+} and Nd^{2+} matched the experimental results in the sense that there is near degeneracy of the $4f^{n+1}$ and $4f^n5d^1$ configurations [133]. In contrast to the other new Ln^{2+} ions discussed above that have $5d_{z^2}$ Ln^{3+} LUMOs, Fig. 5, that match the $5d_{z^2}$ Ln^{2+}

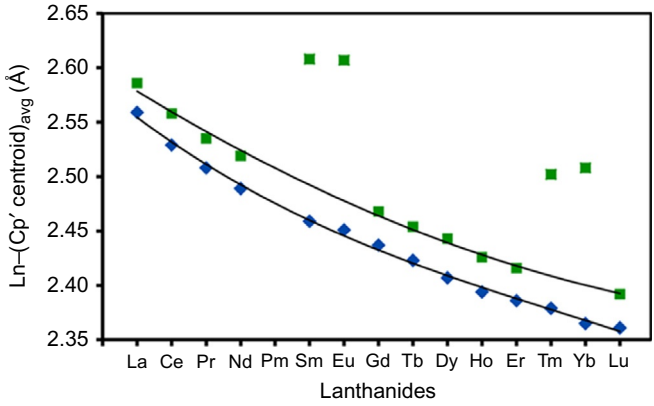

FIG. 7 Plot of average Ln-(Cp′ centroid) distances in Cp'_3Ln (*blue diamonds*) and in [K(2.2.2-cryptand)][Cp'_3Ln] (*green squares*). *Reproduced with permission from M.E. Fieser, M.R. MacDonald, B.T. Krull, J.E. Bates, J.W. Ziller, F. Furche, W.J. Evans, Structural, spectroscopic, and theoretical comparison of traditional vs recently discovered Ln^{2+} ions in the [K(2.2.2-cryptand)][$(C_5H_4SiMe_3)_3Ln$] complexes: the variable nature of Dy^{2+} and Nd^{2+}, J. Am. Chem. Soc. 137 (2015) 369–382, © 2015, American Chemical Society.*

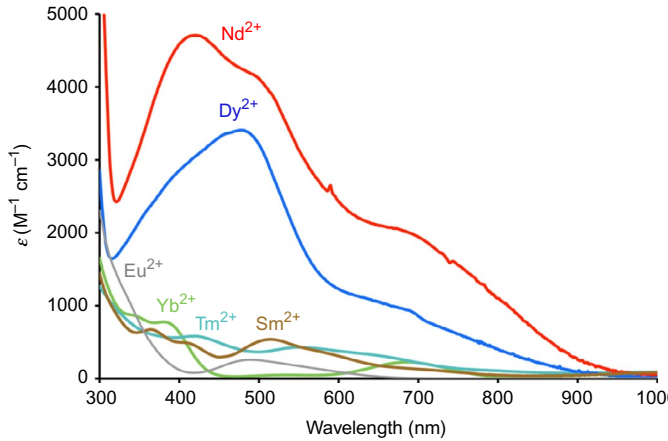

FIG. 8 UV–visible spectra of [K(2.2.2-cryptand)][Cp'_3Ln] (Ln = Nd, Dy, Eu, Yb, Tm, Sm) in THF at room temperature. *Adapted with permission from M.E. Fieser, M.R. MacDonald, B.T. Krull, J.E. Bates, J.W. Ziller, F. Furche, W.J. Evans, Structural, spectroscopic, and theoretical comparison of traditional vs recently discovered Ln^{2+} ions in the [K(2.2.2-cryptand)]-[$(C_5H_4SiMe_3)_3Ln$] complexes: the variable nature of Dy^{2+} and Nd^{2+}, J. Am. Chem. Soc. 137 (2015) 369–382, © 2015, American Chemical Society.*

HOMOs, the Nd^{3+} LUMO does not match the Nd^{2+} HOMO. As shown in Fig. 9, the LUMO for Cp'_3Nd is an f orbital, while the HOMO of $\left(Cp'_3Nd\right)^{1-}$ appears to have a blend of f and d_{z^2} orbital character. Calculations for the dysprosium complexes were more difficult, and a $4f^{n+1}$ ground state was found for Dy^{2+}. However, the simulation of the UV–vis spectrum fits better with a $4f^n5d^1$ ground state. The difficulty in the calculations on these two elements is typical for multi-reference states and reflects the fact that the $4f^{n+1}$ and $4f^n5d^1$ configurations are close in energy. This is consistent with the fact that these ions can adopt either configuration. Since Dy^{2+} and Nd^{2+} can adopt two different electron configurations depending on their coordination environment, they are called "configurational crossover ions" [32,38,134].

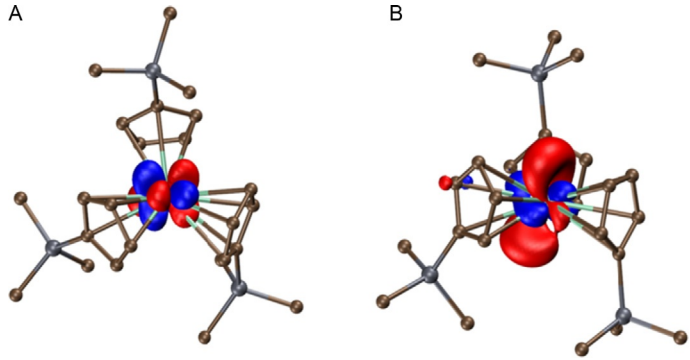

FIG. 9 Contour plots of (A) the LUMO of Cp'_3Nd and (B) the HOMO of $\left(Cp'_3Nd\right)^{1-}$ anion in [K(2.2.2-cryptand)][Cp'_3Nd]. *Reproduced with permission from M.E. Fieser, M.R. MacDonald, B.T. Krull, J.E. Bates, J.W. Ziller, F. Furche, W.J. Evans, Structural, spectroscopic, and theoretical comparison of traditional vs recently discovered Ln^{2+} ions in the [K(2.2.2-cryptand)]-[$(C_5H_4SiMe_3)_3Ln$] complexes: the variable nature of Dy^{2+} and Nd^{2+}, J. Am. Chem. Soc. 137 (2015) 369–382, © 2015, American Chemical Society.*

10 MAGNETIC PROPERTIES OF THE NEW Ln^{2+} IONS IN $(Cp'_3Ln)^{1-}$ COMPLEXES

The synthesis of the complete series of Cp'_3Ln and $\left(Cp'_3Ln\right)^{1-}$ complexes not only allowed the first comprehensive structural comparison of all the Ln^{3+} and Ln^{2+} ions in the same coordination environment, as described in Section 9, but it also provided a complete set of complexes for magnetic analysis [135]. Magnetic susceptibility studies of the Cp'_3Ln complexes provided data consistent with that expected for $4f^n$ Ln^{3+} ions [136,137]. The magnetic moments were well estimated by the $\mu_J = g[J(J+1)]^{1/2}$ formula except for Sm^{3+} and Eu^{3+} which are known to lack the isolated J ground states that allow this formula to apply. The studies on the Cp'_3Ln complexes established that there was nothing unusual about the $\left(Cp'_3\right)^{3-}$ ligand set in terms of affecting magnetic susceptibility.

TABLE 4 Calculated and Experimental Magnetic Moments of [K(2.2.2-cryptand)][Cp'_3Ln] with Calculated Values Closest to Experimental Values Underlined Where Appropriate

Ln	Ln^{2+} Electrons ($n+1$)	μ Calcd $4f^{n+1}$	μ Calcd $4f^n5d^1$ Uncoupled	μ Calcd $4f^n5d^1$ Spin Coupled	μ Found
Eu	7	7.94	1.73	3.46	7.8
Yb	14	0	4.86	5.59	0
Sm	6	3.5[a]	1.94	0	3.64
Tm	13	4.5	7.76	8.59	4.21
Dy	10	10.6	10.77	11.67	11.35
Nd	4	2.68	4.02	2.68	3.01
Pr	3	3.62	3.98	2.65	2.93
Ho	11	9.57	10.75	11.63	11.41
Er	12	7.63	9.74	10.61	9.94
La	1	2.54	1.73	1.73	1.72
Ce	2	3.58	3.07	1.62	2.62
Tb	9	10.63	9.88	10.74	10.48
Gd	8	9.72	8.13	8.94	8.91

[a]*This is the typical value observed experimentally. The moment of $4f^6$ Sm^{2+} does not follow the $\mu_J = g[J(J+1)]^{1/2}$ formula due to the presence of low-lying states.*

The magnetic moments for the $\left(Cp'_3Ln\right)^{1-}$ series are shown in Table 4 along with calculations for their expected values depending on the electron configuration and the coupling scheme used to calculate the magnetic moment [135]. This provided another method to assess the electron configurations assigned to the new Ln^{2+} ions and evaluate the classification of traditional, configurational crossover, and nontraditional ions.

The elements are arranged in the order of Table 1, i.e., in the order of increasing negative values of the calculated reduction potentials. This is done to better allow a comparison of traditional vs configurational crossover vs nontraditional ions. The first column indicates the number of electrons in the ion formed by reducing a $4f^n$ Ln^{3+} ion, i.e., it is $n+1$. The second column gives the magnetic moment expected from a traditional $4f^{n+1}$ Ln^{2+} ion calculated using the $\mu_J = g[J(J+1)]^{1/2}$ formula. The third column gives an estimate of the magnetic moment for a $4f^n5d^1$ Ln^{2+} ion assuming that the magnetism arises from the LS contribution of the $4f^n$ component plus the spin of the

$5d^1$ electron. An angular momentum contribution from the d electron would not be expected since it is in a $d_{z^2} = d_0$ orbital. The fourth column gives the estimated magnetic moment for a $4f^n5d^1$ Ln^{2+} ion if the coupling between the spin of the 4f manifold with the spin of the 5d electron is larger than the LS coupling within the $4f^n$ configuration. In this "spin coupled" model for the magnetic susceptibility, the moment arises from a total angular momentum, J, calculated from the orbital angular momentum, L, of the $4f^n$ component with a total spin angular momentum, $S_{total} = S(4f^n) + S(5d^1)$. The final column contains the experimental values. The calculated values closest to the experimental values are underlined when there is a match [135].

Table 4 shows that the experimental values for the first four ions, Eu^{2+}, Yb^{2+}, Sm^{2+}, and Tm^{2+}, match those expected for $4f^{n+1}$ configurations and they do not match options with $4f^n5d^1$ configurations. These data are consistent with the structural data in Section 9 and UV–visible spectra, Fig. 8, that indicate these are traditional Ln^{2+} ions with $4f^{n+1}$ electron configurations. The next ion in Table 4, Dy^{2+}, has a magnetic moment that does not agree with the $4f^n$ value and best matches with the spin coupled model for $4f^n5d^1$. This is also consistent with the structural and spectral data given above. Unfortunately, the next ion, Nd^{2+}, cannot be evaluated by these magnetic criteria since the predictions for $4f^{n+1}$ and spin coupled $4f^n5d^1$ are identical at 2.68 μ_B and the experimental measurement is closest to that value. For the ions, Pr^{2+}, Ho^{2+}, Er^{2+}, La^{2+}, and Ce^{2+}, as well as for the last ion in Table 4, Gd^{2+}, the measured magnetic moments match best with one of the estimates for the $4f^n5d^1$ configurations. The value for Tb^{2+} is not definitive since the measured value is close to two possibilities.

In summary, the magnetic data do not conflict with the structural, spectral, and theoretical analyses that group Eu^{2+}, Yb^{2+}, Sm^{2+}, and Tm^{2+} as the traditional $4f^n$ Ln^{2+} ions, Dy^{2+} and Nd^{2+} as the configurational crossover ions that are $4f^n5d^1$ in the $\left(Cp'_3\right)^{3-}$ environment, and Pr^{2+}, Ho^{2+}, Er^{2+}, La^{2+}, Ce^{2+}, Tb^{2+}, and Gd^{2+} as the $4f^n5d^1$ Ln^{2+} ions. In addition, the magnetic studies show that the magnetic contribution from a $4f^n$ manifold can be combined with that from a 5d electron to generate magnetic moments higher than ever previously observed for a monometallic complex. The 11.35 and 11.41 μ_B moments of $4f^95d^1$ Dy^{2+} and $4f^{10}5d^1$ Ho^{2+} are the highest reported for monometallic complexes [135]. Traditionally, the highest moments possible are from $4f^9$ ($\mu_J = 10.63$ μ_B) and $4f^{10}$ ($\mu_J = 10.60$ μ_B) lanthanide complexes [136,137].

11 U^{2+} COMPLEXES

Once the new lanthanide ions were discovered as described above, it was conceivable to try to extend this chemistry to uranium. However, there was no basis to expect that uranium would necessarily mimic the rare-earth metals since uranium oxidation state chemistry is quite different with +3, +4, +5, and +6 ions available [138,139]. Moreover since the existence of a U^{2+} ion

in molecular species had been actively pursued for over 30 years, it seemed unlikely that uranium would do similar chemistry. Attempts to synthesize molecules containing U^{2+} were published as early as 1980 [140]. During the 1980s, species such as "$(C_5Me_5)_2U$" were discussed as possible transient intermediates in U^{3+} reduction reactions [141], but it was concluded that "there is no evidence that any uranium(II) species is ever produced" [142]. U^{2+} has also been discussed in compounds containing ligands with ambiguous oxidation states [112,113,143–149]. For example, complexes of the formula $[(anion)_2U]_2(C_6H_6)$ could contain U^{4+} and $(C_6H_6)^{4-}$, U^{3+} and $(C_6H_6)^{2-}$, or U^{2+} and neutral benzene, C_6H_6 [112,113,143]. Since the $(C_6H_6)^{n-}$ moiety in these complexes is not planar and is not displaced by strong neutral donor ligands, the U^{2+} hypothesis was considered unlikely. Solid-state structures formally containing U^{2+}, like some LnX_2 complexes described in Section 2.2, are also in the literature, but are thought to contain uranium in higher oxidation states. For instance, uranium sulfide, US [150], has properties consistent with U^{3+} or U^{4+} with delocalized electrons in the solid-state lattice [151]. U^{2+} has also been reported in the gas phase [152–157], as a transient ion formed by radiolysis [158], and as an OUCO species in a neon matrix [159]. However, molecular U^{2+} species isolable in solution were unknown.

Although molecular complexes of U^{2+} were historically elusive, the reduction of Cp'_3U [160,161] was attempted in analogy to the rare-earth metal reactions in Scheme 17. This resulted in the synthesis of the first molecular complex of U^{2+}, [K(2.2.2-cryptand)][Cp'_3U], identifiable by X-ray crystallography, Scheme 18 [162].

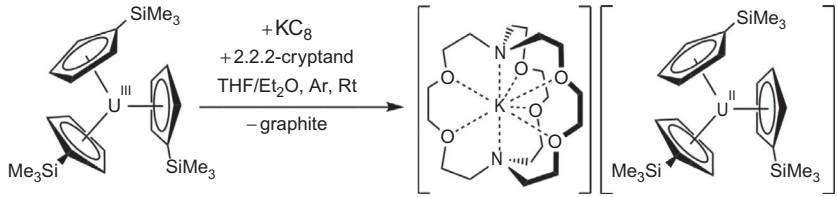

SCHEME 18 Formation of a U^{2+} complex from a Cp'_3U/K reaction.

The uranium complex was found to be isomorphous with the [K(2.2.2-cryptand)][Cp'_3Ln] rare-earth metal complexes. This result was so unexpected that it was necessary to make the corresponding U^{3+} hydride complex, [K(2.2.2-cryptand)][Cp'_3UH], to exclude the possibility that a $(UH)^{2+}$ moiety was at the center of the complex and not a U^{2+} ion. The $[Cp'_3UH]^-$ anion was previously observed spectroscopically [163], but not as the potassium cryptand salt that would allow for direct comparison. [K(2.2.2-cryptand)]-[Cp'_3UH] was prepared according to Scheme 19 and shown to be distinct from [K(2.2.2-cryptand)][Cp'_3]. In fact, the U^{3+} hydride could be made from the U^{2+} complex and hydrogen gas [162].

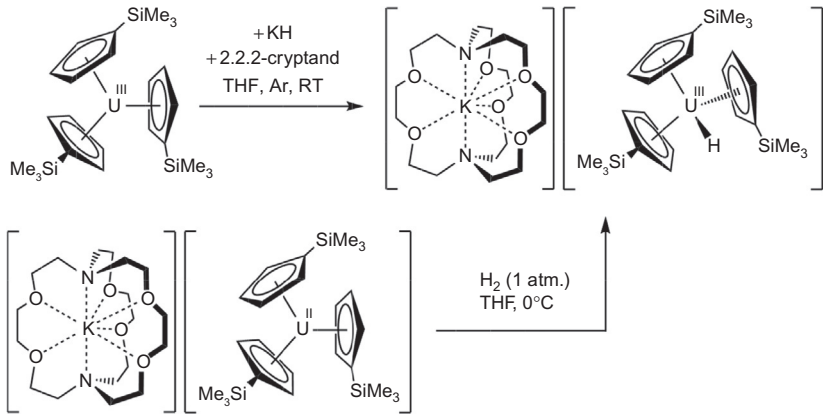

SCHEME 19 Synthesis of [K(2.2.2-cryptand)][Cp'_3UH].

Crystallographic analysis showed that the average U–(Cp′ ring centroid) distance in [K(2.2.2-cryptand)][Cp'_3U] is only 0.013 Å longer than that in Cp'_3U, a small difference similar to the 0.02–0.03 Å differences between $4f^n$ Ln^{3+} Cp'_3Ln and $4f^n5d^1$ Ln^{2+} $\left(Cp'_3Ln\right)^{1-}$ complexes (Table 3). [K(2.2.2-cryptand)][Cp'_3U] was again like the Ln^{2+} complexes in that its UV–visible spectrum was much more intense than those of U^{3+} complexes with the same ligand set, Fig. 10.

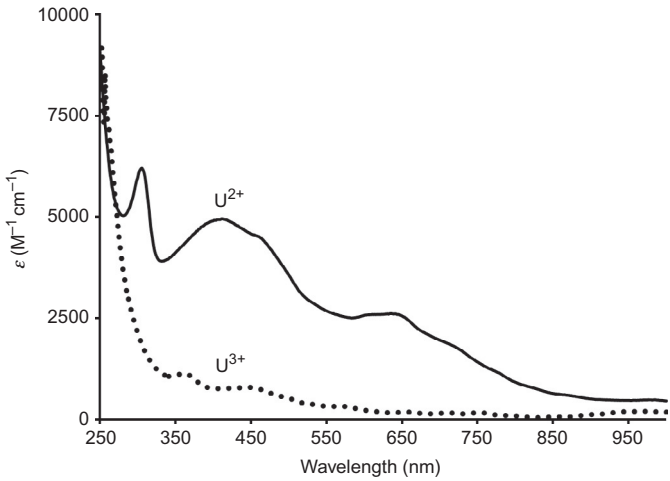

FIG. 10 UV–visible spectra of [K(2.2.2-cryptand)][Cp'_3U] (*solid line*) and Cp'_3U (*dotted line*) in THF. *Adapted with permission from M.R. MacDonald, M.E. Fieser, J.E. Bates, J.W. Ziller, F. Furche, W.J. Evans, Identification of the +2 oxidation state for uranium in a crystalline molecular complex, [K(2.2.2-Cryptand)][$(C_5H_4SiMe_3)_3U$], J. Am. Chem. Soc. 135 (2013) 13310–13313, © 2013, American Chemical Society.*

Although the gas-phase U^{2+} ion is known to have a $5f^4$ configuration [139,164], DFT calculations indicate a $5f^36d^1$ quintet ground state for U^{2+} in the $\left(Cp'_3U\right)^{1-}$ anion [162]. The HOMO has mainly $6d^1$ character and resembles a d_{z^2} orbital, Fig. 11, similar to the HOMOs of the $4f^n5d^1$ Ln^{2+} complexes above, Fig. 5. The stabilization of the $6d_{z^2}$ orbital with respect to the 5f orbitals had previously been noted in studies on trivalent tris(cyclopentadienyl)actinide complexes [130,165].

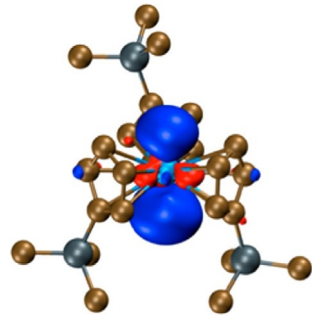

FIG. 11 Contour plot of the HOMO of the $\left[Cp'_3U\right]^-$ anion in [K(2.2.2-cryptand)][Cp'_3U]. *Reproduced with permission from M.R. MacDonald, M.E. Fieser, J.E. Bates, J.W. Ziller, F. Furche, W.J. Evans, Identification of the +2 oxidation state for uranium in a crystalline molecular complex, [K(2.2.2-cryptand)][$(C_5H_4SiMe_3)_3U$], J. Am. Chem. Soc. 135 (2013) 13310–13313,* © *2013, American Chemical Society.*

Analogous studies with Cp″ ligands showed that similar U^{2+} complexes could be obtained with the $\left(Cp''_3\right)^{3-}$ ligand set [166]. As shown in Scheme 20, reduction could be effected with either potassium graphite or sodium and the $\left(Cp''_3U\right)^{1-}$ complexes could be isolated with cryptand or with crown ethers surrounding the alkali metal countercation. The $\left(Cp''_3U\right)^{1-}$ complexes were spectroscopically similar to the $\left(Cp'_3U\right)^{1-}$ complex [162], consistent with a $5f^36d^1$ configuration, but they were thermally more stable [166]. This allowed the ^{29}Si NMR spectra of these U^{2+} complexes to be obtained at room temperature to confirm the trend that silicon-containing uranium complexes exhibit increasingly negative ^{29}Si NMR shifts with decreasing oxidation state for U^{4+}, U^{3+}, and now U^{2+} ions [167].

Following the identification of [K(2.2.2-cryptand)][Cp'_3U] according to Scheme 18, a similar potassium-based reduction of a U^{3+} complex of an arene-anchored tris(aryloxide) ligand was examined and found to produce yet another example of a U^{2+} complex, [K(2.2.2-cryptand)]{[$(^{Ad,Me}ArO)_3$mes]U} (Scheme 21) [168]. Interestingly, in this noncyclopentadienyl coordination environment, the data suggest that the U^{2+} ion has the traditionally expected f^{n+1} electron configuration, i.e., it is $5f^4$. Hence, the ground state of U^{2+} complexes also appears to be dependent on the ligand field.

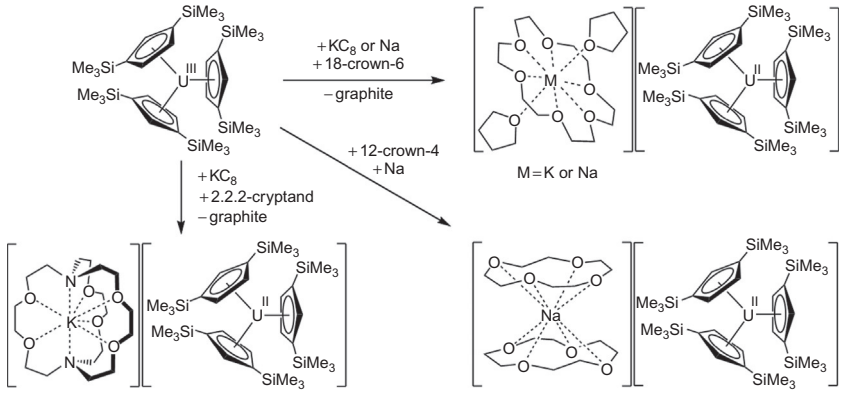

SCHEME 20 Multiple syntheses of $\left(Cp''_3U\right)^{1-}$ complexes.

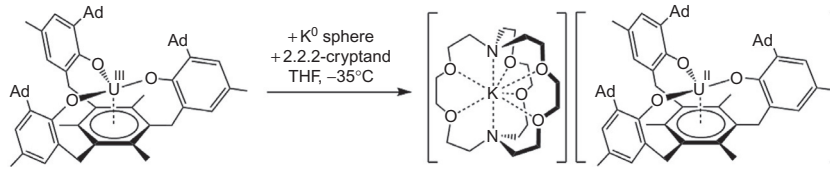

SCHEME 21 Formation of a U^{2+} complex from a U[$(OAr)_3$mes]/K reaction (Ad = adamantyl).

12 Th^{2+} COMPLEXES

Although it was conceivable to attempt the synthesis of Th^{2+} analogs of the new Ln^{2+} and U^{2+} ions described above, it was even less likely that Th^{2+} analogs would form since Th^{3+} complexes are already difficult to obtain. Estimates of the Th^{4+}/Th^{3+} redox potential are between −3.0 and −3.8 V vs SHE [14,15,169,170] and a Th^{3+}/Th^{2+} redox potential of −4.9 V vs SHE has been predicted [14,15,171]. Reduction to metallic thorium would be expected before formation of a Th^{2+} species [22]. Many attempts had been made to synthesize complexes with thorium in oxidation states lower than +4 [172–186]. However, only five Th^{3+} complexes had ever been structurally characterized: three (tris)cyclopentadienyl complexes, $[C_5H_3(SiMe_3)_2]_3Th$ [182], $[C_5H_3(SiMe_2{}^tBu)_2]_3Th$ [183], and $(C_5Me_4H)_3Th$ [184], and two others, $[K(DME)_2]\{[C_8H_6(Si{}^tBuMe_2)_2]_2Th\}$ [184] and $(C_5Me_5)_2[{}^iPrNC(Me)N{}^iPr]Th$ [186]. Experimental data on Th^{2+} ions had been observed only in the gas phase [187,188] and in atomic spectra [189]

Reduction of a precursor analogous to the Cp'_3Ln compounds used in Scheme 17 and Cp'_3U used in Scheme 18 was not possible for thorium since Cp'_3Th is not known. However, Cp''_3Th had been prepared in 1986 [182] and

a reaction similar to Schemes 17 and 18 provided two crystallographically characterizable Th^{2+} complexes, $[K(18\text{-crown-}6)(THF)_2][Cp''_3Th]$ and $[K(2.2.2\text{-cryptand})][Cp''_3Th]$, Scheme 22 [190].

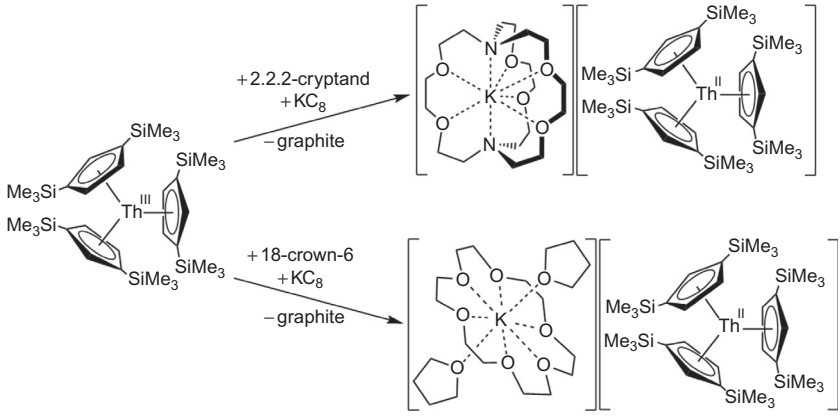

SCHEME 22 Synthesis of two $(Cp''_3Th)^{1-}$ complexes.

The $(Cp''_3Th)^{1-}$ anions in Scheme 22 exhibited physical properties similar to those of the $(Cp'_3M)^{1-}$ complexes of the new Ln^{2+} ions and U^{2+}. The thorium–(ring centroid) distances in the Th^{2+} species were very close to those in the Th^{3+} starting material and the Th^{2+} compounds were intensely colored. This is consistent with an electron configuration containing 6d character. In contrast to the lanthanide and uranium reactions above, the Th^{3+} starting material was already a $6d^1$ ion [191].

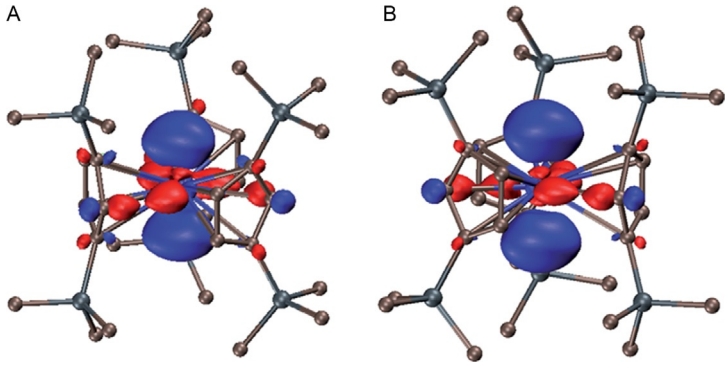

FIG. 12 Contour plots of (A) the LUMO of Cp''_3Th and (B) the HOMO of the $(Cp''_3Th)^{1-}$ anion in $[K(2.2.2\text{-cryptand})][(Cp''_3Th]$. *Adapted with permission from R.R. Langeslay, M.E. Fieser, J.W. Ziller, F. Furche, W.J. Evans, Synthesis, structure, and reactivity of crystalline molecular complexes of the $\{[C_5H_3(SiMe_3)_2]_3Th\}^{1-}$ anion containing thorium in the formal +2 oxidation state, Chem. Sci. 6 (2015) 517–521, © 2015, Royal Society of Chemistry.*

DFT calculations indicate that the ground state of thorium in $\left(Cp''_3Th\right)^{1-}$ is $6d^2$ with the electrons residing in an orbital with d_{z^2} character, Fig. 12. This spin-paired ground state is consistent with the NMR spectrum in the diamagnetic region [190]. The $6d^2$ electron configuration is the first ever observed in an isolable molecular complex since the 6d orbitals are the valence orbitals of the fourth row transition metals, i.e., the superheavy elements like rutherfordium and dubnium. A $6d^2$ configuration might be expected for Rf^{2+} or Db^{3+}. It appears that Th^{2+} compounds like $\left(Cp''_3Th\right)^{1-}$ could be used to model these highly radioactive elements that are only available a few atoms at a time.

13 REACTIVITY OF COMPLEXES OF THE NEW Ln^{2+} AND An^{2+} IONS

13.1 Thermal Stability

Preliminary studies of the stability of the [K(2.2.2-cryptand)][Cp'_3Ln] complexes show that, except for Lu, these compounds follow second-order kinetics in their thermal decomposition with a relative stability order of $Pr^{2+} > Gd^{2+} > Tb^{2+} > Ho^{2+} > Er^{2+} > Y^{2+}$ [126]. The initial half-lives in THF at 298K at 3 mM concentrations span a wide range of 20 days, 3.7 days, 22 h, 3.5 h, 2.5 h, and 2.3 h, respectively. The Lu^{2+} complex is the least stable and decomposition follows first-order kinetics with a half-life of 19 min. Decreasing stability roughly correlates with decreasing radial size, but the details of the decomposition are unknown.

The [K(18-crown-6)][Cp'_3Ln] complexes (Y, Ho, Er, Tb) decompose in Et_2O with first-order kinetics and are much less stable than the 2.2.2-cryptand analogs with half-lives ranging from 1.5 h to 6 min [126]. The proximity of the potassium cation to a cyclopentadienyl ring may facilitate loss of [K(18-crown-6)][Cp′] that could lead to faster decomposition in these cases.

In efforts to identify more stable variants of the $\left(Cp'_3Ln\right)^{1-}$ complexes for physical characterization studies, reductions of other tris(cyclopentadienyl) complexes were explored since these coordination environments should also have d_{z^2} orbitals that could be populated to make analogous complexes [124]. Reductions of $Cp_3Y(THF)$, $Cp''^{Me}_3Y(THF)$, Cp''_3Y, and the mixtures, $Cp''_2YCp/Cp''YCp_2$ and $Cp''_2YCp^{Me}/Cp''YCp^{Me}_2$ ($Cp = C_5H_5$, $Cp^{Me} = C_5H_4Me$) with potassium graphite in the presence of 2.2.2-cryptand generate dark solutions as found in the reduction of Cp'_3Y to make [K(2.2.2-cryptand)][Cp'_3Y], Scheme 17. The solutions had EPR spectra similar to those in Fig. 1 indicative of Y^{2+}. However, in all cases, these complexes were less thermally stable than [K(2.2.2-cryptand)][Cp'_3Y] [126]. The only reaction that produced crystals was a reduction of 3:1 $Cp''_2YCp:Cp''YCp_2$. This allowed crystallographic characterization of [K(2.2.2-cryptand)][Cp''_2YCp], a complex that decomposes 10 times faster than [K(2.2.2-cryptand)][Cp'_3Y]. Reductions of Cp''_3Gd and the mixtures $Cp''_2GdCp/Cp''GdCp_2$ and $Cp''_2GdCp^{Me}/Cp''GdCp^{Me}_2$ gave

similar results: dark EPR active solutions similar to that of [K(2.2.2-cryptand)][Cp'_3Gd] were formed that contained products that were less stable. The only Gd^{2+} complex isolable for X-ray crystallography was [K(2.2.2-cryptand)][Cp''_2GdCp] [124].

[K(2.2.2-cryptand)][Cp'_3U] decomposes via first-order kinetics with a half-life of 1.5 h [162]. The Cp″ U^{2+} complexes, [K(2.2.2-cryptand)][Cp''_3U] and $\left[K(18\text{-crown-}6))\right]\left[Cp''_3U\right]$, also exhibit first-order decomposition kinetics, but they are significantly more stable with 20 and 15 h half-lives, respectively [166]. [K(18-crown-6)$(THF)_2$][Cp''_3Th] is the most stable of all of these compounds and shows only 8% decomposition after 8 days in THF [190].

13.2 Reactivity of Complexes of Ln^{2+} Ions

The reductive capacity of the recently discovered Ln^{2+} complexes, [K(2.2.2-cryptand)][Cp'_3Ln], was probed by examining their reactions with aromatic hydrocarbons [192]. This is a traditional way to characterize lanthanide-based reducing agents too reactive for reproducible electrochemistry [193,51,52,110].

[K(2.2.2-cryptand)][Cp'_3Y] was found to be capable of reducing naphthalene (−2.36 V vs SHE [194]) according to Scheme 23. Two equivalents of the Y^{2+} complex are needed to form the naphthalenide dianion. Since a bis(cyclopentadienyl) naphthalenide product, [K(2.2.2-cryptand)][$Cp'_2Y(\eta^4\text{-}C_{10}H_8)$], is formed from the two tris(cyclopentadienyl) Cp'_3Y precursors, one yttrium center must lose a $(Cp')^{1-}$ anion in the reduction process and one equivalent of Cp'_3Y is also produced. As shown in Scheme 23, these by-products come together and $\left(Cp'_4Y\right)^{1-}$ is isolated. [K(2.2.2-cryptand)][$Cp'_2Ln(\eta^4\text{-}C_{10}H_8)$] products with Ln = La, Ce, and Dy were isolated by reactions analogous to Scheme 23 although only the [K(2.2.2-cryptand)][Cp'_4La] by-product could be identified by X-ray crystallography [192].

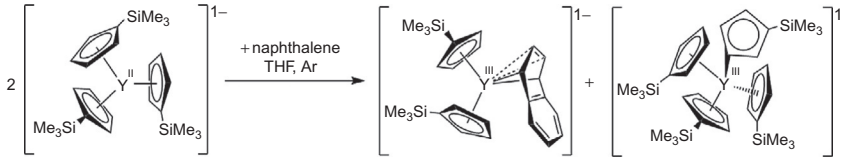

SCHEME 23 Reduction of naphthalene by an Y^{2+} complex.

Reduction of biphenyl (−2.56 V vs SHE [194]) was also observed with [K(2.2.2-cryptand)][Cp'_3Y], Scheme 24, although in this case no by-products could be crystallographically identified. The [K(2.2.2-cryptand)][$Cp'_2Y(\eta^6\text{-}C_6H_5Ph)$] product was unusual since most biphenyl dianion products are bimetallic [192].

Attempts to reduce benzene (−3.18 V vs SHE) with [K(2.2.2-cryptand)][Cp'_3Ln] complexes were not successful. Hence, these aromatic hydrocarbon reactions showed that these divalent ions are capable of reducing substrates

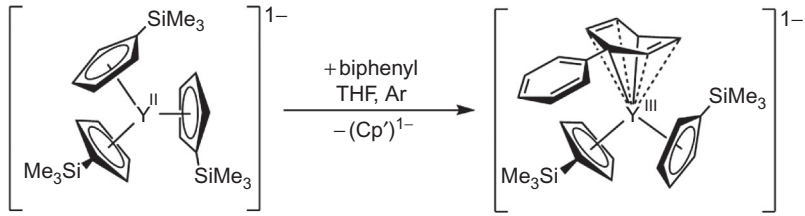

SCHEME 24 Reduction of biphenyl by an Y^{2+} complex.

with reduction potentials as negative as −2.56 V vs SHE. This is consistent with the fact that these Ln^{2+} ions can be synthesized with sodium and potassium which have M^+/M reduction potentials of −2.7 and −2.9 V vs SHE, respectively. The biphenyl reaction demonstrates that these complexes are the strongest rare-earth metallocene reducing agents isolated to date.

Photochemical studies of heteroleptic Ln^{3+} metallocene complexes such as $(C_5Me_5)_2(\eta^3\text{-}C_5Me_4H)Ln$ (Ln = Y, Lu, Dy) and $(C_5Me_5)(C_5Me_4H)(\eta^3\text{-}C_5Me_4H)Lu$ have revealed that when these complexes are excited with visible light under dinitrogen, they can form $(N{=}N)^{2-}$ complexes $[(C_5Me_5)_2Y]_2(\mu\text{-}\eta^2{:}\eta^2\text{-}N_2)$ and $[(C_5Me_5)(C_5Me_4H)Lu]_2(\mu\text{-}\eta^2{:}\eta^2\text{-}N_2)$, respectively, with $(C_5Me_4H)_2$ as a by-product, Scheme 25 [195].

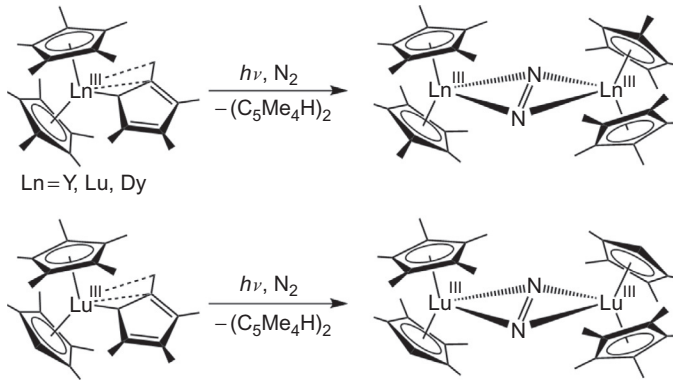

SCHEME 25 Reduction of N_2 to $(N{=}N)^{2-}$ by photolysis of heteroleptic Ln^{3+} metallocenes.

DFT studies indicate that excitation of a ligand-to-metal charge transfer absorption from the $(\eta^3\text{-}C_5Me_4H)^{1-}$ ligand to the Ln^{3+} ion could generate C_5Me_4H radicals and intermediates in these reactions that are formally Ln^{2+} complexes such as "$(C_5Me_5)_2Ln$" [195]. These species would be expected to have the high reactivity needed to reduce dinitrogen. Photolysis of the allyl complexes $(C_5Me_5)_2Ln(\eta^3\text{-}C_3H_4R)$ (Ln = Y, Lu, R = H, Me) under dinitrogen also forms the $(N{=}N)^{2-}$ products, $[(C_5Me_5)_2Y]_2(\mu\text{-}\eta^2{:}\eta^2\text{-}N_2)$, and photolysis

of $(\eta^5\text{-}C_5Me_5)_2Ln(\eta^3\text{-}C_3H_5)$ (Ln = Y, Lu) in the presence of sulfur leads to the $(S)^{2-}$ complexes $[(C_5Me_5)_2Ln]_2(\mu\text{-}S)$ [196]. Although Ln^{2+} complexes have not been identified in these reactions, this photochemistry could be another route to access Ln^{2+}-like reductive reactivity.

13.3 Reactivity of Complexes of An^{2+} Ions

The reactivity of the first U^{2+} complex, [K(2.2.2-cryptand)][Cp'_3U], was initially examined with H_2. This reaction forms the U^{3+} hydride, [K(2.2.2-cryptand)][Cp'_3UH], Scheme 19 [162]. The Cp″ analog, $\left(Cp''_3U\right)^{1-}$, reacts similarly, Scheme 26, and it was found that $PhSiH_3$ can also be used as a reagent to make the analogous hydride complex. The $PhSiH_3$ reaction also generates a hydride product with [K(2.2.2-cryptand)][Cp'_3U] as summarized in Scheme 26 [166].

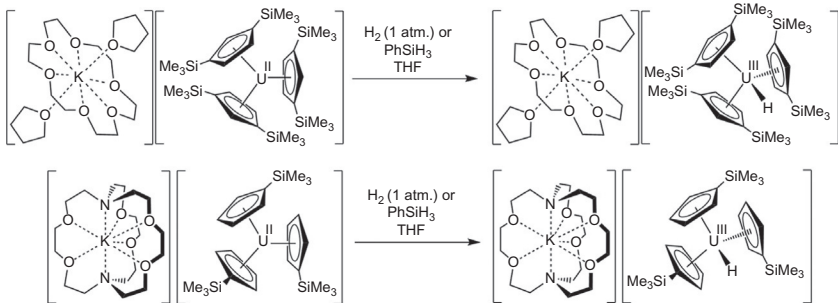

SCHEME 26 Reactivity of U^{2+} complexes with H_2 and $PhSiH_3$.

The Th^{2+} complex [K(18-crown-6)$(THF)_2$][Cp''_3Th] reacts quite differently with H_2 making [K(18-crown-6)(Et_2O)][$Cp''_2Th(\mu\text{-}H)_3ThHCp''_2$] and Cp''_3Th as shown in Scheme 27 [197]. The hydride product is another example

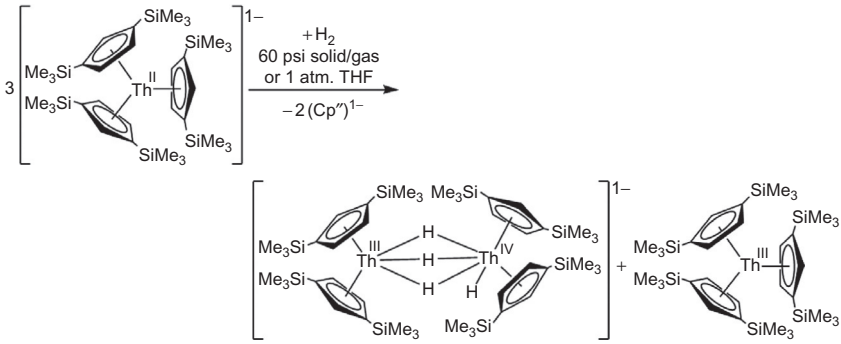

SCHEME 27 Reactivity of a Th^{2+} complex with H_2.

of the rare class of crystallographically characterizable Th^{3+} complexes, the first Th^{3+} hydride complex, and the first mixed-valence thorium complex. The mechanisms of these An^{2+} hydrogen reactions are unknown.

Another substrate that has been examined with both U^{2+} and Th^{2+} complexes is 1,3,5,7-cyclooctatetraene, C_8H_8. With the Th^{2+} complex, [K(18-crown-6)(THF)$_2$][Cp''_3Th], a net two-electron reduction of C_8H_8 occurs to make a Th^{4+} complex of $(C_8H_8)^{2-}$ as shown in Scheme 28 [190]. This was the first two-electron metal-based reduction observed for thorium.

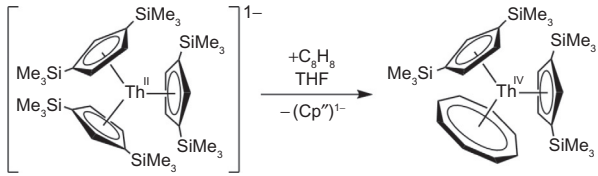

SCHEME 28 Two-electron reduction of C_8H_8 to $(C_8H_8)^{2-}$ by Th^{2+}.

The reaction chemistry of cyclooctatetraene with the Cp′ and Cp″ tris(cyclopentadienyl) U^{2+} complexes is different in that uranocene, $(C_8H_8)_2U$, is the $(C_8H_8)^{2-}$ product [166]. In the case of $\left(Cp''_3U\right)^{1-}$, Cp''_3U and $(Cp'')^{1-}$ are the by-products, Scheme 29. In the case of $\left(Cp'_3U\right)^{1-}$ the two analogous by-products combine and $\left(Cp'_4U\right)^{1-}$ is isolated, Scheme 30. $\left(Cp'_4U\right)^{1-}$ was the first example of a crystallographically characterizable tetrakis(cyclopentadienyl) U^{3+} complex [166].

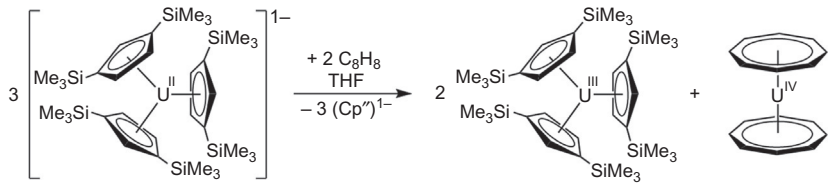

SCHEME 29 Formation of uranocene from C_8H_8 and a U^{2+} complex.

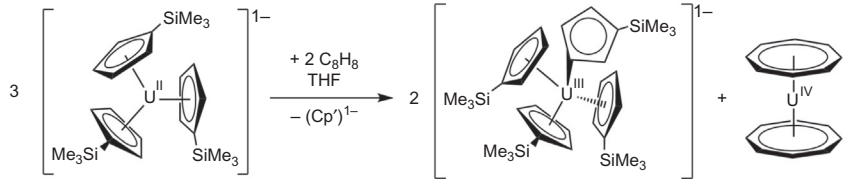

SCHEME 30 Formation of a tetrakis(cyclopentadienyl) uranium by-product in the reduction of C_8H_8 to $(C_8H_8)^{2-}$ by U^{2+}.

14 BIMETALLIC RARE-EARTH METAL COMPLEXES WITH THE NEW Ln^{2+} IONS

Although the [K(2.2.2-cryptand)][Cp'_3Ln] complexes were not found to be capable of reducing benzene as described in Section 13.2, reduced arene complexes had been reported by Lappert from Cp''_3Ln/K and Cp^{tt}_3Ln/K reactions that were postulated to make Ln^{2+} intermediates. As shown in Schemes 10 and 11 in Section 4.2, monometallic Ln^{3+} $(C_6H_6)^{2-}$ complexes, [K(18-crown-6)][$(C_6H_6)LnCp''_2$] (Ln = La, Ce, Pr, Nd) [96,99] and bimetallic Ln^{2+} $(C_6H_6)^{1-}$ complexes, [K(18-crown-6)][$(Cp^{tt}_2La)_2(C_6H_6)$] [98], could be isolated with Cp″ and Cp^{tt} ligands. When analogous LnA_3/M reactions were conducted with the Cp′ complexes, Cp'_3Ln (Ln = La, Ce), yet another result was obtained [198]. In this case, [K(2.2.2-cryptand)]$_2$[$(Cp'_2Ln)_2(\mu\text{-}\eta^6\text{:}\eta^6\text{-}C_6H_6)$] complexes assigned as Ln^{2+} complexes of $(C_6H_6)^{2-}$ ligands were isolated according to Scheme 31 (Ln = La, Ce).

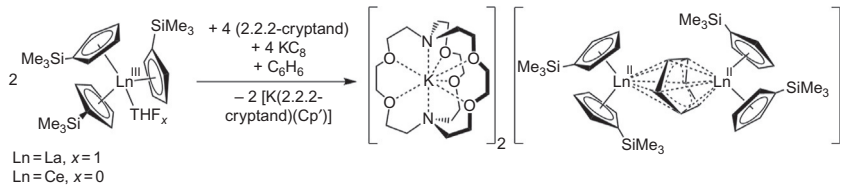

SCHEME 31 Formation of $(C_6H_6)^{2-}$ Ln^{2+} complexes from Cp'_3Ln/K reactions.

Like the [K(18-crown-6)][$(Cp^{tt}_2La)(C_6H_6)$] complexes isolated earlier by Lappert, there could be ambiguity in metal oxidation state for [K(2.2.2-cryptand)]$_2$[$(Cp'_2La)_2(\mu\text{-}\eta^6\text{:}\eta^6\text{-}C_6H_6)$]. However, structural and spectroscopic data as well as the DFT analysis are consistent with the presence of La^{2+} and $(C_6H_6)^{2-}$. In any case, the compounds function as four-electron reductants with naphthalene, Scheme 32 (Ln = La, Ce) [198].

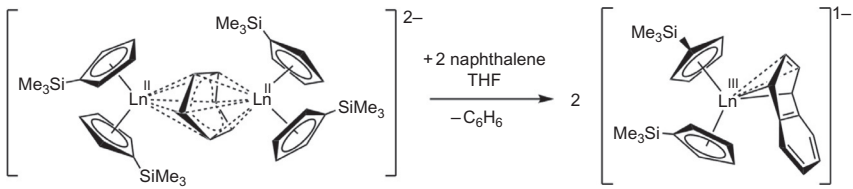

SCHEME 32 Four-electron reduction of two molecules of naphthalene by $\left[(Cp'_2Ln)_2(C_6H_6)\right]^{2-}$.

These LnA_3/M arene reduction reactions show a large variation in products as a function of small changes in the substitution pattern of the cyclopentadienyl ring and the exact reaction conditions. This suggests that the factors controlling reductions of arenes to mono- and di-anions vs the

reduction of Ln^{3+} to Ln^{2+} are closely matched. This is a complicated system to analyze since identification of specific products relies on isolation of crystallographically characterizable compounds. The product of least solubility that crystallizes best may not represent the overall reaction. The fact that these reduced benzene complexes are formed in LnA_3/M reactions and not from isolated Ln^{2+} complexes suggests that there is still much to be discovered about rare-earth metal reduction chemistry.

It should be noted that both of the crystallographically characterized La^{2+} reduced benzene complexes, $[K(18\text{-crown-}6)][(Cp^{tt}_2La)_2(C_6H_6)]$ and $[K(2.2.2\text{-cryptand})]_2[(Cp'_2La)_2(\mu\text{-}\eta^6\text{:}\eta^6\text{-}C_6H_6)]$, have the La^{2+} ions surrounded by three anionic carbocyclic rings as found in $\left(Cp''_3Ln\right)^{1-}$ and $\left(Cp'_3Ln\right)^{1-}$. In the bimetallic complexes, a $(C_6H_6)^{2-}$ dianion shared between two metals takes the place of one of the cyclopentadienyl anions in the tris(cyclopentadienyl) monometallic Ln^{2+} systems.

15 EARLIER LITERATURE REGARDING THE NEW IONS

In light of the large expansion of rare earth and actinide metal oxidation state chemistry since 2011, it is interesting to reflect on what hints were in the earlier literature that might have suggested these breakthroughs. It is always easier to do this in retrospect, but it is worthwhile to make this analysis to help identify information currently in the literature that could help accelerate the discoveries of the future.

As detailed in earlier sections, data from atomic spectra, gas-phase studies, matrix isolation studies, and radiolysis reactions showed that unusual oxidation states could be accessed under special conditions. However, there are also several earlier papers that contain information, suggesting that these new oxidation states could be obtained in molecular species. These results were either not taken seriously or not pursued because the extension of the ideas did not seem reasonable given the current beliefs and level of knowledge. Hopefully, the summary of these papers in this section will stimulate critical analysis of information currently being reported that points to future advances.

One of the key aspects in isolating the new oxidation states described in this chapter was population of d orbitals to access $4f^n5d^1$, $5f^n6d^1$, and $6d^2$ electron configurations. This accessibility of the d orbitals was in the literature as early as 1949 when the $6d^2$ electron configuration was predicted for Th^{2+} [7].

The existence of $4f^n5d^1$ ions for the lanthanides was inherent in the assignment of the LnX_2 compounds of Ln = La, Ce, Pr, and Gd as $(Ln^{3+})(X^{1-})_2(e^{1-})$ species since the (e^{1-}) in the formula was assigned to be in a band comprised of 5d orbitals [5,13,32,33]. This was not controversial at the time probably because these were solid-state species and band structure could accommodate many possibilities. In any case, this solid-state assignment of the energetic accessibility of the 5d orbitals could have been used as a basis to pursue molecular complexes containing $4f^n5d^1$ configurations.

Solid-state studies also showed that the crystal field of a rare-earth metal ion could be changed to make the 5d orbitals more accessible. Beck showed in 1976 that applying pressure to NdI_2, which had salt-like properties consistent with $Nd^{2+}(I^{1-})_2$, converted this compound to a species with the properties of a $(Ln^{3+})(I^{1-})_2(e^{1-})$ material [199]. This was an early example of configurational crossover behavior [32,38,134] in which Nd^{2+} transformed from a $4f^4$ ion to a $4f^35d^1$ ion by changing the crystal field, in this case by pressure. This information also could have been used as a basis to design molecular species with strong crystal fields that would make the 5d orbital accessible.

Other evidence that Nd^{2+} could be a configurational crossover ion was found in the structure of $[(C_5H_2{}^tBu_3)_2Nd(\mu\text{-}I)K(18\text{-crown-}6)]$ [87]. This Nd^{2+} complex had a solid-state structure with the Nd–(ring centroid) distance only 0.05 Å larger than that in $(C_5H_2{}^tBu_3)_2Nd(\mu\text{-}Cl)AlMe_3$ [200], the closest example cited for comparison. This 0.05 Å difference was much smaller than the 0.16–0.19 Å ranges previously observed for traditional Ln^{2+} complexes (Section 2.1). This small difference could arise because the Nd^{2+} in this complex could be $4f^35d^1$ and not $4f^4$. The 2.8 μ_B magnetic moment reported on this compound could not distinguish these two configurations, Table 4.

There were similar small differences in bond distances between the Dy^{2+} complexes $[(C_5H_2{}^tBu_3)_2Dy(\mu\text{-}X)K(18\text{-crown-}6)]$ (X = Br and BH_4) and their Dy^{3+} analogs, 0.038 and 0.01 Å, respectively [86]. However, this information was not discussed and only later analyzed from the Cambridge Structural Database [133]. It seems possible that these Dy^{2+} complexes could have $4f^95d^1$ configurations rather than $4f^{10}$ and therefore would constitute early molecular examples that Dy^{2+} is a configurational crossover ion.

Reviews by Kamenskaya and Mikheev consistently pointed out that Gd^{2+} should have a 4^75d^1 configuration [18–21]. Even the analysis of Nugent that led to the reduction potentials in Table 1 suggested a $4f^75d^1$ configuration for Gd^{2+}, although it was not reflected in the very negative −3.9 V vs SHE predicted Gd^{3+}/Gd^{2+} reduction potential [14,15]. Kamenskaya and Mikheev also repeatedly made the point that Ce^{2+} and Tb^{2+} could have $4f^n5d^1$ configurations and that periodic predictions of Ln^{2+} properties should not include these ions or Gd^{2+}. The predicted reduction potentials of Kamenskaya and Mikheev, Table 2, indicated that potassium could be a strong enough reductant to form new Ln^{2+} ions. However, the complicated manner in which these data were obtained from molten salt studies raised questions about their validity vs the Table 1 values [4]. A 1986 paper on electrochemistry of tris(cyclopentadienyl) complexes by Deacon *et al.* also suggested that new Ln^{2+} ions could be accessed electrochemically [62].

The accessibility of the 5d orbitals for lanthanides was suggested in another way by the research of Cloke *et al.* on the zero valent bis(arene) complexes, $Ln[C_6H_3(CMe_3)_3]_2$, which were crystallographically characterized for Ln = Gd [201] and Ho [202]. The metals in these complexes were assigned $4f^n5d^16s^2$ configurations. Interestingly, since the $6s^2$ electron pair does not

contribute to the magnetism, the magnetic moments predicted for these bis(arene) complexes [201,202] are the same as those in Table 4 [135].

Just the existence of the Ln^0 complex, $Gd[C_6H_3(CMe_3)_3]_2$, in 1987 [201] could be taken to suggest that oxidation states between Ln^0 and Ln^{3+} could be accessible. However, since Ln^0 complexes were not isolable for Ln = La, Ce, Pr, Sm, Eu, Tm, and Yb [202,203], the general implications in lanthanide oxidation state chemistry were not clear. This was complicated by the fact that two different rationales were presented to explain the instability of bis(arene) complexes with these metals: the first three metals were too large and the last four had 5d orbitals too high in energy. Since the stable examples of this class could only be made by cocondensing metal vapor with the ligand at −196°C, these compounds were regarded as rather specialized, trapped valence species.

The reports of spectroscopically characterized Sc^0 and Sc^{2+} complexes in 1991 [204] and the crystallographically characterized Sc^0 and Sc^{1+} complexes, $[Sc(C_6{}^tBu_3MeH_2)_2]$ [205,206] and $[\{(\eta^5\text{-}P_3C_2{}^tBu_2)Sc\}_2(\mu\text{-}\eta^6\text{:}\eta^6\text{-}P_3C_3{}^tBu_3)]$ [206], respectively, in 1996 could also be taken to suggest other rare-earth metal oxidation states are possible. However, these complexes were also generated by metal vapor methods at low temperature. In addition, since scandium is a transition metal, it was possible that this would not extend to the lanthanides.

Another early suggestion of broader lanthanide reduction chemistry was provided by Floriani and coworkers in 1998 when they reported that dinitrogen could be reduced by sodium naphthalenide and octaethylporphyrinogen complexes of Pr and Nd [72]. Prior to this time only Sm had been found to reduce dinitrogen [67–71]. This reactivity, which was unexpected for Pr and Nd at that time, was attributed to the unusual nature of the porphyrinogen ligand and was not recognized as an LnA_3/M reaction (Scheme 8) that could have generality.

Lappert and coworkers had an example in 1998 of La^{2+} in the crystal structure of $[K(18\text{-crown-}6)][(Cp^{tt}_2La)_2(C_6H_6)]$ [98], but the unusual nature of the bridging $(C_6H_6)^{1-}$ monoanion, the lack of precision in the crystal structure, and the possibility that this could be a Ln^{3+} complex of $(C_6H_6)^{3-}$ clouded the issue. It was also likely that Lappert and coworkers had an example of $6d^2$ Th^{2+} 14 years before definitive crystallographic evidence was obtained! A 2001 paper [184] describes the reduction Cp''_3Th with excess Na–K reduction to form a diamagnetic green compound that could not be fully characterized and did not give reproducible analytical results. It was postulated that this "was a mixture of spin-paired Th(II) d^2 complexes of composition $[K(THF)_x][ThCp''_3]$ and/or $ThCp''_2(THF)_x$." This mixture probably contained the green $\left(Cp''_3Th\right)^{1-}$ complex shown in Scheme 22, a complex that has a diamagnetic NMR spectrum. The Th^{2+} claim was not taken seriously in 2001 and it was surprising that it even got past the referees at that time with the minimal evidence available.

Although all these suggestions on the existence of molecular, isolable, Ln^{2+} and An^{2+} complexes with electron configurations that include the d orbitals were in the literature, they were not pursued into publishable new results. This is probably because the beliefs about the limits of oxidation states and electron configurations were too strong to pursue these ideas. It is possible that attempts were made to make the new oxidation states, but were unsuccessful because the reactions were not done under the appropriate conditions, e.g., under argon to avoid reduction of dinitrogen or at low temperature to avoid thermal decomposition. As demonstrated with Th^{2+} in the 2015 [190] vs 2001 [184] papers, the presence of a 2.2.2-cryptand or 18-crown-6 chelate was important to isolating crystallographically characterizable examples of the new oxidation states.

16 SUMMARY AND OUTLOOK

Knowledge of the availability of +2 ions in molecular complexes in the lanthanide series has evolved considerably over the years. As discussed in Section 2, for many years Eu^{2+}, Yb^{2+}, and Sm^{2+} were considered the only Ln^{2+} ions believed to be accessible in solution. The discovery that Tm^{2+}, Dy^{2+}, and Nd^{2+} were accessible in solution led to these ions being called the "new" divalent lanthanides [39] or the "uncommon low-valent states" [1]. All six of these ions were previously considered the traditional divalent ions of the lanthanide series by the solid-state community because they could be obtained as $(Ln^{2+})(X^{1-})_2$ salts in contrast to the other lanthanide metals that formed $(Ln^{3+})(X^{1-})_2(e^{1-})$ compounds. We now know that Ln^{2+} ions are available in soluble, crystalline molecular complexes for all the lanthanides except the radioactive promethium. On the basis of these data, it is expected that Pm^{2+} should be accessible also.

The extension of the +2 oxidation state to all the lanthanides was possible because coordination environments involving three cyclopentadienyl rings allowed a d_{z^2} orbital to become comparable in energy to the 4f orbitals. This allowed reduction of a $4f^n$ Ln^{3+} ion to a $4f^n5d^1$ ion instead of the traditional $4f^n$ to $4f^{n+1}$ reduction previously known for Eu, Yb, Sm, Tm, Dy, and Nd. This meant that the calculated $4f^n$ to $4f^{n+1}$ reduction potentials of Table 1 did not apply to these new $4f^n5d^1$ Ln^{2+} ions. Since the new ions can be formed by potassium reduction, it appears that the less negative reduction potentials of Kamenskaya and Mikheev in Table 2 may be more appropriate. However, since some of the new ions can be formed by reduction with sodium (−2.7 V vs SHE), even these less negative reduction potentials may not apply. Of course, the calculated redox potentials in the Tables and for K and Na are just general values useful as a guide and they do not apply exactly to specific complexes under specific conditions. The error limits for Table 1 of ±0.2 V should always be considered when using calculated values.

The tris(cyclopentadienyl) coordination environment not only allowed nine new +2 rare-earth metal oxidation states to be accessed, but it also changed the boundaries of the grouping of ions from the traditional six and the nontraditional others. With the realization that Dy^{2+} and Nd^{2+} can be either traditional $4f^{n+1}$ Ln^{2+} ions or nontraditional $4f^n5d^1$ Ln^{2+} ions depending on the ligand set, a third category has emerged. These two ions, which can switch categories, are termed the configurational crossover Ln^{2+} ions [32,38,134].

Hence, at the present time, there are only four traditional lanthanide +2 ions: Eu^{2+}, Yb^{2+}, Sm^{2+}, and Tm^{2+}. The +2 species Pr^{2+}, Gd^{2+}, Tb^{2+}, Ho^{2+}, Er^{2+}, and Lu^{2+} are considered nontraditional lanthanides since they have only been isolated as $4f^n5d^1$ species. Dy^{2+} and Nd^{2+} are the third category of configurational crossover species. These three categories line up nicely with 4f–5d promotion energies that are shown in Fig. 13 [133] as a function of the Ln^{3+}/Ln^{2+} bond distance differences discussed in Section 9, Table 3, and Fig. 7.

The horizontal line in Fig. 13 is defined by the $\left(Cp'_3\right)^{3-}$ ligand set. With these ligands, the crystal field stabilization of the 5d orbitals is sufficient that $4f^n5d^1$ configurations are preferred to $4f^{n+1}$ for all but Eu, Yb, Sm, and Tm, which have the highest promotion energies. Other ligand sets will set the limit at different energies. The fact that Nd and Dy are near the borderline is

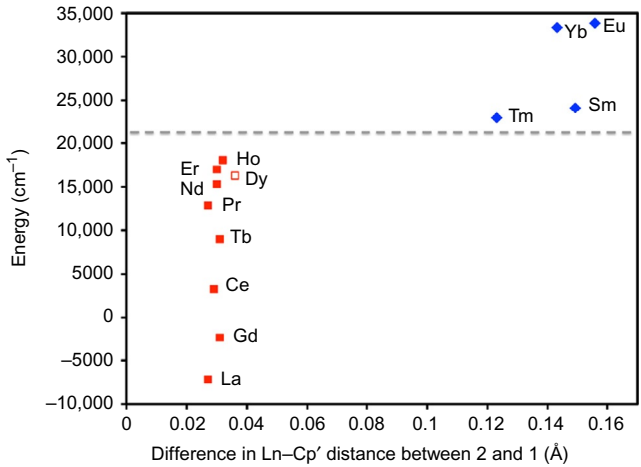

FIG. 13 Plot of the $4f^{n+1}$ to $4f^n5d^1$ promotion energies (only an estimated energy is available for Dy) vs the differences in Ln–(Cp′ centroid) distances of $[K(2.2.2\text{-cryptand})]\left[\left(Cp'_3Ln\right]\right.$ and Cp'_3Ln (Table 3). The *gray dashed line* indicates the barrier in promotion energies to reduce the $4f^n$ Cp'_3Ln to the $4f^{n+1}$ (*diamonds on right*) or $4f^n5d^1$ (*squares on left*) configuration of $\left(Cp'_3Ln\right)^{1-}$. *Adapted with permission from M.E. Fieser, M.R. MacDonald, B.T. Krull, J.E. Bates, J.W. Ziller, F. Furche, W.J. Evans, Structural, spectroscopic, and theoretical comparison of traditional vs recently discovered Ln^{2+} ions in the [K(2.2.2-cryptand)][$(C_5H_4SiMe_3)_3Ln$] complexes: the variable nature of Dy^{2+} and Nd^{2+}, J. Am. Chem. Soc. 137 (2015) 369–382, © 2015, American Chemical Society.*

consistent with the fact that they are configurational crossover ions. However, this plot clearly shows that Er and Ho are also in this "borderline" region. This raises the question about the possibility of isolating Er^{2+} and Ho^{2+} ions with traditional $4f^{12}$ and $4f^{10}$ configurations, respectively, if the "right" ligand set were used. If this were possible, the number of configurational crossover ions would expand to four! Likewise, it seems possible that a ligand set with even more stabilization of a 5d orbital would move the horizontal line in Fig. 13 slightly higher and could lead to isolation of Tm^{2+} and Sm^{2+} as $4f^{12}5d^1$ and $4f^{5}5d^1$ ions with the appropriate ligand set.

Future studies, therefore, should carefully consider the effect of coordination environment on the 5d orbitals and how this can be used to make new oxidation states and electron configurations. It seems likely that coordination environments other than tris(cyclopentadienyl) should be able to stabilize a d orbital to get $4f^n5d^1$ electron configurations. The bis(cyclopentadienyl) arene anion complexes, $\left[\left(Cp'_2Ln\right)_2\left(\mu\text{-}\eta^6:\eta^6\text{-}C_6H_6\right)\right]^{2-}$ [198], constitute another example, but they are closely related tris(carbocyclic anion) species. In addition to searching for $4f^{n+1}$ Er^{2+} and Ho^{2+} and $4f^n5d^1$ Tm^{2+} and Sm^{2+} complexes, it seems that synthesis of Ln^{1+} is a worthy goal as already suggested by Meyer [207]. Sc^{1+} complexes are known [206,208] and the $6d^2$ electron configuration is accessible in Th^{2+}, so it seems that $4f^n5d^2$ or $4f^{n+1}5d^1$ electron configurations are not unreasonable for Ln^{1+} ions. Complexes of Th^{1+} and U^{1+} should also be pursued as well as An^{2+} complexes of other actinides. As in the case of the tris(cyclopentadienyl) Ln^{2+} and An^{2+} complexes in this chapter and the bis(tri-*tert*-butylbenzene) Ln^0 complexes in Section 16 [202], a key component in the new discoveries will be finding the appropriate ligand system under the appropriate conditions which are likely to include low temperature.

Although it is exciting to isolate new classes of complexes as "trophy" molecules, the importance of these discoveries lies in the new chemical opportunities that they provide in terms of physical properties and reactivity. Preliminary examples of this include the unprecedented high magnetic moments found for the Dy^{2+} and Ho^{2+} complexes (Section 10) [135], and the discovery of the first mixed-valent thorium complex and first Th^{3+} hydride complex (Section 13.3) [197]. These aspects of these new oxidation states are just being developed and hopefully will provide the basis for a future chapter. It also seems likely that someday a chapter like this will be written on new +4 oxidation states for the lanthanides!

ACKNOWLEDGMENTS

We thank the National Science Foundation (CHE-1565776) and the Chemical Sciences, Geosciences, and Biosciences Division of the Office of Basic Energy Sciences of the Department of Energy (DE-SC0004739) for support of the rare-earth metal and actinide metal parts of this chapter, respectively.

LIST OF SYMBOLS AND ACRONYMS

An	actinide element
Cp	cyclopentadienyl, C_5H_5
Cp′	$C_5H_4SiMe_3$
Cp″	$C_5H_3(SiMe_3)_2$-1,3
Cp^{Me}	C_5H_4Me
Cp^{tt}	$C_5H_3(CMe_3)_2$-1,3
DFT	density functional theory
DME	dimethoxyethane
HOMO	highest occupied molecular orbital
KC_8	potassium graphite
Ln	yttrium and the lanthanide elements
LUMO	lowest unoccupied molecular orbital
SHE	standard hydrogen electrode
THF	tetrahydrofuran
V	volts

REFERENCES

[1] F. Nief, Molecular chemistry of the rare-earth elements in uncommon low-valent states, in: K.A. Gschneidner Jr., J.-C.G. Bünzli, V.K. Pecharsky (Eds.), Handbook on the Physics and Chemistry of Rare Earths, vol. 1, Elsevier Science, Amsterdam, 2010 (Chapter 246).

[2] J.D. Corbett, Reduced halides of the rare earth elements, Rev. Chim. Mineral 10 (1973) 239–257.

[3] L.R. Morss, Thermochemical properties of yttrium, lanthanum, and the lanthanide elements and ions, Chem. Rev. 76 (1976) 827–841.

[4] L.R. Morss, Comparative thermochemical and oxidation-reduction properties of lanthanides and actinides, in: K.A. Gschneidner Jr., L. Eyring, G.R. Choppin, G.H. Lander (Eds.), Handbook on the Physics and Chemistry of Rare Earths, vol. 18, Elsevier Science, Amsterdam, 1994 (Chapter 122).

[5] G. Meyer, The divalent state in solid rare earth metal halides, in: D.A. Atwood (Ed.), The Rare Earth Elements: Fundamentals and Applications, Wiley, New York, 2012.

[6] T.J. Marks, R.D. Ernst, Scandium, yttrium and the lanthanides and actinides, in: G. Wilkinson, F.G.A. Stone, E.W. Abel (Eds.), Comprehensive Organometallic Chemistry, Pergamon, Oxford, UK, 1982 (Chapter 21).

[7] R.E. Connick, Oxidation states of the rare-earth and actinide elements, J. Chem. Soc. (Suppl.) (1949) 235–241.

[8] A.J. Freeman, R.E. Watson, Theoretical investigation of some magnetic and spectroscopic properties of rare-earth ions, Phys. Rev. 127 (1962) 2058–2075.

[9] C. Matignon, E. Cazes, Un nouveau type de composé dans le group des métaux rares, C. R. Acad. Sci. 142 (1906) 83–85.

[10] C. Matignon, E. Cazes, Le chlorure samareux, Ann. Chim. Phys. 8 (1906) 417–426.

[11] G. Urbain, F. Bourion, Métaux rares. Sur le chlorure europeux, C. R. Acad. Sci. 153 (1911) 1155–1158.

[12] W. Klemm, W. Schüth, Messungen an zwei- und vierwertigen Verbindungen der seltenen Erden. III. Ytterbiumdichlorid, Z. Anorg. Allg. Chem. 184 (1929) 352–358.
[13] G. Meyer, Reduced halides of the rare-earth elements, Chem. Rev. 88 (1988) 93–107.
[14] L.J. Nugent, R.D. Baybarz, J.L. Burnett, J.L. Ryan, Electron-transfer and f-d absorption bands of some lanthanide and actinide complexes and the standard (II-III) oxidation potential for each member of the lanthanide and actinide series, J. Phys. Chem. 77 (1973) 1528–1539.
[15] L.J. Nugent, Chemical oxidation states of the lanthanides and actinides, in: K.W. Bagnall (Ed.), International Review of Science, Inorganic Chemistry Series Two, vol. 7, University Park Press, Baltimore, 1975, pp. 195–219 (Chapter 6).
[16] D.A. Johnson, Relative stabilities of dipositive and tripositive lanthanoid ions in aqueous solution, J. Chem. Soc., Dalton Trans. (1974) 1671–1675.
[17] A.N. Kamenskaya, The lower oxidation state of the lanthanides in solution, Russ. J. Inorg. Chem. 29 (1984) 251–258.
[18] N.B. Mikheev, The lower oxidation states of the lanthanides and actinides in relation to the development of Mendeleev's Periodic Law, Russ. J. Inorg. Chem. 29 (1984) 258–263.
[19] N.B. Mikheev, Lower oxidation states of lanthanides and actinides, Inorg. Chim. Acta 94 (1984) 241–248.
[20] N.B. Mikheev, A.N. Kamenskaya, Complex formation of the lanthanides and actinides in lower oxidation states, Coord. Chem. Rev. 109 (1991) 1–59.
[21] N.B. Mikheev, L.N. Auerman, I.A. Rumer, A.N. Kamenskaya, M.Z. Kazakevich, The anomalous stabilization of the oxidation state 2+ of lanthanides and actinides, Russ. Chem. Rev. 61 (1992) 990–998.
[22] F.H. David, About low oxidation states, hydration and covalence properties of *f*-elements, Radiochim. Acta 96 (2008) 135–144.
[23] A.F. Holleman, E. Wiberg, Inorganic Chemistry, Academic Press de Gruyter, New York, 2001.
[24] D.A. Johnson, Inter-electron repulsion and irregularities in the chemistry of transition series, in: G. Meyer, D. Naumann, L. Wesemann (Eds.), Inorganic Chemistry in Focus III, Wiley-VCH, Weinheim, 2006 (Chapter 1).
[25] R.D. Shannon, Revised effective ionic radii and systematic studies of interatomic distances in halides and chalcogenides, Acta Crystallogr. A A32 (1976) 751–767.
[26] W.J. Evans, S.E. Foster, Structural trends in bis(pentamethylcyclopentadienyl)lanthanide and yttrium complexes, J. Organomet. Chem. 433 (1992) 79–94.
[27] K.N. Raymond, C.W. Eigenbrot Jr., Structural criteria for the mode of bonding of organoactinides and lanthanides and related compounds, Acc. Chem. Res. 13 (1980) 276–283.
[28] W.J. Evans, J.W. Grate, H.W. Choi, I. Bloom, W.E. Hunter, J.L. Atwood, Solution synthesis and crystallographic characterization of the divalent organosamarium complexes $(C_5Me_5)_2Sm(THF)_2$ and $[(C_5Me_5)Sm(\mu\text{-}I)(THF)_2]_2$, J. Am. Chem. Soc. 107 (1985) 941–946.
[29] W.J. Evans, C.A. Seibel, J.W. Ziller, Unsolvated lanthanide metallocene cations $[(C_5Me_5)_2Ln][BPh_4]$: multiple syntheses, structural characterization, and reactivity including the formation of $(C_5Me_5)_3Nd$, J. Am. Chem. Soc. 120 (1998) 6745–6752.
[30] M. Seitz, A.G. Oliver, K.N. Raymond, The lanthanide contraction revisited, J. Am. Chem. Soc. 129 (2007) 11153–11160.
[31] E.A. Quadrelli, Lanthanide contraction over the 4f series follows a quadratic decay, Inorg. Chem. 41 (2002) 167–169.

[32] G. Meyer, H.-J. Meyer, Unusual valences in rare-earth halides, Chem. Mater. 4 (1992) 1157–1168.
[33] G. Meyer, M.S. Wickleder, Simple and complex halides, in: Handbook on the Physics and Chemistry of Rare Earths, vol. 28, Elsevier Science B.V., Amsterdam, 2000.
[34] L.F. Druding, J.D. Corbett, Rare earth metal-metal halide systems. The preparation of neodymium(II) halides, J. Am. Chem. Soc. 81 (1959) 5512–5512.
[35] L.F. Druding, J.D. Corbett, Lower oxidation states of the lanthanides. Neodymium(II) chloride and iodide, J. Am. Chem. Soc. 83 (1961) 2462–2467.
[36] L.B. Asprey, F.H. Kruse, Divalent thulium. Thulium di-iodide, J. Inorg. Nucl. Chem. 13 (1960) 32–35.
[37] J.D. Corbett, B.C. McCollum, Rare earth metal-metal halide systems. IX. Dysprosium-dysprosium(III) chloride system and the preparation of dysprosium(II) chloride, Inorg. Chem. 5 (1966) 938–940.
[38] G. Meyer, A. Palasyuk, Forty-five years of praseodymium di-iodide, PrI_2, in: G. Meyer, D. Naumann, L. Wesemann (Eds.), Inorganic Chemistry in Focus III, Wiley-VCH, Weinheim, 2006 (Chapter 4).
[39] M.N. Bochkarev, Molecular compounds of "new" divalent lanthanides, Coord. Chem. Rev. 248 (2004) 835–851.
[40] L.B. Asprey, B.B. Cunningham, Unusual oxidation states of some actinide and lanthanide elements, Prog. Inorg. Chem. 2 (1960) 267–301.
[41] A.N. Kamenskaya, N.B. Mikheev, N.A. Konovalova, Reduction of thulium, samarium, and ytterbium halides to the bivalent state in hexamethylphosphoramide solutions, Russ. J. Inorg. Chem. 22 (1977) 1152–1155.
[42] A.N. Kamenskaya, K. Bukietynska, N.B. Mikheev, V.I. Spitsyn, B. Jezowska-Trzebiatowska, Properties of non-aqueous solutions of lanthanide dihalides, Russ. J. Inorg. Chem. 24 (1979) 633–637.
[43] A.N. Kamenskaya, N.B. Mikheev, N. Kholmogorova, Solutions of lanthanide di-iodides in tetrahydrofuran, Russ. J. Inorg. Chem. 28 (1983) 1420–1423.
[44] K.E. Johnson, J.N. Sandoe, Interpretation of the spectra of bivalent rare-earth ions in crystals, J. Chem. Soc. A (1969) 1694–1697.
[45] G.H. Dieke, H.M. Crosswhite, H. Crosswhite, Spectra and Energy Levels of Rare Earth Ions in Crystals, Interscience Publishers, New York, 1968.
[46] L. Brewer, Systematics of the properties of the lanthanides, in: S.P. Sinha, D. Reidel (Eds.), Systematics and the Properties of the Lanthanides, Reidel, Dordrecht, 1983, pp. 17–69.
[47] W.C. Martin, R. Zalubas, L. Hagan, Atomic Energy Levels—The Rare-Earth Elements, the Spectra of La, Ce, Pr, Nd, Pm, Sm, Eu, Gd, Tb, Dy, Ho, Er, Tm, Yb, Lu, National Bureau of Standards, U.S. Department of Commerce, Washington, DC, 1978.
[48] P.J. Dorenbos, $f \rightarrow d$ transition energies of divalent lanthanides in inorganic compounds, J. Phys. Condens. Matter 15 (2003) 575–594.
[49] A.N. Kamenskaya, N.B. Mikheev, V.I. Spytsin, Complex compounds of bivalent samarium and thulium with crown ethers, Dokl. Akad. Nauk SSSR 275 (1984) 913–916.
[50] M.N. Bochkarev, I.L. Fedushkin, A.A. Fagin, T.V. Petrovskaya, J.W. Ziller, R.N.R.Broomhall-Dillard, W.J. Evans, Synthesis and structure of the first molecular thulium(II) complex: $[TmI_2(MeOCH_2CH_2OMe)_3]$, Angew. Chem. Int. Ed. 36 (1997) 133–135.
[51] M.N. Bochkarev, A.A. Fagin, A new route to neodymium(II) and dysprosium(II) iodides, Chem. Eur. J. 5 (1999) 2990–2992.

[52] W.J. Evans, N.T. Allen, J.W. Ziller, The availability of dysprosium diiodide as a powerful reducing agent in organic synthesis: reactivity studies and structural analysis of $DyI_2((DME)_3$ and its naphthalene reduction product, J. Am. Chem. Soc. 122 (2000) 11749–11750.

[53] M.N. Bochkarev, I.L. Fedushkin, S. Dechert, A.A. Fagin, H. Schumann, Organometallic compounds of the lanthanides, Part 152. $[NdI_2(THF)_5]$, the first crystallographically authenticated neodymium(II) complex, Angew. Chem. Int. Ed. 40 (2001) 3176–3178.

[54] G.H. Dieke, H.M. Crosswhite, Spectra of the doubly and triply ionized rare earths, Appl. Opt. 2 (1963) 675–686.

[55] Y. Huang, B.S. Freiser, Doubly charged gas-phase heteronuclear cluster ions: synthesis and reaction of $LaFe^{2+}$ with small hydrocarbons, J. Am. Chem. Soc. 110 (1988) 4434–4435.

[56] Y.A. Ranasinghe, T.J. MacMahon, B.S. Freiser, Gas-phase reactions of lanthanum dication with small alkanes and the photodissociation of $LaC_2H_4^{n+}$ and $LaC_3H_6^{n+}$ (n = 1 and 2), J. Am. Chem. Soc. 114 (1992) 9112–9118.

[57] B.S. Freiser, Selected topics in organometallic ion chemistry, Acc. Chem. Res. 27 (1994) 353–360.

[58] J. Marçalo, M. Santos, A.P. de Matos, J.K. Gibson, R.G. Haire, Gas-phase reactions of doubly charged lanthanide cations with alkanes and alkenes. Trends in metal(2+) reactivity, J. Phys. Chem. A 112 (2008) 12647–12656.

[59] D.S. McClure, Z. Kiss, Spectra of the bivalent rare-earth ions in cubic crystals, J. Chem. Phys. 39 (1963) 3251–3257.

[60] H.R. Bronstein, Electromotive force measurements on solutions of rare earth metals in their molten halides. I. The cerium-cerium chloride, praseodymium-praseodymium chloride, and neodymium-neodymium chloride solutions, J. Phys. Chem. 73 (1969) 1320–1326.

[61] N.B. Mikheev, L.N. Auerman, I.A. Rumer, Correlation between oxidation potentials of the lanthanides in aqueous solutions and chloride melts, Inorg. Chim. Acta 109 (1985) 217–220.

[62] A.M. Bond, G.B. Deacon, R.H. Newnham, Electrochemical reduction of tris(cyclopentadienyl)samarium(III), -ytterbium(III), and -europium(III) compounds in tetrahydrofuran, Organometallics 5 (1986) 2312–2316.

[63] W.J. Evans, N.T. Allen, J.W. Ziller, Facile dinitrogen reduction via organometallic Tm(II) chemistry, J. Am. Chem. Soc. 123 (2001) 7927–7928.

[64] W.J. Evans, N.T. Allen, J.W. Ziller, Expanding divalent organolanthanide chemistry: the first organothulium(II) complex and the in situ organodysprosium (II) reduction of dinitrogen, Angew. Chem. Int. Ed. Engl. 41 (2002) 359–361.

[65] W.J. Evans, G. Zucchi, J.W. Ziller, Dinitrogen reduction by Tm(II), Dy(II), and Nd(II) with simple amide and aryloxide ligands, J. Am. Chem. Soc. 125 (2003) 10–11.

[66] W.J. Evans, M. Fang, G. Zucchi, F. Furche, J.W. Ziller, R.M. Hoekstra, J.I. Zink, Isolation of dysprosium and yttrium complexes of a three-electron reduction product in the activation of dinitrogen, the $(N_2)^{3-}$ radical, J. Am. Chem. Soc. 131 (2009) 11195–11202.

[67] W.J. Evans, T.A. Ulibarri, J.W. Ziller, Isolation and X-ray crystal structure of the first dinitrogen complex of an f-element metal,$[(C_5Me_5)_2Sm]_2N_2$, J. Am. Chem. Soc. 110 (1988) 6877–6879.

[68] J. Jubb, S. Gambarotta, Dinitrogen reduction operated by a samarium macrocyclic complex. Encapsulation of dinitrogen into a Sm_2Li_4 metallic cage, J. Am. Chem. Soc. 116 (1994) 4477–4478.

[69] T. Dubé, S. Conoci, S. Gambarotta, G.P.A. Yap, G. Vasapollo, Tetrametallic reduction of dinitrogen: formation of a tetranuclear samarium dinitrogen complex, Angew. Chem. Int. Ed. 38 (1999) 3657–3659.
[70] J. Guan, T. Dubé, S. Gambarotta, G.P.A. Yap, Dinitrogen labile coordination versus four-electron reduction, THF cleavage, and fragmentation promoted by a (calix-tetrapyrrole)-Sm(II) complex, Organometallics 19 (2000) 4820–4827.
[71] M. Ganesan, S. Gambarotta, G.P.A. Yap, Highly reactive Sm^{II} macrocyclic clusters: precursors to N_2 reduction, Angew. Chem. Int. Ed. 40 (2000) 766–769.
[72] E. Campazzi, E. Solari, C. Floriani, R. Scopelliti, The fixation and reduction of dinitrogen using lanthanides: praseodymium and neodymium *meso*-octaethylporphyrinogen–dinitrogen complexes, Chem. Commun. (1998) 2603–2604.
[73] G. Meyer, The reduction of rare-earth metal halides with unlike metals–Wöhler's metallothermic reduction, Z. Anorg. Chem. 633 (2007) 2537–2552.
[74] G.W. Watt, E.W. Gillow, Samarium (II) dicyclopentadienide 1-tetrahydrofuranate, J. Am. Chem. Soc. 91 (1969) 775–776.
[75] W.J. Evans, N.T. Allen, P.S. Workman, J.C. Meyer, Large scale synthesis of dysprosium and neodymium diiodides, Inorg. Chem. 42 (2003) 3097–3099.
[76] D.C. Bradley, J.S. Ghotra, F.A. Hart, Low coordination numbers in lanthanide and actinide compounds. I. Preparation and characterization of tris[bis(trimethylsilyl) amido] lanthanides, J. Chem. Soc., Dalton Trans. (1973) 1021–1023.
[77] W.J. Evans, D.S. Lee, J.W. Ziller, Reduction of dinitrogen to planar bimetallic $M_2(\mu\text{-}\eta^2\text{:}\eta^2\text{-}N_2)$ complexes of Y, Ho, Tm, and Lu using the $K/Ln[N(SiMe_3)_2]_3$ reduction system, J. Am. Chem. Soc. 126 (2004) 454–455.
[78] W.J. Evans, D.K. Drummond, H. Zhang, J.L. Atwood, Synthesis and x-ray crystal structure of the divalent [bis(trimethylsilyl)amido] samarium complexes $[(Me_3Si)_2N]_2Sm(THF)_2$ and $\{[(Me_3Si)_2N]Sm(\mu\text{-}I)(DME)(THF)\}_2$, Inorg. Chem. 27 (1988) 575–579.
[79] T.D. Tilley, R.A. Andersen, A. Zalkin, Divalent lanthanide chemistry. Preparation and crystal structures of sodium tris[bis(trimethylsilyl)amido]europate(II) and sodium tris[bis(trimethylsilyl)amido]ytterbate(II), $NaM[N(SiMe_3)_2]_3$, Inorg. Chem. 23 (1984) 2271–2276.
[80] W.J. Evans, M.A. Johnston, R.D. Clark, R. Anwander, J.W. Ziller, Heteroleptic and heterometallic divalent lanthanide bis(trimethylsilyl) amide complexes: mixed ligand, inverse sandwich, and alkali metal derivatives, Polyhedron 20 (2001) 2483–2490.
[81] W.J. Evans, D.S. Lee, S.B. Rego, J.M. Perotti, S.A. Kozimor, E.K. Moore, J.W. Ziller, Expanding dinitrogen reduction chemistry to trivalent lanthanides via the LnZ_3/alkali metal reduction system: evaluation of the generality of forming $Ln_2(\mu\text{-}\eta^2\text{:}\eta^2\text{-}N_2)$ complexes via LnZ_3/K, J. Am. Chem. Soc. 126 (2004) 14574–14582.
[82] W.J. Evans, D.S. Lee, C. Lie, J.W. Ziller, Expanding the LnZ_3/alkali-metal reduction system to organometallic and heteroleptic precursors: formation of dinitrogen derivatives of lanthanum, Angew. Chem. Int. Ed. 43 (2004) 5517–5519.
[83] W.J. Evans, D.S. Lee, M.A. Johnston, J.W. Ziller, The elusive $(C_5Me_4H)_3Lu$: its synthesis and $LnZ_3/K/N_2$ reactivity, Organometallics 24 (2005) 6393–6397.
[84] W.J. Evans, D.S. Lee, Early developments in lanthanide-based dinitrogen reduction chemistry, Can. J. Chem. 83 (2005) 375–384.
[85] W.J. Evans, D.B. Rego, J.W. Ziller, Synthesis, structure, and ^{15}N NMR studies of paramagnetic lanthanide complexes obtained by reduction of dinitrogen, Inorg. Chem. 45 (2006) 10790–10798.

[86] F. Jaroschik, F. Nief, X.-F. Le Goff, L. Ricard, Isolation of stable organodysprosium (II) complexes by chemical reduction of dysprosium (III) precursors, Organometallics 26 (2007) 1123–1125.

[87] F. Jaroschik, A. Momin, F. Nief, X.-F. Le Goff, G.B. Deacon, P.C. Junk, Dinitrogen reduction and C–H activation by the divalent organoneodymium complex $[(C_5H_2{}^tBu_3)_2Nd(\mu\text{-}I)K([18]crown\text{-}6)]$, Angew. Chem. Int. Ed. 48 (2009) 1117–1121.

[88] W.J. Evans, M. Fang, G. Zucchi, F. Furche, J.W. Ziller, R.M. Hoekstra, J.I. Zink, Isolation of dysprosium and yttrium complexes of a three-electron reduction product in the activation of dinitrogen, the $(N_2)^{3-}$ radical, J. Am. Chem. Soc. 133 (2009) 11195–11202.

[89] S.E. Lorenz, B.M. Schmiege, D.S. Lee, J.W. Ziller, W.J. Evans, Synthesis and reactivity of bis(tetramethylcyclopentadienyl) yttrium metallocenes including the reduction of Me_3SiN_3 to $[(Me_3Si)_2N]^-$ with $[(C_5Me_4H)_2Y(THF)]_2(\mu\text{-}\eta^2{:}\eta^2\text{-}N_2)$, Inorg. Chem. 49 (2010) 6655–6663.

[90] B.M. Schmiege, J.W. Ziller, W.J. Evans, Reduction of dinitrogen with an yttrium metallocene hydride precursor, $[(C_5Me_5)_2YH]_2$, Inorg. Chem. 49 (2010) 10506–10511.

[91] S. Demir, S.E. Lorenz, M. Fang, F. Furche, G. Meyer, J.W. Ziller, W.J. Evans, Synthesis, structure, and density functional theory analysis of a scandium dinitrogen complex, $[(C_5Me_4H)_2Sc]_2(\mu\text{-}\eta^2{:}\eta^2\text{-}N_2)$, J. Am. Chem. Soc. 132 (2010) 11151–11158.

[92] M. Fang, J.E. Bates, S.E. Lorenz, D.S. Lee, D.B. Rego, J.W. Ziller, F. Furche, W.J. Evans, $(N_2)^{3-}$ radical chemistry via trivalent lanthanide salt/alkali metal reduction of dinitrogen: new syntheses and examples of $(N_2)^{2-}$ and $(N_2)^{3-}$ complexes and density functional theory comparisons of closed shell Sc^{3+}, Y^{3+}, and Lu^{3+} versus $4f^9$ Dy^{3+}, Inorg. Chem. 50 (2011) 1459–1469.

[93] M. Fang, D.S. Lee, J.W. Ziller, R.J. Doedens, J.E. Bates, F. Furche, W.J. Evans, Synthesis of the $(N_2)^{3-}$ radical from Y^{2+} and its protonolysis reactivity to form $(N_2H_2)^{2-}$ via the $Y[N(SiMe_3)_2]_3/KC_8$ reduction system, J. Am. Chem. Soc. 133 (2011) 3784–3787.

[94] F. Wöhler, Uber das beryllium und yttrium, Poggendorfs, Ann. Phys. Chem. 13 (1828) 577–582.

[95] Y.K. Gun'ko, P.B. Hitchcock, M.F. Lappert, Activation of a C–O bond by reaction of a tris(cyclopentadienyl)lanthanide complex with an alkali metal in dimethoxyethane (DME); crystal structures of $[Nd\eta\text{-}C_5H_3(SiMe_3)_2\text{-}1,3_2(\mu\text{-}OMe)_2Li(DME)]$ and $[\{Ce(\eta\text{-}C_5H_3{}^tBu_2\text{-}1,3)_2(\mu\text{-}OMe)_2]$, J. Organomet. Chem. 499 (1995) 213–219.

[96] M.C. Cassani, Y.K. Gun'ko, P.B. Hitchcock, M.F. Lappert, The first metal complexes containing the 1,4-cyclohexa-2,5-dienyl ligand (benzene 1,4-dianion); synthesis and structures of $[K(18\text{-}crown\text{-}6)][Ln\{\eta^5\text{-}C_5H_3(SiMe_3)_2\text{-}1,3\}_2(C_6H_6)]$(Ln = La, Ce), Chem. Commun. (1996) 1987–1988.

[97] M.C. Cassani, M.F. Lappert, F. Laschi, First identification by EPR spectra of lanthanum(II) organometallic intermediates (and $E_{½}$ for $La^{3+} \rightarrow La^{2+}$) in the C–O bond activation of dimethoxyethane, Chem. Commun. (1997) 1563–1564.

[98] M.C. Cassani, D.J. Duncalf, M.F. Lappert, The first example of a crystalline subvalent organolanthanum complex: $[K([18]crown\text{-}6)\text{-}(\eta^2\text{-}C_6H_6)_2][(LaCp^{tt}_2)_2(\mu\text{-}\eta^6{:}\eta^6\text{-}C_6H_6)]\cdot 2C_6H_6$ ($Cp^{tt} = \eta^5\text{-}C_5H_3Bu^t{}_2\text{-}1,3$), J. Am. Chem. Soc. 120 (1998) 12958–12959.

[99] M.C. Cassani, Y.K. Gun'ko, P.B. Hitchcock, M.F. Lappert, F. Laschi, Synthesis and characterization of organolanthanidocene(III) (Ln = La, Ce, Pr, Nd) complexes containing the 1,4-cyclohexa-2,5-dienyl ligand (benzene 1,4-dianion): structures of $[K([18]\text{-}crown\text{-}6)][Ln\{\eta^5\text{-}C_5H_3(SiMe_3)_2\text{-}1,3\}_2(C6H6)]$ [$Cp'' = \eta^5\text{-}C_5H_3(SiMe_3)_2\text{-}1,3$; Ln = La, Ce, Nd], Organometallics 18 (1999) 5539–5547.

[100] Y.K. Gun'ko, P.B. Hitchcock, M.F. Lappert, Nonclassical organolanthanoid metal chemistry: [K([18]-crown-6)(η^2-PhMe)$_2$]X (X = [(LnCp$^t_3$)$_2$(μ-H)], [(LnCp$''_2$)$_2$(μ-η^6:η^6-PhMe)]) from [LnCp$^x_3$], K, and [18]-crown-6 in Toluene (Ln = La, Ce; Cp^t = η^5-C$_5$H$_4$SiMe$_2$Bu^t; Cp$''$ = η^5-C$_5$H$_3$(SiMe$_3$)$_2$-1,3), Organometallics 19 (2000) 2832–2834.

[101] M.C. Cassani, Y.K. Gun'ko, P.B. Hitchcock, A.G. Hulkes, A.V. Khvostov, M.F. Lappert, A.V. Protchenko, Aspects of non-classical organolanthanide chemistry, J. Organomet. Chem. 647 (2002) 71–83.

[102] P.B. Hitchcock, M.F. Lappert, L. Maron, A.V. Protchenko, Lanthanum does form stable molecular compounds in the +2 oxidation state, Angew. Chem. Int. Ed. 47 (2008) 1488–1491.

[103] M.P. Coles, P.B. Hitchcock, M.F. Lappert, A.V. Protchenko, Syntheses and structures of the crystalline, highly crowded 1,3-bis(trimethylsilyl)cyclopentadienyls [MCp$''_3$] (M = Y, Er, Yb), [PbCp$''_2$], [{YCp$''_2$(μ-OH)}$_2$], [(ScCp$''_2$)$_2$ (μ-η^2:η^2-C$_2$H$_4$)], [YbCp$''_2$Cl (μ-Cl) K (18-crown-6)], and [{KCp$''$}$_\infty$], Organometallics 31 (2012) 2682–2690.

[104] A. Greco, S. Cesca, G. Bertolini, New π-cyclooctatetraenyl and π-cyclopentadienyl complexes of cerium, J. Organomet. Chem. 113 (1976) 321–330.

[105] M. Wedler, R. Recknagel, F.T. Edelman, Nichtklassische organolanthanoid (II) komplexe: Darstellung und reaktivität der ersten organoneodym (II) verbindung, J. Organomet. Chem. 395 (1990) C26–C29.

[106] E.N. Kirillov, A.A. Trifonov, S.E. Nefedov, I.L. Eremenko, F.T. Edelmann, M.N. Bochkarev, Attempted synthesis of divalent neodymium derivatives. Crystal structure of the Nd(III) complex [{NdCl$_2$(2,4,6-*t*-Bu$_3$C$_6$H$_2$O)(μ-Cl)(THF)}Li(THF)$_2$]$_2$, Z. Naturforsch. B 54 (1999) 1379–1384.

[107] M.N. Bochkarev, I.L. Fedushkin, V.I. Nevodchikov, V.K. Cherkasov, H. Schumann, H. Hemling, R. Weimann, Synthesis and ESR-characterization of radical anion complexes of lanthanum. X-ray crystal structure of the mixed bipy, bipy^{-1} complex of lanthanum(III) [LaI$_2$(bipy)(bipy)(DME)]: evidence for an inter-ligand charge transfer, J. Organomet. Chem. 524 (1996) 125–131.

[108] M.D. Fryzuk, J.B. Love, S.J. Rettig, Arene coordination to yttrium(III) via carbon-carbon bond formation, J. Am. Chem. Soc. 119 (1997) 9071–9072.

[109] M.D. Fryzuk, L. Jafarpour, F.M. Kerton, J.B. Love, B.O. Patrick, S.J. Rettig, Carbon-carbon bond formation using yttrium(III) and the lanthanide elements, Organometallics 20 (2001) 1387–1396.

[110] M.N. Bochkarev, Synthesis, arrangement, and reactivity of arene-lanthanide compounds, Chem. Rev. 102 (2002) 2089–2117.

[111] W. Huang, F. Dulong, T. Wu, S.I. Khan, J.T. Miller, T. Cantat, P.L. Diaconescu, A six-carbon 10π-electron aromatic system supported by group 3 metals, Nat. Commun. 4 (2013) 1448–1455.

[112] P.L. Diaconescu, P.L. Arnold, T.A. Baker, D.J. Mindiola, C.C. Cummins, Arene-bridged diuranium complexes: inverted sandwiches supported by δ backbonding, J. Am. Chem. Soc. 122 (2000) 6108–6109.

[113] W.J. Evans, S.A. Kozimor, J.W. Ziller, N. Kaltsoyannis, Structure, reactivity, and density functional theory analysis of the six-electron reductant, [(C$_5$Me$_5$)$_2$U]$_2$(μ-η^6:η^6-C$_6$H$_6$), synthesized via a new mode of (C$_5$Me$_5$)$_3$M reactivity, J. Am. Chem. Soc. 126 (2004) 14533–14547.

[114] P.L. Arnold, S.M. Mansell, L. Maron, D. McKay, Spontaneous reduction and C–H borylation of arenes mediated by uranium(III) disproportionation, Nat. Chem. 4 (2012) 668–674.

[115] D. Patel, F. Tuna, E.J.L. McInnes, J. McMaster, W. Lewis, A.J. Blake, S.T. Liddle, A triamido-uranium(V) inverse-sandwich 10π-toluene tetraanion arene complex, Dalton Trans. 42 (2013) 5224–5227.

[116] C. Camp, V. Mougel, J. Pécaut, L. Maron, M. Mazzanti, A triamido-uranium(v) inverse-sandwich 10π-toluene tetraanion arene complex, Chem. Eur. J. 19 (2013) 17528–17540.

[117] E. Rogers, P. Dorenbos, E. van der Kolk, Systematics in the optical and electronic properties of the binary lanthanide halide, chalcogenide and pnictide compounds: an overview, New J. Phys. 13 (2011) 093038/1–093038/32.

[118] A. Clearfield, D.K. Warner, C.H. Saldarriaga-Molina, R. Ropal, I. Bernal, Structural studies of $(\pi\text{-}C_5H_5)_2MX_2$ complexes and their derivatives. The structure of bis(π-cyclopentadienyl) titanium dichloride, Can. J. Chem. 53 (1975) 1622–1629.

[119] R. Jungst, D. Sekutowski, J. Davis, M. Luly, G. Stucky, Structural and magnetic properties of di-μ-chloro-bis[bis(η^5-cyclopentadienyl)titanium(III)] and di-μ-bromo-bis[bis(η^5-methylcyclopentadienyl)titanium(III)], Inorg. Chem. 16 (1977) 1645–1655.

[120] R.D. Rogers, R.V. Bynum, J.L. Atwood, Crystal and molecular structure of tetra(cyclopentadienyl)zirconium, J. Am. Chem. Soc. 100 (1978) 5238–5239.

[121] W.L. Lukens Jr., R.A. Andersen, Synthesis, structure, and reactions of $(\eta^5\text{-}C_5H_5)_3Zr$, Organometallics 14 (1995) 3435–3439.

[122] M.R. MacDonald, J.W. Ziller, W.J. Evans, Synthesis of a crystalline molecular complex of Y^{2+}, $[(18\text{-crown-6})K][(C_5H_4SiMe_3)_3Y]$, J. Am. Chem. Soc. 133 (2011) 15914–15917.

[123] M.F. Lappert, A. Singh, J.L. Atwood, W.E. Hunter, Organometallic complexes of the group 3A and lanthanoid metals containing $M(\mu\text{-}Cl)_2Li$ bridging units; the x-ray structure of $[Nd\{\eta\text{-}[C_5H_3(SiMe_3)_2]\}_2(\mu\text{-}Cl)_2Li(thf)_2]$(thf = tetrahydrofuran), J. Chem. Soc. Chem. Commun. (1981) 1190–1191.

[124] J.F. Corbey, D.H. Woen, C.T. Palumbo, M.E. Fieser, J.W. Ziller, F. Furche, W.J. Evans, Ligand effects in the synthesis of Ln^{2+} complexes by reduction of tris(cyclopentadienyl) precursors including C–H bond activation of an indenyl anion, Organometallics 34 (2015) 3909–3921.

[125] M.R. MacDonald, J.E. Bates, M.E. Fieser, J.W. Ziller, F. Furche, W.J. Evans, Expanding rare-earth oxidation state chemistry to molecular complexes of holmium(II) and erbium(II), J. Am. Chem. Soc. 134 (2012) 8420–8423.

[126] M.R. MacDonald, J.E. Bates, J.W. Ziller, F. Furche, W.J. Evans, Completing the series of +2 ions for the lanthanide elements: synthesis of molecular complexes of Pr^{2+}, Gd^{2+}, Tb^{2+}, and Lu^{2+}, J. Am. Chem. Soc. 135 (2013) 9857–9868.

[127] J.W. Lauher, R. Hoffmann, Structure and chemistry of bis(cyclopentadienyl)-MLn complexes, J. Am. Chem. Soc. 98 (1976) 1729–1742.

[128] B.E. Bursten, L.F. Rhodes, R.J. Strittmatter, Bonding in tris(η^5-cyclopentadienyl) actinide complexes. 2. The ground electronic configurations of "base-free" Cp_3An complexes (An = thorium, protactinium, uranium, neptunium, plutonium), J. Am. Chem. Soc. 111 (1989) 2756–2758.

[129] B.E. Bursten, L.F. Rhodes, R.J. Strittmatter, Bonding of tris(η^5-cyclopentadienyl)-actinide complexes. 3. Interaction of π-neutral, π-acidic, and π-basic ligands with $(\eta^5\text{-}C_5H_5)_3U$, J. Am. Chem. Soc. 111 (1989) 2758–2766.

[130] R.J. Strittmatter, B.E. Bursten, Bonding in tris(η^5-cyclopentadienyl) actinide complexes. 5. A comparison of the bonding in neptunium, plutonium, and transplutonium compounds with that in lanthanide compounds and a transition-metal analog, J. Am. Chem. Soc. 113 (1991) 552–559.

[131] R.G. Denning, J. Harmer, J.C. Green, M. Irwin, Covalency in the 4f shell of tris-cyclopentadienyl ytterbium ($YbCp_3$)—a spectroscopic evaluation, J. Am. Chem. Soc. 133 (2011) 20644–20660.

[132] G. Meyer, All the lanthanides do it and even uranium does oxidation state +2, Angew. Chem. Int. Ed. 53 (2014) 3550–3551.

[133] M.E. Fieser, M.R. MacDonald, B.T. Krull, J.E. Bates, J.W. Ziller, F. Furche, W.J. Evans, Structural, spectroscopic, and theoretical comparison of traditional vs recently discovered Ln^{2+} ions in the $[K(2.2.2\text{-cryptand})][(C_5H_4SiMe_3)_3Ln]$ complexes: the variable nature of Dy^{2+} and Nd^{2+}, J. Am. Chem. Soc. 137 (2015) 369–382.

[134] J.A. Wilson, A generalized configuration-dependent band model for lanthanide compounds and conditions for interconfiguration fluctuations, Struct. Bond. 32 (1977) 57–91.

[135] K.R. Meihaus, M.E. Fieser, J.F. Corbey, W.J. Evans, J.R. Long, Record high single-ion magnetic moments through $4f^n5d^1$ electron configurations in the divalent lanthanide complexes $[(C_5H_4SiMe_3)_3Ln]^-$, J. Am. Chem. Soc. 137 (2015) 9855–9860.

[136] B.-W. Wang, S. Gao, Molecular magnetic materials, in: D.A. Atwood (Ed.), The Rare Earth Elements: Fundamentals and Applications, Wiley, New York, 2012.

[137] R.L. Dutta, A. Syamal, Elements of Magnetochemistry, Affiliated East-West Press Pvt. Ltd., New Delhi, 2007.

[138] N.M. Edelstein, J. Fuger, J.J. Katz, L.R. Morss, Summary of comparison of properties of the actinide and transactinide elements, in: L.R. Morss, N.M. Edelstein, J. Fuger (Eds.), The Chemistry of the Actinide and Transactinide Elements, fourth ed., Springer, The Netherlands, 2010 (Chapter 15).

[139] E.F. Worden, J. Blaise, M. Fred, N. Trautmann, J.-F. Wyart, Spectra and electronic structures of free actinide atoms and ions, in: L.R. Morss, N.M. Edelstein, J. Fuger (Eds.), The Chemistry of the Actinide and Transactinide Elements, fourth ed., Springer, The Netherlands, 2010 (Chapter 16).

[140] A.B. McLaren, B. Kanellakopulos, E. Dornberger, Unexpected chemistry in the reduction of uranium cyclopentadienides, Inorg. Nucl. Chem. Lett. 16 (1980) 223–225.

[141] P.J. Fagan, J.M. Manriquez, T.J. Marks, C.S. Day, S.H. Vollmer, V.W. Day, Synthesis and properties of a new class of highly reactive trivalent actinide organometallic compounds. Derivatives of bis(pentamethylcyclopentadienyl)uranium(III), Organometallics 1 (1982) 170–180.

[142] B.P. Warner, B.L. Scott, C.J. Burns, A simple preparative route to bis(imido)uranium(VI) complexes by the direct reductions of diazenes and azides, Angew. Chem. Int. Ed. 37 (1998) 959–960.

[143] P.L. Diaconescu, C.C. Cummins, μ-η^6,η^6-Arene-bridged diuranium hexakisketimide complexes isolable in two states of charge, Inorg. Chem. 51 (2012) 2902–2916.

[144] T. Mehdoui, J.-C. Berthet, P. Thuéry, L. Salmon, E. Rivière, M. Ephritikhine, Lanthanide(III)/actinide(III) differentiation in the cerium and uranium complexes $[M(C_5Me_5)_2(L)]^{0,+}$ (L = 2,2′-bipyridine, 2,2′:6′,2″-terpyridine): structural, magnetic, and reactivity studies, Chem. Eur. J. 11 (2005) 6994–7006.

[145] G. Zi, L. Jia, E.L. Werkema, M.D. Walter, J.P. Gottfriedsen, R.A. Anderson, Preparation and reactions of base-free bis(1,2,4-tri-*tert*-butylcyclopentadienyl)uranium oxide, Cp'_2UO, Organometallics 24 (2005) 4251–4264.

[146] I. Korobkov, S. Gorelsky, S. Gambarotta, Reduced uranium complexes: synthetic and DFT study of the role of π ligation in the stabilization of uranium species in a *formal* low-valent state, J. Am. Chem. Soc. 131 (2009) 10406–10420.

[147] S.J. Kraft, P.E. Fanwick, S.C. Bart, Synthesis and characterization of a uranium(III) complex containing a redox-active 2,2′-bipyridine ligand, Inorg. Chem. 49 (2010) 1103–1110.
[148] S.J. Kraft, U.J. Williams, S.R. Daly, E.J. Schelter, S.A. Kozimor, K.S. Boland, J.M. Kikkawa, W.P. Forrest, C.N. Christensen, D.E. Schwarz, P.E. Fanwick, D.L. Clark, S.D. Conradson, S.C. Bart, Synthesis, characterization, and multielectron reduction chemistry of uranium supported by redox-active α-diimine ligands, Inorg. Chem. 50 (2011) 9838–9848.
[149] D.P. Mills, F. Moro, J. McMaster, J. van Slageren, W. Lewis, A.J. Blake, S.T. Liddle, A delocalized arene-bridged diuranium single-molecule magnet, Nat. Chem. 3 (2011) 454–460.
[150] E.D. Eastman, L. Brewer, L.A. Bromley, P.W. Gilles, N.L. Lofgren, Preparation and properties of the sulfides of thorium and uranium, J. Am. Chem. Soc. 72 (1950) 4019–4023.
[151] A.F. Wells, Structural Inorganic Chemistry, fourth ed., Clarendon Press, Oxford, 1975.
[152] J.E. Sansonetti, W.C. Martin, Handbook of basic atomic spectroscopic data, J. Phys. Chem. Ref. Data 34 (2005) 1559–2259.
[153] E. Di Santo, M. Santos, M.C. Michelini, J. Marçalo, N. Russo, J.K. Gibson, Gas-phase reactions of the bare Th^{2+} and U^{2+} ions with small alkanes, CH_4, C_2H_6, and C_3H_8: experimental and theoretical study of elementary organoactinide chemistry, J. Am. Chem. Soc. 133 (2011) 1955–1970.
[154] H.H. Cornehl, C. Heinemann, J. Marçalo, A. Pires de Matos, H. Schwarz, The "bare" uranyl(2+) ion, UO_2^{2+}, Angew. Chem. Int. Ed. Engl. 35 (1996) 891–894.
[155] G.P. Jackson, F.L. King, D.E. Goeringer, D.C. Duckworth, Gas-phase reactions of U^+ and U^{2+} with O_2 and H_2O in a quadrupole ion trap, J. Phys. Chem. A 10 (2002) 7788–7794.
[156] J. Marçalo, J.P. Leal, A. Pires de Matos, A.G. Marshall, Gas-phase actinide ion chemistry: FT-ICR/MS study of the reactions of thorium and uranium metal and oxide ions with arenes, Organometallics 16 (1997) 4581–4588.
[157] M.C. Heaven, J.K. Gibson, J. Marçalo, Molecular spectroscopy and reactions of actinides in the gas phase and cryogenic matrices, in: L.R. Morss, N.M. Edelstein, J. Fuger (Eds.), The Chemistry of the Actinide and Transactinide Elements, fourth ed., Springer, The Netherlands, 2010 (Chapter 38).
[158] B. Le Motais, J.-F. Le Marechal, A.-M. Koulkes-Pujo, Reduction of a trivalent uranium complex in tetrahydrofuran by pulse radiolysis: first direct evidence of the uranium II oxidation state, C. R. Acad. Sci. 306 (1988) 519–521.
[159] L. Andrews, M. Zhou, B. Liang, J. Li, B.E. Bursten, Reactions of laser-ablated U and Th with CO_2: neon matrix infrared spectra and density functional calculations of OUCO, OThCO, and other products, J. Am. Chem. Soc. 122 (2000) 11440–11449.
[160] J.G. Brennan, R.A. Andersen, A. Zalkin, Chemistry of trivalent uranium metallocenes: electron-transfer reactions with carbon disulfide. Formation of $[(RC_5H_4)_3U]_2[\mu\text{-}\eta^1,\eta^2\text{-}CS_2]$, Inorg. Chem. 25 (1986) 1756–1760.
[161] A. Zalkin, J.G. Brennan, R.A. Andersen, Tris(trimethylsilylcyclopentadienyl)-uranium(III), Acta Crystallogr. C C44 (1988) 2104–2106.
[162] M.R. MacDonald, M.E. Fieser, J.E. Bates, J.W. Ziller, F. Furche, W.J. Evans, Identification of the +2 oxidation state for uranium in a crystalline molecular complex, [K(2.2.2-cryptand)][$(C_5H_4SiMe_3)_3U$], J. Am. Chem. Soc. 135 (2013) 13310–13313.
[163] J.-C. Berthet, C. Villiers, J.-F. Le Maréchal, B. Delavaux-Nicot, M. Lance, M. Nierlich, J. Vigner, M. Ephritikhine, Anionic triscyclopentadienyluranium(III) hydrides, J. Organomet. Chem. 440 (1992) 53–65.

[164] J. Blaise, J.-F. Wyart, Energy levels and atomic spectra of actinides, in: International Tables of Selected Constants, vol. 20, Pergamon Press, Oxford, 1992.
[165] X. Cao, M. Dolg, Segmented contraction scheme for small-core actinide pseudopotential basis sets, J. Mol. Struct. (THEOCHEM) 673 (2004) 203–209.
[166] C.J. Windorff, M.R. MacDonald, K.R. Meihaus, J.W. Ziller, J.R. Long, W.J. Evans, Expanding the chemistry of molecular U^{2+} complexes: synthesis, characterization, and reactivity of the $\{[C_5H_3(SiMe_3)_2]_3U\}^-$ anion, Chem. Eur. J. 22 (2016) 772–778.
[167] C.J. Windorff, W.J. Evans, ^{29}Si NMR spectra of silicon-containing uranium complexes, Organometallics 33 (2014) 3786–3791.
[168] H.S. La Pierre, A. Scheurer, F.W. Heinemann, W. Hieringer, K. Meyer, Synthesis and characterization of a uranium(II) monoarene complex supported by δ backbonding, synthesis and characterization of a uranium(II) monoarene complex supported by δ backbonding, Angew. Chem. Int. Ed. 53 (2014) 7158–7162.
[169] S.G. Bratsch, J.J. Lagowski, Actinide thermodynamic predictions. 3. Thermodynamics of compounds and aquo-ions of the 2+, 3+, and 4+ oxidation states and standard electrode potentials at 298.15 K, J. Phys. Chem. 90 (1986) 307–312.
[170] G. Ionova, C. Madic, R. Guillaumont, About the existence of Th(III) in aqueous solution, Polyhedron 17 (1998) 1991–1995.
[171] R.J.M. Konings, L.R. Morss, J. Fuger, Thermodynamic properties of actinides and actinide compounds, in: L.R. Morss, N.M. Edelstein, J. Fuger (Eds.), The Chemistry of the Actinide and Transactinide Elements, fourth ed., Springer, The Netherlands, 2010 (Chapter 19).
[172] R.J. Clark, J.D. Corbett, Preparation of metallic thorium diiodide, Inorg. Chem. 2 (1963) 460–463.
[173] D.E. Scaife, A.W. Wylie, New lower iodides of thorium, J. Chem. Soc. (1964) 5450–5458.
[174] L.J. Guggenberger, R.A. Jacobson, Crystal structure of thorium diiodide, Inorg. Chem. 7 (1968) 2257–2260.
[175] B. Kanellakopulos, E. Dornberger, F. Baumgaertner, Das erste dreiwertige thorium in einem aromatenkomplex: tris(cyclopentadienyl) thorium(III), Inorg. Nucl. Chem. Lett. 10 (1974) 155–160.
[176] E. Dornberger, R. Klenze, B. Kanellakopulos, Über eine neue präparative methode zur synthese metallorganischer verbindungen, Inorg. Nucl. Chem. Lett. 14 (1978) 319–324.
[177] J.W. Bruno, D.G. Kalina, E.A. Mintz, T.J. Marks, Mechanistic study of photoinduced . beta.-hydride elimination. The facile photochemical synthesis of low-valent thorium and uranium organometallics, J. Am. Chem. Soc. 104 (1982) 1860–1869.
[178] W.K. Kot, G.V. Shalimoff, N.M. Edelstein, M.A. Edelman, M.F. Lappert, [Th(III)[η^5-$C_5H_3(SiMe_3)_2]_3$], an actinide compound with a $6d^1$ ground state, J. Am. Chem. Soc. 110 (1988) 986–987.
[179] I. Korobkov, S. Gambarotta, G.P.A. Yap, The first thorium arene complex: a divalent synthon, Angew. Chem. Int. Ed. 42 (2003) 814–818.
[180] I. Korobkov, S. Gambarotta, G.P.A. Yap, Amide from dinitrogen by in situ cleavage and partial hydrogenation promoted by a transient zero-valent thorium synthon, Angew. Chem. Int. Ed. 42 (2003) 4958–4961.
[181] A. Arunachalampillai, P. Crewdson, I. Korobkov, S. Gambarotta, Ring opening and C–O and C–N bond cleavage by transient reduced thorium species, Organometallics 25 (2006) 3856–3866.
[182] P.C. Blake, M.F. Lappert, J.L. Atwood, H. Zhang, The synthesis and characterisation, including X-ray diffraction study, of [Th{η-$C_5H_3(SiMe_3)_2$}$_3$]; the first thorium(III) crystal structure, J. Chem. Soc. Chem. Commun. (1986) 1148–1149.

[183] J.S. Parry, F.G.N. Cloke, S.J. Coles, M.B. Hursthouse, Synthesis and characterization of the first sandwich complex of trivalent thorium: a structural comparison with the uranium analogue, J. Am. Chem. Soc. 121 (1999) 6867–6871.

[184] P.C. Blake, N.M. Edelstein, P.B. Hitchcock, W.K. Kot, M.F. Lappert, G.V. Shalimoff, S. Tian, Synthesis, properties and structures of the tris(cyclopentadienyl)thorium(III) complexes $[Th\{\eta^5\text{-}C_5H_3(SiMe_2R)_2\text{-}1,3\}_3]$ (R = Me or ^{t}Bu), J. Organomet. Chem. 636 (2001) 124–129.

[185] J.R. Walensky, R.L. Martin, J.W. Ziller, W.J. Evans, Importance of energy level matching for bonding in Th^{3+}-Am^{3+} actinide metallocene amidinates, $(C_5Me_5)_2[^iPrNC(Me)N^iPr]An$, Inorg. Chem. 49 (2010) 10007–10012.

[186] N.A. Siladke, C.L. Webster, J.R. Walensky, M.K. Takase, J.W. Ziller, D.J. Grant, L. Gagliardi, W.J. Evans, Actinide metallocene hydride chemistry: C–H activation in tetramethylcyclopentadienyl ligands to form $[\mu\text{-}\eta^5\text{-}C_5Me_3H(CH_2)\text{-}\kappa C]^{2-}$ tuck-over ligands in a tetrathorium octahydride complex, Organometallics 32 (2013) 6522–6531.

[187] K.J. de Almeida, H.A. Duarte, Dehydrogenation of methane by gas-phase Th, Th^+, and Th^{2+}: theoretical insights into actinide chemistry, Organometallics 29 (2010) 3735–3745.

[188] B.J. Barker, I.O. Antonov, M.C. Heaven, K.A. Peterson, Spectroscopic investigations of ThF and ThF^+, J. Chem. Phys. 136 (2012) 104305/1–104305/9.

[189] M.S. Wickleder, B. Fourest, P.K. Dorhout, Thorium, in: L.R. Morss, N.M. Edelstein, J. Fuger (Eds.), The Chemistry of the Actinide and Transactinide Elements, fourth ed., Springer, The Netherlands, 2010 (Chapter 3)

[190] R.R. Langeslay, M.E. Fieser, J.W. Ziller, F. Furche, W.J. Evans, Synthesis, structure, and reactivity of crystalline molecular complexes of the $\{[C_5H_3(SiMe_3)_2]_3Th\}^{1-}$ anion containing thorium in the formal +2 oxidation state, Chem. Sci. 6 (2015) 517–521.

[191] W.K. Kot, G.V. Shalimoff, N.M. Edelstein, M.A. Edelman, M.F. Lappert, $[Th^{III}\{\eta^5\text{-}C_5H_3(SiMe_3)_2\}_3]$, an actinide compound with a $6d^1$ ground state, J. Am. Chem. Soc. 110 (1988) 986–987.

[192] C.M. Kotyk, M.R. MacDonald, J.W. Ziller, W.J. Evans, Reactivity of the Ln^{2+} complexes [K (2.2.2-cryptand)][$(C_5H_4SiMe_3)_3Ln$]: reduction of naphthalene and biphenyl, Organometallics 34 (2015) 2287–2295.

[193] W.J. Evans, S.L. Gonzales, J.W. Ziller, Reactivity of decamethylsamarocene with polycyclic aromatic hydrocarbons, J. Am. Chem. Soc. 116 (1994) 2600–2608.

[194] S. Bank, D.A. Juckett, Reactions of aromatic radical anions. 12. Kinetic studies of the reaction of radical anions of varying reduction potential with n-hexyl bromides, iodides, and chlorides, J. Am. Chem. Soc. 98 (1976) 7742–7746.

[195] M.E. Fieser, C.W. Johnson, J.E. Bates, J.W. Ziller, F. Furche, W.J. Evans, Dinitrogen reduction, sulfur reduction, and isoprene polymerization via photochemical activation of trivalent bis(cyclopentadienyl) rare earth allyl complexes, Organometallics 34 (2015) 4387–4393.

[196] M.E. Fieser, J.E. Bates, J.W. Ziller, F. Furche, W.J. Evans, Dinitrogen reduction via photochemical activation of heteroleptic tris(cyclopentadienyl) rare earth complexes, J. Am. Chem. Soc. 135 (2013) 3804–3807.

[197] R.R. Langeslay, M.E. Fieser, J.W. Ziller, F. Furche, W.J. Evans, Expanding thorium hydride chemistry through Th^{2+}, including the synthesis of a mixed-valent Th^{4+}/Th^{3+} hydride complex, J. Am. Chem. Soc. 138 (2016) 4036–4045.

[198] C.M. Kotyk, M.E. Fieser, C.T. Palumbo, J.W. Ziller, L.E. Darago, J.R. Long, F. Furche, W.J. Evans, Isolation of +2 rare earth metal ions with three anionic carbocyclic rings: bimetallic bis(cyclopentadienyl) reduced arene complexes of La^{2+} and Ce^{2+} are four electron reductants, Chem. Sci. 6 (2015) 7267–7273.

[199] H.P. Beck, NdI_2, a metallic high pressure modification, Z. Naturforsh. B 31b (1976) 1548–1549.

[200] M.D. Walter, D. Bentz, F. Weber, O. Schmitt, G. Wolmershäuser, H. Sitzmann, Cation size dependent reactivity of lanthanide trihalides with bulky alkylcyclopentadienyl anions, New J. Chem. 31 (2007) 305–318.

[201] J.G. Brennan, F.G.N. Cloke, A.A. Sameh, A. Zalkin, Synthesis of bis(η-1,3,5-tri-t-butylbenzene) sandwich complexes of yttrium(0) and gadolinium(0); the X-ray crystal structure of the first authentic lanthanide(0) complex, [Gd(η-$Bu^t{}_3C_6H_3)_2$], J. Chem. Soc. Chem. Commun. (1987) 1668–1669.

[202] F.G.N. Cloke, Zero oxidation state compounds of scandium, yttrium, and the lanthanides, Chem. Soc. Rev. 22 (1993) 17–24.

[203] D.M. Anderson, F.G.N. Cloke, P.A. Cox, N. Edelstein, J.C. Green, T. Pang, A.A. Sameh, G. Shalimoff, On the stability and bonding in bis(η-arene)lanthanide complexes, J. Chem. Soc., Chem. Commun. (1) (1989) 53–55.

[204] P.L. Arnold, F.G.N. Cloke, J.F. Nixon, The first stable scandocene: synthesis and characterisation of bis(η-2,4,5-tri-tert-butyl-1,3-diphosphacyclopentadienyl)scandium(II), Chem. Commun. (1998) 797–798.

[205] K.D. Khan, Sandwich compounds of scandium and the early transition metals, D. Phil. Thesis, University of Sussex, 1992.

[206] P.L. Arnold, F.G.N. Cloke, P.B. Hitchcock, J.F. Nixon, The first example of a formal scandium(I) complex: synthesis and molecular structure of a 22-electron scandium triple decker incorporating the novel 1,3,5-triphosphabenzene ring, J. Am. Chem. Soc. 118 (1996) 7630–7631.

[207] G. Meyer, Superbulky ligands and trapped electrons: new perspectives in divalent lanthanide chemistry, Angew. Chem. Int. Ed. 47 (2008) 4962–4964.

[208] G.K.B. Clentsmith, F.G.N. Cloke, J.C. Green, J. Hanks, P.B. Hitchcock, J.F. Nixon, Stabilization of low-oxidation-state early transition-metal complexes bearing 1,2,4-triphosphacyclopentadienyl ligands: structure of [{$Sc(P_3C_2{}^tBu_2)_2$}$_2$]; Sc^{II} or mixed oxidation state? Angew. Chem. Int. Ed. 42 (2003) 1038–1041.

Chapter 294

Coordination Chemistry in Rare Earth Containing Ionic Liquids

Denis Prodius and Anja-Verena Mudring[1]
Iowa State University and Ames Laboratory, Ames, IA, United States
[1]*Corresponding author: e-mail: mudring@iastate.edu*

Coordination chemistry of rare earths has developed rapidly during the last 30 years due to an enormous number of diverse applications. Medicine, clean energy, telecommunications, ceramics, permanent magnets, and industrial catalysts are only a few examples without which we cannot imagine the modern world. The continuous development and improvement of rare earth-based materials for advanced applications together with the fact that some of the lanthanides are considered critical elements calls for more elaborate, nontrivial, and advanced technological approaches. But before starting to develop these basic properties, more specifically, the coordination abilities of rare earth ions need to be known. This quest is driven by the academic and industrial interest for use of rare earth coordination compounds in separation processes, catalysis, biomedical, and other applications. It is well known that one of the characteristic properties of rare earth ions is their large ionic radii, which decrease systematically from La (1.032 Å) to Lu (0.861 Å). Since splitting of the degenerate f-orbitals in crystal fields is insignificant, the preferences between different coordination numbers (CNs) and geometries of lanthanides are predominantly driven by ligand steric effects. The total number of metal-to-ligands bonds in coordination compound determines the CN and can range between 2 and 12 for rare earth complexes (Fig. 1).

Regardless of numerous advancements in the coordination chemistry of rare earths, compounds with $CN < 8$ are still unusual. Normally, CNs between 8 and 12 are common for rare earth metal ions; species with CN 8 and 9 make up for more than 60% of the identified structures. The most prominent coordination polyhedra are a bicapped trigonal prism, square antiprism, triangular dodecahedron ($CN = 8$), a monocapped square antiprism or tricapped trigonal prism ($CN = 9$), a bicapped dodecahedron, bicapped square antiprism or tetrakaidecahedron ($CN = 10$), and the icosahedron ($CN = 12$).

Handbook on the Physics and Chemistry of Rare Earths, Vol. 50. http://dx.doi.org/10.1016/bs.hpcre.2016.09.002

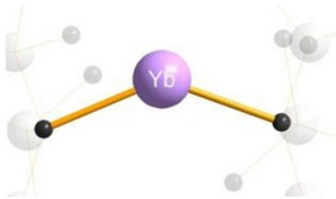

2: $Yb\{C(SiMe_3)_3\}_2$

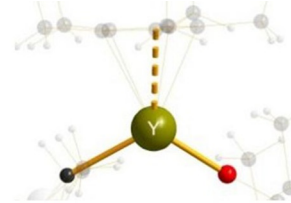

3: $(C_5Me_5)Y(OAr)\{CH(SiMe_3)_2\}$

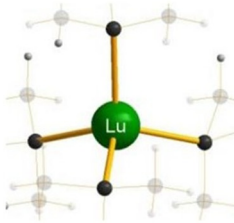

4: $[Lu(t\text{-}But)_4]^-$

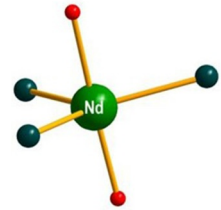

5: $[Nd\{P(SiMe_3)_2\}_3(THF)_2]$

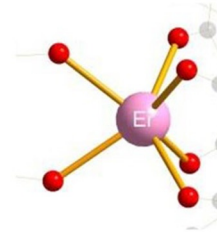

6: $Er(THD)_3$

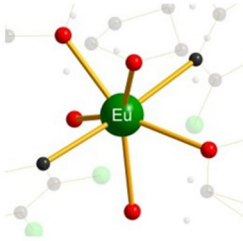

7: $[Eu(C_6F_5)_2(THF)_5]$

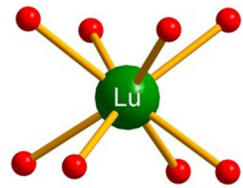

8: $[Lu(H_2O)_8]^{3+}$

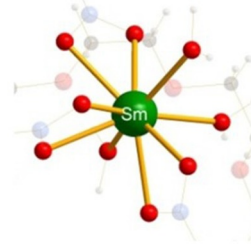

9: $[Sm(NO_3)_3(H_2O)_3]\cdot 18\text{-crown-6}$

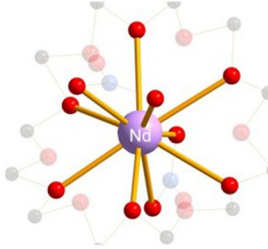

10: $[Nd(NO_3)_2(18\text{-crown-6})]^+$

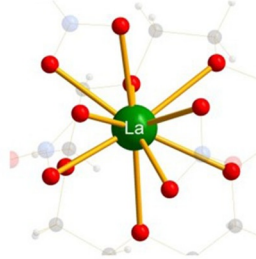

11: $[La(NO_3)_3(15\text{-crown-5})]$

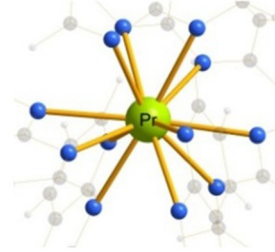

12: $[Pr(1,8\text{-naphthyridine})_6]^{3+}$

FIG. 1 The versatility of Ln ions and their coordination polyhedra as evidenced in the solid state [1].

It has been realized that ionic liquids (ILs), as liquid, purely ionic media, can provide unique coordination environments for metal cations. The exploration of ILs as unique, unusual solvents is one of the most rapidly developing areas over the past few decades, also, with the focus on the crucial target of large-scale industrial applications. It is a known fact that the ILs can provide some properties which cannot be realized in traditional solvents such as, for example, negligible vapor pressure at room temperature (RT), high conductivity, nonflammability, high thermal, and chemical stability over a wide temperature range.

In accordance with a generally accepted definition, ILs are salts with a melting point below the boiling point of water (100°C), a huge number of them are even liquid at ambient temperature and below. In the majority of cases, ILs are assembled of large organic cations and inorganic or organic anions (Fig. 2 is showing classic examples of ions used in the design of ILs). As a rule, the high-profile ILs include alkylphosphonium, alkylammonium, N-alkylpyridinium as well as N,N′-dialkylimidazolium cations [2–5]. The anions may be as simple as halides or common oxyanions like nitrate or perchlorate. In many cases, complex ions of high symmetry like $[AlCl_4]^-$, $[BF_4]^-$, $[SbF_6]^-$, or $[PF_6]^-$ are suitable IL anions, too (Fig. 2).

At present, alkylsulfonates and alkylsulfates and a variety of perfluorinated anions such as bis(trifluoromethylsulfonyl)amide $[(CF_3SO_2)_2N]^-$ (Tf_2N^-) or triflate, $[CF_3SO_3]^-$, are commonly utilized in ILs. Making a metal ion part of the ILs can lead to interesting new systems where the general features of RT ILs can be combined with those related to the metal ion (optical properties like luminescence, magnetic moments, or catalytic centers). Lanthanide-based ILs give us new prospects to create processes, devices, and products which can combine unique properties of both the rare earth ion and an IL. For this, a thorough knowledge about the coordination chemistry of rare earth ions in these unusual liquid media is an indispensable tool for design an appropriate rare earth-based IL. Despite its importance, this area is still largely underexplored, and little information exists. In the following, we will discuss the coordination of rare earth ions by the most prominent IL ions in detail.

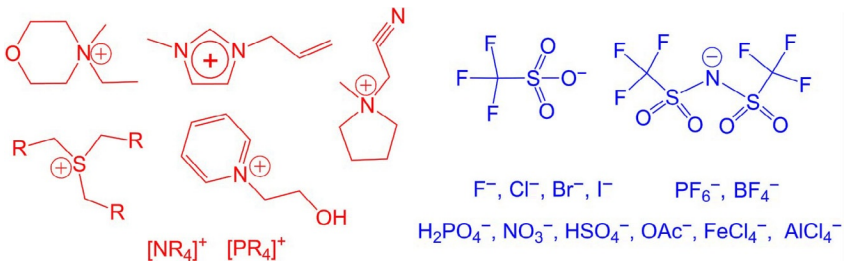

FIG. 2 The basic ionic liquid "toolbox".

The Tf_2N^- ion remains an important "building block" for creating RT ILs from the time when it was found that anions with diffuse charges and negligible capability to create hydrogen-bonding contacts have high capacity to form salts that are liquid at RT and below. As expected, no significant hydrogen bonding between the ions in the majority of (solid-state) crystal structures of ILs with the $[(CF_3SO_2)_2N]^-$ ion was observed [6–9]. This is one of the reasons why the Tf_2N^- ion is only weakly interacting with counterions and why it generally is considered as a "weak" or even noncoordinating ligand. However, in 2005, Mudring and coworkers demonstrated the synthesis of an unprecedented homoleptic Tf_2N^- compound by the reaction of YbI_2 and the IL $[C_1C_3pyrr][Tf_2N]$ (C_1C_3pyrr = 1-methyl-1-propylpyrrolidinium) [10]. The compound crystallizes in the monoclinic space group $P2_1/n$ with four formula units in the unit cell. The asymmetric unit of the crystal structure consists of two cations of the IL with Yb^{II} being coordinated through oxygen atoms of four Tf_2N^- anions (Fig. 3). The distorted square antiprism environment of Yb^{2+} is built by eight oxygen atoms. Actually, this was the first example presenting the Tf_2N^- anion coordinating in a η^2-bidentate fashion to a metal ion to produce isolated anions.

In 2010, the same group of authors investigated the solvation and ligand exchange synthesis of Yb(III) as a reference example for the heavy lanthanides [11,12]. Crystalline $[C_1C_4pyrr][Yb(Tf_2N)_4]$ (C_1C_4pyrr = 1-methyl-1-butyl-pyrrolidinium) was synthesized by carefully cooling a supersaturated

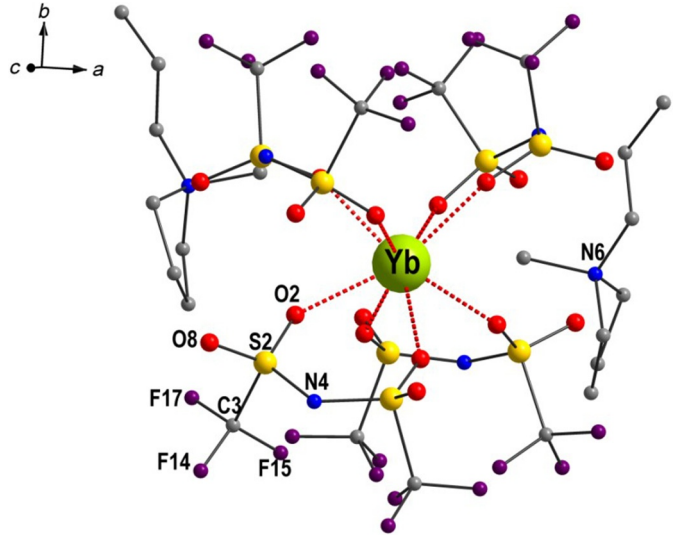

FIG. 3 An asymmetric unit of the crystal structure of $[C_1C_3pyrr]_2[Yb(Tf_2N)_4]$. Hydrogen atoms omitted for clarity.

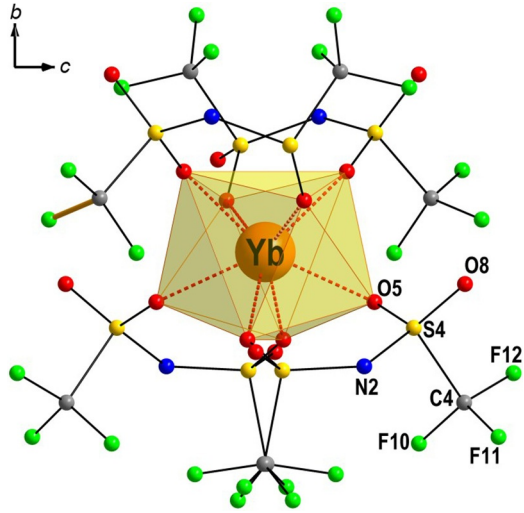

FIG. 4 Coordination of Yb(III) in $[C_1C_4pyrr][Yb(Tf_2N)_4]$.

solution of $Yb(Tf_2N)_3$ in $[C_4C_1pyrr][Tf_2N]$ at 25°C. The structural analysis confirmed that the asymmetric unit of $[C_1C_4pyrr][Yb(Tf_2N)_4]$ contains two crystallographically independent ytterbium(III) cations both with a trigonal dodecahedral coordination environment of oxygens (Fig. 4).

Such a polyhedron is typically favored over a cube when ligand–ligand repulsion, as present in the case of the Tf_2N^- ions, becomes important for CN eight. The construction of an unprecedented homoleptic triflate compound $[C_1C_4pyrr]_3[Yb(OTf)_6]$ [11] from a solution of $Yb(OTf)_3$ in $[C_1C_4pyrr][OTf]$ indicates that all OTf^- anions are acting as monodentate ligands in a nonbridging fashion. This fact results in isolated $[Yb(OTf)_6]^{3-}$ octahedra being embedded in a $[C_1C_4pyrr]$ matrix (Fig. 5).

To explore the ligand exchange reactions, the interaction between $Yb(Tf_2N)_3$ and $[C_1C_4pyrr][OTf]$ IL was investigated. Such intraligand exchange was detected in the complex compound $[C_1C_4pyrr]_4[Yb(OTf)_6][Tf_2N]$ (Fig. 5B), where Tf_2N^- ions are integrated into the crystal structure only in a noncoordinating manner. Thus the powerful coordinating OTf^- ion completely substitutes the less Lewis basic Tf_2N^- ion in the first coordination sphere of the Yb^{3+} ion (Fig. 5). The Yb^{3+} ion is bound uniquely to OTf^- ions in an octahedral manner as in $[C_4C_1pyrr]_3[Yb(OTf)_6]$. For $Yb(OTf)_3$ in $[C_4C_1pyrr][Tf_2N]$ such a ligand exchange reaction could not be detected. Using cyclic voltammetry allows one to efficiently monitor the ion exchange in the rare earth metal coordination sphere concluding that the measured half-wave potentials of the investigated complexes can be associated with the electron–donor properties of the rare earth ion [12].

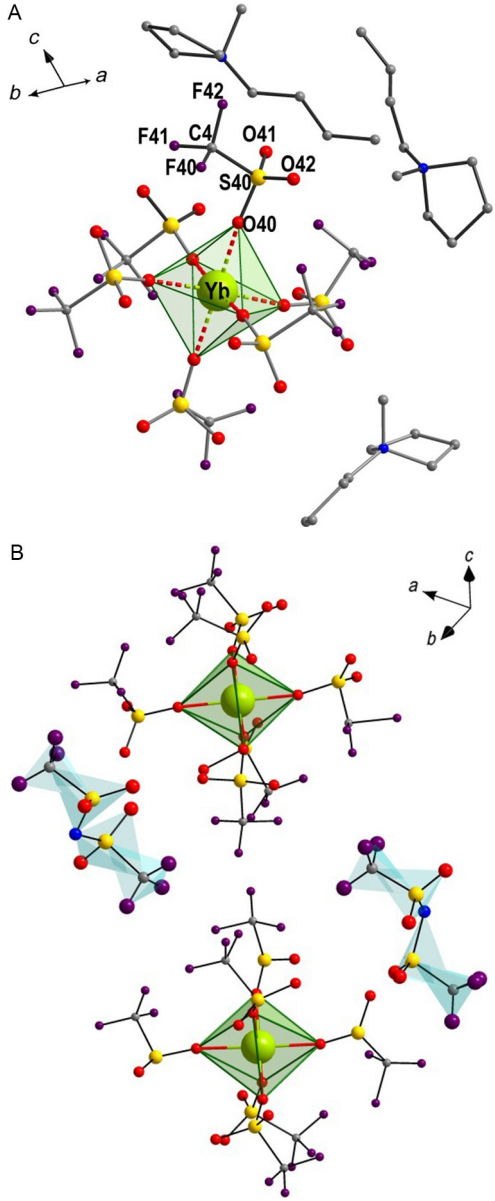

FIG. 5 (A) The asymmetric unit of $[C_1C_4pyrr]_3[Yb(OTf)_6]$ and (B) fragment of the crystal structure of $[C_1C_4pyrr]_4[Yb(OTf)_6][Tf_2N]$ where two noncoordinating Tf_2N-anions are encircled with a *gray background*. $[C_1C_4pyrr]^+$ cations and hydrogen atoms were omitted for clarity.

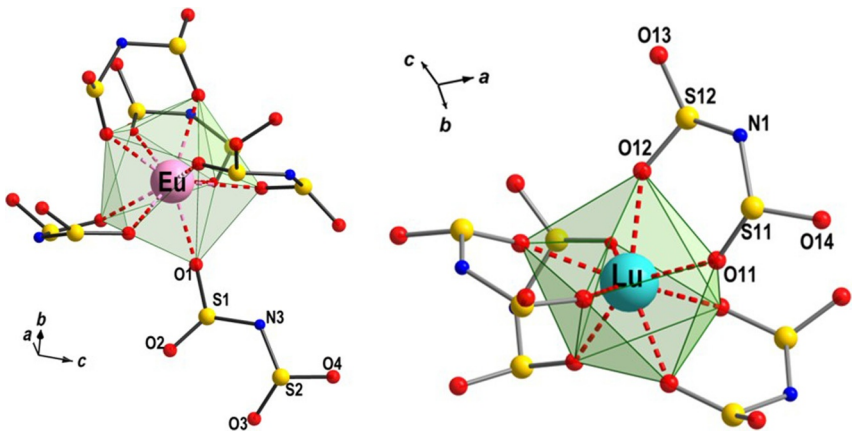

FIG. 6 Coordination environment for the larger (Ln = La–Tb; CN = 9) and smaller (Ln = Dy–Lu; CN = 8) trivalent rare earth cations in $[C_4C_1pyrr]_m[Ln(Tf_2N)_{3+m}]$, the CF_3-groups are removed for clarity.

With an eye to clarify the coordination features of Ln(III) in popular bis(trifluoromethylsulfonyl)amide-based ILs, rare earth complexes with bis(trifluoromethylsulfonyl)amides, $Ln(Tf_2N)_3$ (Ln = Nd–Lu), were processed in $[C_4C_1pyrr][Tf_2N]$. It was demonstrated that these complexes with a formula of $[C_4C_1pyrr]_2[Ln(Tf_2N)_5]$ for the larger radius lanthanides (Ln = Pr–Tb) and $[C_4C_1pyrr][Ln(Tf_2N)_4]$ for the smaller lanthanides (Ln = Dy–Lu), could be crystallized from the solutions. The rare earths with larger ionic radius are ninefold coordinated by four bis(trifluoromethylsulfonyl)amide anions binding in a chelating manner and one extra Tf_2N^- ion binding in a monodentate mode to the lanthanide (Fig. 6) [13,14].

The rare earths with smaller radius prefer a CN = 8, which is built by four Tf_2N^- ions binding in a chelating mode. The same coordination environment was also observed in the crystal structure of $[C_4mim][Y(Tf_2N)_4]$ [15]. The series of compounds $[C_4mpyrr]_2[Ln(Tf_2N)_5]$ (Ln = La–Tb) are ILs with $T_m < 100°C$ (Fig. 7).

A handful of results with ILs containing the pyrrolidine cations encouraged investigation of ILs with the more prominent imidazolium cations. Investigations in that field led to the synthesis of the novel imidazolium Eu-based ILs and their identification as a soft luminescent materials [16]. It was found that these low melting, highly luminescent ILs (Fig. 7B, inset), $[C_1C_3im][Eu(Tf_2N)_4]$ (C_1C_3im = 1-butyl-methylimidazolium), $[C_1C_4im][Eu(Tf_2N)_4]$ (C_1C_4im = 1-propyl-methylimidazolium), and $[C_1C_4pyrr]_2[Eu(Tf_2N)_5]$ exhibit outstanding features such as long lifetimes of luminescence even at the large europium(III) concentration, small line width, and high color purity of the emitted light.

Nevertheless, for the design of novel low-melting rare earth-based ILs is not practical to limit research to perfluorinated anions. To improve the

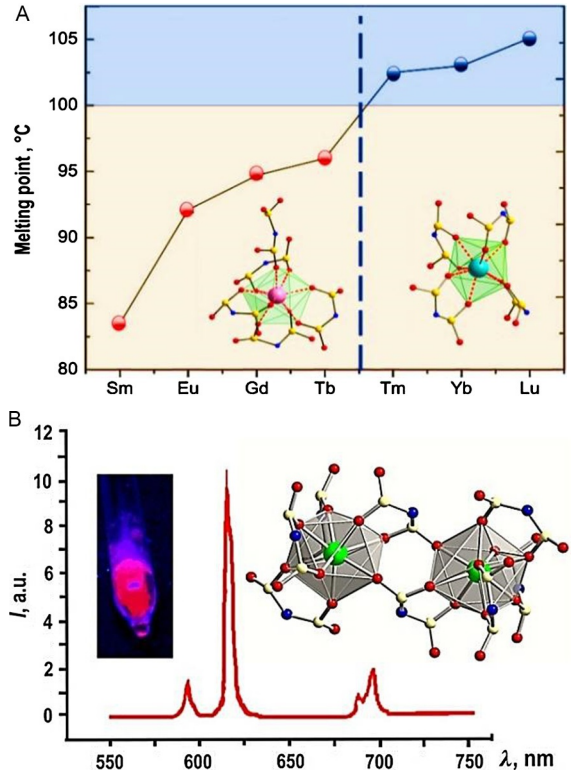

FIG. 7 (A) Melting points of $[C_1C_4pyrr]_n[Ln(Tf_2N)_{3+n}]$ and (B) emission spectrum and structure (as *inset*, *right side*) of $[C_1C_3im][Eu(Tf_2N)_4]$ with photograph of a sample under UV light (*inset*, *left side*).

photophysical properties, Mudring and coworkers continued their research by switching the CF_3 groups of the Tf_2N anion with the toluene "block" in the ditoluenesulfonylamide (DTSA) in the hope that the new one can assist as a better light-absorbing chromophore (antenna). As a result, two new europium-based IL complexes, $[C_1C_4im][Eu(DTSA)_4]$ and $[C_1C_4im]_2[Eu(DTSA)_5]$, were obtained at 120°C under inert conditions using $[C_1C_4im]^+$ as cation [17]. The purity and identity of new complexes were proven by Raman, IR, and ^1H NMR spectroscopy.

Fluorescence measurements demonstrate that the complexes display a strong red luminescence of high color purity.

In 2006, Nockmann with coauthors reported rare earth ions being incorporated in ILs based on the $[C_1C_4im]^+$ cation and rare earth complex anions with SCN^- as the ligand with the general composition $[Ln(NCS)_n(H_2O)_x]_{3-n}$, where $n = 6–8$; $x = 0–2$ (Fig. 8) [18]. The complexes were obtained by a metathesis reaction between $Ln(ClO_4)_3$, NH_4NCS, and an imidazolium-thiocyanate IL. The majority of described ILs is found to be fluids or supercooled liquids at RTs and showed the tendency to solidify

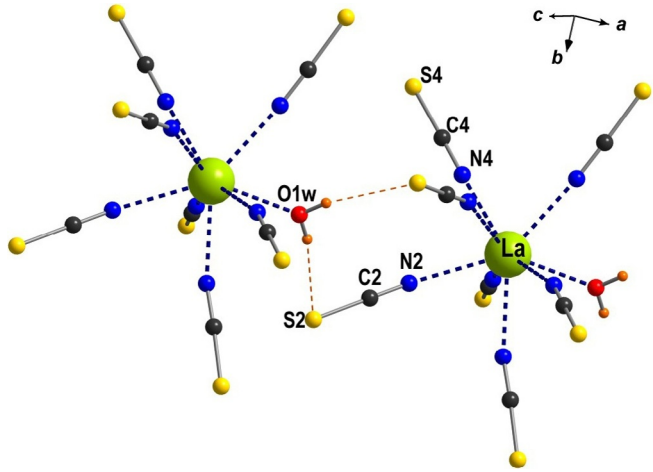

FIG. 8 An anionic $[La(NCS)_7(H_2O)]^{4-}$ unit displaying the hydrogen bonding between coordinated H_2O molecules and NCS ions. The 1-butyl-3-methylimidazolium cations were omitted for clarity.

upon cooling as glasses rather than crystals. Some of these complexes, $[C_1C_4im]_{n-3}[Ln(NCS)_n(H_2O)_x]$ where $n=6$ (Y) or 7 (Pr, La, Nd), and $x=1$ (Pr, La, Nd) or 2 (Y); were crystallized at about 16°C from the molten state while other representatives are liquids below RT.

The crystal structure of $[C_1C_4im]_4[La(NCS)_7(H_2O)]$ (Fig. 8) shows that coordination polyhedron of the Ln(III) ion can be designated as a slightly distorted square antiprism and which is completed by one water molecule and seven isothiocyanate anions. The coordinated H_2O molecule build up strong hydrogen bonds to the NCS ions of the neighboring $[La(NCS)_7(H_2O)]^{4-}$ unit thus resulting in a polymeric stacking of the anions.

This can be an explanation of their better ability to crystallize. All complexes exhibit a full miscibility with other imidazolium-functionalized ILs, including hydrophobic ILs, and in some cases ($x=7$ and 8) even in apolar solvents such as dichloromethane. They are also soluble in H_2O, but undergo complete hydrolysis.

The integration of rare earth ions into ILs provides the benefit of a metal ion that has a significantly higher effective magnetic moment than any known transition metal, and thus can give the best response to an external magnetic field. Separation of such fluids due to their density and magnetic susceptibility has been demonstrated [19]. From this point of view, the new ILs $[C_1C_6im]_{5-n}[Dy(SCN)_{8-n}(H_2O)_y]$ ($n=0$–2, $C_1C_6im=1$-hexyl-3-methylimidazolium) were obtained from KSCN, $[C_1C_6im]SCN$, and dysprosium perchlorate according to a slightly modified method for similar rare earth-based ILs. All reported dysprosium-based liquids $[C_1C_6im]_4[Dy(SCN)_7(H_2O)]$, $[C_1C_6im]_3[Dy(SCN)_6(H_2O)_2]$, and $[C_1C_6im]_5[Dy(SCN)_8]$ comprise Dy^{III} as the magnetically active ion with a $4f^9$ electron configuration and reacting to the attraction of commercial Nd–Fe–B magnets (Fig. 9) [20].

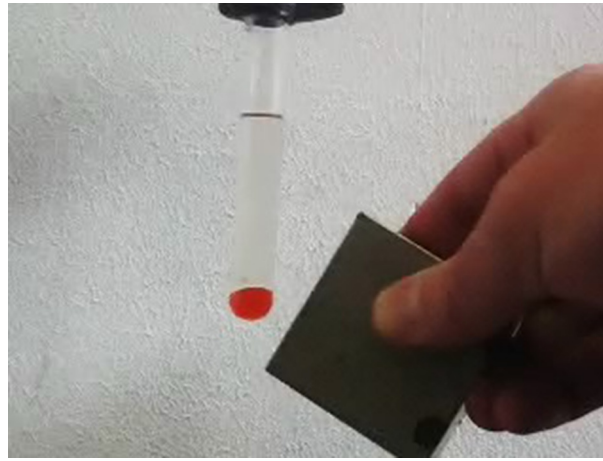

FIG. 9 Response of the *orange-colored* IL $[C_1C_6im]_3[Dy(SCN)_6(H_2O)_2]$ to a Nd–Fe–B magnet.

All these dysprosium-based RT ILs exhibit an intense yellow emission under UV light excitation, which is typical for Dy(III). The excitation spectra and the emission spectra of these compounds show the characteristic Dy^{III} transitions with $^4F_{9/2} \rightarrow {}^6H_{13/2}$ transition as the most intense for all complexes and its lineshape is immensely sharp thus showing high color purity. For these complexes, a monoexponential intensity decay was identified, demonstrating that only one Dy(III) type is existent.

Using organic cations can thus be an alternative approach for creating new magnetic liquids and magnetorheological fluids. Such cations lack acidic protons which participate in the formation of hydrogen-bonded systems as for example in the case of $(C_1C_2im)[LaCl_6]$ ($C_1C_2im \equiv$ 1-ethyl-3-methylimidazolium) [21]. The large trihexyl(tetradecyl)phosphonium cation is another good candidate for the establishment of metal ion containing RT ILs, as the massive cation is not beneficial to crystallization. Reaction of trihexyl(tetradecyl) phosphonium chloride, $[P_{66614}]Cl$, with $GdCl_3$ yield the corresponding paramagnetic $[P_{66614}]_3[GdCl_6]$ IL with χT value equal to 7.72 emu mol^{-1} K (measured at 300 K and $H = 0.1$ T) [22].

The sizes and shapes of cations in ILs are vital in defining the melting points of the salts and, as a rule, the large ions tend essentially to decrease the melting point temperature. One of such materials, $[C_1C_{12}im]_3[DyBr_6]$ ($C_1C_{12}im =$ 1-dodecyl-3-methylimidazolium), has remarkable luminescent behavior as well as magnetic and mesomorphic properties [23]. The reaction of $DyBr_3$ with $[C_1C_{12}im]Br$ at 120°C produces a highly viscous yellowish material which after recrystallization from MeCN (cooling to 5°C) results in a single crystalline product $[C_1C_{12}im]_3[DyBr_6]\cdot 2CH_3CN$ as colorless needles. Single crystal X-ray structure analysis shows that compound crystallizes in

the orthorhombic space group *Pbca* (No. 61) ($a = 14.888(4)$, $b = 18.240(7)$, $c = 49.411(13)$ Å, $Z = 8$, $V = 13{,}417(7)$ Å^3). The asymmetric unit comprises three crystallographically independent $[C_1C_{12}im]^+$ cations, one unique $[DyBr_6]^{3-}$ octahedron and two acetonitrile molecules. The dysprosium ion is six coordinated, resulting in a practically ideal $[DyBr_6]^{3-}$ octahedron (Fig. 10).

The crystal structure features three 1-dodecyl-3-methyl-imidazolium cations. Cations "1" and "2" (as dodecyl chains) accept all-*trans* conformations (Fig. 10A), while cation "3," exhibits a gauche conformation ("crank-handle"-like arrangement) around the C7–C8 bond with a torsion angle of 54 degree. The complex possesses liquid crystalline behavior and takes the form of smectic mesophases which were studied by hot-stage polarizing optical microscopy and differential scanning calorimetry. The emission color of $[C_1C_{12}im]_3[DyBr_6]$ can be tuned from white to orange-yellow depending

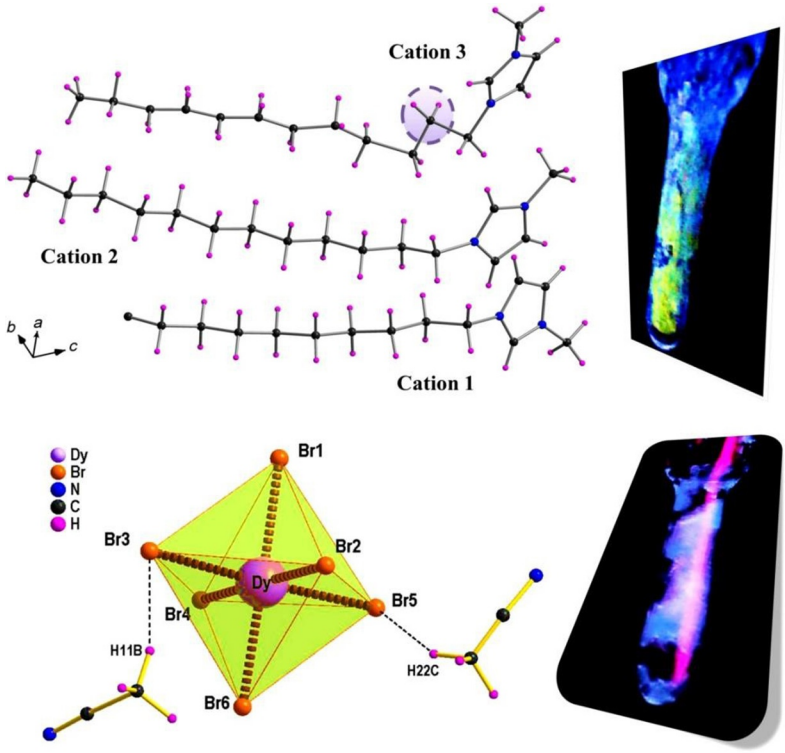

FIG.10 Components of the asymmetric unit in the crystal structure of $[C_1C_{12}im]_3[DyBr_6]$ $2CH_3CN$: three unique $[C_1C_{12}im]^+$ cations (*left top*); $[DyBr_6]^{3-}$ octahedron with hydrogen-bonded acetonitrile molecules, viewed along the *b*-axis (*left bottom*). Luminescence of liquid crystalline $[C_1C_{12}im]_3[DyBr_6]$ at room temperature under excitation of a standard UV lamp.

on the excitation wavelength (Fig. 10B and C). With $\lambda_{ex} = 254$ nm, the classical Dy(III) emission is detected which mainly arises from the $^4F_{9/2} \rightarrow {}^6H_{13/2}$ transition and, due to this, the material looks orange (Fig. 10B). An excitation with $\lambda_{ex} = 366$ nm provides the blue-whitish luminescence from the imidazolium cation itself. Measurement of magnetic properties displays for dysprosium(III) in $[C_1C_{12}im]_3[DyBr_6]$ yielded an effective magnetic moment of $\mu_{eff} = 9.6$ μB at RT. The complex indicates typical superparamagnetic behavior and can be handled by an external magnetic field.

Analogous systems were also investigated [24], where the IL crystal (ILC) C_1C_{12}im Br was 1% doped with $EuBr_2$, $SmBr_3$, $TbBr_3$, and $DyBr_3$ salts, which allows obtaining ILC materials that display luminescence in the three basic colors. In the case of Tb and Dy, it was possible to tune the emission color by a simple variation of the excitation light wavelength.

Heating of the complex to the RT causes the elimination of acetonitrile molecules and results in the formation of an RTIL of composition $[C_{12}mim]_4[EuBr_6]Br$ (Fig. 11). The structure–temperature relationship has been studied by differential scanning calorimetry and hot-stage polarizing optical microscopy. In the temperature range of −3 to 98°C this compound assumes a smectic liquid crystal phase. At 77 K, it displays a strong red emission with a lifetime of 2.6 ms [25].

Heating stoichiometric amounts of triazolium iodide, $AgNO_3$, and $La(NO_3)_3 \cdot 6H_2O$ under reflux in CH_3CN in the darkness yielded viscous liquids resulted after removing of solvent and AgI (Fig. 12). All these reaction products have been characterized as thermally stable RTILs in a nitrogen atmosphere over 185/235°C temperature range. Because nitrate is an energetic oxidizing anion, these ILs can be used as an oxidizer module in energetic ILs [26].

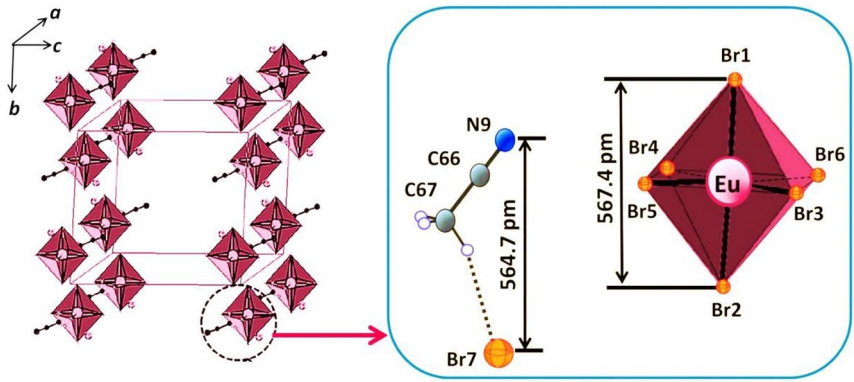

FIG. 11 Anion packing in the unit cell of $[C_1C_{12}im]_4[EuBr_6]Br \cdot CH_3CN$ (*left*) and evaluation of the space requirements of a $Br \cdots CH_3CN$ moiety and a $[EuBr_6]$ octahedron (*right*). $[EuBr_6]^{3-}$ octahedral units are shaded in *red* with open front faces.

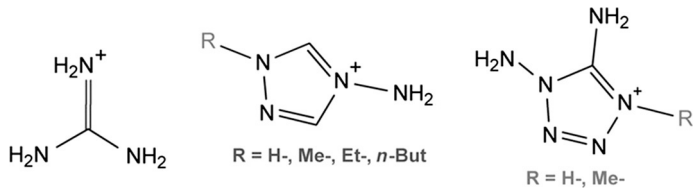

FIG. 12 Cations used in ILs based on La and Ce nitrate complex anions.

A

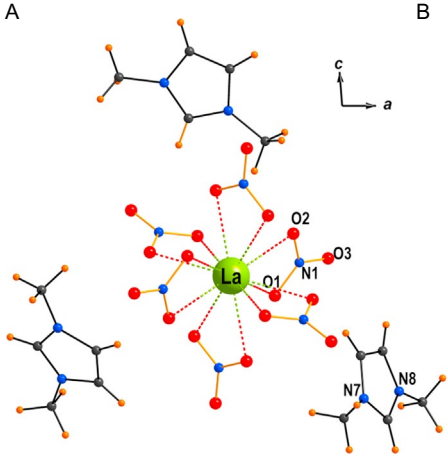

B

n	T_m [°C]	T_d [°C]	ρ [g·cm^{-3}]
1	115	303	1.74
2	51	319	1.70
n-4	29	304	1.67
iso-4	–28	310	1.62
iso-5	84	316	1.54
6	68	315	1.55
8	57	318	1.46
12	<RT	320	1.40
14	36	322	1.25
16	51	324	1.23
18	63	322	1.20

T_m = melting point; T_d = decomposition temperature; ρ = density at 25°C

FIG. 13 Molecular structure of $[C_1C_1im]_3[La(NO_3)_6]$ (A) and physicochemical properties of complexes $[C_1C_nim]_3[La(NO_3)_6]$ (B).

Later Tao and coauthors have presented the synthesis and characterization of new series of La-based ILs with general formula $[C_1C_nim]_3[La(NO_3)_6]$, where ($n = 1$–18) (Fig. 13) [27]. The crystal structure of compound with the symmetrical $[C_1C_1im]^+$ cation (C_1C_1im = 1,3-dimethylimidazolium) was investigated by single-crystal X-ray diffraction, with the subsequent crystallographic parameters: monoclinic space group $P2_1/c$; $a = 15.3170(3)$, $b = 14.2340(2)$, $c = 13.8954(2)$ Å; $\beta = 94.3453(15)$ degree, $V = 3020.80(9)$ Å^3, $Z = 4$, $\rho = 1.764$ g cm^{-3}. The coordination environment of La^{3+} ion is formed by 6 nitrate ions with 12 oxygen atoms without any water molecule or hydrogen-bonding network (Fig. 13A). Each anion is surrounded by three 1,3-dimethylimidazolium cations. All hexanitratolanthanate ILs were found to be stable against moisture and decomposed at a temperature above 300°C. Compounds with $n = 8$, 12, 14, 16, 18 which were found to be ILCs (DSC, POM) forming a smectic a liquid-crystalline phase.

Nitrogen-/oxygen-rich anions, for example, nitrile-/nitroso-/nitro-containing molecules can be used for creating not only energetic ILs. Some

polynitrile anions such as tricyanomethanide (tcm) and dicyanamide (dca) have been integrated into a number of ILs used already in organic chemistry and solar cells technology. Their high charge delocalization and low point symmetry make them ideal for the design of new ILs. The dicyanonitrosomethanide (dcnm) anion (Fig. 14) had been revealed to freely coordinate to Ln(III) ions via η^2-nitroso groups resulting 12-coordinate homoleptic compounds with $[Ln(dcnm)_6]^{3-}$ anions (Ln = La–Gd) [28,29]. The compound $(N_{2222})_3[Ln(dcnm)_6]$ (N_{2222} = tetraethylammonium) with $T_m = 126°C$ suggested that lower melting points of other rare earth-based ILs can be reached by variation with larger cation. This hypothesis was confirmed in [30,31], where was described the synthesis of the new family of Ln-containing ILs with dicyanonitrosomethanide ligand, $(N_{4444})_3[Ln(dcnm)_6]$ (Ln = La–Nd), which displayed polymorph-dependent melting points. This phenomenon was established by a temperature-dependent in situ synchrotron-based X-ray powder diffraction. An extension of the series of $[Ln(dcnm)_6]^{3-}$ ion containing ILs with variety of cations could be realized via double replacement reaction between $LnCl_3{\cdot}xH_2O$, the silver dicyanonitrosomethanide and a desired IL-halide salt (CatX) in an alcoholic solution (Eq. 1):

$$6Ag(dcnm) + 3(Cat)X + LnCl_3 \cdot xH_2O \rightarrow (Cat)_3\left[Ln(dcnm)_6\right] + 3AgX\downarrow + 3AgCl\downarrow + xH_2O \quad (1)$$

This produces an insoluble AgHal, which is separated from the reaction media by simple filtration, leaving the main product in solution. Rapid crystallization of the product was observed by cooling in combination with reducing the solution volume under vacuum.

The above-mentioned procedure yielded a number of ILs with imidazolium (C_1C_2im = 1-ethyl-3-methylimidazolium, $C_2C_1C_1im$ = 1,2-dimethyl-3-ethylimidzolium), pyridinium (C_1C_4Py = N-methyl-*N*-propylpyrrolidinium), and ammonium (N_{1114} = trimethylbutylammonium, N_{1112OH} = triethylhydroxyethylammonium) cations (Table 1).

Efforts to produce complexes containing lanthanides heavier than gadolinium proved to be difficult, probably due to the smaller radii of these Ln(III) hindering building-up of 12-coordinated units. This obstruction was met in earlier attempts to make $[Ln(dcnm)_6]^{3-}$ compounds with the smaller tetramethylammonium and $[NEt_4]^+$ cations. Thermal stability investigation of complexes showed that they all can be attributed to the class of ILs ($T_m < 100°C$). The thermal properties of complexes containing $[Ln(dcnm)_6]^{3-}$ anion are presented in Table 1. Complex $(C_1C_4py)_3[Ce(dcnm)_6]$ has $T_m = 38.1°C$, the lowest value within the compounds comprising the $[Ln(dcnm)_6]^{3-}$ anion. The melt did not recrystallize upon cooling and forms a supercooled glass at −28.7°C.

Using ammonium-based cations produces complexes with higher melting points than those having the pyridinium or imidazolium cations. While $(N_{1114})_3[Ln(dcnm)_6]$ (Ln = Sm, Gd) are ILs, the analogs comprising lighter Ln(III) melt above 100°C. The compound $(N_{1112OH})_3[Ce(dcnm)_6]$ was not

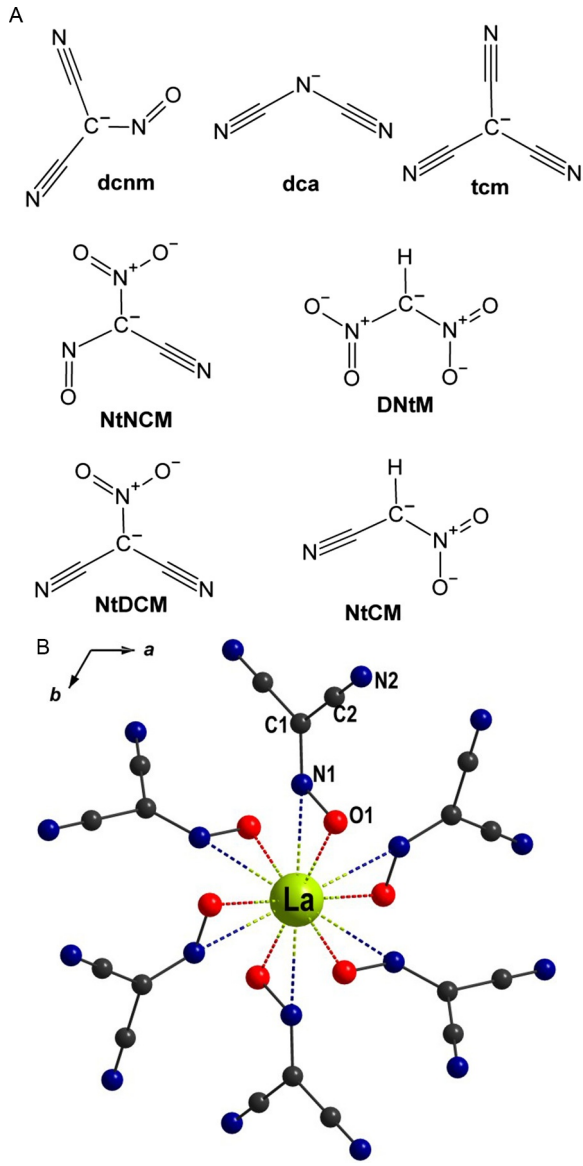

FIG. 14 (A) Nitroso-/nitrile-/nitro-containing units that have been used in the synthesis of new ILs; NtCM = cyanonitromethanide, DNtM = dinitromethanide, NtNCM = cyanonitronitrosomethanide, NtDCM = dicyanonitromethanide and (B) the $[La(dcnm)_6]^{3-}$ ion from the crystal structure of $(C_1C_2im)_3[La(dcnm)_6]$ with dicyanonitrosomethanide (dcnm) anions [31].

detected to melt below 160°C due to the presence of stronger intermolecular hydrogen bonds, found in the crystal structure (Fig. 14B).

Ligands which can form stable rare earth complexes with a variety of interesting properties are important tools in coordination chemistry of

TABLE 1 Thermal Properties of Compounds Comprising $[Ln(Dcnm)_6]^{3-}$ Anion[a]

Compound	Cycle	Heating Transition	T (°C)	ΔH (kJ mol^{-1})	Cooling Transition	T (°C)	ΔH (kJ mol^{-1})
$(C_2mim)_3[La(dcnm)_6]$	1	S → L	57.7	72.92	L → S (P)	6.4	−20.56
	2	L → S (P)	−7.4	−38.08			
	2	S → L	59.2	71.15			
$(C_2mim)_3[Ce(dcnm)_6]$	1	S → L	43.4	60.79	L → G	−30.6	
	2	G → L	−31.9				
$(C_2mim)_3[Pr(dcnm)_6]$	1	S → L	64.7	83.01	L → G	−43.4	
	2	G → L	−47.4				
	2	L → S (P)	−6.0	−34.16			
	2	L → S (P)	15.6	−25.23			
	2	S → L	62.4	83.24			
$(C_2mim)_3[Nd(dcnm)_6]$	1	S → L	60.9	74.89	L → S	23.1	−38.95
	2	–	13.9	0.82			
	2	S → L	40.1	37.82	L → S	20.3	−39.24
$(C_2C_1mim)_3[Pr(dcnm)_6]$	1	S → L	62.9	60.79	L → G	−32.0	
	2	G → L	−33.5				
	2	L → S	5.1	−41.81			
	2	S → L	61.4	63.83			
$(C_4C_1py)_3[Ce(dcnm)_6]$	1	S → L	38.1	44.16	L → G	−28.7	
	2	G → L	−29.8				
$(N_{1114})_3[La(dcnm)_6]$	2	S → L	109.1	68.67	L → S	105.2	−68.2

$(N_{1114})_3[Ce(dcnm)_6]$	2	S→L	106.3	55.63	L→S	93.8	−46.72
$(N_{1114})_3[Pr(dcnm)_6]$	2	S→L	104.8	69.72	L→S	96.9	−65.54
$(N_{1114})_3[Nd(dcnm)_6]$	2	S→L	102.5	74.28	L→S	90.6	−71.71
$(N_{1114})_3[Sm(dcnm)_6]$	2	S→L	83.7	47.31	L→S	75.4	−50.33
$(N_{1114})_3[Gd(dcnm)_6]$	2	S→L	74.8	45.02	L→S	55.8	−44.68
$(N_{1114OH})_3[Ce(dcnm)_6]$	1	No transition observed					

[a](P) denotes partial transition; T, the onset temperature of transition; L→S, liquid-to-solid transition; S→L, solid-to-liquid transition; L→G, liquid-to-glass transition; G→L, glass-to-liquid transition; △H, enthalpy of transition.

lanthanides and the family of 1,3-diketone-based ligands is one of them [32,33]. Nevertheless, only limited attempts have been made to incorporate 1,3-diketones as part of ILs for the reason that some 1,3-diketonates are unstable in aqueous solution. The europium β-diketonate compound [34], $[C_1C_6im][Eu(tta)_4]$ (C_1C_6im = 1-hexyl-3-methylimidazolium; $Eu(tta)_4$ = tetrakis(2-thenoyltrifluoroacetonato)europate(III)), with deprotonated 2-thenoyltrifluoroacetonate (tta) ligand is stable against hydrolysis in ethanol/water mixtures and in the IL $[C_1C_6im][Tf_2N]$. This compound demonstrated outstanding features such as a high quantum yield. By combination of one or two mesogenic components (cholesterol or cyanobiphenyl) with an imidazolium cation, ILCs were produced with the $[Eu(tta)_4]^-$ anion [35]. Other work aiming at luminescent soft materials were devoted to investigations on samarium(III) β-diketonate complexes: $[C_1C_6im][Sm(tta)_4]$, $[C_1C_6im][Sm(hfa)_4]$, and $[C_1C_6im][Sm(nta)_4]$ (where nta ≡ 2-naphtoyltrifluoroacetonate, tta ≡ 2-thenoyltrifluoroacetonate, and hfa ≡ hexafluoroacetylacetonate), in the IL $[C_1C_6im][Tf_2N]$ [36]. Extraction of neodymium as $[C_1C_4im][Nd(hfac)_4]$ in IL phase from aqueous solution was reported [37]. Unfortunately, the thermal behavior of $[C_1C_4im][Nd(hfac)_4]$ was not investigated, thus offering no proof of their IL origin.

In 2009, Tang and Mudring prepared two new terbium complexes with hexafluoroacetylacetone (Hhfacac) as the ligand [38]. Mixing of H[hfacac] ligand with $[C_1C_4im]Cl$ or $[C_1C_4pyrr]Br$ ($[C_1C_4pyrr]$ = N-methyl-*N*-propylpyrrolidinium) and $TbCl_3$ in basic $EtOH/H_2O$ solutions produced the new complexes with general formula $[C_4mpyrr][Tb(hfacac)_4]$ and $[C_1C_4im][Tb(hfacac)_4]$. $[C_1C_4im][Tb(hfacac)_4]$ crystallizes in *Pbca* with eight formula units per unit cell with two terbium(III) ions, two $[C_4C_1im]^+$ cations, and eight [hfacac] anions in the asymmetric unit (Fig. 15).

Each terbium(III) ion is coordinated by eight oxygen atoms provided from four (hexafluoroacetyl)acetonate anions as chelating ligands. The coordination environment around terbium(III) can be designated as a square antiprism. The Tb–O distances range 2.34(2)/2.42(2)Å which is analogous to those described for other Tb(III) acetylacetonates. A huge number of C–H···F hydrogen bonds can be detected within the $[Tb(hfacac)_4]^-$ ion as well as between the $[C_1C_4im]^+$ cations and $[Tb(hfacac)_4]^-$ anions. They play a very important role in assembling the structure: through the linkage of intra- and intermolecular C–H···F interactions, they form a 2D layer in the *bc* plane (Fig. 15B, top) which further build a 3D construction (Fig. 15B, bottom). The structure of compound $[C_1C_4pyr][Tb(hfacac)_4]$ is very similar to that with the $[C_1C_4im]^+$ cation but the asymmetric unit only has one cation $[C_1C_4pyr]^+$ and one $[Tb(hfacac)_4]^-$ anion. Numerous intra- and intermolecular hydrogen bonding were also observed in this compound. From the DSC traces of these two compounds, it is clear that they have fully different thermal performance. Complex $[C_1C_4im][Tb(hfacac)_4]$ starts melting at 116.2°C (onset) and crystallizes at 102.3°C upon cooling while thermobehavior of $[C_1C_4pyr][Tb(hfacac)_4]$ is complicated and can be described as for an organic plastic

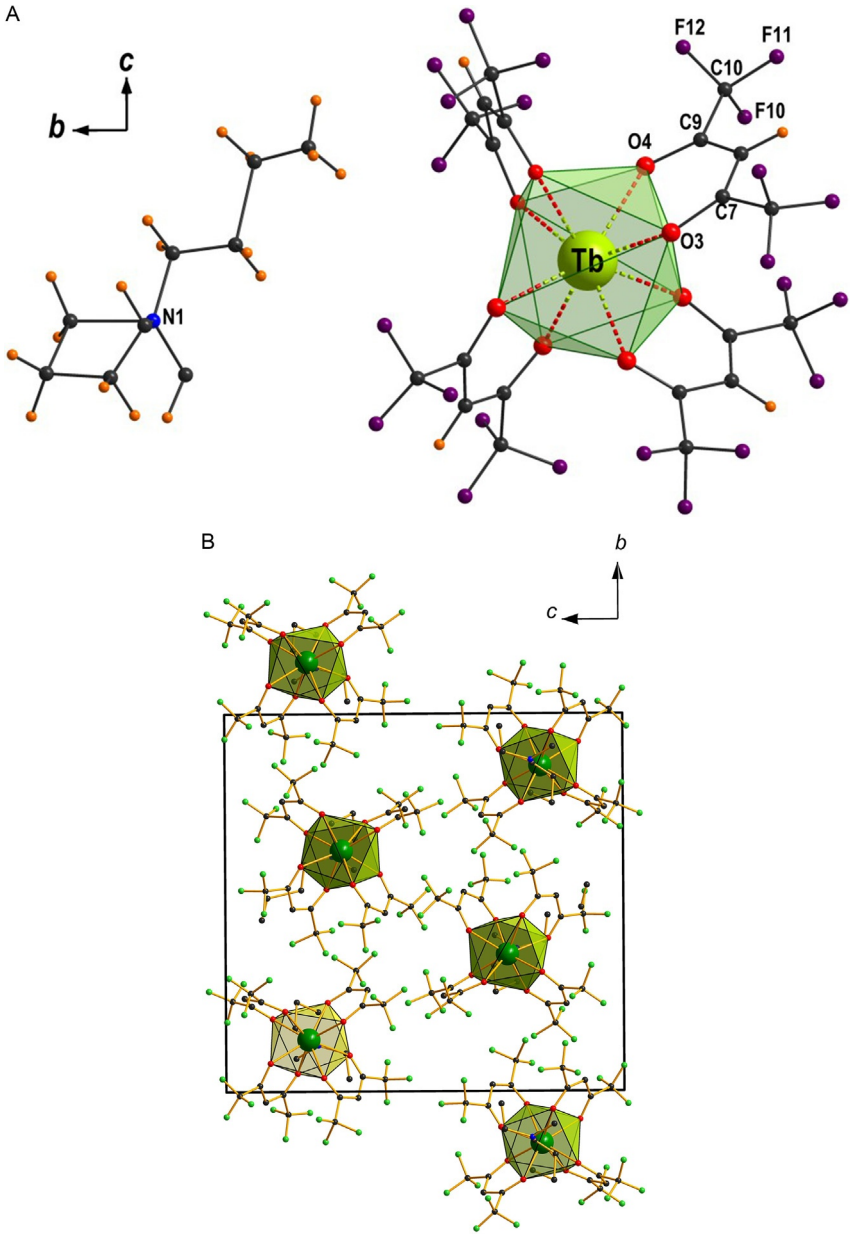

FIG. 15 (A) Molecular structure of the asymmetric unit in $[C_1C_4im][Tb(hfacac)_4]$. (B) 2D layer of $[C_1C_4im][Tb(hfacac)_4]$ in the *bc* plane (*up*) and its 3D supramolecular structure along the *b*-axis (*bottom*). TbO_8 antiprisms are shaded in *green*.

crystal. There are overall four distinct endothermic solid → solid-phase transitions (38.0, 57.7, 85.8, and 98.4°C) between 20 and 150°C with final melting at 111.4°C. Both complexes display very strong emission in the visible region which are typical for the Tb(III) ion.

An easy access to a similar set of compounds was achieved by reacting water/ethanol solutions of 1-ethyl-3-methylimidazolium chloride (C_1C_2im), or 1-butyl-4-methylimidazolium chloride (C_1C_4im), the respective rare earth trichloride and diethyl-2,2,2-trichloroacetylphosphoramidate (DETCAP). The resulting compounds have a general composition of [cat][Ln(DETCAP)4] (cat = 1-ethyl-3-methylimidazolium, Ln = Eu (1) and Tb (2); R = 1-butyl-3-methylimidazolium (C_4mim), Ln = Eu (3), and Tb (4)), with rare earth ions connected by four chelating pseudobetadiketonate ligands $(DETCAP)^-$, resulting in the corresponding complex anions. Fluorescence measurements (at RT and −196°C) demonstrate strong red Eu(III) or green Tb(III) emissions and long decay times for all samples with quantum yields about 30–49% [39].

Ever among all of the above-mentioned functional groups, the carboxyl functional group seems to be the most powerful and useful for the generation of ILs based on complex rare earth ion. In 2006, the interesting practical application of protonated betaine bis(trifluoromethylsulfonyl)amide ILs as a dissolving agent for large quantities of metal oxides with selective metal-solubilizing power was shown [40]. Among metal oxides used was Dy_2O_3, which after solubilization in [Hbet][Tf_2N] (Hbet = betainium) and slow evaporation at RT from an aqueous solution gave single crystals of $[Dy_2(bet)_8(H_2O)_4][Tf_2N]_6$. The structure contains dimeric $[Dy_2(bet)_8(H_2O)_4]^{6+}$ cations and bis(trifluoromethylsulfonyl)amide anions. In the structural motif which is common for rare earth carboxylates, each Dy(III) ion is connected with oxygen atoms from six monodentately coordinating betaine zwitterions; four of them are μ_2-bridging so that Dy(III) ions occur as dimers (Fig. 16).

Two H_2O molecules complete the Dy(III) coordination environment (CN = 8) to a polyhedron which can be defined as a slightly distorted square antiprism. The Tf_2N^- anions participate in the formation of weak hydrogen bonds with one of these water molecules from both sides of the dimer. A series of similar rare earth containing ILs with bis(trifluoromethylsulfonyl)amide anion and variety of different cations such as betainium, P-carboxymethyl-tributylphosphonium, N-carboxymethyl (or ethyl)-methylpyrrolidinium, N-carboxymethyl-methylmorpholinium, N-carboxymethyl-methylpiperidinium, carnitine, N-carboxymethyl-methylpyridinium, N-dymethyl-*N*-butyl-betainium, and N-dymethyl-*N*-hexyl-betainium were patented as "Novel ionic liquids" in Ref. [41].

This group of authors continued further their research on new carboxyl-functionalized task-specific ILs for solubilizing metal oxides. In Refs. [42,43], a series of investigations on yttrium(III) and europium(III) compounds with general formula $[R_2(RCOO)_6(H_2O)_4]^{6+}$ and Tf_2N^- as the anion were reported (where RCOO ≡ betainium and N-carboxymethylmorpholinium).

A

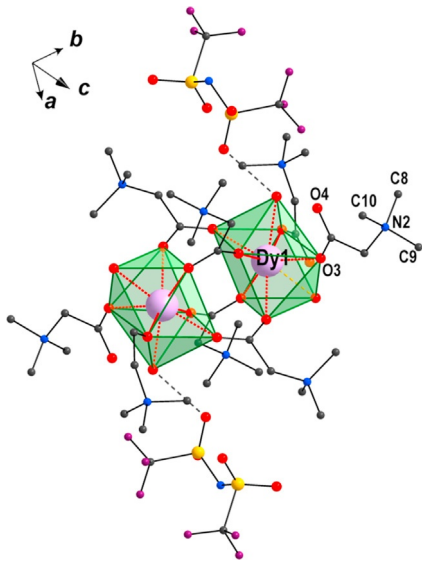

B

Rare earth complex	Melting point (°C)
$[Y_2(bet)_8(H_2O)_2][Tf_2N]_6$	109
$[La_2(bet)_8(H_2O)_2][Tf_2N]_6$	78
$[Pr_2(bet)_8(H_2O)_2][Tf_2N]_6$	86
$[Nd_2(bet)_8(H_2O)_4][Tf_2N]_6$	90
$[Sm_2(bet)_8(H_2O)_2][Tf_2N]_6$	88
$[Eu_2(bet)_8(H_2O)_2][Tf_2N]_6$	95
$[Gd_2(bet)_8(H_2O)_2][Tf_2N]_6$	94
$[Tb_2(bet)_8(H_2O)_2][Tf_2N]_6$	88
$[Dy_2(bet)_8(H_2O)_2][Tf_2N]_6$	88
$[Ho_2(bet)_8(H_2O)_2][Tf_2N]_6$	80
$[Er_2(bet)_8(H_2O)_2][Tf_2N]_6$	94
$[Tm_2(bet)_8(H_2O)_2][Tf_2N]_6$	97
$[Yb_2(bet)_8(H_2O)_2][Tf_2N]_6$	89
$[Lu_2(bet)_8(H_2O)_2][Tf_2N]_6$	88

FIG. 16 (A) Cationic dimer $[Dy_2(bet)_8(H_2O)_4]^{6+}$ in the structure of $[Dy_2(bet)_8(H_2O)_4][Tf_2N]_6$ with hydrogen bonding from coordinated water molecules to two bis(trifluoromethylsulfonyl) imide anions and (B) melting points for the rare earth complexes $[R_2(bet)_8(H_2O)_4][Tf_2N]_6$ [41].

Recently, Powell and coworkers presented the synthesis and structural investigation of three Dy-containing ILs with the N-carboxymethyl(or ethyl) imidazolium moiety [44]. These compounds were identified as efficient catalysts in the three-component synthesis of ethyl 2-methyl-4-(2-*oxo*-2,3-dihydro-1H-3-indolyl)-5-phenyl-1H-3-pyrrolecarboxylate. In addition, at low temperatures, they possess the properties of single-ion magnets. As single crystal needles of $\{[Dy(cmim)_3(H_2O)_2](Tf_2N)_3\}_n$ and $\{[Dy(cmim)_4(H_2O)_2](PF_6)_3{\cdot}2H_2O\}_n$ (where cmim ≡ N-carboxymethylimidazolium) were extremely thin, synchrotron radiation was necessary to clarify their crystal structures.

The polymeric chains built up by the complex cations are linked by two carboxylate groups through neighboring pairs of Dy(III) ions. Two aqua ligands and a chelating carboxylate group from a cmmim ligand complete the coordination environment of Dy. The coordination geometry can be best described as a bicapped trigonal prism. Within the crystal structure of $\{[Dy(cmim)_3(H_2O)_2](Tf_2N)_3\}_n$, the 1D chains are well separated by the Tf_2N^- ions, as is clear when viewed along the *c*-axis. Weak interactions through hydrogen bonding between C–H bonds of ligands to either O or F atoms of the anions have been identified. The compound $\{[Dy(cmim)_4(H_2O)_2](PF_6)_3{\cdot}2H_2O\}_n$ also crystallizes in $P2_1/c$ with $Z = 4$ with the polymeric chains running parallel to the *c*-axis. Nevertheless, the connections are different and the polymeric chain has a *zig–zag* structure (Fig. 17B). The

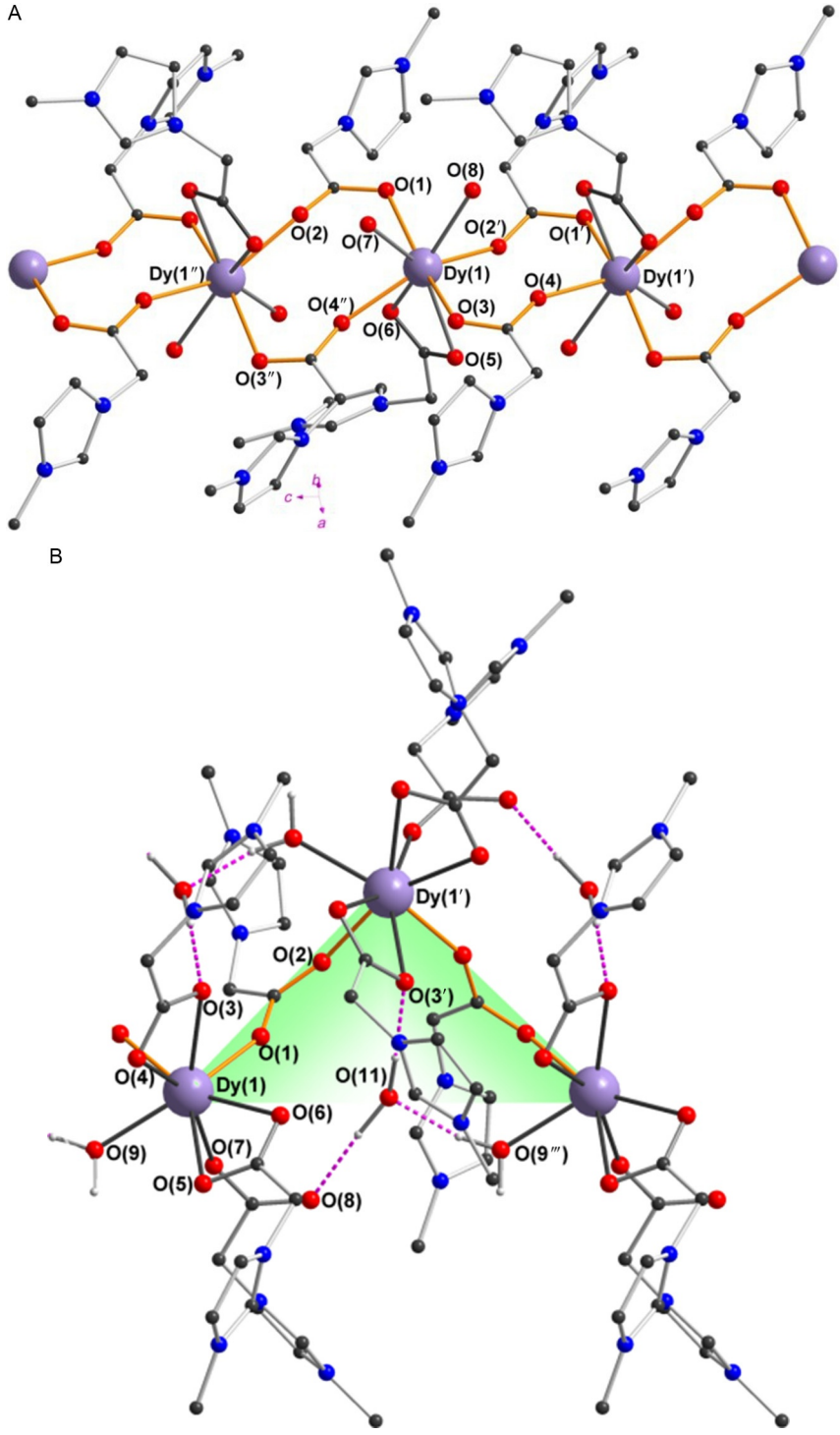

FIG. 17 (A) Assembly of the cationic polymer in $\{[Dy(cmim)_3(H_2O)_2](Tf_2N)_3\}_n$ (carboxylate bridges in *orange*) and (B) a fragment of the cationic polymer in $\{[Dy(cmim)_4(H_2O)_2](PF_6)_3{\cdot}2H_2O\}_n$ (carboxylate bridges in *orange*, hydrogen bonds as *pink dotted lines*).

coordination polyhedron around Dy is built up by two chelating carboxylate ligands, a monodentate carboxylate group and a coordinated water molecule. A lattice water is located within a triangle of the zig–zag chain network with all three Dy^{3+} cations and therefore gives rigidity to the structure (Fig. 17B). The differences between the two types of structural motifs in these complexes were confirmed by IR spectroscopy.

At the same time, the carboxylate group can be used simultaneously with other polydentate ligands which also can bind rare earth ions. Recently, novel luminescent soft materials yielded from the reaction of Eu^{3+}-containing carboxyl functionalized ILs with functionalized terpyridine–imidazolium complexes were reported (Fig. 18).

These ligands are constructed from an imidazolium ring modified on one side with a terpyridine derivative and, on the opposite side, various paraffin chains [45]. These samples are either paste-like materials or viscous liquids, depending on the nature of anions of the carboxylate incorporated ILs (Fig. 18). Due to the energy transfer from the task-specific terpyridine–imidazolium ligands to the Eu^{3+} ions, all these materials display intense, bright red emission under irradiation with UV light.

In conclusion, despite the fact that coordination chemistry can essentially contribute to the creating of new nontrivial rare earth containing materials—

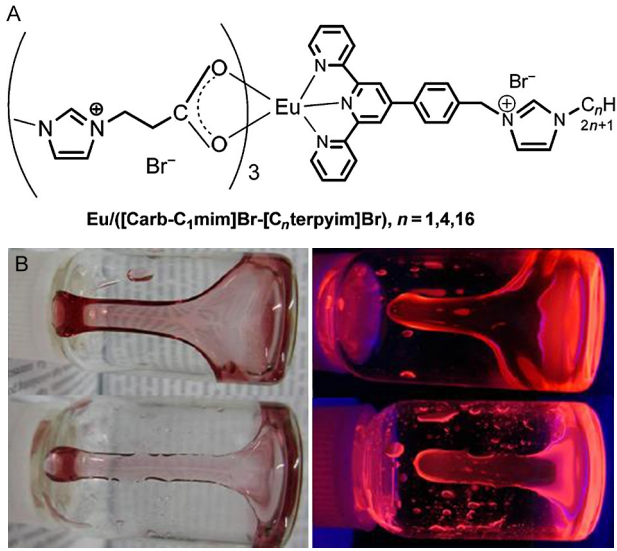

FIG. 18 (A) Probable structure of europium(III) compounds incorporated in the soft materials; (B) images of the synthesized complexes: {Eu-[Carb-C_1mim]Tf_2N-[C_4terpyim]Br} (*up*) and {Eu-[Carb-C_1mim]Tf_2N-[C_4terpyim]Tf_2N} (*bottom*) at day (*left*) and UV (*right*) lights. *Adapted with permission from D. Wang, H. Wang, H. Li, Novel luminescent soft materials of terpyridine-containing ionic liquids and europium(III), ACS Appl. Mater. Interfaces 5 (2013) 6268.*

rare earth-based ILs—this field of coordination and materials chemistry still can be considered as poorly explored. New systems and amazing results appear promptly and possess boundless innovation potential.

ACKNOWLEDGMENTS

This work is supported in part by the Critical Materials Institute, an Energy Innovation Hub funded by the US Department of Energy, Office of Energy Efficiency and Renewable Energy, Advanced Manufacturing Office and the National Science Foundation.

REFERENCES

[1] S. Cotton, Rare Earth and Actinide Chemistry, John Wiley & Sons, Chichester, 2013. p. 272.
[2] P. Bonhôte, A.P. Dias, N. Papageorgiou, K. Kalyanasundaram, M. Grätzel, Hydrophobic, highly conductive ambient-temperature molten salts, Inorg. Chem. 35 (1996) 1168.
[3] M. Earle, K.R. Seddon, Ionic liquids: green solvents for the future, Pure Appl. Chem. 72 (2000) 1391.
[4] P. Wasserscheid, W. Keim, Ionic liquids—new "solutions" for transition metal catalysis, Angew. Chem. Int. Ed. 39 (2000) 3772.
[5] J.D. Holbrey, W.M. Reichert, R.D. Rogers, Crystal structures of imidazolium bis(trifluoromethanesulfonyl)imide 'ionic liquid' salts: the first organic salt with a cis-TFSI anion conformation, Dalton Trans. 15 (2004) 2267.
[6] C.M. Forsyth, D.R. MacFarlane, J.J. Golding, J. Huang, J. Sun, M. Forsyth, Structural characterization of novel ionic materials incorporating the bis(trifluoromethanesulfonyl)amide anion, Chem. Mater. 14 (2002) 2103.
[7] V. Montanari, D.D. Desmarteau, W.T. Pennington, Synthesis and structure of novel perfluorinated iodinanes, J. Mol. Struct. 550/551 (2000) 337.
[8] M.G. Davidson, P.R. Raithby, A.L. Johnson, P.D. Bolton, Structural diversity in Lewis-base complexes of lithium triflamide, Eur. J. Inorg. Chem. 18 (2003) 3445.
[9] D.D. DesMarteau, W.T. Pennington, V. Montanari, B.H. Thomas, Iodonium zwitterions, J. Fluorine Chem. 122 (2003) 122.
[10] A.-V. Mudring, A. Babai, S. Arenz, R. Giernoth, The "noncoordinating" anion Tf_2N^- coordinates to Yb^{2+}: a structurally characterized Tf_2N^- complex from the ionic liquid [mppyr][Tf_2N], Angew. Chem. Int. Ed. 44 (2005) 5485.
[11] A. Babai, S. Pitula, A.-V. Mudring, Structural and electrochemical properties of Yb^{III} in various ionic liquids, Eur. J. Inorg. Chem. 31 (2010) 4933.
[12] A. Babai, G. Kopiec, A. Lackmann, B. Mallick, S. Pitula, S. Tang, A.-V. Mudring, Eu^{3+} as a dual probe for the determination of IL anion donor power: a combined luminescence spectroscopic and electrochemical approach, J. Mol. Liq. 192 (2014) 191.
[13] A. Babai, A.-V. Mudring, The first homoleptic bis(trifluoromethanesulfonyl)amide complex compounds of trivalent f-elements, Dalton Trans. 15 (2006) 1828.
[14] A. Babai, A.-V. Mudring, Anhydrous praseodymium salts in the ionic liquid [bmpyr][Tf2N]: structural and optical properties of [bmpyr]4[PrI6][Tf2N] and [bmyr]2[Pr(Tf2N)5], Chem. Mater. 17 (2005) 6230.
[15] A. Babai, A.-V. Mudring, The first homoleptic bis(trifluoromethanesulfonyl)amide complex of yttrium: [bmim][$Y(Tf_2N)(4)$], Z. Anorg. Allg. Chem. 634 (2008) 938.

[16] S. Tang, A. Babai, A.-V. Mudring, Europium-based ionic liquids as luminescent soft materials, Angew. Chem. Int. Ed. 47 (2008) 7631.
[17] S. Tang, J. Cybinska, A.-V. Mudring, Luminescent soft material: two new europium-based ionic liquids, Helv. Chim. Acta 92 (2009) 2375.
[18] P. Nockemann, B. Thijs, N. Postelmans, K. Van Hecke, L. Van Meervelt, K. Binnemans, Anionic rare-earth thiocyanate complexes as building blocks for low-melting metal-containing ionic liquids, J. Am. Chem. Soc. 128 (2006) 13658.
[19] M. Okuno, H.-O. Hamaguchi, S. Hayashi, Magnetic manipulation of materials in a magnetic ionic liquid, Appl. Phys. Lett. 89 (2006) 132506.
[20] B. Mallick, B. Balke, C. Felser, A.-V. Mudring, Dysprosium room-temperature ionic liquids with strong luminescence and response to magnetic fields, Angew. Chem. Int. Ed. 47 (2008) 7635.
[21] K. Matsumoto, T. Tsuda, T. Nohira, R. Hagiwara, Y. Ito, O. Tamada, Tris(1-ethyl-3-methylimidazolium) hexachlorolanthanate, Acta Cryst. C58 (2002) m186.
[22] R.E. Del Sesto, T.M. McCleskey, A.K. Burrell, G.A. Baker, J.D. Thompson, B.L. Scott, J. -Wilkes, P. Williams, Structure and magnetic behavior of transition metal based ionic liquids, Chem. Commun. 4 (2008) 447.
[23] A. Getsis, B. Balke, C. Felser, A.-V. Mudring, Dysprosium-based ionic liquid crystals: thermal, structural, photo- and magnetophysical properties, Cryst. Growth Des. 9 (2009) 4429.
[24] A. Getsis, A.-V. Mudring, Rare earth containing ionic liquid crystals: $EuBr_2$, $SmBr_3$, $TbBr_3$ and $DyBr_3$ in C_{12}mimBr, Z. Anorg. Allg. Chem. 636 (2010) 1726.
[25] A. Getsis, S. Tang, A.-V. Mudring, A luminescent ionic liquid crystal: [C(12)mim](4)[$EuBr_6$]Br, Eur. J. Inorg. Chem. 14 (2010) 2172.
[26] G.-H. Tao, Y. Huang, J.A. Boatz, J.M. Shreeve, Energetic ionic liquids based on rare earth nitrate complex anions, Chem. Eur. J. 14 (2008) 11167.
[27] S.-P. Ji, M. Tang, L. He, G.-H. Tao, Water-free rare-earth-metal ionic liquids/ionic liquid crystals based on hexanitratolanthanate(III) anion, Chem. Eur. J. 19 (2013) 4452.
[28] A.S.R. Chesman, D.R. Turner, E.I. Izgorodina, S.R. Batten, G.B. Deacon, Homoleptic 12-coordinate lanthanoids with eta(2)-nitroso ligands, Dalton Trans. 14 (2007) 1371.
[29] A.S.R. Chesman, D.R. Turner, G.B. Deacon, S.R. Batten, New approaches to 12-coordination: structural consequences of steric stress, lanthanoid contraction and hydrogen bonding, Eur. J. Inorg. Chem. 18 (2010) 2798.
[30] A.S.R. Chesman, M. Yang, B. Mallick, T.M. Ross, I.A. Gass, G.B. Deacon, S.R. Batten, A.-V. Mudring, Melting point suppression in new lanthanoid(III) ionic liquids by trapping of kinetic polymorphs: an in situ synchrotron powder diffraction study, Chem. Commun. 48 (2012) 124.
[31] A.S.R. Chesman, M. Yang, N.D. Spiccia, G.B. Deacon, S.R. Batten, A.-V. Mudring, Lanthanoid-based ionic liquids incorporating the dicyanonitrosomethanide anion, Chem. Eur. J. 18 (2012) 9580.
[32] K. Binnemans, Rare-earth beta-diketonates, in: K.A. Gschneidner, J.C.G. Bünzli, V.K. Pecharsky (Eds.), Handbook on the Physics and Chemistry of Rare Earths, vol. 35 (225), Elsevier, The Netherlands, 2005, pp. 107–272.
[33] P. Zhang, Y.-N. Guo, J. Tang, Recent advances in dysprosium-based single molecule magnets: structural overview and synthetic strategies, Coord. Chem. Rev. 257 (2013) 1728.
[34] P. Nockemann, E. Beurer, K. Driesen, R. Van Deun, K. Van Hecke, L. Van Meervelt, K. Binnemans, Photostability of a highly luminescent europium β-diketonate complex in imidazolium ionic liquids, Chem. Commun. 34 (2005) 4354.

[35] K. Goossens, P. Nockemann, K. Driesen, B. Goderis, C. Görller-Walrand, K. Van Hecke, L. Van Meervelt, E. Pouzet, K. Binnemans, T. Cardinaels, Imidazolium ionic liquid crystals with pendant mesogenic groups, Chem. Mater. 20 (2008) 157.

[36] K. Lunstroot, P. Nockemann, K. Van Hecke, L. Van Meervelt, C. Görller-Walrand, K. Binnemans, K. Driesen, Visible and near-infrared emission by samarium(III)-containing ionic liquid mixtures, Inorg. Chem. 48 (2009) 3018.

[37] H. Mehdi, K. Binnemans, K. Van Hecke, L. Van Meervelt, P. Nockemann, Hydrophobic ionic liquids with strongly coordinating anions, Chem. Commun. 46 (2010) 234.

[38] S. Tang, A.-V. Mudring, Terbium β-diketonate based highly luminescent soft materials, Eur. J. Inorg. Chem. 19 (2009) 2769.

[39] S. Tang, C. Lorbeer, X. Wang, P. Ghosh, A.-V. Mudring, Highly luminescent salts containing well-shielded lanthanide-centered complex anions and bulky imidazolium countercations, Inorg. Chem. 53 (2014) 9027.

[40] P. Nockemann, B. Thijs, S. Pittois, J. Thoen, C. Glorieux, K. Van Hecke, L. Van Meervelt, B. Kirchner, K. Binnemans, Task-specific ionic liquid for solubilizing metal oxides, J. Phys. Chem. B 110 (2006) 20978.

[41] K. Binnemans, C.-A. Goerller-Walrand, P. Nockemann, B. Thijs, Novel ionic liquids, WO2007147222A3, 2007.

[42] P. Nockemann, B. Thijs, T.N. Parac-Vogt, K. Van Hecke, L. Van Meervelt, B. Tinant, I. Hartenbach, T. Schleid, V.T. Ngan, M.T. Nguyen, K. Binnemans, Carboxyl-functionalized task-specific ionic liquids for solubilizing metal oxides, Inorg. Chem. 47 (2008) 9987.

[43] P. Nockemann, B. Thijs, K. Lunstroot, T.N. Parac-Vogt, C. Görller-Walrand, K. Binnemans, K. Van Hecke, L. Van Meervelt, S. Nikitenko, J. Daniels, C. Hennig, R. Van Deun, Speciation of rare-earth metal complexes in ionic liquids: a multiple-technique approach, Chem. Eur. J. 15 (2009) 1449.

[44] D. Prodius, F. Macaev, Y. Lan, G. Novitchi, S. Pogrebnoi, E. Stingaci, V. Mereacre, C.E. Anson, A.K. Powell, Evidence of slow relaxation of magnetization in dysprosium-based ionic liquids, Chem. Commun. 49 (2013) 9215.

[45] D. Wang, H. Wang, H. Li, Novel luminescent soft materials of terpyridine-containing ionic liquids and europium(III), ACS Appl. Mater. Interfaces 5 (2013) 6268.

Index

Note: Page numbers followed by "*f*" indicate figures, "*t*" indicate tables, and "*s*" indicate schemes.

A

B

C

D

E

F

G

H

I

J

K

L

M

N

O

P

Q

R

S

T